Heteronuclear Polycationic Clusters from Group 15 and 16 Elements Synthesized in Chlorido Gallate Melts

Dissertation

zur

Erlangung des Doktorgrades (Dr. rer. nat.)

der

Mathematisch-Naturwissenschaftlichen Fakultät

der

Rheinischen Friedrich-Wilhelms-Universität Bonn

vorgelegt von

Dipl. Chem. Andreas Eich

aus

Wenden

Bonn, 2015

Angefertigt mit Genehmigung der Mathematisch-Naturwissenschaftlichen Fakultät der Rheinischen Friedrich-Wilhelms-Universität Bonn.

1. Gutachter: Prof. Dr. Johannes Beck
2. Gutachter: Prof. Dr. Werner Mader

Tag der Promotion: 26.6.2015

Erscheinungsjahr: 2015

This is the final cruise of the Starship *Enterprise* under my command. This ship and her history will shortly become the care of another crew. To them and their posterity will we commit our future. They will continue the voyages we have begun and journey to all the undiscovered countries, boldly going where no man – where no *one* – has gone before.

Captain James T. Kirk, Stardate 9529.1 (Star Trek VI - The Undiscovered Country)

Acknowledgements

The presented work had only been possible with the help of the following people.

At first I would like to appreciate the supervision of the work by Prof. Dr. Johannes Beck. He supported me in various scientific questions and problems. Specially I am thankful for the possibility to publish my results with him.

As a second important person I have to mention Dr. Gregor Schnakenburg. Several experimental results could only be fully understood or confirmed with the help of theoretical considerations. In this connection I have to thank Prof. Alexander C. Filippou for committing Dr. Schnakenburg's expertise and for the supply of measuring time on the single crystal diffractometers of the central X-ray facility.

I appreaciate the support of Prof. Dr. Thomas Bredow. Few results could only be confirmed with the help of specific theoretical considerations.

Furthermore I am thankful to:

- Dr. Jörg Daniels for the recording of single crystal diffraction datasets, especially for the measurements of phase transitions and modulated crystal structures,

- Dr. Jürgen Tirrèe for high number of high quality Raman measurements,

- Christian Landvogt and Charlotte Rödde for the recording single crystal diffraction datasets,

- Axel Pelka for the recording of single crystal diffraction datasets and the introduction to the Nonius Kappa CCD diffractometer,

- Dr. Wilfried Hoffbauer for the recording ^{77}Se and ^{125}Te solid state NMR spectra,

- Dr. Marianne Engeser, Christine Sondag and Nora Schocher for the recording and analysis of mass spectra,

- Dr. Ralf Weisbarth for the introduction to the Zeiss DSM 940 scanning electron microscope

- Norbert Wagner for magnetic measurements and the attempts for measuring the electrical conductivity of crystals,

- Dr. Yaser NejatyJahromy for EPR measurements,

- Prof. Dr. Hartmut Bärnighausen for the explanation of Drilling calculations,

- Dr. Jonas Sundberg (University of Southern Denmark, Odense) for the introduction to the Bruker Kappa ApexII diffractometer

and all students of the Inorganic Advanced Practical Course for their experimental contributions.

Abstract

Reactions of the pentele elements arsenic, antimony and bismuth with the chalcogen elements selenium and tellurium in chlorido gallate melts in the presence of oxidants arsenic trichloride, antimony trichloride and bismuth trichloride yielded various new polycationic clusters.

Experiments were carried out in moisture free and sealed vacuum glass ampoules. The preparative work was performed in an argon filled glove box, exclusively. All investigated compounds are highly moisture sensitive. Certain added salt-like compounds have a huge influence on the reactions. Several mono-charged cations like Li^+, Na^+, K^+, Rb^+, Cs^+, NH_4^+, In^+, Tl^+, Cu^+, Ag^+, Au^+, Hg_2^{2+}, PPh_4^+, used as the respective chlorides and the pentele oxides, were added as the reaction triggering adjuvants.

Depending on the compositions of these melts, monomeric clusters as well as cationic and neutral bridged chains could be obtained. The monomeric clusters form polyhedra like prisms, cubes and double cubes. The polymeric chains show motifs of helices, ladders and connected rings.

The new compounds mainly made of main group elements are characterized by their crystal structures, by chemical analyses via energy dispersive electron-beam X-ray fluorescence, Raman spectroscopy, solid state NMR, mass spectrometry, electron paramagnetic resonance, differential scanning calorimetry and powder diffraction. Additional supporting density functional calculations were carried out for various purposes. Some of the new compounds show crystallographic phenomena like phase transitions and systematic crystal twinning, which are demonstrated and discussed.

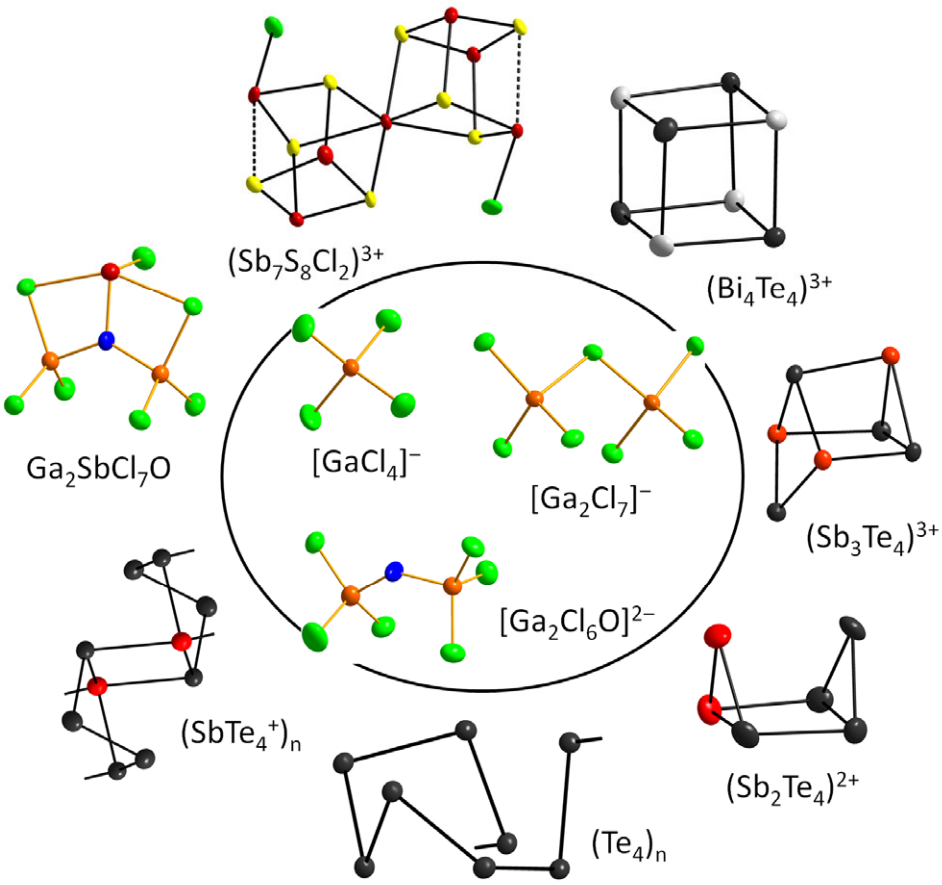

By oxidation and Lewis acid-base reactions in $GaCl_3$-based melts, polycationic clusters of various structures are formed emerging as cubes, double cubes, prisms and as chains. The weakly coordinating anions $[GaCl_4]^-$, $[Ga_2Cl_7]^-$ and $[Ga_2Cl_6O]^{2-}$ stabilize the highly reactive, naked clusters.

Table of Contents

1.0 Introduction

1.1 Definition and Historical Beginning of the Search for Polycationic Clusters 1
1.2 Mixed Polycationic Clusters from Group 15 and 16 and Their Syntheses 2
1.3 The Pecularities in Chemical Bonding between Heavy Electron-Rich Atoms and the Advantage of Formation of Heteronuclear Clusters 10
1.4 Motivation 10
1.5 General Syntheses in $M[GaCl_4]$ Melts 11

2.0 Experimentals and Results

2.1 The Double Cube Shaped Cluster $(Sb_7Te_8)^{5+}$ 14
2.1.1 Syntheses and EDX Analyses of Compounds Containing the $(Sb_7Te_8)^{5+}$ Cluster 14
2.1.2 The Reactions Leading to Compounds Containing the $(Sb_7Te_8)^{5+}$ Cluster 18
2.1.3 Crystal Structures of Compounds Containing the $(Sb_7Te_8)^{5+}$ Cluster 19
2.1.4 The $(Sb_7Te_8)^{5+}$ Polycationic Cluster 21
2.1.5 The Phase Transition of $Ag(Sb_7Te_8)[GaCl_4]_6$ 26
2.1.6 The Novel $Cu[GaCl_4]_2^-$ Anion in $Cu(Sb_7Te_8)[GaCl_4]_6$ 32
2.1.7 Mass Spektrometric Analysis of the $(Sb_7Te_8)^{5+}$ Cluster 36

2.2 The Double Cube Shaped Polycationic Clusters $(Sb_7Se_8)^{5+}$, $(Sb_7Se_8Cl_2)^{3+}$ and $(Sb_7S_8Cl_2)^{3+}$ 37
2.2.1 Syntheses and EDX Analyses 37
2.2.2 The Reactions Leading to Compounds Containing the $(Sb_7Se_8)^{5+}$, $(Sb_7Se_8Cl_2)^{3+}$ and $(Sb_7S_8Cl_2)^{3+}$ Cluster 39
2.2.3 Crystal Structures of $(Sb_7Se_8)[GaCl_4]_2[Ga_2Cl_7]_3$, $(Sb_7Se_8Cl_2)[GaCl_4]_3$ and $(Sb_7S_8Cl_2)[GaCl_4]_3$ 40
2.2.4 ^{77}Se Solid State NMR of $(Sb_7Se_8)[GaCl_4]_2[Ga_2Cl_7]_3$ and $(Sb_7Se_8Cl_2)[GaCl_4]_3$ 46

2.3 Raman Examination of Double Cube Shaped Clusters 51

2.4 Comparison of All Double Cube Shaped Clusters 54

2.5 The Cube Shaped Polycationic Clusters $(Sb_4Te_4)^{4+}$ and $(Sb_4Se_4)^{4+}$ 54
2.5.1 Syntheses and EDX Analyses of $(Sb_4Te_4)[GaCl_4]_4$ and $(Sb_4Se_4)[GaCl_4]_4$ 54
2.5.2 The Reactions Leading to $(Sb_4Ch_4)[GaCl_4]_4$ (Ch = Te, Se) 58
2.5.3 Crystal Structures of $(Sb_4Te_4)[GaCl_4]_4$ and $(Sb_4Se_4)[GaCl_4]_4$ 58
2.5.4 Raman Spectroscopy Study of $(Sb_4Te_4)[GaCl_4]_4$ and $(Sb_4Se_4)[GaCl_4]_4$ 59

2.6 The Mixed Heptanuclear Cluster $(Sb_3Te_4)^{3+}$ 61
2.6.1 Syntheses and EDX Analyses of $(Sb_3Te_4)[Ga_2Cl_7]_3$ 61
2.6.2 Crystal Structure of $(Sb_3Te_4)[Ga_2Cl_7]_3$ 62

2.7 The Prism Shaped Polycationic Clusters $(Pn_2Te_4)^{2+}$ (Pn = As, Te) 64

2.7.1 Syntheses and EDX Analyses of Compounds Containing the $(Pn_2Te_4)^{2+}$ Clusters 64
2.7.2 The Reactions Leading to $(Pn_2Te_4)^{2+}$ Containing Compounds 69
2.7.3 Crystal Structures of Compounds Containing the $(Pn_2Te_4)^{2+}$ Clusters 70
2.7.4 The Drilling Refinement of $M(Pn_2Te_4)[GaCl_4]_3$ 75
2.7.5 Examination of Compounds Containing the $(Pn_2Te_4)^{2+}$ Clusters by Raman Spectroscopy 80
2.7.6 Summary and Evaluation of the Analytical Results of the $(Pn_2Te_4)^{2+}$ Cluster 90

2.8 The Sequence of Cluster Degradation 92

2.9 Mixed Pentele-Chalcogen Cationic Chains 92
2.9.1 Syntheses and EDX Analyses of Compounds Containing Mixed Pentele-Chalcogen Cationic Chains 93
2.9.2 The Reactions Leading to Compounds Containing Mixed Pentele-Chalcogen Cationic Chains 97
2.9.3 Crystal Structures of Compounds Containing a $(Pn_2Ch_2^{1+/2+})_n$ Polymeric Cation 98
2.9.4 The Crystal Structure of $(Sb_3Te_4)[GaCl_4]$ 102
2.9.5 The Statistical Disorder in the Anionic Part in the Structures of $(Sb_2Te_4)I[AlI_4]$, $(Bi_2Te_2)Cl[GaCl_4]$, $(Bi_2Se_2)Cl[GaCl_4]$ and $(Sb_3Te_4)[GaCl_4]$ 103
2.9.6 The Crystal Structure of $(SbTe_4)[Ga_2Cl_7]$ 107

2.10 β-$(SbI_2)[AlI_4]$ - A New Polymorph of Diiodoantimony-Tetraiodidoaluminate 110
2.10.1 Syntheses and EDX Analyses of β-$(SbI_2)[AlI_4]$ 110
2.10.2 Crystal Structure of β-$(SbI_2)[AlI_4]$ 111
2.10.3 Comparison of the Structures of α- and β-$(SbI_2)[AlI_4]$ 112
2.10.4 Raman Spectroscopy Study of $(SbI_2)[AlI_4]$ 113

2.11 Structural and Raman Spectroscopic Characterization of $Cu[AlI_4]$ 115
2.11.1 Syntheses and EDX Analysis of $Cu[AlI_4]$ 115
2.11.2 Crystal Structure and Raman Spectrum of $Cu[AlI_4]$ 116

2.12 $Se_4Cu[GaCl_4]$, $Te_4Cu[GaCl_4]$ and $Se_7Cu_2[GaCl_4]_2$ - A New Class of Compounds Containing Neutral Chalcogen Chains 118
2.12.1 Syntheses and EDX Analyses of Compounds Containing Neutral Chalcogen Chains 119
2.12.2 The Reactions Leading to Compounds Containing Neutral Chalcogen Chains 121
2.12.3 Crystal Structures of $CuTe_4[GaCl_4]$, $CuSe_4[GaCl_4]$ and $Cu_2Se_7[GaCl_4]_2$ 123
2.12.4 Raman and EPR Examination of $CuSe_4[GaCl_4]$, $CuTe_4[GaCl_4]$ and $Cu_2Se_7[GaCl_4]_2$ 125

2.13 The Square Planar Cluster $(Te_4)^{2+}$ and the Novel Anion $[Ga_2Cl_6O]^{2-}$ in $Te_4[Ga_2Cl_6O]$ 127
2.13.1 Syntheses of $Te_4[Ga_2Cl_6O]$ 127
2.13.2 Crystal Structure of $Te_4[Ga_2Cl_6O]$ 128

2.14 $(Pn_2Te_4)^{2+}$ vs. $(Pn_2Te_4)^{4+}$ Clusters (Pn = As, Sb) and the Hexachlorido Oxo Digallate Anion $[Ga_2Cl_6O]^{2-}$ 129

2.14.1 Syntheses and EDX Analyses of Compounds Containing the $(Pn_2Te_4)^{2+/4+}$ Clusters .. 130
2.14.2 The Reactions Leading to $(Sb_2Te_4)^{2+/4+}$ Clusters and $[Ga_2Cl_6O]^{2-}$ Anions 133
2.14.3 Crystal Structures of Compounds Containing $(Pn_2Te_4)^{2+/4+}$ Clusters and $[Ga_2Cl_6O]^{2-}$ Anions 133
2.14.4 Raman Spectroscopy Study of $(Pn_2Te_4)[Ga_2Cl_6O]_2$ 139

2.15 Ga_2SbCl_7O - A Molecular Gallium Antimony Chloride Oxide 141
2.15.1 Synthesis and EDX Analysis of Ga_2SbCl_7O 142
2.15.2 The Reaction Leading to Ga_2SbCl_7O 142
2.15.2 Crystal Structure of Ga_2SbCl_7O 143

2.16 The Cube Shaped Clusters $(Bi_4Ch_4)^{3+}$ (Ch = Te, Se) and the Novel Anion $[SeGa_3Cl_9]^{2-}$ 148
2.16.1 Syntheses and EDX Analyses 149
2.16.2 Crystal Structures of $(Bi_4Te_4)[GaCl_4]_2[Ga_2Cl_7]$ and $(Bi_4Se_4)[GaCl_4][SeGa_3Cl_9]$ 151
2.16.3 Analysis of the Electronic Structure of the $(Bi_4Te_4)^{3+}$ Cluster 156

3.0 Synopsis and Perspective 158

4.0 Literature 161

5.0 Appendix 166
A 5.1 Instruments, Analytics and Preparation 166
A 5.1.1 The Vacuum System and Tube Furnaces 166
A 5.1.2 The Glovebox 167
A 5.1.3 Crystal Structure Determination 168
A 5.1.4 Energy Dispersive Electron-Beam X-ray Fluorescence Analysis (EDX) 169
A 5.1.5 Characterization by Raman Spectroscopy 171
A 5.1.6 ^{77}Se and ^{125}Te Solid State NMR Spectroscopy 173
A 5.1.7 Electron Paramagnetic Resonance Spectroscopy (EPR) 173
A 5.1.8 X-ray Powder Diffraction 175
A 5.1.9 Differential Scanning Calorimetry (DSC) 175
A 5.1.10 Mass Spectrometry (MS) 176
A 5.1.11 Magnetic Measurements 177
A 5.1.12 Crystal Photos 177
A 5.2 Crystallographic Data 178
A 5.3 Occupation Factors of Heavy Atom Positions in Sb-Te Polycationic Clusters 202
A 5.4 Intramolecular Bond Lengths in Polycationic Clusters 209
A 5.5 Sb···Cl and Te···Cl Distances Around Polycationic Clusters 217
A 5.6 Coordination Spheres of Discrete Polycationic Clusters 222
A 5.7 Calculated Raman Vibration Modes of Polycationic Clusters and Anions 229
A 5.8 Programs and Chemicals 245
A 5.8.1 Synthesis of Gallium(III) Chloride 245
A 5.8.2 Synthesis of Indium(I) Chloride 245
A 5.8.3 Programs 248
A 5.8.4 Chemicals and Purifications 249
A 5.8.5 Summary of Successful Syntheses 250

1.0 Introduction

1.1 Definition and Historical Beginning of the Search for Polycationic Clusters

Polycationic clusters are positive charged molecules made up of main group elements. They need weakly coordinating, weakly basic and hardly oxidizable anions to be stable as cations in salt-like compounds.

The documented history of polycationic clusters began 1798 when M. Klaproth published his observations on dissolving elemental tellurium in concentrated sulfuric acid.[1] The solutions reported are of yellow, blue and red colour obtained from elemental sulfur in oleum depending on the SO_3 concentration.[2] In 1827 G. Magnus reported on green solutions from selenium in the same solvent.[3,4] For about 160 years no reasonable explanation could be given for these observations and the nature of the coloured species remained unclear.
In 1960 N. Bartlett and D. Lohmann described the platinum oxyfluoride $PtOF_4$[5] which was corrected in 1962 to be $O_2[PtF_6]$.[6] The O_2^+ cation was the first identified polycationic chalcogen "cluster". It was synthesized by oxidation of molecular oxygen with platinum hexafluoride. In the following years the O_2^+ cation was additionally found in salts with the anions $[AsF_6]^-$, $[SbF_6]^-$ and $[BF_4]^-$.[7,8,9,10,11]
In 1968 the first selenium clusters Se_4^{2+} and Se_8^{2+} could be obtained in strong acidic solvents.[12] The square planar structure of Se_4^{2+} could be determined by an X-Ray study in the same year.[13,14]
In the same period of time, experiments with tellurium in $Na[AlCl_4]$ melts led to the assumtion of the existence of a tellurium cluster assumed to be Te_4^{2+}.[15,16] It was confirmed by single crystal X-ray diffraction in 1972 to have the analogous structure as Se_4^{2+}.[17]
With the upcoming availability of single crystal structure determinations the number of publications on chalcogen clusters arised. It was no longer necessary to rely on spectroscopy or conductivity measurements only.

Besides homonuclear chalcogen clusters various mixed pentele - chalcogen clusters were found during the last 45 years and analyzed by several analytical methods. The focus in this work is the synthesis and analysis of novel mixed polycationic clusters made up from elements of group 15 and 16 of the periodic table.

1.2 Mixed Polycationic Clusters From Group 15 and 16 and Their Syntheses

The first stable mixed polycationic cluster of group 15 and 16 elements was found in 1969.
The heart-shaped $(S_5N_5)^+$ was obtained by reaction of tetrasulphur tetranitride and aluminium trichloride in thionyl chloride at 35 °C as the tetrachlorido aluminate salt (Fig. 1.2.1).[18]

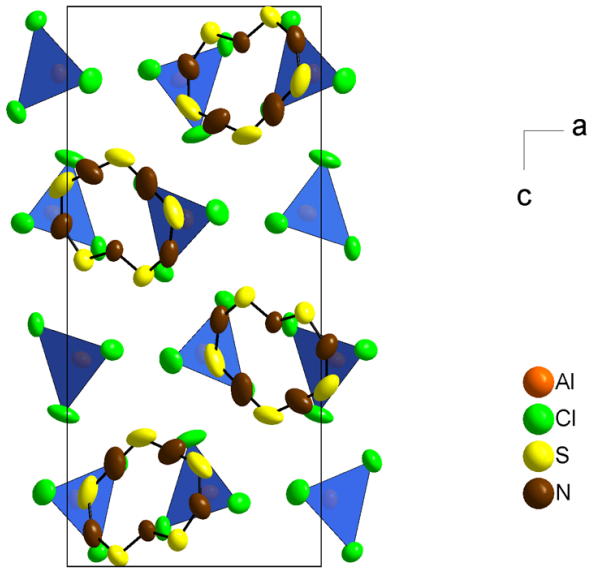

Fig. 1.2.1 The unit cell of $(S_5N_5)[AlCl_4]$.[19] The atoms are represented by thermal ellipsoids scaled to include a probability of 50 %. The $[AlCl_4]^-$ ions are shown as discrete tetrahedra.

In 1985 the $(S_5N_5)^+$ cluster was obtained as the corresponding tetrachlorido gallate salt by the reaction of gallium metal with trithiazyl chloride in dichloromethane at 30 °C. Adding an equimolar amount of gallium trichloride to a suspension of $(S_5N_5)[GaCl_4]$ in dichloromethane formed $(S_5N_5)[Ga_2Cl_7]$, which contains an "azulene-shaped" isomer of $(S_5N_5)^+$ (Fig. 1.2.2).[20]

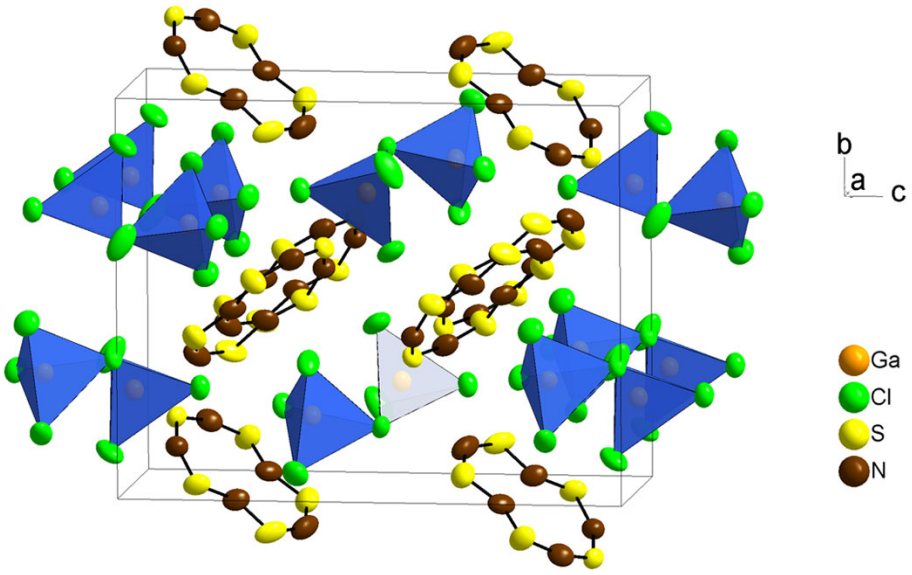

Fig. 1.2.2 The unit cell of $(S_5N_5)[Ga_2Cl_7]$.[20] The atoms are represented by thermal ellipsoids scaled to include a probability of 50 %. The $[Ga_2Cl_7]^-$ ions are shown as discrete double tetrahedra.

In the period between the discovery of these two isomers several further polycationic S-N-clusters were found and characterized such as $(S_4N_4)^{2+}$[21], $(S_4N_5)^{+}$[22] and $(S_3N_2)^{+}$[23,24,25]. Further S-N-clusters, $(S_3N_2)^{+}$ and $(S_4N_3)^{+}$,[26] were obtained in 2001, which shows the ongoing research on this kind of molecules. The syntheses have in common that they proceed in liquid SO_2 or dichloromethane as the appropriate solvents.

In 1980 the cage shaped $(As_3S_4)^{+}$(Fig. 1.2.3) and $(As_3Se_4)^{+}$ (Fig. 1.2.4) were found. They were synthesized in liquid SO_2 by dissolving As_4S_4 and mixtures of arsenic and selenium in liquid AsF_5 and SbF_5, respectively.[27] Both clusters have been isolated as the hexafluorido arsenate and antimonate salts.

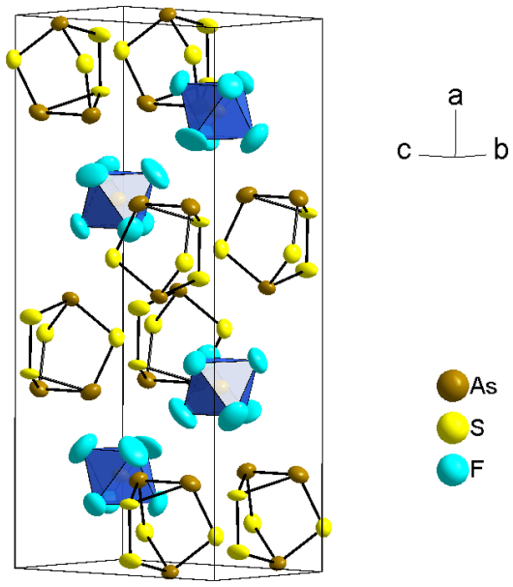

Fig. 1.2.3 The unit cell of $(As_3S_4)[AsF_6]$.[27] The atoms are represented by thermal ellipsoids scaled to include a probability of 50 %. The $[AsF_6]^-$ ions are shown as discrete octaheda.

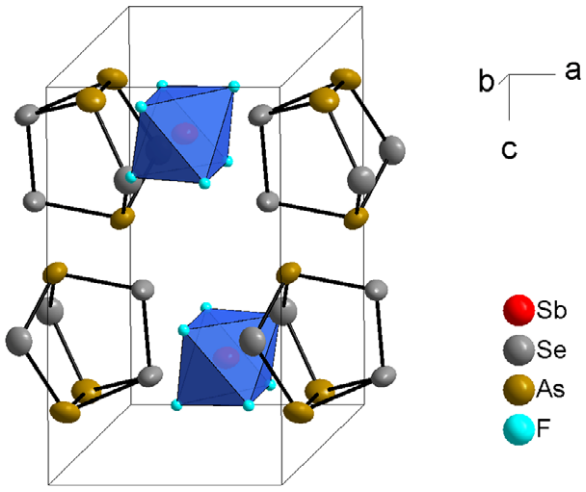

Fig. 1.2.4 The unit cell of $(As_3Se_4)[SbF_6]$.[27] Sb, Se and As atoms are represented by thermal ellipsoids scaled to include a probability of 50 %. F atoms are shown as spheres of arbitrary radii. The $[SbF_6]^-$ ions are shown as discrete octaheda.

An extended cluster as a derivative of $(As_3S_4)^+$, namely $(As_3S_5)^+$, was obtained in 2005 by the oxidation of the elements arsenic and sulphur with arsenic trichloride in a Lewis acidic aluminium trichloride melt at 80 °C (Fig. 1.2.5).[28]

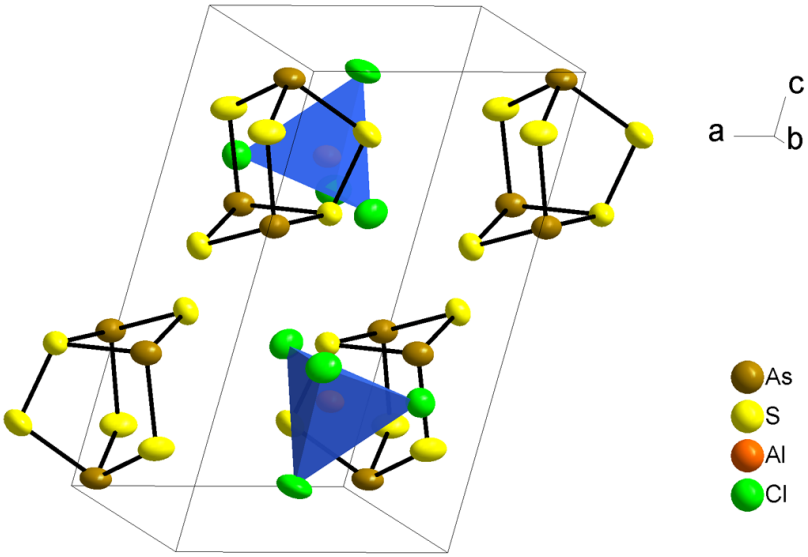

Fig. 1.2.5 The unit cell of $(As_3S_5)[AlCl_4]$.[28] The atoms are represented by thermal ellipsoids scaled to include a probability of 50 %. The $[AlCl_4]^-$ ions are shown as discrete octaheda.

The first bismuth-tellurium polycationic cluster was the cube shaped $(Bi_4Te_4)^{4+}$ (Fig. 1.2.6). It was realized by the oxidation of the elements bismuth and tellurium with bismuth trichloride in a sodium aluminate melt at 130 °C and introduced with its cuboiddal structure a new structural principle among the polycationic main group element clusters.[29] The selenium and sulphur congeners were obtained in the analogous way.[30] The three isotypic tetragonal structures are characterized by high symmetrical clusters.

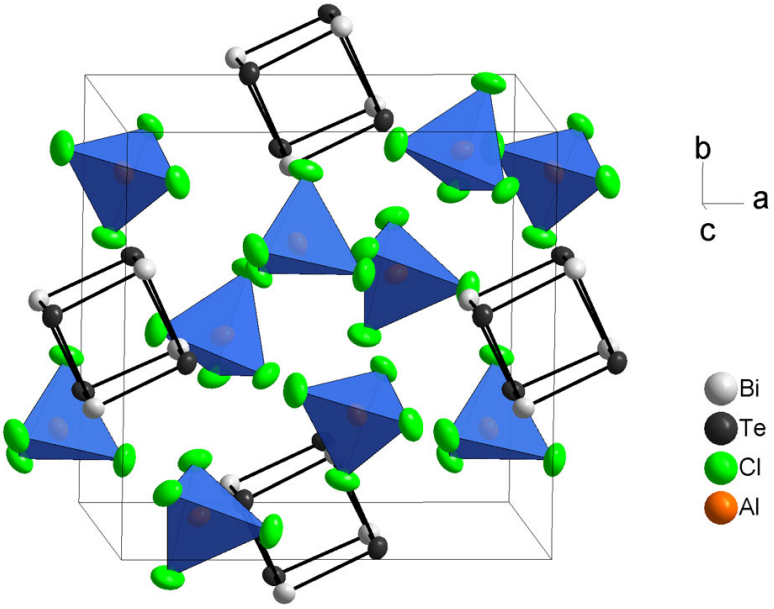

Fig. 1.2.6 The unit cell of $(Bi_4Te_4)[AlCl_4]_4$.[29] The atoms are represented by thermal ellipsoids scaled to include a probability of 70 %. The $[AlCl_4]^-$ ions are shown as discrete tetrahedra.

Besides discrete mixed pentele-chalcogen clusters polymeric arrangements are known.
In 2004 S. Schlüter presented $(Bi_2Se_2^{2+})_n$ and $(Bi_2Te_2^{2+})_n$ (Fig. 1.2.7) in their isotypic structures.[31] The two polycations form double zigzag chains. They were synthesized in aluminium trichloride melts at relatively high temperatures of 420 °C by oxidation of the elements with bismuth trichloride.

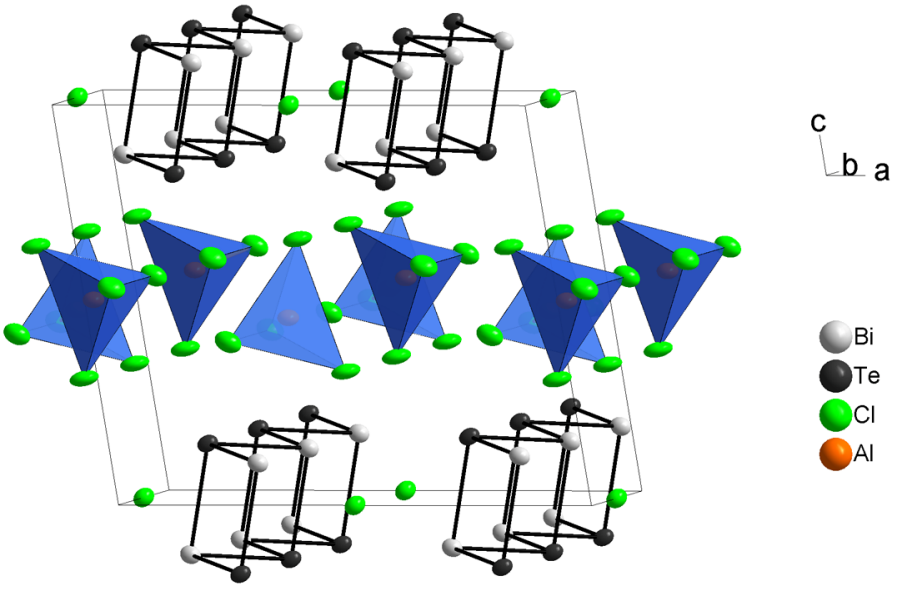

Fig. 1.2.7 The unit cell of $(Bi_2Te_2)Cl[AlCl_4]$.[31] The atoms are represented by thermal ellipsoids scaled to include a probability of 50 %. The $[AlCl_4]^-$ ions are shown as discrete tetrahedra.

In 2010 the isotypic $(Bi_2Te_2)Br[AlCl_4]$ and $(Sb_2Te_2)Br[AlCl_4]$ were obtained from the respective elements in the ionic liquid EMIMBr-$AlCl_3$ (EMIM = 1-ethyl-3-methylimidazolim) at 165 °C.[32]
Three years later the isostructural compound $(Bi_2Se_2)Br[AlCl_4]$ was synthesized in the analogous way.[33]
A remarkable fact in these structures is the presence of bridging chloride and bromide anions between the clusters. These anions are rather basic and are expected to cause a decomposition of the clusters.
Other known polymeric polycationic clusters are the antimony-tellurium chains $(Sb_3Te_4)_n^{+}$[31] (Fig. 1.2.8) and $(Sb_2Te_2^{+})_n$[34] (Fig. 1.2.9). $(Sb_3Te_4^{+})_n$ can be described as a connection of two double zigzag chains. The structure motiv of $(Bi_2Te_2^{2+})_n$ is simply duplicated.

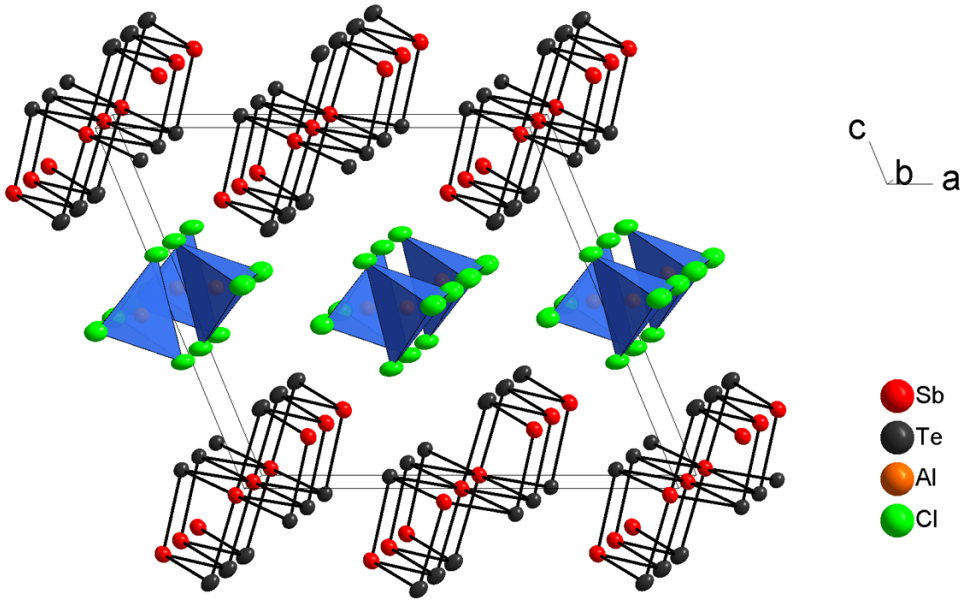

Fig. 1.2.8 The unit cell of $(Sb_3Te_4)[AlCl_4]$.[31] The atoms are represented by thermal ellipsoids scaled to include a probability of 60 %. The $[AlCl_4]^-$ ions are shown as discrete tetrahedra.

The structure of the polymeric $(Sb_2Te_2^+)_n$ can be described as a chain consisting of connected square planar (Sb_2Te_2) units arranged in roughly parallel alignment.

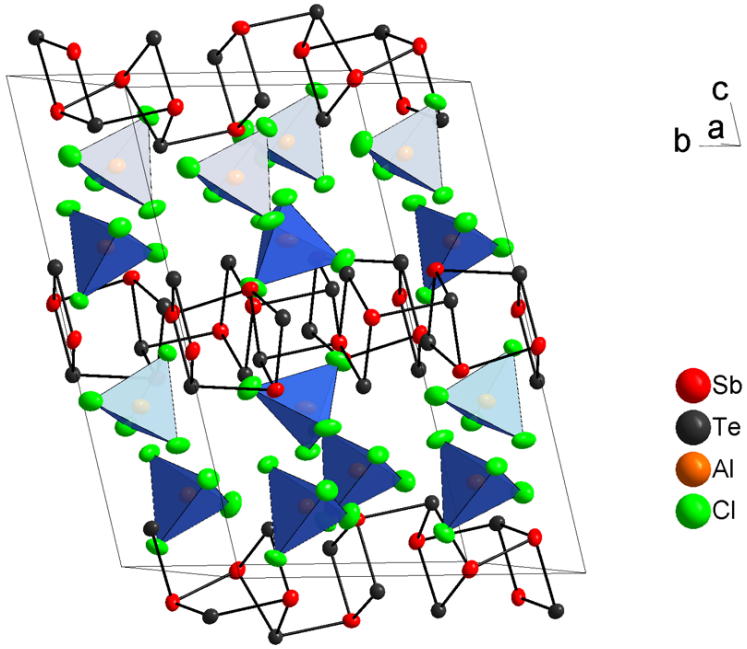

Fig. 1.2.9 The unit cell of $(Sb_2Te_2)[AlCl_4]$.[34] The atoms are represented by thermal ellipsoids scaled to include a probability of 50 %. The $[AlCl_4]^-$ ions are shown as discrete tetrahedra.

Both antimony-tellurium polycationic polymers were obtained from an aluminium trichloride melt at 130 °C, $(Sb_2Te_2)[AlCl_4]$ in the presence of additional sodium chloride.
The first prism shaped heteronuclear clusters build from group 15 and 16 elements were $(BiTe_5)^{3+}$ (Fig. 1.2.10) and $(SbTe_5)^{3+}$.[35]

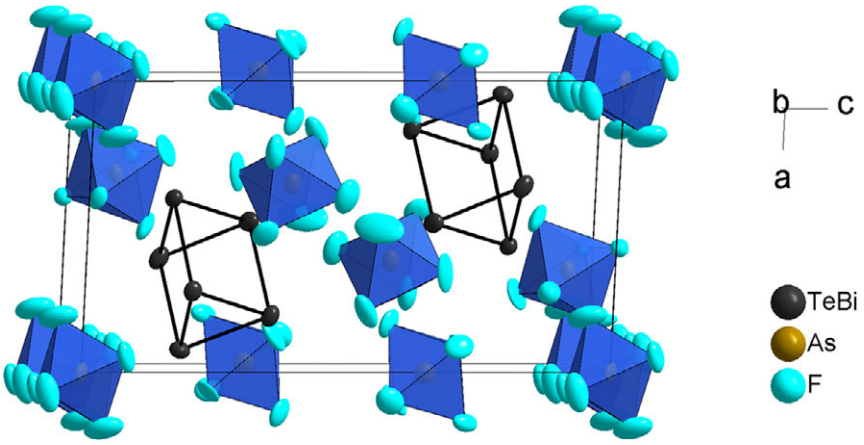

Fig. 1.2.10 The unit cell of $(Te_6)(BiTe_5)[AsF_6]_7$.[35] The atoms are represented by thermal ellipsoids scaled to include a probability of 50 %. The $[AlCl_4]^-$ ions are shown as discrete tetrahedra.

The two isotypic compounds $(Te_6)(BiTe_5)[AsF_6]_7$ and $(Te_6)(SbTe_5)[AsF_6]_7$ were synthesized by the reaction of bismuth telluride and antimony telluride with arsenic pentafluoride in liquid sulphur dioxide.

The first published antimony-selenium polycationic cluster was obtained from a mixture of antimony, selenium and selenium tetrachloride in the ionic liquid BMIMCl-$AlCl_3$ (BMIM = 1-n-butyl-3-methylimidazolium) at room temperature. The resulting discrete $(Sb_{10}Se_{10})^{2+}$ polycation consists of two (Sb_4Se_4) cages connected by a square planar (Sb_2Te_2) unit (Fig. 1.2.11).[36]

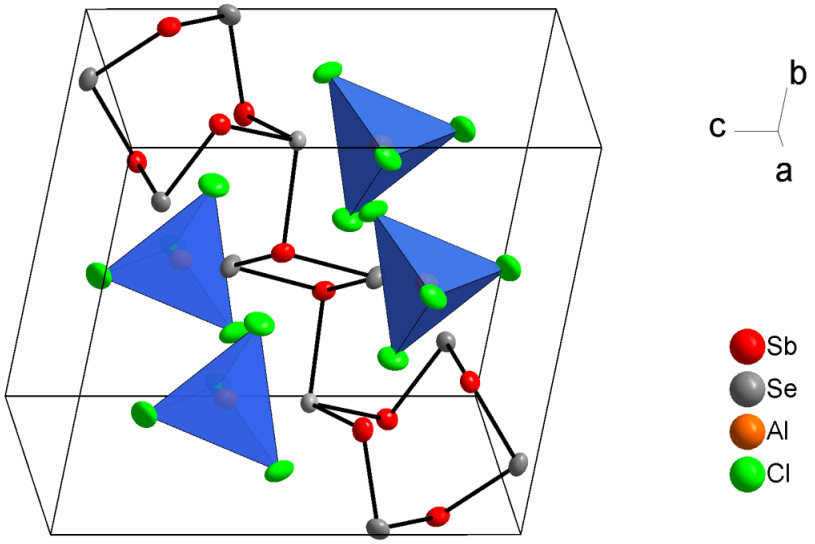

Fig. 1.2.11 The unit cell of $(Sb_{10}Se_{10})[AlCl_4]_2$.[36] The atoms are represented by thermal ellipsoids scaled to include a probability of 50 %. The $[AlCl_4]^-$ ions are shown as discrete tetrahedra.

Another antimony-selenium cluster, the double cube shaped $(Sb_7Se_8Cl_2)^{3+}$, was found in the reaction of the elements with antimony trichloride in a sodium chloridoaluminate melt at 136 °. In an analogous reaction the sulphur cogener $(Sb_7S_8Cl_2)^{3+}$ could be synthesized.[31] Both compounds were crystallized as isotypic tetrachlorido aluminate salts.

Additionally the bromine congener of the $(Sb_7S_8Cl_2)^{3+}$ (Fig. 1.2.12) could be obtained in the reaction of the elements in the ionic liquid EMIMBr-$AlCl_3$ at 165 °C.[37] The double cube polyhedra was a novel structural feature in the chemistry of polycationic clusters.

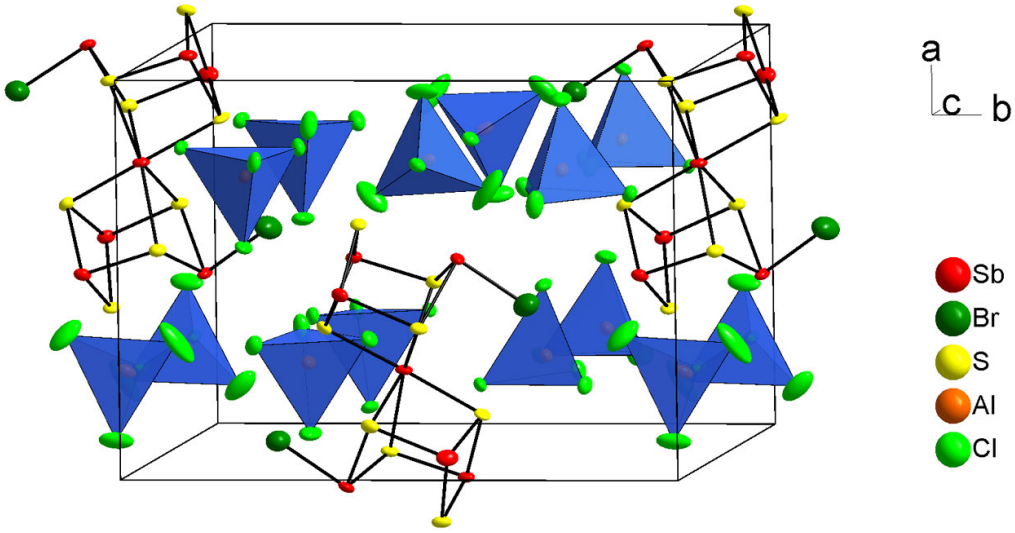

Fig. 1.2.12 The unit cell of $(Sb_7S_8Br_2)[AlCl_4]_3$.[37] The atoms are represented by thermal ellipsoids scaled to include a probability of 90 %. The $[AlCl_4]^-$ ions are shown as discrete tetrahedra. Half of $(Sb_7S_8Br_2)^{3+}$ clusters are omitted for clarity.

The most recent result reported in 2014 is the isolation of $(Sb_7Se_8Br_2)^{3+}$ from the reaction mixture of antimony, selenium and niob pentachloride in the ionic liquid BMIMBr-$AlBr_3$ in a glass ampoule at 160°C. The same procedure without niob pentachloride yielded $(Sb_{13}Se_{16}Br_2)[AlCl_{3.2}Br_{0.8}]$. These two compounds can even be crystallized together as $(Sb_7Se_8Br_2)(Sb_{13}Se_{16}Br_2)[AlBr_4]_8$ (Fig. 1.2.13).[38] $(Sb_{13}Se_{16}Br_2)^{5+}$ is a spiro-connected double cube shaped cluster and the most complex polycationic cluster known until today. In general, the use of ionic liquids turned out to be advantageous for the synthesis of larger clusters.

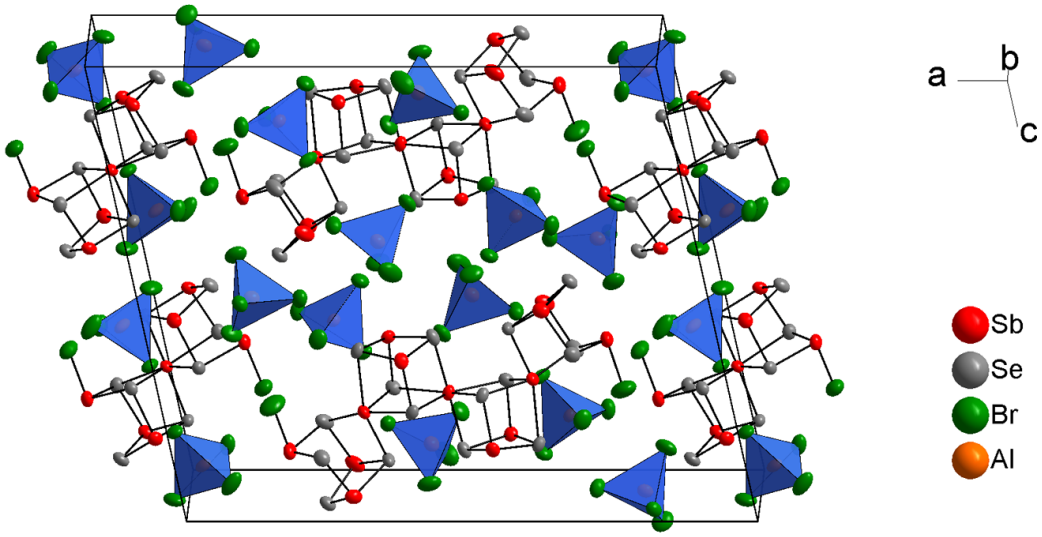

Fig. 1.2.13 The unit cell of $(Sb_7Se_8Br_2)(Sb_{13}Se_{16}Br_2)[AlBr_4]_8$.[38] The atoms are represented by thermal ellipsoids scaled to include a probability of 70 %. The $[AlBr_4]^-$ ions are shown as discrete tetrahedra.

The special characteristics of these cube-structured clusters are the chlorine and bromine atoms bound covalently to antimony. Despite the presence of basic halide anions the clusters do not decompose into antimony or chalcogen chlorides or bromides. A comparable situation can be found in the clusters $(Se_6I_2)^{2+}$ and $(Te_{15}X_4^{2+})_n$ (X = Cl, Br).[39]
Another heteronuclear antimony-tellurium polycationic cluster is the almost regular double cube shaped $(Sb_7Te_8)^{5+}$ in the structure of $Na(Sb_7Te_8)[AlCl_4]_6$ (Fig. 1.2.14). It was synthesized in the analogous way to the antimony-selenium and antimony-sulphur double cube shaped clusters in a sodium chlorido aluminate melt.[31]

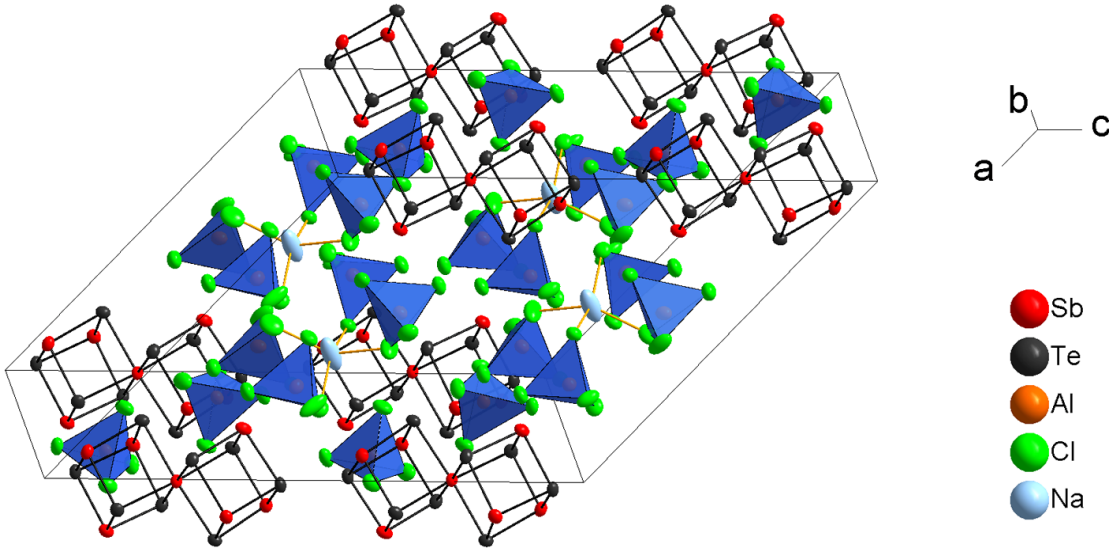

Fig. 1.2.14 The unit cell of $Na(Sb_7Te_8)[AlCl_4]_6$.[31] The atoms are represented by thermal ellipsoids scaled to include a probability of 90 %. The $[AlCl_4]^-$ ions are shown as discrete tetrahedra.

The compound undergoes a phase transition at 177 K. Above this temperature the sodium atom is dynamically disordered over two positions. Lowering the temperature results in ordering of the Na^+ ions in two positions under loss of the symmetry centre and doubling the size of the unit cell.

A common feature in all these clusters mentioned above is the alternating heavy atom distribution. The amount of heteronuclear bonds is maximized to gain additional ionic bonds and thereby a higher overall stability.
The presence of simple anions with unequivocal charge in polycationic cluster containing structures allows for the determination of the clusters' charges. This is highly advantagous if the single crystal data limit the distinction of elements, which is a known difficulty in the case of neighbouring elements like Sb/Te or As/Se.

1.3 The Pecularities in Chemical Bonding Between Heavy Electron-Rich Atoms and the Advantage of Formation of Heteronuclear Clusters

The heavier elements of group 15 and 16 show a higher variety in the formation of polycationic clusters compared to their lighter homologues (see chapter 1.2). The choice of certain element combinations in the performed experiments is based on this fact.

The reason for this deviant chemical behaviour of the heavier elements is on the one hand the increasing possibility of hypervalent bonding like present in the clusters $(Sb_3Te_4)^+$ and $(Sb_7Te_8)^{5+}$[31]. On the other hand, the energy difference between occupied np^2 orbitals with lone pair character and antibonding $n\sigma^*$ orbitals of bonds between theses elements decreases with increasing n. Regarding tellurium, $5p^2 \rightarrow 5\sigma^*$ intra- and intermolecular bonding is observed. The lone pairs transfer electron density into the empty $5\sigma^*$ orbitals of suitable Te-Te bonds. The consequence is a slight lengthening of the σ bonds and the generation of new, secondary bonds within the clusters or between neighbouring clusters. The covalent bonds range generally from 2.75 - 2.85 Å. The secondary bonds are present between 3.00 and 3.50 Å.[40]

Intermolecular interactions can be observed for example in the structures of $Te_6[MOCl_4]_2$ (M = Nb, W) [41,42] and $Te_8[VOCl_4]_2$[43]. The individual tellurium clusters are arranged in a linear way with a minimum distance between adjacent clusters of 4.61 Å in the case of Te_6^{2+} and 3.59 Å in the case of Te_8^{4+}. This trend leads to dimers of clusters in the structure of $Te_8[HfCl_6]$[44] with an intermolecular distance of 3.47 Å. In $Te_8[WCl_6]_2$[45] the Te_8^{2+} clusters are strung as an endless ondulated chain with an intermolecular distance of only 3.42 Å.[40]

The next group besides polycationic clusters are positively charged polymers connected by covalent bonds like present in the structure of $(Te_4)(Te_{10})[Bi_4Cl_{16}]$[46]. Here, Te_4^{2+} cations are connected to a polymeric chain with two and three-fold bonded Te atoms. The positive charge is delocalized over the whole chain, which can be understood as donation of electron density from the $5p^2$ lone pairs of the two-fold bonded tellurium atoms into the empty antibonding $5\sigma^*$ orbital of the three-fold bonded tellurium atoms. The more interactions of this type are present, the lower the total energy is.[47]

Further polycationic tellurium polymers are for example $(Te_6^{2+})_n$[48] or $(Te_7^{2+})_n$[49]. Besides the discrete 2e-2c bonds secondary Te-Te interactions in the range mentioned above are present.[40]

Comparable heteronuclear chains are $(Bi_2Te_2)^{2+}$[32], $(Sb_2Te_2)^+$[33], $(Sb_2Te_2)^{2+}$[32] and $(Sb_3Te_4)^+$[31]. However, comparable short intermolecular interactions between heteronuclear tellurium clusters have not been observed until today. Admittedly, research on homonuclear tellurium clusters has been performed much more intensively than the approach to the heteronuclear side of this chemistry.

1.4 Motivation

The motivation for this work is based on the desire to enhance the knowledge on novel polycationic heteronuclear clusters made of group 15 and 16 elements. The chosen synthetic approach are reactions in gallium trichloride melts and low pressure inert gas atmospheres. Gallium trichloride acts as a solvent and provides the anionic part in the final compounds in form of $[GaCl_4]^-$ and $[Ga_2Cl_7]^-$ anions, which are weakly coordinating, weakly basic and hardly oxidizable. An additional aim was set to the incorporation of positive single charged anions to the crystal structures of polycationic clusters containing compounds. During the practical work, it was found that the addition of such single charged cations to the melts has a substantial influence on the product formation. Due to this awareness melts were examined in various ways to obtain intentional products.

1.5 General Synthesis Procedures in M[$GaCl_4$] Melts

The main focus of the present work is the Sb/Te system. Additional experiments were done in the systems As/Te, Sb/Se, Bi/Te and to a smaller extent for Sb/S and Bi/Se. In all experiments the ratio Pn/Ch was 1:1 and $GaCl_3$ was used in large excess serving as a solvent and providing the later anionic part of the compounds. A disadvantage of this method is occasionally the fallacious impression of a crystalline product formation. As sometimes observed, crystalline $GaCl_3$ absorbs coloured species from the melt and takes the appearance of polycationic clusters containing crystals. With some experience a distinction was possible. It turned out as essential for the success of the reactions to use $SbCl_3$ in double excess with respect to the amount of Sb and Te.
A similar approach to the syntheses of polycationic clusters in acidic melts can be found in the Ph.D. thesis of S. Schlüter on heteronuclear clusters of group 15 and 16 in chlorido aluminate melts [31]. In the present work S. Schlüter's melt composition was modified by cutting the amounts of Pn, Ch, $PnCl_3$ and the solvent $GaCl_3$ in half. The adjuvant X was expanded from the solely used NaCl to many other single charged cations as chlorides and to the pentele and chalcogen oxides. Besides that the amount of X was retained at the original quantity for a stronger effect on the melt and the product formation. Additional chlorine anions lower the melt basicity due to a higher concentration of $[GaCl_4]^-$ and $[Ga_2Cl_7]^-$ anions. Additional cations alter the redox potential of the melts depending on their charge and size. In the case of Hg_2Cl_2 and the oxides Pn_2O_3 and Pn_2O_5, the stoichiometric amount was divided by two and three. In some cases two adjuvants were combined. Experiments without the adjuvants were additionally undertaken.

In general, the composition of the educts was chosen as follows:

0.24 mmol Pn + 0.36 mmol Ch + 0.12 mmol $PnCl_3$/$PnCl_5$ + 0.99 mmol $GaCl_3$ + 0.18 mmol X

The following tested additives X in the respective Pn/Ch systems ordered by priority were used:

Sb/Te: LiCl, NaCl, KCl, RbCl, CsCl, NH_4Cl, InCl, TlCl, CuCl, AgCl, AuCl, Hg_2Cl_2, $CuCl_2$, $InCl_2$, Ga_2O_3, Sb_2O_3, Sb_2O_5, TeO_2, TeO_3, PPh_4Cl
As/Te: LiCl, NaCl, KCl, RbCl, CsCl, NH_4Cl, InCl, TlCl, CuCl, AgCl, AuCl, Hg_2Cl_2, $CuCl_2$, $InCl_2$, As_2O_3, As_2O_5, TeO_2, PPh_4Cl
Sb/Se: LiCl, NaCl, KCl, RbCl, CsCl, NH_4Cl, InCl, TlCl, CuCl, AgCl, AuCl, Hg_2Cl_2, $CuCl_2$, Sb_2O_3, Sb_2O_5, PPh_4Cl
Bi/Te: LiCl, NaCl, KCl, RbCl, CsCl, NH_4Cl, InCl, TlCl, CuCl, AgCl, Hg_2Cl_2, $CuCl_2$, PPh_4Cl
Sb/S: LiCl, NaCl, KCl, RbCl, CsCl, NH_4Cl, InCl, TlCl, CuCl, AgCl, Hg_2Cl_2, Sb_2O_3, Sb_2O_5, PPh_4Cl
Bi/Se: LiCl, NaCl, KCl, RbCl, CsCl, NH_4Cl, InCl, TlCl, CuCl, AgCl, Hg_2Cl_2, $CuCl_2$, PPh_4Cl

Syntheses were performed between 50 and 200 °C. Temperatures above 160 °C turned out to be not efficient because antimony recrystallized under these conditions as hexagonal, metallic, plate shaped crystals. Since $GaCl_3$ based melts are liquid already slightly above room temperature, the reaction conditions may be adjusted similar to those in ionic liquids. In general, the use of $GaCl_3$ as the main component of the melt, which serves as the reaction medium for the synthesis of polycationic main group element clusters allows for much lower reactions temperatures in comparison to $AlCl_3$.
For all reactions, self-built pressure stable glass ampoules (Simax glass, length approx. 90 mm, outer diameter 14 mm, wall thickness 1.5 mm) were used (Fig. 1.5.1). Before filling with starting materials in

an argon filled glove box, ampoules were heated once for 3 minutes under dynamic vacuum with a heat gun to remove adsorbed moisture (approx. 500 °C / $5 \cdot 10^{-2}$ mbar). In later periods of the experimental work they were heated with a gas oxygen burner almost to the melting point of the glass. The advantage of the use of glass ampoules is the possibility to observe the progress of the reactions visually.

Fig. 1.5.1 Argon filled ampoule before filling with starting materials.

Arsenic, antimony, bismuth, selenium and tellurium were purified by vacuum sublimation to remove the impurities As_2O_3, As_2O_5, Sb_2O_3, Sb_2O_5, Bi_2O_3, SeO_2, SeO_3, TeO_2 and TeO_3. Commercial tellurium turned out as heavily contaminated by tellurium dioxide.
Other educts, which had been delivered in closed ampoules or bottles were used without further treatment and handled in the glovebox. Compounds which were in stock in the institute were dried at specific temperatures under low pressure. For the exact conditions see table 5.8.4.1 in the appendix. All starting materials were stored under strict exclusion of atmospheric moisture.
Ampoules were filled in the glovebox with calculated amounts of educts. On weighing the masses of the starting materials the used balance allowed for an accuracy of ± 0.1 mg. In all experiments, a submolar amount of any starting compound was avoided and the accuracy of the used amount ranged between 0 and + 2 mg.

The ampoules were evacuated and flame sealed at the vacuum system (approx. $3 \cdot 10^{-2}$ mbar) (Fig. A 5.1.1.1). In the case of liquid educts the mixture was frozen with liquid nitrogen during flame sealing.
Tube furnaces used for syntheses were aligned in an angle of about 30° to the horizontal for keeping the melt compact in the hot zone (Fig. A 5.1.1.2). Ampoules were positioned in the lower end of the furnaces so that the other sides of the ampoules were closer to the hottest zone. In this way it was ensured that gallium trichloride did not escape from the reaction mixture by sublimation.
In intervalls of about five days the ampoules were taken out of the furnaces and inspected under the microscope. Admittedly this procedure supported the growth of twinned crystals which were sometimes quite problematic. However, the use of heavy elements allowed for the choice of relatively small crystals for single crystal diffraction, which compensated the twinning problems. If the formation of crystals was observed, the ampoules were tilted reversely while still being hot to decant the melt from the solids (Fig. 1.5.3).

Fig. 1.5.3 Ampoules after synthesis.

Depending on the pentele/chalcogen combinations, the melts differed in colour and viscosity. In general, melts with the combinations Sb/Te, Bi/Te and Bi/Se were black, As/Te dark orange, Sb/Se dark red and Sb/S yellow - green. Especially the use of PPh_4Cl made the melts much more liquid compared to the cases without this additive. The melt was easier to separate from the solids in the respective ampoules, which helped for the crystal separation.

Summarizing all performed experiments it has to be admitted that this way of synthesis can not be described as “clean” because the isolated products were always contaminated by melt residues and often amorphous as well as crystalline byproducts. In all experiments, variable amounts of a $GaCl_3$-rich melt and unreacted pentele and chalcogen elements remained. In most cases it was possible to obtain pure phases of the desired polycation containing compounds.

After cooling to ambient temperature, the ampoules were scratched with a glass cutter and opened in the glove box. Since all investigated compounds are very sensitive towards air and evaporate excessive gallium trichloride, residual ampoules were sealed with parafilm and stored under argon atmosphere.

For all analytics, crystals were prepared under the glovebox microscope. In general, they had a to be separated from a viscous melt and cleaned from adherences in perfluorinated polyether (Fomblin Y, Sigma Aldrich) or a higher viscous polyether (NVH Oil, Jena Bioscience). In these media, the crystals were examined by single crystal diffraction, Raman spectroscopy, EPR measurements, UV-vis measurements, electrical conductivity and solid state NMR measurements. Only for EDX measurements the polyethers had to be avoided because the electron beam was absorbed in the oil film on the crystals surface.

2.0 Experimentals and Results

2.1 The Double Cube Shaped Polycationic Cluster $(Sb_7Te_8)^{5+}$

2.1.1 Syntheses and EDX Analyses of Compounds Containing the $(Sb_7Te_8)^{5+}$ Cluster

$(Sb_7Te_8)[GaCl_4]_2[Ga_2Cl_7]_3$ and $(Sb_7Te_8)[GaCl_4]_3[Ga_2Cl_7]_2$

45.9 mg (0.36 mmol) tellurium, 29.2 mg (0.24 mmol) antimony, 27.4 mg (0.12 mmol) antimony trichloride and 174.3 mg (0.99 mmol) gallium trichloride were filled in a glass ampoule under argon atmosphere. In the case of $(Sb_7Te_8)[GaCl_4]_2[Ga_2Cl_7]_3$ 10.5 mg (0.18 mmol) sodium chloride and in the case of $(Sb_7Te_8)[GaCl_4]_3[Ga_2Cl_7]_2$ 17.8 mg (0.18 mmol) copper (I) chloride were added. After 15 days at 100 °C for $(Sb_7Te_8)[GaCl_4]_2[Ga_2Cl_7]_3$ and 60 days for $(Sb_7Te_8)[GaCl_4]_3[Ga_2Cl_7]_2$, orange rod shaped crystals appeared in the black melt (Fig. 2.1.1.1 right). Most of the crystals are covered by a metallic shiny surface which turned out in EDX measurement to consist of a layer of tellurium. $(Sb_7Te_8)[GaCl_4]_3[Ga_2Cl_7]_2$ was additionally formed with the respective amount of InCl and $InCl_2$. $(Sb_7Te_8)[GaCl_4]_2[Ga_2Cl_7]_3$ may be obtained alternatively using a mixture of PPh_4Cl/Hg_2Cl_2 (0.18 mmol each) after about 3 weeks days at 100 °C in a solidified melt. The crystal quality obtained by this method, however, was relatively bad.
The synthesis of $(Sb_7Te_8)[GaCl_4]_2[Ga_2Cl_7]_3$ can be improved substantially by using antimony telluride instead of the elements. Even with copper(I) chloride and antimony telluride this compound is formed in high yield. To obtain clean orange crystals for Raman spectroscopy the compound can be recrystallized by reaction with further antimony trichloride and tetraphenylphosphonium chloride in an ampoule at 100 °C. Unfortunately, the orange rod shaped crystals (Fig. 2.1.1.1) are very thin and sensitive towards mechanical preparation, so sufficient material for a Raman measurement could not be obtained.

Tentative reaction equations are:

$16\ Sb + 24\ Te + 5\ SbCl_3 + 24\ GaCl_3 \rightarrow 3\ (Sb_7Te_8)[GaCl_4]_2[Ga_2Cl_7]_3$
$16\ Sb + 24\ Te + 5\ SbCl_3 + 21\ GaCl_3 \rightarrow 3\ (Sb_7Te_8)[GaCl_4]_3[Ga_2Cl_7]_2$

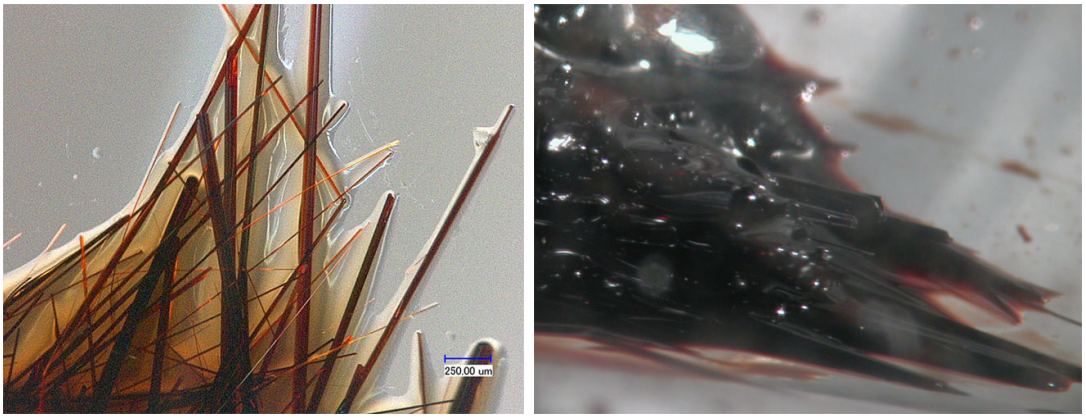

Fig. 2.1.1.1 Crystals of $(Sb_7Te_8)[GaCl_4]_2[Ga_2Cl_7]_3$ after recrystallization (left) and $(Sb_7Te_8)[GaCl_4]_3[Ga_2Cl_7]_2$ in the original melt (right).

The EDX analyses of both compounds support the sum formulae. Despite deviating values from the calculated composition due to adherences on the crystals surfaces depending on the chosen way of syntheses the Sb:Te relation is close to the expected one (Tab. 2.1.1.1).

Tab. 2.1.1.1 Elemental composition of $(Sb_7Te_8)[GaCl_4]_2[Ga_2Cl_7]_3$ and $(Sb_7Te_8)[GaCl_4]_3[Ga_2Cl_7]_2$ in atom-% and the Sb : Te ratio. Standard deviations given in brackets refer to the last significant digit.

	Sb	Te	Ga	Cl	Sb : Te
$(Sb_7Te_8)[GaCl_4]_2[Ga_2Cl_7]_3$	12.6(9)	13(1)	29(1)	44.8(9)	1 : 1.06
Calculated	13.46	15.38	15.38	55.70	1 : 1.14
$(Sb_7Te_8)[GaCl_4]_3[Ga_2Cl_7]_2$	14.8(2)	16.5(3)	18.1(3)	50.1(5)	1 : 1.11
Calculated	14.58	16.67	14.58	54.17	1 : 1.14

$Na(Sb_7Te_8)[GaCl_4]_6$

45.9 mg (0.36 mmol) tellurium, 29.2 mg (0.24 mmol) antimony, 27.4 mg (0.12 mmol) antimony trichloride, 174.3 mg (0.99 mmol) gallium trichloride, 7.6 mg (0.18 mmol) lithium chloride and 10.5 mg (0.18 mmol) sodium chloride were filled in a glass ampoule under argon atmosphere. After 69 days at 88 °C black shiny rhombic and trapezoidal crystals appeared in yellow brown drops outside the melt. During mechanical cleaning in perfluorinated polyether the crystals showd their actual orange colour.
Another much more effective synthetic procedure could be applied by following the route of synthesis of $Ag(Sb_7Te_8)[GaCl_4]_6$ and changing the respective amount of lithium chloride to tetraphenylphosphonium chloride. After 15 days at 100 °C, a large amount of relative big red rod shaped crystals were obtained in a black melt.
The advantage of this synthesis was the possibility to obtain crystals containing the $(Sb_7Te_8)^{5+}$ cluster free from any coverage by finely dispersed tellurium (Fig. 2.1.1.2). This made samples of $Na(Sb_7Te_8)[GaCl_4]_6$ accessible for Raman spectroscopy.

A tentative reaction equation is:

$$16\ Sb + 24\ Te + 5\ SbCl_3 + 3\ NaCl + 3\ GaCl_3 \rightarrow 3\ Na(Sb_7Te_8)[GaCl_4]_6$$

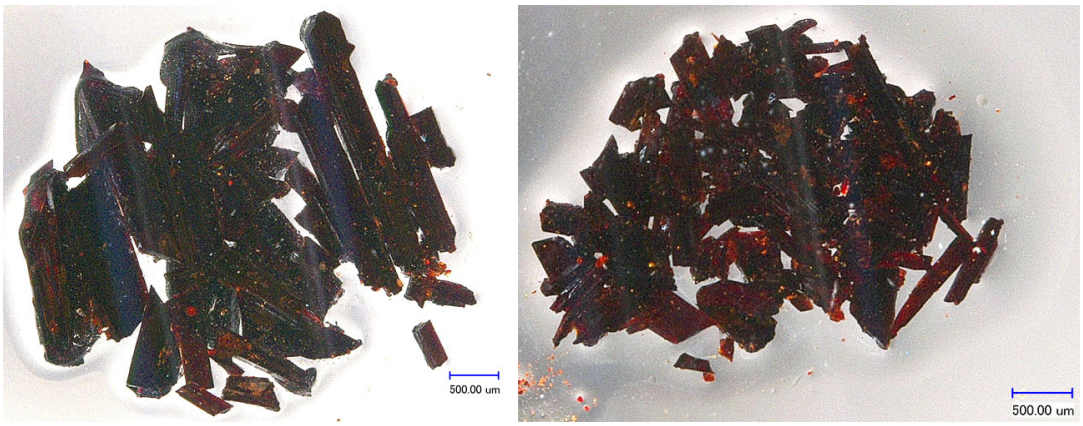

Fig. 2.1.1.2 Crystals of $Na(Sb_7Te_8)[GaCl_4]_6$ in different crystal sizes immersed in perfluorinated polyether prepared for Raman measurements.

The EDX analysis supports the sum formula of $Na(Sb_7Te_8)[GaCl_4]_6$. An uncertainty of the determination of both sodium and gallium is caused by the overlap of the Na-*L* and Ga-*L* X-ray emission line. Thus the sodium content is detected too high (Tab. 2.1.1.2).

Tab. 2.1.1.2 Elemental composition of $Na(Sb_7Te_8)[GaCl_4]_6$ in atom-% and the Sb : Te ratio. Standard deviations given in brackets refer to the last significant digit.

$Na(Sb_7Te_8)[GaCl_4]_6$	Na	Sb	Te	Ga	Cl	Sb : Te
Found	10.0(7)	13.8(4)	15.0(5)	15.2(6)	45.8(4)	1 : 1.09
Calculated	2.17	15.22	17.39	13.04	52.17	1 : 1.14

$Ag(Sb_7Te_8)[GaCl_4]_6$

45.2 mg (0.36 mmol) tellurium, 29.2 mg (0.24 mmol) antimony, 27.4 mg (0.12 mmol) antimony trichloride, 174.3 mg (0.99 mmol) gallium trichloride, 25.8 mg (0.18 mmol) silver(I) chloride and 60.0 mg (0.16 mmol) tetraphenylphosphonium chloride were heated in an ampoule to 100 °C. After 19 days, silvery shiny rod shaped crystals appeared in a liquid black melt. During crystal preparation, they turned out to be red. Using antimony telluride instead of the elements was not successful. Additionally the compound was obtained with lithium chloride instead of tetraphenylphosphonium chloride after 69 days in form of thick rod and rhomb shaped black crystals. The metallic layer on the crystals surface was identified via EDX as tellurium.
Another way of synthesis was the dissolution of $(Sb_7Te_8)[GaCl_4]_2[Ga_2Cl_7]_3$ in $PPh_4[GaCl_4]$ and reaction with AgCl at 100 °C.

A tentative reaction equation according to the formation of the sodium congener is:

$$16\ Sb + 24\ Te + 5\ SbCl_3 + 3\ AgCl + 3\ GaCl_3 \rightarrow 3\ Ag(Sb_7Te_8)[GaCl_4]_6$$

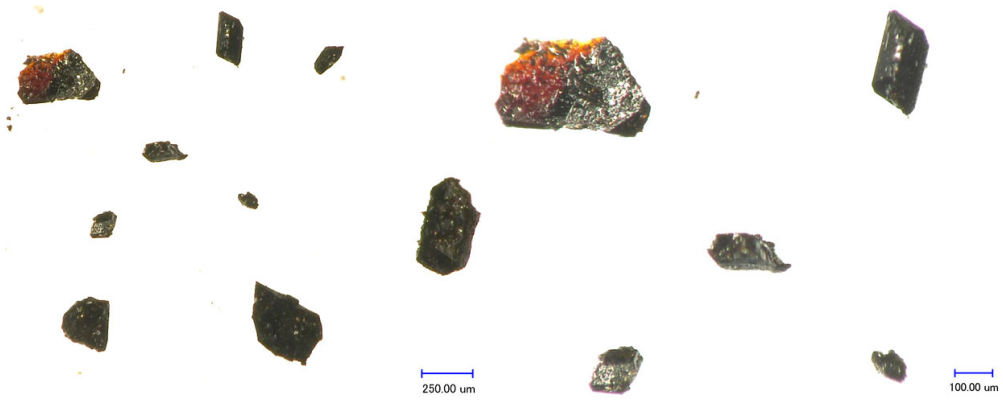

Fig. 2.1.1.3 Crystals of $Ag(Sb_7Te_8)[GaCl_4]_6$ immersed in perfluorinated polyether.

The EDX analysis is in fair agreement with the sum formula $Ag(Sb_7Te_8)[GaCl_4]_6$ (Tab. 2.1.1.3).

Tab. 2.1.1.3 Elemental composition of $Ag(Sb_7Te_8)[GaCl_4]_6$ in atom-% and the Sb : Te ratio. Standard deviations given in brackets refer to the last significant digit.

$Ag(Sb_7Te_8)[GaCl_4]_6$	Ag	Sb	Te	Ga	Cl	Sb : Te
Found	2.4(2)	13.4(1)	15.1(9)	16.0(9)	52(2)	1 : 1.13
Calculated	2.17	15.22	17.39	13.04	52.17	1 : 1.14

$Cu(Sb_7Te_8)[GaCl_4]_6$

The original motive of this synthesis was the crystallization of an $(Sb_7Te_8)^{5+}$ cluster with the hexachlorido oxogallate anion $[Ga_2Cl_6O]^{2-}$, which will be presented later (chapter 2.14).
122.3 mg (0.20 mmol) antimony telluride, 36.5 mg (0.16 mmol) antimony trichloride, 174.3 mg (0.99 mmol) gallium trichloride and 17.8 mg (0.18 mmol) copper(I) chloride and 35.0 mg (0.12 mmol) antimony(III) oxide were filled into a glass ampoule under argon atmosphere. The ampoule was evacuated and flame sealed. After 45 days at 100 °C black, relatively big, black rod shaped crystals were found next to the melt on the inner wall of the ampoule. The crystals are highly light absorbing. Small particles formed on mechanical cleavage of the crystals showed the actual orange colour of the compound in transmitted light (Fig. 2.1.1.4). The residual black melt solidified at ambient temperature and contained only few more, smaller crystals of $Cu(Sb_7Te_8)[GaCl_4]_6$.

A tentative reaction equation is:

$$8\ Sb_2Te_3 + 5\ SbCl_3 + 18\ GaCl_3 + 3\ CuCl \rightarrow 3\ Cu(Sb_7Te_8)[GaCl_4]_6$$

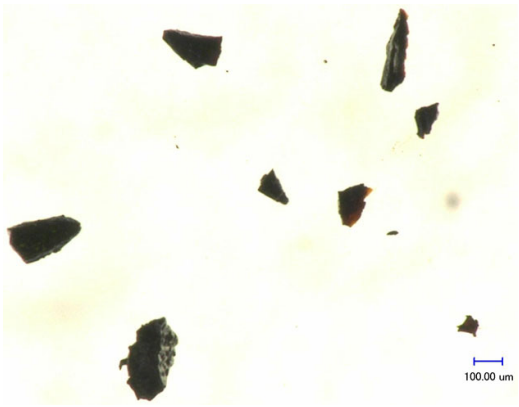

Fig. 2.1.1.4 Crystals of $Cu(Sb_7Te_8)[GaCl_4]_6$ immersed in perfluorinated polyether.

The EDX analysis of $Cu(Sb_7Te_8)[GaCl_4]_6$ is in fair agreement with the sum formula (Tab. 2.1.1.4).

Tab. 2.1.1.4 Elemental composition of $Cu(Sb_7Te_8)[GaCl_4]_6$ in atom-% and the Sb : Te ratio. Standard deviations given in brackets refer to the last significant digit.

$Cu(Sb_7Te_8)[GaCl_4]_6$	Cu	Sb	Te	Ga	Cl	Sb : Te
Found	2.8(1)	15.7(2)	16.5(2)	15.0(4)	49.9(4)	1 : 1.05
Calculated	2.17	15.22	17.39	13.04	52.17	1 : 1.14

2.1.2 The Reactions Leading to Compounds Containing the $(Sb_7Te_8)^{5+}$ Cluster

The compounds containing the $(Sb_7Te_8)^{5+}$ cluster were obtained from elemental antimony and tellurium as well as from antimony telluride with $SbCl_3$ as the oxidant. In the synproportionation reaction between Sb, Te and $SbCl_3$, the Lewis acid $GaCl_3$ takes up the chloride ions of $SbCl_3$ and of the used monochlorides, forming the respective chloridogallate anions (Eqn. 1-5).

$$16\ Sb + 24\ Te + 5\ SbCl_3 + 21\ GaCl_3 \rightarrow 3\ (Sb_7Te_8)[GaCl_4]_3[Ga_2Cl_7]_2 \quad (1)$$
$$16\ Sb + 24\ Te + 5\ SbCl_3 + 24\ GaCl_3 \rightarrow 3\ (Sb_7Te_8)[GaCl_4]_2[Ga_2Cl_7]_3 \quad (2)$$
$$16\ Sb + 24\ Te + 5\ SbCl_3 + 3\ NaCl + 3\ GaCl_3 \rightarrow 3\ Na(Sb_7Te_8)[GaCl_4]_6 \quad (3)$$
$$16\ Sb + 24\ Te + 5\ SbCl_3 + 3\ AgCl + 3\ GaCl_3 \rightarrow 3\ Ag(Sb_7Te_8)[GaCl_4]_6 \quad (4)$$
$$8\ Sb_2Te_3 + 5\ SbCl_3 + 18\ GaCl_3 + 3\ CuCl \rightarrow 3\ Cu(Sb_7Te_8)[GaCl_4]_6 \quad (5)$$

It turned out as essential for the success of the reactions to use $SbCl_3$ in double excess with respect to the amount of Sb and Te and to add a metal monochloride like LiCl, NaCl, InCl, CuCl, AgCl or antimony(III) oxide. When using stoichiometric amounts of $SbCl_3$, compounds containing the $(Sb_7Te_8)^{5+}$ cluster were formed only in very small yields. In the absence of the monochlorides, the compounds were not formed at all. In the case of $(Sb_7Te_8)[GaCl_4]_2[Ga_2Cl_7]_3$ and $(Sb_7Te_8)[GaCl_4]_3[Ga_2Cl_7]_2$, the monovalent cations are not incorporated into the structure of the two chloridogallate salts. The nature of the metal monochloride influences the product formation, as with NaCl $(Sb_7Te_8)[GaCl_4]_3[Ga_2Cl_7]_2$ and with CuCl or InCl $(Sb_7Te_8)[GaCl_4]_2[Ga_2Cl_7]_3$ was isolated. In the cases of $Na(Sb_7Te_8)[GaCl_4]_6$, $Ag(Sb_7Te_8)[GaCl_4]_6$ and $Cu(Sb_7Te_8)[GaCl_4]_6$, Na^+, Ag^+ and Cu^+ are embedded in the structures. The role of the metal monochlorides as additives in the reactions is not fully understood. One effect of the addition of MCl is the lowering of the acidity of the $GaCl_3$ melts caused by an acid-base reaction leading to $M[GaCl_4]$ and $M[Ga_2Cl_7]$. Sb_2O_3 has pesumably a similar effect on the entire melt due to dissolving O^{2-} anions. Without this adjuvant, $(Sb_7Te_8)[GaCl_4]_2[Ga_2Cl_7]_3$ is formed at the applied temperature. In comparison with the isotypic sodium and silver congeners, the copper(I) containing compound crystallizes in much lower yield. Only a few, relatively big crystals are formed in the ampoule besides the residual solidified melt. No other crystalline byproducts could be isolated.
Tetraphenylphosphonium chloride turned out as quite effective, as it lowers the viscosity of the corresponding melts.

2.1.3 Crystal Structures of Compounds Containing the $(Sb_7Te_8)^{5+}$ Cluster

The crystal structures of $(Sb_7Te_8)[GaCl_4]_3[Ga_2Cl_7]_2$, $(Sb_7Te_8)[GaCl_4]_2[Ga_2Cl_7]_3$ (Fig. 2.1.3.1), $Na(Sb_7Te_8)[GaCl_4]_6$, $Ag(Sb_7Te_8)[GaCl_4]_6$ and $Cu(Sb_7Te_8)[GaCl_4]_6$ all consist of double cube shaped $(Sb_7Te_8)^{5+}$ cluster cations and chloridogallate anions. The crystallographic data are shown in Tab. A 5.2.1 - A 5.2.3 in the appendix.

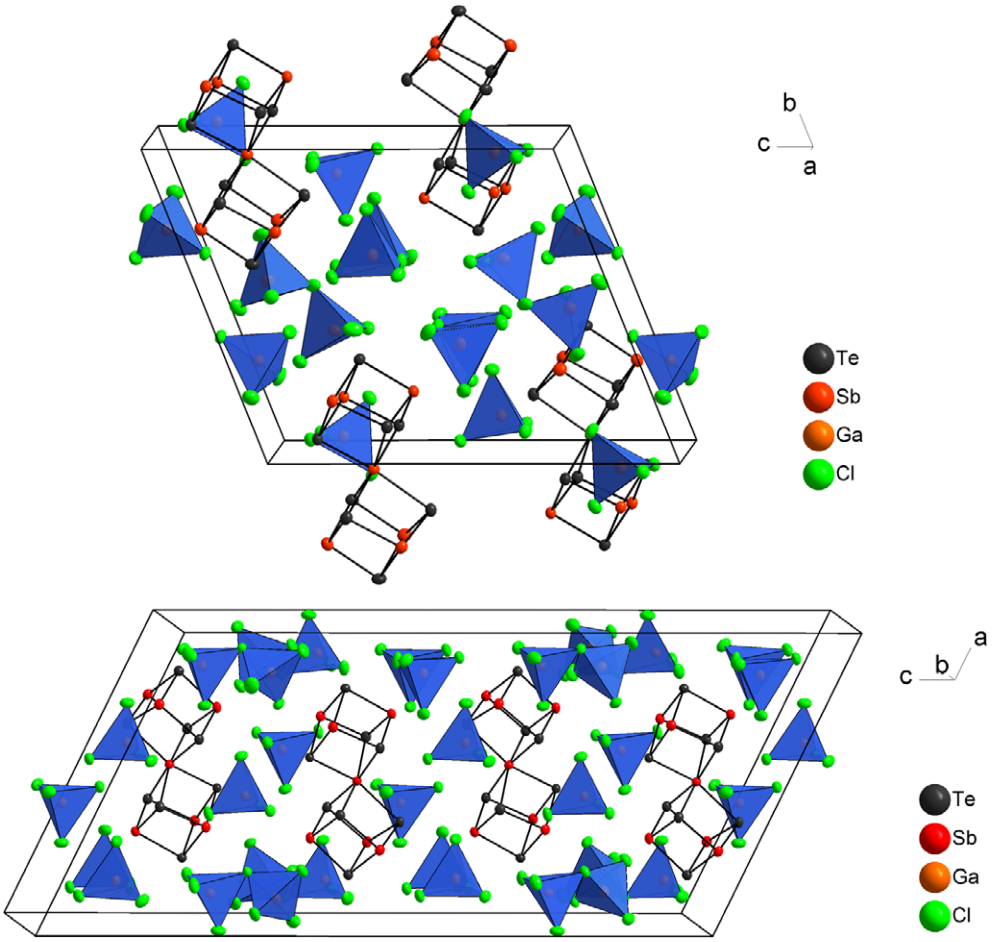

Fig. 2.1.3.1 The unit cells of the structures of $(Sb_7Te_8)[GaCl_4]_3[Ga_2Cl_7]_2$ (top) and $(Sb_7Te_8)[GaCl_4]_2[Ga_2Cl_7]_3$ (bottom). The $[GaCl_4]^-$ and $[Ga_2Cl_7]^-$ ions are represented by discrete tetrahedra and double-tetrahedra. Atoms are represented by thermal ellipsoids scaled to include a probability of 70 %.

The chloridogallate anions in all structures are almost regular tetrahedra $[GaCl_4]^-$ or double tetrahedra $[Ga_2Cl_7]^-$. The bond lengths and angles within the anions are within normal boundaries, ranging from 2.11(1) to 2.37(1) Å for Ga–Cl and from 2.09(1) to 2.18(1) Å for Al–Cl. The Cl–Ga–Cl and Cl–Al–Cl angles deviate maximally by 11.71° from the ideal tetrahedron angle of 109.45°. These parameters are in line with those found for the anions in $K[GaCl_4]$[50] and $K[Ga_2Cl_7]$.[51]

Fig. 2.1.3.1 shows the triclinic unit cell of $(Sb_7Te_8)[GaCl_4]_2[Ga_2Cl_7]_3$, which includes two formula units, and the monoclinic unit cell of $(Sb_7Te_8)[GaCl_4]_3[Ga_2Cl_7]_2$, which contains four formula units. The ratio of tetrachloridogallate to heptachloridodigallate anions is the significant difference between the two compounds. Formally, one $[GaCl_4]^-$ anion in $(Sb_7Te_8)[GaCl_4]_2[Ga_2Cl_7]_3$ is replaced by a dinuclear $[Ga_2Cl_7]^-$ ion in $(Sb_7Te_8)[GaCl_4]_3[Ga_2Cl_7]_2$. The crystal structures of $Na(Sb_7Te_8)[GaCl_4]_6$ and $Ag(Sb_7Te_8)[GaCl_4]_6$ are isotypic. The unit cell of the sodium containing structure is shown in Fig. 2.1.3.2. The Na^+ and Ag^+ ions that are additionally embedded in the structure are coordinated by Cl atoms of surrounding $[GaCl_4]^-$ ions.

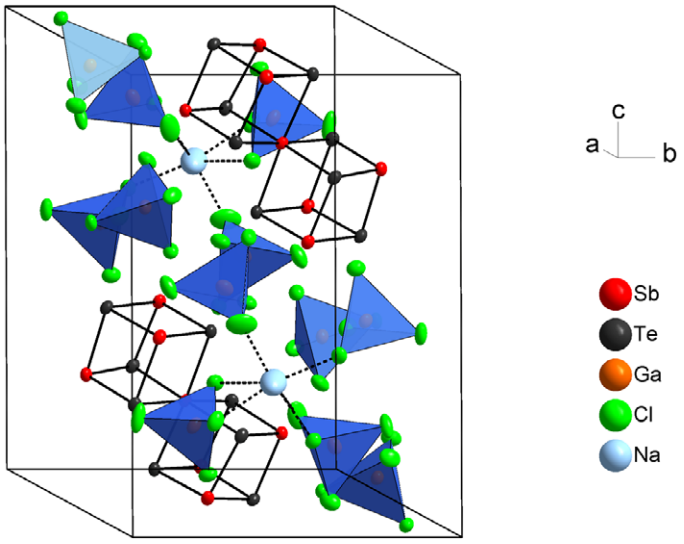

Fig. 2.1.3.2 The unit cell of the structure of $Na(Sb_7Te_8)[GaCl_4]_6$ at 100 K. The $[GaCl_4]^-$ ions are represented by discrete tetrahedra. The atoms are represented by thermal ellipsoids scaled to include a probability of 60 %.

The high charge of the polycation and the low charge of the chloridogallate anions cause a high anion to cation ratio in all compounds. As a consequence, the large polycationic clusters gain high coordination numbers by surrounding anions in the crystal structures. If Sb···Cl and Te···Cl distances up to 4 Å are taken into consideration, the cation in the structure of $(Sb_7Te_8)[GaCl_4]_2[Ga_2Cl_7]_3$ is coordinated by 16 anions, six $[GaCl_4]^-$ and ten $[Ga_2Cl_7]^-$ ions (Fig. 2.1.3.3). In the structure of $(Sb_7Te_8)[GaCl_4]_3[Ga_2Cl_7]_2$, the respective coordination number is 16 (nine $[GaCl_4]^-$ and seven $[Ga_2Cl_7]^-$ ions), and in the structures of $Na(Sb_7Te_8)[GaCl_4]_6$, $Na(Sb_7Te_8)[GaCl_4]_6$ and $Cu(Sb_7Te_8)[GaCl_4]_6$, 18 $[GaCl_4]^-$ anions surround each cation.

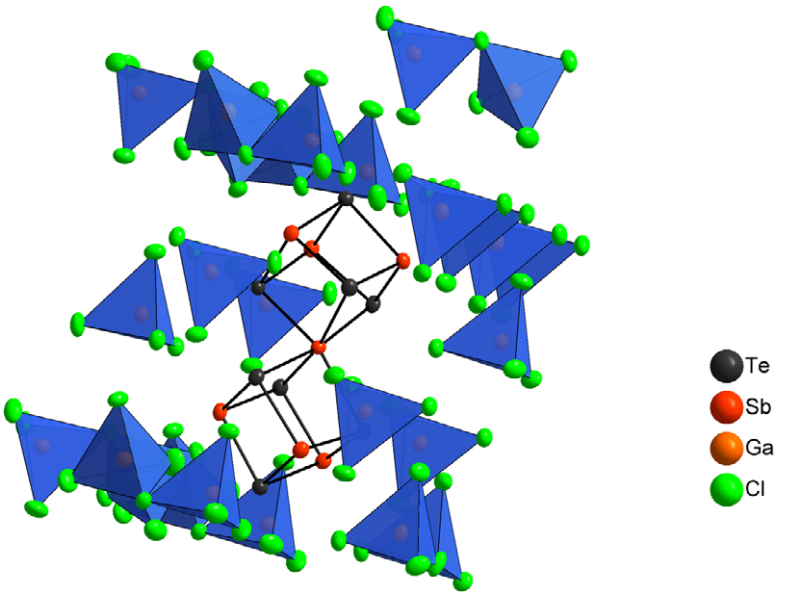

Fig. 2.1.3.3 The coordination sphere of the $(Sb_7Te_8)^{5+}$ cluster by surrounding $[GaCl_4]^-$ and $[Ga_2Cl_7]^-$ ions in the structure of $(Sb_7Te_8)[GaCl_4]_2[Ga_2Cl_7]_3$. The atoms are represented by thermal ellipsoids scaled to include a probability of 80 %. The $[GaCl_4]^-$ and $[Ga_2Cl_7]^-$ ions are shown as discrete tetrahedra and double tetrahedra.

The other coordination spheres of the $(Sb_7Te_8)^{5+}$ clusters are shown in the appendix in Figs. A 5.6.1 - 5.6.4.

2.1.4 The $(Sb_7Te_8)^{5+}$ Polycationic Cluster

The $(Sb_7Te_8)^{5+}$ cations all crystal structures have the shape of two distorted cubes sharing one corner (Fig. 2.1.4.1).

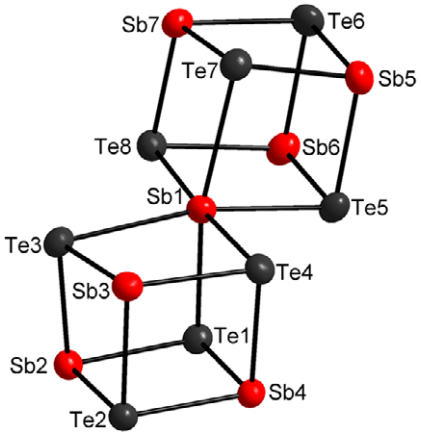

Fig. 2.1.4.1 The $(Sb_7Te_8)^{5+}$ cluster in the crystal structure of $(Sb_7Te_8)[GaCl_4]_2[Ga_2Cl_7]_3$. The atoms are represented by thermal ellipsoids scaled to include a probability of 80 %.

The assignment of Sb and Te to the respective atom positions is ensured by the statistical interpretation of the occupation factors based on the diffraction data (*vide supra*) (Fig. 2.1.4.2) and is in line with the atomic arrangement in $(Sb_7S_8Br_2)^{3+}$, where the significant difference in the scattering factors between Sb and S leads to an unequivocal assignment of the two kinds of atoms within this structurally closely related cluster ion.[37]

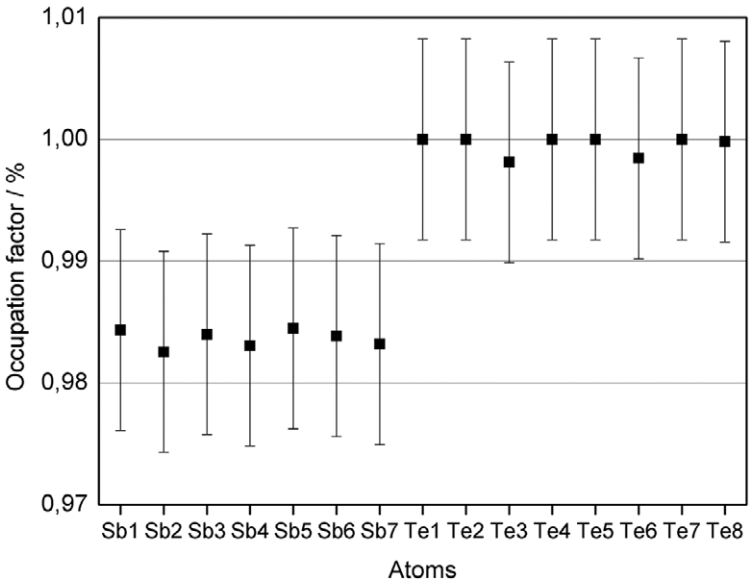

Fig. 2.1.4.2 Graphical representation of the Sb/Te atom assignments in the structure of $(Sb_7Te_8)[GaCl_4]_2[Ga_2Cl_7]_3$. Depicted are the obtained occupation factors of the atomic sites of the $(Sb_7Te_8)^{5+}$ cluster when the structure is refined with all atom positions assumed to be occupied by Te exclusively. The standard deviations are indicated by vertical bars.

Representations of occupation factors of other $(Sb_7Te_8)^{5+}$ clusters are shown in Figs. A 5.3.1 - A 5.3.4 in the appendix.

The clusters are located in general positions for $(Sb_7Te_8)[GaCl_4]_3[Ga_2Cl_7]_2$, $(Sb_7Te_8)[GaCl_4]_2[Ga_2Cl_7]_3$ and the low temperature forms of $Na(Sb_7Te_8)[GaCl_4]_6$, $Ag(Sb_7Te_8)[GaCl_4]_6$ with all 15 atoms being symmetrically independent. In $Cu(Sb_7Te_8)[GaCl_4]_6$ and the higher symmetric room temperature forms of $Na(Sb_7Te_8)[GaCl_4]_6$ and $Ag(Sb_7Te_8)[GaCl_4]_6$, the $(Sb_7Te_8)^{5+}$ cation is located in an inversion centre at the position of the central Sb atom, giving the cluster C_i symmetry.

The analysis of the Sb···Cl and Te···Cl distances between the Sb and Te atoms of the cluster and the Cl atoms of the coordinating chloridogallate ions also supports the selected Sb/Te assignment (Tabs. A 5.5.1 - A 5.5.5). There is a clear distinction between two sets of distances, beginning at 3.07 Å for Sb···Cl and at 3.43 Å for Te···Cl (Tabs. A 5.5.1 - 5.5.5). It has previously been observed on all members of the series of the cube shaped cationic clusters $(Bi_4Ch_4)^{4+}$ that the distances between the pentele atoms and the coordinating atoms of the $[AlCl_4]^-$ anions are significantly shorter than the respective chalcogen···chloride distances.[29,30] The slightly higher electronegativity of Te diminishes the positive charge on the chalcogen atoms and enhances the ionic interaction between the anions and the Sb atoms.

The atoms in the clusters are arranged in alternating order, which maximizes the number of heteronuclear bonds, enhancing the polar character of the bonds. The central Sb atom is six-fold coordinated in a distorted octahedral environment; all other atoms have three-fold coordination in trigonal pyramidal shape with angles close to 90°. The Sb–Te bond lengths fall in two groups. All bonds involving the central atom Sb1 range between 2.90(1) and 3.23(1) Å with an average of 3.04 Å. The respective Sb–Te bonds involving only three-fold coordinated atoms in the periphery of the two cube subunits are in the range of 2.80(1) to 2.91(1) Å with an average of 2.86 Å (compare Tabs. A 5.4.1 - A 5.4.5). As shown in Fig. 2.1.4.4, the $(Sb_7Te_8)^{5+}$ cations are distorted to a different amount (see Fig. 2.1.4.1 for the numbering).

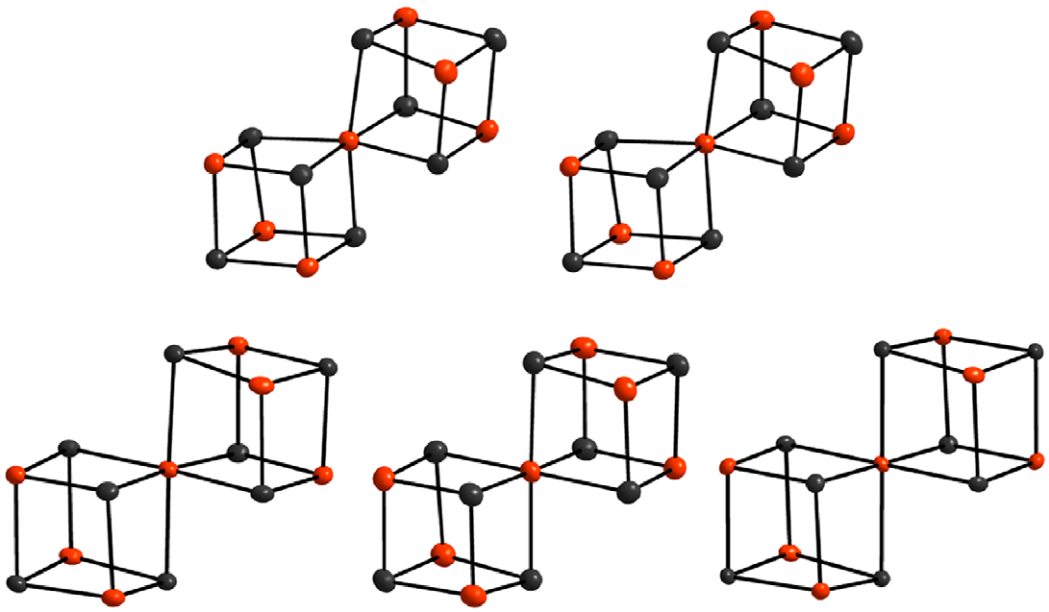

Fig. 2.1.4.4 The $(Sb_7Te_8)^{5+}$ clusters in the structures of $(Sb_7Te_8)[GaCl_4]_3[Ga_2Cl_7]_2$ (123 K, top left), $(Sb_7Te_8)[GaCl_4]_2[Ga_2Cl_7]_3$ (123 K, top right), $Na(Sb_7Te_8)[GaCl_4]_6$ (100 K, bottom left), $Ag(Sb_7Te_8)[GaCl_4]_6$ (123 K, bottom middle) and $Cu(Sb_7Te_8)[GaCl_4]_6$ (100 K, bottom right). The atoms are represented by thermal ellipsoids scaled to include a probability of 80 %.

In the structures of $Na(Sb_7Te_8)[GaCl_4]_6$, $Ag(Sb_7Te_8)[GaCl_4]_6$ and $Cu(Sb_7Te_8)[GaCl_4]_6$, the clusters are quite regular with angles deviating not more than by 5° from rectangularity or linearity, thus nearly showing the highest possible local symmetry D_{3d}. In the structure of $(Sb_7Te_8)[GaCl_4]_2[Ga_2Cl_7]_3$, the distortion is substantial and affects mainly the bonds around the central atom Sb1, where Te–Sb–Te angle deviations up to 17° are present. Additionally, the Sb–Te bonds are separated into three short and three long bonds (Sb1–Te1 2.903(1), Sb1–Te5 2.960(1), Sb1–Te8 2.951(1), Sb1–Te3 3.135(1), Sb1–Te4 3.155(1), Sb1–Te7 3.23(1) Å) with the short and long bonds in *trans* position, giving the Sb1 atom a 3+3 coordination environment (compare Tabs. A 5.4.1 - 5.4.5). Apparently, the long bonds around Sb1 are weak and the angular distortion is caused by the crystal packing and the interaction with the anions. The structural parameters in the $(Sb_7Te_8)^{5+}$ cluster in $(Sb_7Te_8)[GaCl_4]_3[Ga_2Cl_7]_2$ corresponds to the parameters found in $(Sb_7Te_8)[GaCl_4]_2[Ga_2Cl_7]_3$.

The bonding within the $(Sb_7Te_8)^{5+}$ cationic cluster can be described by different models. Treating the cluster as a Zintl ion works only for the peripheral, three-fold coordinated atoms. Assuming an electron octet, each atom forms three two-electron covalent bonds and carries one lone pair. For Sb, this situation implies an uncharged state, while for Te the formal charge is +1. All eight Te atoms are three-fold coordinated, resulting in eight positive charges. Regarding the central six-coordinate Sb atom as bonded with six covalent bonds makes it necessary to assume a 14 valence electron shell including one lone pair. The electron counting rules assign a formal charge of −3 to this Sb atom, so the overall charge +5 for the cluster is explained by this method. The degree of hypervalency for the central Sb atom, however, is overstressed by this model. A normal valency for the central Sb atom with an electron octet can only be achieved with three bonds and one lone pair. This leads to the setup of two electronic resonance forms (Fig. 2.1.4.5), each consisting of a $(Sb_4Te_4)^{4+}$ cube and a heptatomic $(Sb_3Te_4)^{+}$ unit.

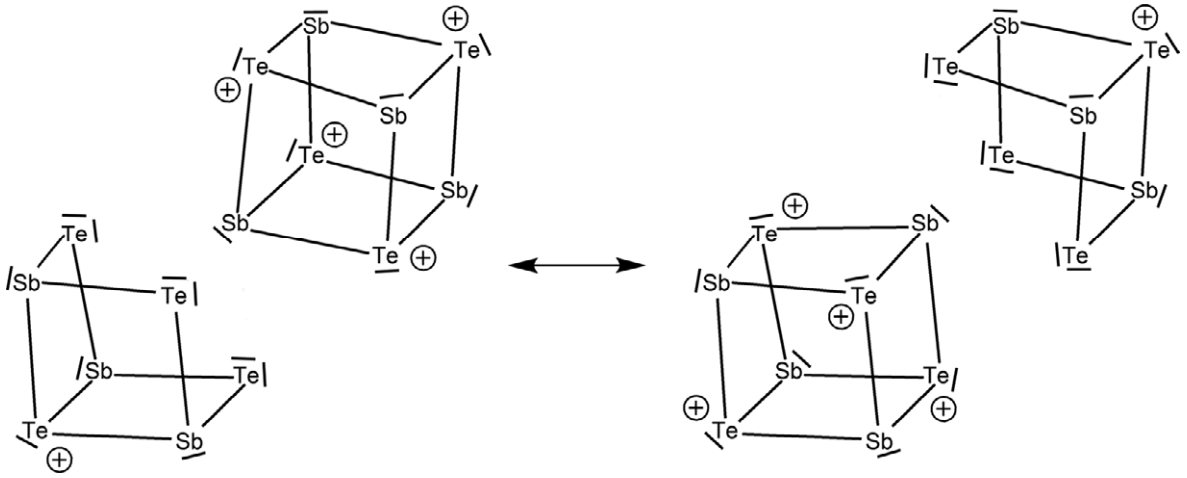

Fig. 2.1.4.5 Two resonance formulae for the $(Sb_7Te_8)^{5+}$ cluster ion. According to this model, the six bonds of the central antimony atom are understood as the resonance of two sets of three two center-two electron bonds.

According to this model, the bond order of each of the six Sb1–Te bonds is 0.5, which is in line with the elongated bond lengths. The almost undistorted cluster as found in the structures of $Na(Sb_7Te_8)[GaCl_4]_6$, $Ag(Sb_7Te_8)[GaCl_4]_6$ and $Cu(Sb_7Te_8)[GaCl_4]_6$ can be understood by an equal contribution of both forms. The distorted cluster as present in the structure of $(Sb_7Te_8)[GaCl_4]_2[Ga_2Cl_7]_3$ contains a higher contribution of one of the two forms, which leads to an unsymmetrical 3+3 coordination at the central Sb atom and explains the angular distortions.

Density functional calculations of the $(Sb_7Te_8)^{5+}$ polycationic cluster at the B3LYP/DEF2-TZVPPD level of theory corroborate the picture stated below.

The molecular orbitals describing the binding between the central Sb atom and its bond partners comprise three bonding, three non-bonding, and three antibonding orbitals, leading to an overall bond order of 0.5 in terms of classical three-centre, four-electron bonds (Fig. 2.1.4.6). Analysis of the wave function using the natural bond orbital partitioning scheme reveals a best Lewis formula describing the corresponding bonds using three natural bond orbitals between the central Sb atom and three adjacent Te atoms and three lone pair natural orbitals of appropriate symmetry at the Te atoms located *trans* to the former ones forming three-centre, four-electron natural hyperbond orbitals. These hyperbonds are equally comprised from the NBO and the lone pair orbitals. According to NBO theory, the six Sb–Te bonds are polarised towards the Te atoms (65 vs. 35 %) and are build up from almost pure *p* atomic orbitals. The calculated NPA charges of the central Sb atom (0.00) versus the six connected Te atoms (+0.06), the three-coordinate Sb atoms (+0.71) and the two Te atoms at the top (+0.20) are in perfect agreement with the Lewis formula depicted in Fig. 2.1.4.5, as well as the results of the resonance calculations.

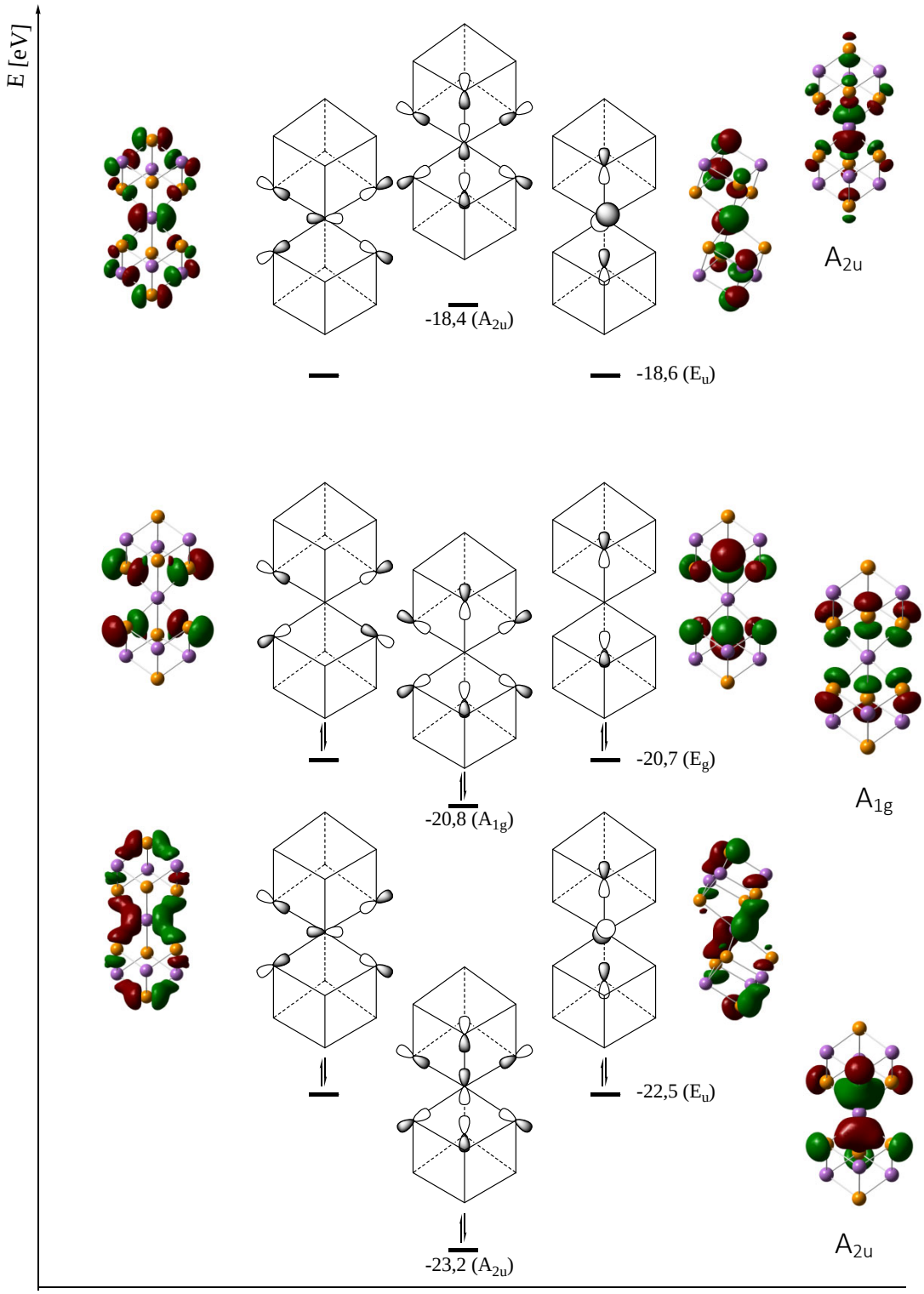

Fig. 2.1.4.6 MO scheme of the $(Sb_7Te_8)^{5+}$ cluster in the HOMO-LUMO region and the shape of the respective MOs. Energies are given in electron volt. The symmetry races given in parentheses correspond to the D_{3d} point group of the cluster.*

* The theoretical treatment of the $(Sb_7Te_8)^{5+}$ cluster was performed by Dr. Gregor Schnakenburg.

The structure motive of the $(Sb_7Te_8)^{5+}$ cluster is only new as a discrete cluster. The double cube motive can already be found in the structure of Sb_2Te_3.[52] The layered structure of this compound prevents the formation of the complete polyhedron. One corner of the Sb_7Te_8- fragment occupied by antimony is missing in the structure of Sb_2Te_3 (Fig. 2.1.4.7).

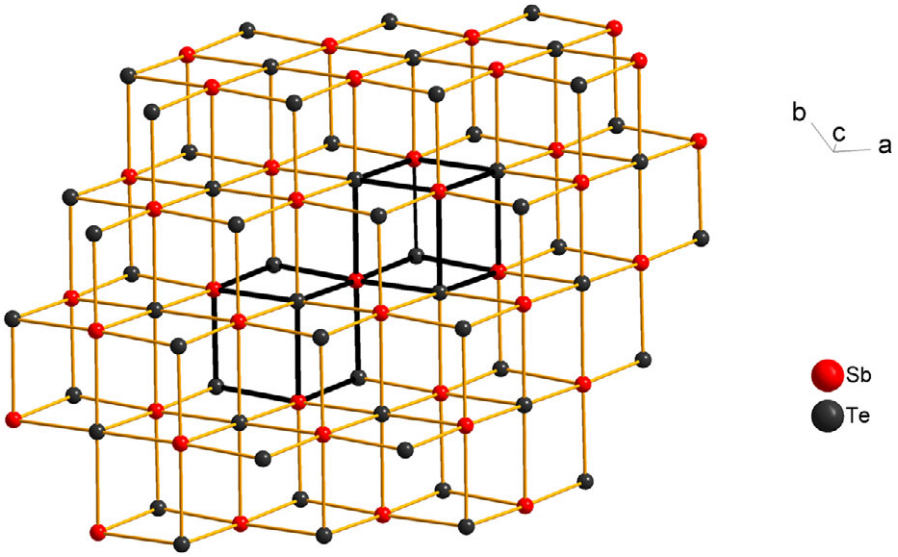

Fig. 2.1.4.7 The crystal structure of Sb_2Te_3.[54] The atoms are represented by thermal ellipsoids scaled to include a probability of 90 %. By bold black lines a Sb_7Te_8 fragment is emphasized.

2.1.5 The Phase Transition of $Ag(Sb_7Te_8)[GaCl_4]_6$

$Na(Sb_7Te_8)[GaCl_4]_6$ is isotypic to $Na(Sb_7Te_8)[AlCl_4]_6$ [31], which undergoes a phase transition at 177 K. Due to a high similarity of the two compounds an examination for a phase transition was not performed for the chloridogallate.

$Ag(Sb_7Te_8)[GaCl_4]_6$ is the isotypic silver cognener of $Na(Sb_7Te_8)[MCl_4]_6$ (M = Al, Ga). The $(Sb_7Te_8)^{5+}$ cluster is rather regular. The angular distortions from linearity and rectangularity are throughout less than 9°. The structure is close to the highest possible point symmetry D_{3d}. Fig. 2.1.5.1 shows the unit cell of $Ag(Sb_7Te_8)[GaCl_4]_6$ at 123 K in the setting with a = 12.246(1) Å, b = 12.780(1) Å, c = 18.297(1) Å, α = 91.755(1)°, β = 90.553(1)° and γ = 105.899(1)°.

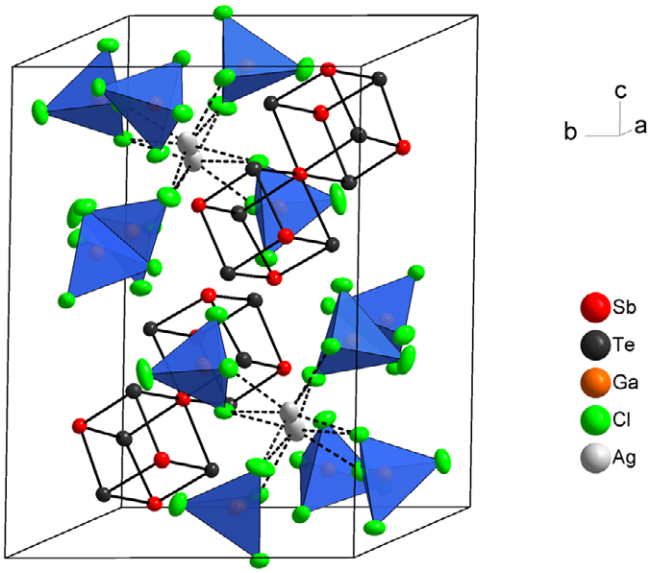

Fig. 2.1.5.1 The original unit cell of $Ag(Sb_7Te_8)[GaCl_4]_6$ at 123 K. The atoms are represented by thermal ellipsoids scaled to include a probability of 70 %. The $[GaCl_4]^-$ ions are shown as discrete tetrahedra. Ag···Cl contacts up to 3.3 Å are shown with dashed lines.

In analogy to $Na(Sb_7Te_8)[GaCl_4]_6$, the Ag^+ containing compound undergoes a phase transition in the solid state. In the Na^+ containing chlorido aluminate congener the phase transition of mainly second order with a critical temperature at T_c = 177 K is accompanied by a order-disorder transition of the Na^+ cations, which below T_c occupy two separate positions, but show dynamical disorder above T_c. An analogous transition with cutting in half the unit cell volume was found for $Ag(Sb_7Te_8)[GaCl_4]_6$ after transforming the original low temperature cell (93 K) by the operation (0 0 -1/0 1 0/1 -1 1) (Fig. 2.1.5.2) and warming the crystal until 183 K. The cell transformation above the phase transition is performed by the operation (-1 1 0 / 1 1 1 / 0 -1 -1).* Fig. 2.1.5.2 shows the unit cells of $Ag(Sb_7Te_8)[GaCl_4]_6$ above and below the critical temperature and Tab. 2.1.5.1 the transformed unit cell parameters, respectively.

* Transformation matrixes were taken from Ref. [31] and verified for the chloridogallate structures with KPLOT. [55]

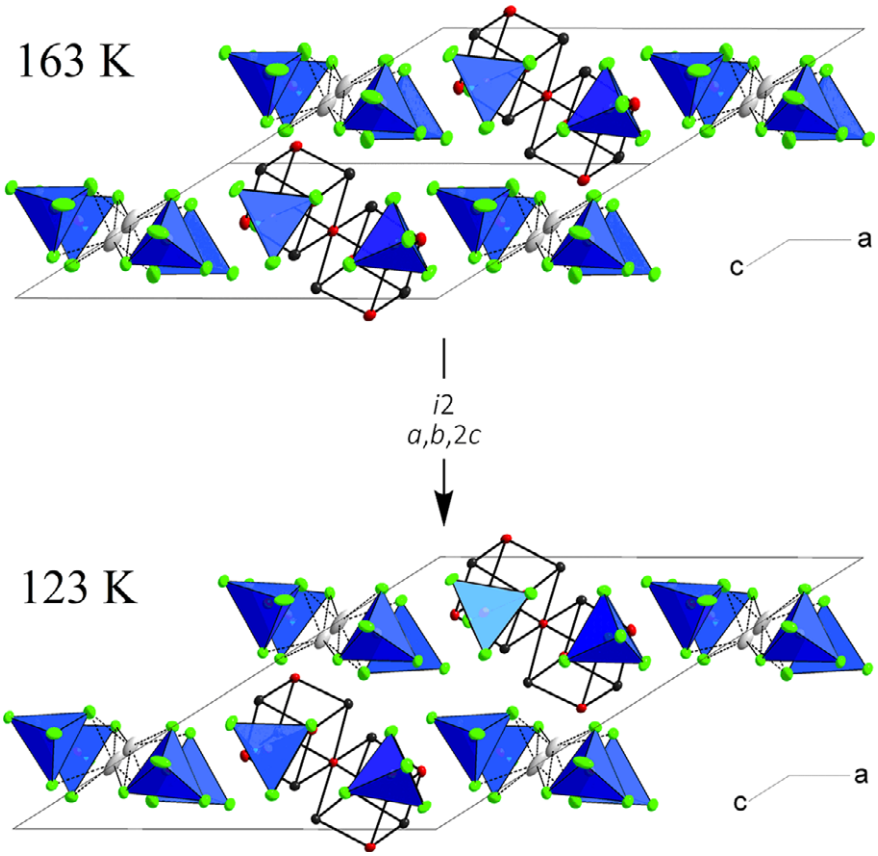

Fig. 2.1.5.2 The structure of $Ag(Sb_7Te_8)[GaCl_4]_6$ at 163 K (top) and 123 K (bottom). For 163 K two unit cells are shown. The transition is of the *isomorphic* type with index 2 (*i*2) under doubling of one unit cell axis and doubling of the cell volume and retention of the crystal symmetry ($P\bar{1}$ in both forms).

Tab. 2.1.5.1 Original and transformed unit cell parameters of $Ag(Sb_7Te_8)[GaCl_4]_6$ at 123 and 163 K. Standard deviations given in brackets refer to the last significant digit.

Unit cell (123K)	Unit cell (transf.)
a = 12.2469(2)	*a* = 18.2976(3)
b = 12.7805(1)	*b* = 12.7806(2)
c = 18.2967(3)	*c* = 26.9053(4)
α = 91.755(1)	α = 125.369(1)
β = 90.553(1)	β = 132.064(1)
γ = 105.899(1)	γ = 91.756(1)
V = 2752.49(7)	V = 2752.47(7)

(163 K)	Unit cell (transf.)
a = 11.665(1)	*a* = 18.3421(7)
b = 12.0847(5)	*b* = 12.7815(4)
c = 12.2879(13)	*c* = 13.5212(5)
α = 111.987(6)	α = 125.385(2)
β = 111.325(7)	β = 132.236(1)
γ = 101.325(7)	γ = 91.585(2)
V = 1383.7(2)	V = 1383.71(1)

The critical temperature for $Ag(Sb_7Te_8)[GaCl_4]_6$ is lower and was determined to 143.5 K. All reflections *hkl* with *l* odd of the low temperature form diminish smoothly in intensity with rising temperature and vanish completely at 143.5 K. The intensities of three selected, strong superstructure reflections of the low temperature form of $Ag(Sb_7Te_8)[GaCl_4]_6$ (7 -5 7, 4 -11 15, and 14 2 -17, all with *l* odd) were monitored over a larger temperature interval. Applying the Landau theory for second order solid state

transitions $I(T) \propto \left(\frac{T_c - T}{T_c}\right)^{\beta}$ [53], critical exponents β = 0.5(1) gave the best fit to the experimental data, indicating long range ordering processes (Fig. 2.1.5.3).

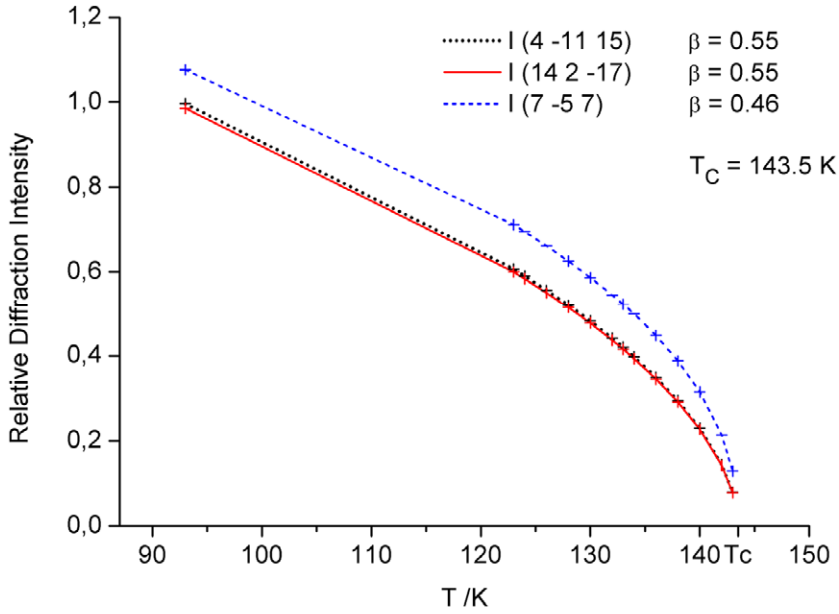

Fig. 2.1.5.3 The experimental diffraction intensity of three selected reflections as a function of temperature for $Ag(Sb_7Te_8)[GaCl_4]_6$. The intensities are normalized to unity for the lowest measured temperature (93 K). The vertical bars indicate the intensity standard deviations, horizontal bars the temperature uncertainty of 2 K. Approaching the critical temperature of 143.5 K, diffraction intensities diminish to 10 % of the initial values and then vanish completely within a temperature interval of less than 1 K.

Fig. 2.1.5.4 and 2.1.5.5 show the simulated precession diagrams of $Ag(Sb_7Te_8)[GaCl_4]_6$ at 123 and 163 K. At 163 K every second row of reflections in the *c** direction disappeared.

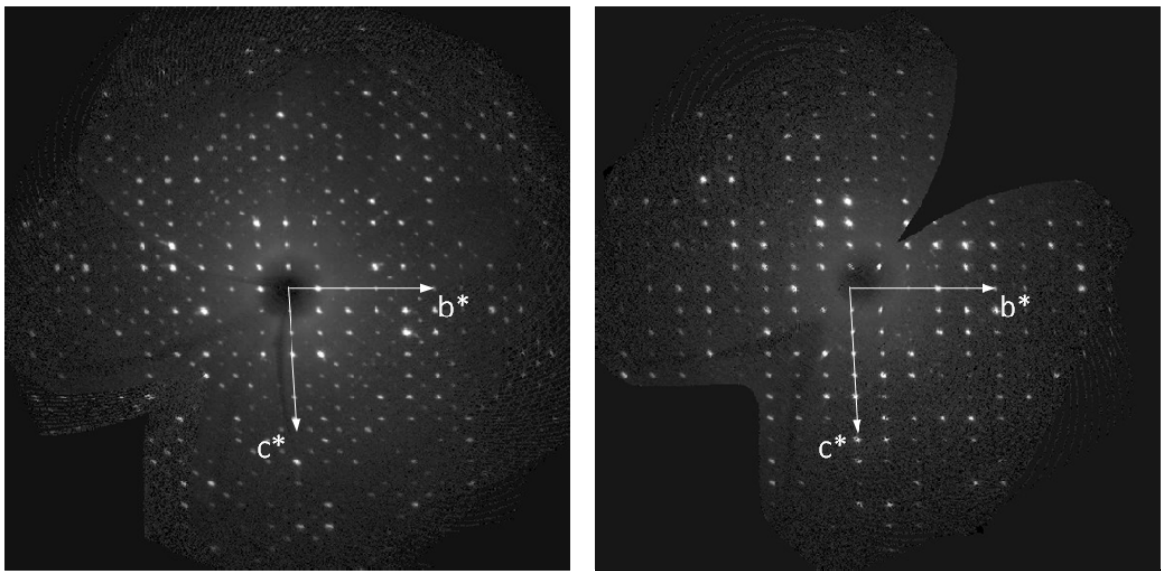

Fig. 2.1.5.4 Simulated precession images, derived from the area detector data, of the 0*kl* layer of $Ag(Sb_7Te_8)[GaCl_4]_6$ at 123 (left) and 163 K (right).

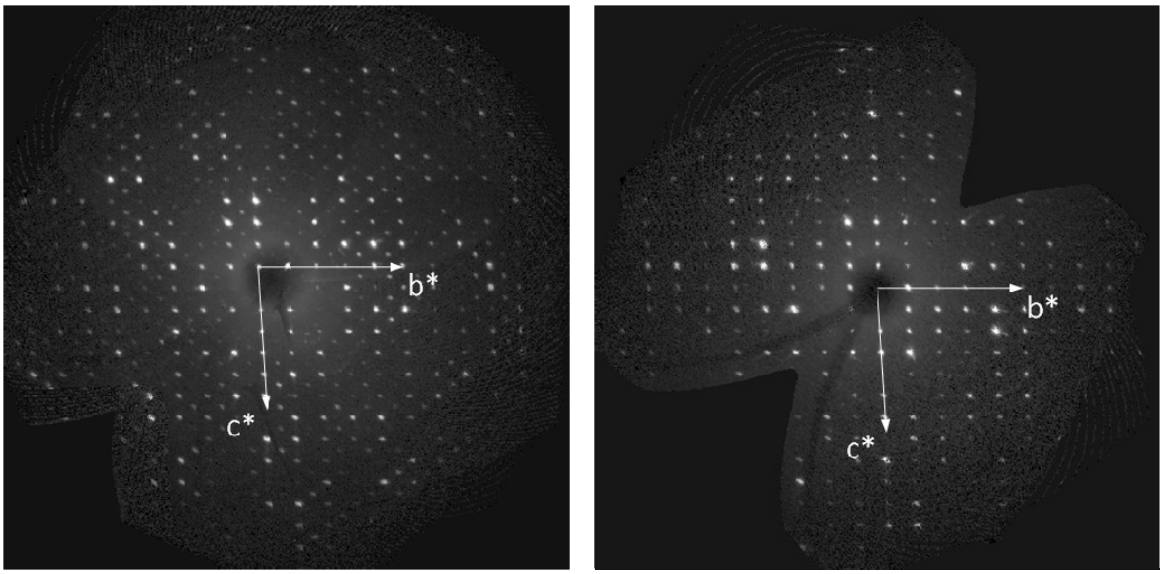

Fig. 2.1.5.5 Simulated precession images, derived from the area detector data, of the 1*kl* layer of $Ag(Sb_7Te_8)[GaCl_4]_6$ at 123 (left) and 163 K (right).

Since the requirements of a direct group-subgroup relation and a critical exponent of close to 0.5 are fulfilled, a second order transition can be assumed. There is, however, a discontinuous change in the reflection intensities close to the transition temperature. The overall mechanism is thus understood as a continuous dislocation below T_c on increasing temperature. On reaching the actual critical temperature of 177 K, the last movements of the atoms in the crystal are discontinuous and belong to a first order transition.

Fig. 2.1.5.6 shows the structural changes in the Ag^+ coordination sphere.

Above T_c the Ag^+ ion occupies two closely neighboured positions, which are symmetry related by an inversion centre and occupation factors of 50:50. Below the transition temperature, at 123 K the occupation changes to 75:25 under loss of the inversion centre. At 93 K, a third position for Ag^+ emerges, the occupation factors amount to 81:13:6. The structural changes during the phase transition are rather small and all constituents of the structure contribute by slight changes of the respective spatial orientations. Distinct effects of the phase transition are present among the Ag···Cl distances between the Ag^+ ion and the Cl atoms of the surrounding $[GaCl_4]^-$ anions (2.394(9) - 3.27(1) Å at 123 K in the low temperature form, 2.428(8) - 3.106(6) Å at 163 K in the high temperature form) and among the distance between the two split positions of the Ag^+ ion. This separation increases with rising temperature and amounts to 1.055(5) Å at 123 K, 1.129(5) Å at 163 K, and 1.133(4) Å at 183 K. Lowering the temperature leads to an increasing localisation on distinct positions. But even at 93 K, the localisation of Ag^+ is incomplete. The dynamical behaviour of the structure is manifested by structural changes, which proceed over a broad range of temperature.

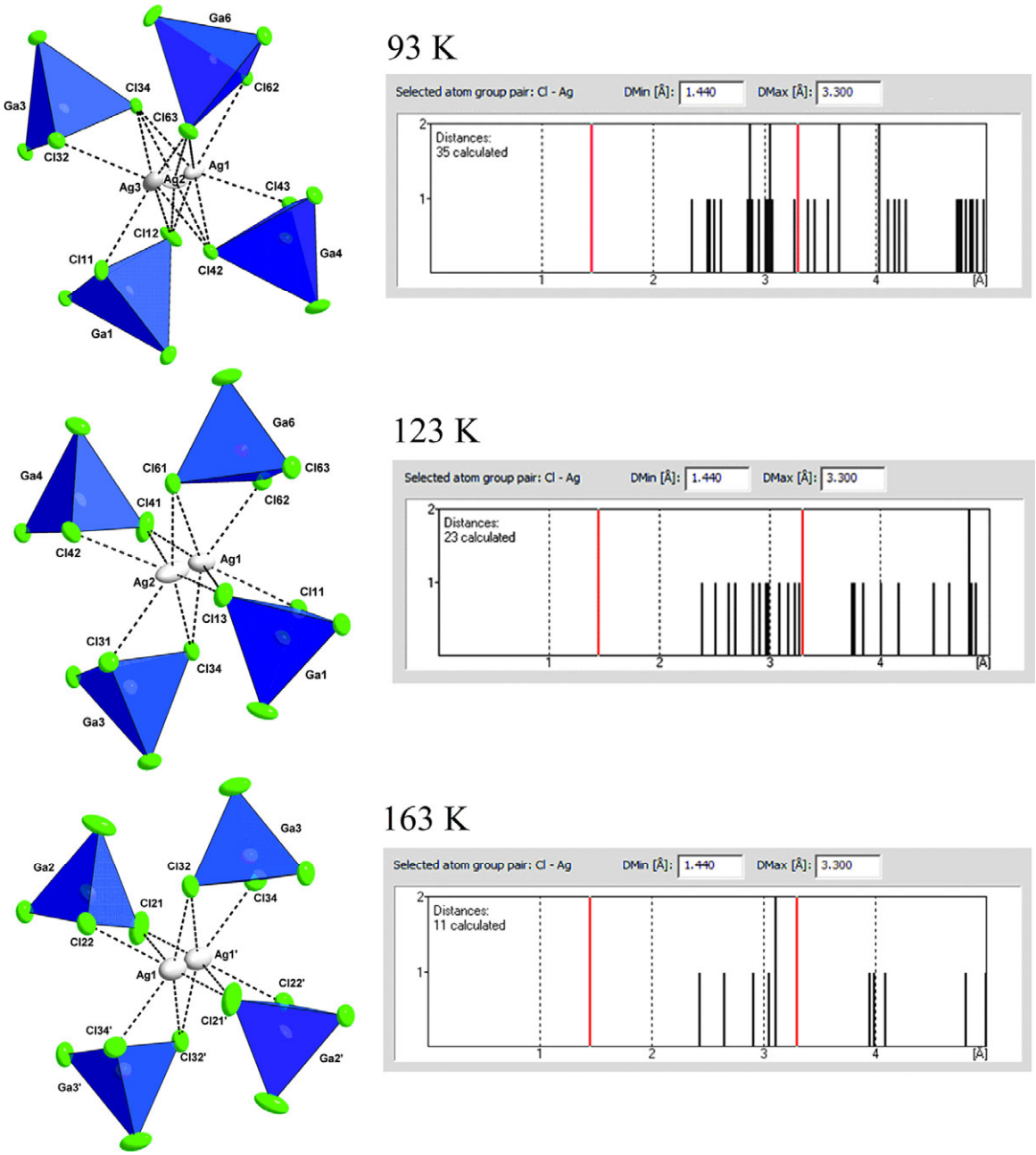

Fig. 2.1.5.6 The silver ion coordination sphere (left) and Ag···Cl contacts (right) in $Ag(Sb_7Te_8)[GaCl_4]_6$ at three different temperatures. Ag-Cl contacts are demonstrated with dashed lines. The $[GaCl_4]^-$ ions are shown as discrete tetrahedra. The atoms are represented by thermal ellipsoids scaled to include a probability of 70 %.

This might be the reason why the phase transition could not be observed as a distinct thermal effect by differential scanning calorimetry (Fig. 2.1.5.7).

The inversion centre within the $(Sb_7Te_8)^{5+}$ ion also vanishes but the structure of the cluster is not substantially altered.

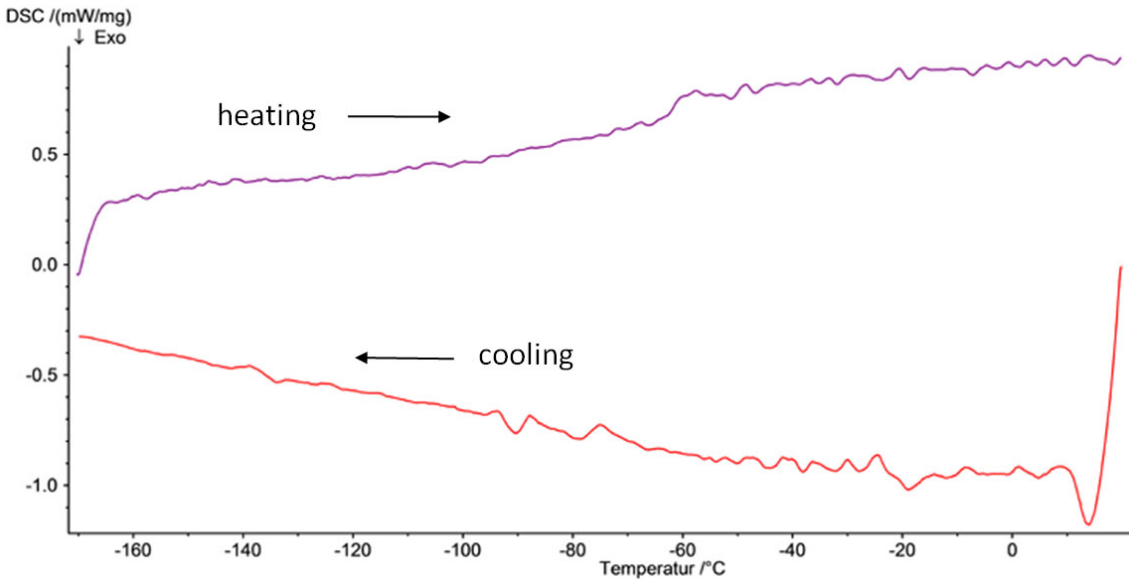

Fig. 2.1.5.7 Differential scanning calorimetric plot of $Ag(Sb_7Te_8)[GaCl_4]_6$ between 103 and 293 K. All termal effects are caused by the perfluorinated polyether FomblinY (compare Fig. A 5.1.9.1). Curve 1 (top) demonstrates the heating process, curve 2 (bottom) the cooling process.

Unfortunately the trial failed to follow the phase transition in a ^{107}Ag solid state NMR spectrum to determine the activation energy for the movement of the silver ion. The reason was a metallic layer on the crystal surfaces, which turned out in EDX measurements to be an excess of tellurium and silver. As soon as there is a paramagnetic or metallic substance in the magnetic field, the rotation frequency of the sample holder is not stable any more and and recording of spectra is hindered.

2.1.6 The Novel $[CuGa_2Cl_8]_2^-$ Anion in $Cu(Sb_7Te_8)[GaCl_4]_6$

The crystal structure of $Cu(Sb_7Te_8)[GaCl_4]_6$ (Fig. 2.1.6.1) is as a first approximation isotypic to the room temperature structures of the respective sodium and silver containing congeners $Na(Sb_7Te_8)[AlCl_4]_6$, $Na(Sb_7Te_8)[GaCl_4]_6$, and $Ag(Sb_7Te_8)[GaCl_4]_6$. The structure contains three independent tetrachlorido gallate anions, mixed antimony-tellurium clusters $(Sb_7Te_8)^{5+}$ with the shape of two connected cubes and Cu(I) ions. The polycationic cluster bears a center of symmetry at the central Sb1 atom and is fairly regular with Sb–Te bond lengths between 3.057(3) and 3.0171(3) Å around Sb1 and between 2.8225(4) and 2.8946(4) Å for the three-fold coordinated atoms in the periphery of the two cuboidal subunits (Tab. A 5.4.5). Significant distortions from the ideal D_{3d} symmetry are present among the Sb–Te–Sb and Te–Sb–Te angles, which range between 84.54(1) and 98.32(1)°.

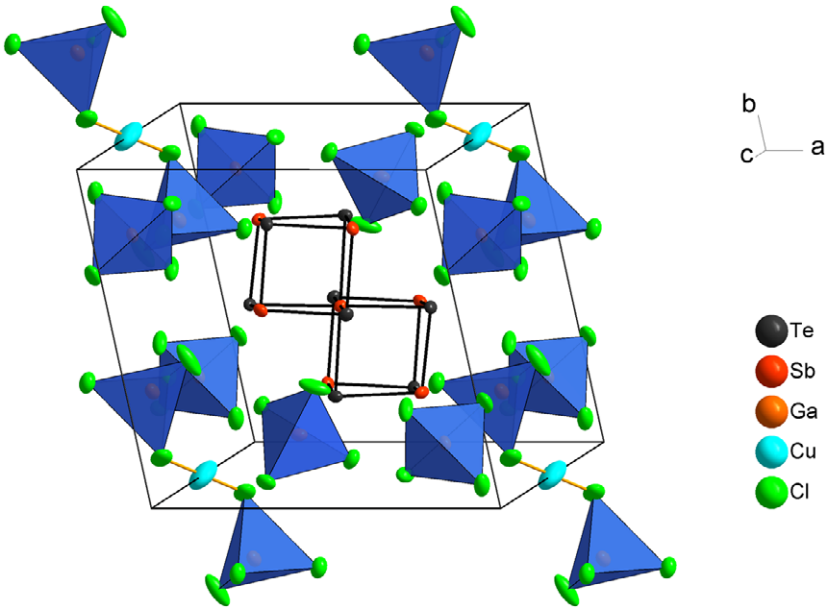

Fig. 2.1.6.1 The unit cell of the structure of $Cu(Sb_7Te_8)[GaCl_4]_6$ at 100 K. The $[GaCl_4]^-$ ions are represented by discrete tetrahedra. The atoms are represented by thermal ellipsoids scaled to include a probability of 80 %.

This representative does not show this characteristic phase transition in contrast to the predecessor compounds due to a different bonding situation of the copper(I) cation.

In all other representatives of this structure family known so far, the monovalent cation is surrounded by four neighbouring $[MCl_4]^-$ anions (M = Al, Ga). The four coordinating tetrahedral anions face towards the cation with one edge each, thus forming a distorted cube of eight Cl atoms, which contains the cation. The large coordination polyhedron allows for a dynamic dislocation of the cations. Na^+ and Ag^+ show a strong temperature dependence of their respective positions. In the structure of $Cu(Sb_7Te_8)[GaCl_4]_6$ two of the eight surrounding Cl atoms coordinate to Cu^+ with short Cu–Cl bonds of 2.188(2) Å, the other Cu–Cl distances are substantially longer (3.036(1) Å, 3.524(1) Å, 3.546(1) Å). The strength of the Cu(I) coordinative bonds corresponds to the weakening of the respective Ga–Cl bonds. Two of three symmetrically independent $[GaCl_4]^-$ anions show slight deviations from ideal tetrahedral symmetry manifested in elongated Ga–Cl bonds of those Cl atoms, which exhibit short bonds to the Cu^+ ion (Ga1–Cl11 2.228(1) Å, Ga3–Cl32 2.200(1) Å) (Fig. 2.1.6.2) All other Ga–Cl bond lengths are in the expected range between 2.136(1) and 2.188(1) Å, as found for $Na[GaCl_4]$. The two short and symmetric Cu–Cl11 bonds give rise to the presence of a covalently bound, linear dichloridocuprate(I) complex anion $[CuCl_2]^-$ in the structure of $Cu(Sb_7Te_8)[GaCl_4]_6$. The two Cu–Cl bonds are much shorter than the shortest Cu–Cl distances present in the structure of $Cu[GaCl_4]$ (2.356 Å) [55], in CuCl [56] (2.382 Å) or in $CuCl_2$ [57] (2.263 Å). The $[CuCl_2]^-$ ion is well known. It is generally linear with Cu–Cl bond lengths of averaged 2.085Å. [59] In the structure of $Cu(Sb_7Te_8)[GaCl_4]_6$, the Cu–Cl bond is elongated by only 0.1 Å. Since the $[CuCl_2]^-$ anion in $Cu(Sb_7Te_8)[GaCl_4]_6$ is coordinated by two $GaCl_3$ molecules, the entity $[Cl_3Ga\cdots Cl–Cu–Cl\cdots GaCl_3]^-$ may be understood as novel coordination unit build from a soft $[CuCl_2]^-$ anion and two strong Lewis-acidic $GaCl_3$ molecules. This unit may alternatively treated as a Cu^+ ion coordinated by two $[GaCl_4]^-$ anions $[Cl_3GaCl\cdots Cu\cdots ClGaCl_3]^-$. Due to the two strong covalent bonds the Cu^+ ions are no longer mobile, but only exhibit a pronounced thermal vibration perpendicular to the linear Cl–Cu–Cl axis (Fig. 2.1.6.2).

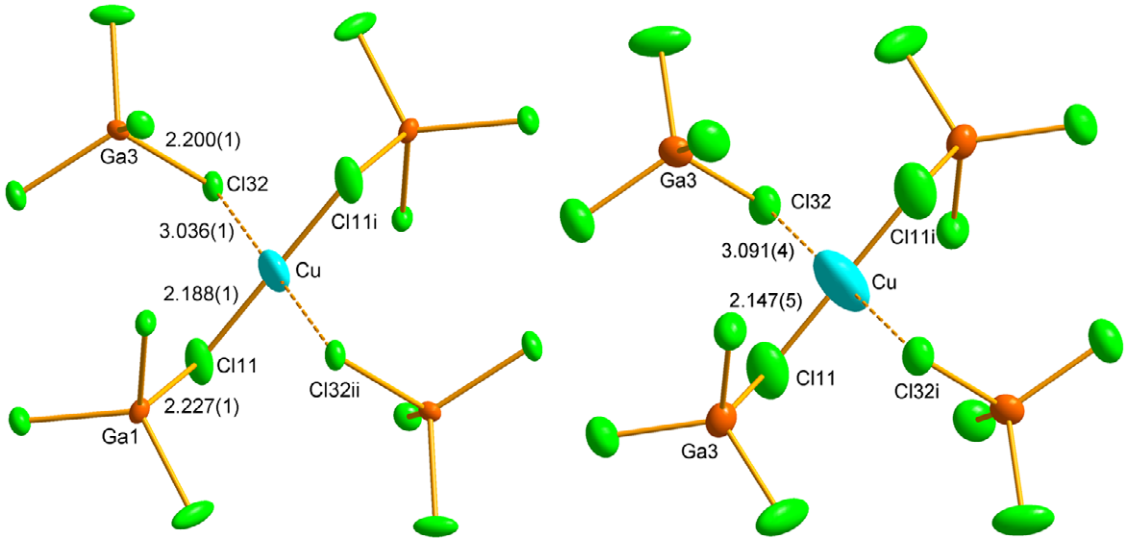

Fig. 2.1.6.2 The coordination of Cu(I) cations by $[GaCl_4]^-$ anions in the structure of $Cu(Sb_7Te_8)[GaCl_4]_6$ at 100 K (left) and 223 K (right). Symmetry code: i: 2-x, -y, 1-z, bond lengths are given in Å, long Cu···Cl bonds are drawn with dashed lines. The atoms are represented by thermal ellipsoids scaled to include a probability of 50 %.

A phase transition, as observed for the Na^+ und Ag^+ containing congeners, was not detected in the investigated temperature interval between 100 and 223 K and no change of the cell volume or vanishing superstructure reflections were observed in the simulated pecession images (Fig. 2.1.6.3). Only the expected decrease of intensity with increasing temperature due to the enhanced thermal motion of the atoms within the crystal was visible.

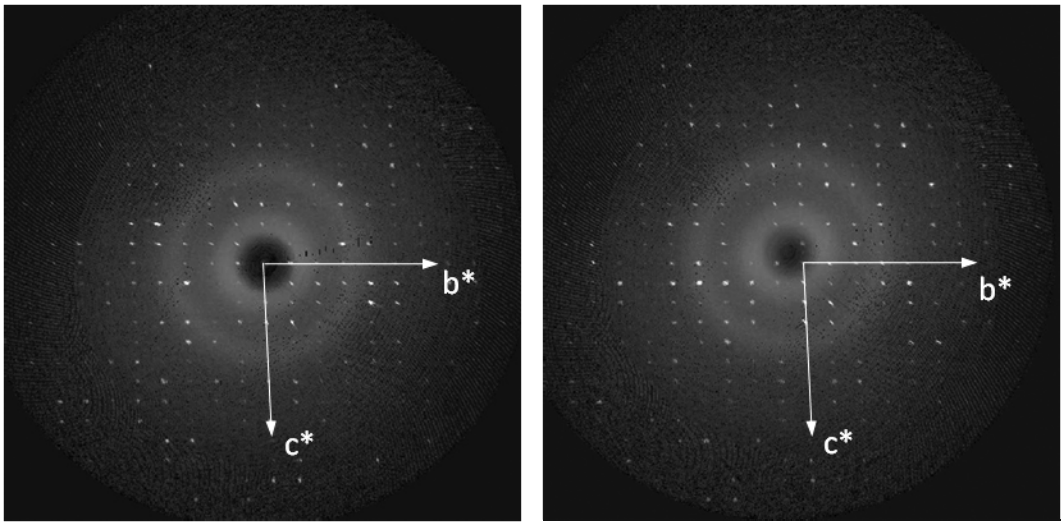

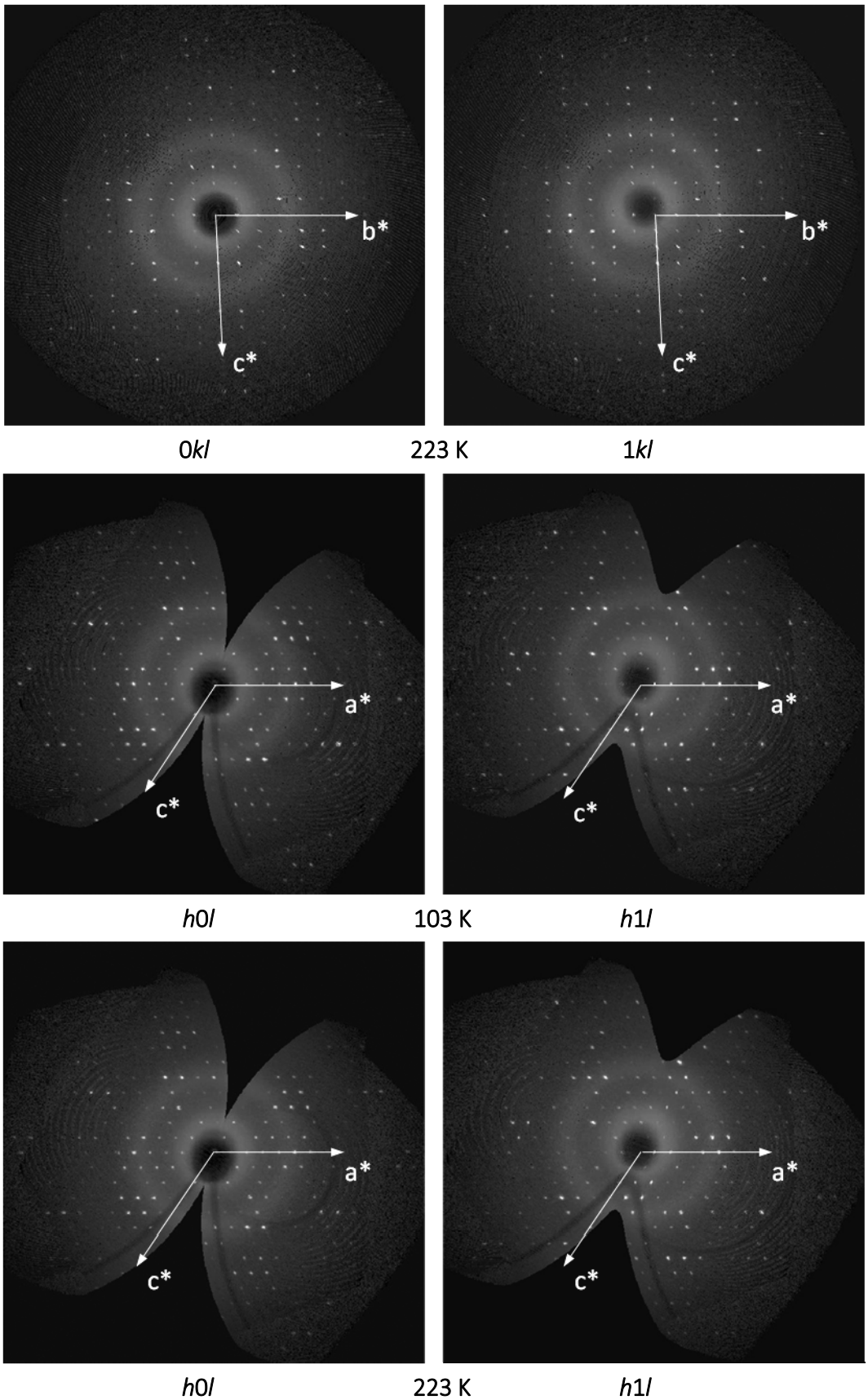

Fig. 2.1.6.3 Simulated precession images, derived from the area detector data, of two layers of $Cu(Sb_7Te_8)[GaCl_4]_6$ at 103 and 223 K. There are no superstructure reflections observed in the *c** direction.

2.1.7 Mass Spektrometric Analysis of the $(Sb_7Te_8)^{5+}$ Cluster

The mesomeric formulae of the $(Sb_7Te_8)^{5+}$ cluster (compare Fig. 2.1.4.5) gave a motive for mass spectrometric investigations. Point of interest was the possible fragmentation of the cluster into $(Sb_4Te_4)^{4+}$ and $(Sb_3Te_4)^{+}$ units. Fig. 2.1.7.1 shows the spectra of five unequivocally identified fragments of the $(Sb_7Te_8)^{5+}$ cluster of $(Sb_7Te_8)[GaCl_4]_2[Ga_2Cl_7]_3$ in a MALDI spectrum.

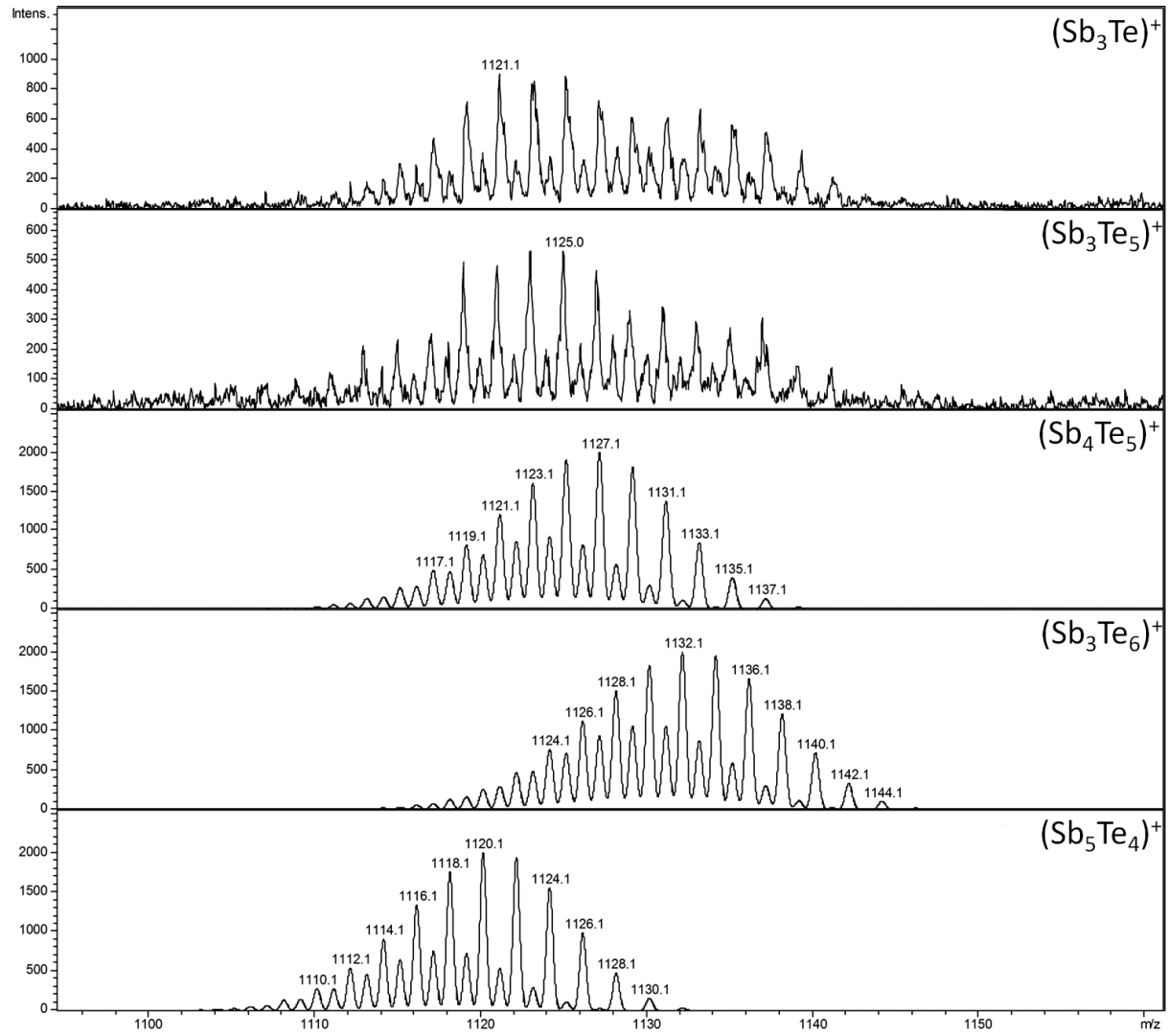

Fig. 2.1.7.1 The isotopic patterns of $(Sb_7Te_8)[GaCl_4]_2[Ga_2Cl_7]_3$ in positive MALDI mode. Identified fragments are $(Sb_3Te)^+$ (first), $(Sb_3Te_5)^+$ (second), $(Sb_4Te_5)^+$ (third), $(Sb_3Te_6)^+$ (fourth) and $(Sb_5Te_4)^+$ (fifth).

Additionally, $(Sb_5Te_5)^+$ and $(Sb_4Te_6)^+$ are possible but difficult to identify unequivocally in the spectra due to overlaps with other fragments. The disadvantage of this method is that only single positive charged ions are visible in the spectra which excludes the detection of the $(Sb_4Te_4)^{4+}$ cluster.
Unfortunately the same fragmentation was obtained with the reference substance Sb_2Te_3 but with more overlaps. At least, the existence of the $(Sb_3Te_4)^+$ and other single charged clusters could be proved in the gas phase.

2.2 The Double Cube Shaped Polycationic Clusters $(Sb_7Se_8)^{5+}$, $(Sb_7Se_8Cl_2)^{3+}$ and $(Sb_7S_8Cl_2)^{3+}$

2.2.1 Syntheses and EDX Analyses

$(Sb_7Se_8)[GaCl_4]_2[Ga_2Cl_7]_3$

By using copper(I) chloride cube (see below) and double cube shaped polycationic clusters from antimony and tellurium could be obtained. Further investigations of $Cu[GaCl_4]$ melts in the Sb/Se system led to $(Sb_7Se_8)[GaCl_4]_2[Ga_2Cl_7]_3$, the isotypic selenium congener of $(Sb_7Te_8)[GaCl_4]_2[Ga_2Cl_7]_3$.
28.4 mg (0.36 mmol) selenium, 29.2 mg (0.24 mmol) antimony, 27.4 mg (0.12 mmol) antimony trichloride, 174.3 mg (0.99 mmol) gallium trichloride and 17.8 mg (0.18 mmol) copper (I) chloride were filled in a glass ampoule under argon atmosphere. After one week at 100°C orange/green crystals (Fig. 2.2.1.1) - depending on the point of view - became visible in a solidified orange melt. At 88°C the yield decreased and at 50 °C the rods became thinner and could not be examined on the single crystal diffractometer anymore.
Additionally, $(Sb_7Se_8)[GaCl_4]_2[Ga_2Cl_7]_3$ crystallized in lower yield using AgCl, $Au(tht)Cl/PPh_4Cl$, $CuCl/PPh_4Cl$ and Sb_2O_3/PPh_4Cl instead of CuCl.

A tentative reaction equation according to the tellurium congener is:

$$16\ Sb + 24\ Se + 5\ SbCl_3 + 24\ GaCl_3 \rightarrow 3\ (Sb_7Se_8)[GaCl_4]_2[Ga_2Cl_7]_3$$

Fig. 2.2.1.1 Crystals of $(Sb_7Se_8)[GaCl_4]_2[Ga_2Cl_7]_3$ immersed in perfluorinated polyether.

The EDX analysis is in fair agreement with the sum formula $(Sb_7Se_8)[GaCl_4]_2[Ga_2Cl_7]_3$ (Tab. 2.2.1.1). Te reason for the too high Ga value is not clear.

Tab. 2.2.1.1 Elemental composition of $(Sb_7Se_8)[GaCl_4]_2[Ga_2Cl_7]_3$ in atom-% and the Sb : Se ratio.

$(Sb_7Se_8)[GaCl_4]_2[Ga_2Cl_7]_3$	Sb	Se	Ga	Cl	Sb : Se
Found	13.8(7)	15.1(6)	20(1)	50.6(4)	1 : 1.10
Calculated	13.46	15.38	15.38	55.70	1 : 1.14

$(Sb_7Se_8Cl_2)[GaCl_4]_3$

For $(Sb_7Se_8Cl_2)[GaCl_4]_3$, the synthesis of $(Sb_7Se_8)[GaCl_4]_2[Ga_2Cl_7]_3$ was modified. Copper(I) chloride was replaced by the respective amount of tetraphenylphosphonium chloride.
28.4 mg (0.36 mmol) selenium, 29.2 mg (0.24 mmol) antimony, 27.4 mg (0.12 mmol) antimony trichloride and 174.3 mg (0.99 mmol) gallium trichloride were filled in a glass ampoule and heated to 100 °C whereupon a melt formed. After 16 days orange, rod and cube-shaped crystals (Fig. 2.2.1.2) were visible in a green, mushy melt. Additionally adding 68.3 mg (0.18 mmol) tetraphenylphosphonium chloride the yield, crystal size and quality were improved. The melt was dark red and of relative low viscosity, which allowed it to be decanted from the crystals. With CuCl as the additive the reaction time is shortened to 7 days and the temperature interval for a successful synthesis is broader (90 °C -140 °C). The highest yield is obtained at 100 °C in about 80 %.
Instead of using a tetraphenylphosphonium tetrachloridogallate melt as the reaction medium, $(Sb_7Se_8Cl_2)[GaCl_4]_3$ is also formed, but in significant lower yield in the presence of one the following adjuvants: LiCl, NaCl, KCl, RbCl, NH_4Cl/PPh_4Cl and $CsCl/PPh_4Cl$.

A tentative reaction equation is:

$$16\ Sb + 24\ Se + 5\ SbCl_3 + 9\ GaCl_3 \rightarrow 3\ (Sb_7Se_8Cl_2)[GaCl_4]_3$$

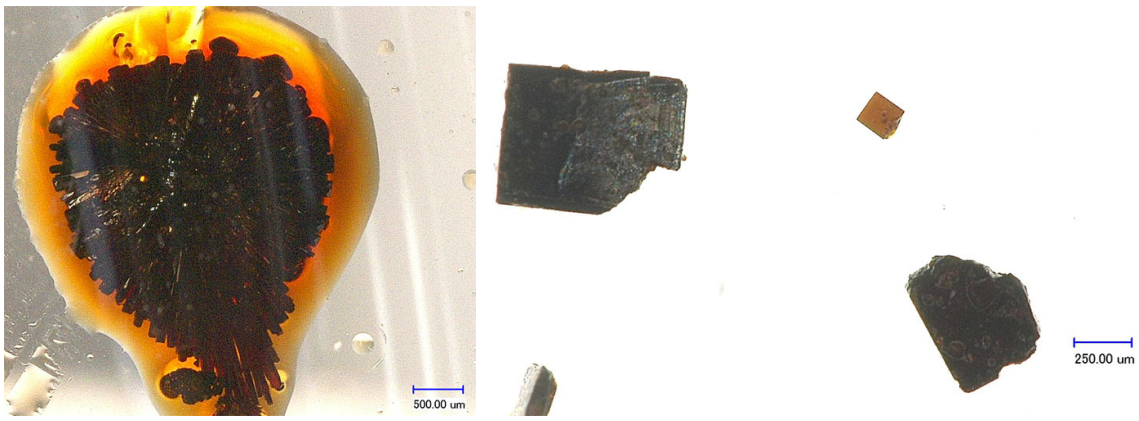

Fig. 2.2.1.2 Crystals of $(Sb_7Se_8Cl_2)[GaCl_4]_3$ in the reaction melt (left) and separated crystals immersed in perfluorinated polyether (right).

The EDX analysis is in fair agreement with the sum formula $(Sb_7Se_8Cl_2)[GaCl_4]_3$ (Tab. 2.2.1.1). The too high results for Ga and Cl can be explained by $GaCl_3$ adherences on the crystal surface.

Tab. 2.2.1.2 Elemental composition of $(Sb_7Se_8Cl_2)[GaCl_4]_3$ in % and Sb : Se ratio.

$(Sb_7Se_8Cl_2)[GaCl_4]_3$	Sb	Se	Ga	Cl	Sb : Se
Found	20.0(6)	23.1(9)	13.2(6)	43(1)	1 : 1.16
Calculated	21.88	25.00	9.38	37.50	1 : 1.14

$(Sb_7S_8Cl_2)[GaCl_4]_3$

122.3 mg (0.36 mmol) antimony sulfide, 36.5 mg (0.16 mmol) antimony trichloride, 174.3 mg (0.99 mmol) gallium trichloride and 17.8 mg (0.18 mmol) copper(I) chloride were filled in a glass ampoule under argon atmosphere. The ampoule was evacuated and flame sealed. After 10 days at 100 °C, orange crystals (Fig. 2.2.1.3) with the habitus of needles of hexagonal cross section were crystalllized in a mushy yellow-green melt. The estimated yield is about 20 %. Syntheses using the entire elements antimony and sulphur did not succeed.

A tentative reaction equation is:

$8\ Sb_2S_3 + 5\ SbCl_3 + 9\ GaCl_3 \rightarrow 3\ (Sb_7S_8Cl_2)[GaCl_4]_3$

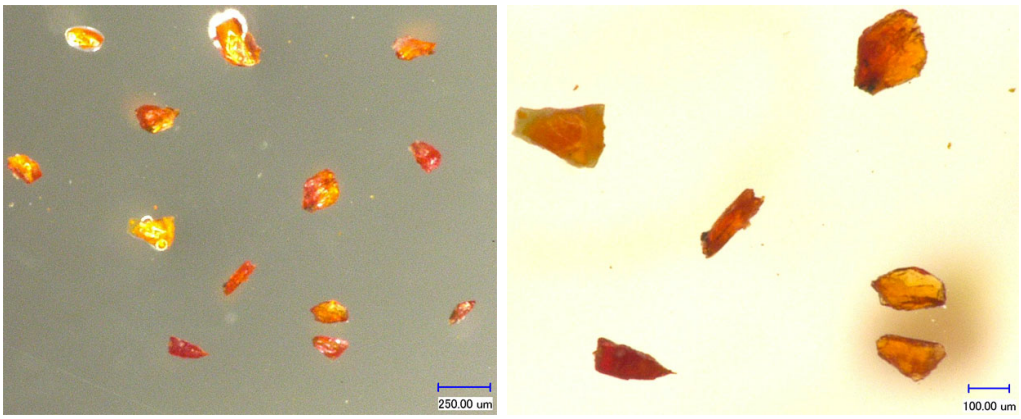

Fig. 2.2.1.3 Crystals of $(Sb_7S_8Cl_2)[GaCl_4]_3$ immersed in perfluorinated polyether. The photo was taken after 16 months of storage of the opened ampoule in the glovebox. The shape of the crystals changed. Apparently, the solidified melt still acts as a solvent and interacts with the crystals in dissolution/crystallization equilibrium. The colour of the crystals, however, was unchanged.

The EDX analysis is in fair agreement with the sum formula $(Sb_7S_8Cl_2)[GaCl_4]_3$ (Tab. 2.2.1.3).

Tab. 2.2.1.3 Elemental composition of $(Sb_7S_8Cl_2)[GaCl_4]_3$ in atom-% and the Sb : S ratio.

$(Sb_7S_8Cl_2)[GaCl_4]_3$	Sb	S	Ga	Cl	Sb : S
Found	22.7(2)	24.9(2)	9.1(3)	43.1(4)	1 : 1.10
Calculated	21.88	25.00	9.38	37.50	1 : 1.14

2.2.2 The Reactions Leading to Compounds Containing Sb/Se and Sb/S Double Cube Shaped Clusters

It is remarkable, that no crystalline byproducts are formed in the syntheses of $(Sb_7Se_8Cl_2)[GaCl_4]_3$ and $(Sb_7S_8Cl_2)[GaCl_4]_3$. $(Sb_7Se_8)[GaCl_4]_2[Ga_2Cl_7]_3$ is obtained in high yield leaving only small residues of the orange solidified melt. In an EDX analysis, copper chloridogallates could be identified to be present in the melt in form of relatively small inconspicuous crystals. $(Sb_7Se_8Cl_2)[GaCl_4]_3$ crystallizes in good yields but some residual educts in form of excess melt are left over. $(Sb_7S_8Cl_2)[GaCl_4]_3$ is obtained in lower

yield with larger residual amounts of an amorphous mushy melt and no improvement of the synthetic procedure could be found. In all cases, $SbCl_3$ was used at least in double excess to obtain higher yields. It was found empirically that the reactions proceed in the desired way only by adding adjuvants. Tetraphenylphosphonium chloride turned out as most effective, as it lowers the viscosity of the melts. The addition of copper(I) chloride in stochiometric amounts is essential for the synthesis of $(Sb_7Se_8)[GaCl_4]_2[Ga_2Cl_7]_3$. Without addition of CuCl, only $(Sb_7Se_8Cl_2)[GaCl_4]_3$ is formed. Apparently, the presence of CuCl lowers the acidity of the $GaCl_3$ melt and causes an increase of the concentration of free chloride ions. $(Sb_7S_8Cl_2)[GaCl_4]_3$ is synthesized successfully only in the presence of CuCl and Sb_2S_3, not by using elemental antimony and sulphur. For the combination Sb/Se, several synthetic attempts with different starting compositions were explored. The only crystalline products observed so far were $(Sb_7Se_8)[GaCl_4]_2[Ga_2Cl_7]_3$ or $(Sb_7Se_8Cl_2)[GaCl_4]_3$, respectively. They seem to be the thermodynamically most preferred clusters of this pentele/chalcogen combination in the melt approach.

2.2.3 Crystal Structures of $(Sb_7Se_8)[GaCl_4]_2[Ga_2Cl_7]_3$, $(Sb_7Se_8Cl_2)[GaCl_4]_3$ and $(Sb_7S_8Cl_2)[GaCl_4]_3$

The crystal structures consist of double cube shaped $(Sb_7Se_8)^{5+}$ and $(Sb_7Ch_8Cl_2)^{3+}$ (Ch = Se, S) polycationic clusters. The anions are tetrachloridogallate and heptachloridodigallate ions. The crystallographic data are shown in Tab. A 5.2.4 - A 5.2.5 in the appendix.
Both types of chloridogallate anions are of regular shape and are in line with the structures of the respective ions in the alkaline tetrachloridogallates $A[GaCl_4]$ (A = Li [59], Na, K [50], Rb [60], Cs [61]) and $K[Ga_2Cl_7]$ [51]. The Ga–Cl bond lengths in all three structures are in the range from 2.132(4) to 2.322(4) Å and the Cl–Ga–Cl angles in the range from 98.4(1) to 117.1(1)°.

$(Sb_7Se_8)[GaCl_4]_2[Ga_2Cl_7]_3$ is the selenium containing congener of $(Sb_7Te_8)[GaCl_4]_2[Ga_2Cl_7]_3$ and crystallizes isotypically. Fig. 2.2.3.1 shows the unit cell, which includes two formula units, and Fig. 2.2.3.2 the structure of an individual $(Sb_7Se_8)^{5+}$ cluster.

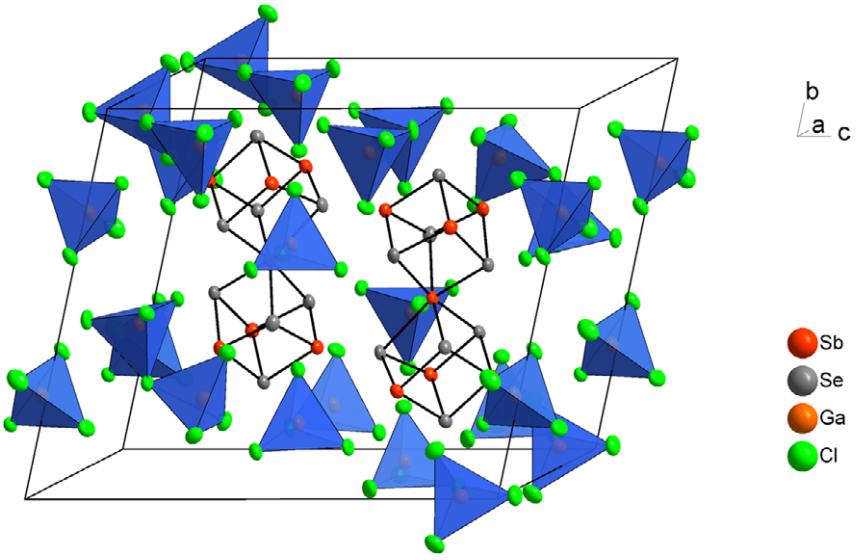

Fig. 2.2.3.1 The unit cell of the structure of $(Sb_7Se_8)[GaCl_4]_2[Ga_2Cl_7]_3$. The $[GaCl_4]^-$ and $[Ga_2Cl_7]^-$ ions are represented by discrete tetrahedra and corner sharing double-tetrahedra. The atoms are represented by thermal ellipsoids scaled to include a probability of 70 %.

The Sb–Se bonds in the periphery are in the range between 2.580(2) and 2.714(1) Å, the respective bonds involving the central atom Sb1 are separated into three short and three long bonds (2.719(2), 2.730(2), 2.752(2) and 2.978(2), 3.014(2), 3.112(2) Å). The short and the long bonds are in mutual *trans* position, so the central Sb1 atom gains a [3+3] coordination. These structural peculiarities imply that the bonding considerations developed for $(Sb_7Te_8)^{5+}$ are analogously valid for $(Sb_7Se_8)^{5+}$ (Fig. 2.2.3.2). The bond lengths separation in $(Sb_7Se_8)^{5+}$, however, is more pronounced compared with the tellurium containing congener (compare Tab. A 5.4.6).

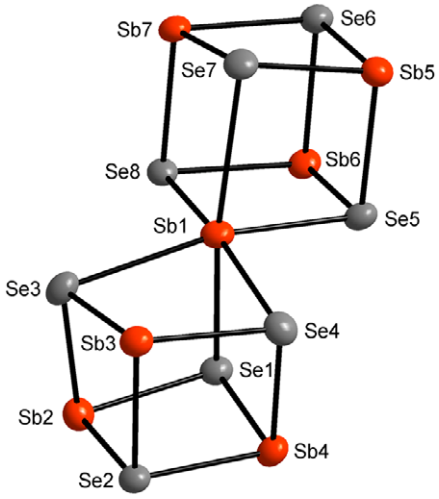

Fig. 2.2.3.2 The $(Sb_7Se_8)^{5+}$ cluster in the crystal structure of $(Sb_7Se_8)[GaCl_4]_2[Ga_2Cl_7]_3$. The atoms are represented by thermal ellipsoids scaled to include a probability of 80 %.

$(Sb_7Se_8Cl_2)[GaCl_4]_3$ crystallizes isotypically to the known $(Sb_7S_8Br_2)[AlCl_4]_3$[37] in the acentric space group $P2_12_12_1$ (Fig. 2.2.3.3 top). Two additional chlorine atoms are bound to two peripheral Sb atoms of an underlying $(Sb_7Se_8)^{5+}$ cluster, which lowers the charge from +5 to +3 and results in the $(Sb_7Se_8Cl_2)^{3+}$ cation (Fig. 2.2.3.3, middle).

In *trans* positions to the Sb–Cl bonds the edges of the cuboidal clusters are opened (Sb2···Se2 3.235(1), Sb5···Se6 3.240(1) Å). The substitution with the two terminal Cl atoms lowers the ideal point symmetry of the cluster from D_{3d} to C_{2h}. In the structure all atoms occupy general positions and actually no higher point symmetry than C_1 is present. Strong distortions from the ideal C_{2h} symmetry are observed, which is manifested in angle deviations by more than 10° from rectangularity and linearity for the Se–Sb1–Se angles and a strong tilting of the two cubes. The angle Se2···Sb1···Se6 amounts to 155.5°, but is expected to be linear if the D_{3d} symmetry of the ideal $(Sb_7Se_8)^{5+}$ cluster was preserved. The six Sb–Se bonds of the central atom Sb1 bonds fall into three groups, two short, two middle and two long bonds (Sb1–Se1 2.7316(7), –Se5 2.7652(7); –Se4 2.8397(7), –Se8 2.8440(7); –Se3 3.0306(7), –Se7 3.0542(7) Å). All other Sb–Se bond lengths are in the normal range between 2.575(1) and 2.696(1) Å (compare Tab. A 5.4.7). The Sb–Cl bond lengths (Sb2–Cl1 2.377(1), Sb5–Cl2 2.402(1) Å) correlate with those in $SbCl_3$. [62]

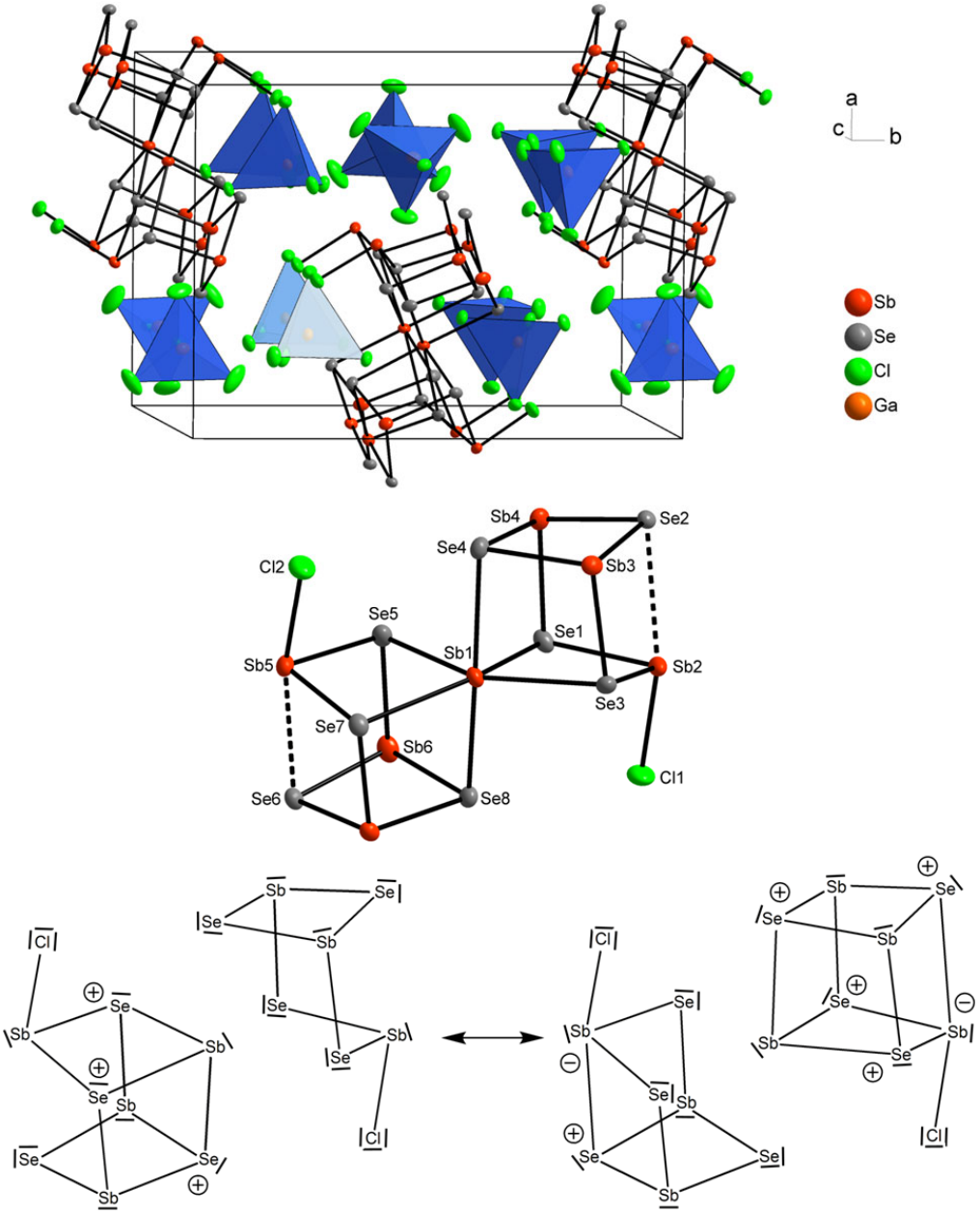

Fig. 2.2.3.3 The unit cell of the structure of $(Sb_7Se_8Cl_2)[GaCl_4]_3$ (top). The $[GaCl_4]^-$ ions are represented by discrete tetrahedra. The individual $(Sb_7Se_8Cl_2)^{3+}$ cluster cation is shown in the middle. The atoms are represented by thermal ellipsoids scaled to include a probability of 80 %. On bottom two of the several mesomeric Lewis formulae (extensions from those of $(Sb_7Te_8)^{5+}$, Fig. 2.1.4.5) for the cation are given.

$(Sb_7S_8Cl_2)[GaCl_4]_3$ is the sulphur containing congener of $(Sb_7Se_8Cl_2)[GaCl_4]_3$ and the chlorine/gallium containing congener of $(Sb_7S_8Br_2)[AlCl_4]_3$[37]. It crystallizes in the monoclinic system in the space group $P2_1$, which represents a direct subgroup of $P2_12_12_1$ (Fig. 2.2.3.4). The $(Sb_7S_8Cl_2)^{3+}$ cluster is isostructural to $(Sb_7S_8Br_2)^{3+}$ and $(Sb_7Se_8Br_2)^{3+}$ [38] with an analogous bond lengths distribution. The replacement of selenium by sulphur shortens as expected the Sb-chalcogen bond lengths.

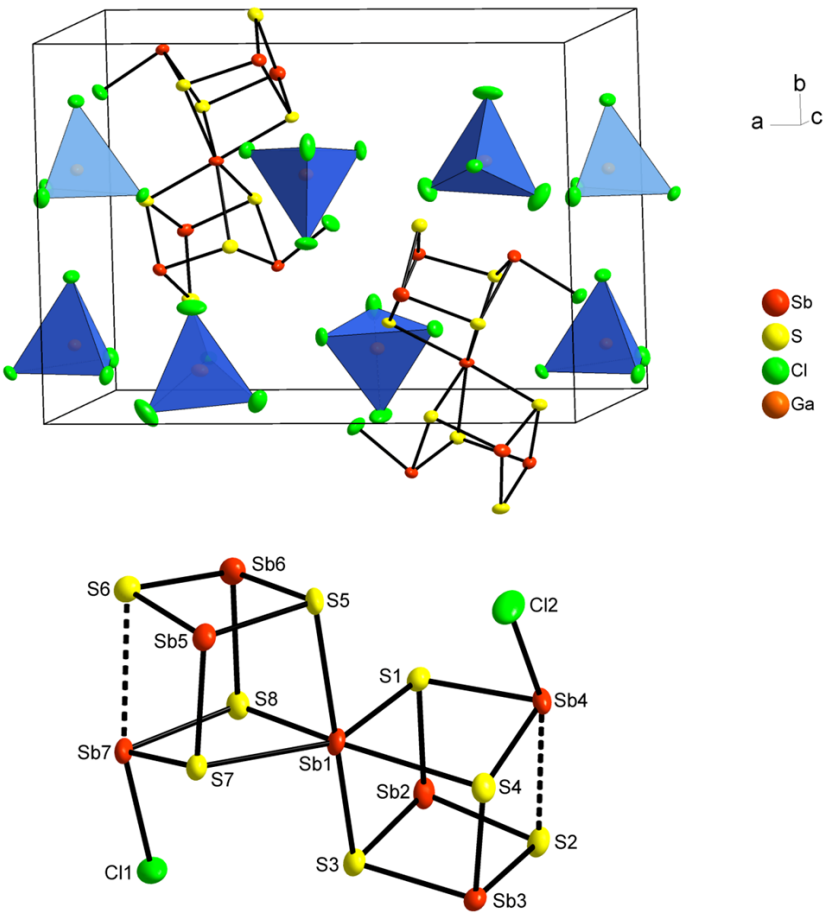

Fig. 2.2.3.4 The unit cell of the structure of $(Sb_7S_8Cl_2)[GaCl_4]_3$ (top). The $[GaCl_4]^-$ ions are represented by discrete tetrahedra. The individual $(Sb_7S_8Cl_2)^{3+}$ cluster cation is shown at the bottom. The atoms are represented by thermal ellipsoids scaled to include a probability of 80 %.

The Sb–S bonds in the periphery of the double-cube shaped cluster are in the range between 2.427(3) and 2.585(4) Å and like in the structure of $(Sb_7Se_8Cl_2)^{3+}$ the six Sb–S bonds of the central atom Sb1 fall into three groups (Sb1–S1 2.581(4), –S8 2.607(4); –S3 2.708(4), –S5 2.744(4); –S7 2.984(7), –S4 2.969(4) Å). Two edges of the cluster, in *trans* positions to the Sb–Cl bonds, are elongated (Sb4···S2 3.140(4), Sb7···S6 3.119(4) Å). The Sb–Cl bonds are equivalent to those in $(Sb_7Se_8Cl_2)^{3+}$ (Sb7–Cl1 2.389(4), Sb4–Cl2 2.367(4) Å) (Tab. A 5.4.8). The degree of distortion from a regular C_{2h} shape is as high as found for the $(Sb_7Se_8Cl_2)^{3+}$ cluster. The angle S2···Sb1···S6 amounts to 154.3° and deviates thus strongly from linearity, indicating a strong tilting of the both cubes. The bonding in the cationic clusters $(Sb_7Ch_8X_2)^{3+}$ (Ch = S, Se, X = Cl, Br) can be understood in classical terms. Applying the octet rule for all atoms, a series of mesomeric Lewis formulae results, analogous to $(Sb_7Se_8Cl_2)^{3+}$ (compare Fig. 2.2.3.3). The AIM analysis of the $(Sb_7S_8Cl_2)^{3+}$ cluster, however, reveals that even the elongated Sb···Ch cube edges *trans* to the Sb–Cl bonds in $(Sb_7Se_8Cl_2)[GaCl_4]_3$ and $(Sb_7S_8Cl_2)[GaCl_4]_3$ still feature a bond critical point, showing the double-cube cluster bonding is persisting on going from $(Sb_7Ch_8)^{5+}$ to $(Sb_7Ch_8Cl_2)^{3+}$. The Lewis basic chlorine atoms are strongly Coulomb attracted by the $(Sb_7Ch_8)^{5+}$ core as seen by the existence of two additional bond critical points to one adjacent sulphur and antimony atom, respectively (Fig. 2.2.3.5).

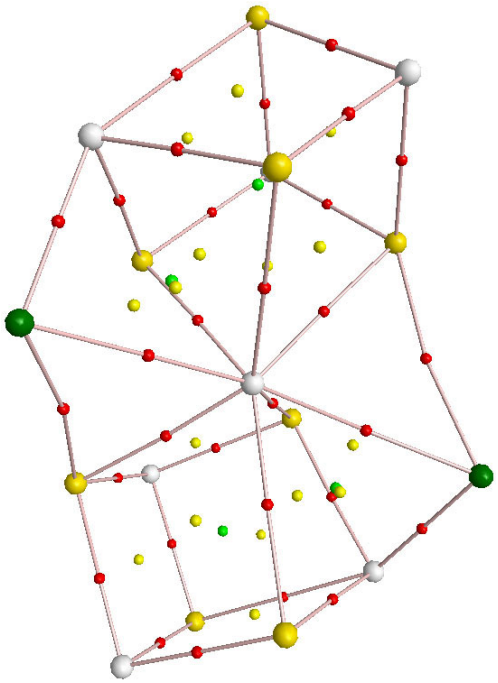

Fig. 2.2.3.5 AIM analysis of $(Sb_7S_8Cl_2)^{3+}$.** Colour code: yellow = sulphur, gray = antimony, green = chlorine; sticks between the atoms represent the constructive bonds between the atoms, bonding critical points are depicted as red spheres, ring critical points are yellow and cage critical points are green spheres.

The crystals of $(Sb_7S_8Cl_2)[GaCl_4]_3$ turned out as systematically twinned in a non-merohedral way by a 180° rotation along the direct *a* axis. Several crystals were tested, which all showed the same type of diffraction pattern (Fig. 2.2.3.6). The unit cell relationship of the two main twin components in direct space are $a_{TWIN} = -a$, $b_{TWIN} = b$ and $c_{TWIN} = -c$, in reciprocal space $a^*_{TWIN} = -a^* + 0{,}056\ c^*$, $b^*_{TWIN} = -b^*$ and $c^*_{TWIN} = c^*$ (Fig. 2.2.3.6) with the superposition matrix $h_{TWIN} = h, 0, 0$ / $k_{TWIN} = 0, -k, 0$ / $l_{TWIN} = -0.0566\ h, 0, -l$. As only a few reflections of both individuals should overlap, the structure refinement was initially carried out using a HKLF5 file. This refinement procedure, however, did not lead to convincing results, caused by the presence of additional twin components. The axis length ratio of *a* = 17.0025 Å to *c* = 8.6105 Å is 1.975, approximately 2. Thus a repeated rotation of 93.19° (which represents the monoclinic unit cell angle) around *b** results in further twin components with additional overlapping of the reciprocal lattice points. Accordingly, the HKLF5 processing was not effective and a reliable space-group determination was not possible. Refinement was then performed using only reflections originating from one domain of the twinned crystal with no or minimal overlap. Best results were obtained in space-group $P2_1$. The non-centrosymmetry was ensured by a Flack *x* parameter close to zero.*

* The crystallographic treatment of the twinning and the precession representations were performed by Dr. Jörg Daniels.

** The AIM analysis was perfomed by Dr. Gregor Schnakenburg.

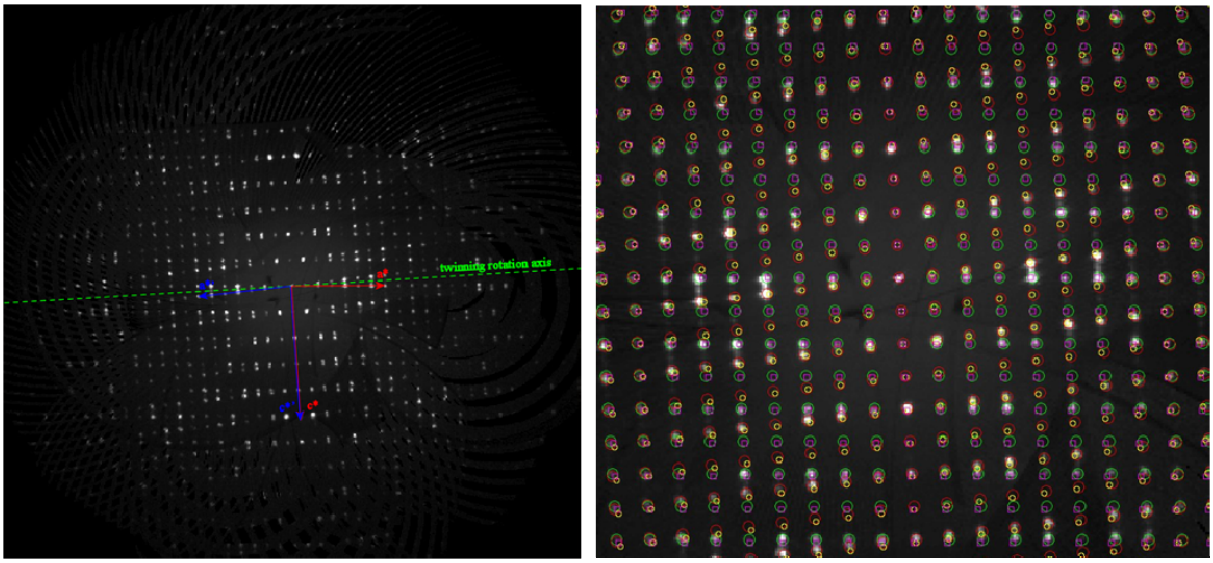

Fig. 2.2.3.6 **left:** The reciprocal lattice plane (*h*2*l*) of crystals of $(Sb_7S_8Cl_2)[GaCl_4]_3$ with reciprocal lattice directions of two the non-merohedrally twinned individuals in red and blue. The *b** axis of the "red" individual points towards the viewer, *b** axis of "blue" individual points opposite to the viewer. The twinning rotation axis (-a* + 0,028 c*) is figured in green colour.
right: The reciprocal lattice plane (*h*2*l*) of crystals of $(Sb_7S_8Cl_2)[GaCl_4]_3$ (reconstructed from single crystal diffractometer data) with the expected reflection positions (in red and green) of two non-merohedrally twinned individuals originated by a 180° rotation around the direct *a* axis and the reflection positions of two additional twin components generated by rotation of 93.19° (which represents the monoclinic unit cell angle) around *b** presented in magenta and yellow.

$(Sb_7S_8Cl_2)[GaCl_4]_3$ was examined by differential scanning calorimetry in the temperature range between -30 °C and +240 °C applying heating rates of 10 °C/min. The only detectable thermal effect occurs on heating at 180 °C and represents an irreversible decomposition since on cooling no inverse thermal effect was detected at this temperature (Fig. 2.2.3.7). A solid state phase transition in the observed temperature range may be excluded by this measurement.

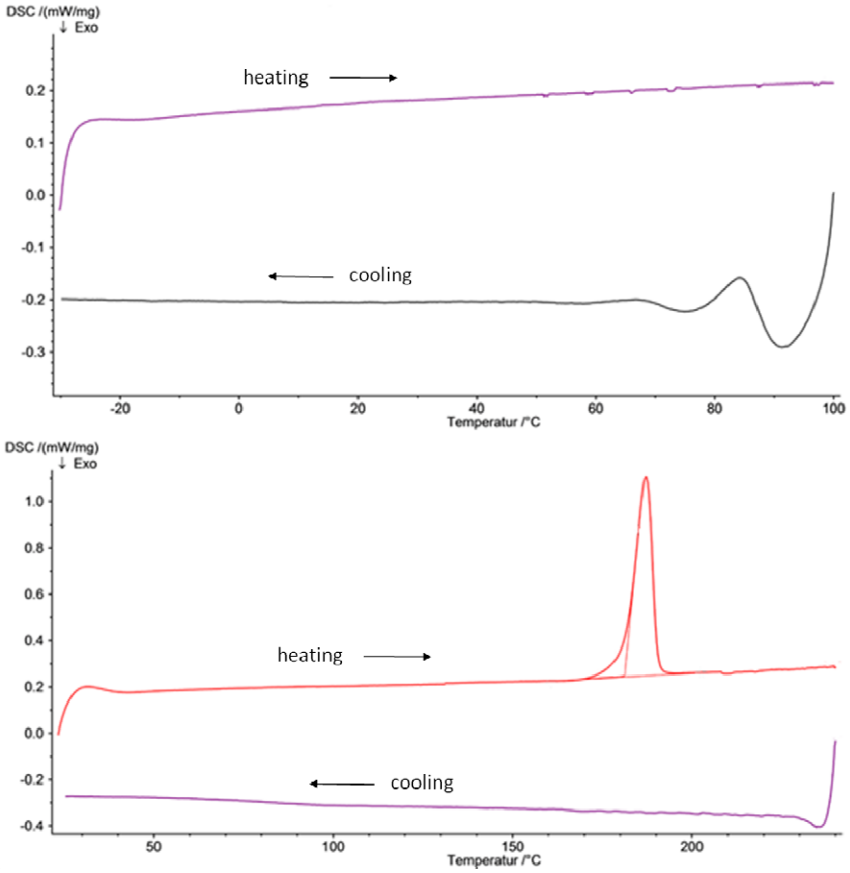

Fig. 2.2.3.7 Differential scanning calorimetric plot of $(Sb_7S_8Cl_2)[GaCl_4]_3$ between -30 and +240 °C. Curve 1 (top) demonstrated the heating process, curve 2 (bottom) the cooling process, respectively.

In all crystal structures the polycations are coordinated by Cl atoms of the surrounding chloridogallate anions (Fig. A 5.6.6 - A 5.6.8). Due to the lower charge of +3 and additional repulsive interactions between the chlorine ligands and the coordinating anions, the $(Sb_7Ch_8Cl_2)^{3+}$ (Ch = Se, S) clusters are less intensively coordinated by chloridogallate anions than the $(Sb_7Ch_8)^{5+}$ (Ch = Te, Se) clusters. The shortest distances are present throughout to the Sb atoms, the chalcogen···Cl distances being substantially longer ($(Sb_7Se_8)[GaCl_4]_2[Ga_2Cl_7]_3$: Sb···Cl > 3.01 Å, Se···Cl > 3.27 Å; $(Sb_7Se_8Cl_2)[GaCl_4]_3$: Sb···Cl > 3.16 Å, Se···Cl > 3.33 Å; $(Sb_7S_8Cl_2)[GaCl_4]_3$: Sb···Cl > 3.13 Å, S···Cl > 3.29 Å). A. This is caused by the higher electronegativity of the chalcogen atoms compared to Sb. The positive charges of the clusters are mainly localized on the Sb atoms.

2.2.4 ^{77}Se Solid State NMR Spectroscopy on $(Sb_7Se_8)[GaCl_4]_2[Ga_2Cl_7]_3$ and $(Sb_7Se_8Cl_2)[GaCl_4]_3$

The two title compounds crystallize in high yields, which are a prerequisite for a solid state NMR experiment. The point of interest was the question if the different chemical selenium environments and especially the multiple-centre bonds around the six-fold coordinated antimony atom are visible in the NMR spectra.

The spectrum of $(Sb_7Se_8)[GaCl_4]_2[Ga_2Cl_7]_3$ consists of six resolved isotropic signals at -301 ppm, -354 ppm, -610 ppm, -654 ppm, -693 ppm, and -818 ppm (Fig. 2.2.4.1).

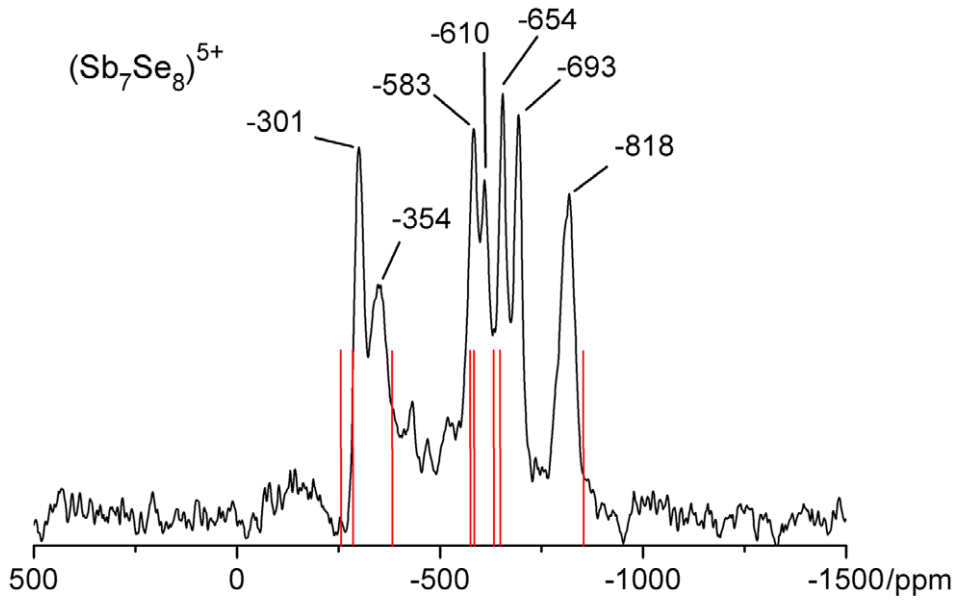

Fig. 2.2.4.1 ^{77}Se solid state NMR spectrum of $(Sb_7Se_8)[GaCl_4]_2[Ga_2Cl_7]_3$. The red vertical lines indicate the calculated positions of the resonance signals according to periodic DFT calculations. Not assigned signals are spinning side bands.

The signal at -583 ppm originates from the byproduct $(Sb_4Se_4)[GaCl_4]_4$ present in the reaction melt and forming adherences on the surface of the selected crystals (compare chapt. 2.5). The solidified reaction melt itself shows one isotropic signal at -592 ppm, which matches the signal at -583 ppm within the limits of the measurement accuracy (Fig. 2.2.4.2).

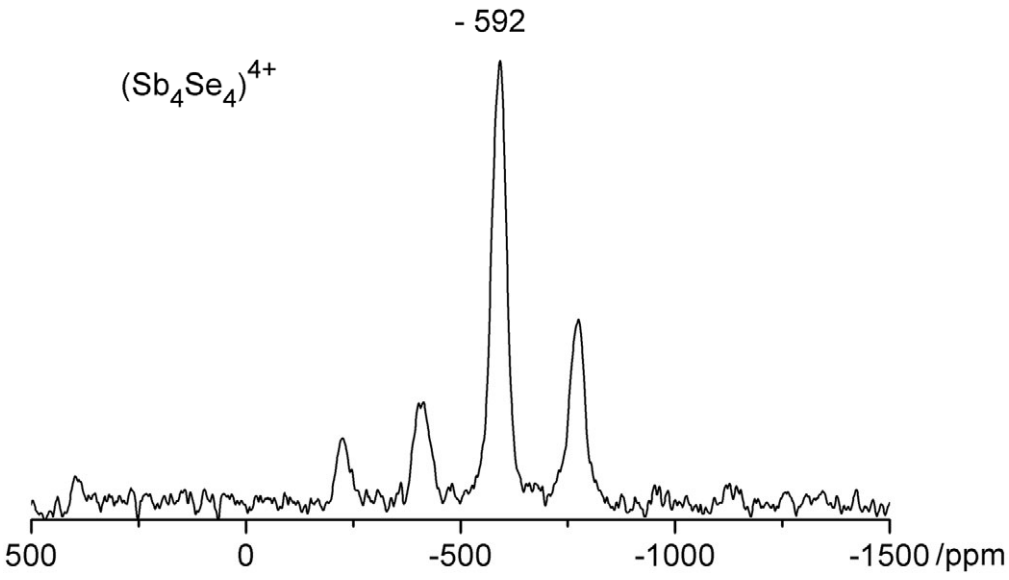

Fig. 2.2.4.2 ^{77}Se solid state NMR spectrum of the solidified orange reaction melt formed in the synthesis of $(Sb_7Se_8)[GaCl_4]_2[GaCl_4]_3$. One isotropic signal is obtained at -592 ppm. Not assigned signals are side bands.

In the spectrum of $(Sb_7Se_8Cl_2)[GaCl_4]_3$ four isotropic lines at 148 ppm, -162 ppm, -411 ppm and -578 ppm are observed. The isotropic line position was determined by variation of the rotation frequency up to 17 kHz (Fig. 2.2.4.3).

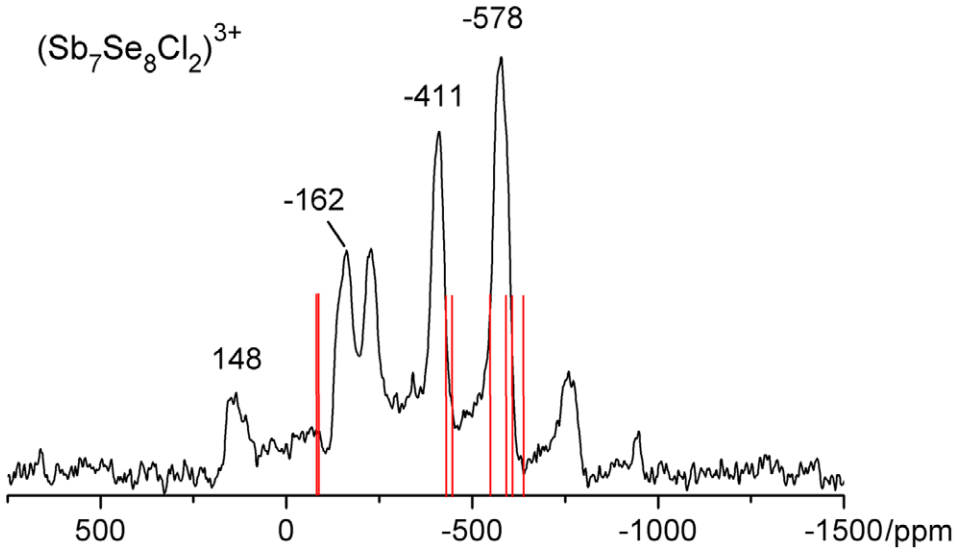

Fig. 2.2.4.3 ^{77}Se solid state NMR spectra of $(Sb_7Se_8Cl_2)[GaCl_4]_3$. The red vertical lines indicate the calculated positions of the resonance signals according to periodic DFT calculations. Not assigned signals are spinning side bands.

In ideal D_{3d} symmetry one expects for the cluster $(Sb_7Se_8)^{5+}$ two ^{77}Se resonances for the two symmetrically different Se atoms. In the crystal structure all atoms are in general positions and the cluster deviates significantly from the ideal symmetry. Therefore, Se atoms are no longer symmetrically equivalent and up to eight resonance signals are expected. In ideal C_{2h} symmetry the $(Sb_7Se_8Cl_2)^{3+}$ cluster in $(Sb_7Se_8Cl_2)[GaCl_4]_3$ has three different Se atoms. In the crystal, this cluster is also strongly distorted from the ideal symmetry. Since all atoms are located on general positions, eight different Se atoms are present. The number of observed resonances is lower for both clusters, six lines for $(Sb_7Se_8)^{5+}$ and four lines for $(Sb_7Se_8Cl_2)^{3+}$.

The chemical shifts of the ^{77}Se resonances were calculated via DFT. A general difficulty in comparison of the discrete calculated resonance frequencies with the experimentally found ones arises from the large experimental signal widths. In the gas phase approach and referenced to Me_2Se*, the calculated chemical shifts for the $(Sb_7Se_8)^{5+}$ cluster in $(Sb_7Se_8)[GaCl_4]_2[Ga_2Cl_7]_3$ fall into five groups for Se3/Se7 (+110/+96 ppm), Se8 (-450 ppm), Se4 (-731 ppm), Se5/Se1 (-1185/-1113 ppm), Se2/Se6 (-1494/-1462 ppm) (see Fig. 2.2.3.2 for the atom numbering). For the $(Sb_7Se_8Cl_2)^{3+}$ cluster the calculated shifts fall into four groups for Se3/Se7 (+149/+139 ppm), Se6/Se2 (-349/-311 ppm), Se1/Se5/Se4 (-867/-791/-778 ppm), Se8 (-1028 ppm) (see Fig. 2.2.3.3 for the atom numbering). In contrast to the calculated vibrational frequencies, the NMR shifts calculated by this method do not match the experiments well, the agreement is only roughly and the absolute shifts differ substantially.
The discrepancies between cluster calculations and experiment are most likely due to missing interactions with neighbour atoms. In order to investigate this effect, periodic DFT calculations of the ^{77}Se chemical shifts were performed. Also for this method Me_2Se was taken as internal reference. The

* The calculations were performed by Dr. Gregor Schnakenburg.

absolute agreement with the experiment is also not perfect. Taking the calculated chemical shift of Me_2Se as the standard, the splittings of the signals are shifted by approx. 110 ppm with respect to the observed spectra to lower field. Using the Me_2Se shift obtained by molecular DFT, however, a good agreement is obtained. In the further discussion and for a clear comparison, the obtained chemical shifts for the individual Se atoms were adjusted by the molecular calculation value. For the molecular reference a large cubic box of 15×15×15 Å was used. For $(Sb_7Se_8)[GaCl_4]_2[Ga_2Cl_7]_3$ there are five groups of resonance signals as found for the cluster calculation but with a different grouping, Se3/Se4 (-261/-290 ppm), Se7 (-377 ppm), Se5/Se8 (-574/-581 ppm), Se1/Se2 (-629/-648 ppm), Se6 (-851 ppm). The separation of the calculated shifts is thus much better described than based on the cluster models. The differences are within 20-70 ppm of the experimental values.
Therefore the periodic calculations were taken as basis for a tentative explanation of the splitting of the signals. One criterion is of course the local environment of the atoms. Each Se atom of the $(Sb_7Se_8)^{5+}$ ion is coordinated by Cl atoms of surrounding chloridogallate anions. The overall coordination is rather uniform. Within a sphere of radius 4 Å each Se atom is coordinated by five to seven Cl atoms. The different local environment has no straightforward connection with the calculated chemical shifts. However, the close similarity of Se3 and Se4 is evident, and also the large number of Cl neighbours for Se6 is consistent with the large negative shift. For all other atoms, however, there is no clear trend of the chemical shift with the number of Se and Cl neighbours within the selected sphere. In order to rationalize the shifts in terms of long-range electrostatic interaction, the electrostatic potential at the nuclear positions was calculated. In Fig. 2.2.4.4 the correlation between shift and potential is shown. Since the reference charge is +1, a more negative potential indicates a higher electron density at or near the nucleus position, which is consistent with a negative chemical shift.

Similar analyses were performed for $(Sb_7Se_8Cl_2)[GaCl_4]_3$. In this case the calculations reveal three groups of signals for the $(Sb_7Se_8Cl_2)^{3+}$ cluster, Se3/Se7 (-87/-93 ppm), Se6/Se2 (-446/-460 ppm), and Se1/Se5/Se8/Se4 (-551/-591/-614/-638 ppm). Here, the deviations of the calculated shifts from the measured peaks amount up to 240 ppm and are even larger than for $(Sb_7Se_8)[GaCl_4]_2[Ga_2Cl_7]_3$ (compare Fig. 2.2.4.3). Apparently this structure is less reliably described with the present approach. Nevertheless, an attempt was made to rationalize the shifts with the coordination sphere. The calculated shifts as function of the calculated electrostatic potential at the Se position shows no clear correlation. In particular the Se3/Se7 group does not fit to the proposed linear behaviour (Fig. 2.2.4.4). The reason is not yet clear.*

* Periodical DFT ^{77}Se NMR calculations were performed by Prof. Dr. Thomas Bredow.

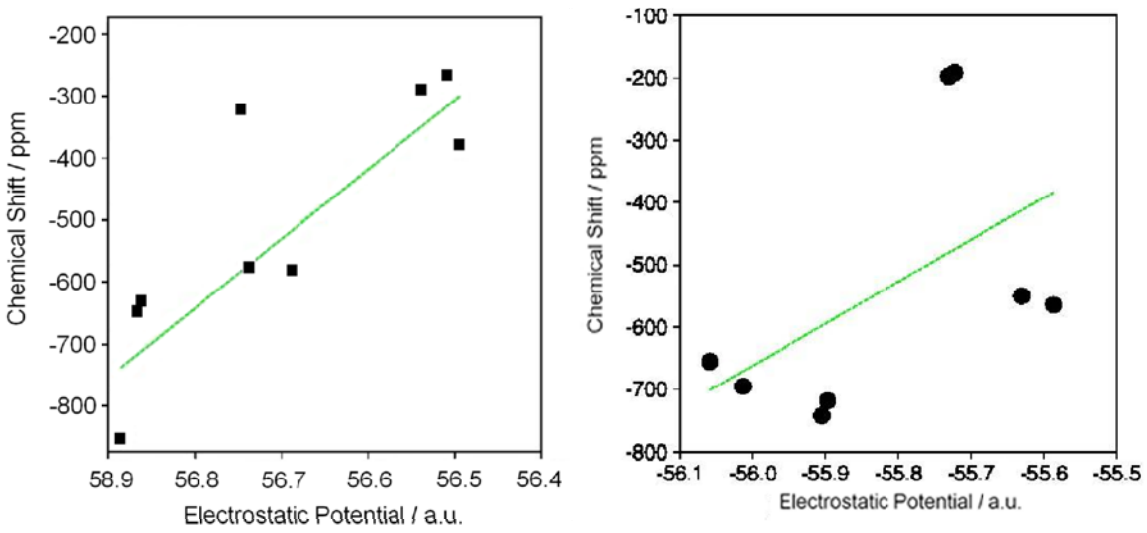

Fig. 2.2.4 4 Calculated ^{77}Se chemical shift as a function of the electrostatic potential at the nucleus position of the Se atoms in the structure of $(Sb_7Se_8)[GaCl_4]_2[Ga_2Cl_7]_3$ (left) and $(Sb_7Se_8Cl_2)^{3+}$ (right) (PBE/VASP results).*

Polycationic clusters have already been examined by ^{77}Se NMR spectroscopy in SO_2 or H_2SO_4 solution. These investigations show the presence of equilibria between different mixed chalcogen polycations [63, 64] and the solution dynamics of the species Se_8^{2+} and Se_{10}^{2+}.[65] More recently, the solution dynamics of selenium-halogen cations like $Se_6I_2^{2+}$ was investigated by NMR, showing even more complex equilibria of several species.[66] The chemical shifts of the cationic Se species in solution are generally observed in the region between +1000 and +2000 ppm. A survey of the ^{77}Se resonances in the solid state NMR spectra of several inorganic compounds showed that selenides containing Se^{2-} appear around -500 ppm, elemental selenium at +800 ppm and formally positive Se like Se(IV) in SeO_3^{2-} around +1300 ppm.[67] NMR is thus a sensitive probe for the valence state of Se in molecules and solids. The chemical shifts found for the Se resonances in the positively charged clusters of $(Sb_7Se_8)[GaCl_4]_2[Ga_2Cl_7]_3$ and $(Sb_7Se_8Cl_2)[GaCl_4]_3$ show a remarkable high-field shift. This is in line with the observation of the stronger coordination of the Sb atoms by the chloridogallate anions in comparison to the chalcogen atoms in the crystal structures. Since the positive charges are mainly localized on the Sb atoms and strong covalent bonding is present, the nuclei of the Se atoms are substantially shielded by a high electron density.

* The figures were provided by Prof. Dr. Thomas Bredow.

2.3 Raman Examination of the Double Cube Shaped Clusters

Raman spectra of $Na(Sb_7Te_8)[GaCl_4]_6$, $(Sb_7Se_8)[GaCl_4]_2[Ga_2Cl_7]_3$, $(Sb_7Se_8Cl_2)[GaCl_4]_3$ and $(Sb_7S_8Cl_2)[GaCl_4]_3$ were recorded in the region between 80 and 420 cm^{-1} and compared with the calculated spectra (Fig. 2.3.1 - 2.3.2).* The vibration frequencies of the cluster cations, the tetrachloridogallate and the heptachloridodigallate anions were calculated for comparison and assignment (Fig. A 5.7.1 - A 5.7.6), since the typical vibrations appear all in the same spectral region between 60 cm^{-1} and 400 cm^{-1}. They were adjusted to the experimental obtained spectra by means of the strongest signal, respectively. Both, experimental and calculated spectra get more complex from the tellurium to the sulphur containing compound.

In aqueous solution, Raman bands at 114(s), 149(s), 346(vs) and 386(w) cm^{-1} have been assigned for the $[GaCl_4]^-$ anion,[68] which are in line with the present experiments if slight deviations due to the solid state of the samples and overlaps with the cluster bands are considered. In the spectra of $Na(Sb_7Te_8)[GaCl_4]_6$ and $(Sb_7Se_8Cl_2)[GaCl_4]_3$ the band at 345 cm^{-1} can unequivocally attributed to the A_2 vibration mode. In the spectrum of $Sb_8[GaCl_4]_2$[69] only this band was observed. In the spectrum of $(Sb_7S_8Cl_2)[GaCl_4]_3$ this band overlaps completely with the strongest band of the $(Sb_7S_8Cl_2)^{3+}$ cluster. The second F_2 vibration mode at 386 cm^{-1} is not observed in any of the spectra. According to literature, the $[Ga_2Cl_7]^-$ anion in $K[Ga_2Cl_7]$ shows Raman bands at 63(vs), 96(s), 107(m), 130(m), 141(m), 284(m), 365(vs) and 407(m) cm^{-1}.[70] In the spectrum of $(Sb_7Se_8)[GaCl_4]_2[Ga_2Cl_7]_3$ the band around 63 cm^{-1} could not be detected due to the overlap with the laser excitation. The bands at 95, a shoulder at 108 and bands at 282 and 412 cm^{-1} are in line with the expectation. At 372 cm^{-1} the characteristic and strongest signal for the $[Ga_2Cl_7]^-$ anion is found. Signals expected around 130 and 141 cm^{-1} overlap with signals of the cluster. The observed signals are supported by the calculated spectrum of $[Ga_2Cl_7]^-$ considering slight deviations (Fig. 2.3.1). In the spectrum of $(Sb_7Se_8)[GaCl_4]_2[Ga_2Cl_7]_3$, the only band arising from the mononuclear $[GaCl_4]^-$ ion is found at 349 cm^{-1}. The vibration modes of the clusters $(Sb_7Te_8)^{5+}$, $(Sb_7Se_8)^{5+}$, $(Sb_7Se_8Cl_2)^{3+}$, and $(Sb_7S_8Cl_2)^{3+}$ as well as the chlorido gallate anions, which occur in the region between 80 and 370 cm^{-1} have been calculated by DFT methods in the gas phase approximation. All clusters gain on the structure optimization procedure rather irregular structures with no internal molecular symmetry. Various individual throughout non-degenerate vibration modes arise from the low symmetry. The vibration modes are depicted in the appendix (Figs. A 5.7.1 - A 5.7.6). In the region above 180 cm^{-1} the calculated signals are generally in accurate agreement with the experimental data. Below 180 cm^{-1} some deviations between theory and experiment are present, which might be explained by the less accurate description of weaker forces by DFT methods and/or grid effects. The influences of the crystal lattice on the molecular vibration frequencies are not considered in the calculations. Additionally, bands of the clusters overlap with bands of the exciting laser close to 80 cm^{-1} in the spectra of $(Sb_7Se_8)[GaCl_4]_2[Ga_2Cl_7]_3$ and $(Sb_7Se_8Cl_2)[GaCl_4]_3$, which increases and falsifies their intensities.

* The DFT calculations were performed by Dr. Gregor Schakenburg.

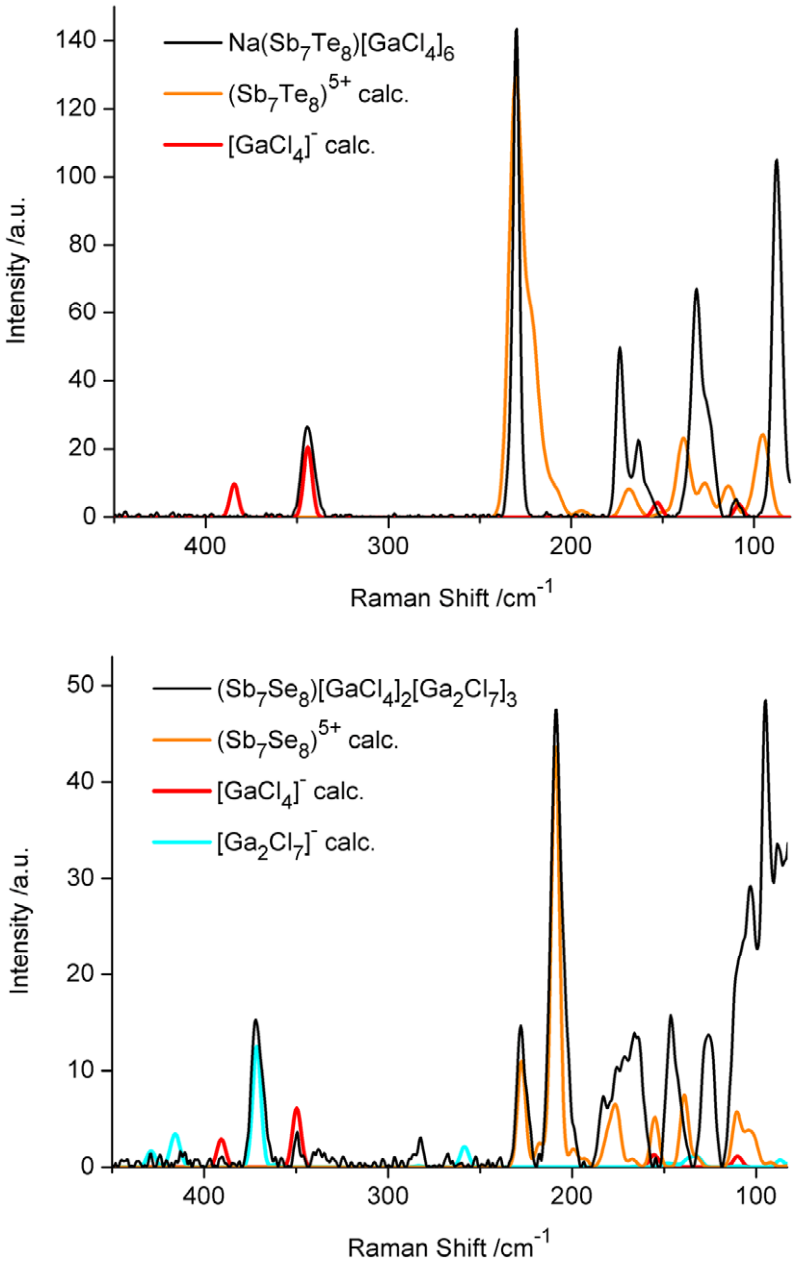

Fig. 2.3.1 Comparison between experimental and calculated Raman spectra of $Na(Sb_7Te_8)[GaCl_4]_6$ (top) and $(Sb_7Se_8)[GaCl_4]_2[Ga_2Cl_7]_3$ (bottom). Experimental spectra are drawn with black lines, the calculated spectra of the clusters with orange and of the chloridogallate anions with blue and red lines.

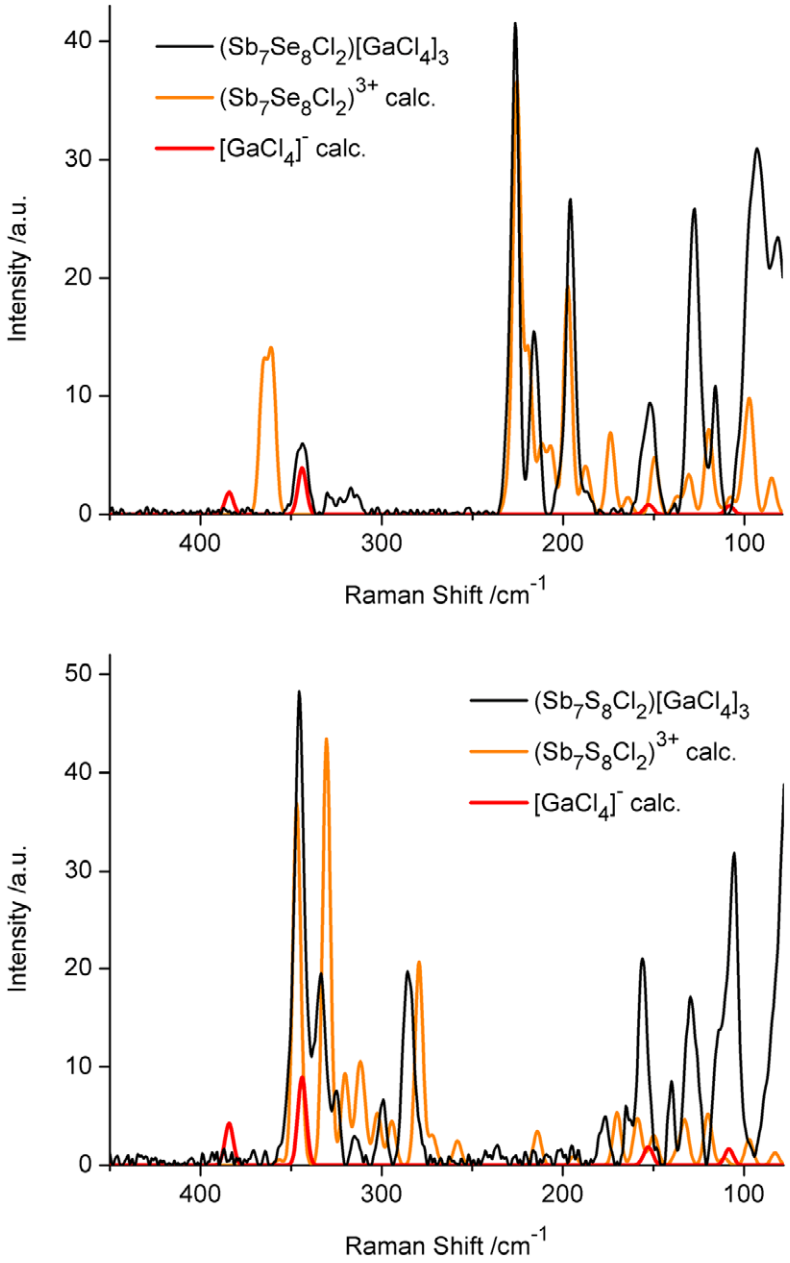

Fig. 2.3.2 Comparison between experimental and calculated Raman spectra of $(Sb_7Se_8Cl_2)[GaCl_4]_3$ (top) and $(Sb_7S_8Cl_2)[GaCl_4]_3$ (bottom). Experimental spectra are drawn with black lines, the calculated spectra of the clusters with orange and of the tetrachlorido gallate anions with red lines.

2.4 Comparison of the Double Cube Shaped Clusters

The $(Sb_7Te_8)^{5+}$ cluster in $(Sb_7Te_8)[GaCl_4]_2[Ga_2Cl_7]_3$ is extremely distorted compared with those in $(Sb_7Te_8)[GaCl_4]_3[Ga_2Cl_7]_2$ and $M(Sb_7Te_8)[GaCl_4]_6$ (M = Na, Ag, Cu), which show smaller distortions from the highest possible symmetry. However, generally the distortion increases from the tellurium containing clusters to the sulphur congeners due to the irregular bond length distribution and angle deviations from 90 and 180° around the six-fold coordinated Sb atom. In the $(Sb_7Ch_8Cl_2)^{3+}$ clusters additionally the elongated bonds along the Cl-Sb-Se edge contribute to the degree of distortion. Fig. 2.4.1 shows a compilation of the double cube shaped clusters.

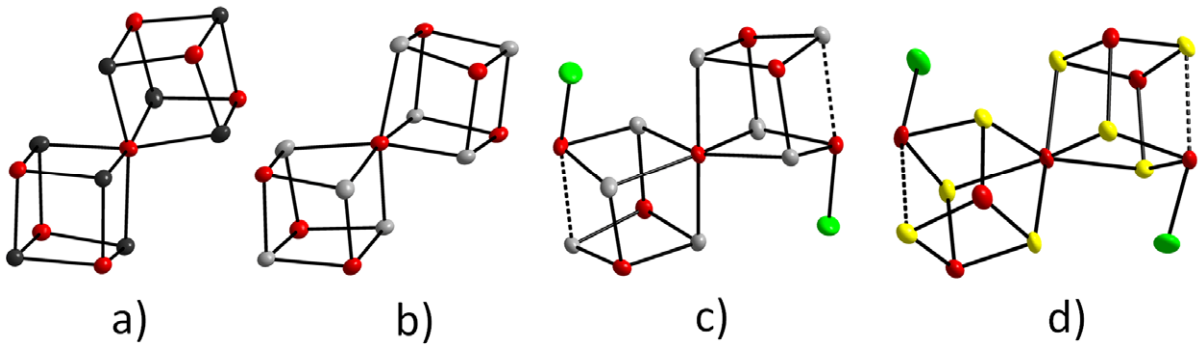

Fig. 2.4.1 The double cube shaped clusters $(Sb_7Te_8)^{5+}$ of $(Sb_7Te_8)[GaCl_4]_2[Ga_2Cl_7]_3$ (a), $(Sb_7Se_8)^{5+}$ (b), $(Sb_7Se_8Cl_2)^{3+}$ (c) and $(Sb_7S_8Cl_2)^{3+}$ (d).

2.5 The Cube Shaped Clusters $(Sb_4Te_4)^{4+}$ and $(Sb_4Se_4)^{4+}$

2.5.1 Syntheses and EDX Analyses of $(Sb_4Ch_4)[GaCl_4]_4$ (Ch = Te, Se)

$(Sb_4Te_4)[GaCl_4]_4$

45.9 mg (0.36 mmol) tellurium, 29.2 mg (0.24 mmol) antimony, 27.4 mg (0.12 mmol) antimony trichloride, 174.3 mg (0.99 mmol) gallium trichloride and 17.8 mg (0.18 mmol) of copper (I) chloride were filled in a glass ampoule under argon atmosphere. After 26 days at 88 °C orange crystals (Fig. 2.5.1.1) appeared in a black melt with an estimated yield of 20 %. It is remarkable that $(Sb_4Te_4)[GaCl_4]_4$ appears in the same experiment as $(Sb_7Te_8)[GaCl_4]_3[Ga_2Cl_7]_2$ after approx. half the time and a 12 °C lower temperature.

A tentative reaction equation is:

$8\ Sb + 12\ Te + 4\ SbCl_3 + 12\ GaCl_3 \rightarrow 3\ (Sb_4Te_4)[GaCl_4]_4$

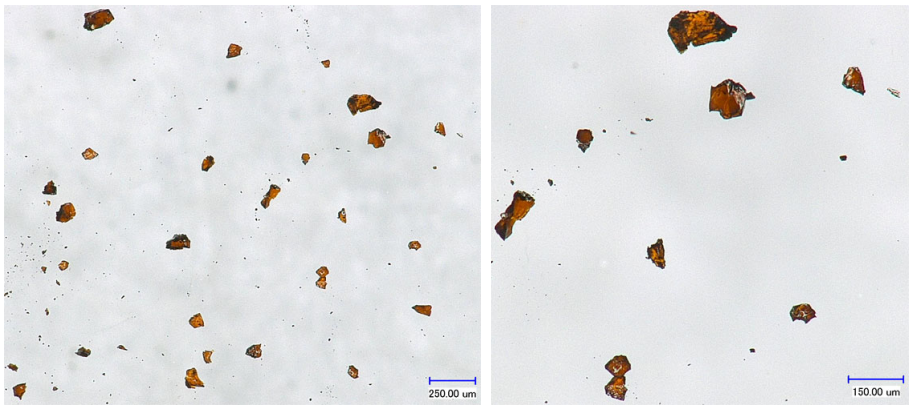

Fig. 2.5.1.1 Crystals of $(Sb_4Te_4)[GaCl_4]_4$ immersed in perfluorinated polyether.

The EDX analysis is in fair agreement with the sum formula $(Sb_4Te_4)[GaCl_4]_4$ (Tab. 2.5.1.1).

Tab. 2.5.1.1 Elemental composition of $(Sb_4Te_4)[GaCl_4]_4$ in atom-% and the Sb : Te ratio. Standard deviations given in brackets refer to the last significant digit.

$(Sb_4Te_4)[GaCl_4]_4$	Sb	Te	Ga	Cl	Sb : Te
Found	15.1(8)	15.5(7)	16.1(6)	53(1)	1 : 1.03
Calculated	14.29	14.29	14.29	57.14	1 : 1

$(Sb_4Se_4)[GaCl_4]_4$

The synthesis of $(Sb_4Se_4)[GaCl_4]_4$ was performed as for $(Sb_7Se_8)[GaCl_4]_2[Ga_2Cl_7]_3$. After 10 days crystals of $(Sb_7Se_8)[GaCl_4]_2[Ga_2Cl_7]_3$ were obtained in one end of the ampoule. By decanting, the hot melt was transferred in the other end of the ampoule and cooled down to room temperature with 6 °C/h. $(Sb_4Se_4)[GaCl_4]_4$ crystallized during the cooling process in form of small orange crystals in an orange solidified melt with an estimated yield of 30 % (Fig. 2.5.1.5). The powder pattern of the solidified melt is very similar to the calculated pattern of $(Bi_4Se_4)[AlCl_4]_4$[30]. The calculated patterns of $(Sb_4Se_4)[GaCl_4]_4$ and $(Bi_4Se_4)[AlCl_4]_4$ correspond.
Additionally, crystalline $GaCl_3$ and presumably $Cu[GaCl_4]$ are present in the melt (Fig. 2.5.1.2). $Cu[GaCl_4]_2$ shows a rather complex powder diffractogram and its presence in the melt can be excluded.

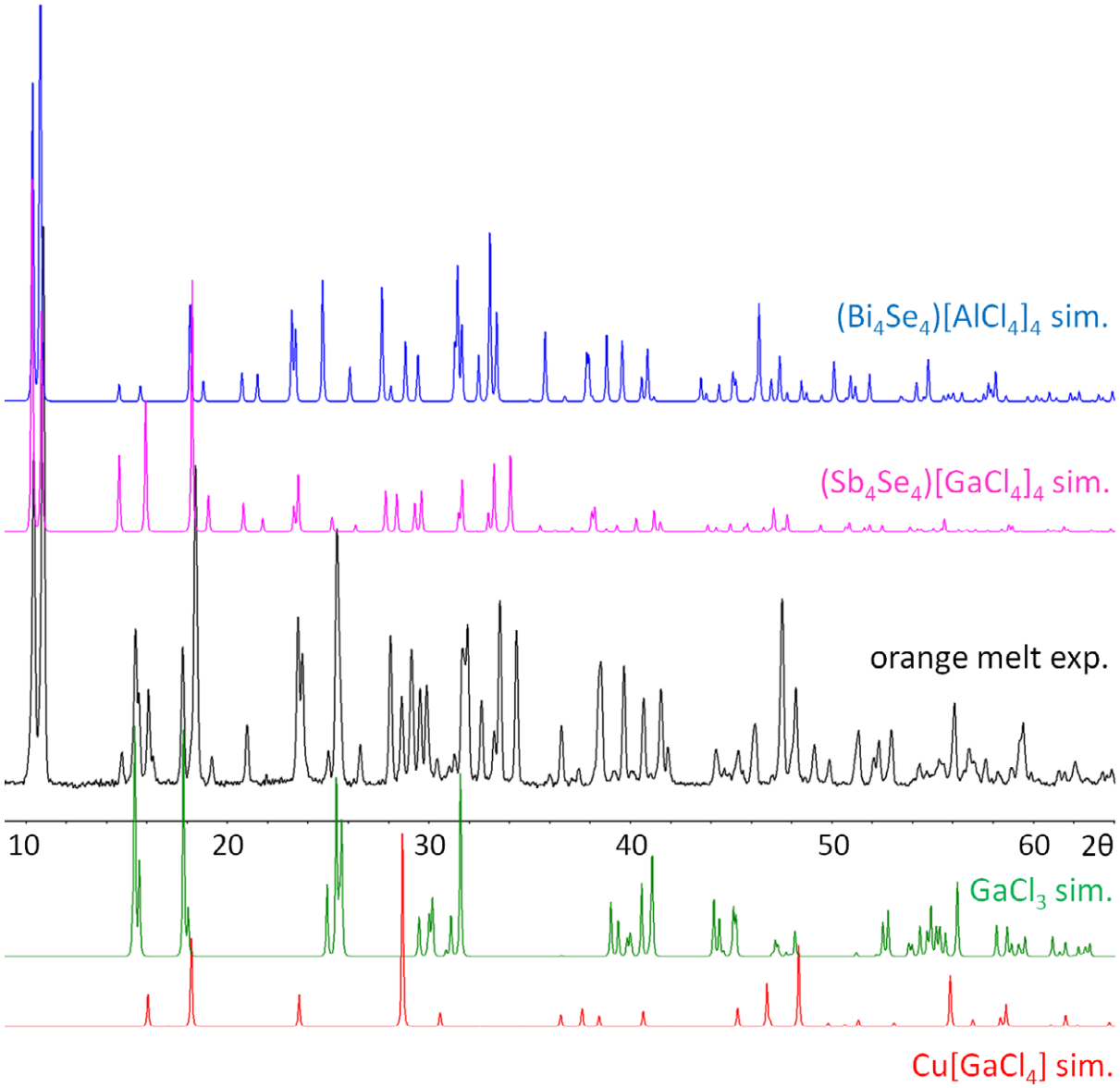

Fig. 2.5.1.2 Experimental powder diffractogram of the orange melt (black) and simulated patterns of $(Sb_4Se_4)[GaCl_4]_4$ (pink), $(Bi_4Se_4)[AlCl_4]_4$[30] (blue), $GaCl_3$ (green) and $Cu[GaCl_4]$ (red) [71] for comparison.

A tentative reaction equation may be set up in accordance to the tellurium congener:

$$8\ Sb + 12\ Se + 4\ SbCl_3 + 12\ GaCl_3 \rightarrow 3\ (Sb_4Se_4)[GaCl_4]_4$$

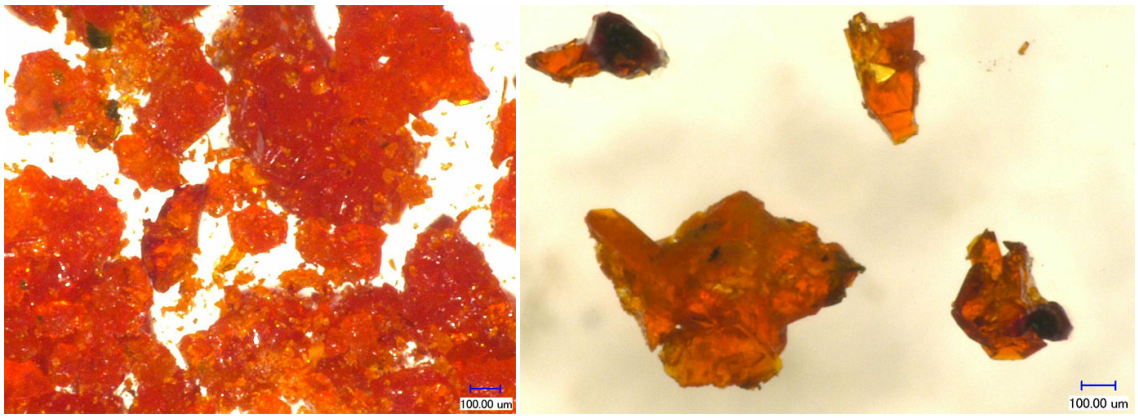

Fig. 2.5.1.3 Crystals of $(Sb_4Se_4)[GaCl_4]_4$ immersed in perfluorinated polyether.

The EDX analysis for Sb and Se is in accurate agreement with the sum formula $(Sb_4Se_4)[GaCl_4]_4$ (Tab. 2.5.1.2). The reason for the high Ga und low Cl content is not clear.

Tab. 2.5.1.2 Elemental composition of $(Sb_4Se_4)[GaCl_4]_4$ in atom-% and the Sb : Se ratio. Standard deviations given in brackets refer to the last significant digit.

$(Sb_4Se_4)[GaCl_4]_4$	Sb	Se	Ga	Cl	Sb : Se
Found	14.7(4)	14.5(8)	21.4(6)	49.2(8)	1 : 0.99
Calculated	14.29	14.29	14.29	57.14	1 : 1

2.5.2 The Reactions Leading to $(Sb_4Ch_4)[GaCl_4]_4$ (Ch = Te, Se)

As described in chapters 2.1.1 and 2.2.1, the product formation is controlled by the use of specific adjuvants. Both compounds $(Sb_4Ch_4)[GaCl_4]_4$ (Ch = Te, Se) are accessible with the use of CuCl. During the synthesis of $(Sb_4Te_4)[GaCl_4]_4$, a large amount of the black melt remained. The synthesis of $(Sb_4Se_4)[GaCl_4]_4$ yielded mainly $(Sb_7Se_8)[GaCl_4]_2[Ga_2Cl_7]_3$ and an orange melt, which after crystallzation at ambient temperature turned out by X-ray powder diffractometry and EDX analysis to be a mixture of $(Sb_4Se_4)[GaCl_4]_4$ and finely dispersed, crystalline copper chloridogallates. In the ^{77}Se-NMR spectrum of the melt, only one selenium signal is found as expected for the highly symmetric $(Sb_4Se_4)^{4+}$cluster (compare Fig. 2.2.4.2).

Both syntheses are related to those of $(Sb_7Te_8)[GaCl_4]_2[Ga_2Cl_7]_3$ and $(Sb_7Se_8)[GaCl_4]_2[Ga_2Cl_7]_3$. $(Sb_7Te_8)[GaCl_4]_2[Ga_2Cl_7]_3$ was obtained with a reaction temperature of 12 °C higher after the double time. $(Sb_7Se_8)[GaCl_4]_2[Ga_2Cl_7]_3$ was found in the same reaction as $(Sb_4Se_4)[GaCl_4]_4$. The adjuvant CuCl has a generally unknown effect on the melts, but leads reliably to the formation of single and double cube shaped polycationic clusters.

2.5.3 Crystal Structures of $(Sb_4Te_4)[GaCl_4]_4$ and $(Sb_4Se_4)[GaCl_4]_4$

The crystallographic data of $(Sb_4Te_4)[GaCl_4]_4$ and $(Sb_4Se_4)[GaCl_4]_4$ are listed in Tab. A 5.2.6 in the appendix.

Both compounds crystallize isotypically to their bismuth - aluminium congeners $(Bi_4Ch_4)[AlCl_4]_4$ (Ch = Te, Se) [29,30] in the acentric space group $I\bar{4}$. The cube shaped pentele - chalcogen clusters are build from two independent atoms. In the structure of $(Sb_4Te_4)[GaCl_4]_4$ the distances between the Sb and Te atoms of the cluster and the coordinating chlorine atoms of the chloridogallate anions (Fig. A 5.6.9) support the atom assignment within the cluster based on the occupation factors. Assigning both positions as occupied with tellurium leads to free occupation factors of 0.983(1) and 0.998(1) and a clear distinction of the pentele and chalcogen positions (Tab. A 5.3.5). Sb-Cl distances range from 2.975(1) - 3.702(1) Å, Te-Cl distances from 3.5785(9) - 3.8537(9) Å (Tab. A 5.5.6).

As described in Ref. [30], the crystal examined of $(Bi_4Se_4)[AlCl_4]_4$ exhibits the inverse structure compared to the examined crystal for $(Bi_4Te_4)[AlCl_4]_4$. The same unequivocal assignment can be made in the structures of both title compounds. They consist of slightly distorted cube shaped $(Sb_4Ch_4)^{4+}$ (Ch = Te, Se) polycationic clusters and tetrahedral $[GaCl_4]^-$ anions. Figure 2.5.3.1 shows the unit cell of $(Sb_4Te_4)[GaCl_4]_4$ with the corresponding $(Sb_4Te_4)^{4+}$ cation and its Lewis formula. The pentele - chalcogen bond lengths range from 2.8635(4) - 2.9377(4) Å in $(Sb_4Te_4)[GaCl_4]_4$ and from 2.6627(6) - 2.7631(7) Å in $(Sb_4Se_4)[GaCl_4]_4$ (Tab. A 5.4.9). With Sb-Te-Sb angles of 88.0 - 91.0 ° and Te-Sb-Te angles of 87.7 - 92.0° the $(Sb_4Te_4)^{4+}$ is slightly less distorted than the $(Sb_4Se_4)^{4+}$ (Sb-Se-Sb 89.3 - 93.2°, Se-Sb-Se 86.6 - 90.6°)

The coordinating tetrachlorido gallate anions (Figs. A 5.6.9 - A 5.6.10) occupy general positions. With Ga–Cl bond lengths of 2.146(1) - 2.206(1) in the structure of $(Sb_4Te_4)[GaCl_4]_4$ and 2.142(1) - 2.217(1) in the structure of $(Sb_4Se_4)[GaCl_4]_4$ the ions show a slight distortion from ideal tetrahedral symmetry. This fact is underlined by the Cl-Ga-Cl angles of 103 - 116° in the tellurium and 102 - 118° in the selenium containing structure.

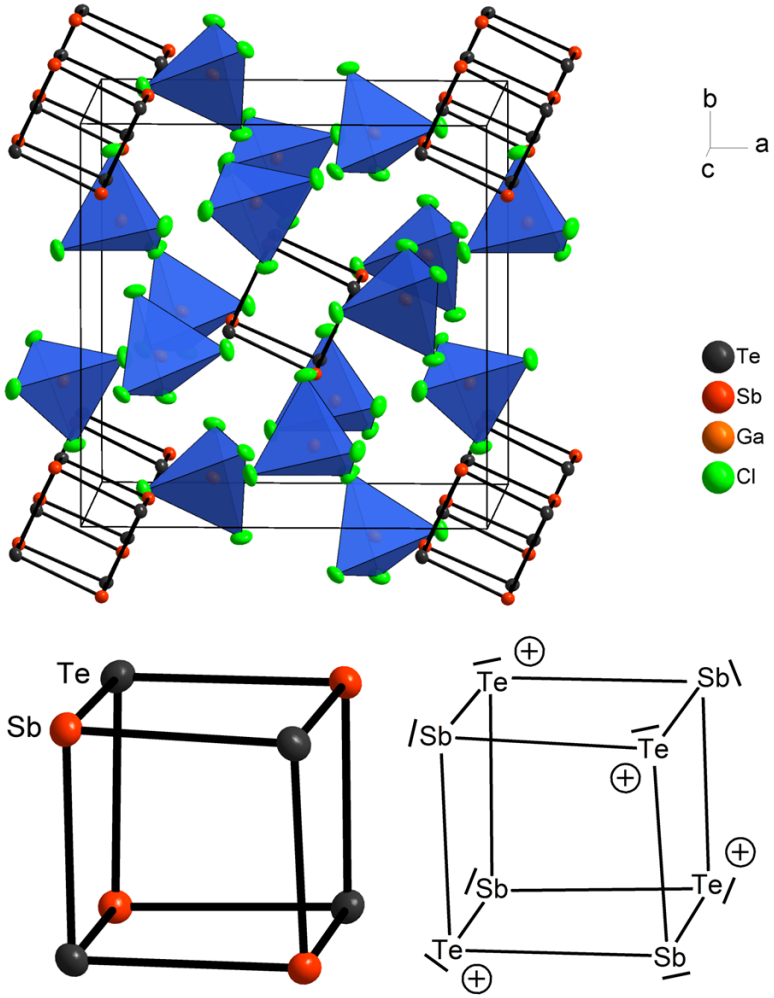

Fig. 2.5.3.1 The unit cell of the structure of $(Sb_4Te_4)[GaCl_4]_4$ (top). The $[GaCl_4]^-$ ions are represented by discrete tetrahedra. On bottom the individual $(Sb_4Te_4)^{4+}$ cluster cation (left) and the corresponding Lewis formula (right) is given which is analogous to $(Sb_4Se_4)^{4+}$. The atoms are represented by thermal ellipsoids scaled to include a probability of 80 %.

2.5.4 Raman Spectroscopy Study of $(Sb_4Te_4)[GaCl_4]_4$ and $(Sb_4Se_4)[GaCl_4]_4$

Raman spectra were recorded for $(Sb_4Te_4)[GaCl_4]_4$ and $(Sb_4Se_4)[GaCl_4]_4$ and calculated by DFT methods in the gas phase approximation. The vibration frequencies of the cluster cations and of the tetrachloridogallate and heptachloridodigallate anions were calculated for comparison and assignment. In general, reliable statements can be given for the resonances higher than 85 cm^{-1} because the exciting laser generates Raman bands at 75 and 78 cm^{-1}. The calculated spectra were adjusted to the experimental spectra by means of the strongest signal, respectively. Besides that, the intensities of the calculated signals were chosen lower compared to those obtained from the experiment for clarity. Fig. 2.5.4.1 shows the comparison between the experimental and calculated Raman spectra of $(Sb_4Te_4)[GaCl_4]_4$ and $(Sb_4Se_4)[GaCl_4]_4$.

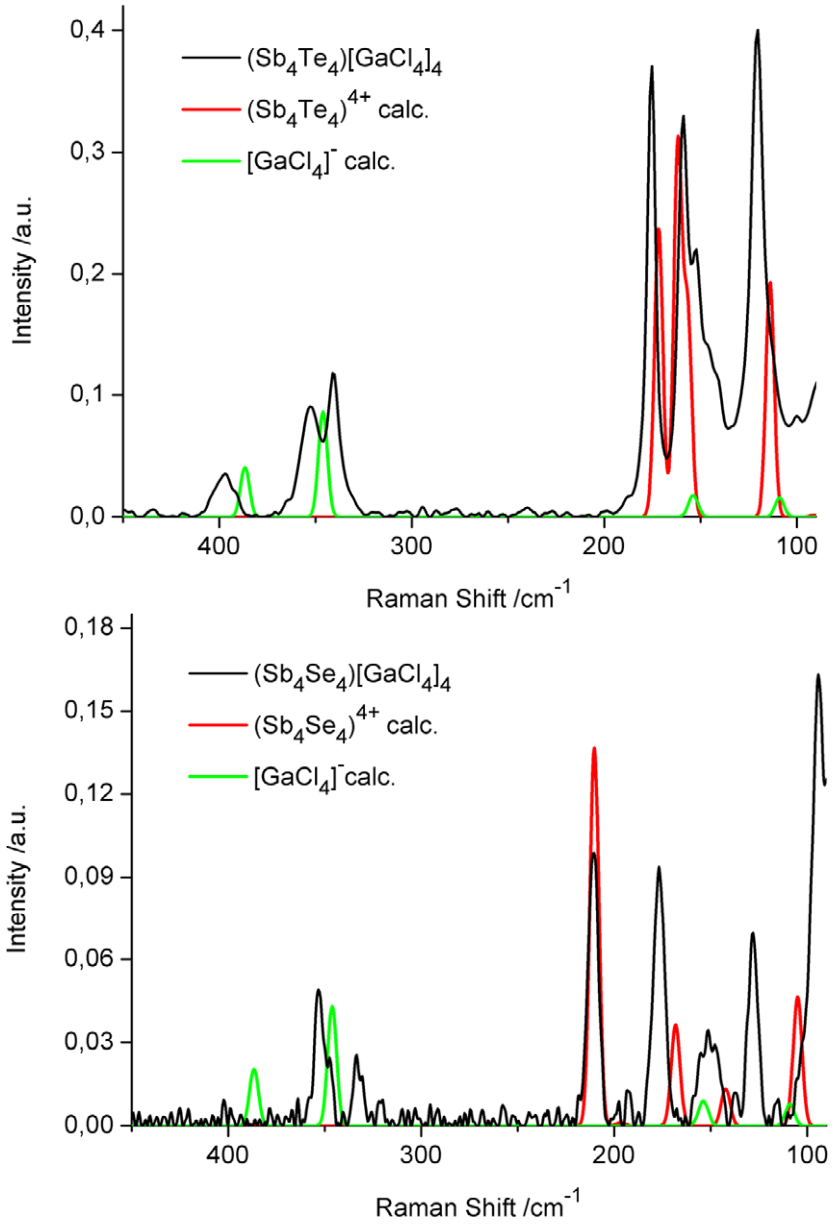

Fig. 2.5.4.1 Comparison between experimental and calculated Raman spectra of $(Sb_4Te_4)[GaCl_4]_4$ (top) and $(Sb_4Se_4)[GaCl_4]_4$ (bottom). Experimental spectra are drawn with black lines, the calculated spectra of the clusters are red and those of the tetrachloridogallate anions are green.

Since $(Sb_4Ch_4)^{4+}$ clusters are highly symmetrical, assessable spectra are obtained. The bands at 345 cm^{-1} can be unequivocally attributed to the A_2 vibration mode of the $[GaCl_4]^-$ anion.[70] The other typical Raman bands for this anions in aqueous solution at 114(s), 149(s) and 386(w) cm^{-1} can not be identified due to overlap with the cluster bands.[68] The calculated spectrum of $(Sb_4Te_4)[GaCl_4]_4$ fits the experiment accurately. Four signals are confirmed between 120 and 180 cm^{-1}. A large background is found in the region of the cluster signals, for which the reason is not clear. In the experimental spectrum of $(Sb_4Se_4)[GaCl_4]_4$, five sharp cluster bands are obtained between 90 and 220 cm^{-1}, which fits to five calculated bands in this region. However, one of the bands at 196 cm^{-1} is extremely weak in relation to the others. Presumably the split signal at 151 cm^{-1} is explained by the calculated spectrum, which does not support the experimental spectrum as well as compared to $(Sb_4Te_4)[GaCl_4]_4$. The corresponding signal may be present in the shoulder between 140 and 150 cm^{-1} in the spectrum of $(Sb_4Te_4)[GaCl_4]_4$ since the two spectra are expected to be similar. Probably the signal at 162 cm^{-1} in the

calculated spectrum of $(Sb_4Te_4)[GaCl_4]_4$ splits into multiple signals in the solid state which is already indicated by the shoulder at 158 cm^{-1}. In the experimental spectrum a clear band at 152 cm^{-1} is found. The reason for the large difference in intensity between the band at 94 cm^{-1} in the spectrum of $(Sb_4Se_4)[GaCl_4]_4$ and the calculated band is the partial overlap with the laser band in this region.
The calculated vibration modes of the $(Sb_4Ch_4)^{4+}$ clusters are shown in Figs. A 5.7.7 and A 5.7.8.

2.6 The Mixed Heptanuclear Cluster $(Sb_3Te_4)^{3+}$

2.6.1 Syntheses and EDX Analyis of $(Sb_3Te_4)[Ga_2Cl_7]_3$

The synthesis of $(Sb_3Te_4)[Ga_2Cl_7]_3$ could be performed analogously to the synthesis of $(Sb_4Te_4)[GaCl_4]_4$ by replacing CuCl by the respective amount of AgCl. Heating to 100 °C for 18 days yielded orange crystals in a black melt. Unfortunately, this way of synthesis was not reproducible like an analogous experiment with sodium chloride as the adjuvant at 200 °C which had already led to $(Sb_3Te_4)[Ga_2Cl_7]_3$. A more reliable way to obtain the title compound is the use of gallium oxide as an adjuvant. Starting from the same amounts of tellurium, animony, antimony trichloride and gallium trichloride and adding 75.0 mg (0.40 mmol) Ga_2O_3 led to $(Sb_3Te_4)[Ga_2Cl_7]_3$ after heating the ampoule to 50 °C for 10 days and 70 °C for further 19 days. Crystals are orange and plate shaped (Fig. 2.6.1.1). The yield did not exceed 5 % in all runs.

A tentative reaction equation is:

$2\ Sb + 4\ Te + SbCl_3 + 6\ GaCl_3 \rightarrow (Sb_3Te_4)[Ga_2Cl_7]_3$

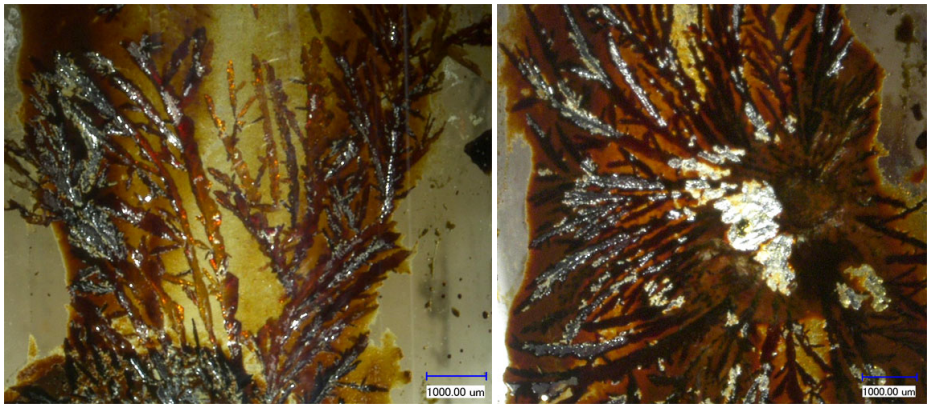

Fig. 2.6.1.1 Crystals of $(Sb_3Te_4)[Ga_2Cl_7]_3$ in the reaction ampoule. The silvery shimmer on the crystal surface is caused by tellurium excess.

The EDX analysis is in excellent agreement with the sum formula $(Sb_3Te_4)[Ga_2Cl_7]_3$ concerning the Sb:Te ratio (Tab. 2.6.1.1). The higher obtained results for Sb and Te lead to a lower result for Cl. Only the Ga content is in accurate agreement with the expectation.

Tab. 2.6.1.1 Elemental composition of $(Sb_3Te_4)[Ga_2Cl_7]_3$ in atom-% and the Sb : Te ratio. Standard deviations given in brackets refer to the last significant digit.

$(Sb_3Te_4)[Ga_2Cl_7]_3$	Sb	Te	Ga	Cl	Sb : Te
Found	13.8(3)	18.4(5)	17.0(6)	50.6(3)	1 : 1.33
Calculated	8.8	11.8	17.6	61.8	1 : 1.33

2.6.2 Crystal Structure of $(Sb_3Te_4)[Ga_2Cl_7]_3$

The triclinic structure of $(Sb_3Te_4)[Ga_2Cl_7]_3$ consists of $(Sb_3Te_4)^{3+}$ polycationic clusters and $[Ga_2Cl_7]^-$ anions. The cluster may be understood as either as a prism with an extended corner or a cube with a missing corner (Fig. 2.6.2.1). The crystallographic data are listed in Tab. A 5.2.7.

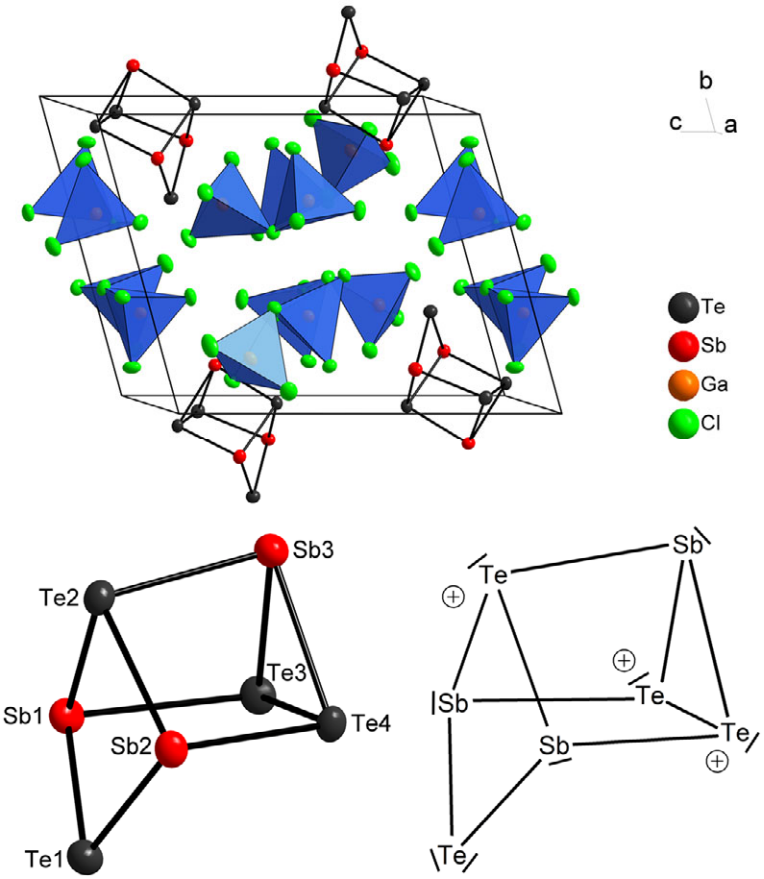

Fig. 2.6.2.1 The unit cell of the structure of $(Sb_3Te_4)[Ga_2Cl_7]_3$ (top). The $[Ga_2Cl_7]^-$ ions are represented by discrete tetrahedra. On bottom the individual $(Sb_3Te_4)^{3+}$ cluster cation (left) with Sb/Te site assignments of the lowest-energy isomer and the respective Lewis formula (right) are are given. The atoms are represented by thermal ellipsoids scaled to include a probability of 70 %.

In the $(Sb_3Te_4)^{3+}$ cluster seven independent atom positions are present with occupation factors of 0.951(2), 0.961(2), 0.961(1), 0.969(2), 0.989(2), 0.990(2) and 0.994(2) when refined as occupied with tellurium with free occupation factors (Fig. A 5.3.6). For the composition Sb_3Te_4, one expects three "small" occupation factors <1 and four "large" occupation factors of approximately 1. The observed occupation is almost in line with the sum formula $(Sb_3Te_4)^{3+}$ for the cationic cluster since four "small" and three "large" occupation factors are found.

Following, the occupation factors within the cluster based on the diffraction data give unambigous assignments for the atom positions Sb1, Sb2, Sb3, Te2, Te3 and Te4 are unambiguous (Fig. A 5.3.6). The occupation factor of Te1 is, however, not in line with the atom site distribution of this lowest-energy isomer. Charge neutrality demands a charge of +3 for the cluster and from the experience with mixed polycationic pentele/chalcogen or pure chalcogen clusters, three-fold coordinated chalcogen atoms cause the positive charge [29,30,32,33,34,36,38,40,51] following the Lewis formalism. The EDX analysis supports antimony-tellurium ratio of 3:4 unequivocally (Tab. 2.6.1.1).
The depicted isomer in Figure 2.6.2.1 is the one of 21 conceivable isomers (Fig. 2.6.2.2) with the maximized number of heteronuclear bonds and one homonuclear bond.

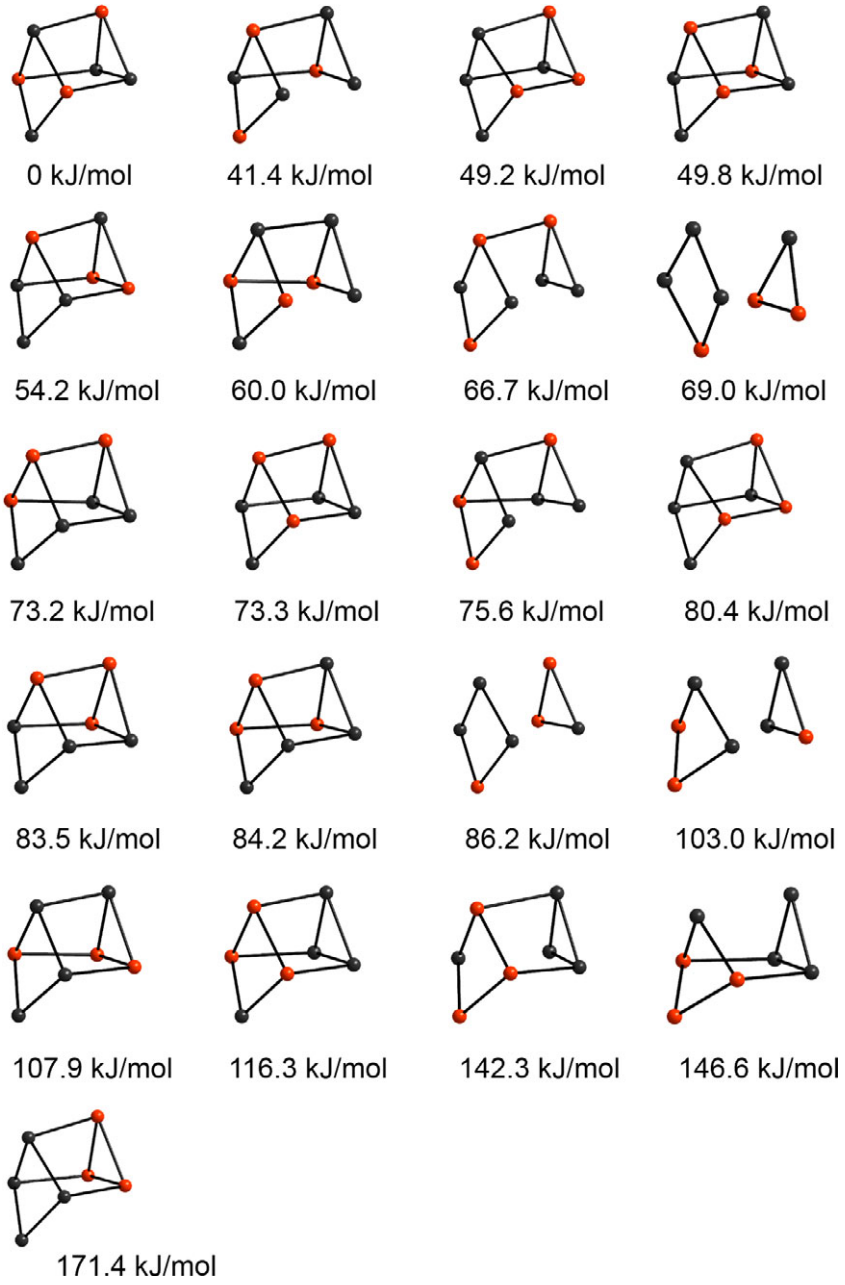

Fig. 2.6.2.2 Graphical representation of the 21 possible isomers of the $(Sb_3Te_4)^{3+}$ cluster with calculated potential energies (B3LYP/TZV(2d/sp)) normalized to the isomer with the lowest energy. Bonds are considered up to 3.1 Å.*

* The calculations were performed by Dr. Gregor Schnakenburg.

All other isomers have at least two homonuclear bonds. Furthermore the minimum number +3 of formel charges is present. A DFT calculation of the relative energetic levels of all these isomers normalized to the expected isomer shows the next more unfavourable isomer to be 41.4 kJ/mol higher. The most improbable isomer with the maximized number of homonuclear bonds is found at a level of 171.4 kJ/mol. Considering the distances to the coordinating chlorine atoms of the $[Ga_2Cl_7]^-$ anions (Fig. A 5.6.11) the atom assignments of all positions besides Te3 are supported (Tab. A 5.5.7). Shorter contacts are indicative for Sb, longer contacts for Te (Sb1–Cl 3.242(2) - 3.951(2) Å, Sb2–Cl 3.201(2) - 3.685(2) Å, Sb3–Cl 3.220(2) - 3.738(2) Å, Te1–Cl 3.6742(1) - 3.986(2) Å, Te2–Cl 3.472(1) - 3.754(1) Å, Te4–Cl 3.499(2) - 4.007(2) Å). The Te3–Cl distances range from 3.2312) to 3.879(2) Å.
The intramolecular Sb–Te bond lengths range between 2.7367(5) and 2.9752(5) Å. The only homonuclear bond within the triangular site plane between Te3 and Te4 is 2.7471(5) Å which is close to the average Te–Te bond length of 2.724(1) Å in Te_8^{2+} [72] in the structure of $Te_8[ReCl_6]$ (Tab. A 5.4.10). The distortion of the cluster is mainly observed on the Sb1-Te3-Te4 and Sb2-Te4-Te3 angles of 100.12(2)° and 101.17(2)°. The Sb1-Sb2 distance is straddled by the two-fold coordinated Te1 to reach angles close to 90° within the square plane (Sb1-Te1-Sb2 89.12(2)°, Sb1-Te2-Sb2 84.96(2)°, Te1-Sb1-Te2 90.09(2), Te1-Sb2-Te2 89.87(2)°).
The heptachlorido digallate anions in $(Sb_3Te_4)[Ga_2Cl_7]_3$ are located on general positions and do not show any remarkable deviations from those found in $K[Ga_2Cl_7]$[51].

2.7 The Prism Shaped Polycationic Clusters $(Pn_2Te_4)^{2+}$ (Pn = As, Sb)

2.7.1 Syntheses and EDX Analyses of Compounds Containing the $(Pn_2Te_4)^{2+}$ Clusters

$(As_2Te_4)[Ga_2Cl_7]_2$

A glass ampoule was filled with 45.9 mg (0.36 mmol) tellurium, 18.0 mg (0.24 mmol) arsenic, 21.8 mg (0.12 mmol) arsenic trichloride, 174.0 mg (0.99 mmol) gallium trichloride and 60.0 mg (0.16 mmol) tetraphenyl phosphonium chloride. Arsenic trichloride had to be added with a small syringe, which did not allow for an exact weighing of this compound. The amount was calculated from the weight of individual drops. After 1-2 weeks at 50 - 100 °C orange crystals were obtained (Fig. 2.7.1.1) in a liquid, orange-yellowish melt. The highest yield was achieved at 100 °C with about 25 %. Alternatively, $(As_2Te_4)[Ga_2Cl_7]_2$ can be synthesized be replacing tetraphenyl phosphonium chloride by the respective amount of both, diarsenic trioxide and sodium chloride and heating the mixture to 100 °C. The yields are comparable but the almost solidified melt using this pair of adjuvants makes it more difficult to separate the crystals.

A tentative reaction equation is:

$$4\ As + 12\ Te + 2\ AsCl_3 + 12\ GaCl_3 \rightarrow 3\ (As_2Te_4)[Ga_2Cl_7]_2$$

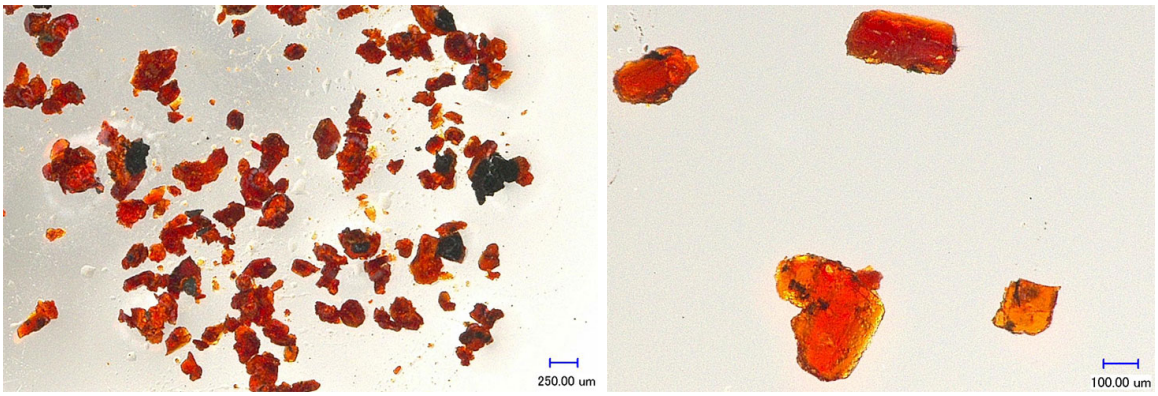

Fig. 2.7.1.1 Crystals of $(As_2Te_4)[Ga_2Cl_7]_2$ immersed in perfluorinated polyether.

The EDX analysis of $(As_2Te_4)[Ga_2Cl_7]_2$ is in fair agreement with the sum formula (Tab. 2.7.1.1) for As and Te. The too high Ga result leads to a lower value for Cl. The reason for the higher Ga value is not clear.

Tab. 2.7.1.1 Elemental composition of $(As_2Te_4)[Ga_2Cl_7]_2$ in atom-% and the As : Te ratio. Standard deviations given in brackets refer to the last significant digit.

$(As_2Te_4)[Ga_2Cl_7]_2$	As	Te	Ga	Cl	As : Te
Found	8.3(5)	16.3(7)	20.4(4)	54.8(7)	1 : 1.96
Calculated	8.3	16.6	16.7	58.3	1 : 2.00

$(Sb_2Te_4)[Ga_2Cl_7]_2$

23.0 mg (0.18 mmol) tellurium, 14.6 mg (0.12 mmol) antimony, 13.7 mg (0.06 mmol) antimony trichloride, 87.1 mg (0.49 mmol) gallium trichloride, 16.7 mg (0,09 mmol) indium(II) chloride and 30.0 mg (0.08 mmol) tetraphenylphosphonium chloride were sealed in a glass ampoule and annealed at 100 °C for 11 days. $(Sb_2Te_4)[Ga_2Cl_7]_2$ forms square plate shaped crystals (Fig. 2.7.1.2) in a black melt in an estimated yield of 30 %. As a byproduct, $(Sb_7Te_8)[GaCl_4]_3[Ga_2Cl_7]_2$ (chapter 2.1) crystallizes as orange rod shaped crystals in low yield. Without the addition of PPh_4Cl, only this compound forms.

A tentative reaction equation is:

$$9\ Sb + 20\ Te + 4\ SbCl_3 + 20\ GaCl_3 + InCl_2 \rightarrow 3\ (Sb_2Te_4)[Ga_2Cl_7]_2 + (Sb_7Te_8)[GaCl_4]_2[Ga_2Cl_7]_3 + InCl_3$$

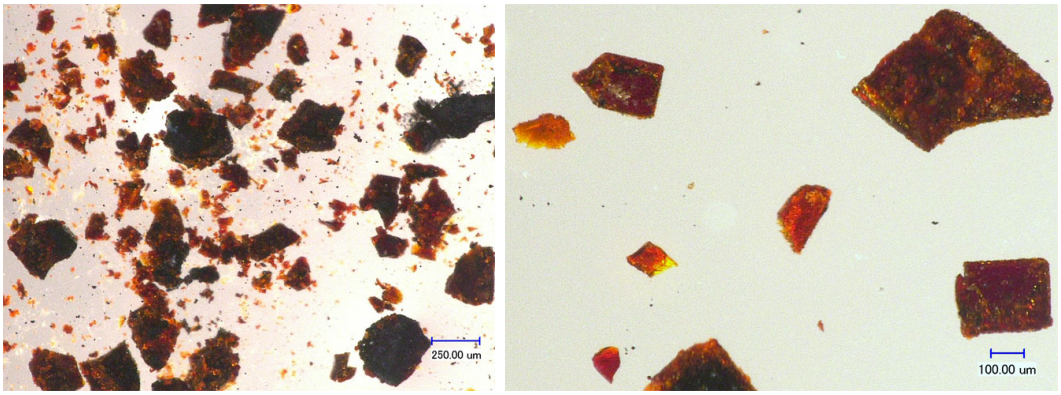

Fig. 2.7.1.2 Crystals of $(Sb_2Te_4)[Ga_2Cl_7]_2$ immersed in perfluorinated polyether.

The EDX analysis reveals too high contents for Sb, Te and Ga. Nevertheless, the Sb:Te ratio is in line with the calculated ratio of 1:2.

Tab. 2.7.1.2 Elemental composition of $(Sb_2Te_4)[Ga_2Cl_7]_2$ in atom-% and the Sb : Te ratio. Standard deviations given in brackets refer to the last significant digit.

$(Sb_2Te_4)[Ga_2Cl_7]_2$	Sb	Te	Ga	Cl	Sb : Te
Found	10.3(3)	20.9(4)	20.1(4)	48.6(5)	1 : 2.03
Calculated	8.3	16.6	16.7	58.3	1 : 2.00

$(Sb_2Te_4)[GaCl_4]_2$

45.2 mg (0.36 mmol) tellurium, 29.2 mg (0.24 mmol) antimony, 27.4 mg (0.12 mmol) antimony trichloride, 174.3 mg (0.99 mmol) gallium trichloride and 68.2 mg (0.18 mmol) tetraphenylphosphonium chloride were filled in glass ampoule, which was evacuated and sealed. On annealing at 88 °C crystals appear within 26 days as a byproduct in form of orange, plate shaped crystals in an estimated yield of 10 % (Fig. 2.7.1.3). As a main product, $(Sb_3Te_4)[GaCl_4]$ (chapter 2.9) crystallizes in a light greenish, liquid melt. Additionally, $(Sb_2Te_4)[GaCl_4]_2$ is formed during the synthesis of $CuTe_4[GaCl_4]$ (chapter 2.12) in a comparable amount. By the use of 6.4 mg (0.18 mmol) lithium chloride as an additional adjuvant, only $(Sb_2Te_4)[GaCl_4]_2$ is formed in higher yield of about 30 % at 100 °C within 11 days.

A tentative reaction equation for the experiment leading to $(Sb_3Te_4)[GaCl_4]$ is:

$$4\ Sb + 8\ Te + SbCl_3 + 3\ GaCl_3 \rightarrow (Sb_2Te_4)[GaCl_4]_2 + (Sb_3Te_4)[GaCl_4]$$

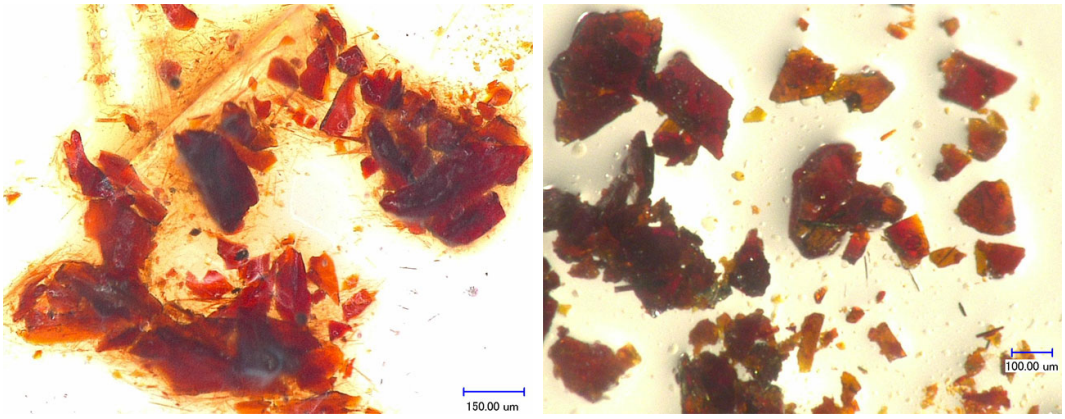

Fig. 2.7.1.3 Crystals of $(Sb_2Te_4)[GaCl_4]_2$ immersed in perfluorinated polyether. Left as a byproduct from the synthesis of $(Sb_3Te_4)[GaCl_4]$, right as as a byproduct from the synthesis of $CuTe_4[GaCl_4]$ (metallic rod shaped crystals).

In the EDX analysis, three crystals of $(Sb_2Te_4)[GaCl_4]_2$ were examined. The results show a too high Ga content, which is a general problem in most analyses performed during this work. Considering these deviations, the results for Sb, Te and Cl are in the expected ranges and support the sum formula. The Sb:Te ratio is in accurate agreement with the calculation.

Tab. 2.7.1.3 Elemental composition of $(Sb_2Te_4)[GaCl_4]_2$ in atom-% and the Sb : Te ratio. Standard deviations given in brackets refer to the last significant digit.

$(Sb_2Te_4)[GaCl_4]_2$	Sb	Te	Ga	Cl	Sb : Te
Found	10.9(3)	21.6(5)	18.9(6)	48.9(7)	1 : 1.98
Calculated	12.5	25	12.5	50	1 : 2.00

$M(As_2Te_4)[GaCl_4]_3$ (M = K, Rb, Cs, NH_4, In, Tl)

45.9 mg (0.36 mmol) tellurium, 18.0 mg (0.24 mmol) arsenic, 21.8 mg (0.12 mmol) arsenic trichloride, 174.3 mg (0.99 mmol) gallium trichloride and 0.18 mmol of the respective monochloride (KCl, RbCl, CsCl, NH_4Cl, InCl, TlCl) were filled in a glass ampoule under argon atmosphere and heated to 100 - 120 °C. After 1 - 2 weeks, $M(As_2Te_4)[GaCl_4]_3$ crystallized as orange crystals in a liquid orange-yellowish melt in an estimated yield of 30-40 % (Fig. 2.7.1.4). The yield of $Cs(As_2Te_4)[GaCl_4]_3$ could be improved to about 50 % by adding 60.0 mg (0.16 mmol) PPh_4Cl.

A tentative reaction equation is:

$4\ As + 12\ Te + 2\ AsCl_3 + 9\ GaCl_3 + 3\ MCl \rightarrow 3\ M(As_2Te_4)[GaCl_4]_3$

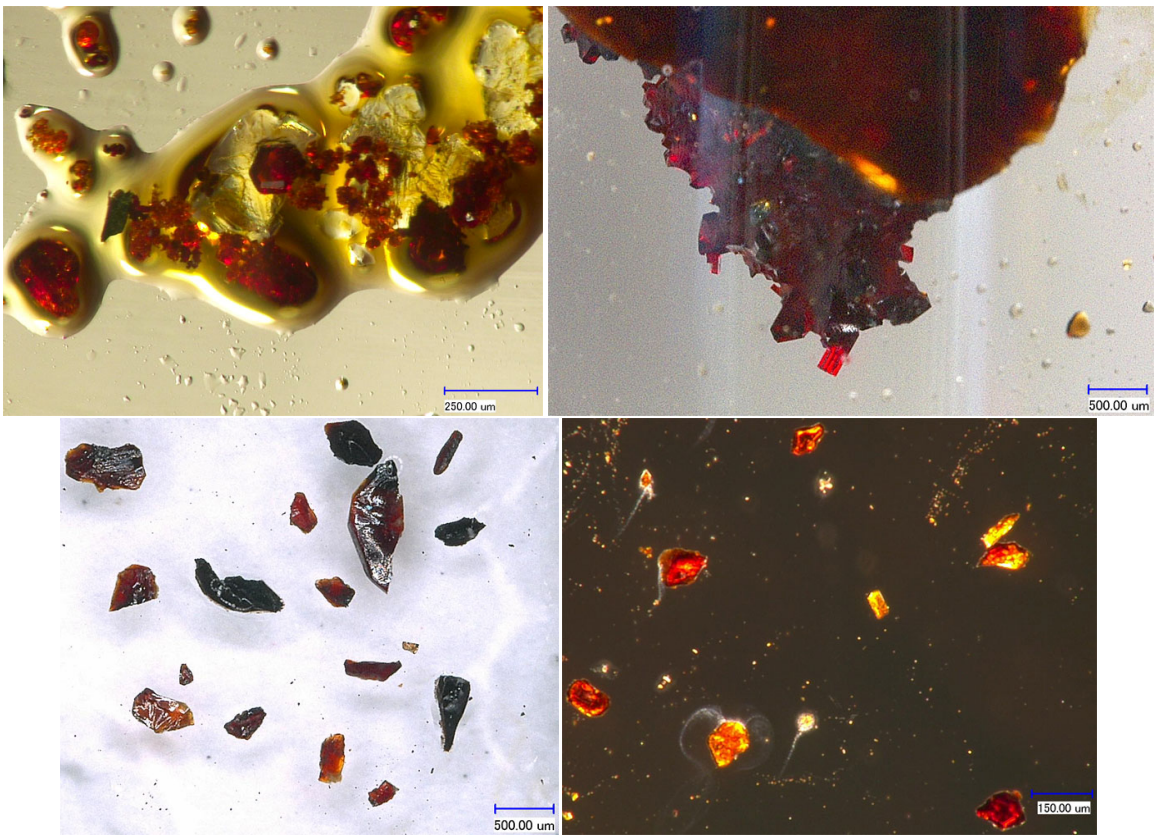

Fig. 2.7.1.4 Crystals of $K(As_2Te_4)[GaCl_4]_3$ (top left), $Cs(As_2Te_4)[GaCl_4]_3$ (top right), $In(As_2Te_4)[GaCl_4]_3$ (bottom left) and $Tl(As_2Te_4)[GaCl_4]_3$ (bottom right) immersed in perfluorinated polyether or in the reaction ampoule.

The EDX analyses of all $M(As_2Te_4)[GaCl_4]_3$ are in fair agreement with the sum formula (Tab. 2.7.1.4). The As and Te contents reveal a constant ratio of 1:2 for all obtained compounds. The reason for the too high Ga values in some cases is not clear.

Tab. 2.7.1.4 Elemental composition of $M(As_2Te_4)[GaCl_4]_3$ in atom-% and the As : Te ratio. Standard deviations given in brackets refer to the last significant digit.

$M(As_2Te_4)[GaCl_4]_3$	M	As	Te	Ga	Cl	As : Te
$K(As_2Te_4)[GaCl_4]_3$	4.2(2)	7.4(5)	15.2(7)	23.3(15)	49.7(5)	1 : 2.03
$Rb(As_2Te_4)[GaCl_4]_3$	3.5(1)	8.7(4)	17.5(4)	16.9(4)	53.1(3)	1 : 2.00
$Cs(As_2Te_4)[GaCl_4]_3$	4.8(1)	8.8(2)	18.2(1)	15.72)	52.2(1)	1 : 2.06
$NH_4(As_2Te_4)[GaCl_4]_3$	-	10.0(3)	19.5(2)	19.4(7)	50.9(5)	1 : 1.94
$In(As_2Te_4)[GaCl_4]_3$	3.95(6)	9.8(2)	20.2(2)	14.9(2)	50.9(2)	1 : 2.05
$Tl(As_2Te_4)[GaCl_4]_3$	4.5(1)	8.1(3)	16.3(2)	20.1(4)	50.8(3)	1 : 2.02
Calculated	4.5	9.1	18.2	13.6	54.5	1 : 2.00

$M(Sb_2Te_4)[GaCl_4]_3$ (M = K, Rb, Cs, NH_4, Tl)

For the synthesis of $M(Sb_2Te_4)[GaCl_4]_3$, arsenic and arsenic trichloride (as used for the synthesis of $M(As_2Te_4)[GaCl_4]_3$) were replaced by the respective amounts of antimony and antimony trichloride. Crystals of $M(Sb_2Te_4)[GaCl_4]_3$ were formed during 3 - 5 weeks at 100 - 120 °C. All compounds were obtained as orange crystals in yields of about 10 % (Fig. 2.7.1.5). The yields of $Rb(Sb_2Te_4)[GaCl_4]_3$ and $Cs(Sb_2Te_4)[GaCl_4]_3$ can be improved to about 30 % by adding 60.0 mg (0.16 mmol) PPh_4Cl. Yields of $K(Sb_2Te_4)[GaCl_4]_3$, $NH_4(Sb_2Te_4)[GaCl_4]_3$ and $Tl(Sb_2Te_4)[GaCl_4]_3$ can be improved to about 50 % by replacing the elements by Sb_2Te_3.

A tentative reaction equation can be set up according to the arsenic congener:

$$Sb + 12\ Te + 2\ SbCl_3 + 9\ GaCl_3 + 3\ MCl \rightarrow 3\ M(Sb_2Te_4)[GaCl_4]_3$$

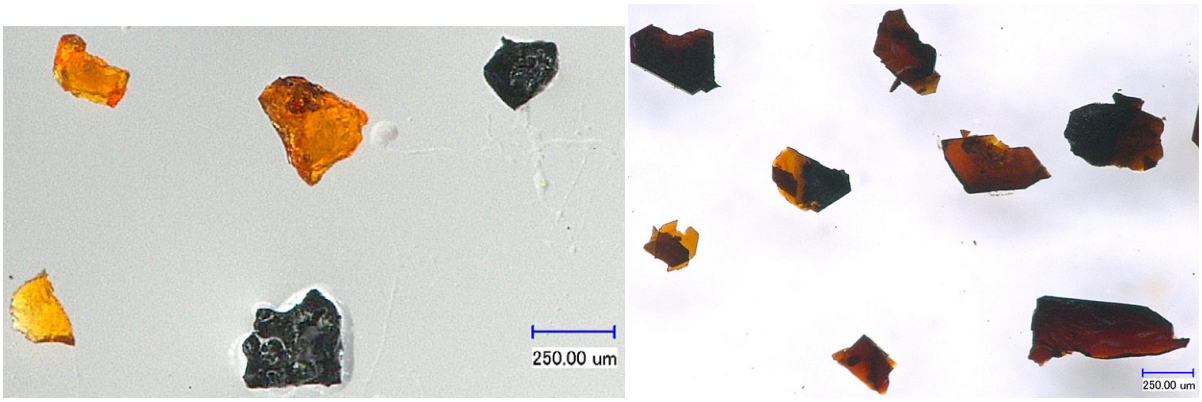

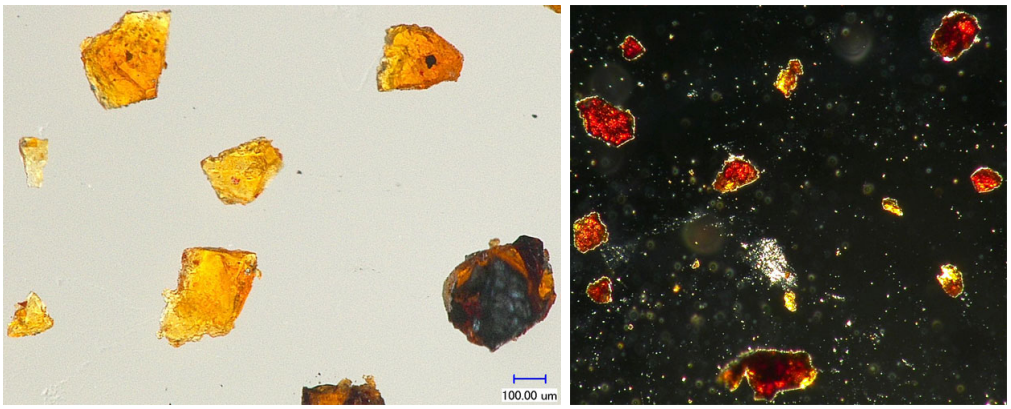

Fig. 2.7.1.5 Crystals of $K(Sb_2Te_4)[GaCl_4]_3$ (top left), $Rb(Sb_2Te_4)[GaCl_4]_3$ (top right), $NH_4(Sb_2Te_4)[GaCl_4]_3$ (bottom left) and $Tl(Sb_2Te_4)[GaCl_4]_3$ (bottom right) immersed in perfluorinated polyether.

In general, the EDX analyses of all $M(Sb_2Te_4)[GaCl_4]_3$ agree with the sum formula (Tab. 2.7.1.5). Only $Rb(Sb_2Te_4)[GaCl_4]_3$ and $Cs(Sb_2Te_4)[GaCl_4]_3$ show remarkable deviations in the expected Sb:Te ratio of 1:2. Additionally, a too high result for Ga in the analysis of $NH_4(Sb_2Te_4)[GaCl_4]_3$ is obtained. N can not be quantified with this method due to a too low energy of the N-*L* X-ray emission line.

Tab. 2.7.1.5 Elemental composition of $M(Sb_2Te_4)[GaCl_4]_3$ in atom-% and the Sb : Te ratio. Standard deviations given in brackets refer to the last significant digit.

$M(Sb_2Te_4)[GaCl_4]_3$	M	Sb	Te	Ga	Cl	Sb : Te
$K(Sb_2Te_4)[GaCl_4]_3$	5.0(5)	9.8(4)	19.0(8)	15(1)	50.5(4)	1 : 1.94
$Rb(Sb_2Te_4)[GaCl_4]_3$	4.1(2)	9.5(2)	17.2(3)	15.3(4)	53.7(3)	1 : 1.80
$Cs(Sb_2Te_4)[GaCl_4]_3$	4.31(9)	9.0(2)	16.7(3)	16.6(8)	53.3(5)	1 : 1.84
$NH_4(Sb_2Te_4)[GaCl_4]_3$	-	8.0(5)	16(1)	21(1)	53(2)	1 : 1.99
$Tl(Sb_2Te_4)[GaCl_4]_3$	5.3(1)	8.7(2)	16.7(4)	16.8(5)	52.4(5)	1 : 1.92
Calculated	4.5	9.1	18.2	13.6	54.5	1 : 2.00

2.7.2 The Reactions Leading to $(Pn_2Te_4)^{2+}$ Containing Compounds

In the synthesis of $(As_2Te_4)[Ga_2Cl_7]_2$ containing PPh_4Cl only the liquid reaction melt and negligible amounts of As and Te remind. None of the adjuvants used in the syntheses of $(As_2Te_4)[Ga_2Cl_7]_2$, $(Sb_2Te_4)[Ga_2Cl_7]_2$ and $(Sb_2Te_4)[GaCl_4]_2$ was incorporated in the final products.

In the structures of $M(Pn_2Te_4)[GaCl_4]_3$, the adjuvants are incooperated in the crystalline products. The synthesis of $Cs(Sb_2Te_4)[GaCl_4]_3$ without the use of PPh_4Cl leads to a large amount of additional $Cs[GaCl_4]$ and lowers the yield of the intended product. By adding PPh_4Cl, the formation of $Cs[GaCl_4]$ is avoided. In all other cases, only small amounts of $M[GaCl_4]$ are observed. In general, the syntheses of $M(As_2Te_4)[GaCl_4]_3$ proceed much faster and with higher yields than the analogous antimony congeners. All compounds $M(Pn_2Te_4)[GaCl_4]_3$ could be obtained at temperatures between 88 and 140 °C. The highest yields were obtained at 100 °C, only for $Tl(As_2Te_4)[GaCl_4]_3$ the optimal temperature was 120 °C.

The reaction ampoules of $M(Sb_2Te_4)[GaCl_4]_3$ contain a large amount of residual solidified black melt, which makes it generally difficult to separate the crystals for analytics. The liquid melt of

$M(As_2Te_4)[GaCl_4]_3$ is mainly decantable from the crystals at room temperature. $In(Sb_2Te_4)[GaCl_4]_3$ could not be obtained, because InCl acts an adjuvant for the synthesis of $(Sb_7Te_8)[GaCl_4]_2[Ga_2Cl_7]_3$.
The used adjuvants M^+ (M = K, Rb, Cs, NH_4, In, Tl) are spherical cations. The attempt to incorporate the non spherical cations NH_3Me^+ and NH_3Et^+ as chlorides did not succeed. Obviously the structure of $M(Pn_2Te_4)[GaCl_4]_3$ can only be realized with spherical cations M^+. Attempts to synthesize a hypothetical $(Bi_2Te_4)^{2+}$ prismatic cluster were not successful.

2.7.3 Crystal Structures of Compounds Containing the $(Pn_2Te_4)^{2+}$ Clusters

$(As_2Te_4)[Ga_2Cl_7]_2$ crystallizes in the space group *C*2/*c* and consists of prism shaped $(As_2Te_4)^{2+}$ polycationic clusters and $[Ga_2Cl_7]^-$ anions (Fig. 2.7.3.1). The crystallograpic data are shown in table A 5.2.8.
The correct atom assignment of the arsenic and tellurium positions was not possible on basis of the diffraction data due to a statistical disorder of all heavy atom positions caused by an arbitrary orientation of the prisms in the crystal structure along their approximated three-fold axis. Due to two $[Ga_2Cl_7]^-$ anions in the asymmetric unit, the As:Te relation is expected to be 1:2 to formulate a $(As_2Te_4)^{2+}$ polycationic cluster to obtain charge balance. EDX measurements confirm the clusters' composition unequivocally (Tab. 2.7.1.1). The polycationic cluster is build of three crystallographical independent positions refined as tellurium. In a distance of 0.5 - 0.8 Å high electron densities are found, which were refined as occupied by arsenic (As1, As2) and tellurium (Te3b). Using the same positional and displacement factors for both kinds of atoms with the ShelXL commands EXYZ and EADP did not succeed due to the formation of new electron densities next to the combined positions. Free refinements of the double occupied positions led to 50:50 occupations for As:Te on two positions and 50:50 occupation for Te:Te on the third position. Different crystals of $(As_2Te_4)[Ga_2Cl_7]_2$ were examined several times on different diffractometers at different temperatures. All measurements led to the same results.
Concerning the As and Te distribution within the clusters, an aggregation of arsenic on only two positions could be detected (Te1/As1, Te2/As2). The third position is occupied solely by Te and Te3b (Fig. 2.7.3.1).

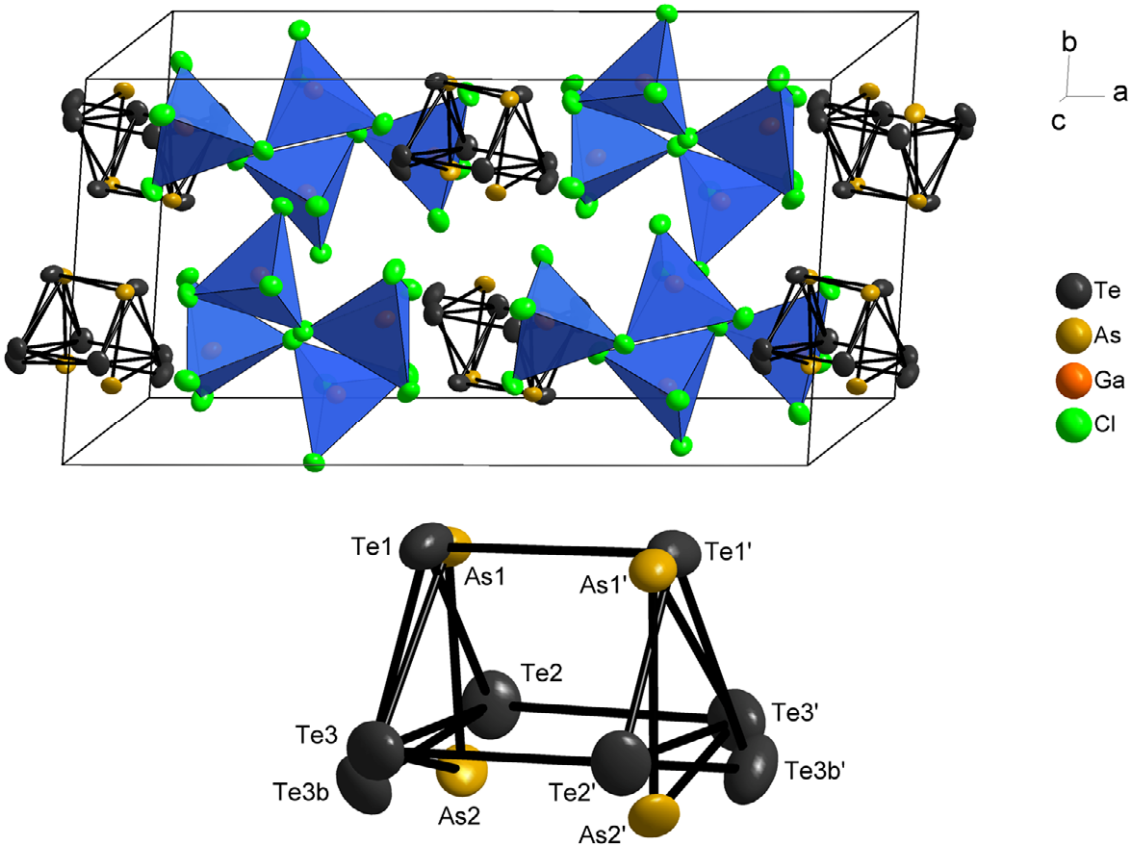

Fig. 2.7.3.1 The unit cell of the structure of $(As_2Te_4)[Ga_2Cl_7]_2$ (top). The $[Ga_2Cl_7]^-$ ions are represented by discrete tetrahedra. On bottom the disordered $(As_2Te_4)^{2+}$ cluster is shown. The atoms are represented by thermal ellipsoids scaled to include a probability of 50 %.

Due to the disorder the intermolecular distances of the cluster atoms to surrounding chlorine atoms can not be taken as evidence for the presence of arsenic or tellurium on the respective positions. The charge balance demands a cluster with a charge of +2, which can only be realized by the sum formula $(As_2Te_4)^{2+}$. Additionally, three different isomers of this cluster have to be considered being present in the structure. A more detailed insight the question of isomers will be demonstrated below in the Raman analysis.

Fig. 2.7.3.2 shows the potential energies of the three isomers, respectively, normalized to the isomer of the lowest energy and the maximized number of heteronuclear bonds and no As–As contacts. The cleaved Te–Te bond is 3.35 Å. Generally, all calculated isomers are open prisms after structure optimization. In the case of the lowest energy isomer two enantiomorphs have to be considered. The next more unfavourable isomer holds an As–As bond within the rectangular plane. Two weak bonds with 3.25 Å are found. The As–As bond of the highest energetic isomer is located in the triangular site plane of the prisms. The cleaved bond is 3.26 Å. The 2c-2e bonds in all calculated $(As_2Te_4)^{2+}$ clusters are max. 3.0 Å.

The bonding situation in the corresponding calculated $(Sb_2Te_4)^{2+}$ isomers is similar to this found for the $(As_2Te_4)^{2+}$ isomers. 2c-2e bonds are considered up to 3.17 Å. Cleaved Te–Te bonds are 3.43 Å and weak bonds 3.26 Å.

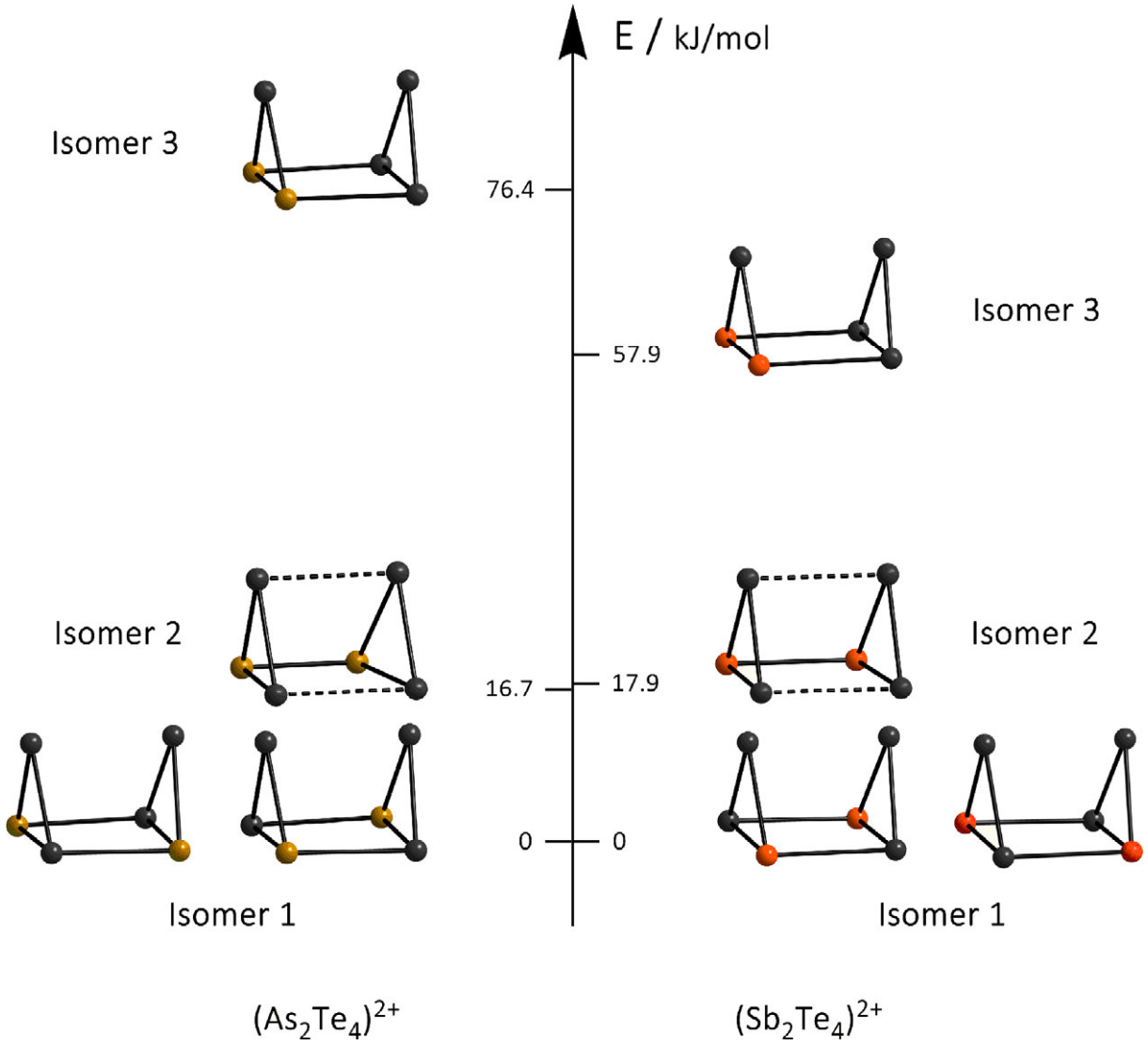

Fig. 2.7.3.2 Calculated Gibbs free enthalpie of three isomers of $(As_2Te_4)^{2+}$ (left) and $(Sb_2Te_4)^{2+}$ (right) (B3LYP/TZV(2d/sp))*. Full bonds are considered up to 3.0 Å (left) and 3.17 Å (right). Dashed lines illustrate weak bonds of 3.25 (left) and 3.26 Å (right).

The compounds $(Sb_2Te_4)[Ga_2Cl_7]_2$ and $(Sb_2Te_4)[GaCl_4]_2$ crystallize in the azentric space groups $Pca2_1$ and $P2_12_12_1$. They consist of $(Sb_2Te_4)^{2+}$ polycationic clusters in boat conformation and chloridogallate anions (Fig. 2.7.3.3). In the structure of $(Sb_2Te_4)[Ga_2Cl_7]_2$ the $(Sb_2Te_4)^{2+}$ clusters form two layers with opposed orientations of the slightly tilted clusters, respectively. In the structure of $(Sb_2Te_4)[GaCl_4]_2$, the $(Sb_2Te_4)^{2+}$ clusters have the same orientation and are slightly tilted along the *c*-direction The clusters are defined by six independent atom positions, respectively. The crystallographicc data are shown in Tabs. A 5.2.8 and A 5.2.9.

* The calculations were performed by Dr. Gregor Schnakenburg.

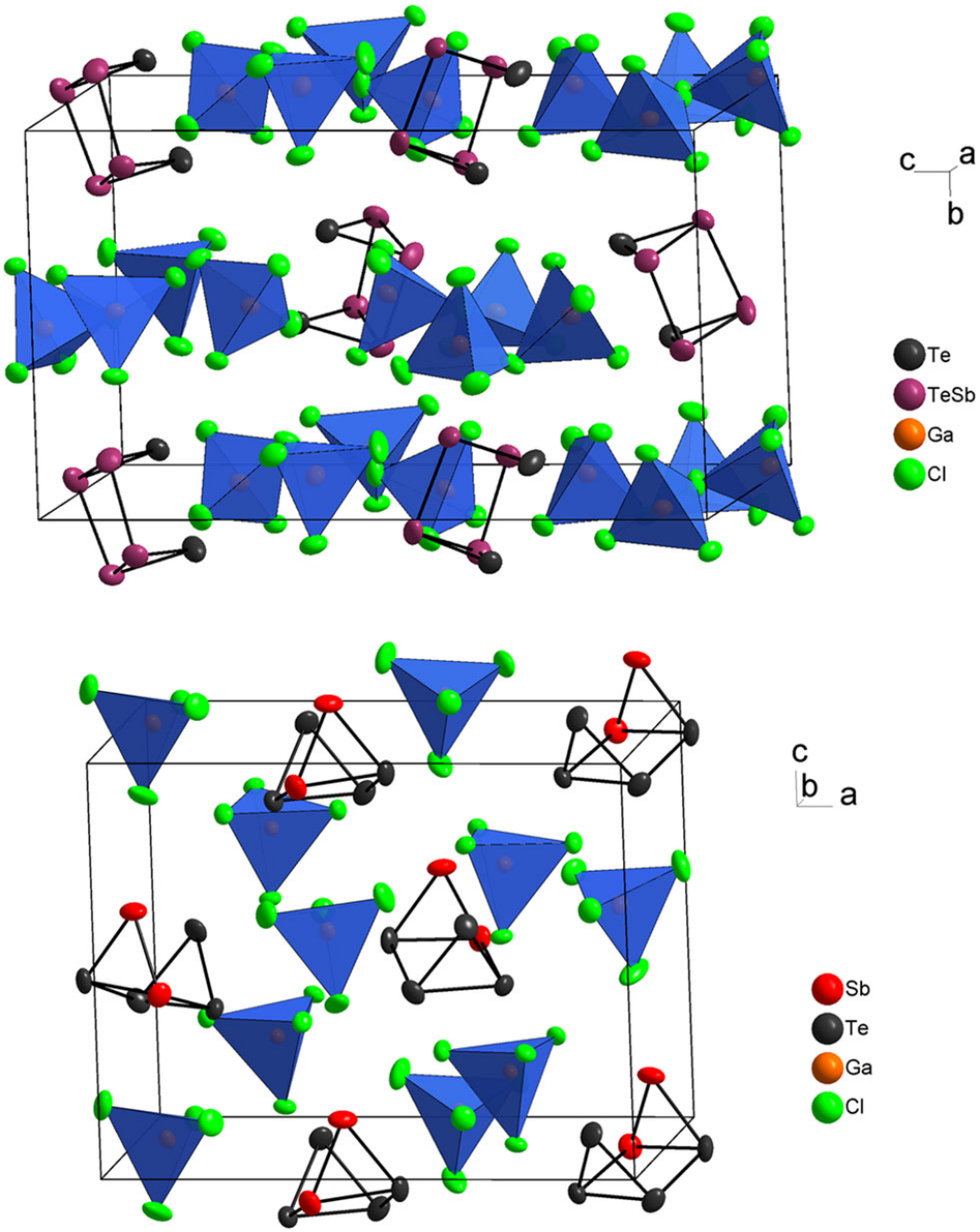

Fig. 2.7.3.3 The unit cells of the structures of $(Sb_2Te_4)[Ga_2Cl_7]_2$ (top) and $(Sb_2Te_4)[GaCl_4]_2$ (bottom). The $[Ga_2Cl_7]^-$ and $[GaCl_4]^-$ ions are represented by discrete tetrahedra and double tetrahedra. The atoms are represented by thermal ellipsoids scaled to include a probability of 70 %. Some anions are omitted for clarity.

In the $(Sb_2Te_4)^{2+}$ cluster in the structure of $(Sb_2Te_4)[Ga_2Cl_7]_2$, four under-occupied atom sites with occupation factors of 0.975(6), 0.983(5) and 0.977(5) (2x) are obtained when refined as occupied by tellurium with free ocupation factors. Two sites give occupation factors of 1.004(5) and 1.003(5) (Fig. A 5.3.7). The four lower occupied sites were refined as half occupied by both Te and Sb, the two full occupied sites were set to Te, solely. This disorder can be conceived as a mixture of both enatiomorphs of the lowest energy isomer 1 of the $(Sb_2Te_4)^{2+}$ cluster (compare Fig. 2.7.3.2). The Sb–Te bond lengths in the triangular plane of the prism are uniform with an average of 2.726 Å. Along the prism edges, three different bond lengths are present. The mixed atom sites bind with 3.069(2) and 3.116(2) Å to each other. The Te–Te distance is significantly longer with 3.305(2) Å and indicates a

weak homonuclear interaction. The parameters obtained for the calculated isomer 1 of the $(Sb_2Te_4)^{2+}$ cluster are in line with the experimental values. The average calculated bond length in the triangular plane of the cluster is 2.88 Å, the prism edges are 3.10 Å and the weak interaction is 3.43 Å. An analysis of the closest Te/Sb···Cl and Te···Cl interactions indicates a preferred occupation of Sb on the position of Te/Sb3 (Sb/Te3···Cl 3.285(4) - 3.903(3)). All other interactions to coordinating Cl atoms are approximately uniform and inconspicuous for the respective elements (Tab. A 5.5.8).
Due to the crystallization in an acentric space group, only one enantiomorph is expected in the crystal, which is ensured by a Flack *x* parameter of –0.01(1). However, the disorder erases the enatiomeric purity.

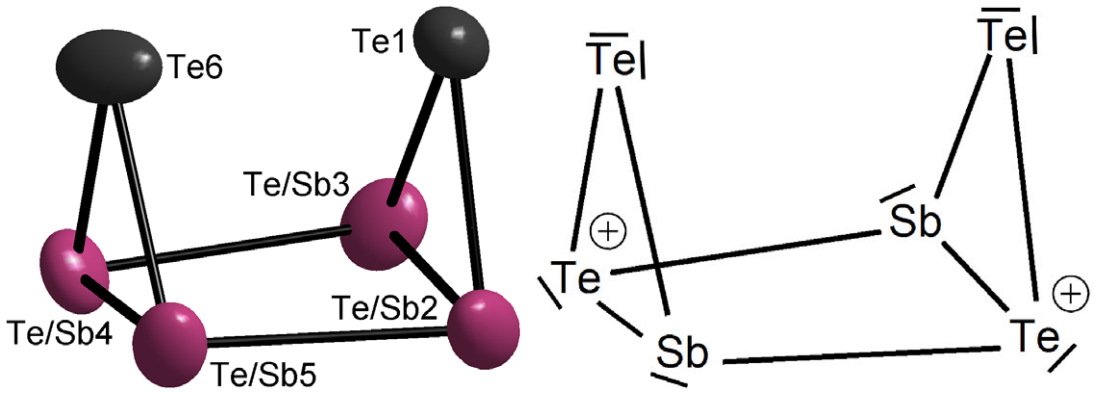

Fig. 2.7.3.4 The individual disordered $(Sb_2Te_4)^{2+}$ polycation in the structure of $(Sb_2Te_4)[Ga_2Cl_7]_2$ with four sites occupied by both Te and Sb (left). The atoms are represented by thermal ellipsoids scaled to include a probability of 70 %. On the right the Lewis formula of one enatiomorph of the isomer 1 of the $(Sb_2Te_4)^{2+}$ cluster is given.

In the $(Sb_2Te_4)^{2+}$ cluster of $(Sb_2Te_4)[GaCl_4]_2$, two atom sites give occupation factors of 0.963(6) and 0.965(6) when refined as occupied by tellurium with free occupation factors. In contrast, the other four atom sites reveal occupation factors of 0.980(6), 0.977(6), 0.982(6) and 0.990(6) (Fig. A 5.3.8). Consequently, the two lower occupied sites were set to be occupied by Sb, so that a homonuclear Sb–Sb bond is present in the triangular plane (Fig. 2.7.3.5). The shorter edges of the rectangular plane of the prisms are slightly elongated (2.795(2), 2.788(2) Å) compared to the corresponding bonds in the $(Sb_2Te_4)^{2+}$ cluster in $(Sb_2Te_4)[Ga_2Cl_7]_2$ (2.752(2), 2.754(2) Å). Even the non-bonding interaction along the open edge of the prism is elongated to 3.596(2) Å (Tab. A 5.4.11). An analysis of the intermolecular interactions to coordinating Cl atoms did not reveal any preferred occupation of Sb or Te on specific positions (Tab. A 5.5.9).

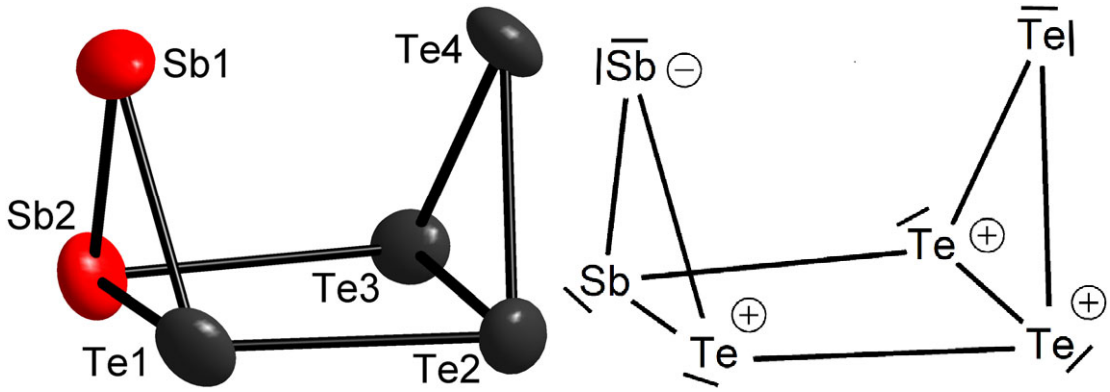

Fig. 2.7.3.5 The individual $(Sb_2Te_4)^{2+}$ cluster in the structure of $(Sb_2Te_4)[GaCl_4]_2$ (left). The atoms are represented by thermal ellipsoids scaled to include a probability of 70 %. On the right the Lewis formula of one enatiomorph of the isomer 1 of the $(Sb_2Te_4)^{2+}$ cluster is given.

Compared with the calculated isomer 3 of the $(Sb_2Te_4)^{2+}$ cluster (Fig. 2.7.3.2), the two Sb atoms occupy different positions. In the calculated isomer, the open edge of the prism is occupied by Te at both sites. Unfortunately, it was not possible to calculate an optimized cluster of the isomer present in the crystal structure. Structure optimizations led to isomer 3 with an open edge at the Te-Te side of the prism, which is lower in energy. Only two positive formal charges are necessary to describe the clusters charge and the Te–Te bond is cleaved.
The structural parameters of the anions found in $(Sb_2Te_4)[Ga_2Cl_7]_2$ and $(Sb_2Te_4)[GaCl_4]_2$ are in line with those found in $(As_2Te_4)[Ga_2Cl_7]_2$ and $(Sb_4Te_4)[GaCl_4]_4$.

2.7.4 Crystal Structures and Drilling Refinement of $M(Pn_2Te_4)[GaCl_4]_3$

The eleven isotypic compounds with the common sum formula $M(Pn_2Te_4)[GaCl_4]_3$ are build from M^+ cations (M = K, Rb, Cs, NH_4, In, Tl), $(Pn_2Te_4)^{2+}$ clusters (Pn = As, Te) and $[GaCl_4]^-$ anions. The clusters show the analogous disorder as present in the structure of $(As_2Te_4)[Ga_2Cl_7]_2$. The crystallographic data of all $M(Pn_2Te_4)[GaCl_4]_3$ compounds are listed in Tabs. A 5.2.11 and A 5.2.12.
Fig. 2.7.4.1 shows the unit cell of $K(Sb_2Te_4)[GaCl_4]_3$ representatively for all compounds $M(Pn_2Te_4)[GaCl_4]_3$, which are homeotypic to the structure of $Bi_5[GaCl_4]_3$ [73]. Polycationic clusters and $[GaCl_4]^-$ anions occupy equivalent positions in the same space group. The incorporated M^+ cations in $M(Pn_2Te_4)[GaCl_4]_3$ elongate the crystallographic *c*-axis by about 2-3 Å from 30.0 to 32.2 Å in $M(As_2Te_4)[GaCl_4]_3$ and 32.8 Å in $M(Pn_2Te_4)[GaCl_4]_3$.

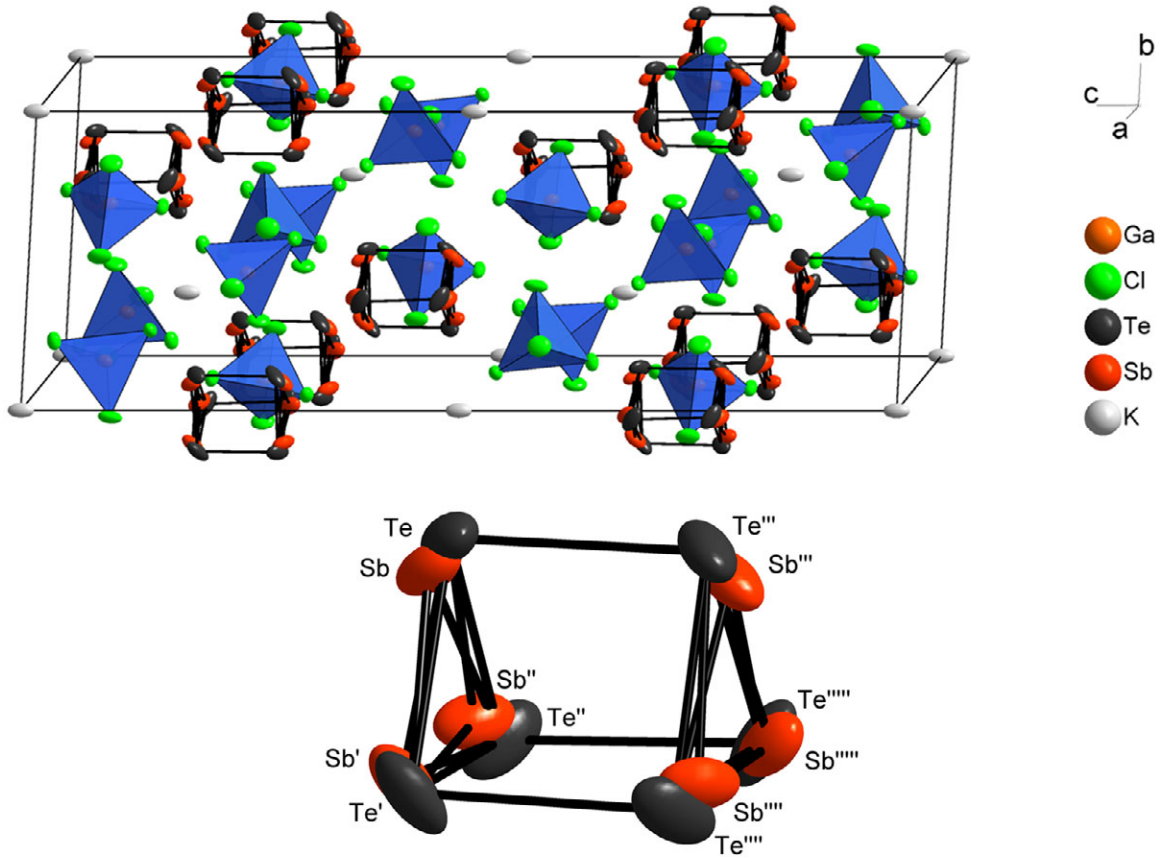

Fig. 2.7.4.1 The unit cell of the structure of $K(Sb_2Te_4)[GaCl_4]_3$ (top). The $[GaCl_4]^-$ ions are represented by discrete tetrahedra. On bottom the disordered $(Sb_2Te_4)^{2+}$ cluster is shown. The atoms are represented by thermal ellipsoids scaled to include a probability of 50 %.

Due to the high symmetry of the space group $R\bar{3}c$, the prismatic clusters are build of only one crystallographic independent atom position. The cluster has the local symmetry $D_3(32)$. Distances between the positions refined as occupied by tellurium and the neighbouring electron densities are about 0.31 Å in the $(Sb_2Te_4)^{2+}$ clusters and 0.4 - 0.5 Å in the $(As_2Te_4)^{2+}$ clusters, which are below the experiments resolution. Because of some suspicous weighting schemes in the SHELX refinements and to obtain more insight in the statistical disorder, the structures were refined as pseudo-merohedral Drillings in the monoclinic subgroups *C*2/*c* (Fig. 2.7.4.2) and *Cc* with three and six independent atom positions in the clusters, respectively. The transformation from the trigonal cell to the cell in *C*2/*c* is described with $a_{mon} = 2a_{hex} + b_{hex}$, $b_{mon} = -b_{hex}$, $c_{mon} = -2/3a_{hex} - 1/3b_{hex} - 1/3\ c_{hex}$ and the transformation matrix (2 1 0, 0 -1 0, -2/3 -1/3 -1/3). The following 120° rotation of the monoclinic cell is described as $a' = -1/2a_{mon} - 3/2\ b_{mon}$, $b' = 1/2\ a_{mon} - 1/2\ b_{mon}$, $c' = 1/2\ a_{mon} - 1/2\ b_{mon} + c_{mon}$ with the rotation matrix (-1/2 -3/2 0, 1/2 -1/2 0, 1/2 1/2 1). To obtain the structure in *Cc* an additional inversion was applied.

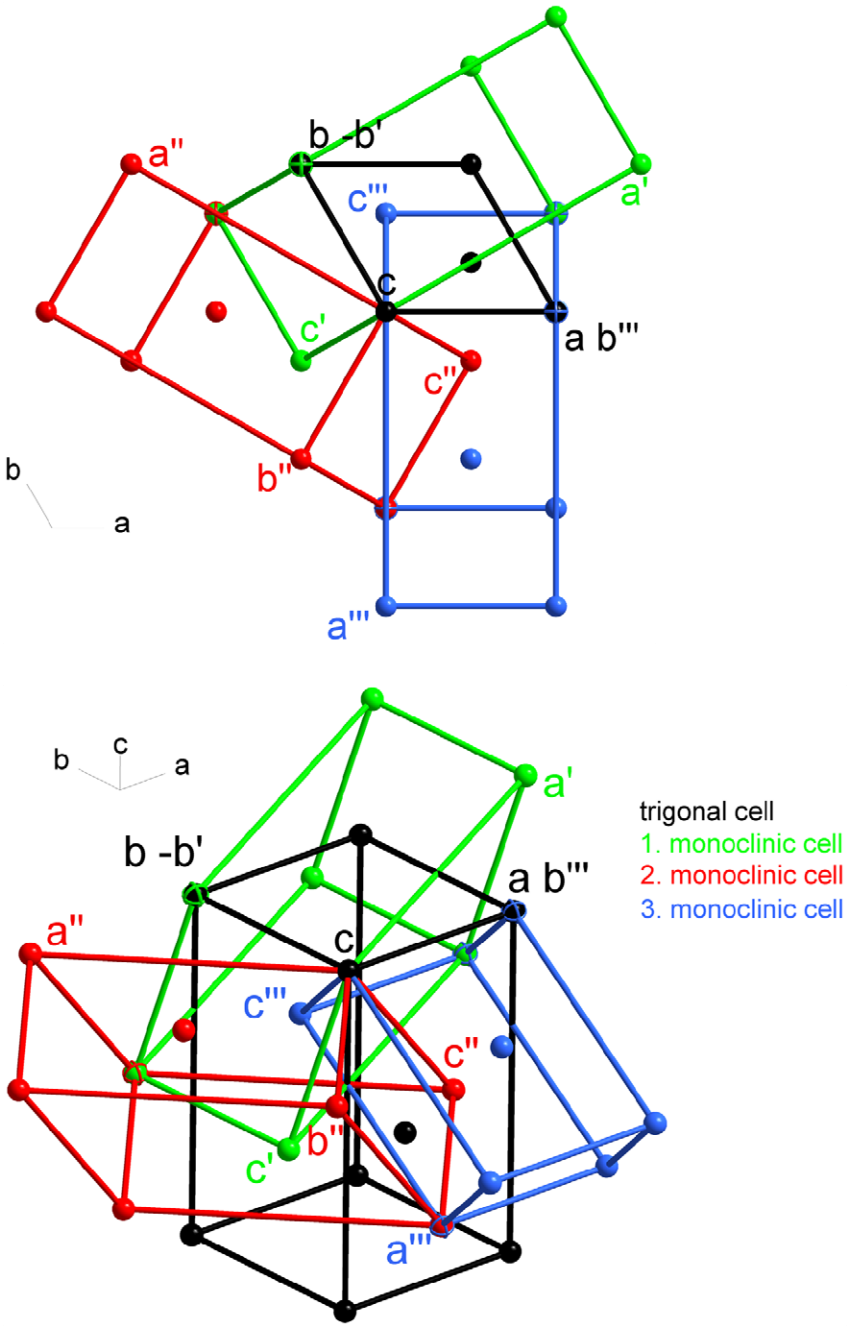

Fig. 2.7.4.2 Graphical representation of the relation between the original trigonal cell and the lower symmetric monoclinic cells in the space group *C*2/*c* viewed from two different directions.

The refinements in the monoclinic space groups *C*2/*c* and *Cc* led to slightly distorted prisms and likewise different occupation factors of the pentele and tellurium sites, respectively. The double occupations of each postion could not be resolved by the Drilling refinement. Like in the structure of $(As_2Te_4)[Ga_2Cl_7]_2$, the prismatic clusters in $M(Pn_2Te_4)[GaCl_4]_3$ still show the typical disorder for the $(Pn_2Te_4)^{2+}$ clusters. The crystallographic quality factors R1 and wR2 als well as the Goodness-of-fit and the weighting scheme could not be improved.

Partly the reciprocal lattices of the eleven isotypic structures of $M(Pn_2Te_4)[GaCl_4]_3$ show some disturbations but in general the refinement in $R\bar{3}c$ led to the best results. Free refinements of the arsenic and tellurium position gave occupation factors of 0.32-0.36 (As) and 0.63 - 0.68 (Te), which are in line with the expected 1:3 relation of As:Te on each position. The EDX analyses confirm the

pentele:chalcogen relation of 1:2 in all cases unequivocally (Tabs. 2.7.1.2, 2.7.1.3). Consequently, in the refinements the As and Te occupations were set to 0.33 and 0.66 for all structures. Hydrogen atoms of NH_4^+ cations $NH_4(Pn_2Te_4)[GaCl_4]_3$ were implemented as rigid groups. The identification of the respective isomers of the $(Pn_2Te_4)^{2+}$ clusters will be shown below.

The $(Pn_2Te_4)^{2+}$ clusters can be derived from the Te_6^{4+} cluster by adding pentele atoms which is accompanied by lowering of the charge. In 2002 F. Steden presented the $(SbTe_5)^{3+}$ and $(BiTe_5)^{3+}$ clusters [35] as the hexafluorido arsenates. The way of stepwise substitution of tellurium atoms by pentele atoms demonstrates a procedure to decrease the cluster charge and keep a closed trigonal prism without degradation of bonds. Fig. 2.7.4.3 shows the respective known 32 valence electron clusters.

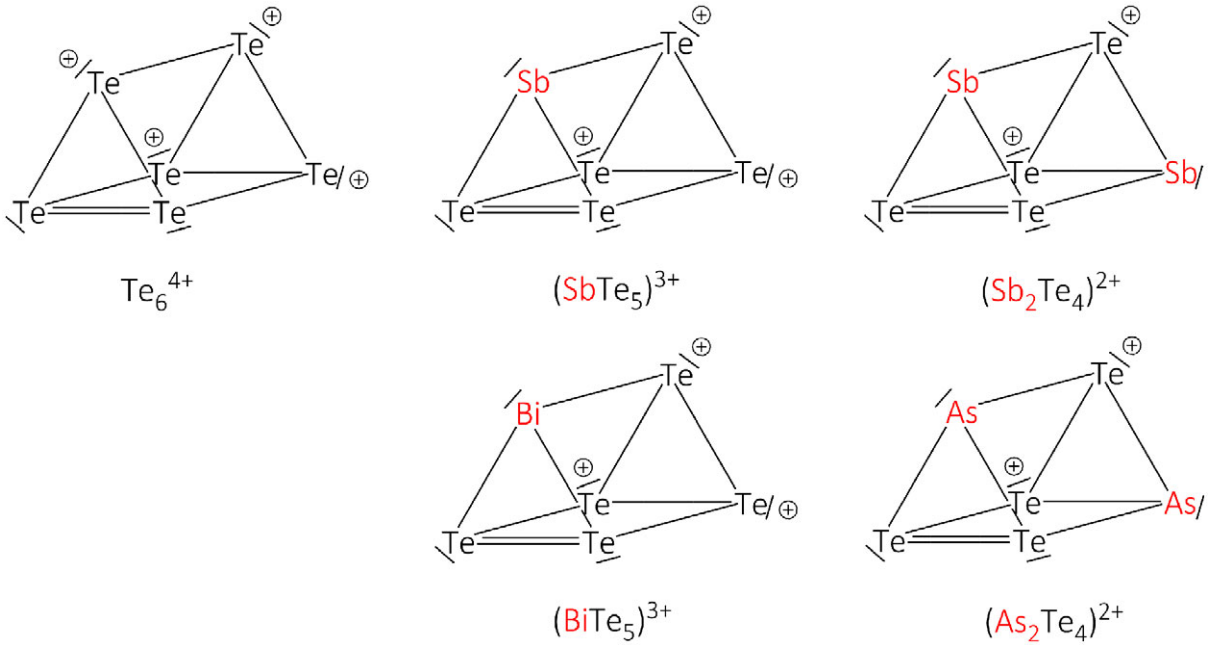

Fig. 2.7.4.3 Stepwise substitution of tellurium atoms in Te_6^{4+} by pentele atoms in trigonal prismatic clusters.

The $(Pn_2Te_4)^{2+}$ clusters are Wade clusters.[74] Calculation of the skeleton electron pairs leads to an attribution as hypho-type clusters derived from a tricapped trigonal prism by elimination of three atoms (Fig. 2.7.4.4).
The hypothetical closo cluster might be $(Sb_5Te_4)^{11+}$ (SKEP: ½ · [5 · (5 - 2) + 4 · (6 - 2) - 11] = 10). The degradation to the respective arachno type occurs via formal elimination of three Sb^{3+}.

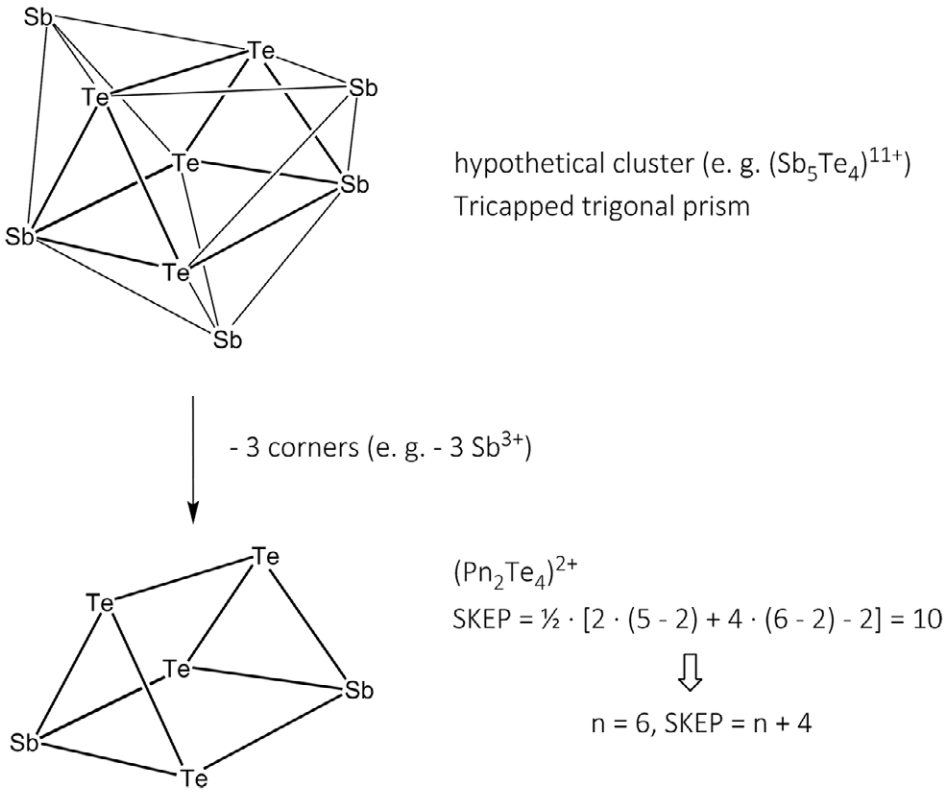

Fig. 2.7.4.4 Derivation of the trigonal prismatic clusters $(Pn_2Te_4)^{2+}$ according to the Wade rules and calculation of the skeleton electron pairs.

The compounds $M(As_2Te_4)[GaCl_4]_3$ (M = Na, Ag) and $Na(Sb_2Te_4)[GaCl_4]_3$ were accessible from the same educt basis like the 11 isotypic structures and the adjuvants NaCl, AgCl and PPh_4Cl. They crystallize in the space group *C*2/*c* but with a different structure and show a temperature - depending one - dimensional modulation in the *b* direction. These structures are not discussed in the present work.

2.7.5 Examination of Compounds Containing the $(Pn_2Te_4)^{2+}$ Clusters by Raman Spectroscopy

Raman investigations of all compounds containing the $(Pn_2Te_4)^{2+}$ clusters were necessary to identify the $(As_2Te_4)^{2+}$ and $(Sb_2Te_4)^{2+}$ isomers within the crystals.
Figures 2.5.7.1 and 2.5.7.2 show the Raman spectra of the calculated isomers of $(Sb_2Te_4)^{2+}$ and $(As_2Te_4)^{2+}$ (Fig. 2.7.3.2). In the summarized spectrum of all $(Sb_2Te_4)^{2+}$ isomers, three separate ranges of Raman bands between 80 and 250 cm^{-1} are visible whereas the calculated Raman bands of the $(As_2Te_4)^{2+}$ isomers show a quasi-continuous spectrum with three broad bands.

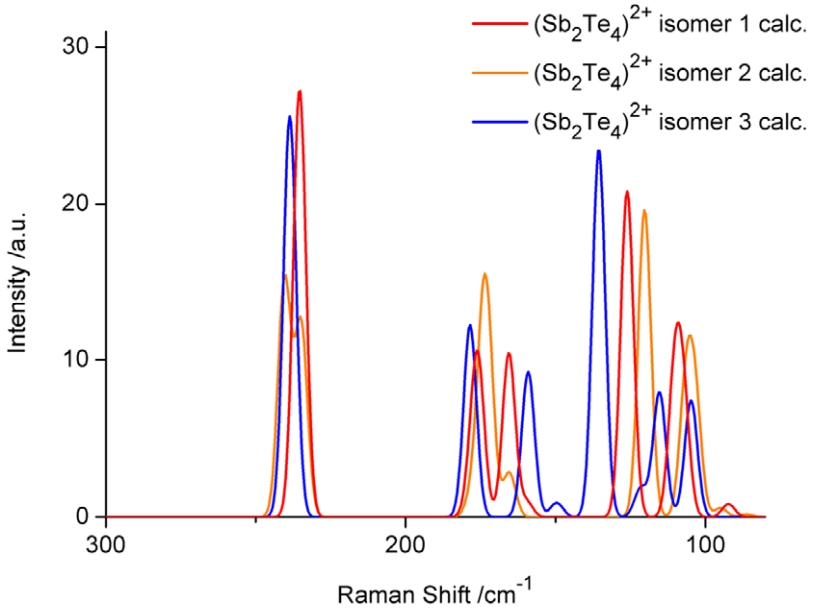

Fig. 2.5.7.1 Calculated Raman spectra of three isomers of the $(Sb_2Te_4)^{2+}$ cluster (B3LYP/TZV(2d/sp)).*

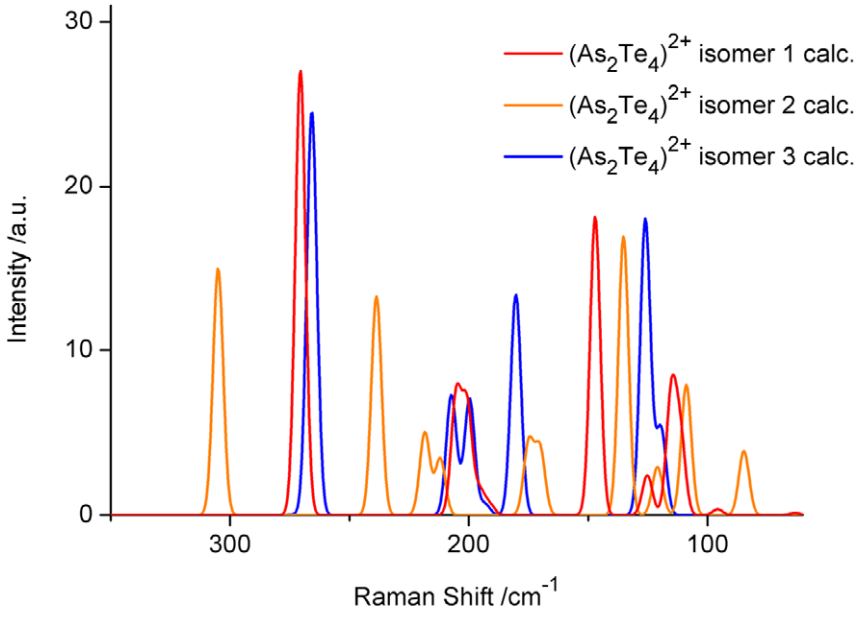

Fig. 2.5.7.2 Calculated Raman spectra of three isomers of the $(As_2Te_4)^{2+}$ cluster (B3LYP/TZV(2d/sp)).*

* The calculations of the Raman spectra were performed by Dr. Gregor Schnakenburg.

All theoretical spectra of $(Pn_2Te_4)^{2+}$ shown below were adjusted on the highest experimental vibration frequency due to higher accuracy of the calculation in this region. The highest-energy vibration mode in the region of 270 cm^{-1} for $(As_2Te_4)^{2+}$ and 235 cm^{-1} for $(Sb_2Te_4)^{2+}$ is a symmetrical breath vibration of one or both triangular side planes (Figs. A 5.7.9 - A 5.7.14). Besides that, the intensities of the calculated signals were chosen lower compared to those obtained from the experiment for clarity. A general difficulty of the comparison of the experimental and theoretical spectra is the inaccuracy of the calculations, which increases below 150 cm^{-1} significantly. The vibration modes of all $(Pn_2Te_4)^{2+}$ isomers are depicted in the appendix (Figs. A 5.7.9 - A 5.7.14).

The experimental spectrum of $(As_2Te_4)[Ga_2Cl_7]_2$ shows clear signals at 103, 106, 122, 139, 146, 157, 163, 187, 196, 202 and 272 cm^{-1} and presumably at 82 and 87 cm^{-1} (Fig. 2.5.7.3). At 366 cm^{-1} the characteristic strong Raman band of the $[Ga_2Cl_7]^-$ anion is visible. The other observed bands in $K[Ga_2Cl_7]$ at 63(vs), 96(s), 107(m), 130(m), 141(m), 284(m) and 407(m) cm^{-1} could not be detected in the present spectrum due to the overlap with the cluster signals.[70] The observed signal at 366 cm^{-1} is additionally supported by the calculated spectrum of $[Ga_2Cl_7]^-$. The very weak obtained signals at 255 and 355 and 122 cm^{-1} are also in line with the calculation. Comparison with the adjusted Raman spectra of the calculated isomers of the $(As_2Te_4)^{2+}$ cluster shows that only the spectrum of isomer 2 is suitable to explain the experiment considering signal shifts and additional splitting due to lattice effects like the site symmetry influence on the vibration frequencies. Theoretical Raman bands below 220 cm^{-1} were generally calculated with too high energies.

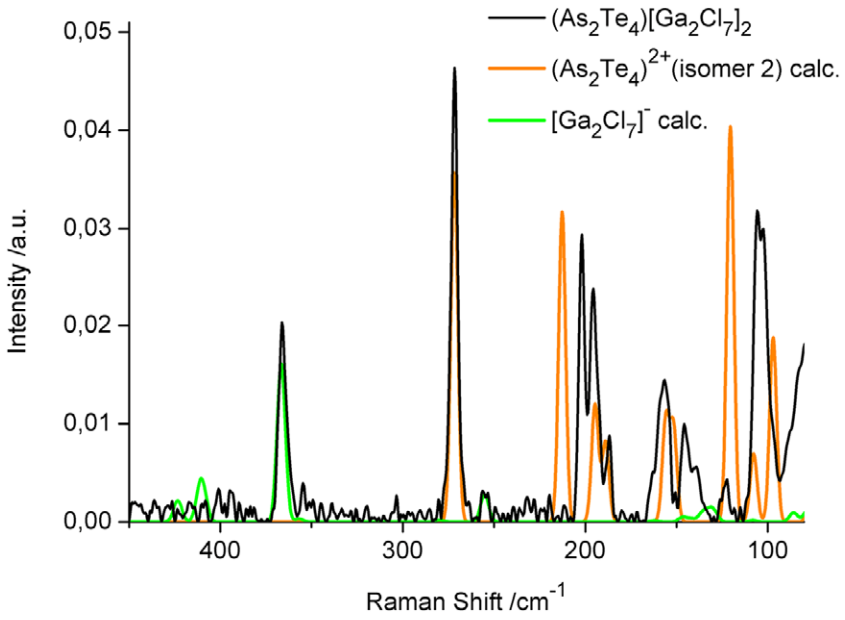

Figure 2.5.7.3 Comparison of the experimental Raman spectrum of $(As_2Te_4)[Ga_2Cl_7]_2$ with the calculated spectrum of the isomer 2 of the $(As_2Te_4)^{2+}$ cluster. The calculated spectrum of the chloridogallate anion is shown in green.

The spectrum of $(Sb_2Te_4)[Ga_2Cl_7]_2$ gives signals at 87, 129, 164, 174 and 230 cm^{-1} for the $(Sb_2Te_4)^{2+}$ cluster and 365 cm^{-1} for the $[Ga_2Cl_7]^-$ anion. The signals obtained for the cluster are in line with the calculated spectrum of the respective isomer 1 (Fig. 2.5.7.4) and confirm the crystal structure, which was refined to incoorporate two enatiomorphs of isomer 1 of the $(Sb_2Te_4)^{2+}$ cluster.

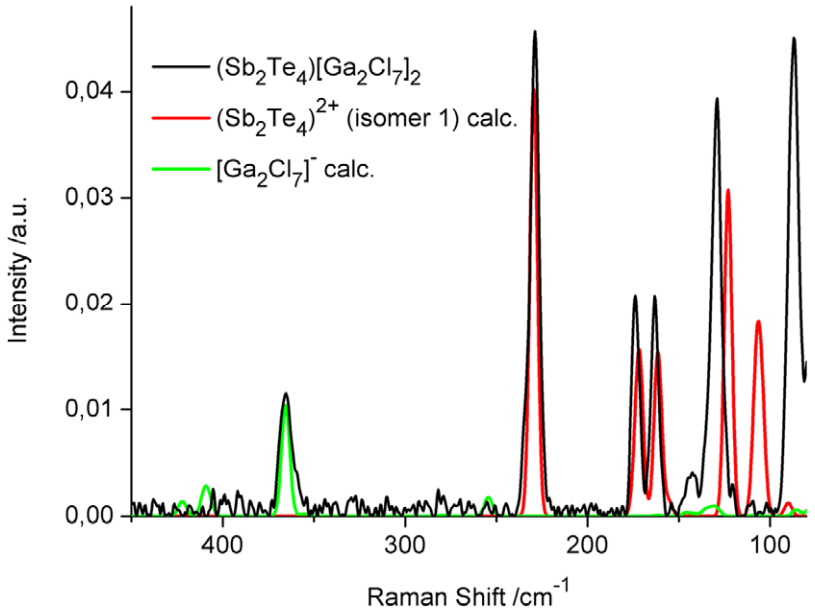

Fig. 2.5.7.4 Comparison between the experimental spectrum of $(Sb_2Te_4)[Ga_2Cl_7]_2$ and the calculated Raman spectrum of $(Sb_2Te_4)^{2+}$ isomer 1. The experimental spectrum is drawn with black lines, the calculated spectrum of the cluster is red and the spectrum of the chloridogallate anion is shown in green.

The Raman spectrum recorded for $(Sb_2Te_4)[GaCl_4]_2$ shows the best correlation with the calculated spectrum of the isomer 3 of the $(Sb_2Te_4)^{2+}$ cluster (Fig. 2.5.7.5). Signals are obtained at 88, 100, 130, 145, 164, 174 and 231 cm^{-1}. The bands at 100 and 145 cm^{-1} are not present in the spectrum of $(Sb_2Te_4)[Ga_2Cl_7]_2$. The agreement of the experimental spectrum of $(Sb_2Te_4)[GaCl_4]_2$ and the calculation is not accurate below 170 cm^{-1}.

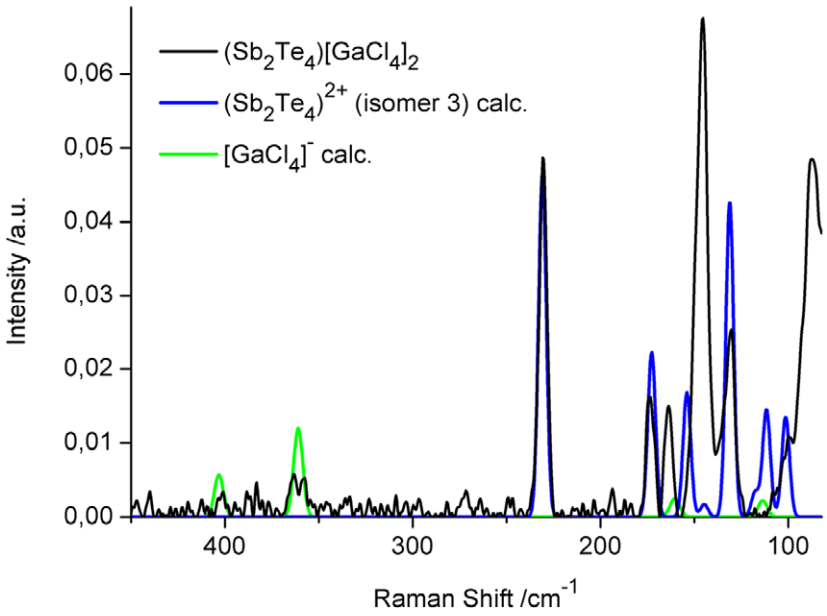

Fig. 2.5.7.5 Comparison between the experimental spectrum of $(Sb_2Te_4)[GaCl_4]_2$ and the calculated Raman spectrum of $(Sb_2Te_4)^{2+}$ isomer 3. The experimental spectrum is drawn with black lines, the calculated spectrum of the cluster is blue and the spectrum of the chloridogallate anion is shown in green.

The Sb atoms in the calculated isomer 3 of the $(Sb_2Te_4)^{2+}$ cluster occupy positions in the rectangular plane of the prism in contrast to the crystal structure (Figs. 2.7.3.2, 2.7.3.5). Unfortunately, the attempt to calculate a Raman spectrum of an optimized cluster corresponding to the isomer present in the crystal structure led to the isomer 3 again after structure optimization. Consequently, the agreement of the experimental spectrum and the calculation is limited. The calculated Raman spectrum of the unoptimized cluster, which is actually present in the crystal structure, shows even higher deviations from the experimental spectrum. Calculations of all other conceivable unoptimized isomers of the $(Sb_2Te_4)^{2+}$ cluster - even with Sb occupying the adjacent positions of the cleaved bond - did not lead to a better agreement.
The signals obtained for the $[GaCl_4]^-$ anion also show remarkable deviations compared to the spectra of $M(Pn_2Te_4)[GaCl_4]_3$ (see below). A rather low intensiv split Raman band at 357 and 363 cm^{-1} demonstrates a shift of approximately 15 cm^{-1} compared to the expected Raman signal for the anion around 345 cm^{-1}.

In all spectra recorded for $M(Pn_2Te_4)[GaCl_4]_3$, the only band arising from the mononuclear $[GaCl_4]^-$ ion is the A_2 vibration found at 343 - 344 cm^{-1}. Like already described in chapter 2.3, this is a general fact in Raman investigations of solid compounds containg this anion. The other expected signals for $[GaCl_4]^-$ [68] turn out as too weak or not visible due to overlap with the cluster bands in the solid state.
In general, the experimental spectra of $M(As_2Te_4)[GaCl_4]_3$ show signals at 88, 103, 106, 127, 155, 187, 195, 201, 264 and 271 cm^{-1} considering minimal deviations and individual splitting of max. 2 cm^{-1} (Figs. 2.5.7.6 - 2.5.7.11). In contrast to the Raman spectrum of $(As_2Te_4)[Ga_2Cl_7]_2$ all signals in the spectra of $M(As_2Te_4)[GaCl_4]_3$ can only be explained by the presence of both isomers 1 and 3 of the $(As_2Te_4)^{2+}$ cluster.

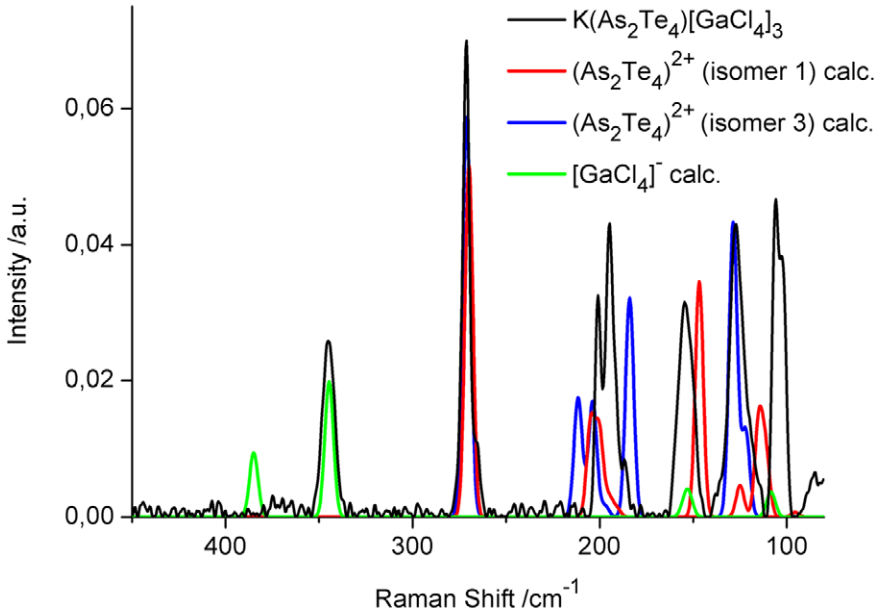

Fig. 2.5.7.6 Comparison between the experimental spectrum of $K(As_2Te_4)[GaCl_4]_3$ and the calculated Raman spectra of $(As_2Te_4)^{2+}$ isomer 1 and 3. Experimental spectra are drawn with black lines, the calculated spectra of the clusters are red and blue and the spectrum of the chloridogallate anion is shown in green.

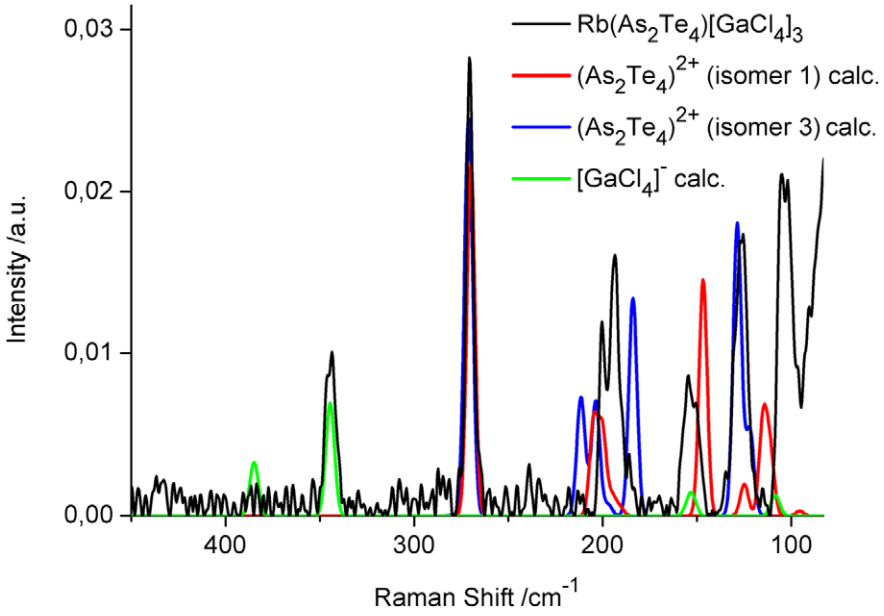

Fig. 2.5.7.7 Comparison between the experimental spectrum of $Rb(As_2Te_4)[GaCl_4]_3$ and the calculated Raman spectra of $(As_2Te_4)^{2+}$ isomer 1 and 3. Experimental spectra are drawn with black lines, the calculated spectra of the clusters are red and blue and the spectrum of the chloridogallate anion is shown in green.

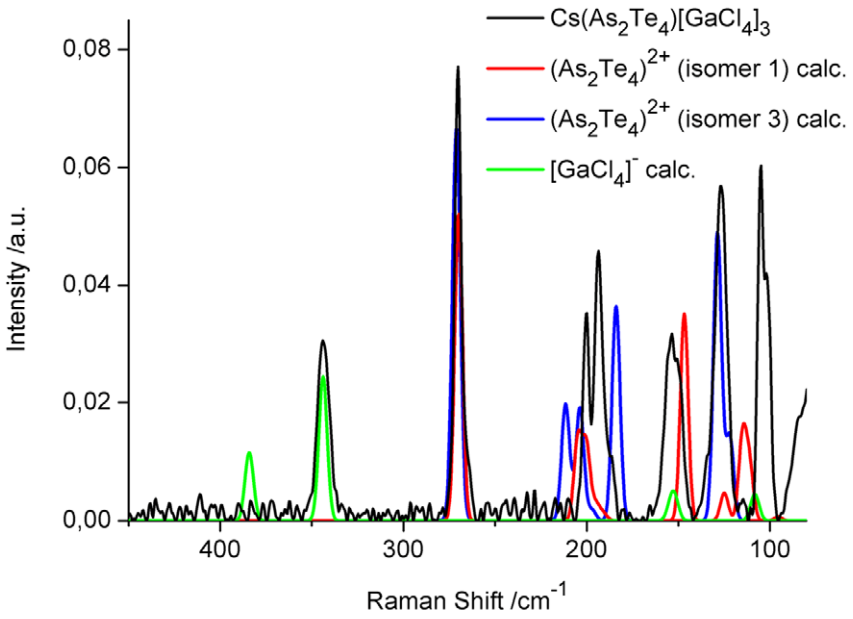

Fig. 2.5.7.8 Comparison between the experimental spectrum of $Cs(As_2Te_4)[GaCl_4]_3$ and the calculated Raman spectra of $(As_2Te_4)^{2+}$ isomer 1 and 3. Experimental spectra are drawn with black lines, the calculated spectra of the clusters are red and blue and the spectrum of the chloridogallate anion is shown in green.

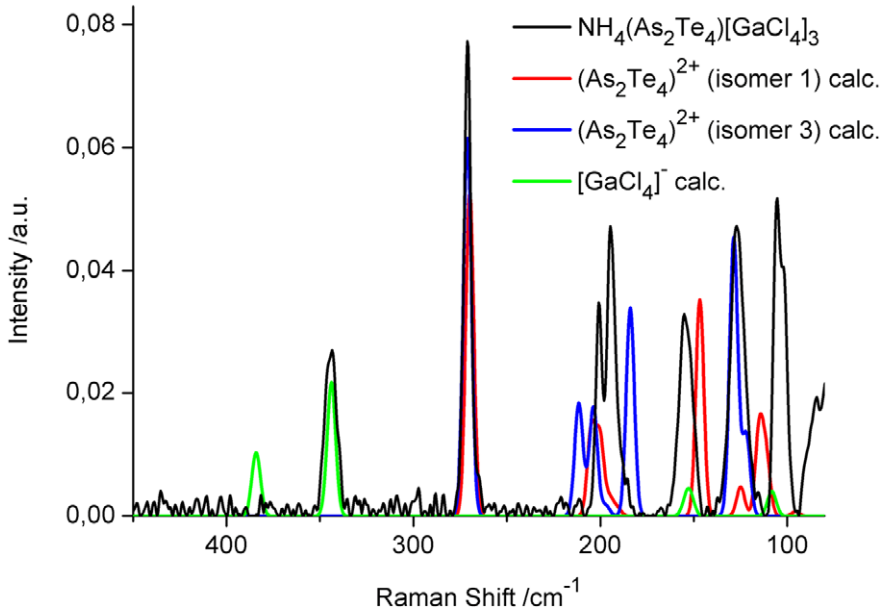

Fig. 2.5.7.9 Comparison between the experimental spectrum of $NH_4(As_2Te_4)[GaCl_4]_3$ and the calculated Raman spectra of $(As_2Te_4)^{2+}$ isomer 1 and 3. Experimental spectra are drawn with black lines, the calculated spectra of the clusters are red and blue and the spectrum of the chloridogallate anion is shown in green.

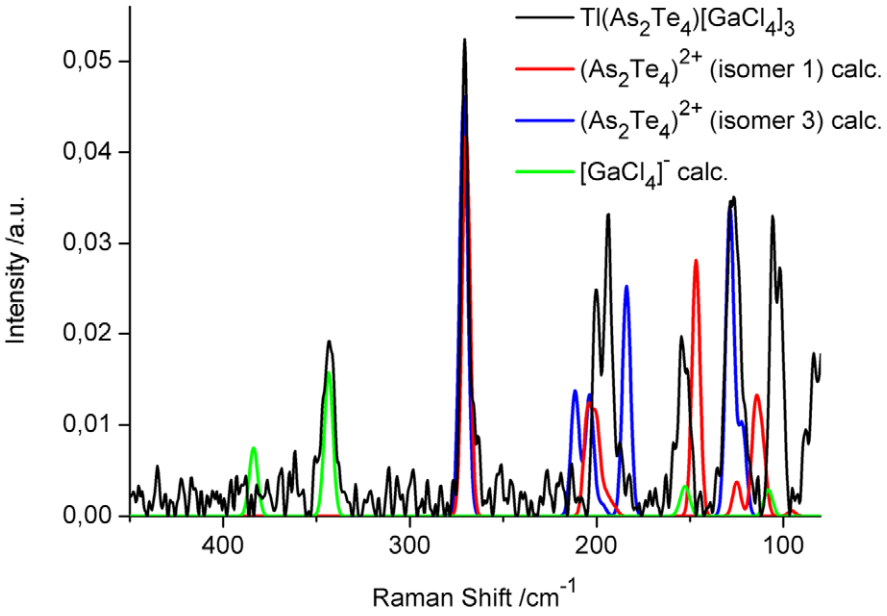

Fig. 2.5.7.10 Comparison between the experimental spectrum of $Tl(As_2Te_4)[GaCl_4]_3$ and the calculated Raman spectra of $(As_2Te_4)^{2+}$ isomer 1 and 3. Experimental spectra are drawn with black lines, the calculated spectra of the clusters are red and blue and the spectrum of the chloridogallate anion is shown green.

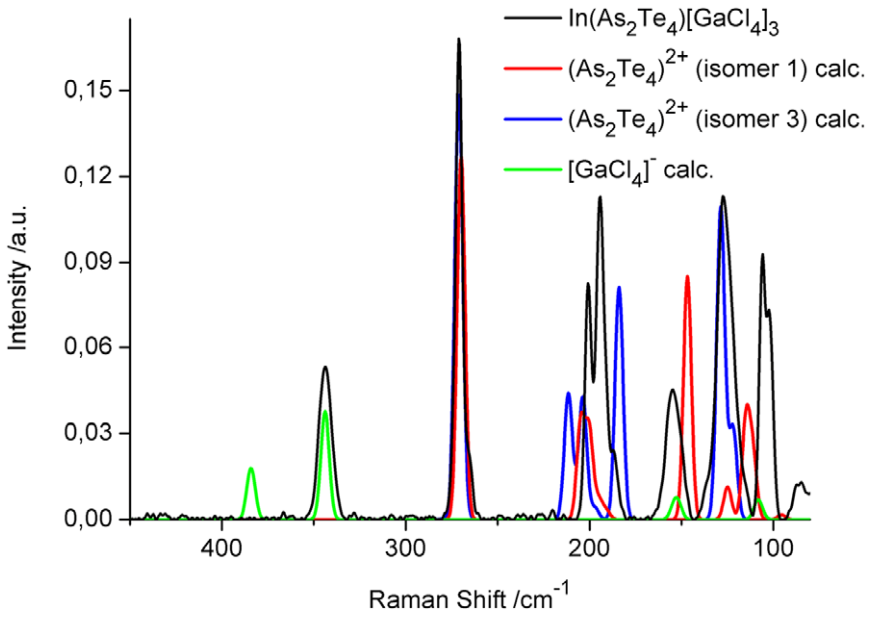

Fig. 2.5.7.11 Comparison between the experimental spectrum of $In(As_2Te_4)[GaCl_4]_3$ and the calculated Raman spectra of $(As_2Te_4)^{2+}$ isomer 1 and 3. Experimental spectra are drawn with black lines, the calculated spectra of the clusters are blue and red and the spectrum of the chloridogallate anion is shown in green.

The characteristic region between 95 and 165 cm^{-1} shows three intensive Raman bands, which are not in line with the presence of one isomer exclusively. Like in the spectrum of $(As_2Te_4)[Ga_2Cl_7]_2$, the calculated vibration frequencies below 220 cm^{-1} are calculated with too high energies. The lower the frequency of the Raman bands, the more inaccurate is the coincidence with the experiment. The absolute values of the calculated signals have to be shifted by a higher extent in the region of lower wavenumbers.

In contrast to the mixture of $(As_2Te_4)^{2+}$ isomers in $M(As_2Te_4)[GaCl_4]_3$, an incorporation of only one $(Sb_2Te_4)^{2+}$ isomer is observed in $M(Sb_2Te_4)[GaCl_4]_3$, respectively. For $M(Sb_2Te_4)[GaCl_4]_3$ (M = Rb, Cs) all experimental Raman bands are explained by the calculated spectrum of isomer 1 of the $(Sb_2Te_4)^{2+}$ cluster (Figs. 2.5.7.12, 2.5.7.13). In general, the two spectra show signals at 89, 127, 129, 136, 167, 174, and 230 cm^{-1} for the cluster and 345 cm^{-1} for the $[GaCl_4]^-$ anion. The characteristic region between 150 and 180 cm^{-1} shows a well resolved split signal at 166 and 174 cm^{-1} for M = Rb (M = Cs: 165, 173 cm^{-1}) for isomer 1 of the $(Sb_2Te_4)^{2+}$ cluster, which is line with the calculation.

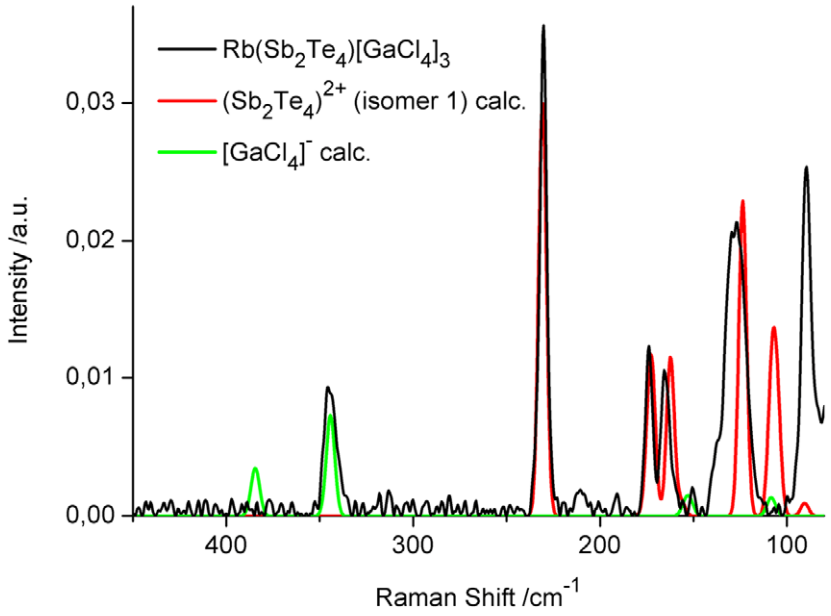

Fig. 2.5.7.12 Comparison between the experimental spectrum of $Rb(Sb_2Te_4)[GaCl_4]_3$ and the calculated Raman spectrum of $(Sb_2Te_4)^{2+}$ isomer 1. The experimental spectrum is drawn with black lines, the calculated spectrum of the cluster is red and the spectrum of the chloridogallate anion is shown in green.

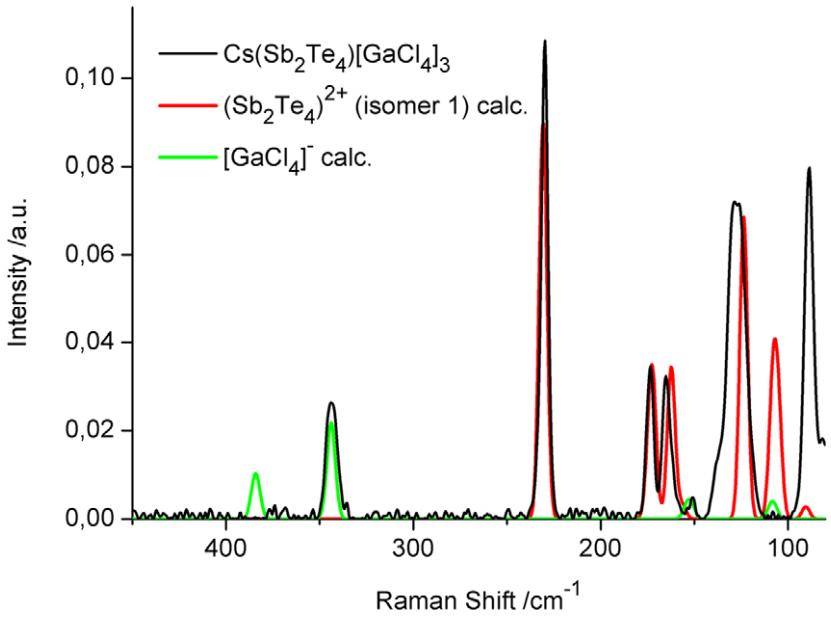

Fig. 2.5.7.13 Comparison between the experimental spectrum of $Cs(Sb_2Te_4)[GaCl_4]_3$ and the calculated spectrum of $(Sb_2Te_4)^{2+}$ isomer 1. The experimental spectrum is drawn with black lines, the calculated spectrum of the cluster is blue and the spectrum of the anion is green.

The spectrum of $NH_4(Sb_2Te_4)[GaCl_4]_3$ is in full agreement with the calculated spectrum of isomer 2 of the $(Sb_2Te_4)^{2+}$ cluster (Fig. 2.5.7.14). Clear signals from the cluster are visible at 89, 129, 230 and 235. Furthermore a multiplett at 167, 169, 173 and 178 resolves. Two unequivocal characteristics for the isomer 2 of $(Sb_2Te_4)^{2+}$ are the most intensive signal at 129 cm^{-1} on the one hand and the split band at 230 and 235 cm^{-1} on the other hand. Both show accurate agreement with the calculation.

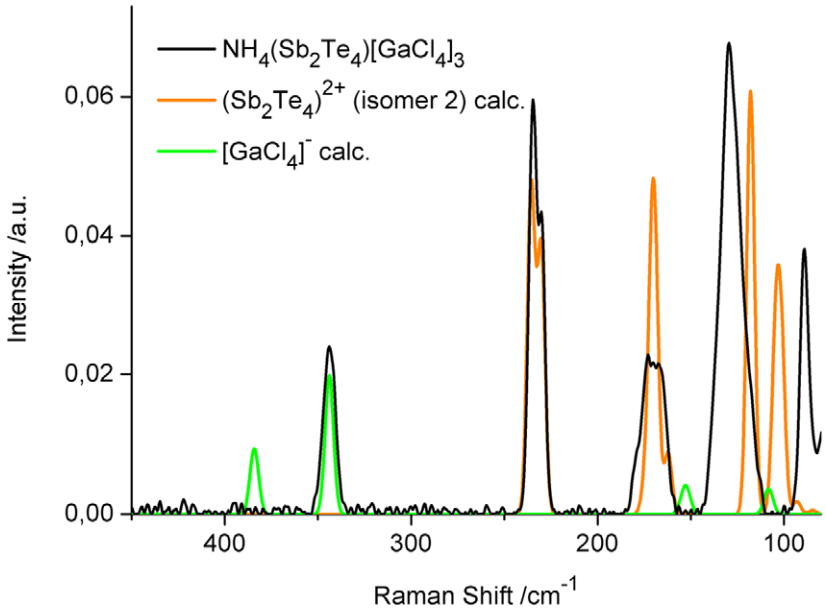

Fig. 2.5.7.14 Comparison between the experimental spectrum of $NH_4(Sb_2Te_4)[GaCl_4]_3$ and the calculated Raman spectrum of $(Sb_2Te_4)^{2+}$ isomer 2. The experimental spectrum is drawn with black lines, the calculated spectrum of the cluster is orange and the spectrum of the chloridogallate anion is shown in green.

In the spectra of $M(Sb_2Te_4)[GaCl_4]_3$ (M = K, Tl) the signal between 150 and 180 cm^{-1} is not well resolved and both individual bands show a significant difference in their intensities. Besides that, this split signal and the highest energetic signal for both compounds are shifted by 5 cm^{-1} to higher wavenumbers compared to $M(Sb_2Te_4)[GaCl_4]_3$ (M = Rb, Cs). A further signal arises in a shoulder at 120 cm^{-1}. Nonetheless, the calculated spectrum of isomer 1 of the $(Sb_2Te_4)^{2+}$ cluster exhibits the best correlation (Figs. 2.5.7.15, 2.5.7.16).

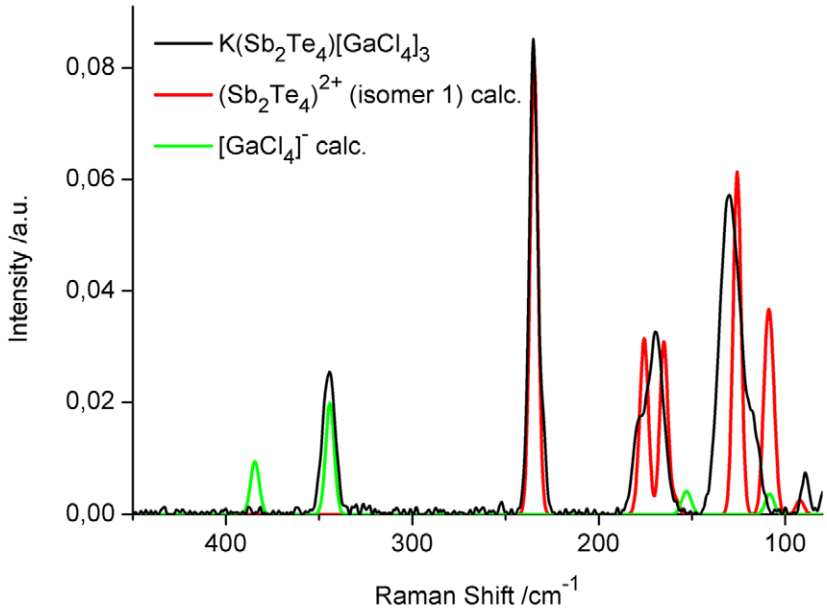

Fig. 2.5.7.15 Comparison between the experimental spectrum of $K(Sb_2Te_4)[GaCl_4]_3$ and the calculated Raman spectrum of $(Sb_2Te_4)^{2+}$ isomer 1. The experimental spectrum is drawn with black lines, the calculated spectrum of the cluster is red and the spectrum of the chloridogallate anion is shown in green.

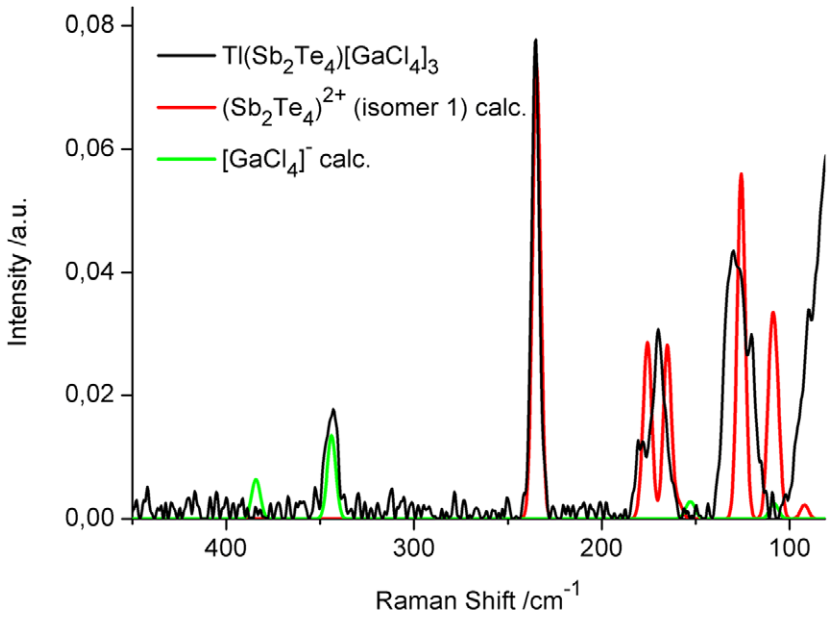

Fig. 2.5.7.16 Comparison between the experimental spectrum of $Tl(Sb_2Te_4)[GaCl_4]_3$ and the calculated Raman spectrum of $(Sb_2Te_4)^{2+}$ isomer 1. The experimental spectrum is drawn with black lines, the calculated spectrum of the cluster is red and the spectrum of the chloridogallate anion is shown in green.

The big intensity difference between the signals at 89 cm^{-1} in all spectra of $M(Sb_2Te_4)[GaCl_4]_3$ and the corresponding calculated signal, which is shifted to higher wavenumbers, can presumably be explained by the partial overlap with the laser signal at 76 and 78 cm^{-1}. The laser signal was hidden in all spectra for clarity. If higher laser energies were chosen due to a smaller amount of substance, especially the signal at 89 cm^{-1} increased in intensity. A comparison of all spectra, which are presented in this work, reveal a clear correlation between the intensity of the signal at 89 cm^{-1} and the laser energy.

Each spectrum of all $M(Pn_2Te_4)[GaCl_4]_3$ compounds was recorded at least twice to confirm the results. The spectra show the same wavenumbers of signals and the same splittings in all cases. The temperatures during all syntheses were approximately the same. Each compound was synthesized repeatedly with slightly divergent reaction times of 1-2 weeks, respectively.

The comparison of the unit cell parameters of $M(As_2Te_4)[GaCl_4]_3$ and $M(Sb_2Te_4)[GaCl_4]_3$ shows a slight difference of about 0.1 Å in the *a*-axis, but about 0.6 Å in the *c*-axis (Tabs. A 5.2.9, A 5.2.10). The $(Sb_2Te_4)^{2+}$ cation is expected to demand a bigger volume in the structure compared to the $(As_2Te_4)^{2+}$ cluster due to the larger single-bond covalent radius of Sb (140 pm) compared to As (121 pm)[75]. The unit cell parameters of $(Bi_5)[GaCl_4]_3$ are extended by additional M^+ cations to the unit cell parameters of the structures of $M(As_2Te_4)[GaCl_4]_3$. The further exchange of As by Sb in $M(As_2Te_4)[GaCl_4]_3$ leads to an further increase of the unit cell volume.

The reason for the incorporation of only one isomer in the structures of $M(Sb_2Te_4)[GaCl_4]_3$, respectively, is not clear. The only obvious difference in all structures of $M(Pn_2Te_4)[GaCl_4]_3$ is the incorporation of different M^+ cations. Presumably, the $(As_2Te_4)^{2+}$ and $(Sb_2Te_4)^{2+}$ clusters are formed in different isomers due to different properties of the melt. The basicity of the melts increase with increasing radius of the M^+ cations. Additionally the interactions between Sb and As, respectively, and the M^+ cations are presumably different during reaction in the melt. At least, no relation was found between the formation of specific isomers and the radii of the M^+ cations (K^+ 149 pm, Rb^+ 163 pm, Cs^+ 186 pm, NH_4^+ 148 pm, Tl^+ 144 pm[75]).

2.7.6 Summary and Evaluation of the Analytical Results of the $(Pn_2Te_4)^{2+}$ Cluster

The compound $(Sb_2Te_4)[Ga_2Cl_7]_2$ contains a partially disordered $(Sb_2Te_4)^{2+}$ cluster due to the presence of both enatiomorphs, which occupy the identical crystallographic site. So both enantiomorphs are present simultanously in crystallographic superposition. $(Sb_2Te_4)[GaCl_4]_2$ is the only compound with a not disordered $(Pn_2Te_4)^{2+}$ cluster found in this work. Two positions with clearly lower occupation factors for Te reveal occupation with Sb. Unfortunately, the respective isomer could not be confirmed by Raman spectroscopy.

The refinement of the single crystal diffraction data of the compounds $(As_2Te_4)[Ga_2Cl_7]_2$ and $M(Pn_2Te_4)[GaCl_4]_3$ did not lead to unambigous results due to statistically disordered polycationic clusters. Analyses of the pentele and chalcogen occupation factors, EDX analysis and charge neutrality demand a cluster with a pentele : chalcogen ratio of 1:2. Examination of the compounds by Raman spectroscopy and supporting DFT calculations proved the presence of different isomers of $(Pn_2Te_4)^{2+}$ clusters in the crystal structures.

Finally, the structure of $Cs(Sb_2Te_4)[GaCl_4]_3$ is representatively modelled for the compounds $(As_2Te_4)[Ga_2Cl_7]_2$ and $M(Pn_2Te_4)[GaCl_4]_3$ with resolved disorder. The construction of isomer 1 is performed according to the optimized polyhedron (Fig. 2.7.3.2) and deleting respective electron densities from the disordered cluster.

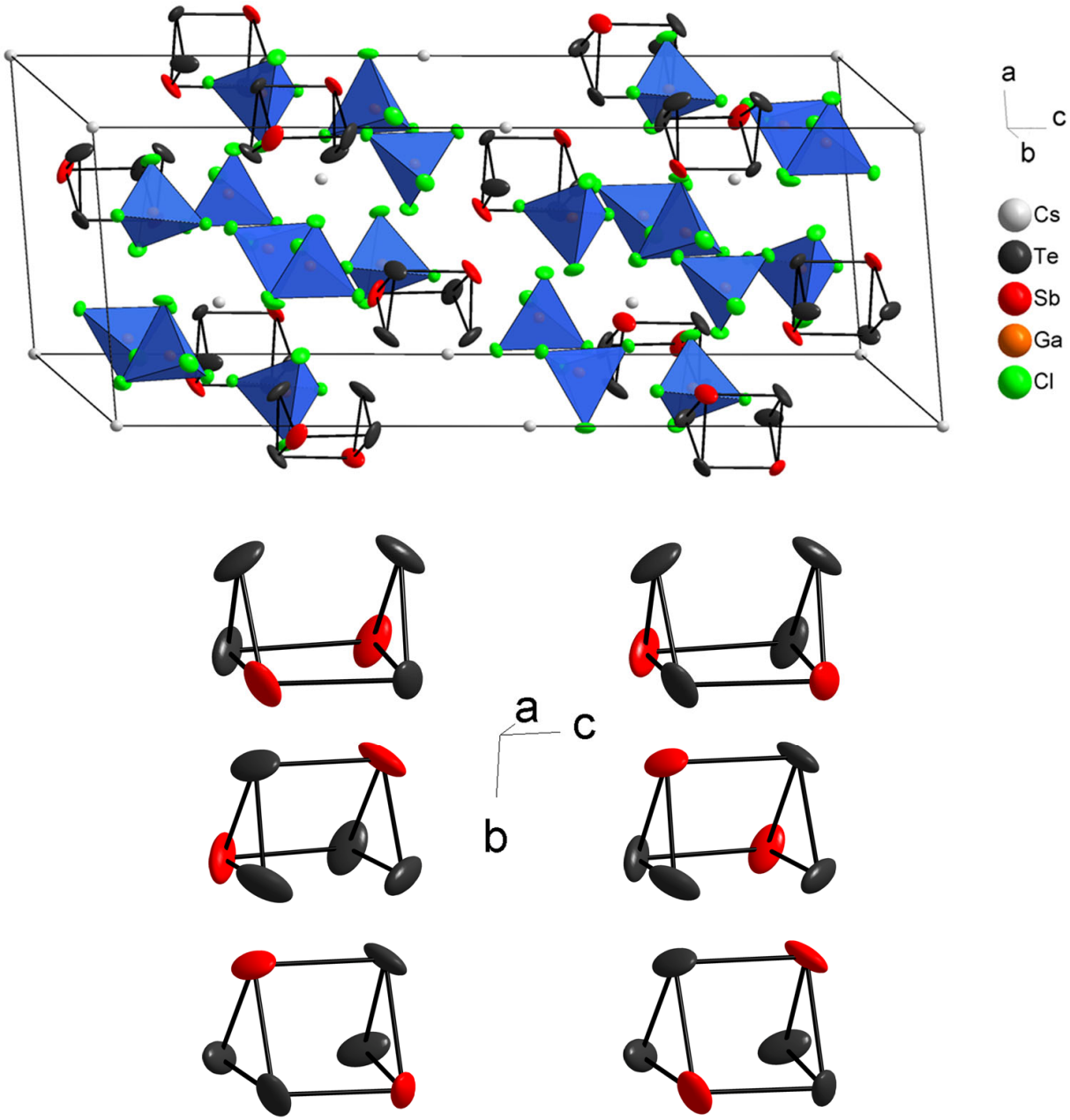

Fig. 2.5.7.17 The unit cell of the structure of $Cs(Sb_2Te_4)[GaCl_4]_3$ (top). The $[GaCl_4]^-$ ions are represented by discrete tetrahedra. On bottom the six possibilities of the Sb/Te distribution in the isomer 1 of the $(Sb_2Te_4)^{2+}$ cluster are shown. The atoms are represented by thermal ellipsoids scaled to include a probability of 70 %. Due to the presence of high residual electron desities, the ellipsoids are enlarged.

2.8 The Sequence of Cluster Degradation

Taking the $(Sb_7Te_8)^{5+}$, $(Sb_4Te_4)^{4+}$, $(Sb_3Te_4)^{3+}$ and $(Sb_2Te_4)^{2+}$ clusters and the Sb/Te clusters into account as reported above, the set up of a correlation between these clusters is possible (Fig. 2.8.1).
The $(Sb_3Te_4)^{3+}$ cluster is a link between cube and prism shaped clusters. It can be found additionally as a fragment in the mesomeric formulation of the $(Sb_7Te_8)^{5+}$ cluster (compare Fig. 2.1.4.5) Unfortunately attempts to synthesize the hypothetical isostructural clusters $(As_3Te_4)^{3+}$, $(As_3Se_4)^{3+}$, $(Sb_3Se_4)^{3+}$, $(Bi_3Te_4)^{3+}$ and $(Bi_3Se_4)^{3+}$ to answer the question of the pentele and chalcogen positions within the cluster unequivocally were not successful.

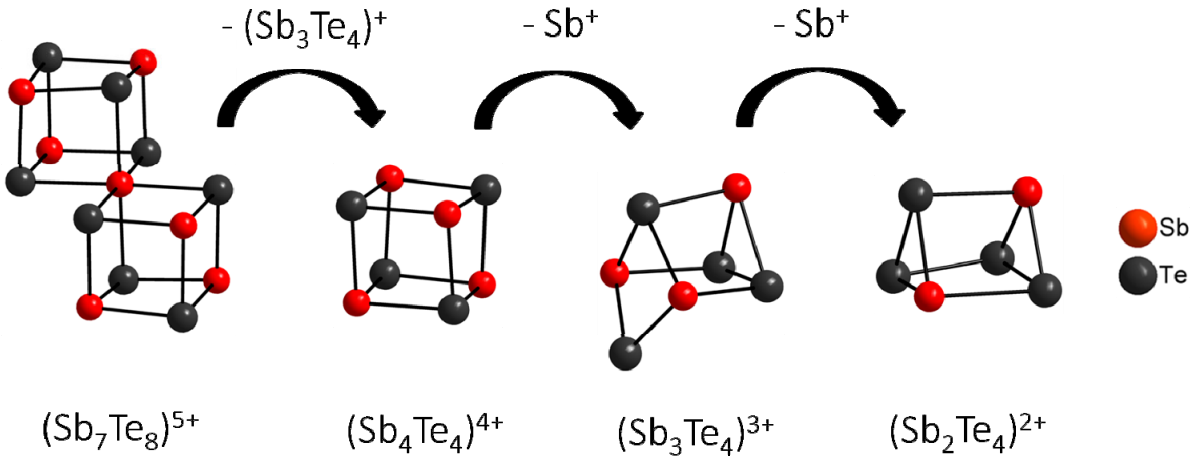

Fig. 2.8.1 Formal degradation of the $(Sb_7Te_8)^{5+}$ cluster to $(Sb_4Te_4)^{4+}$, $(Sb_3Te_4)^{3+}$ and $(Sb_2Te_4)^{2+}$. The atoms are shown as spheres of arbitrary radii.

2.9 Mixed Pentele-Chalcogen Cationic Chains

Besides the large number of discrete, molecular polycationic clusters, the class of polymeric polycations is plentiful with various homo and heteronuclear species and different structural realizations. $(Te_7^{2+})_n$ exists in two modifications, as a folded band in $Te_7[WOX_4]_2$ (X = Cl, Br) and $Te_7[Be_2Cl_6]$ [76] and as strands made of connected six membered rings in $Te_7[AsF_6]_2$.[77] $(Te_8^{2+})_n$ occurs as two diversely folded chains of connected six membered rings in $Te_8[Bi_4Cl_{14}]$, $Te_8[U_2Br_{10}]$ and $Te_8[NbOCl_4]_2$.[78] A combination of two different polymeric tellurium strands is present in $(Te_4)(Te_{10})[Bi_4Cl_{16}]$.[76] $(Te_6^{2+})_n$ is built of strands consisting of remarkable five-membered Te_5 rings.[79] Mixed tellurium/selenium polymeric chains built of connected four and five-membered rings are present in the structures of $(Se_4Te_3)[WOCl_4]_2$ and $(Se_{4.85}Te_{3.15})[WOCl_4]_2$.[80] The general structural principle of these 1D strands of connected chalcogen atoms is connected rings.
The number of known polymeric heteronuclear pentele/chalcogen cations is limited to $(Sb_2Te_2^{+})_n$, [34] $(Sb_2Te_2^{2+})_n$, $(Bi_2Te_2^{2+})_n$, [32] $(Bi_2Se_2^{2+})_n$ and $(Bi_4Te_4^{2+})_n$, [33] (compare chapter 1.2) which show interesting electrical transport properties like anisotropic or n-type semiconductivity. $(Sb_2Te_2^{+})_n$ consists of connected four-membered rings comparable to $(Te_4^{2+})_n$ in $(Te_4)(Te_{10})[Bi_4Cl_6]$.[75] The other known mixed chains establish the structure motive of ladder shaped strands related to those known for the homonuclear tellurium strands in Te_2Br and $(Te_{15}X_4)_n[MOX_4]_{2n}$ (X = Cl, Br; M = Mo, W).[81]

By synthetic work in chloridogallate and iodidoaluminate melts the polymeric ladder shaped cations $(Sb_2Te_2^{+})_n$, $(Sb_2Te_2^{2+})_n$, $(Bi_2Te_2^{2+})_n$ and $(Bi_2Se_2^{2+})_n$ were found in new compounds. Moreover, the unprecedented polymeric cations $(Sb_3Te_4^{+})_n$ with a "double ladder" structure and $(SbTe_4^{+})_n$ with a unique structure of connected five-membered rings could be isolated.

2.9.1 Syntheses and EDX Analyses of Compounds Containing Mixed Pentele-Chalcogen Cationic Chains

$(Sb_2Te_2)[GaCl_4]$

Under argon atmosphere, 91.8 mg (0.72 mmol) tellurium, 58.4 mg (0.48 mmol) antimony, 54.7 mg (0.24 mmol) antimony trichloride, 348.6 mg (1.98 mmol) gallium trichloride and 10.5 mg (0.18 mmol) sodium chloride were filled in a glass ampoule, which was evacuated to approx. $6 \cdot 10^{-2}$ mbar, flame sealed, and placed in a horizontal tube furnace. After 13 days at 125 °C silvery shiny, thin square-plate shaped crystals (Fig. 2.9.1.1) were obtained in estimated yield of 30 % in a black melt.

A tentative reaction equation is:

$5\ Sb + 6\ Te + SbCl_3 + 3\ GaCl_3 \rightarrow 3\ (Sb_2Te_2)[GaCl_4]$

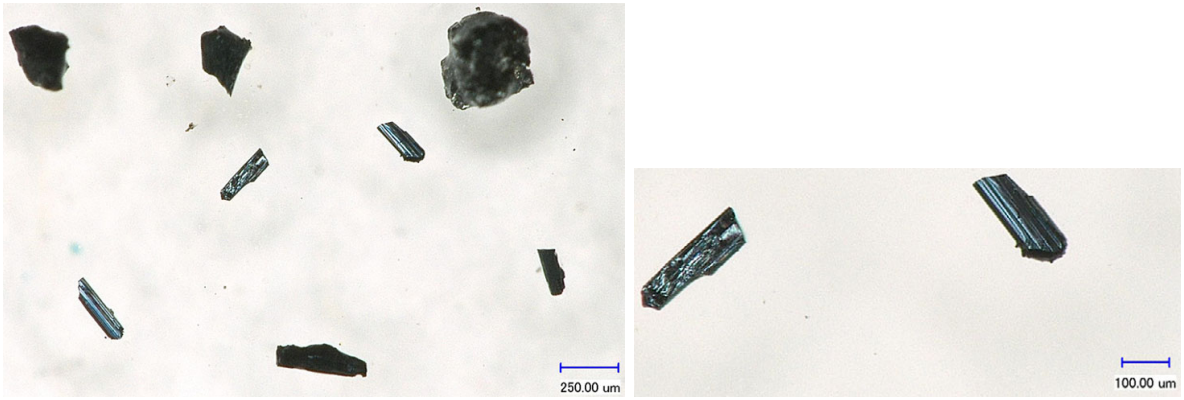

Fig. 2.9.1.1 Crystals of $(Sb_2Te_2)[GaCl_4]$ immersed in perfluorinated polyether.

The EDX analysis of $(Sb_2Te_2)[GaCl_4]$ supports generally the sum formula tolerably. All examined crystals show a slight tellurium, but a high gallium and chlorine excess and on their surfaces. The higher results for Ga and Cl can be explained by $GaCl_3$ adherences on the crystal surfaces.

Tab. 2.9.1.1 Elemental composition of $(Sb_2Te_2)[GaCl_4]$ in atom-% and the Sb : Te ratio. Standard deviations given in brackets refer to the last significant digit.

$(Sb_2Te_2)[GaCl_4]$	Sb	Te	Ga	Cl	Sb : Te
Found	12.1(6)	13.7(6)	17.3(4)	56.7(8)	1 : 1.13
Calculated	22.22	22.22	11.11	44.44	1 : 1

$(Sb_2Te_2)I[AlI_4]$

122.3 mg (0.20 mmol) antimony telluride, 80.4 mg (0.16 mmol) antimony triiodide, 403.6 mg (0.99 mmol) aluminium triiodide and 26.9 mg (0.18 mmol) sodium iodide were heated in an evacuated glass ampoule at 100 °C for 7 days and to 170 °C for further 5 days. $(Sb_2Te_2)I[AlI_4]$ forms black cube-shaped crystals emerging from an orange melt, which solidified at ambient temperature. During the manual separation the crystals turned out to be intergrown agglomerates of silvery shiny thin square plate shaped crystals.
An increased yield can be achieved by replacing sodium iodide by copper(I) iodide or silver iodide and heating the ampoules stepwise to 100 °C for 7 days, 170 °C for 5 days to finally keeping at 190 °C for 8 days. Cooling down to room temperature with 6 °C/h yielded $(Sb_2Te_2)I[AlI_4]$ in approx. yield of 30 %. In the case of the adjuvant CuI, black block shaped crystals and with AgI, silvery rod shaped crystals were formed, the identity of which was confirmed by lattice constants determinations on isolated single crystals. The crystals of $(Sb_2Te_2)I[AlI_4]$ from batches run with the adjuvant AgI are mechanically sensitive and easily fan out on mechanical strain (Fig. 2.9.1.2).

A tentative reaction equation is:

$4\ Sb + 6\ Te + 2\ SbI_3 + 3\ AlI_3 \rightarrow 3\ (Sb_2Te_2)I[AlI_4]$

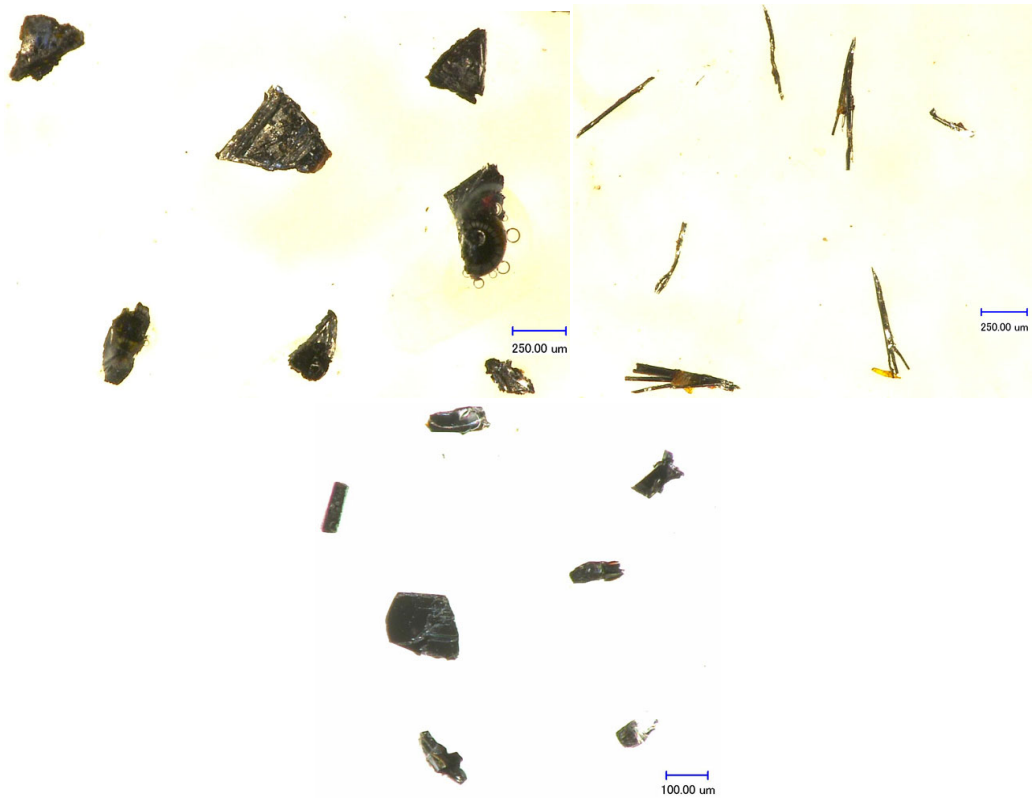

Fig. 2.9.1.2 Crystals of $(Sb_2Te_2)I[AlI_4]$ immersed in perfluorinated polyether from experiments with the adjuvants sodium chloride (top left), silver chloride (top right) and copper(I) chloride (bottom).

The EDX analysis supports the composition of $(Sb_2Te_2)I[AlI_4]$. A constant slight excess of antimony is found on all examined crystals (Tab. 2.9.1.2).

Tab. 2.9.1.2 Elemental composition of $(Sb_2Te_2)I[AlI_4]$ in atom-% and the Sb : Te ratio. Standard deviations given in brackets refer to the last significant digit.

$(Sb_2Te_2)I[AlI_4]$	Sb	Te	Al	I	Sb : Te
Found	21.2(4)	18.4(2)	9.5(5)	50.6(4)	1 : 0.87
Calculated	20	20	10	50	1 : 1

$(Bi_2Te_2)Cl[GaCl_4]$ and $(Bi_2Se_2)Cl[GaCl_4]$

For the synthesis of $(Bi_2Te_2)Cl[GaCl_4]$ 76.6 mg (0.6 mmol) tellurium, 83.6 mg (0.4 mmol) bismuth, 63.1 mg (0.2 mmol) bismuth trichloride and 105.6 mg (0.6 mmol) gallium trichloride were loaded into a glass ampoule, which was sealed under vacuum. For $(Bi_2Se_2)Cl[GaCl_4]$, tellurium was replaced by the respective molar amount of selenium. The ampoules were placed in tube furnaces aligned in an angle of about 30° to the horizontal. For $(Bi_2Te_2)Cl[GaCl_4]$ the ampoule was heated to 120 °C for six days and to 140 °C for additional seven days. For $(Bi_2Se_2)Cl[GaCl_4]$ the ampoule was heated to 50 °C for 11 days and to 100 °C for additional nine days. $(Bi_2Te_2)Cl[GaCl_4]$ crystallizes in form of black needles, $(Bi_2Se_2)Cl[GaCl_4]$ as dark red needles (Fig. 2.9.1.3). Crystals isolated from the black melt had a pronounced tendency to form intergrown agglomerates. In the synthesis of $(Bi_2Te_2)Cl[GaCl_4]$, sodium chloride or tetraphenylphosphonium chloride may be added to the reaction mixture as an adjuvant. The use of $[P(C_6H_5)_4]Cl$ is advantageous since a less viscous melt is obtained, which alleviates the separation of the crystals.
By adding sodium chloride to the reaction mixture for the synthesis of $(Bi_2Se_2)Cl[GaCl_4]$, $(Bi_4Se_4)[GaCl_4]_4$ is obtained instead in form of yellow crystals. This compound crystallizes isotypically to the aluminium containing congener $(Bi_4Se_4)[AlCl_4]_4$.[30]

Tentative reaction equations are:

$4\ Bi + 6\ Te + 2\ BiCl_3 + 3\ GaCl_3 \rightarrow 3\ (Bi_2Te_2)Cl[GaCl_4]$
$4\ Bi + 6\ Se + 2\ BiCl_3 + 3\ GaCl_3 \rightarrow 3\ (Bi_2Se_2)Cl[GaCl_4]$

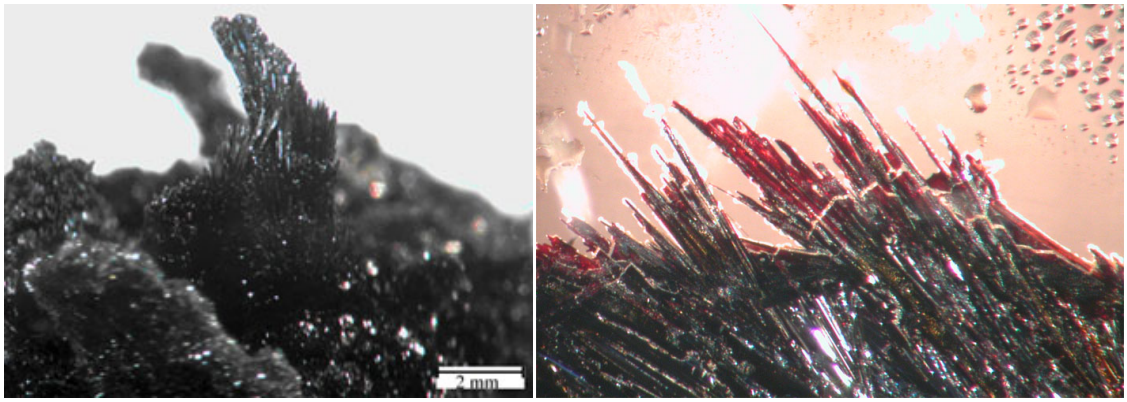

Fig. 2.9.1.3 Crystals of $(Bi_2Te_2)Cl[GaCl_4]$ (left) and $(Bi_2Se_2)Cl[GaCl_4]$ (right) in the reaction ampoules.

Besides slightly too high Ga and too low Cl contents, the EDX analyses of all crystals confirm the compostions of $(Bi_2Ch_2)Cl[GaCl_4]$ accurately.

Tab. 2.9.1.3 Elemental composition of $(Bi_2Te_2)Cl[GaCl_4]$ and $(Bi_2Se_2)Cl[GaCl_4]$ in atom-% and the Sb : Te ratio. Standard deviations given in brackets refer to the last significant digit.

	Bi	Ch	Ga	Cl	Bi : Ch
$(Bi_2Te_2)Cl[GaCl_4]$	19.3(2)	19.5(2)	12.4(2)	48.6(2)	1 : 1.01
$(Bi_2Se_2)Cl[GaCl_4]$	20.1(7)	20.5(7)	13.2(14)	46.1(3)	1 : 1.02
calculated	20	20	10	50	1 : 1

$(Sb_3Te_4)[GaCl_4]$

45.2 mg (0.36 mmol) tellurium, 29.2 mg (0.24 mmol) antimony, 27.4 mg (0.12 mmol) antimony trichloride, 174.0 mg (0.99 mmol) gallium trichloride and 60.0 mg (0.16 mmol) tetraphenylphosphonium chloride were filled in a glass ampoule, which was evacuated and sealed. On heating to temperatures between 50 and 140 °C, crystals appeared within one to three weeks in form of silvery, metallic shiny rods in an estimated yield of 15 % (Fig. 2.9.1.4). Tetraphenylphosphonium chloride may be replaced by sodium chloride. Unsing this adjuvant, at slightly higher reaction temperatures between 130 and 160 °C crystallization starts after three days. The disadvantage of this variant is the much higher viscosity of the melt, which hampers the manual separation of the crystals. $(Sb_2Te_4)[GaCl_4]_2$ (chapter 2.7) is obtained as a byproduct in comparable yield.

A tentative reaction equation is:

$$8\ Sb + 12\ Te + SbCl_3 + 3\ GaCl_3 \rightarrow 3\ (Sb_3Te_4)[GaCl_4]$$

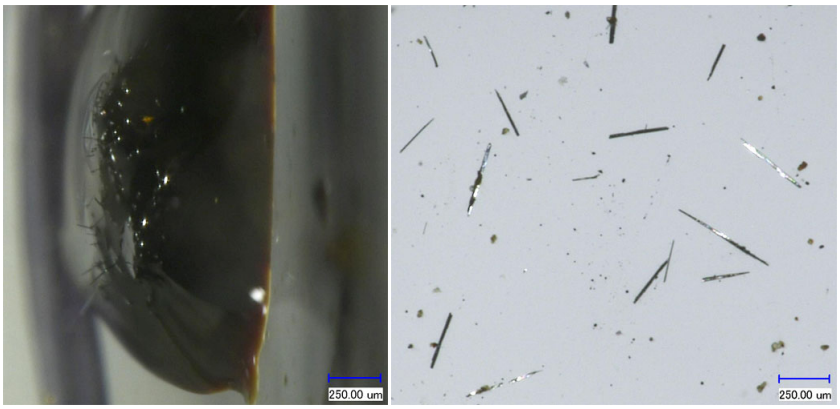

Fig. 2.9.1.4 Crystals of $(Sb_3Te_4)[GaCl_4]$ from two different experiments in the reaction ampoule with the adjuvant sodium chloride (left) and immersed in perfluorinated polyether from an experiment with the adjuvant tetraphenyl phosponium chloride.

Considering slight deviations from the calculated composition like in the EDX analysis of $(Bi_2Te_2)Cl[GaCl_4]$, the sum formula $(Sb_3Te_4)[GaCl_4]$ is supported by the analysis (Tab. 2.9.1.4).

Tab. 2.9.1.4 Elemental composition of $(Sb_3Te_4)[GaCl_4]$ in atom-% and the Sb : Te ratio. Standard deviations given in brackets refer to the last significant digit.

$(Sb_3Te_4)[GaCl_4]$	Sb	Te	Ga	Cl	Sb : Te
Found	26.3(2)	32.0(4)	12.4(2)	29.1(4)	1 : 1.22
Calculated	25	33.33	8.33	33.33	1 : 1.33

$(SbTe_4)[Ga_2Cl_7]$

45.2 mg (0.36 mmol) tellurium, 29.2 mg (0.24 mmol) antimony, 27.4 mg (0.12 mmol) antimony trichloride, 174.0 mg (0.99 mmol) gallium trichloride, 60.0 mg (0.16 mmol) tetraphenylphosphonium chloride and 14.4 mg (0.09 mmol) tellurium dioxide were placed in a glass ampoule, which was flame-sealed under dynamic vacuum. After 60 days at 50 °C compound $(SbTe_4)[Ga_2Cl_7]$ was obtained as black needles in an estimated yield of 70 % (Fig. 2.9.1.5) with small residues of unreacted antimony in a colourless melt.

A tentative reaction equation is:

$2\ Sb + 12\ Te + SbCl_3 + 6\ GaCl_3 \rightarrow 3\ (SbTe_4)[Ga_2Cl_7]$

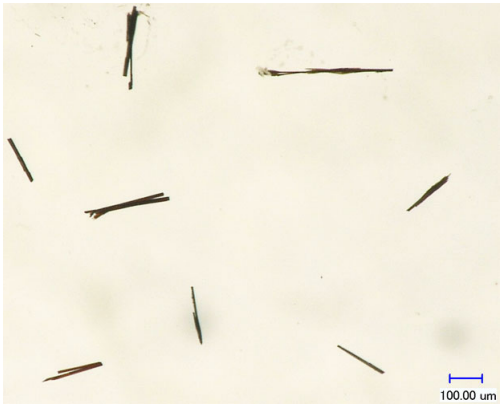

Fig. 2.9.1.5 Crystals of $(SbTe_4)[Ga_2Cl_7]$ immersed in perfluorinated polyether.

The EDX analysis shows deviations from the calculated composition concerning the Sb:Te ratio due to a slight Sb excess on the crystal surfaces (Tab. 2.9.1.5). Despite this, the sum formula of $(SbTe_4)[Ga_2Cl_7]$ is confirmed.

Tab. 2.9.1.5 Elemental composition of $(SbTe_4)[Ga_2Cl_7]$ in atom-% and the Sb : Te ratio. Standard deviations given in brackets refer to the last significant digit.

$(SbTe_4)[Ga_2Cl_7]$	Sb	Te	Ga	Cl	Sb : Te
Found	7.48(1)	26.66(3)	16.28(3)	49.58(3)	1 : 3.56
Calculated	7.14	28.57	14.29	50	1 : 4

2.9.2 The Reactions Leading to Compounds Containing Mixed Pentele-Chalcogen Cationic Chains

All compounds were obtained from melts mainly composed of gallium trichloride and in one case AlI_3. Antimony or bismuth trihalides were use as mild oxidants towards the respective elements.
The addition of sodium chloride or sodium iodide turned out as essential in the syntheses of $(Sb_2Te_2)[GaCl_4]$ and $(Sb_3Te_4)[GaCl_4]$. Without the addition of NaCl, no crystalline products at all were formed in attempted reactions for $(Sb_3Te_4)[GaCl_4]$. Sodium halides dissolve in the reaction melts

forming $Na[GaCl_4]$ and $Na[AlI_4]$ lowering the Lewis acidity of the melts. The adjuvant sodium halides were not incorporated into the crystals as shown by EDX analyses and remained in the viscous melts. Crystals of all compounds under study are black or shiny metallic, only $(Bi_2Se_2)Cl[GaCl_4]$ forms dark red crystals. $(Sb_2Te_2)[GaCl_4]$ and particularly $(Sb_3Te_4)[GaCl_4]$ were obtained in intergrown crystal bundles. For the separation of single crystals, mechanical cleavage along their long axes had to be performed. $(Bi_2Te_2)Cl[GaCl_4]$ and $(Bi_2Se_2)Cl[GaCl_4]$ crystallize in extreme thin needles sensitive against splitting during any mechanical tratment. Crystals of $(Sb_2Te_2)I[AlI_4]$ grow in block shaped crystals, but show analogously a high sensitivity against mechanical manipulation. All these compounds crystallize from the melts in estimated yields of 10 - 30 %. All attempts to synthesize a compound of the composition $(Bi_3Te_4)[GaCl_4]$ in analogous way to the synthesis of $(Sb_3Te_4)[GaCl_4]$ were unceccessful, since only $(Bi_2Te_2)Cl[GaCl_4]$ was obtained.

Tellurium dioxide, which dissolves in the acidic reaction melt, turned out as the crucial adjuvant in the synthesis of $(SbTe_4)[Ga_2Cl_7]$. Compared to the rather low yields of the other compounds containing mixed pentele-chalcogen chains, $(SbTe_4)[Ga_2Cl_7]$ crystallizes in high yield of about 70 %. No other products besides unreacted antimony and small residues of an almost colourless melt were present in the closed reaction ampoules and no oxygen was detected in the reaction product.

In the course of the investigations, tetraphenylphosphonium chloride turned out as an invaluable adjuvant. $[P(C_6H_5)_4]Cl$ has an improving influence on the products on the one hand and it allows for new products on the other hand. The synthesis of $Ag(Sb_7Te_8)[GaCl_4]_6$ (chapter 2.1) was only possible in the presence this adjuvant. Mixtures of $[P(C_6H_5)_4]Cl$ and $GaCl_3$ become liquid at room temperature instantaneously by forming $PPh_4[GaCl_4]$ and can be conceived as a ionic liquid. Additionally, $[P(C_6H_5)_4]Cl$ lowers the acidity of the melts by providing Cl^- anions similar to NaCl. During the syntheses of $Na(Sb_7Te_8)[GaCl_4]_6$ and $(Sb_7Se_8Cl_2)[GaCl_4]_3$ (chapter 2.1, 2.2) the yield, crystal quality and crystal size could be improved substantially by adding tetraphenylphosphonium chloride to the basic educt mixture. The reason may be attributed to the lower viscosity of the melts and a higher ion mobility.

Dark-red block-shaped crystals of $Cu[AlI_4]$ were obtained as by-products in the synthesis of $(Sb_2Te_2)I[AlI_4]$ with CuI used as the adjuvant. In all three applied synthetic procedures for $(Sb_2Te_2)I[AlI_4]$, yellow rod shaped crystals were found, which were identified as $(SbI_2)[AlI_4]$. Both compounds can be obtained individually by reacting CuI and SbI_3 with AlI_3 at 190 °C, respectively. These two compounds are presented in chapters 2.10 and 2.11.

All attempts to measure the electrical conductivity of selected crystals were hampered by the brittleness and mechanical instability of the crystals of all compounds. However, semiconducting behaviour is expected as reported for $(Bi_2Se_2)Cl[AlCl_4]$, $[(Bi_4Te_4)Br_2(Al_2Cl_{6-x}Br_x)]Cl_2$ [33] and $(Bi_2Te_2)Br[AlCl_4]$. [32]

2.9.3 Crystal Structures of Compounds Containing a $(Pn_2Ch_2^{1+/2+})_n$ Polymeric Cation

1D-polymeric $(Pn_2Ch_2^{1+/2+})_n$ cations are present in the crystal structures of $(Sb_2Te_2)[GaCl_4]$, $(Sb_2Te_2)I[AlI_4]$, $(Bi_2Te_2)Cl[GaCl_4]$ and $(Bi_2Se_2)Cl[GaCl_4]$. $(Sb_2Te_2)[GaCl_4]$ contains the polymeric cation $(Sb_2Te_2^+)_n$ and is isotypic to known the aluminium containing analogue $(Sb_2Te_2)[AlCl_4]$.[13] The structure consists of discrete $[GaCl_4]^-$ anions and two symmetrically independent polymeric cations, which are built of approximately parallel arranged four-memberd Sb_2Te_2 rings. These rings are connected by Sb–Sb and Sb–Te bonds to infinite chains. Tellurium occupies both, the two-fold and three-fold coordinated positions, the latter ones carrying formally the positive charges (Fig. 2.9.3.1). The

distinction of Sb and Te was possible on basis of the diffraction data (Fig. A 5.3.9). An additional analysis of the coordination environment of the Sb and Te atoms by Cl atoms, did not lead to unambigous results for Te2B and Te3B (Tab. A 5.5.10). The crystallographic data of $(Sb_2Te_2)[GaCl_4]$ are shown in Tab. A 5.2.12.

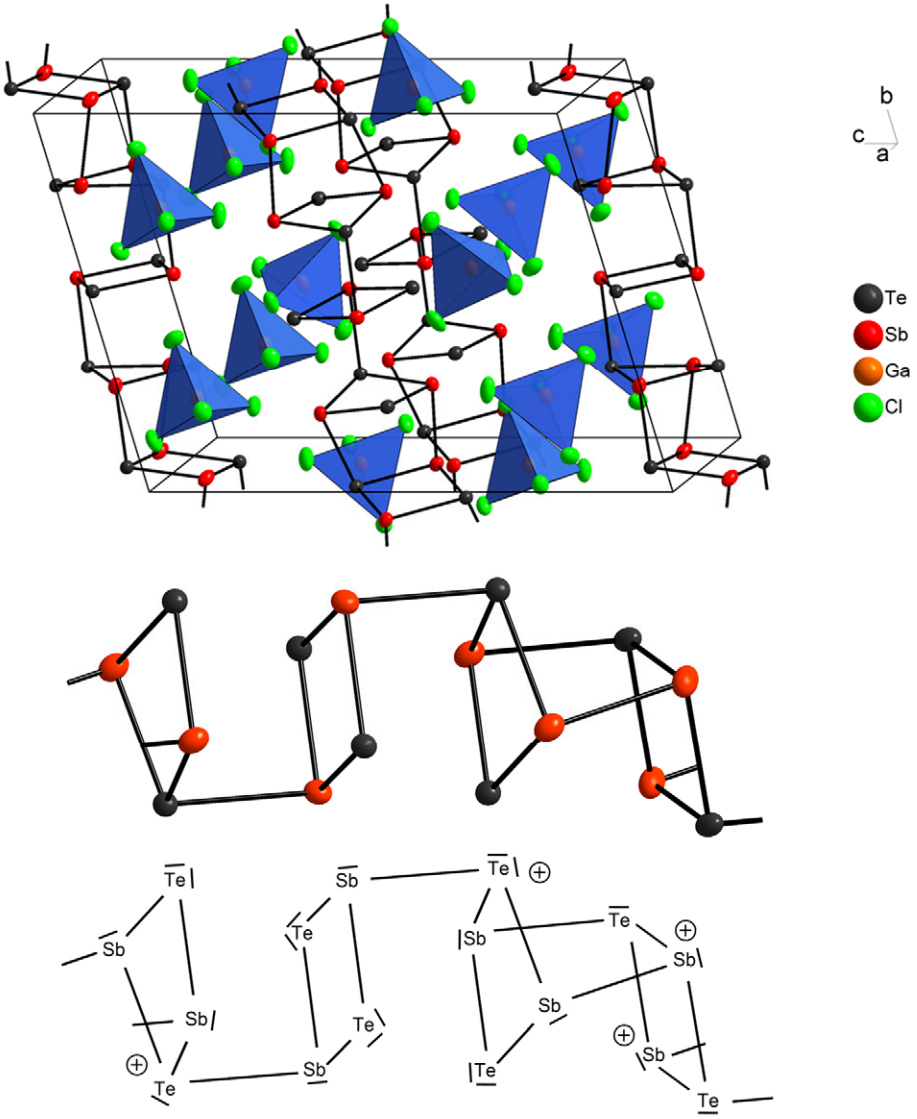

Fig. 2.9.3.1 The unit cell of the structure of $(Sb_2Te_2)[GaCl_4]$. The $[GaCl_4]^-$ ions are represented by discrete tetrahedra. The atoms are represented by thermal ellipsoids scaled to include a probability of 70 %. A section of the $(Sb_2Te_2^+)_n$ chain is shown in the middle. The atoms are represented by thermal ellipsoids scaled to include a probability of 70 %. On bottom the Lewis formula for the cation is given.

According to the Zintl rules, any change of the charge of the cation will lead to an altered structure. This rule holds, since the structures of $(Sb_2Te_2)I[AlI_4]$, $(Bi_2Te_2)Cl[GaCl_4]$ and $(Bi_2Se_2)Cl[GaCl_4]$, containing the polymeric cation $(Pn_2Ch_2^{2+})_n$ exhibit as a consequence of the charge +2 on each Pn_2Ch_2 unit a different connection between the Pn_2Ch_2 ring units with respect to the structure of $(Sb_2Te_2)[GaCl_4]$. The three compounds crystallize all in space group *C*2/*m*, but only $(Bi_2Te)Cl[GaCl_4]$ and $(Bi_2Se_2)Cl[GaCl_4]$ are isotypic. All heavy atoms occupy exclusively special positions in the mirror planes and all pentele and chalcogen atoms are triply coordinated (Fig. 2.9.3.2).

The Sb/Te distribution within the the $(Sb_2Te_2^{2+})_n$ chain is confirmed by an analysis of the free occupation factors when all heavy atom pasotions are refined as occupied by tellurium (Fig. A 5.3.10). Pn–Ch dumbbells are connected to infinite ladder-shaped bands with zig zag conformation running along the crystallographic *b* direction. In the bands of $(Bi_2Te_2)Cl[GaCl_4]$ and $(Bi_2Se_2)Cl[GaCl_4]$, two different Pn–Ch bonds are present, one along, the other across the band. The bond lengths are uniform in the bismuth containing compounds $(Bi_2Te_2)Cl[GaCl_4]$ and $(Bi_2Se_2)Cl[GaCl_4]$ (Bi–Te 2.9631(5) and 2.9673(3) Å, Bi–Se 2.781(1) and 2.782(2) Å). In $(Sb_2Te_2)I[AlI_4]$ the Sb–Te bond lengths across the band are 2.805(1) and 2.823(1) Å. In contrast to this, the bond lengths along the band are significantly longer and found in the range between 2.918(1) and 3.095(1) Å (Tabs. A 5.4.12 and A 5.4.13). The bond angles within the ladder-shaped cations are uniform in all three structures and close to 90°. The structures of the cations thus resemble the ternary pentele chalcogenide halides SbTeI, [82] BiTeCl, [83] and BiSeCl [84], from which they are formally derived by replacing every second halide ion by halogenido aluminates and -gallates. The remaining halide ions have different functions. In the structures of $(Bi_2Te_2)Cl[GaCl_4]$ and $(Bi_2Se_2)Cl[GaCl_4]$ the chloride ions bridge between the Bi atoms of neighboring polymeric chains with Bi–Cl distances of 3.1396(2) Å for $(Bi_2Te_2)Cl[GaCl_4]$ and 3.0875(5) Å for $(Bi_2Se_2)Cl[GaCl_4]$ and give the two structures a pronounced layered character. The arrangement of $[AlI_4]^-$ and I^- ions in the structure of $(Sb_2Te_2)I[AlI_4]$ is different. No bridging halide atoms between adjacent cationic strands are present, instead the cationic strands are all around surrounded by $[AlI_4]^-$ anions, retaining the one-dimensional character. The discrete iodine atoms form asymmetric bridges over each two Sb atoms with Sb–I bonds of 3.051(1) and 3.199(2) Å. The crystallographic data of all structures containing ladder shaped polycationic chains are shown in tables A 5.2.12 and 5.2.13.

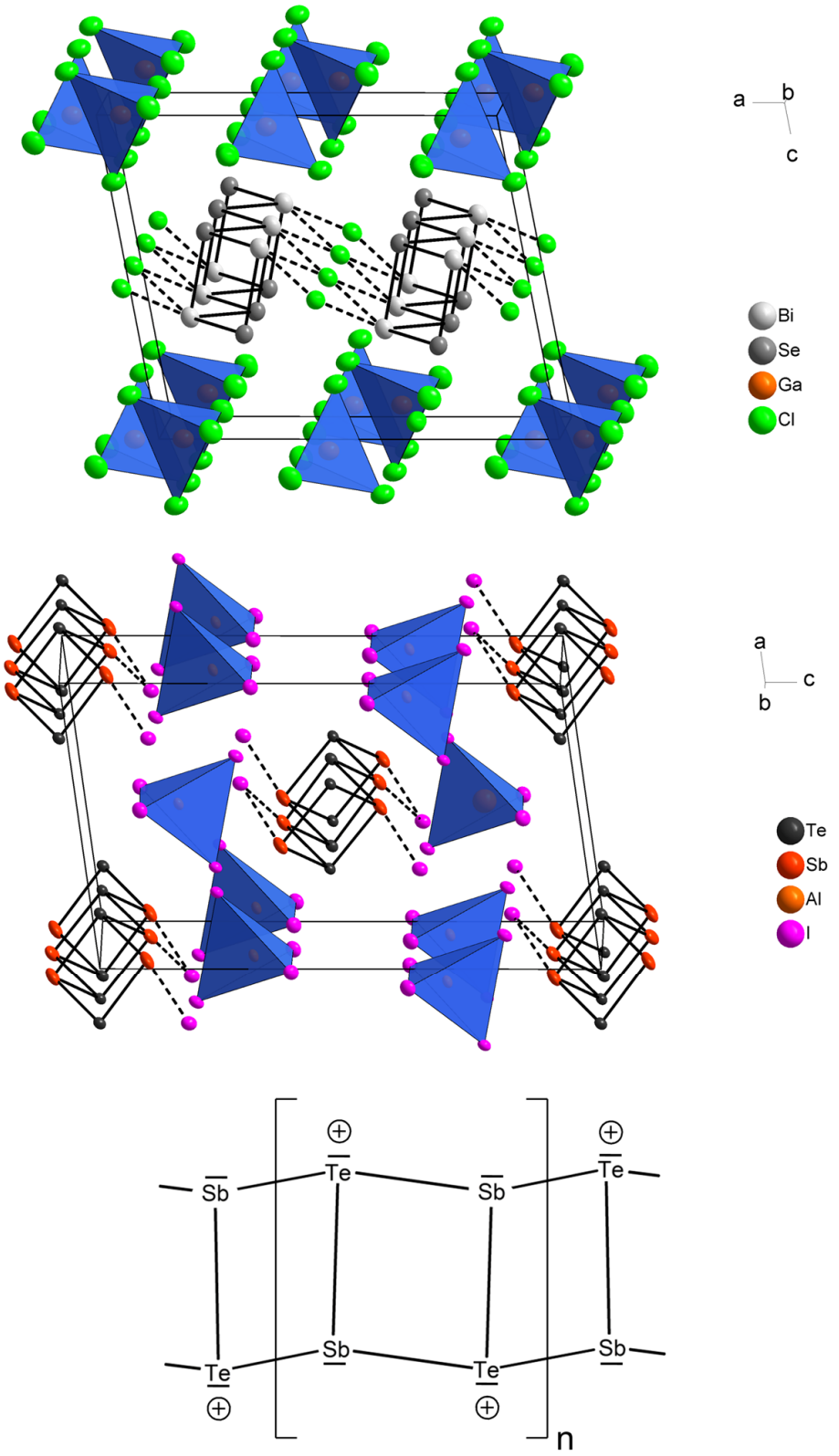

Fig. 2.9.3.2 The unit cells of the structures of $(Bi_2Se_2)Cl[GaCl_4]$ (top) and $(Sb_2Te_2)I[AlI_4]$ (middle). The $[GaCl_4]^-$ and $[AlI_4]^-$ ions are shown as discrete tetrahedra. The atoms are represented by thermal ellipsoids scaled to include a probability of 70 %. Both structures are depicted in an idealized way since only one half of the disordered Ga and Al atoms is shown. For $(Sb_2Te_2)I[AlI_4]$ only the atoms sites Al(1) with 85 % occupation are depicted. On bottom a Lewis formula for the $(Sb_2Te_2^{2+})_n$ polymeric cation is given. Formulae for $(Bi_2Te_2^{2+})_n$ and $(Bi_2Se_2^{2+})_n$ are analogous.

2.9.4 The Crystal Structure of $(Sb_3Te_4)[GaCl_4]$

The crystal structure of $(Sb_3Te_4)[GaCl_4]$ contains a novel polymeric pentele/chalcogen cation. Fig. 2.9.4.1 shows the unit cell of $(Sb_3Te_4)[GaCl_4]$ and a section of the cationic chain. The structure of the cation may be understood as the product of a formal condensation of two $(Sb_2Te_2)^{2+}$ chains under loss of one Sb^{3+} ion for each two Sb_2Te_2 groups (Fig. 2.9.4.2). As a peculiarity, one of the three Sb atoms of the formula entity has a six-fold coordination in form of an almost undistorted $SbTe_6$ octahedron.

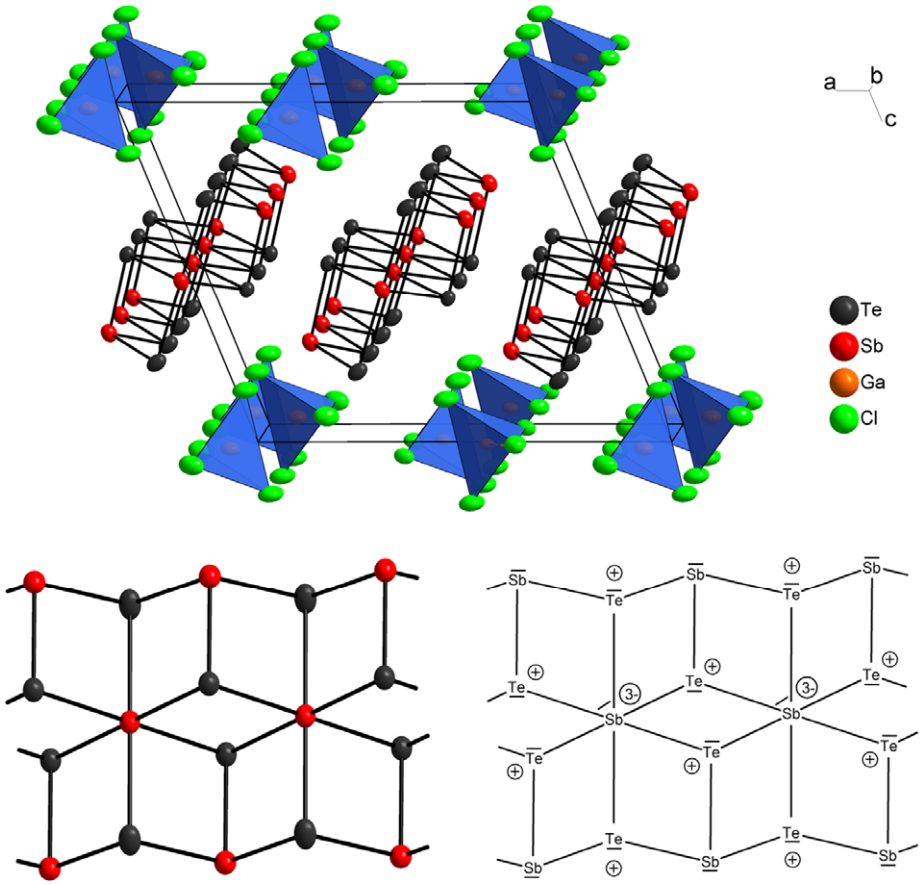

Fig. 2.9.4.1 The unit cell of the structure of $(Sb_3Te_4)[GaCl_4]$ (top). The $[GaCl_4]^-$ ions are shown as discrete tetrahedra. A section of the $(Sb_3Te_4^+)_n$ chain is shown left at the bottom. The atoms are represented by thermal ellipsoids scaled to include a probability of 70 %. The structure is depicted in an idealized way since only one half of the disordered Ga atoms is shown. On bottom right a Lewis formula for the $(Sb_3Te_4^+)_n$ polymeric cation is given.

The correct assignment of the Sb and Te position was possible on basis of the diffraction data. Free refinements with all positions occupied by Te leads to a clear distinction of lower and higher occupation factors (Fig. A 5.3.11).

The bond lengths within the $(Sb_3Te_4^+)_n$ cation fall into two groups. Sb–Te bonds within the $SbTe_6$ octahedra are long with 3.0257(5) and 3.0281(7) Å (Tab. A 5.4.14) and are in line with the corresponding bonds in the double-cube shaped $(Sb_7Te_8)^{5+}$ cluster in $Na(Sb_7Te_8)[GaCl_4]_6$ (3.012 Å) (compare chapter 2.1.4). The Te–Sb–Te angles at the central Sb(1) atom are close to the ideal values with distortions of less than 3°. The Sb–Te bond lengths at the peripheral three-fold coordinated Sb atoms are significantly shorter with 2.8685(9) Å. The bond angles at Sb(2) are in turn all close to rectangularity in the range between 87.18(1)° and 95.56(2)°. The octahedral $SbTe_6$ coordination entity

is known from the molecular double-cube shaped $(Sb_7Te_8)^{5+}$. A classical Lewis formula implies for the central Sb atom six covalent bonds and a lone pair (Fig. 2.9.4.1). With 14 valence electrons this model is allowedly overstressed and the bonding situation of this hypervalent Sb atom is better understood in non-classical terms with three perpendicular three center-four electron bonds. The individual strands approach each other in direction of the *a*-axis. Secondary Sb–Te bonds of 3.5375(8) Å connect the strands to an undulating layer parallel to the *a*-*b*-plane, which resembles a section of the 2D sheets as present in the structure of Sb_2Te_3. The individual $(Sb_3Te_4^+)_n$ strand may be considered as a section of the layer structure of Sb_2Te_3 under formal loss of telluride ions: $Sb_2Te_3 = Sb_6Te_9 = Sb_6Te_8^{2+} + Te^{2-}$; $Sb_6Te_8^{2+} = Sb_3Te_4^+$. Alternatively, the structure of the cation may be understood as the product of a formal condensation of two $(Sb_2Te_2)^{2+}$ chains under loss of one Sb^{3+} ion for each two Sb_2Te_2 groups. The structure motif of the $(Sb_3Te_4^+)_n$ chain is also present in the double-cube shaped discrete cation $(Sb_7Te_8)^{5+}$ with the typical six-fold coordinated central Sb atom. These structural relations are summarized in Fig. 2.9.4.2.

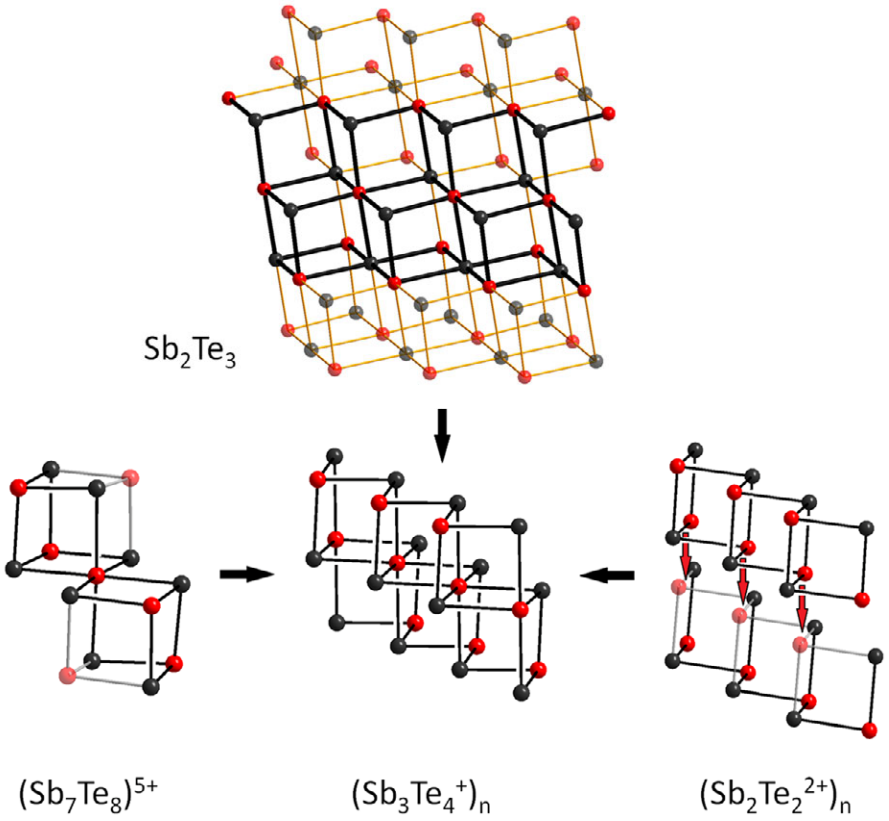

Fig. 2.9.4.2 The structure of the 1D polymeric cation $(Sb_3Te_4^+)_n$ with the intrinsic "double-ladder" structure in $(Sb_3Te_4)[GaCl_4]$ and the structural relation to Sb_2Te_3 (top), $(Sb_7Te_8)^{5+}$ (bottom left) and $(Sb_2Te_2^{2+})_n$ (bottom right).

2.9.5 The Statistical Disorder in the Anionic Part in the Structures of $(Sb_2Te_4)I[AlI_4]$, $(Bi_2Te_2)Cl[GaCl_4]$, $(Bi_2Se_2)Cl[GaCl_4]$ and $(Sb_3Te_4)[GaCl_4]$

The 1D-polymeric cations as present in compounds $(Sb_2Te_2)I[AlI_4]$, $(Bi_2Te_2)Cl[GaCl_4]$ and $(Bi_2Se_2)Cl[GaCl_4]$ had already been found in the structures of $(Sb_2Te_2)Br[AlCl_4]$, $(Bi_2Te_2)Br[AlCl_4]$ and $(Bi_2Se_2)Br[AlCl_4]$.[32,33] The compounds in this study represent new combinations under exchange of

chlorine for iodine in the case of $(Sb_2Te_2)I[AlI_4]$ and bromine and aluminium for chlorine and gallium for $(Bi_2Te_2)Cl[GaCl_4]$ and $(Bi_2Se_2)Cl[GaCl_4]$. Despite coinciding formulae, the new structures are not isotypic to the reported ones, which crystallize in space group *C*2/*c*. $(Bi_2Te_2)Cl[GaCl_4]$ and $(Bi_2Se_2)Cl[GaCl_4]$ belong to space group *C*2/*m*. Two cell axes are cut in half, the cell volume amounts only one quater with respect to the reported congeners. Careful inspection of the diffraction patterns of several crystals did not show any superstructure reflections (Fig. 2.9.5.1).

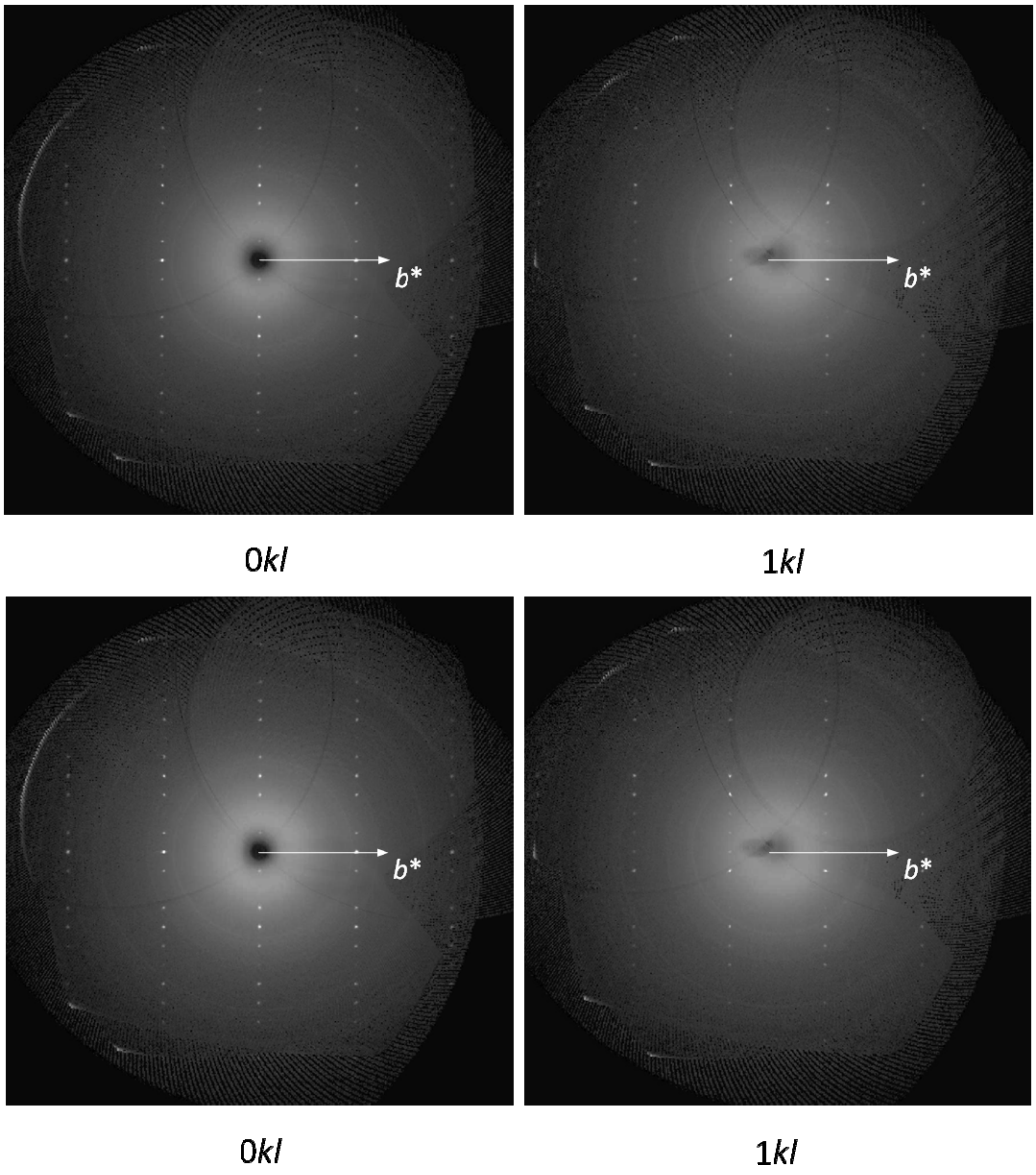

Fig. 2.9.5.1 Simulated precession diagrams, derived from the area detector data, of the layers 0*kl* and 1*kl* of $(Bi_2Te_2)Cl[GaCl_4]$ (top), $(Bi_2Se_2)Cl[GaCl_4]$ (bottom). There are no superstructure reflections observed in the *b** direction.

The consequence is the necessity for a model of statistical disorder of the $[GaCl_4]^-$ groups. The atoms Ga and Cl1 occupy their position in the mirror plane and close to the mirror plane only by 50 %. Rows of tetrahedral $GaCl_4$ groups along the short *b*-axis emerge. The structure model implies order of the occupation of the Ga atoms in the *b* direction but no coherence between the rows and a purly random occupation in the lattice directions *a* and *c.* An analogous disorder phenomenon is present in the structure of $(Sb_3Te_4)[GaCl_4]$, which also belongs to space group *C*2/*m*. No evidence for an enlargement

of the short unit cell axis *b* (4.1958(4) Å) by additional reflections was found on inspection of the diffraction pattern of several crystals (Fig. 2.9.5.2).

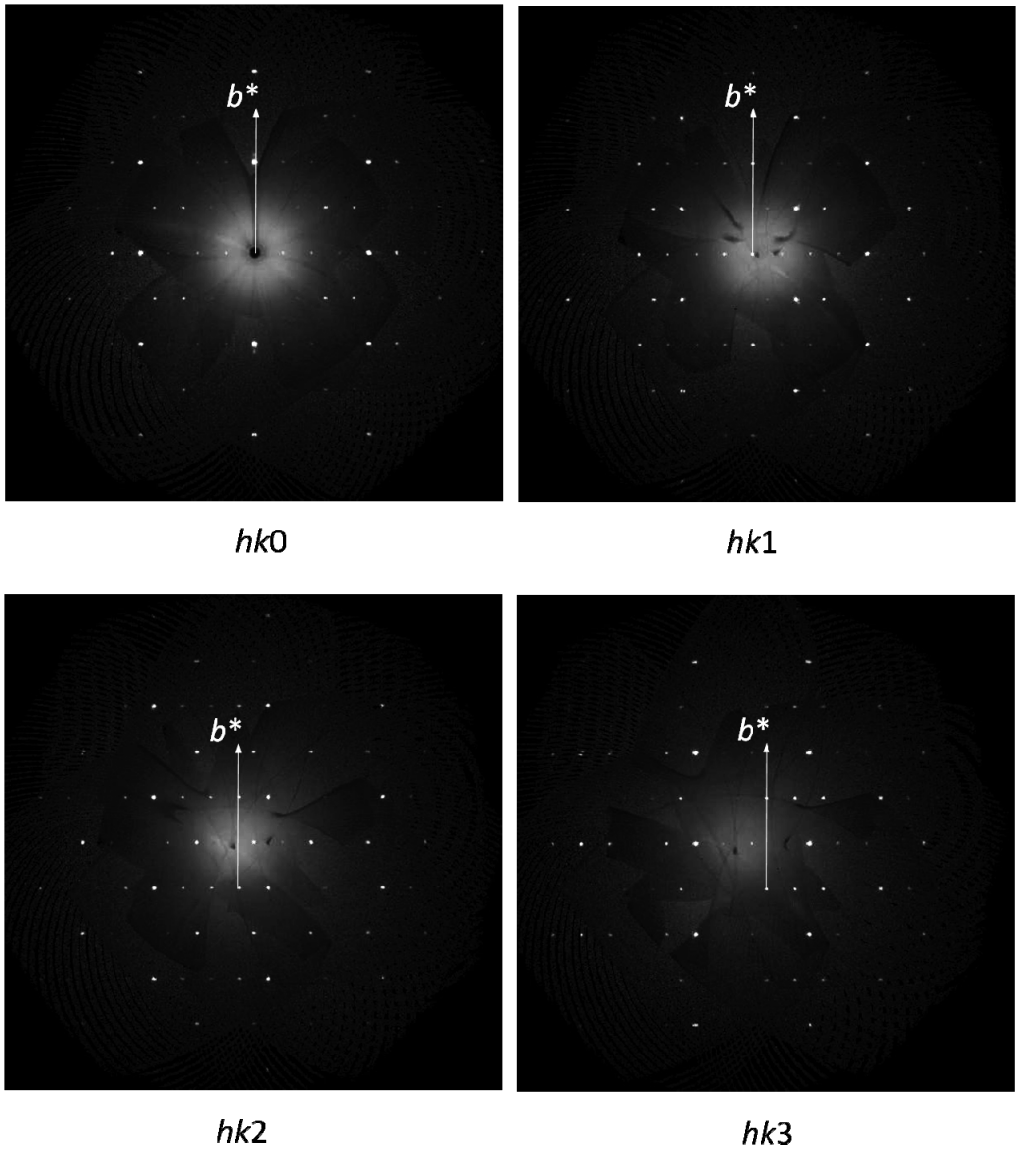

Fig. 2.9.5.2 Simulated precession diagrams of $(Sb_3Te_4)[GaCl_4]$, derived from the area detector data, of the layers *hk*0 (top left), *hk*1 (top right), *hk*2 (bottom left) and *hk*3 (bottom right). There are no superstructure reflections observed.

The structure can only be refined under assumption of a disorder in the anionic part: a 50 % occupation is assigned to the Ga and the Cl1 atom, giving a row of $[GaCl_4]^-$ groups along the *b*-axis. This structure model is only valid if there is no regularity between the occupation of the atom positions of the anions in the directions *a* and *c*. Fig. 2.9.5.3 shows the resolved disorder of the $[GaCl_4]^-$ anions.

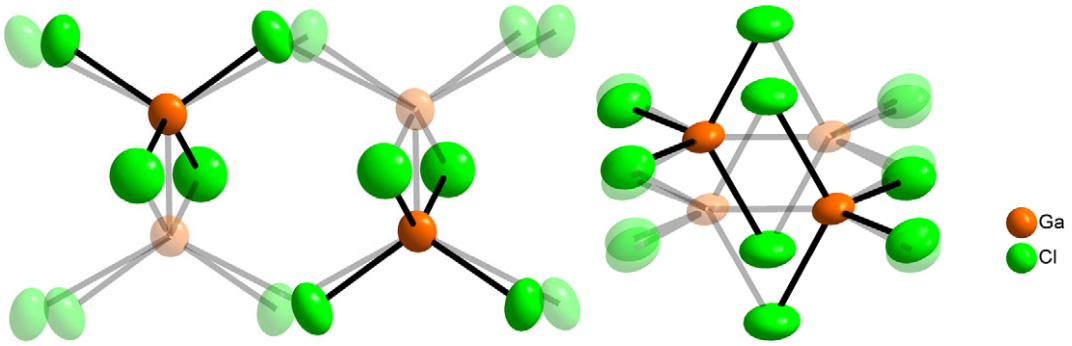

Fig. 2.9.5.3 The $[GaCl_4]^-$ anions in the structures of $(Bi_2Ch_2)Cl[GaCl_4]$ (Pn = Te, Se) and $(Sb_3Te_4)[GaCl_4]$. All atoms generated by symmetry operations of the space group *C*2/*m* are shown. All atoms are occupied by 50 %. Therefore translucent atoms and bonds are used to indicate the disorder.

In contrast, the diffraction patterns of $(Sb_2Te_2)I[AlI_4]$ contain superstructure reflections. Taking these into account leads to a doubled *b*-axis and a primitive cell in space group $P2_1/n$ (Fig. 2.9.5.4).

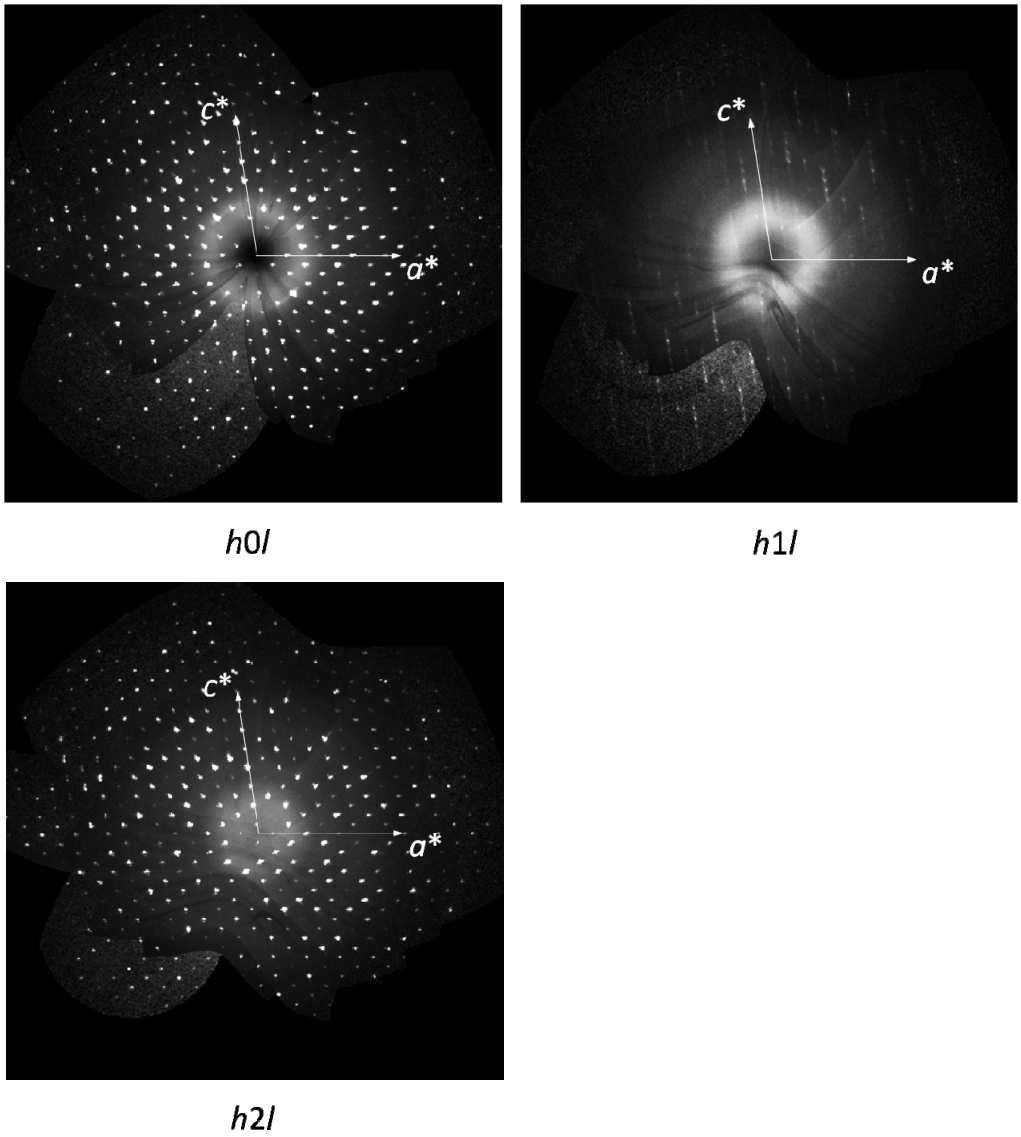

Fig. 2.9.5.4 Simulated precession diagrams of the layers *h*0*l*, *h*1*l* and *h*2*l* of $(Sb_2Te_2)I[AlI_4]$, derived from the area detector data. The layers with *k* = odd contain weak superstructure reflections together with some diffuse streaks.

The Fourier maps reveal a high electron density in the vicinity of Al1 is present. In the final refinement, two Al positions were assumed with a common occupation factor of unity as the sum of two individual ones. The respective positions gained the occupation factors 0.833(9) for Al(1) and 0.166(9) for Al2. The disorder phenomena, as present in the structures of $(Bi_2Te_2)Cl[GaCl_4]$, $(Bi_2Se_2)Cl[GaCl_4]$, and $(Sb_3Te_4)[GaCl_4]$ are partially but not completely resolved in the structure of $(Sb_2Te_2)I[AlI_4]$. Fig. 2.9.5.5 shows the resolved disorder of the $[GaCl_4]^-$ anions.

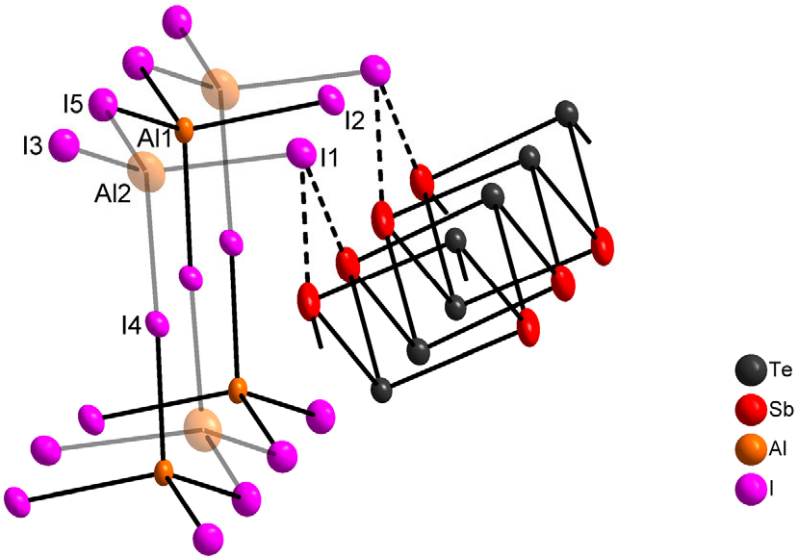

Fig. 2.9.5.5 The disordered $[AlI_4]^-$ and I^- anions in the structures of $(Sb_2Te_2)I[AlI_4]$. The disordered atom Al2 is shown with translucent atoms and bonds.

In all crystal structures, the cationic part is not affected by any disorder. Since strong covalent bonds between penetele and chalogen atoms are present in the directions of the respective strands, the cations determine the crystal lattice and afford different positions for the tetrahedral $[AlI_4]^-$ and $[GaCl_4]^-$ anions in the space between the strands. A similar disorder has been observed in the structure of $[(Bi_4Te_4)Br_2(Al_2Cl_{6-x}Br_x)]Cl_2$. [33]

2.9.6 The Crystal Structure of $(SbTe_4)[Ga_2Cl_7]$

The structure of $(SbTe_4)[Ga_2Cl_7]$ consists of polymeric $(SbTe_4^+)_n$ cations and heptachlorido digallate anions. The $[Ga_2Cl_7]^-$ anions are of regular shape (Ga–Cl bonds 2.13(1) to 2.33(1), Cl–Ga–Cl angles 101.1(2) to 116.9(2)°) and do not show remarkable deviations from those found in $K[Ga_2Cl_7]$[51]. The $(SbTe_4)^+$ cation is a five membered ring in the envelope conformation. Within the ring, the bond lengths are rather equably distributed in the range 2.696(2) to 2.832(2) Å, the angles lie between 92.75(4) and 103.09(4)°. The individual $(SbTe_4)^+$ rings are connected via Sb–Te bonds of 3.059(2) and 3.140(2) Å to a 1D polymer running along the crystallographic *a*-axis (Fig. 2.9.6.1). The intramolecular bond lengths are listet in Tab. A 5.5.15. Each five-membered ring exhibits four heteronuclear bonds to two neighbored rings forming rectangular four-membered Sb_2Te_2 rings with inversion centers in the points of gravity as the linkers between the individual $(SbTe_4)^+$ cations. The two different intermolecular Sb–Te bonds generate a sequence of $(SbTe_4)^+$ clusters that are linked alternately by long and short bonds. This bond length alteration is a typical feature for clusters of the heavy main

group elements and is attributed to the specific $5p^2 \rightarrow \sigma^*$ donor-acceptor bonds. [47,85] If all bonds are assessed as two-center two-electron bonds, Lewis formulae can be set up for the $(SbTe_4^+)_n$ cation, one of which is shown in Fig. 2.9.6.1.

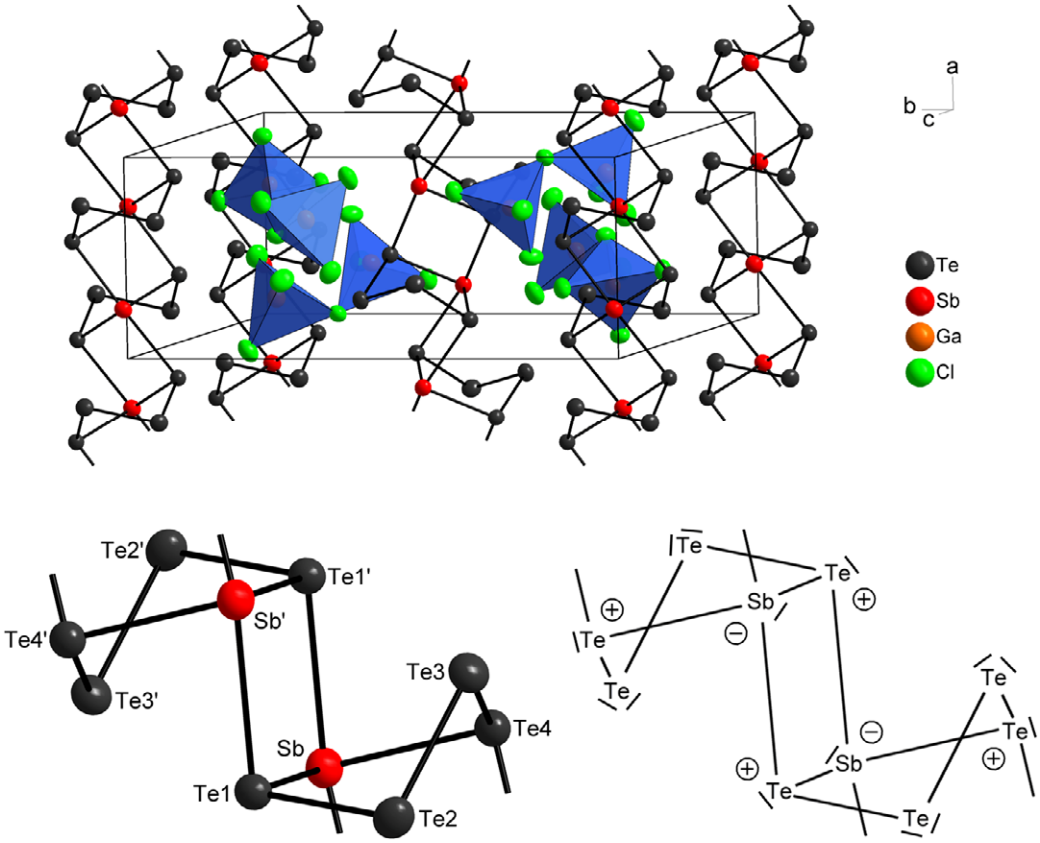

Fig. 2.9.6.1 The unit cell of the structure of $(SbTe_4)[Ga_2Cl_7]$ (top). The $[Ga_2Cl_7]^-$ ions are represented as discrete double tetrahedra. Atoms are drawn by thermal ellipsoids scaled to include a probability of 70 %. On bottom left a detailed view of a section of the cationic chain is given, on bottom right the respective Lewis formula. Symmetry operations *I*: -x, 1-y, 1-z.

Only the Sb atom gains a hypervalency with four bonds, one lone pair, ten valence electrons and a negative formal charge. The Sb atom, however, may be positioned in all positions of the five-membered ring. All respective formulae reveal the charge +1 for the $SbTe_4$ cluster and none of the five isomers can be excluded at the outset. By X-ray diffraction, Sb and Te atoms are difficult to distinguish. The location of the Sb atom in the four-fold coordinated position was, however, supported by the lowest occupation factor of all five crystallographic independent positions when refined as occupied by tellurium (Fig. A 5.3.12)

In order to clarify the atom site distribution, all five conceivable isomers of the $(SbTe_4^+)_n$ cluster were calculated on hybrid DFT level. Full optimization of the atomic positions was performed for each of the resulting unit cells. The results for relative stabilities of the five isomers (Fig. 2.9.6.2), the Sb coordination number and the next-neighbor Sb-Te distances are given in Tab. 2.9.6.1.

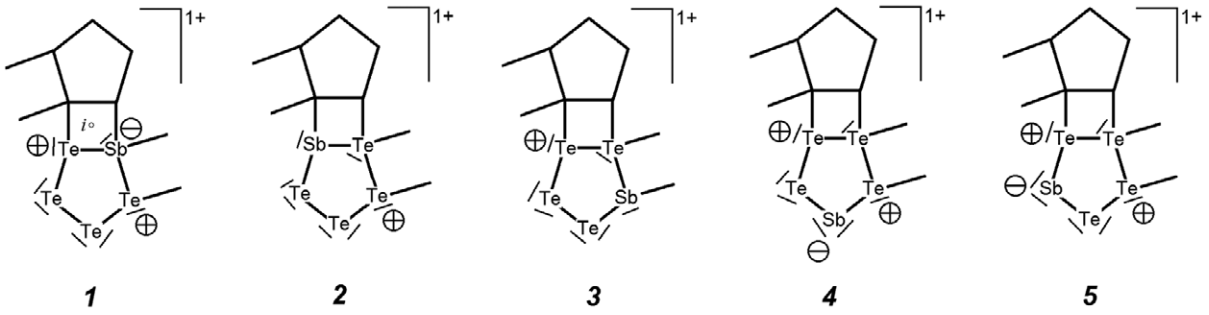

Fig. 2.9.6.2 Lewis formulae of the five conceivable isomers of $(SbTe_4^+)_n$. By X-ray diffraction and by periodical DFT calculations, **1** was determined as the most reliable isomer with Sb in the position with the highest coordination.

Tab. 2.9.6.1 Relative stability and nearest-neighbour Sb–Te distances / Å calculated with PW1PW. The numbering of the sites refers to Fig. 2.9.6.1.

Sb at position	Coordination number	Relative energy / kJ/mol	Calculated nearest neighbour distances / Å
Sb	4	0	2.83, 2.84, 3.05, 3.15
Te1	3	+26	2.76, 2.88, 2.91
Te2	2	+84	2.73, 2.73
Te3	2	+105	2.39, 3.22
Te4	3	+34	2.76, 2.87, 2.87

The energy minimum is clearly the isomer with Sb on the four-fold coordinated position. A direct correlation between the stability and the coordination number was found, the three-fold coordinated positions being 30 kJ/mol, and the two-fold coordinated positions even 80-100 kJ/mol less stable. Even though zero-point, vibration, and entropy effects have been neglected, these differences are large enough so that it is not expected that this affects the conclusions. The calculated Sb–Te bond lengths range between 2.8 and 3.0 Å, similar to the distances obtained from the crystal structure determination, except for the isomer with Sb on the Te3 site (image 4 in Fig. 2.9.6.2) where a very short (2.4 Å) and a rather long (3.2 Å) distance was obtained.
The analysis of the wavefunction based on a Mulliken population analysis led to an alternative explanation for the observed result. For all isomers, the atomic charge on Sb was very close to +1 while the Te atoms were almost neutral. Although atomic charges are no quantum-mechanical observables and results from any population analysis should be regarded with care, this qualitative result is not expected to be method or basis set dependent. It explains why Sb prefers four-fold coordinated sites since this is optimal for Sb^+ with four valence electrons. Since all Te atoms are neutral, they form two covalent bonds to their neighbor atoms, Te or Sb, and all other bonds are coordinative as in bulk Te.*

The attribution of the atoms Sb and Te to the atom sites in the polycation in $(Sb_2Te_2)[GaCl_4]$ was performed on basis of the diffraction data. Fig. A 5.3.12 shows the obtained occupation factors and the subsequent Sb/Te site assignments in the structure of $(SbTe_4)[Ga_2Cl_7]$. The analysis of the coordination of the Sb and Te atoms by Cl atoms of neighbouring anions does not lead to a distinction

* The theoretical calculations and the atom distribution analysis were performed by Prof. Dr. Thomas Bredow.

of Sb···Cl and Te-···Cl contacts since they are rather uniform with approximately 3.55 Å in all cases (Tab. A 5.5.13).

2.10 β-$(SbI_2)[AlI_4]$ - A New Polymorph of Diiodoantimony-Tetraiodidoaluminate

Some adducts of trihalides of groups 13 and 15 were explored at the beginning of the 1980s. In 1981 an 1:1 mixture of $SbCl_3$ and $AlCl_3$ yielded $(SbCl_2)[AlCl_4]$, consisting of $SbAlCl_6$ chains.[86] In 1983 the corresponding iodine congener $(SbI_2)[AlI_4]$ was isolated.[87] The structural feature is tetrameric four-core units $Al_2Sb_2I_{12}$. In the same year $(PI_4)[AlI_4]$ and $(P_2I_5)[AlI_4]$ were found and structurally characterized.[88] One of the characteristics of these iodophosphorous iodoaluminates are attractive iodine-iodine interactions due to differently polarized iodine ions. In 2001 the $(P_2I_5)^+$ cation was obtained as the isotypic gallium congener $(P_2I_5)[GaI_4]$.[89]
All of these adducts were prepared by dissolving the components pentelehalide and aluminium trihalide in CS_2 and crystallization by slow evaporation of the solvent according to Ref. [90].
In the following chapter, a new polymorph of $(SbI_2)[AlI_4]$ is demonstrated, which was synthesized in an aluminium triiodide melt.

2.10.1 Syntheses and EDX Analysis of β-$(SbI_2)[AlI_4]$

β-$(SbI_2)[AlI_4]$ was first found as a byproduct in the various syntheses of $(Sb_2Te_2)I[AlI_4]$ (chapter 2.9), which contained SbI_3 and AlI_3. It can be obtained directly by reacting a 1:1 mixture of SbI_3 and AlI_3 at 190 °C for 1 week in an yield of 100 %. β-$(SbI_2)[AlI_4]$ grows in yellow rod shaped crystals. The bulk material is orange coloured (Fig. 2.10.1.1).
Crystals of β-$(SbI_2)[AlI_4]$ are sensitive towards moisture. During slow decomposition after minutes in perfluorinted polyether they become first orange and powdery under gas elusion. At the end, only a black powder remains.

The reaction equation is:

$SbI_3 + AlI_3 \rightarrow (SbI_2)[AlI_4]$

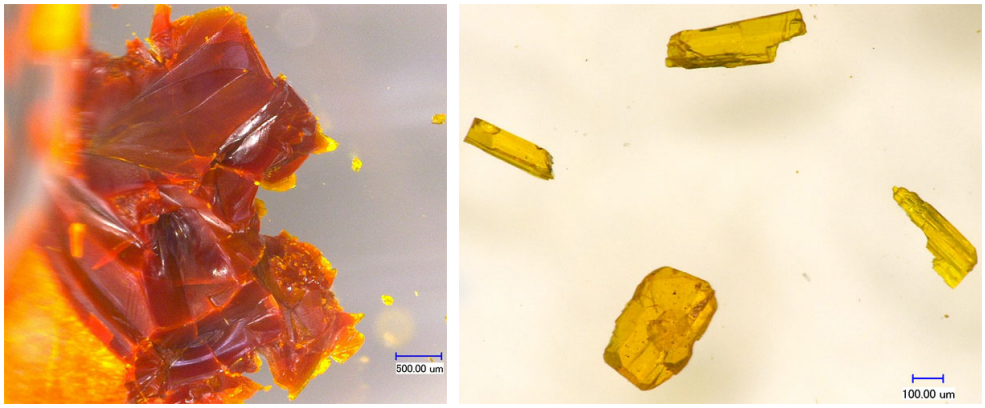

Fig. 2.10.1.1 Microscopic images of β-$(SbI_2)I[AlI_4]$ taken through the walls of the reaction ampoule (left) and of manually separated crystals immersed in perfluorinated polyether (right).

Compared with the calculated compostion of β-(SbI_2)[AlI_4], the values from the EDX analysis for Sb and Al are too high, the iodine content comes out as too low. A possible reason is the release of iodine during the analysis with the electron beam due to heating the sample.

Tab. 2.9.1.5 Elemental composition of β-(SbI_2)[AlI_4] in atom-% and the Sb : Te ratio. Standard deviations given in brackets refer to the last significant digit.

(SbI_2)[AlI_4]	Sb	Al	I
Found	19.3(3)	18.6(9)	61.9(7)
Calculated	12.5	12.5	75.0

2.10.2 Crystal Structure of β-(SbI_2)[AlI_4]

β-(SbI_2)[AlI_4] crystallizes in the space group $P2_1/n$. All atoms occupy general positions. The reaction leading to (SbI_2)[AlI_4] demonstrates the association of SbI_3 and AlI_3 to a structure consisting of $^1_\infty[SbI_{2/1}I_{2/2}AlI_{2/1}I_{2/2}]$ chains (Fig. 2.10.2.1). The Sb–I bond lengths fall into two groups. The Sb–I bond lengths to the terminal iodine atoms are 2.736(1) and 2.727(1) Å. The Sb–I bond lengths to the bridging iodine atoms are significant longer with 3.049(1) and 3.117(1) Å.

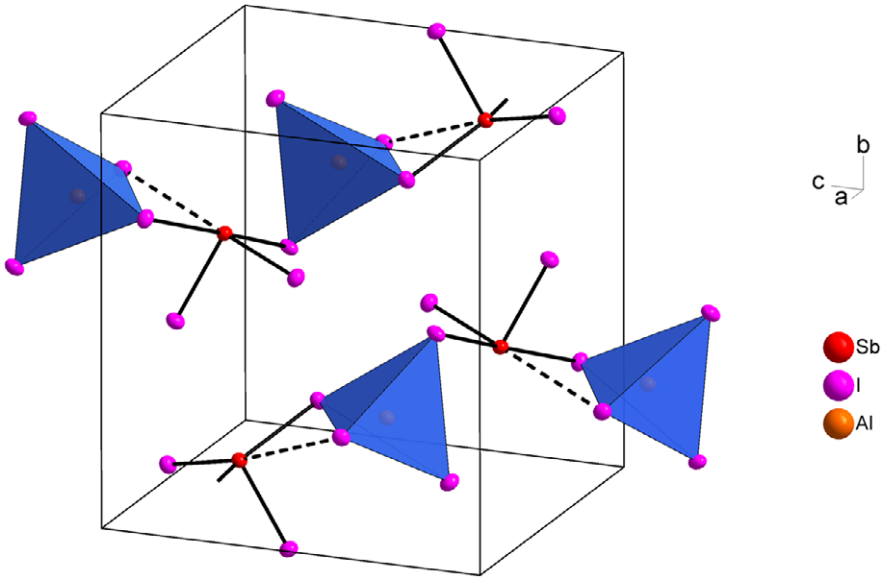

Fig. 2.10.2.1 The arrangement of the $^1_\infty[SbI_{2/1}I_{2/2}AlI_{2/1}I_{2/2}]$ - chains in the unit cell of the structure of (SbI_2)[AlI_4] at 100 K. The $[AlI_4]^-$ ions are represented by discrete tetrahedra. The SbI contact of 3.523(1) Å is shown with dashed lines. The atoms are represented by thermal ellipsoids scaled to include a probability of 70 %.

Comparable to SbI_3, Sb–I bond lengths in the range of 2.68(1) - 2.77(1) Å are observed, [91] which correspond to the shorter bonds in β-(SbI_2)[AlI_4]. Taking the long range Sb···I contacts between 3.540(1) and 3.880(1) Å in SbI_3 into account, antimony is in the center of a strongly distorted SbI_6 octahedron. The Al-I bond lengths in β-(SbI_2)[AlI_4] are rather uniform (Al–I3 2.583(1), Al–I4 2.580(1),

Al–I5 2.511(1), Al–I6 2.489(1) Å). The difference between the bond lengths to bridging (I3, I4) and terminal (I5, I6) iodine atoms is less than 0.1 Å.

The strand in β-(SbI_2)[AlI_4] is similar to the one found in ($SbCl_2$)[$AlCl_4$][86]. Considering Sb···Cl contacts of 3.716(1) and 3.863(1) Å, the Sb atom gets a strongly distorted octahedral coordination. In the structure of (SbI_2)[AlI_4] no corresponding interactions are found below 4 Å. A transformation of the structure of β-(SbI_2)[AlI_4] from $P2_1/n$ to $P2_1/c$ leads to the unit cell parameters α = 10.845(7) Å, β = 11.310(4) Å, γ = 14.800(1) Å and β = 133.00(1)°, which do not match those of ($SbCl_2$)[$AlCl_4$].

Fig. 2.10.2.2 shows a view along the strands in β-(SbI_2)[AlI_4].

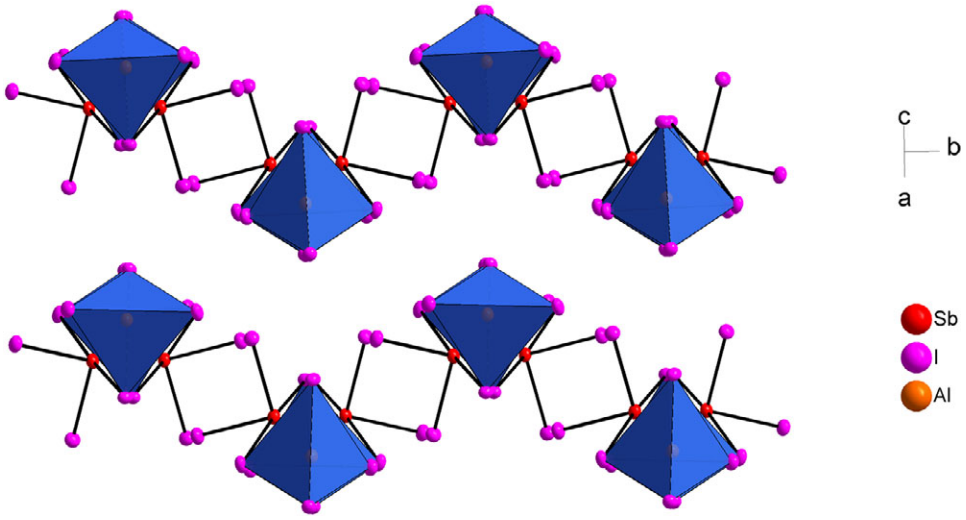

Fig. 2.10.2.2 The arrangement of the (SbI_2)[AlI_4] chains chains along the *ac* angle bisector. The $[AlI_4]^-$ ions are represented by discrete tetrahedra. The atoms are represented by thermal ellipsoids scaled to include a probability of 70 %.

2.10.3 Comparison of the Structures of α- and β-(SbI_2)[AlI_4]

A similar Sb coordination to this found in β-(SbI_2)[AlI_4], is present in the α-form of (SbI_2)[AlI_4][87], where two SbI_3 and two AlI_3 units form an adduct consisting of isolated four membered $[(SbI_2I_{2/2})(AlI_2I_{2/2})]_2$ units. Antimony is in the center of two differently distorted octahedra (Fig. 2.10.3.1).

The Sb–I bond lengths (2.708(2) Å × 2, two 3.123(2) Å × 2, 3.589(2) Å × 2) are in good agreement with those found in β-(SbI_2)[AlI_4]. The significant difference in the structure of β-(SbI_2)[AlI_4] compared to the α-form and SbI_3 is the presence of only one long range Sb···I contact of 3.523(1) Å (Sb···I5). The resulting unusual Sb polyhedron is a distorted square pyramide, which is connected alternatingly over edges and corners to the $[AlI_4]^-$ tetrahedra to form zig zag bands (Fig. 2.10.2.1).

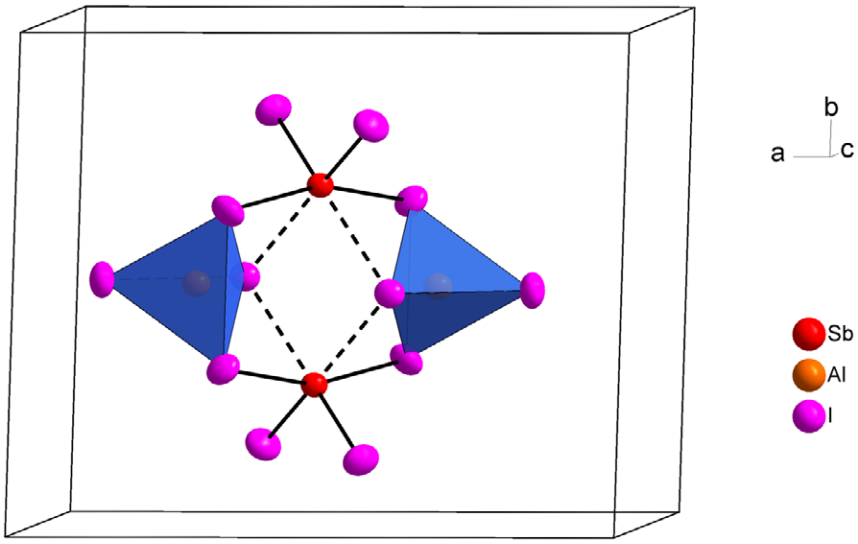

Fig. 2.10.3.1 The unit cell of α-(SbI_2)[AlI_4][87]. The four-membered units on the cell corners and the superposale in the *c*-direction are omitted for clarity. The SbI contact of 3.589(2) Å is shown with dashed lines. The $[AlI_4]^-$ ions are represented by discrete tetrahedra. The atoms are represented by thermal ellipsoids scaled to include a probability of 70 %.

2.10.4 Raman Spectroscopy Study of β-(SbI_2)[AlI_4]

The calculation of the Raman spectrum of discrete $(SbI_2)^+$ and $[AlI_4]^-$ ions in the gas phase approach showed partly slight deviations for the intensive signals found in the experimental spectrum. However, in the region below 100 and above 200 cm^{-1} the calculation was not accurate at all (Fig. 2.10.4.1). An attempt of the calculation of a discrete SbI_2AlI_4 molecule did not show any conformity with the experiment.*

Thus a solid state Raman spectrum of (SbI_2)[AlI_4] was calculated on hybrid DFT level. The Raman spectrum of β-(SbI_2)[AlI_4] shows two very strong signals at 180 and 184 cm^{-1} which are caused by antisymmetrical vibrations of Sb and a terminal I atom. A third signal of less than half the intensity at 148 cm^{-1} results from a symmetrical stretch vibration of the $[AlI_4]^-$ anions (compare Fig. 2.11.2.2 below). All other obtained signals are of low or vanishing low intensity. Generally, many signals came out of the calculation with extremely low intensities. The corresponding signals are not visible in the experimental spectrum. However, all experimental Raman bands (83, 87, 100, 107, 127, 147, 180, 184, 190, 303, 323, 383 cm^{-1}) are explained by the calculation (Fig. 2.10.4.2). The vibration modes of the corresponding calculated signals are depicted in Fig. A 5.7.15.**

The agreement of both spectra militates for a $(SbI_2AlI_4)_n$ polymer since the calculation of discrete $(SbI_2)^+$ and $[AlI_4]^-$ ions can not explain the Raman spectrum satisfactorily.

* The calculations were performed by Dr. Gregor Schnakenburg.
** The calculations were performed by Prof. Dr. Thomas Bredow.

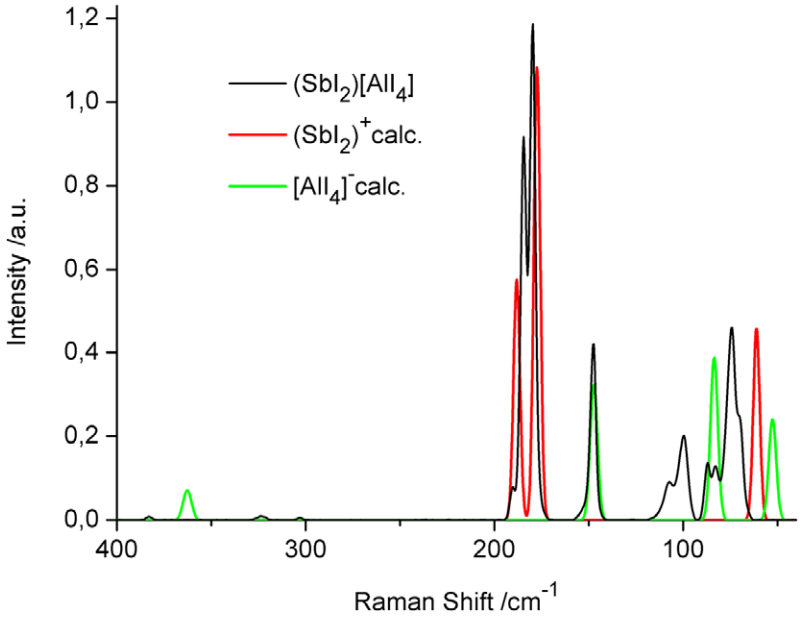

Fig. 2.10.4.1 Comparison between the experimental Raman spectrum of (SbI_2)[AlI_4] (laser energy 30 mW) (top) and the calculated spectrum (B3LYP/def2-TZVPP) of the individual $(SbI_2)^+$ and $[AlI_4]^-$ ions (bottom). The broad double signal between 64 and 80 cm^{-1} in the experimental spectrum is caused by the exciting laser.

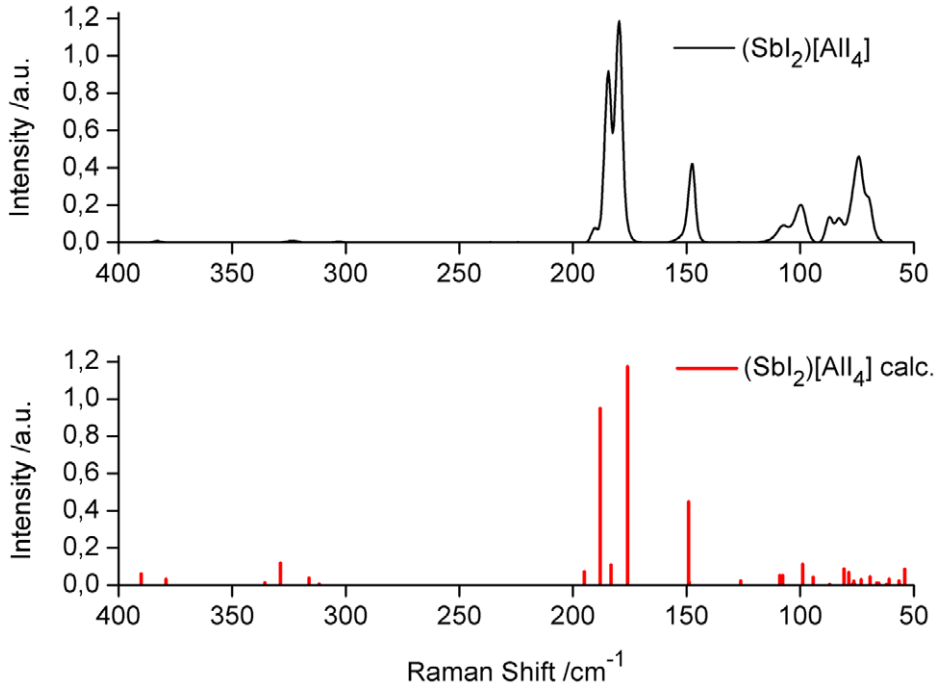

Fig. 2.10.4.2 Comparison between the experimental Raman spectrum of (SbI_2)[AlI_4] (laser energy 30 mW) (top) and the calculated spectrum (PW1PW) (bottom). The broad double signal between 64 and 80 cm^{-1} in the experimental spectrum of is caused by the exciting laser.

2.11 Structural and Raman Spectroscopic Characterization of $Cu[AlI_4]$

The class of copper aluminates and gallates is still rarely explored.
In 1980 $Cu[AlCl_4]_2$ was found to consist of discrete molecules with copper(II) in a square planar coordination.[92] The crystal structure of α-copper(I) tetrachloridoaluminate was first determined in 1982.[93] It consists of a polymeric network made of $CuCl_4$ and $AlCl_4$ tetrahedra. The metastable β-$Cu[AlCl_4]$ was found in 1997 and shows a slightly different stacking of the tetrahedral building blocks.[94] The structure of the isotypic bromine congener of the α-form was determined in 1994 by powder diffraction.[95] $Cu[GaCl_4]_2$ was found two years after its aluminate analogue in 1982 to crystallizes isotypically with discrete molecules as building blocks.[96] The corresponding copper(I) tetrachlorido gallate is likewise isotypic to its aluminate congener.[97]
The only established copper iodo aluminate or gallate is $Cu[GaI_4]$.[98] It shows a polymeric structure made of CuI_4 and GaI_4 tetrahedra with a different occupation of tetrahedral holes compared to $Cu[MCl_4]$ (M = Al, Ga).
In the following chapter the crystal structure and Raman spectrum of $Cu[AlI_4]$ are presented. The structure is related to the structure of $Cu[MCl_4]$ (M = Al, Ga) and $Cu[AlBr_4]$.

2.11.1 Synthesis and EDX Analysis of $Cu[AlI_4]$

$Cu[AlI_4]$

$Cu[AlI_4]$ was found as a byproduct in the synthesis of the polycationic cluster containing compound $(Sb_2Te_2)I[AlI_4]$. Besides antimony, tellurium and antimony triiodide, copper(I) iodide and aluminium iodide were present in the reaction melt. The ampoule was heated stepwise to 100 °C for 7 days, 170 °C for 5 days to finally keeping at 190 °C for 8 days. Cooling down to room temperature with 6°C/h yielded $(Sb_2Te_2)I[AlI_4]$ (chapter 2.9.1), $(SbI_2)[AlI_4]$ (chapter 2.10.1) and $Cu[AlI_4]$. $Cu[AlI_4]$ grows in dark red cube-shaped crystals (Fig. 2.11.1.1) and is highly air sensitive.

The reaction equation is:

$CuI + AlI_3 \rightarrow Cu[AlI_4]$

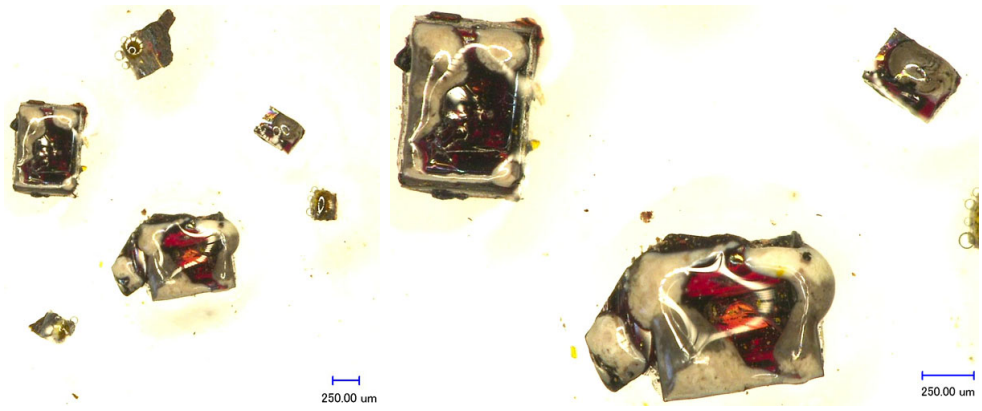

Fig. 2.11.1.1 Microscopic images of crystals of $Cu[AlI_4]$ immersed in perfluorinated polyether.

Like in the EDX analysis of β-$(SbI_2)[AlI_4]$ (Tab. 2.9.1.5), the EDX analysis reveals a too low iodine content. Consequently, the values for Cu and Al come out too high (Tab. 2.11.1.1). Apparently, iodine is released from the crystals in the vacuum chamber of the instrument during the irradiation with the electron beam.

Tab. 2.11.1.1 Elemental composition of $Cu[AlI_4]$ in atom-%. Standard deviations given in brackets refer to the last significant digit.

$Cu[AlI_4]$	Cu	Al	I
Found	25.9(7)	33(1)	40.6(8)
Calculated	16.7	16.7	66.7

2.11.2 Crystal Structure and Raman Spectrum of $Cu[AlI_4]$

$Cu[AlI_4]$ crystallizes in the space group $P\bar{4}2c$ as found for $Cu[MCl_4]$ (M = Al, Ga) and $Cu[AlBr_4]$, but it is not isotypic. All I atoms occupy general, Cu and Al special positions. The I atoms form a cubic close packing. $CuAlI_4$ and AlI_4 tetrahedra build a polymeric network. Al–I bonds are uniform (Al1–I1 2.545(1) Å, Al2–I2 2.547(1) Å, Al3–I3 2.543(2) Å, Al3–I4 2.457(1) Å), Cu–I bonds show slight differences (Cu1–I1 2.669(1) Å, Cu1–I3 2.602(1) Å, Cu2–I2 2.627(1) Å, Cu2–I4 2.630(1) Å).

Compared to the five known $Cu[MX_4]$ (M = Al, Ga; X = Cl, Br, I) phases, $Cu[AlI_4]$ also shows one quarter occupation of tetrahedral holes. The known phases show corner-sharing tetrahedra, exclusively. The packing in $Cu[AlI_4]$ leads to corner and edge connections of MI_4 tetrahedra. Due to these edge connections, Cu1 is shifted from the tetrahedron center because of repulsing interactions with Al1 from the neighbouring polyhedron (Fig. 2.11.2.1). The Cu1–Al1 distance of 3.227(1) Å is significant shorter than all other Cu–Al distances ranging between 4.056(2) and 4.205(1) Å. The resulting unit cell has an approximately 4-6 times bigger volume (1706.98(8) $Å^3$) compared to the known congeners of copper(I) aluminates and gallates (297-431 $Å^3$).

Two different tetrahedra connections and an irregular copper(I) coordination lead to a new structure type in the class of adducts of copper(I) halides and Group 13 trihalides.

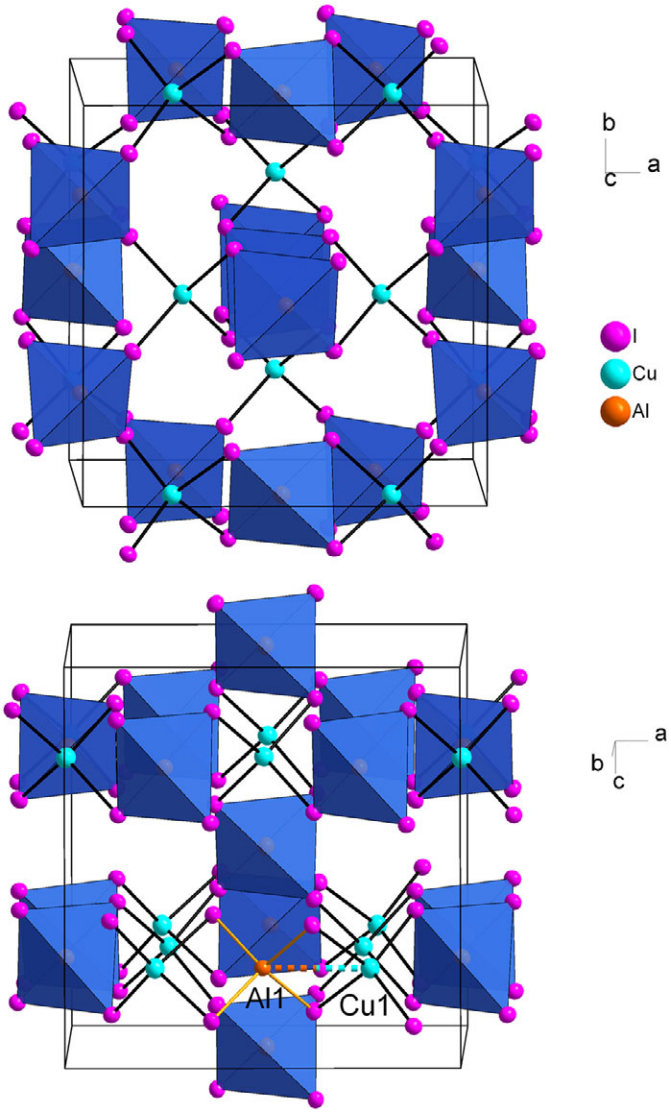

Fig. 2.11.2.1 The unit cell of the structure of Cu[AlI$_4$] at 123 K from two different points of view. The [AlI$_4$]$^-$ ions are represented by discrete tetrahedra. The atoms are represented by thermal ellipsoids scaled to include a probability of 70 %. The Al1-Cu1 repulsing interaction is shown with a dashed line.

The Raman spectrum of Cu[AlI$_4$] shows two clear signals at 104 (m) and 147 cm^{-1} (vs), which are in line with the Raman spectrum recorded for (P_2I_5)[AlI$_4$].[99] The strongest signal at 147 cm^{-1} can be identified as the symmetrical A_1 stretch vibration of the [AlI$_4$]$^-$ ion. The other Raman bands expected for the [AlI$_4$]$^-$ ion (51 cm^{-1} E, 82 cm^{-1} F_2, 336 cm^{-1} F_2) are not present in the spectrum.[100] A third signal is visible as a shoulder at 152 cm^{-1} (m), which can also be attributed to the [AlI$_4$]$^-$ ion due to splitting of the A_1 vibration of the tetrahedral anion. The CuI$_4$ tetrahedron does not cause a signal at this wavenumber [101] (Fig. 2.11.2.2).

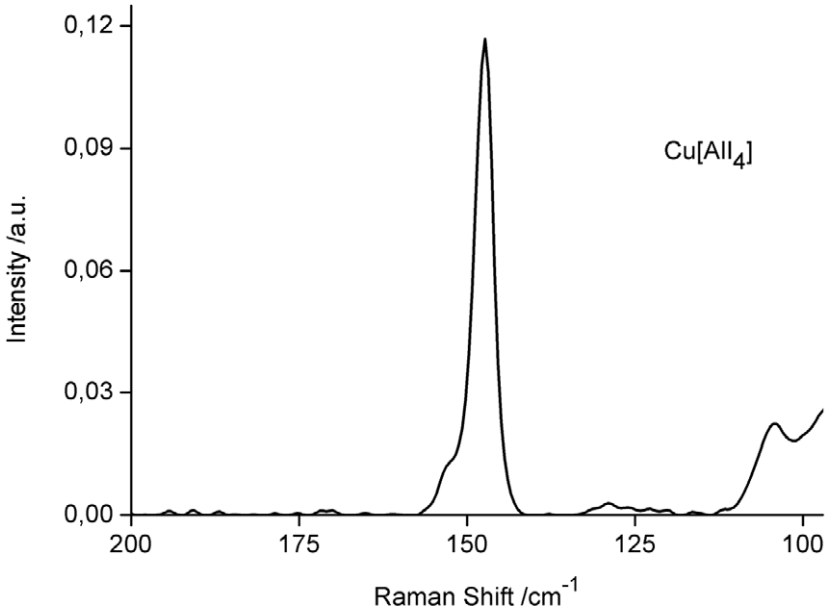

Fig. 2.11.2.2 The Raman spectrum of $Cu[AlI_4]$ (laser energy 25 mW, 512 scans).

2.12 $CuSe_4[GaCl_4]$, $CuTe_4[GaCl_4]$ and $Cu_2Se_7[GaCl_4]_2$ - A New Class of Compounds Containing Neutral Chalcogen Chains

The elements selenium and tellurium are known since 1924 to form one dimensional helical chains in their thermodynamic most stable trigonal forms.[102] Weak secondary interactions to the neighbour chains are present in distances of 3.43 and 3.49 Å.

A positively charged screw-shaped chain of Te atoms with similar conformation as found in the element is observed in the tellurium subchloride Te_3Cl_2. Every third Te atom carries two axial chlorine ligands which have influence on the twisting of the chain. In Te_2X (X = Cl, Br, I) more uniform zig zag chains are present and the halide anions bridge between two Te atoms, respectively.[103] Every second Te atom is three-fold coordinated by Te neighbours. Tellurium has a formal charge of +2/3 and +0.5 in these compounds. A charge of +1 is present for tellurium in α-TeI with an analogous conformation of the chains as in Te_2X. The coordination of iodide ions has bridging and terminal character. In contrast, in α-TeI four membered Te rings are present. [104] During synthetic work on tellurium subhalides the compound $(Te_2)_2(I_2)$ was isolated, which demonstrates an iodine incorporation into tellurium with resulting structural changes to $(Te)_2$ double layers.[105] From the element selenium, only the molecular subhalides Se_2X_2 (X = Cl, Br) are known. [106]

The class of copper(I)chalcogenidohalides was likewise explored and some of the representatives also show related chalcogen chains. In CuTeX [107] and $CuTe_2X$ [108] (X = Cl, Br, I) helical chains are present consisting of tellurium atoms with a formal oxidation state of zero. Besides the specific structural chalcogen motives, which correlate with the elements structures, these compounds show interesting copper(I) ionic conductance. The specific chalcogen screws can even be found in the mixed copper(I) chalcogen halides CuSeTeCl, CuSeTeBr and CuSeTeI [109] and their mixed sulphur congeners [110].

Analogous selenium helices are obtained in $CuSe_2X$ (X = Cl, Br) [111]. Increasing the chalcogen content in $CuSe_3Br$ and $CuSe_3I$ [112] or the corresponding mixed chalcogen congeners $CuSe_{2.36}S_{0.64}Br$, $CuSe_{2.6}S_{0.4}I$, and $CuSe_{1.93}Te_{1.07}I$ [113] leads to corrugated Se_6 rings as the structural feature.

In the following chapter three new representatives with the sum formulae $CuCh_4X$ (Ch = Se, Te) and $Cu_2Se_7X_2$ (X = $GaCl_4$) are presented, which contain chalcogen chains with different conformations and formally neutral chalcogen atoms. They are both isolated and bridged by copper(I) tetrachlorido gallate.

2.12.1 Syntheses and EDX Analyses of Compounds Containing Neutral Chalcogen Chains

$CuSe_4[GaCl_4]$

28.4 mg (0.36 mmol) selenium, 50.5 mg (0.24 mmol) bismuth, 37.8 mg (0.12 mmol) bismuth trichloride, 174.0 mg (0.99 mmol) gallium trichloride, 60.0 mg (0.16 mmol) tetraphenylphosphonium chloride and 24.2 (0.18 mmol) copper(II) chloride were filled in a glass ampoule and heated to 100 °C for 4 weeks. $CuSe_4[GaCl_4]$ forms orange transparent hexagonal rod shaped crystals in a liquid orange melt in an estimated yield of 50 % (Fig. 2.12.1.1).

$CuTe_4[GaCl_4]$

45.9 mg (0.36 mmol) tellurium, 29.2 mg (0.24 mmol) antimony, 27.4 mg (0.12 mmol) antimony trichloride, 174.0 mg (0.99 mmol) gallium trichloride, 60.0 mg (0.16 mmol) tetraphenylphosphonium chloride and 24.2 (0.18 mmol) copper(II) chloride were heated in a glass ampoule. After 1 week at 100 °C, a yield of about 50 % of silvery shiny rod shaped crystals were obtained in a black melt (Fig. 2.12.1.1). By exchanging antimony and antimony trichloride by the respective amounts of bismuth and bismuth trichloride or exchanging copper(II) chloride by copper(I) chloride the same compound is obtained in lower yield. $(Sb_2Te_4)[GaCl_4]_2$ (chapter 2.7) is obtained as a byproduct in comparable yield.

Tentative reaction equations with the assumption of the pentele element as the reductant are:

$12\ Se + Bi + 3\ GaCl_3 + 3\ CuCl_2 \rightarrow 3\ CuSe_4[GaCl_4] + BiCl_3$
$12\ Te + Sb + 3\ GaCl_3 + 3\ CuCl_2 \rightarrow 3\ CuTe_4[GaCl_4] + SbCl_3$

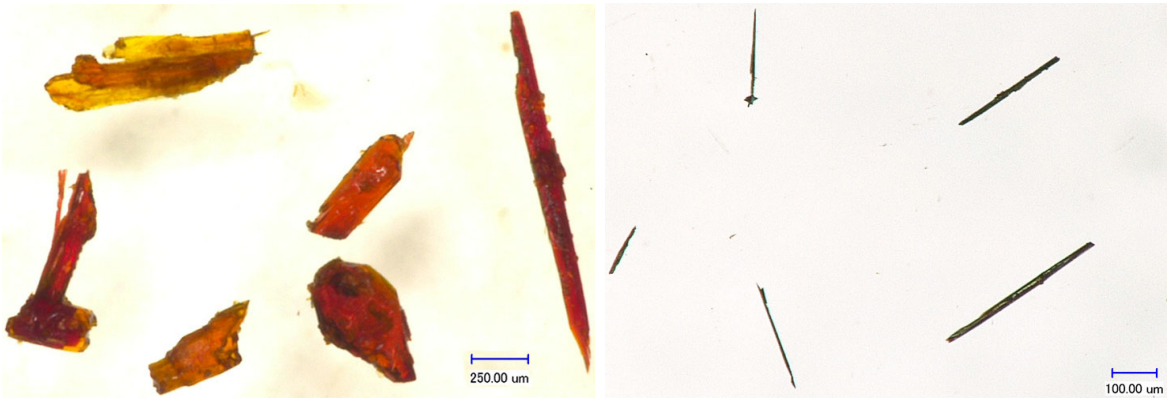

Fig. 2.12.1.1 Crystals of $CuSe_4[GaCl_4]$ (left) and $CuTe_4[GaCl_4]$ (right) immersed in perfluorinated polyether.

Due to an excess of $GaCl_3$ on the crystals surfaces from the synthetic procedures the obtained values for gallium and chlorine came out too high for all substances. Depending on the actual position of the electron beam on the crystal surface the amount of adherences varied, which led to high standard

deviations in general. However, the Ch : Cu ratio is close to the calculated composition. No traces of the pentele elements were found in the analyses, which are required for syntheses.

Tab. 2.12.1.1 Elemental composition of $CuSe_4[GaCl_4]$ and $CuTe_4[GaCl_4]$ in atom-%. Standard deviations given in brackets refer to the last significant digit.

	Ch	Cu	Ga	Cl	Ch : Cu
$CuSe_4[GaCl_4]$	36.5(6)	8.5(3)	13.8(4)	41.0(7)	4.29 : 1
$CuTe_4[GaCl_4]$	31(1)	8.3(4)	18.0(8)	45.5(8)	3.72 : 1
Calculated	40	10	10	40	4 : 1

$Cu_2Se_7[GaCl_4]_2$

28.4 mg (0.36 mmol) selenium, 29.2 mg (0.24 mmol) antimony, 27.4 mg (0.12 mmol) antimony trichloride, 174.0 mg (0.99 mmol) gallium trichloride, 60.0 mg (0.16 mmol) tetraphenylphosphonium chloride and 24.2 mg (0.18 mmol) copper(II) chloride were filled in a glass ampoule and heated to 100 °C for 4 weeks. $Cu_2Se_7[GaCl_4]_2$ forms orange transparent crystals in a liquid orange melt with very low yield.

A much higher yield of about 40 % and bigger crystals can be obtained by replacing antimony, antimony trichloride and copper(II) chloride by the respective amounts of bismuth, bismuth trichloride and copper(I) chloride. $Cu_2Se_7[GaCl_4]_2$ is obtained as orange transparent hexagonal rod shaped crystals (Fig. 2.12.1.2). As a byproduct, yellow crystals of $(Bi_4Se_4)[GaCl_4]_4$, the gallium congener of $(Bi_4Se_4)[AlCl_4]_4$[30], could be identified by unit cell determinations. The exchange of selenium by the respective amount of sulphur in this synthesis leads to $(Bi_4S_4)[GaCl_4]_4$, the gallium congener of $(Bi_4Se_4)[AlCl_4]_4$[30].

A tentative reaction equation of the experiment with copper(I) chloride is:

$$7\ Se + 2\ GaCl_3 + 2\ CuCl \rightarrow Cu_2Se_7[GaCl_4]_2$$

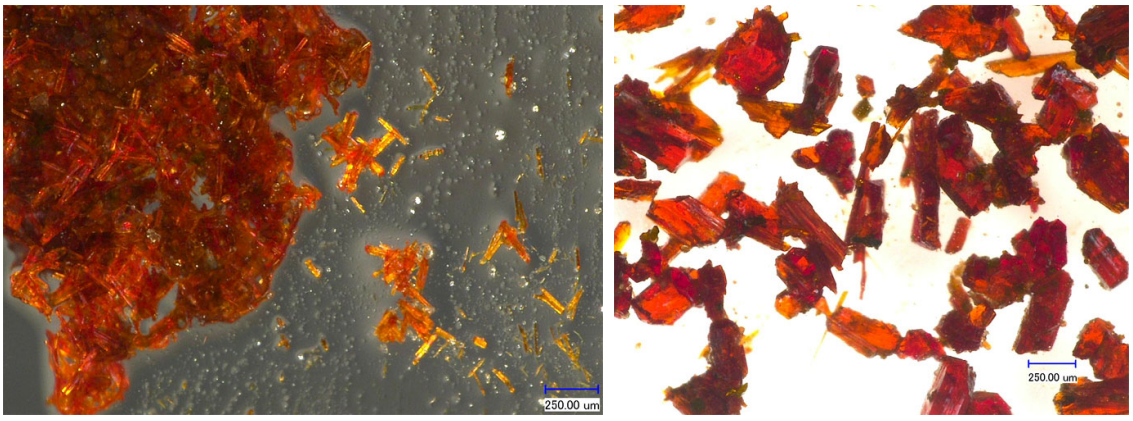

Fig. 2.12.1.2 Crystals of $Cu_2Se_7[GaCl_4]_2$ from two different ampoules and different ticknesses immersed in perfluorinated polyether (left: cumulated crystals for the Raman measurement).

Like in the analyses of $CuSe_4[GaCl_4]$ and $CuTe_4[GaCl_4]$ an excess of $GaCl_3$ on the crystals surfaces hampered the exact analysis of the compound. The values obtained for Se and Cu are too low due to

high values for Ga and Cl. Despite, the Se : Cu ratio is in very good agreement with the calculated composition.

Tab. 2.12.1.2 Elemental composition of $Cu_2Se_7[GaCl_4]_2$ in atom-%. Standard deviations given in brackets refer to the last significant digit.

$Cu_2Se_7[GaCl_4]_2$	Se	Cu	Ga	Cl	Se : Cu
Found	26(3)	7.4(8)	16(1)	49(3)	1 : 3.51
Calculated	37	11	11	42	1 : 3.5

All three examined compounds were prepared in ampoules which contained $PPh_4[GaCl_4]$. The presence of melt adherences on the crystals surfaces can be prooved in such cases by the presence of the additional phosphorous *K* emission line in the EDX spectrum. Figure 2.12.1.3 shows an EDX spectrum of $CuTe_4[GaCl_4]$ as an example for adherences of $PPh_4[GaCl_4]$. The phosphorus content during several measurements of crystals varied between 1 and 5 atom-%. For one atom-% phosphorus, one atom-% of $[GaCl_4]$ has to be considered, which falsifies the EDX result. However, the Ch:Cu ratio is in fair agreement with the expected ratio in all cases.

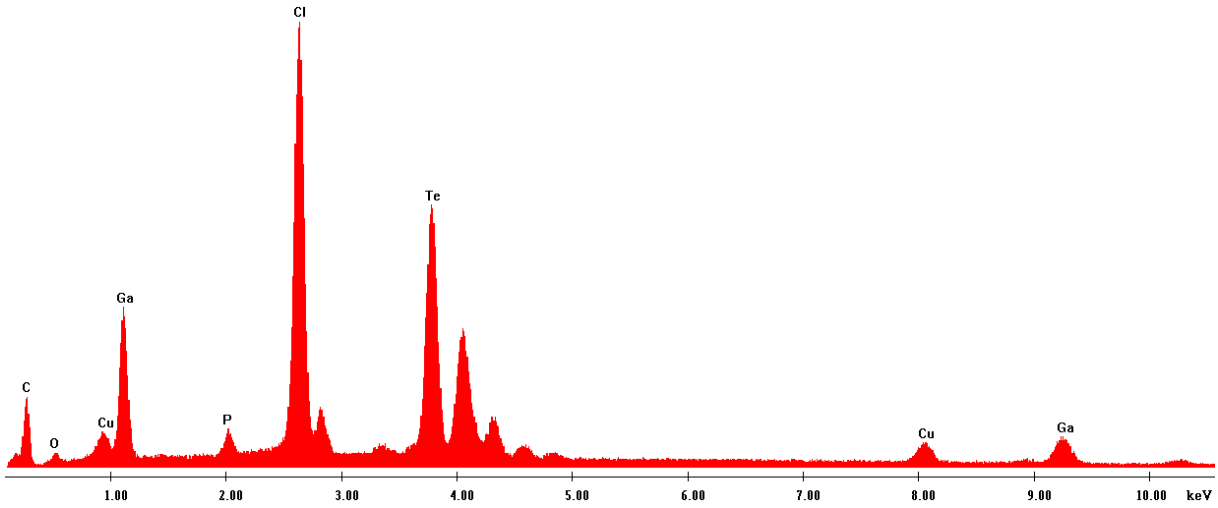

Fig. 2.12.1.3 EDX spectrum of $CuTe_4[GaCl_4]$. All signals are labeled. At 2 keV the P-*K* emission line is found.

2.12.2 The Reactions Leading to Compounds Containing Neutral Calcogen Chains

The primary intention of the preparative work was to synthesize mixed pentele-chalcogen polycationic clusters. CuCl and $CuCl_2$ should take the role of adjuvants without being incorporated in the final products. The reasons for expanding the single positively charged adjuvants to Cu(II) were the plenty successful syntheses with Cu(I) (chapter 2.1, 2.2, 2.5, 2.9, 2.16).

The addition of PPh_4Cl to the $GaCl_3$ based melt forming $PPh_4[GaCl_4]$ as a solvent keeps the melts relatively liquid which facilitates the separation of crystals.

All reactions can only be performend in the presence of the pentele trichlorides $SbCl_3$ or $BiCl_3$. Reactions without these compounds did not succeed in crystalline products. Even the elemental pentele elements are required to obtain the desired compounds. In the synthesis of $CuTe_4[GaCl_4]$ both

antimony or bismuth with the respective trichloride lead to the same product. Even the exchange of copper(II) by copper(I) yields $CuTe_4[GaCl_4]$.

The exchange of bismuth and bismuth trichloride by antimony and antimony trichloride in the synthesis of $CuSe_4[GaCl_4]$ results in the formation of $Cu_2Se_7[GaCl_4]_2$. Applying this synthesis, $Cu_2Se_7[GaCl_4]_2$ can only be found in traces without a specific crystal shape together with a large amount of crystalline copper chloridogallates which turned out in an EDX analysis. Using the educt composition of Bi, Te, $BiCl_3$, CuCl, PPh_4Cl and $GaCl_3$, $Cu_2Se_7[GaCl_4]_2$ is obtaind in high yield and bigger crystals.

In all syntheses Cu(II) is reduced to Cu(I) presumably by the pentele elements. $CuTe_4[GaCl_4]$ and $Cu_2Se_7[GaCl_4]_2$ can be obtained additionally from mixtures containing originally Cu(I).

Crystals of all compounds are sensitive towards moisture. They were obtained from melts mainly composed of gallium trichloride. Covered by perfluorinated polyether the selenium containing compounds were stable for a few days in normal atmosphere. The selenium containing compounds show the same colour and crystal shape and fan out on pressure to orange fibers.

The reaction of As, S, $AsCl_3$, $GaCl_3$, $CuCl_2$ and PPh_4Cl at 100 °C yields bright yellow, octahedral shaped crystals of a yet not fully characterized compound.

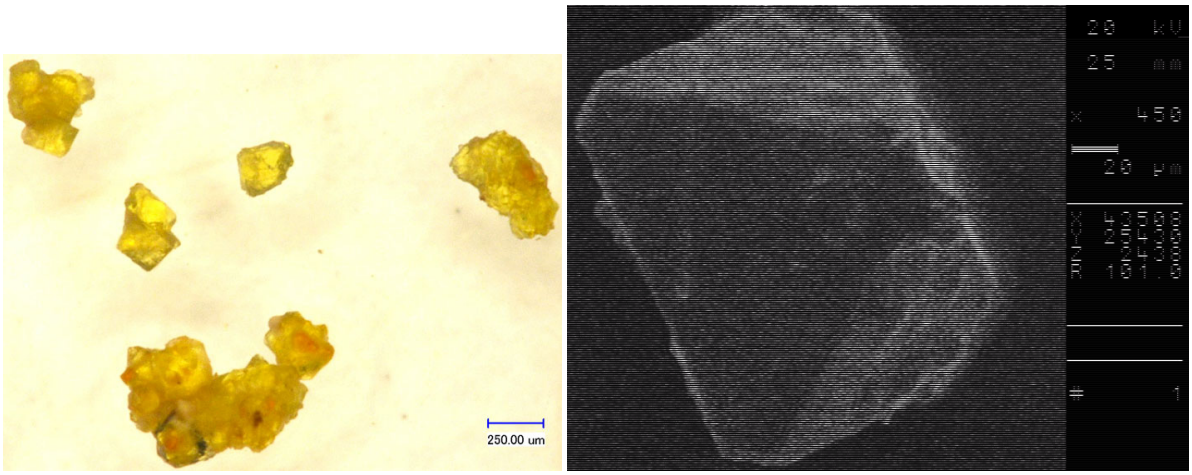

Fig. 2.12.2.1 Adnated crystals of the arsenic-sulphur containing compound immersed in perfluorinated polyether (left). On the right an individual crystal is shown on an scanning electron microscope image.

The structure refinement leads to ring molecules with incorporated $CuGaCl_4$ units with isolating and bridging character. Additionally unknown clusters are incorporated in the voids of the structure. Unfortunately the refinement did not lead to satisfying results due to twinning problems and/or an unresolved disorder. Additionally, the element distribution of As, Ga and Cu is not clear. The only ensured parts of the structure are $[GaCl_4]^-$ and $[Ga_2Cl_7]^-$ anions and the already mentioned $CuGaCl_4$ units.

In the EDX analysis the crystal from Fig. 2.12.2.1 and further, clean fragments of a broken crystal were examined. The partly overlap of the S-*L* and Au-*M* as well as the As-*L* and Ga-*L* X-ray emission lines have an estimated small falsifying influence on the result. The analysis indicates the sum formula $As_3CuCl_8Ga_2S_5$ (15.7(4) % As, Cu, 11.9(4) %, 40(1) % Cl, 4.9(3) % Ga, 26.7(5) % S). A Raman spectrum was recorded but it could not give more insight in the structure. Thus the compound will not be further discussed in this work.

2.12.3 Crystal Structures of $CuSe_4[GaCl_4]$, $CuTe_4[GaCl_4]$ and $Cu_2Se_7[GaCl_4]_2$

The crystallographic data are shown in Tabs. A 5.2.18 and A 5.2.19 in the appendix.
The crystal structures of $CuSe_4[GaCl_4]$ and $CuTe_4[GaCl_4]$ are isotypic. They consist of helical chalcogen chains and copper(I) chloridogallate units (Fig. 2.12.3.1). All atoms occupy general positions. The chalcogen atoms are two-fold bound to neighbouring chalcogen atoms and formally neutral.

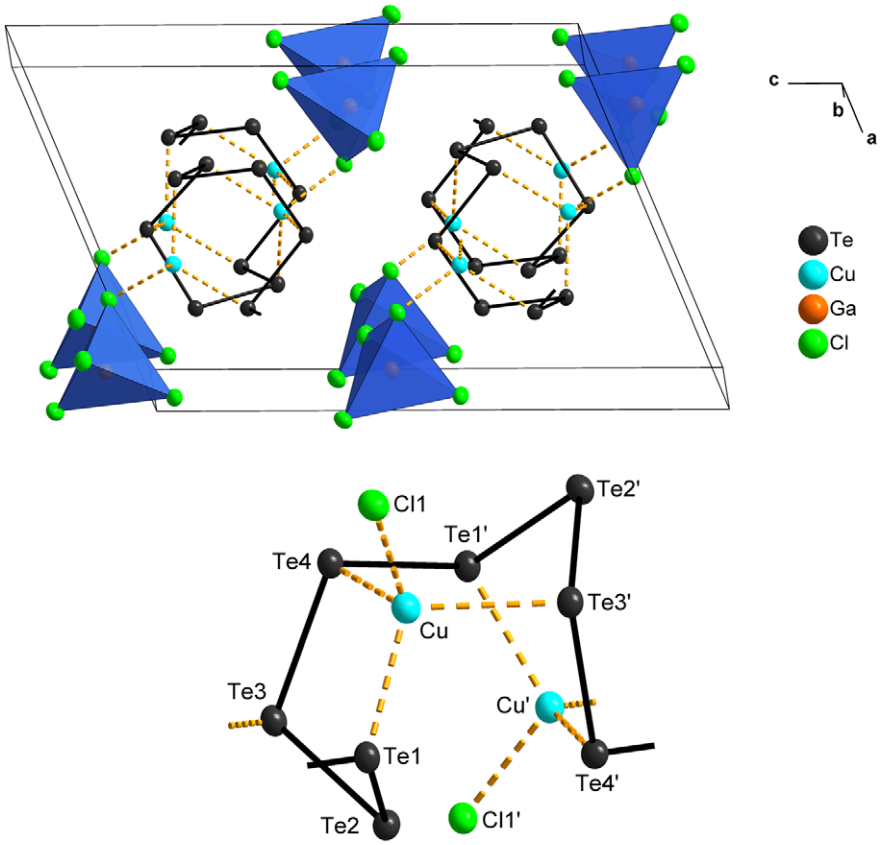

Fig. 2.12.3.1 The unit cell of the structure of $CuTe_4[GaCl_4]$ (top) and a section of the individual tellurium chain (bottom). The $[GaCl_4]$ units are represented by discrete tetrahedra. The atoms are represented by thermal ellipsoids scaled to include a probability of 70 %. Symmetry operations *I*: 1-x, -0.5+y, 0.5-z.

Se–Se bonds range between 2.3225(4) and 2.4321(4) Å. The respective Te–Te bond lengths are 2.7070(6) - 2.8444(6) Å (Tab. A 5.4.16). The bond angles along the chalcogen chains amount to 97.24(1) - 103.34(1)° in $CuSe_4[GaCl_4]$ and 91.78(2) - 100.07(2)° in $CuTe_4[GaCl_4]$. The chalcogen atoms 1, 3 and 4 are additionally coordinated to a $Cu[GaCl_4]$ unit in an average distance of 2.44 Å in $CuSe_4[GaCl_4]$. and 2.58 Å in $CuTe_4[GaCl_4]$. The $[GaCl_4]^-$ anions are bound to copper(I) in a distance of 2.3354(6) Å in $CuSe_4[GaCl_4]$. In the structure of $CuTe_4[GaCl_4]$ this bond is elongated to 2.432(2) Å. Here, neutral units isolate the chalcogen chains from each other due to repulsing interactions between the chlorine atoms of neighbouring chains. The bond lengths and angles within the $[GaCl_4]^-$ anions correspond to those found in $K[GaCl_4]$[50] and $K[Ga_2Cl_7]$[51].

The chains present in $Ch_4Cu[GaCl_4]$ can be regarded as five-membered $CuSe_4$ rings strung along the crystallographic *b* direction and alternatingly rotated by 180°. The conformation of these rings is for example similar to the $SbTe_4$ rings found in the cationic chains of $(SbTe_4)[Ga_2Cl_7]$ (chapter 2.9) or the $CuTe_5$ rings in CuTeI[107] and $CuTe_2Cl$[108]. Cu occupies the centre of a slightly distorted $CuTe_3Cl$ tetrahedron with angles between 105.08(4) and 114.42(3)°.

The conformation of the selenium chain in $Cu_2Se_7[GaCl_4]_2$ differs from the one found in $CuSe_4[GaCl_4]$. It can be described as a helical chain. All selenium atoms are two-fold coordinated by selenium neighbours in distances of 2.3210(8) - 2.3983(8) Å. The bond angles along the chain are rather uniform and range between 100.10(3) and 101.81(4)°. The structure motive of the chain is seven membered Cu_2Se_5 bicycluses consisting of aggregated $CuSe_4$ rings as present in $CuSe_4[GaCl_4]$. These bicycluses are connected by a Se–Se' bridge, which contains the inversion center (Fig. 2.12.3.2).

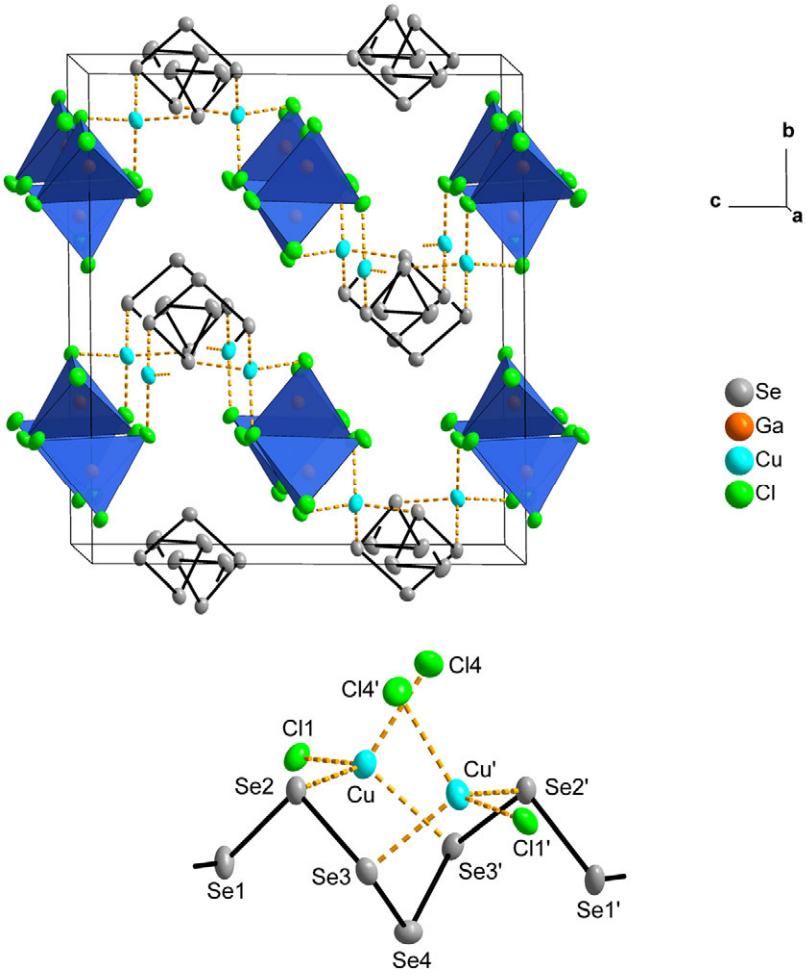

Fig. 2.12.3.2 The unit cell of the structure of $Cu_2Se_7[GaCl_4]_2$ (top), the layer structure (middle) and the individual selenium chain (bottom). The $[GaCl_4]$ units are represented by discrete tetrahedra. The atoms are represented by thermal ellipsoids scaled to include a probability of 70 %. Symmetry operations *I*: 1-x, y, 0.5-z.

In the structure of $Cu_2Se_7[GaCl_4]_2$ two $Cu[GaCl_4]$ units coordinate to two Se atoms of a Se_7 fragment. Se–Cu bond lenghts are insignificantly shorter with 2.399(1) and 2.4091(9) Å (Tab. A 5.4.17). In contrast to the isolating character of the $CuGaCl_4$ units in $CuSe_4[GaCl_4]$ and $CuTe_4[GaCl_4]$, they bridge between the selenium chains in $Cu_2Se_7[GaCl_4]_2$ and build a corrugated layer structure in the *a*-*c* plane

(Fig. 2.12.3.2). Thus two slightly elongated Ga–Cl bonds (Ga–Cl1 2.229(2) Å, Ga–Cl4 2.106(2) Å) are present to the bridging Cl atoms.

The structural feature of all compounds is isolated chalcogen chains. There are no secondary interactions with the neighbour strands. The selenium compounds emerge as orange transparent thick crystals in contast to the known copper(I) selenium halides CuSeBr and $CuSe_2Br$, which are black and needle shaped.

2.12.4 Raman and EPR Examination of $CuSe_4[GaCl_4]$, $CuTe_4[GaCl_4]$ and $Cu_2Se_7[GaCl_4]_2$

$CuSe_4[GaCl_4]$ and $Cu_2Se_7[GaCl_4]_2$ crystallize as orange crystals and were examined by Raman spectroscopy. $CuSe_4[GaCl_4]$ gave no Raman signals, only noise could be detected. $Cu_2Se_7[GaCl_4]_2$ gave only one very weak Raman band at 238 cm^{-1} in repeated measurements (Fig. 2.12.4.1). For comparison, elemental selenium shows Raman signals at 144 (w), 235 (vs) and 237 cm^{-1} (vs). The typical signal at 345 cm^{-1} for the $[GaCl_4]^-$ anions [113] is not observed in the spectrum of $Cu_2Se_7[GaCl_4]_2$.

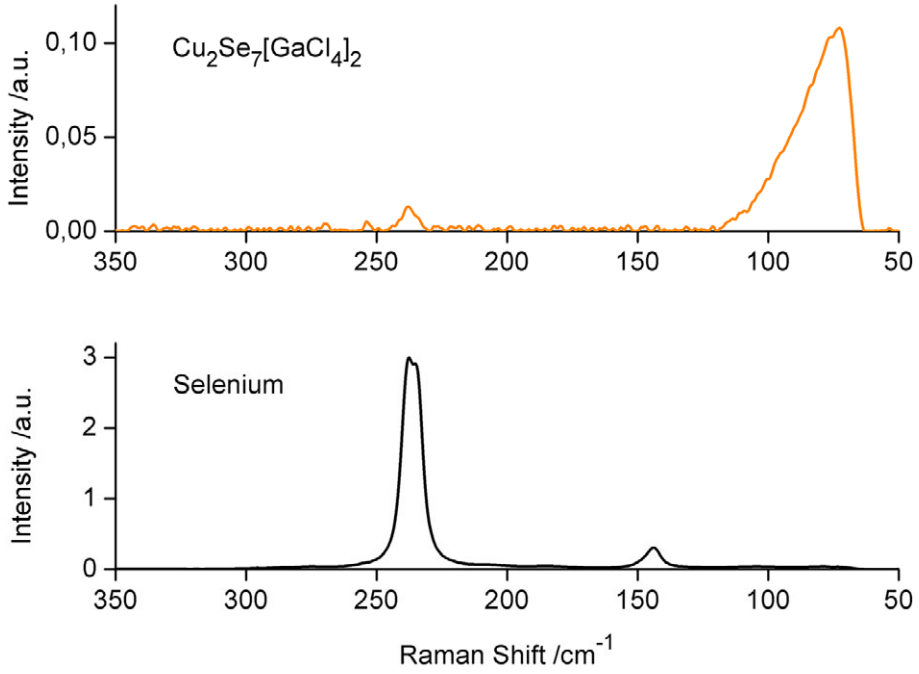

Fig. 2.12.4.1 Comparison between the spectrum of elemental selenium (laser energy 30 mW) and $Cu_2Se_7[GaCl_4]_2$ (laser energy 80 mW). The broad signal between 60 and 170 cm^{-1} in the spectrum of $Cu_2Se_7[GaCl_4]_2$ is caused by the exciting laser.

EPR analyses of all compounds confirm the presence of copper(I). Figs. 2.12.4.2 - 2.12.4.4 show the EPR spectra of all examined compounds and reference spectra of CuCl, $CuCl_2$, $Cu[GaCl_4]$ and $Cu[GaCl_4]_2$ at low temperatures. $Cu[GaCl_4]$ and $Cu[GaCl_4]_2$ were synthesized by reacting CuCl and $CuCl_2$ with the respective amounts of $GaCl_3$ in sealed glass ampoules at temperatures of 100 and 120 °C. After approximately one week colourless crystals of $Cu[GaCl_4]$ and yellow crystals of $Cu[GaCl_4]_2$ were obtained. The compounds were confirmed by unit cell determinations.

In general, the chalcogen containing compounds are EPR silent. At about 3300 G a similar pattern with extremely low intensity like the spectrum of Cu(II) can be intuited, which is explained by minimal Cu(II) adherences at the crystal surface since copper(II) chloride was used for syntheses.

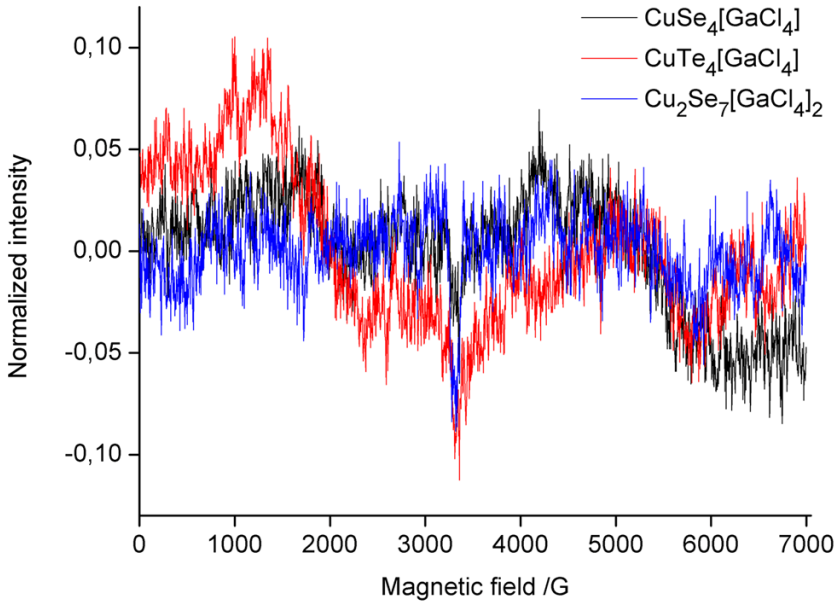

Fig. 2.12.4.2 Continuous wave X-band EPR spectra of crystals of $CuSe_4[GaCl_4]$ (black) and $CuTe_4[GaCl_4]$ (red) at 16 K and $Cu_2Se_7[GaCl_4]_2$ (blue) at 20 K. The spectra of $CuSe_4[GaCl_4]$ and $CuTe_4[GaCl_4]$ were recorded with 2 mM microwave power and 2 G modulation amplitude, the spectrum of $Cu_2Se_7[GaCl_4]_2$ with 20 mW microwave power and 5 G modulation amplitude.

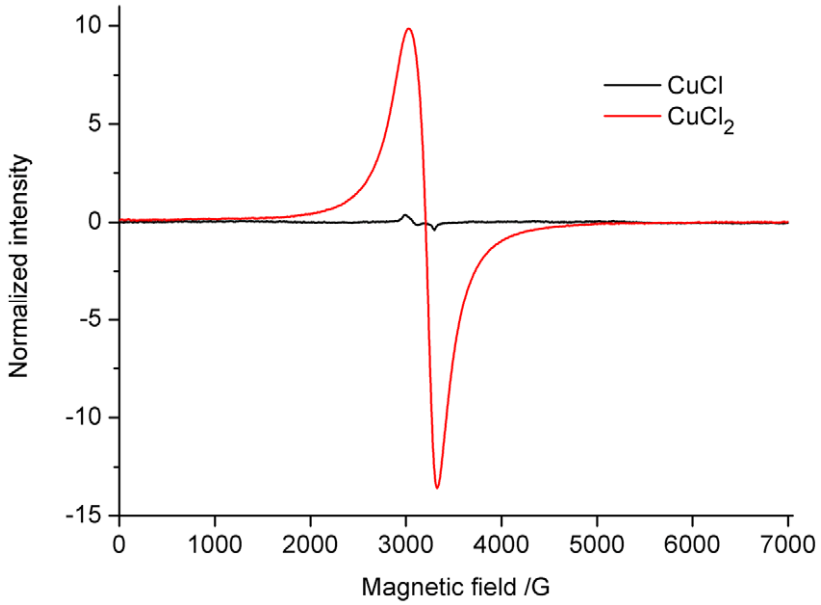

Fig. 2.12.4.3 Continuous wave X-band EPR spectra of crystals of CuCl (black line) and $CuCl_2$ (red line) at 16 K. Both spectra were recorded with 2 mW microwave power and 2 G modulation amplitude.

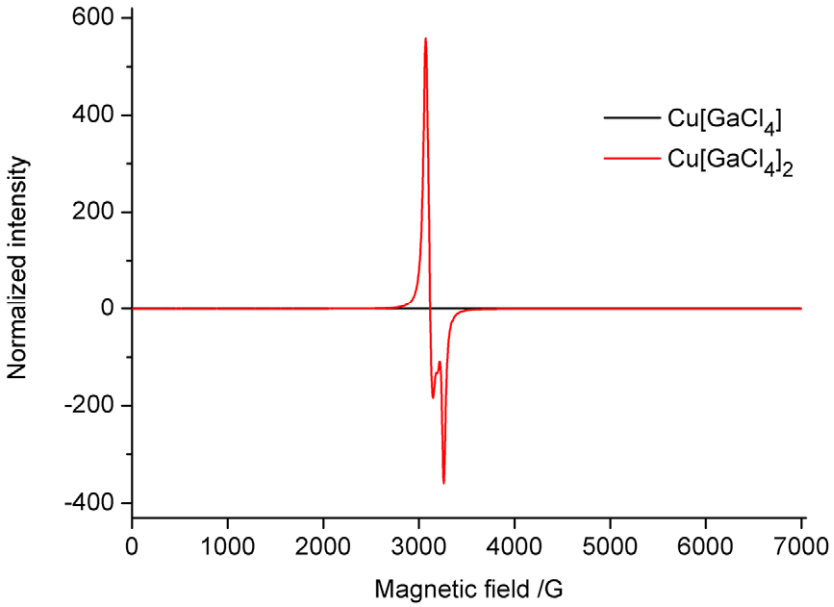

Fig. 2.12.4.4 Continuous wave X-band EPR spectra of crystals of $Cu[GaCl_4]$ (black line) and $Cu[GaCl_4]_2$ (red line) at 16 K. Both spectra were recorded with 2 mW microwave power and 2 G modulation amplitude.

The EPR silence is in line with the magnetic examination of $CuTe_4[GaCl_4]$ and $Cu_2Se_7[GaCl_4]_2$. Both compounds revealed diamagnetic response.

2.13 The Square Planar Cluster Te_4^{2+} and the Novel Anion $[Ga_2Cl_6O]^{2-}$ in $Te_4[Ga_2Cl_6O]$

The structural investigation of polycationic clusters began in 1972. The best known and first structurally characterized polycationic tellurium cluster was the homonuclear Te_4^{2+} in the chloridoaluminate salts $Te_4[AlCl_4]_2$ and $Te_4[Al_2Cl_7]_2$.[114] This square planar cation was found several times during the search for polycationic clusters with various anions like $[Bi_6Cl_{20}]^{2-}$, $[Bi_2Br_8]^{2-}$[115], $[Ga_2Cl_7]^{-}$[116] and $[Ga_2Br_7]^{-}$[117]. This variety of anions was enriched by the polymeric $(Te_4^{2+})_n$ in $(Te_4)(Te_{10})[Bi_4Cl_{16}]$[46] and the mixed tellurium-selenium congeners $(Te_2Se_2)^{2+}$ and $(Te_3Se)^{2+}$, which were isolated as slighly distorted, disordered, square clusters as the respective fluorido antimonate salts [118].

In the following chapter a new compound bearing Te_4^{2+} with the novel anion $[Ga_2Cl_6O]^{2-}$, an oxygen bridged chloridodigallate anion is presented.

2.13.1 Syntheses of $Te_4[Ga_2Cl_6O]$

45.2 mg (0.36 mmol) tellurium, 29.2 mg (0.24 mmol) antimony, 27.4 mg (0.12 mmol) antimony trichloride, 174.3 mg (0.99 mmol) gallium trichloride and 68.2 mg (0.18 mmol) tetraphenylphosphonium chloride were filled in glass ampoule, which was evacuated and sealed. PPh_4Cl was not dried for this experiment but taken as present in stock. On annealing at 88 °C, crystals appeared within 26 days in form of dark violet, plate shaped crystals in a black melt.

The origin of the incorporated oxygen was presumably water from PPh_4Cl. Only a few crystals were found on the glass wall of the ampoule outside the reaction melt. Attempts of reproduction led to dark violett coloured precipitates but no crystals could be obtained. Additionally crystals of $Te_4[Ga_2Cl_6O]$ occur as a byproduct in the synthesis of $(Sb_2Te_4)[Ga_2Cl_6O]_2$ ($P2_1/n$ polymorph) containing Sb_2O_5 (chapter 2.14) in higher yield.

2.13.2 Crystal Structure of $Te_4[Ga_2Cl_6O]$

The crystal structure of $Te_4[Ga_2Cl_6O]$ is build of Te_4^{2+} cations and $[Ga_2Cl_6O]^{2-}$ anions. The cations are aligned along [01-1] and tilted towards each other (Fig. 2.13.2.1). The crystallographic data are shown in Tab. A 5.2.20 in the appendix.

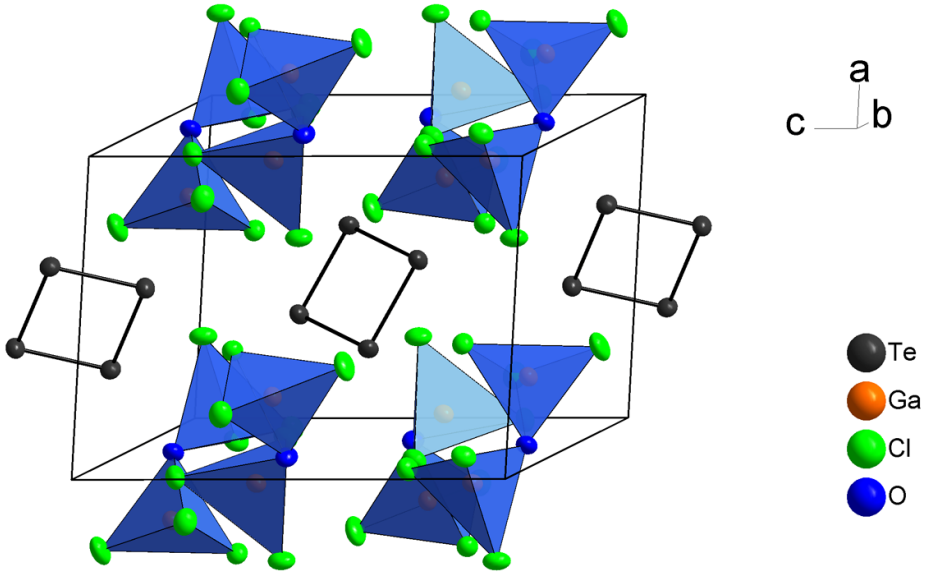

Fig. 2.13.2.1 The unit cell of the structure of $Te_4[Ga_2Cl_6O]$. The $[Ga_2Cl_6O]^{2-}$ anions are represented by discrete double tetrahedra. The atoms are represented by thermal ellipsoids scaled to include a probability of 70 %.

Te–Te bond lengths are 2.6827(5) and 2.6858(5) Å and are line with the bond lengths for Te_4^{2+} found in the halogenido aluminates, bismutates and gallates [114-117]. Te-Te-Te angles of 90.20(2) and 89.80(2) show almost ideal rectangularity of the cluster. the secondary Te···Cl interactions between the clusters and the surrounding $[Ga_2Cl_6O]^{2-}$ anions are in a broad range between 3.284(2) and 3.975(2) Å.
The $[Ga_2Cl_6O]^{2-}$ anion exhibits the same structure as a $[Ga_2Cl_7]^-$ anion, representing a corner sharing double tetrahedron (Fig. 2.13.2.2).

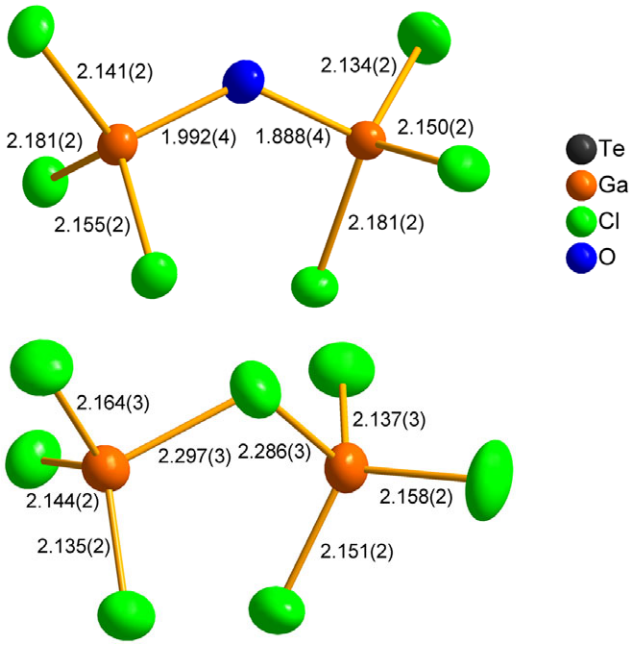

Fig. 2.13.2.2 Structural comparison of the $[Ga_2Cl_6O]^{2-}$ (top) and $[Ga_2Cl_7]^-$ anion as present in the structure of $(As_2Te_4)[Ga_2Cl_4]_2$ (bottom). The atoms are represented by thermal ellipsoids scaled to include a probability of 70 %. Bond lengths are given in Å.

The significant structural differences between $[Ga_2Cl_7]^-$ and $[Ga_2Cl_6O]^{2-}$ are the bond lengths to the bridging oxygen and chlorine atoms. In the structures of compounds presented above, bridging Ga–Cl bond lengths are in the range between 2.25 - 2.35 Å. Due to the formal exchange of the chlorine atom by an oxygen atom, these bond lengths shrink to 1.8 - 2.0 Å, which is in line with the Ga-O-Ga bridge in the anion $[Ga_8\{NH(C_6H_5)\}_2(NH_2)_4(NH)_2OLi]^-$ (Ga–O 1.87 Å, 1.90 Å)[119] and the Ga–O bond lengths in Ga_2O_3 (1.80 - 2.02 Å)[120]. Consequently, the Ga-Ga distance decreases from approximately 3.8 Å in $[Ga_2Cl_7]^-$ to 3.4 Å in $[Ga_2Cl_6O]^{2-}$. In principle, a smaller, weakly coordinating, but more basic gallate anion was generated and can be used to stabilize polycationic clusters. Compared to the high number of $[GaCl_4]^-$ and $[Ga_2Cl_7]^-$ anions, which are necessary to compensate highly positively charged clusters (e. g. $(Sb_7Te_8)^{5+}$)), only the half number of $[Ga_2Cl_6O]^{2-}$ anions is needed instead.

2.14 $(Pn_2Te_4)^{2+}$ vs. $(Pn_2Te_4)^{4+}$ Clusters (Pn = As, Sb) and the Hexachlorido Oxido Digallate Anion $[Ga_2Cl_6O]^{2-}$

Due to the discovery of the novel anion $[Ga_2Cl_6O]^{2-}$, experiments were performed to crystallize this anion with further mixed polycationic clusters. By introducing the specific oxides Pn_2O_3, Pn_2O_5 (Pn = As, Sb) and TeO_3 to the syntheses, the incorporation of oxygen into the chlorido gallate anions succeeded and the desired compounds crystallized in high yield. The generation of the oxygen bridged digallate anion allowed for the formation of prismatic pentele-tellurium clusters and four novel compounds were found. Despite accurate crystal structure refinements, EDX and Raman analyses no unambigous results for the clusters charge were found. In the following chapter this question will be discussed for the cations $(Pn_2Te_4)^{2+}$ and $(Pn_2Te_4)^{4+}$. A $(Pn_2Te_4)^{4+}$ cluster would be isoelectronic to a hypothetical Te_6^{6+} cluster, which could not be obtained until today.

2.14.1 Syntheses and EDX Analyses of Compounds Containing the $(Pn_2Te_4)^{2+/4+}$ Clusters

$(As_2Te_4)[Ga_2Cl_6O]_2$

45.2 mg (0.36 mmol) tellurium, 18.0 mg (0.24 mmol) arsenic, 21.7 mg (0.12 mmol) arsenic trichloride, 174.3 mg (0.99 mmol) gallium trichloride, 60.2 mg (0.16 mmol) tetraphenylphosphonium chloride and 23.7 mg (0.12 mmol) arsenic trioxide were annealed in a sealed ampoule at 100 °C for five days. $(As_2Te_4)[Ga_2Cl_6O]_2$ is obtained as orange, block-like crystals (Fig. 2.14.1.1) in an estimated yield of 50 % in a dark orange melt. At 50 °C the reaction time is expanded to 2-3 months and the yield is lower. An exchange of As_2O_3 by As_2O_5 leads to the same product.
$AsCl_3$ is liquid and had to be added with a syringe. The correct amount was calculated by the weight of individual drops.

A tentative reaction equation is:

$$12\ Te + 2\ As + 12\ GaCl_3 + 2\ As_2O_3 \rightarrow 3\ (As_2Te_4)[Ga_2Cl_6O]_2$$

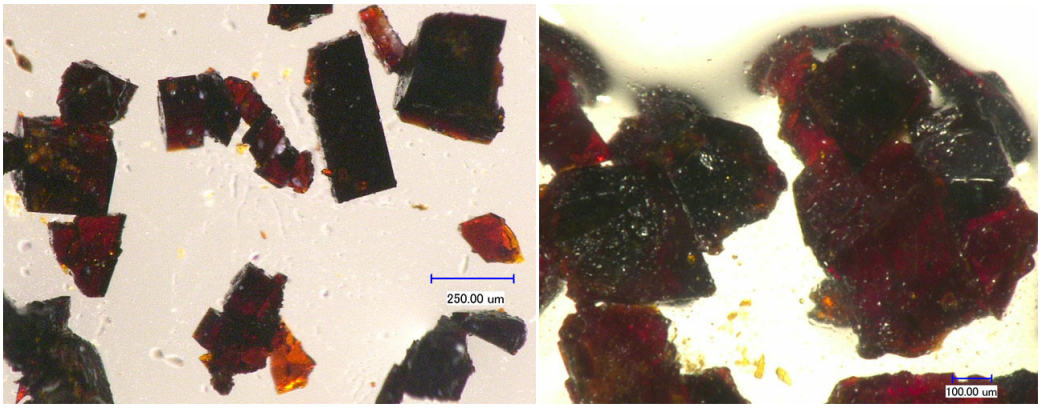

Fig. 2.14.1.1 Crystals of $(As_2Te_4)[Ga_2Cl_6O]_2$ immersed in perfluorinated polyether.

The EDX results (Tab. 2.14.1.1) reveal too high contents for Ga and Cl compared to the respective calculated ratios for $(As_2Te_4)[Ga_2Cl_6O]_2$. Especially a systematically too high Ga content is detected. The reason is not clear. Oxygen can generally not be detected in EDX analyses due to a too low energy of the O-*L* X-ray emission line. A too high result for Cl indicates $GaCl_3$ adherences on the crystals surfaces, which may partly explain the high Ga content. The syntheses in $PPh_4[GaCl_4]$ generally lead to thin films of this solvent on the crystals surfaces (compare Fig. 2.12.1.3). Despite several inaccuracies, the experimental results are very close to the sum formula $(As_2Te_4)[Ga_2Cl_6O]_2$, which favours a charge of +4 for the polycationic cluster. Generally, the As : Te ratio of 1 : 2 was confirmed.

Tab. 2.14.1.1 Elemental composition of $(As_2Te_4)[Ga_2Cl_6O]_2$ in atom-% and the As : Te ratio. Standard deviations given in brackets refer to the last significant digit.

$(As_2Te_4)[Ga_2Cl_6O]_2$	As	Te	Ga	Cl	O	As : Te
Found	7.6(5)	15.7(7)	22(1)	53.8(9)	-	1 : 2.05
Calculated	8.3	16.7	16.7	50.0	8.3	1 : 2.00

$(Sb_2Te_4)[Ga_2Cl_6O]_2$ (*C*2 polymorph)

45.2 mg (0.36 mmol) tellurium, 29.2 mg (0.24 mmol) antimony, 27.4 mg (0.12 mmol) antimony trichloride, 174.3 mg (0.99 mmol) gallium trichloride, 60.2 mg (0.16 mmol) tetraphenylphosphonium chloride and 17.5 to 35.0 mg (0.06 - 0.12 mmol) antimony trioxide were filled in a glass ampoule, sealed and annealed at 50 °C for three weeks. Orange, block-shaped crystals form within two weeks in an estimated yield of 60 % (Fig. 2.14.1.2).

A tentative reaction equation is:

$12\ Te + 2\ Sb + 12\ GaCl_3 + 2\ Sb_2O_3 \rightarrow 3\ (Sb_2Te_4)[Ga_2Cl_6O]_2$

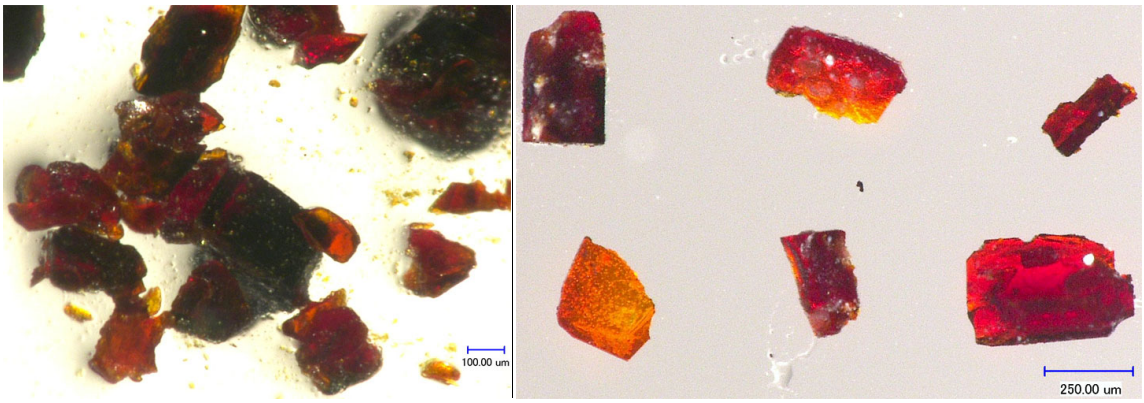

Fig. 2.14.1.2 Crystals of $(Sb_2Te_4)[Ga_2Cl_6O]_2$ immersed in perfluorinated polyether.

The EDX results (Tab. 2.14.1.2) show the same inaccuracies for Ga and Cl like in the analysis of $(As_2Te_4)[Ga_2Cl_6O]_2$. The Sb : Te ratio of 1 : 2 was confirmed and the full analysis is indicative of the sum formula $(Sb_2Te_4)[Ga_2Cl_6O]_2$ with an $(Sb_2Te_4)^{4+}$ cluster.

Tab. 2.14.1.2 Elemental composition of $(Sb_2Te_4)[Ga_2Cl_6O]_2$ in atom-% and the Sb : Te ratio. Standard deviations given in brackets refer to the last significant digit.

$(Sb_2Te_4)[Ga_2Cl_6O]_2$	Sb	Te	Ga	Cl	O	Sb : Te
Found	6.2(5)	11.7(9)	27.5(8)	54.5(9)	-	1 : 1.89
Calculated	8.3	16.7	16.7	50.0	8.3	1 : 2.00

$(Sb_2Te_4)[Ga_2Cl_6O]_2$ ($P2_1/n$ polymorph)

45.2 mg (0.36 mmol) tellurium, 29.2 mg (0.24 mmol) antimony, 27.4 mg (0.12 mmol) antimony trichloride, 174.3 mg (0.99 mmol) gallium trichloride, 60.0 mg (0.16 mmol) tetraphenyl phosphonium chloride and 38.8 mg (0.12 mmol) antimony pentaoxide were filled in a glass ampoule, sealed and annealed at 50 °C for three weeks. By exchanging antimony pentaoxide by tellurium trioxide the same product forms but crystallizes preferably in plate-like crystals. Crystals of $(Sb_2Te_4)[Ga_2Cl_6O]_2$ are orange and block-shaped (Fig. 2.14.1.3). It is obtained in an estimated yield of 50 % in a black liquid melt. The yield in the synthesis with TeO_3 is lower, but the crystal quality improves.

A tentative reaction equation is:

$$20\ Te + 6\ Sb + 20\ GaCl_3 + 2\ Sb_2O_5 \rightarrow 5\ (Sb_2Te_4)[Ga_2Cl_6O]_2$$

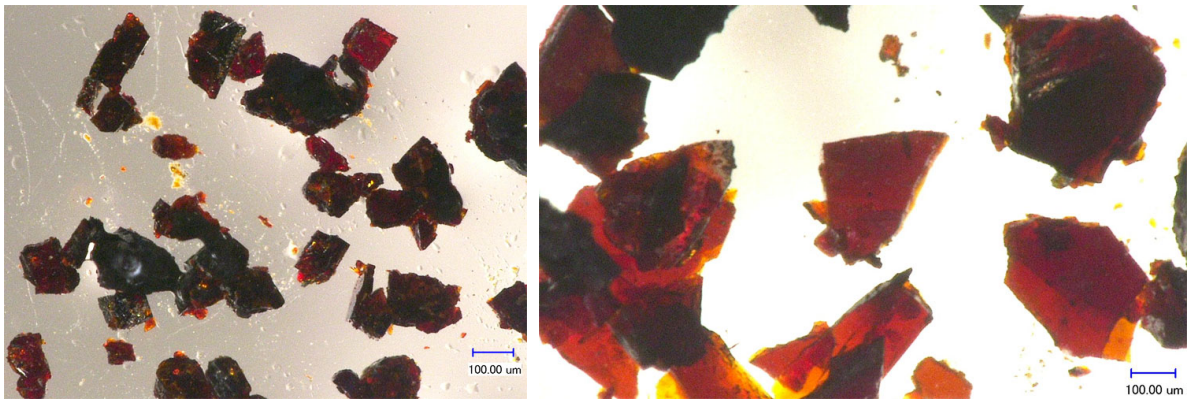

Fig. 2.14.1.3 Crystals of $(Sb_2Te_4)[Ga_2Cl_6O]_2$ immersed in perfluorinated polyether, left from the experiment with Sb_2O_5, right from the experiment with TeO_3.

The EDX results (Tab. 2.14.1.3) correspond to those obtained for $(As_2Te_4)[Ga_2Cl_6O]_2$ and $(Sb_2Te_4)[Ga_2Cl_6O]_2$ (*C*2 polymorph). The the sum formula $(Sb_2Te_4)[Ga_2Cl_6O]_2$ is confirmed.

Tab. 2.14.1.3 Elemental composition of $(Sb_2Te_4)[Ga_2Cl_6O]_2$ in atom-% and the Sb : Te ratio. Standard deviations given in brackets refer to the last significant digit.

$(Sb_2Te_4)[Ga_2Cl_6O]_2$	Sb	Te	Ga	Cl	O	Sb : Te
Found	8.0(2)	15.1(3)	21.3(3)	55.3(4)	-	1 : 1.88
Calculated	8.3	16.7	16.7	50.0	8.3	1 : 2.00

$(Sb_2Te_4)_2[Ga_2Cl_6O]_4$

For $(Sb_2Te_4)_2[Ga_2Cl_6O]_4$, 45.2 mg (0.36 mmol) unsublimated tellurium, 29.2 mg (0.24 mmol) antimony, 27.4 mg (0.12 mmol) antimony trichloride and 174.3 mg (0.99 mmol) gallium trichloride were filled in an evacuated glass ampoule, which was sealed and annealed at 50 °C for 37 days. $(Sb_2Te_4)_2[Ga_2Cl_6O]_4$ crystallizes as orange, plate shaped crystals in very low yield. Unfortunately, attempts of reproduction to obtain samples for further analyses were not successful.

Only few EDX results were taken into account since deviating analyses were performed probably due to the presence of different phases with the same crystal colour. In most cases, the Sb : Te ratio was found to be 1 : 2. Consequently, only these results were considered. The experimental composition is close to the sum formula $(Sb_2Te_4)_2[Ga_2Cl_6O]_4$. Consequently, two $(Sb_2Te_4)^{4+}$ clusters are assumed to be present in the crystal structure.

Tab. 2.14.1.4 Elemental composition of $(Sb_2Te_4)_2[Ga_2Cl_6O]_4$ in atom-% and the Sb : Te ratio. Standard deviations given in brackets refer to the last significant digit.

$(Sb_2Te_4)_2[Ga_2Cl_6O]_4$	Sb	Te	Ga	Cl	O	Sb : Te
Found	9.3(4)	19.9(5)	21(2)	48(2)	-	1 : 2.14
Calculated	8.3	16.7	16.7	50	8.3	1 : 2.00

2.14.2 The Reactions Leading to $(Sb_2Te_4)^{2+/4+}$ Clusters and $[Ga_2Cl_6O]^{2-}$ Anions

All compounds were obtained from melts mainly composed of gallium trichloride. As described in the chapters above the product formation can be controlled by the use of specific adjuvants. $(As_2Te_4)[Ga_2Cl_6O]$ and both polymorphs of $(Sb_2Te_4)[Ga_2Cl_6O]_2$ were synthesized by the use of the oxidic adjuvants Sb_2O_3, Sb_2O_5, As_2O_3, As_2O_5 and TeO_3. The exchange of Sb_2O_3 by Sb_2O_5 led to a different polymorph in the synthesis of $(Sb_2Te_4)[Ga_2Cl_6O]_2$. The corresponding exchange of As_2O_3 by As_2O_5 did not cause any difference in the synthesis of $(As_2Te_4)[Ga_2Cl_6O]_2$. Without the use of PPh_4Cl, yields were much lower and the melts of higher viscosity. PPh_4Cl improves yields, the crystal quality and size.
All syntheses were additionally performed at various temperatures between 50 and 100 °C with different amounts of these oxides, but all experiments led to the same phase pure products in high yield. The oxides dissolve in the acidic melts and build the $[Ga_2Cl_6O]^{2-}$ anion. In contrast, TeO_2 does not generate the oxido hexachlorido digallate anion, since $(SbTe_4)[Ga_2Cl_7]$ is formed instead (chapter 2.9) In the reaction ampoules of $(As_2Te_4)[Ga_2Cl_6O]_2$ and $(Sb_2Te_4)[Ga_2Cl_6O]_2$, unreacted As and Sb was found as a byproduct, respectively. In the synthesis of the *C*2 polymorph of $(Sb_2Te_4)[Ga_2Cl_6O]_2$, metallic shiny needles of $(Sb_3Te_4)[GaCl_4]$ (chapter 2.9) were found as a byproduct in an estimated yield of 10 % at all applied temperatures. In $(Sb_2Te_4)_2[Ga_2Cl_6O]_4$ the incorporated oxygen presumably originates from traces of TeO_2 and/or TeO_3, being present in not sublimated tellurium, which agrees with the low yield of this compound.
All substances described in this chapter form block shaped crystals, which fan out to plates on mechanical pressure.
Analogous attempts to synthesize polycationic clusters with the hypothetical anion $[Ga_2Cl_6S]^{2-}$ anion using Sb_2S_3 did not succeed. Additional experiments to obtain cube and double cube shaped Sb/Te and Sb/Se clusters with the oxygen bridged digallate anion, were also not successful. Only compounds, containing mixed pentele-chalcogen prismatic clusters were obtained. This indicates that these clusters are the preferred clusters to be formed in oxygen containing $GaCl_3$ melts.

2.14.3 Crystal Structures of Compounds Containing $(Pn_2Te_4)^{4+}$ Clusters and $[Ga_2Cl_6O]^{2-}$ Anions

$(As_2Te_4)[Ga_2Cl_6O]_2$ and one polymorph of $(Sb_2Te_4)[Ga_2Cl_6O]_2$ crystallize in the azentric space group *C*2. The other polymorph of $(Sb_2Te_4)[Ga_2Cl_6O]_2$ crystallizes in $P2_1/n$. The structures are build from $(Pn_2Te_4)^{4+}$ polycationic clusters and $[Ga_2Cl_6O]^{2-}$ anions (Fig. 2.14.3.1). The crystallographic data are shown in Tabs. A 5.2.21 and A 5.2.22.
$(As_2Te_4)[Ga_2Cl_6O]_2$ was refined as an inversion twin due to a Flack *x* parameter of 0.58(2). The *C*2 polymorph of $(Sb_2Te_4)[Ga_2Cl_6O]_2$ was obtained as an enatiomeric pure crystal (Flack $x = 0.07(2)$).

The structures of the three compounds $(Pn_2Te_4)[Ga_2Cl_6O]_{1/2}$ (Pn = As, Pn) show the same statistical disorder as found for $(As_2Te_4)[Ga_2Cl_7]_2$ and $M(Pn_2Te_4)[GaCl_4]_3$ (chapter 2.7). All atom sites within the polycationic clusters were refined to be occupied by both, the pentele element and tellurium. Attempts to use the same postitional and displacement parameters for both kinds of atoms with the ShelX commands EXYZ and EADP succeeded only for the structure of $(As_2Te_4)[Ga_2Cl_6O]_2$. Acceptable residual electron densities of 2.5 e·Å^{-3} were obtained. Using the same procedure for the polymorphs of $(Sb_2Te_4)[Ga_2Cl_6O]_2$, yielded new residual electron densities next to the averaged positions higher than 10 e·Å^{-3}. Consequently, all structures were refined in analogous way with disordered atom positions, which led to the lowest crystallographic reliability factors and residual electron densities. Only the position of Te1 in the $P2_1/n$ polymorph of $(Pn_2Te_4)[Ga_2Cl_6O]_2$ did not show any residual electron density in its' direct neighbourhood (see Fig. 2.14.3.2 below for the numbering). Free refinenments of the pentele and tellurium positions confirm the EDX analyses according to the Pn : Te ratio being 1 : 2 in all cases. The occupations of the atoms positions are listed in Tab. 2.14.3.1.

Tab. 2.14.3.1 Obtained occupations for the Pn and Te position in the structures of $(Pn_2Te_4)[Ga_2Cl_6O]_2$ (Pn = As, Sb).

$(As_2Te_4)[Ga_2Cl_6O]_2$		$(Sb_2Te_4)[Ga_2Cl_6O]_2$ ($C2$ polymorph)		$(Sb_2Te_4)[Ga_2Cl_6O]_2$ ($P2_1/n$ polymorph)	
As1 45 %	Te1 55 %	Sb1 20 %	Te1 80 %	Sb1 0%	Te1 100 %
As2 35 %	Te2 65 %	Sb2 30 %	Te2 70 %	Sb2 25 %	Te2 75 %
As2 20 %	Te3 80 %	Sb3 50 %	Te3 50 %	Sb3 11 %	Te3 89 %
				Sb4 24 %	Te4 76 %
				Sb5 30 %	Te5 70 %
				Sb6 35 %	Te6 65 %

In both clusters of $(Pn_2Te_4)[Ga_2Cl_6O]_2$, which crystallize in the space group $C2$, similar occupations of As and Te are obtained (As1/Te1-Sb3/Te3, As2/Te2-Sb2/Te2, As3/Te3-Sb1/Te1).

The crystal structure determinations give unambigous results for the respective sum formulae. Two $[Ga_2Cl_6O]^{2-}$ anions compensate one polycationic cluster. Thus, the presence of $(Pn_2Te_4)^{2+}$ clusters as found in the EDX analyses are obviously confirmed.

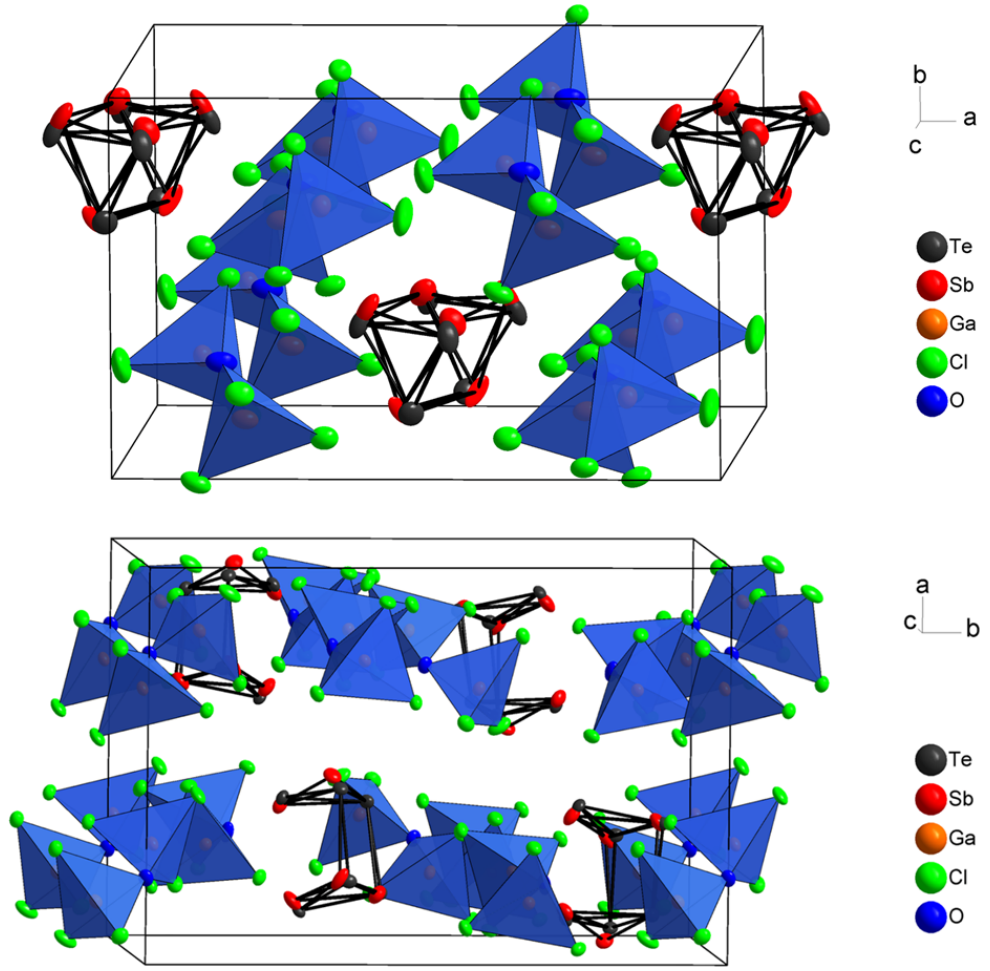

Fig. 2.14.3.1 The unit cell of the structures of $(Sb_2Te_4)[Ga_2Cl_6O]_2$ (*C*2 polymorph) (top) and $(Sb_2Te_4)[Ga_2Cl_6O]_2$ ($P2_1/n$ polymorph) (bottom). The $[Ga_2Cl_6O]^{2-}$ anions are represented by discrete double tetrahedra. The atoms are represented by thermal ellipsoids scaled to include a probability of 50 %.

A detailed analysis of the clusters reveals structural differences. Taking only reasonable Pn–Pn, Pn–Te and Te–Te bond lengths between 2.5 and 3.1 Å into account, leads to a boat conformation of the prismatic cluster of the $P2_1/n$ polymorph of $(Sb_2Te_4)[Ga_2Cl_6O]_2$ (Fig. 2.14.3.2). Furthermore, the position occupied by Te1 is not involved in the disorder. Unfortunately, further analyses of this partly disordered cluster and both completely disordered clusters in the *C*2 structures of $(Pn_2Te_4)[Ga_2Cl_6O]_2$ are hampered.

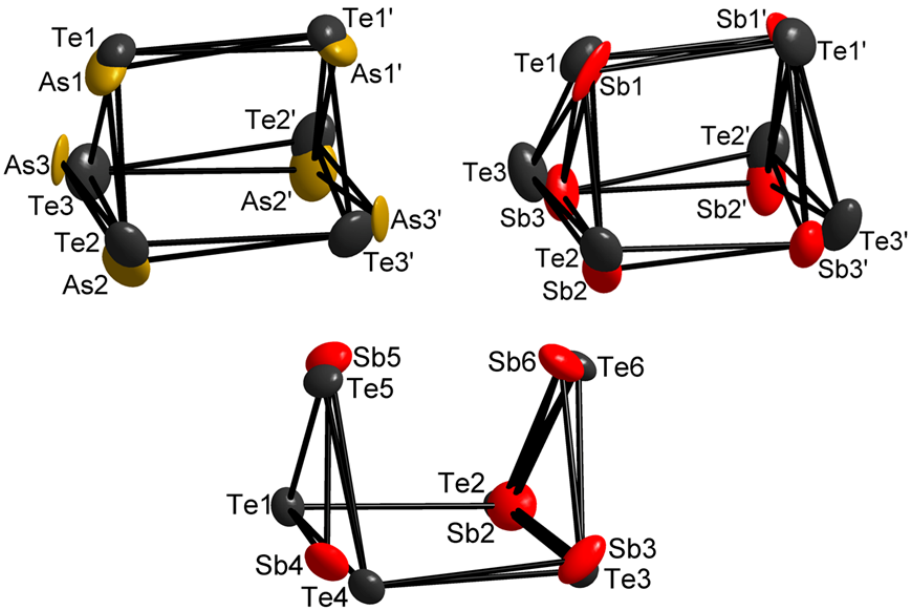

Fig. 2.14.3.2 $(Pn_2Te_4)^{4+}$ clusters in the structures of $(As_2Te_4)[Ga_2Cl_6O]_2$ (top left), $(Sb_2Te_4)[Ga_2Cl_6O]_2$ (*C*2 polymorph) (top right) and $(Sb_2Te_4)[Ga_2Cl_6O]_2$ ($P2_1/n$ polymorph) (bottom). The atoms are represented by thermal ellipsoids scaled to include a probability of 50 %. The symmetry code *I* refers to atoms generated by the two-fold axis with coordinates 1-*x*, *y*, 1- *z*.

The compound $(Sb_2Te_4)_2[Ga_2Cl_6O]_4$ also crystallizes in the azentric space group *C*2. The refinement of the Flack *x* parameter revealed *x* = 0.42(3) indicating an inversion twinning of the examined crystal. Here, two different, not disordered $(Pn_2Te_4)^{4+}$ clusters are present in the crystal structure (Fig. 2.14.3.3). The EDX analysis (Tab. 2.14.1.4) reveals a Sb:Te ratio of 1:2. The examination of the occupation factors (Fig. A 5.3.13) confirms the atom assignment of one prism unequivocally (Fig. 2.14.3.3 left). Two lower and four higher occupied positions are obtained from the diffraction data. Sb occupies positions in the rectangular plane of the prism and at the open edge (Sb2–Te1 3.535(2) Å). The prism edges are 2.712(2) Å (Sb1–Te4) and 3.018(2) Å (Te2–Te3) and the average bond length within the triangular plane is 2.718 Å, which, however, corresponds to the respective bonds in the Te_6^{4+} cation (2.67 Å).[121]

The atom assignment in the other prism (Fig. 2.14.3.3 bottom right) is not supported by the occupation factors based on the diffraction data since three lower occupations are found for three independent atom positions (Fig. A 5.4.14). Presumably, Sb occupies two positions at the shorter edge of the prism, which show an insignificantly lower occupation factor compared to the postions of Te5 and Te6, which mark the open edges of this prism with a weak bond of 3.248(2) Å. The Sb3–Sb3' bond lengths is 2.984(2) Å and the average bond length within the triangular plane 2.716 Å.

Despite an unequivocal charge of +4 for the clusters obtained from the number of anions, Lewis formulae of both clusters are not in line with the proposed charge (Fig. 2.14.3.4). In the first prism Te2, Te3 and Te4 are three-fold coordinated and give a formal charge of +1, respectively. Te1 and Sb1 are formally neutral. Sb2 is two-fold coordinated and carries a formal charge of -1. All these considerations lead to a charge of +2 for the cluster. In the second prism, four Te atoms are 2.5-fold coordinated and carry a formel charge of +0.5 each. Two three-fold coordinated Sb atoms are formally neutral. The resulting charge for the cluster is again +2.

The coordination of the Sb and Te atoms by Cl atoms of the $[Ga_2Cl_6O]^{2-}$ anions does not allow for an distinction of the pentele and chalcogen atoms. All interactions are rather uniform and start with distances of 3.5(1) Å (Tab. A 5.5.14).

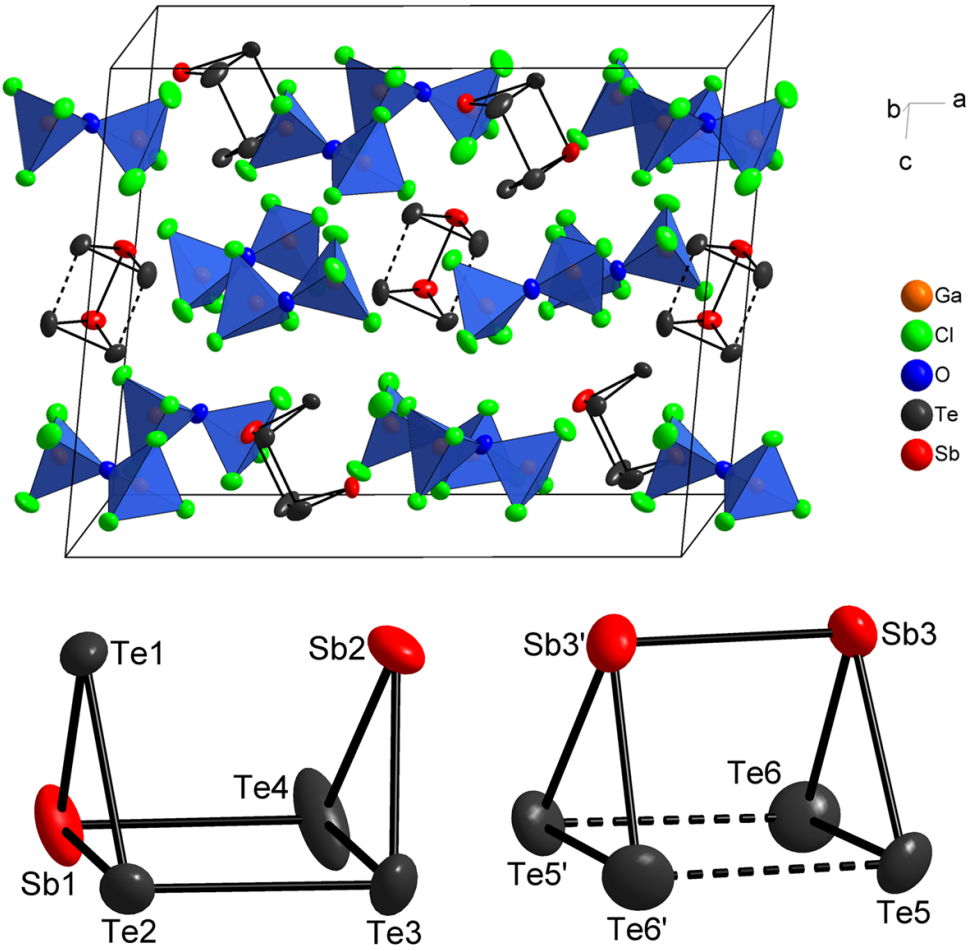

Fig. 2.14.3.3 The unit cell of the structure of $(Sb_2Te_4)_2[Ga_2Cl_6O]_4$ (top). The $[Ga_2Cl_6O]^{2-}$ anions are represented by discrete double tetrahedra. The atoms are represented by thermal ellipsoids scaled to include a probability of 70 %. On bottom the two independet $(Sb_2Te_4)^{4+}$ clusters are shown thermal ellipsoids scaled to include a probability of 50 %.

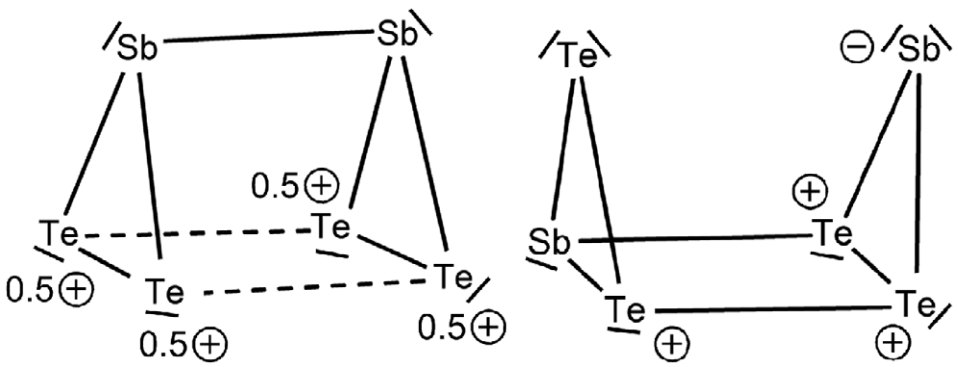

Fig. 2.14.3.4 Lewis valence formulae of the prismatic clusters in the structure of $(Sb_2Te_4)_2[Ga_2Cl_6O]_4$.

The structural parameters of the $[Ga_2Cl_6O]^{2-}$ anion are in line with those in the structure of $Te_4[Ga_2Cl_6O]$ (chapter 2.13).

The datasets of all four crystal structures exhibit rather good quality and the refinements lead to convincing results. The presence of $(Pn_2Te_4)^{4+}$ clusters seem to be confirmend by this method. The reason for the disorder, which occurs only in prismatic clusters during this work, is still not clear. Unfortunately, it was not possible to reproduce the synthesis of $(Sb_2Te_4)_2[Ga_2Cl_6O]_4$ for further analytical investigations such as Raman spectroscopy.

For comparison with the experimental results, the three isomers of the $(Sb_2Te_4)^{4+}$ cluster were calculated (Fig. 2.14.3.5). They are all closed prisms with a maximum bond length of 3.012 Å in isomer 1.

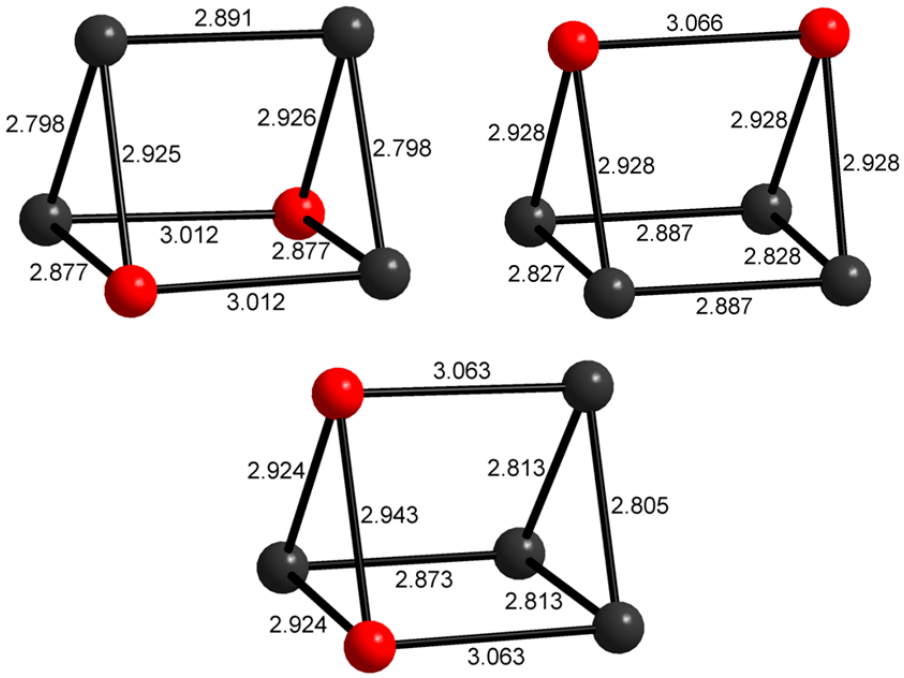

Fig. 2.14.3.5 Calculated structures of the three isomers of the $(Sb_2Te_4)^{4+}$ cluster and the respective bond lengths /Å (B3LYP/TZV(2d/sp)).*

For comparison the first and second calculated isomers from Fig. 2.14.3.5 are relevant. They do not show any coincidence besides a similar Sb–Sb bond length (calculation: 3.066 Å, experiment: 2.984(2) Å). The bonds within the triangular plane of the calculated clusters are elongated in average to 2.866 Å (isomer 1) and 2.894 Å (isomer 3). No weak elongated or cleaved bonds are found in contrast to the experimental data. The structural parameters of the calculated $(Sb_2Te_4)^{2+}$ isomers are generally closer to those found in the crystal structure (Fig. 2.14.3.6).

Consequently, the presence of $(Sb_2Te_4)^{4+}$ clusters could not be confirmed by the calculations.

* The calculations were performed by Dr. Gregor Schnakenburg.

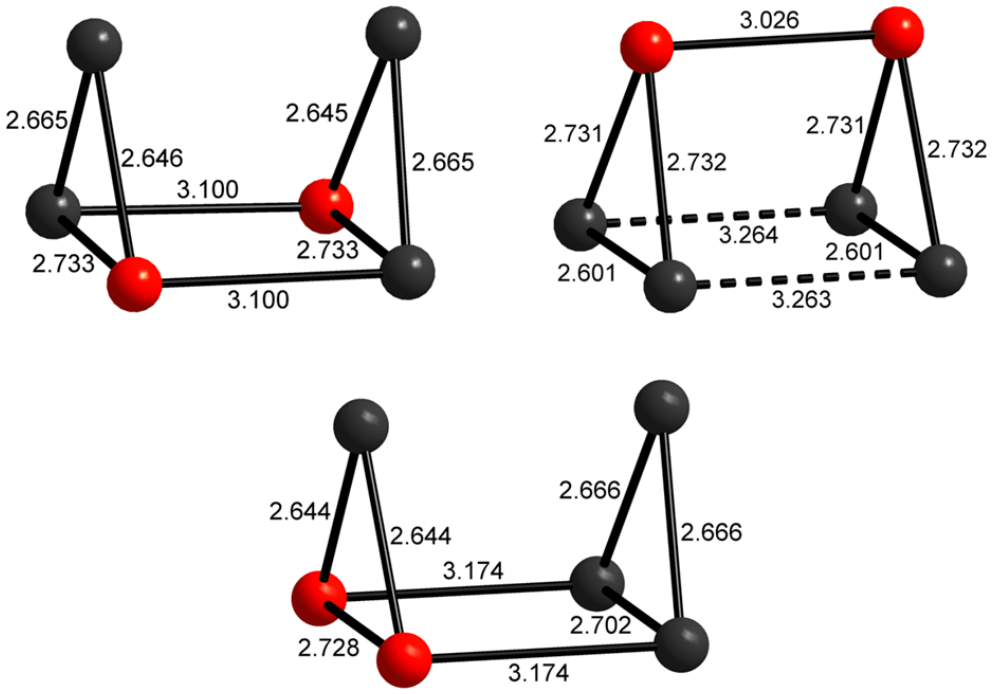

Fig. 2.14.3.6 Calculated three isomers of the $(Sb_2Te_4)^{2+}$ cluster and bond lengths /Å (B3LYP/TZV(2d/sp)).*

2.14.4. Raman Spectroscopy Study of $(Pn_2Te_4)[Ga_2Cl_6O]$

According to the EDX analyses and the crystal structures, $(Sb_2Te_4)^{4+}$ polycationic clusters are present in the compounds described in this chapter. Like in the structures of $M(Pn_2Te_4)[GaCl_4]_3$ (chapter 2.7), both kinds of analyses, crystal structure determination and EDX analysis, can not clarify the presence of specific isomers of the clusters unequivocally. Consequently, Raman analyses of $(As_2Te_4)[Ga_2Cl_6O]$ and both polymorphs of $(Sb_2Te_4)[Ga_2Cl_6O]$ were performed and the obtained spectra were compared with the calculated spectra of these clusters. Generally, reliable statements about Raman signals can be made above about 90 cm^{-1} due to the signals of the exciting laser around 76 and 78 cm^{-1} (compare Fig. A 5.1.5.2). All calculated spectra were adjusted to the experimental spectra by means of a strong signal at high wavenumbers.

The Raman spectrum of $(As_2Te_4)[Ga_2Cl_6O]$ shows intensive bands at 103, 106, 153, 196, 201 and 272 cm^{-1}, which can be attributed to the polycationic cluster (Fig. 2.14.4.1). Additional weak signals are visible at 186 and 265 cm^{-1}, which also originate from the cluster. Besides the intensive signal at 127 cm^{-1}, the spectrum is in full agreement with those obtained for $M(As_2Te_4)[GaCl_4]_3$ (Figs. 2.5.7.6 - 2.5.7.11). In contrast to the presence of two isomers, in the spectrum of $(As_2Te_4)[Ga_2Cl_6O]$ all signals are explained with the calculated spectrum of the isomer 3 of the $(As_2Te_4)^{2+}$ cluster, solely. The band at 88 cm^{-1} is not visible due to overlap with the laser band.
The less well resolved signal around 360 cm^{-1} is caused by the $[Ga_2Cl_6O]^{2-}$ anion. Additional very weak signals are found at 116 and 136, which presumably also belong to vibrations of the anion.

* The calculations were performed by Dr. Gregor Schnakenburg.

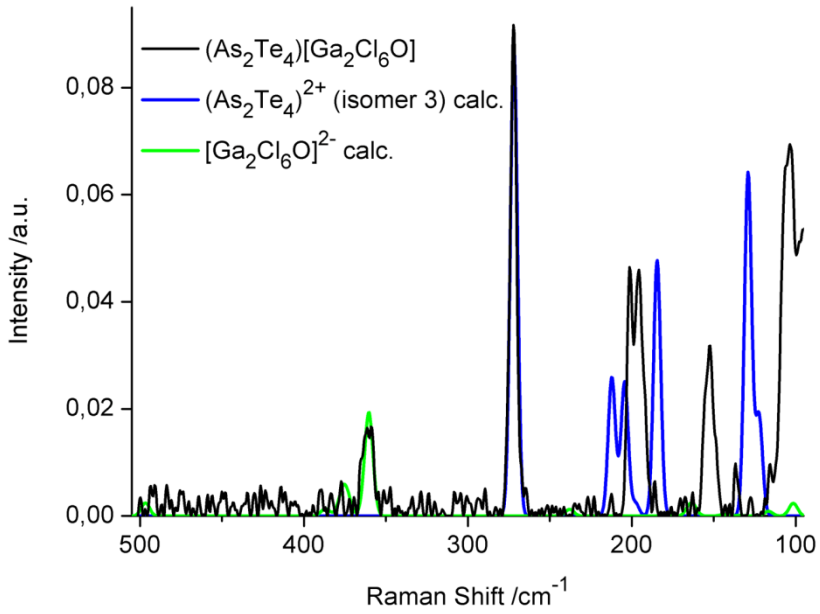

Fig. 2.14.4.1 Comparison between the experimental spectrum of $(As_2Te_4)[Ga_2Cl_6O]$ and the calculated Raman spectrum of $(As_2Te_4)^{2+}$ isomer 3. Experimental spectra are drawn with black lines, the calculated spectrum of the cluster is blue and the spectrum of the anion is shown in green.

The Raman spectrum of $(Sb_2Te_4)[Ga_2Cl_6O]$ (*C*2 polymorph) reveals signals at 89, 130, 164, 174 and 231 cm^{-1} originating from the cluster (Fig. 2.14.4.2) and is in line with the spectra of the $(Sb_2Te_4)^{2+}$ cluster in the spectra of $(Sb_2Te_4)[Ga_2Cl_7]_2$ (Fig. 2.5.7.4) and $M(Sb_2Te_4)[GaCl_4]_3$ (M = Rb, Cs) (Figs. 2.5.7.12, 2.5.7.13), considering no splitting of the signal at 130 cm^{-1}. The coincidence with the calculated isomer 1 of the $(Sb_2Te_4)^{2+}$ cluster is excellent in all these spectra. Two low intensive signals are found at 101 and 145 cm^{-1}, which may be caused by the $[Ga_2Cl_6O]^{2-}$ anion, since the calculations reveal Raman bands at these wavenumbers. The anion causes a split signal at 348 and 360 cm^{-1}, which is visible due to a higher number of scans. Consequently, the background is minimized in contrast to the spectrum of $(As_2Te_4)[Ga_2Cl_6O]$.

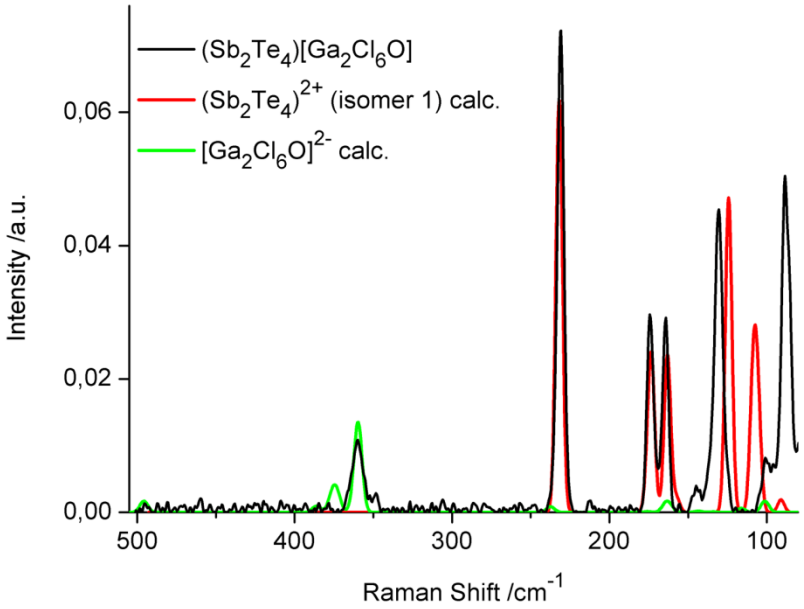

Fig. 2.14.4.2 Comparison between the experimental spectrum of $(Sb_2Te_4)[Ga_2Cl_6O]$ (*C*2 polymorph) and the calculated Raman spectrum of $(Sb_2Te_4)^{2+}$ isomer 1. Experimental spectra are drawn with black lines, the calculated spectrum of the cluster is red and the spectrum of the anion is shown in green.

The Raman spectra of $(Sb_2Te_4)[Ga_2Cl_6O]$ ($P2_1/n$ polymorph), which was obtained from two synthetic runs with different oxides, are almost in full agreement with the spectrum of the corresponding *C*2 polymorph. The same signals are obtained at the same wavenumbers (Fig. 2.14.4.3).

The only remarkable difference is found in the spectrum of $(Sb_2Te_4)[Ga_2Cl_6O]$ from the experiment with TeO_3. The Raman band at 89 cm^{-1} is the most intensive one in the spectrum. The laser signal at 76 and 78 cm^{-1} is hidden for clarity in all spectra, but it overlaps partly with the signal at 89 cm^{-1}. In this specific case the laser signal is much more intensive compared to the two spectra above and the corresponding calculated signal. The reason is a much higher laser energy during recording the spectrum, which was already figured out in the Raman analyses of $M(Sb_2Te_4)[GaCl_4]_3$.

Unfortunately, the anion gives only weak and low resolved signals in both spectra.

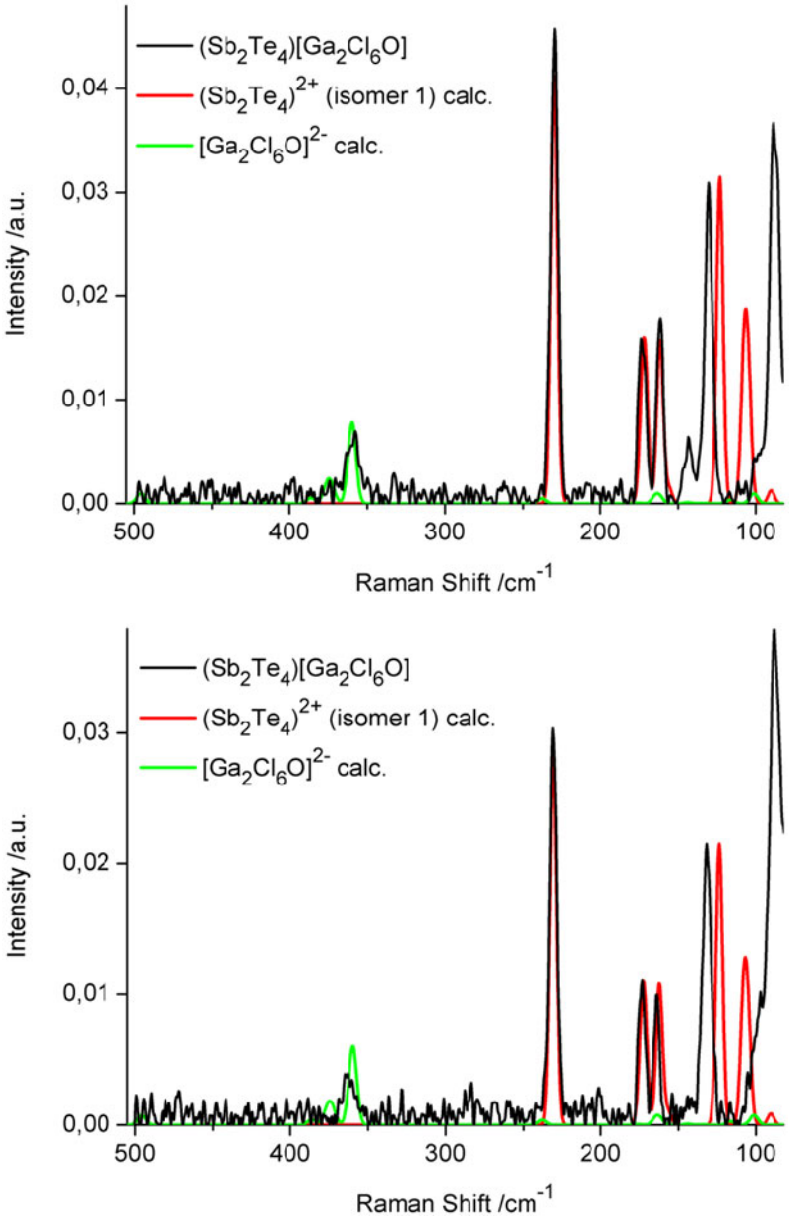

Fig. 2.14.4.3 The experimental spectra of $(Sb_2Te_4)[Ga_2Cl_6O]$ ($P2_1/n$ polymorph) from the synthesis with Sb_2O_5 (top) and TeO_3 (bottom). Both spectra are compared with the calculated Raman spectrum of $(Sb_2Te_4)^{2+}$ isomer 1. Experimental spectra are drawn with black lines, the calculated spectrum of the cluster is red and the spectrum of the anion is shown in green.

Several analyses of different samples of both polymorphs from different ampoules led to the same results. In all cases the isomer 1 of the $(Sb_2Te_4)^{2+}$ cluster was found, which stands in clear contrast to the EDX and crystal structure analyses. The spectra of three isomers of the $(Sb_2Te_4)^{4+}$ cluster, referred to the isomers of the $(Sb_2Te_4)^{2+}$ cluster (compare Fig. 2.7.3.2), were calculated for comparison. They are shown in Fig. 2.14.4.4.

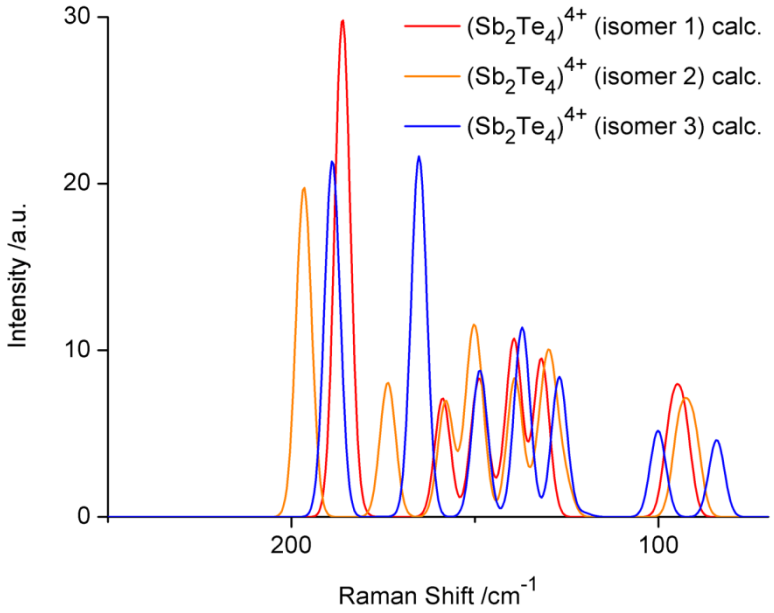

Fig. 2.14.4.4 Calculated Raman spectra of three isomers of the $(Sb_2Te_4)^{4+}$ cluster (B3LYP/TZV(2d/sp)).*

All calculated spectra contain signals in a smaller range between approximately 80 and 200 cm^{-1}, compared to the spectra calculated for the $(Sb_2Te_4)^{2+}$ isomers (compare Fig. 2.5.7.1) Further differences are the higher number of signals and the closer distances between them in the case of the $(Sb_2Te_4)^{4+}$ spectra.

The reason for the contradiction of different analyses is not clear since repeated EDX, crystal structure and Raman analyses led to the same results. All obtained data are of good or very good quality. Any chemical alteration of the examined compounds during analysis is excluded since covalent bonds had to be broken and the crystallinity would get lost. In all cases, mechanically cleaned crystals were examined.

2.15 Ga_2SbCl_7O - A Molecular Gallium Antimony Chloride Oxide

The elements gallium and antimony form stable compounds with oxygen and chlorine. Well known compounds are Ga_2O_3,[120] $GaCl_3$,[71] Sb_2O_3,[122] and $SbCl_3$.[63] $GaCl_3$ is highly Lewis acidic and the chloridogallate anions $[GaCl_4]^-$ [50] and $[Ga_2Cl_7]^-$ [51] appear in many salt-like compounds. Moreover, ternary oxide halides of both elements, namely GaOCl and SbOCl [123] can be obtained from the respective binary compounds. Mixed ternary antimony/gallium chlorides or oxides are rare. The mixed chloride $[SbCl_2][GaCl_4]$ [124], $Sb_8[GaCl_4]_2$, containing a square-antiprismatic Sb_8^{2+} cluster,[125] and the mixed oxide $GaSbO_4$ [126] have been characterized.
In the following chapter, the novel quaternary gallium antimony chloride oxide Ga_2SbCl_7O is presented.

* The calculation of the Raman spectra was performed by Dr. Gregor Schnakenburg.

2.15.1 Synthesis and EDX Analysis of Ga_2SbCl_7O

1.1 mg (0.009 mmol) tellurium, 21.9 mg (0.18 mmol) antimony, 27.4 mg (0.12 mmol) antimony trichloride, 174.0 mg (0.99 mmol) gallium trichloride and 34.9 (0.12 mmol) antimony trioxide were filled in a glass ampoule under argon atmosphere. The ampoule was evacuated to a pressure of $6 \cdot 10^{-2}$ mbar, flame sealed and heated to 50°C. After 19 days colourless crystals are visible in in a yellow-brownish reaction melt (Fig. 2.15.1.1). After opening the ampoule in the glove box, the crystals were separated mechanically from the solidified melt and cleaned from adherences by immersion in perfluorinated polyether.

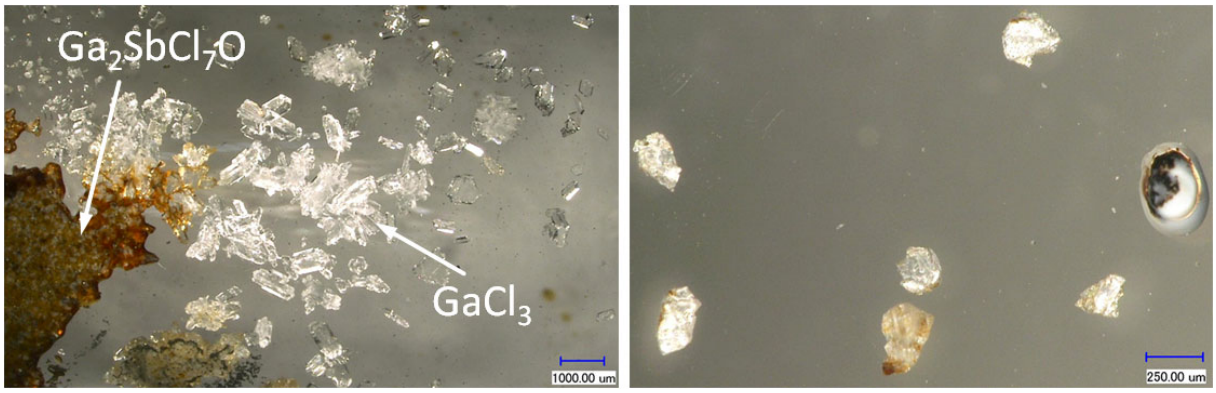

Fig. 2.15.1.1 Left: Photo taken of the reaction ampoule: Crystals of Ga_2SbCl_7O in the reaction melt (left) and $GaCl_3$ deposited outside the melt (right).
Right: Separated crystals of Ga_2SbCl_7O and immersed in perfluorinated polyether.

Due to their extreme sensitivity the prepared crystals for the EDX analysis decomposed during the transfer from the glove box to the vacuum chamber of the scanning electron microscope probably by hydrolysis. The crystals have formed to a foam-shaped material, but could be examined in this state. Ten Ga_2SbCl_7O samples (compare Fig. 2.15.1.1 (right)) were examined by area measurements, respectively. The analysis could only proove the presence of the elements Sb, Ga and Cl. The oxygen content could not be quantified due to the low energy of the respective X-ray emission line. A important result is the fact that no traces of Te were found (Tab. 2.15.1.2).

Tab. 2.15.1.2 Elemental composition of Ga_2SbCl_7O in atom-%. Standard deviations given in brackets refer to the last significant digit.

	Ga	Sb	Cl	O
Found	29(2)	6.3(6)	63(1)	/
Calculated	18.2	9.1	63.6	9.1

2.15.2 The Reaction Leading to Ga_2SbCl_7O

The primary intention of the preparative work was to synthesize mixed Sb/Te polycationic clusters with a $[Ga_2Cl_6O]^{2-}$ anion. Sb_2O_3 was attributed the role of an adjuvant, since it was found empirically, that several added compounds, mainly monovalent metal halides and some oxides, influence the composition of the reaction medium and the product formation without being incorporated in the

final products. The pentele oxides Pn_2O_3 (Pn = As, Sb) and TeO_3 were used in former syntheses to generate the oxo hexachlorido digallate anion (chapter 2.13, 2.14). $GaCl_3$ is generally used in large excess to serve as solvent and as the source for chloridogallates, which act as weakly coordinating anions for the expected positively charged clusters. The above mentioned composition of the starting materials yielded Ga_2SbCl_7O as the only product in high yield and no other crystalline byproducts were found in a yellowish, orange melt. For the formation of Ga_2SbCl_7O the following tentative reaction equation may be set up:

$$SbCl_3 + 6\ GaCl_3 + Sb_2O_3 \longrightarrow 3\ Ga_2SbCl_7O$$

However, reactions carried out according to this equation do not yield the title compound and neither using $GaCl_3$, $SbCl_3$ and Sb_2O_3 nor the reaction of SbOCl with two equivalents $GaCl_3$ carried out under various conditions was successful. Ga_2SbCl_7O is formed from elemental antimony, Sb_2O_3, $GaCl_3$, and tellurium. All attempts to obtain Ga_2SbCl_7O without the presence of elemental tellurium or using different oxides like TeO_2, TeO_3, Ga_2O_3, Sb_2O_5 and Sb_3O_4Cl failed. The presence of tellurium in the reaction mixture is required to cause the dissolution of antimony in the melt. Without tellurium, the used elemental antimony remains undissolved in the melt even after months of annealing. The required amount of Te is low. Even with amounts as small as 1 mg the reaction was successful, indicating that tellurium has a catalytic role. Moreover, using a small amount of Te is advantageous, since larger amounts of Te lead to a dark coloration of the reaction melt. With smaller amounts of Te the reaction melt remains yellowish and the colourless crystals of Ga_2SbCl_7O are better visible. The difficult visual distinction of crystals of Ga_2SbCl_7O from those of $GaCl_3$ is a basic obstacle of the melt approach synthesis.

2.15.3 Crystal Structure of Ga_2SbCl_7O

The crystallographic data are given in Tab. A 5.2.23.

The crystal structure of Ga_2SbCl_7O consists of discrete molecules (Fig. 2.15.3.1). A crystallographic mirror plane bisects the molecule with the atoms Sb, O, and Cl1 located in the plane, giving the molecule C_s point symmetry.

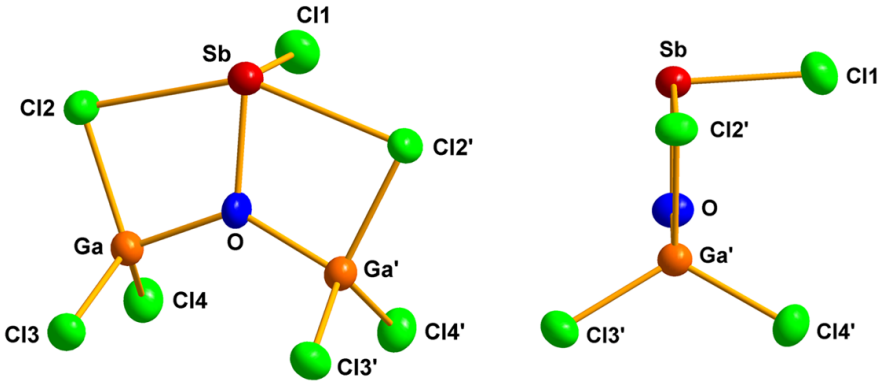

Fig. 2.15.3.1 The Ga_2SbCl_7O molecule shown in two perspectives, perpendicular and parallel to the main molecular plane. The atoms are represented by thermal ellipsoids scaled to include a probability of 70 %. The symmetry code *I* refers to atoms generated by the mirror plane with coordinates *x*, 1.5-*y*, *z*.

Perpendicular to the mirror plane another plane in the molecule is present. The six atoms, Ga, Ga^{I}, Cl2, $Cl2^{I}$, Sb, and O are located in planar arrangement with the largest deviation of an atom position to the least squares plane of less than 0.03 Å. The Ga atoms are in distorted tetrahedral coordination forming a bent Ga–O–Ga bridge with Ga–O bonds of 1.888(3) Å and a Ga–O–Ga^{I} angle of 131.3(4)°. The Sb atom has an irregular coordination by one oxygen atom (Sb–O 2.012(8) Å) and one terminal Cl atom (Sb–Cl1 2.309(3) Å) in the first sphere and two further Cl atoms (Sb–Cl2 = Sb–$Cl2^{I}$ 2.709(3) Å) in the second sphere. Obviously, a distinct lone pair effect at a trivalent Sb atom is present. The Ga–Cl2 (2.232(2) Å) and Sb–Cl2 (2.709(3) Å) bonds are elongated, typical for bridging chlorine atom as present in $[Ga_2Cl_7]^-$.[51] In binuclear chlorido antimonates(III), however, the bridging Sb–Cl–Sb bonds are generally spread over a large distance regime between 2.5 and 3.3 Å and thus significantly longer than found in Ga_2SbCl_7O.[127] The central oxygen atom is in trigonal-planar coordination by two Ga atoms and the Sb atom.

An individual SbOCl molecule may be identified as a building unit within the Ga_2SbCl_7O molecule, which can therefore be understood as a complex formed between two units of gallium trichloride and one unit of molecular antimony oxychloride, according to the alternative formula SbOCl · 2 $GaCl_3$. Monomeric SbOCl has been observed so far only as a gas phase species. It was generated in a Knudsen cell by reaction of gaseous $SbCl_3$ with oxygen over metallic silver at 1313 K and subsequent mass spectrometric detection.[128,129] The central triangular [OGa_2Sb] fragment was already observed in the structure of $[(Me_3SiCH_2)_2GaOSbEt_2]_2$.[130] Generally, the trigonal-planar [M_3O] fragment with one oxygen atom coordinated by three metal atoms is known for several main group and transition metals. Examples are the ions $[(SbMe_2)_3O]^+$ [131], $[(SnMe_3)_3O]^+$ [132] and $[\{O(AlCl_2)(AlCl_3)\}_2]^{2-}$ [133]. Commonly known are the oxygen centered trinuclear transition metals acetates of the type $[M_3O(acetate)_6]^+$ for M = Fe, Ru, Cr.[134] For Au [135, 136] and Hg [137, 138] the respective [M_3O] fragment is known to occur in planar arrangement and in trigonal-pyramidal shape.

Following the Lewis formalism and interpreting all intramolecular bonds as two-center two-electron bonds an alternating sequence of formal charges is obtained along the perimeter of the outer six membered ring of the molecule (Fig. 2.15.3.2). The formal positive charge at the oxygen atom is stabilized by three formally negative charged coordinating atoms.

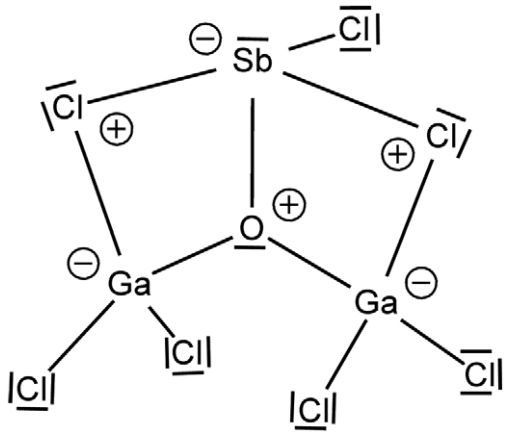

Fig. 2.15.3.2 Lewis valence formula of Ga_2SbCl_7O with alternating formal charges within the six-membered ring.

The calculated gas-phase structure of Ga_2SbCl_7O (B3LYP/def2-TZVPP) compares well the crystal structure, as evidenced for example by comparison of the calculated Sb–O bond length of 2.0147 Å with the experimentally determined of 2.012(8) Å.

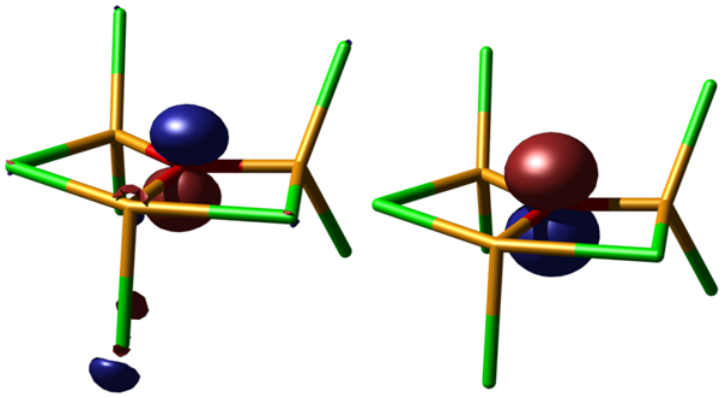

Fig. 2.15.3.3 Kohn-Sham orbital of the oxygen centered lone pair (HOMO-19, left) and its corresponding natural bond orbital (right), both scaled at an isosurface value of 0.08e·bohr^{-3}*.

The low lying (-12.1 eV) molecular orbital (HOMO-19) comprising the lone pair at the oxygen atom shows almost no delocalisation and no steric effect (Fig. 2.16.3.3 left), which is further confirmed by a natural bond orbital analysis of the wave function, which reveals a) a low amount (0.57 %) of electrons in non-Lewis orbitals typical for a highly localised structure, b) an almost fully occupied (1.94e) lone pair NBO at the oxygen atom emerging from a pure p orbital of oxygen (Fig. 2.15.3.3 right) and c) highly localised two-centre two-electron bonds between Sb–O and Ga–O (occpuancies always larger the 1.96 e). This proves that the Lewis formula depicted in Fig. 2.16.3.2 best describes the system. Due to the high polarity of the covalent bonds between the electropositive Ga and Sb atoms and the electronegative oxygen atom the calculated natural partial charge at O remains negative (–1.36e).

The arrangement of the molecules in the unit cell corresponds to a simple hexagonal closest packing with the sequence ABAB. The layers of molecules are stacked perpendicular to the crystallographic *b* axis (Fig. 2.15.3.4).

* The calculation was performend and the figure drawn by Dr. Gregor Schnakenburg.

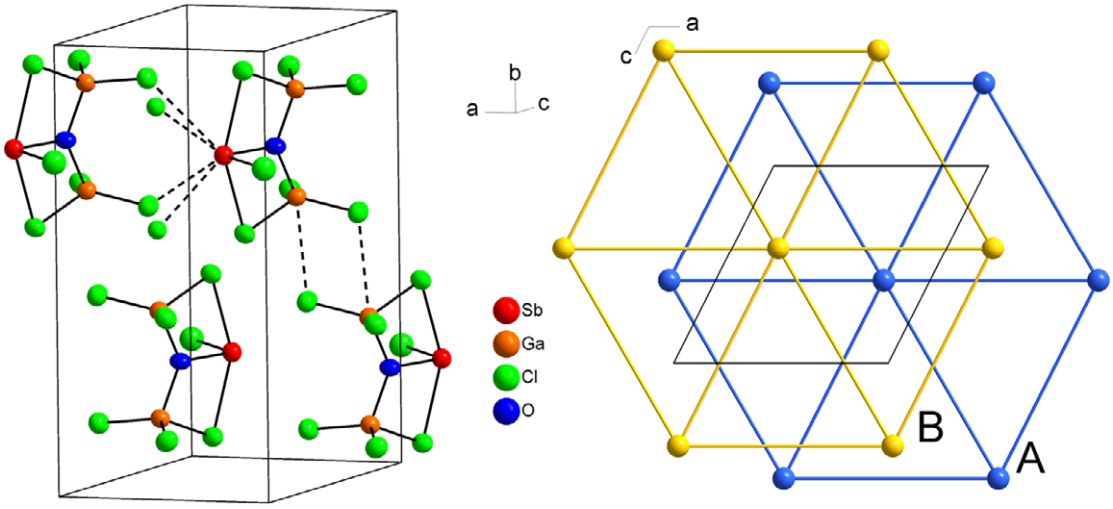

Fig. 2.15.3.4 The unit cell of the crystal structure of Ga_2SbCl_7O. The atoms are represented by thermal ellipsoids scaled to include a probability of 70 % (left). The dotted lines indicate the intermolecular contacts, which are shorter than the van der Waals radii. In the figure on the right, the packing of the molecules is depicted in a view along the *b* axis. The individual molecules have been reduced to spheres at the points of the respective centres of gravity. The molecules form triangular planar nets parallel to the *a*-*c* plane and are stacked in the motif of a hexagonal closest packing with the layer sequence ABAB…

The lattice constants of the actual monoclinic cell reveal the close relation to a hexagonal cell with axes *a* and *c* of almost equal lengths and a monoclinic angle deviating from 120° only by 3°. There are some intermolecular interactions present, which are significantly shorter than the sum of the van der Waals radii of Ga and Cl (3.6 Å) and of Sb and Cl (3.7 Å). Within the layers, each Sb atoms has four contacts to Cl atoms of two neighbouring molecules. The Ga–Cl···Sb bridging bonds lengths amount to Sb···Cl3' 3.355(2) and Sb···Cl4'' 3.703(2) Å. The shorter one of these contacts is close to a normal bridging Sb–Cl–Sb bond [127]. In the stacking direction, the molecules are connected via weak Ga···Cl bonds (Ga···Cl4' 3.501(2) Å) forming four-membered Ga_2Cl_2 rings.

2.16 The Cube Shaped Clusters $(Bi_4Ch_4)^{3+}$ (Ch = Te, Se) and the Novel Anion $[SeGa_3Cl_9]^{2-}$

During the efforts to synthesize the hypothetic compound $(Bi_3Te_4)[GaCl_4]$ with a double ladder shaped $(Bi_3Te_4^+)_n$ cationic chain in a sodium tetrachlorido gallate melt, only $(Bi_2Te_2)Cl[GaCl_4]$ with a simple ladder shaped BiTe chain was obtained (chapter 2.9). The corresponding experiment with selenium led to $(Bi_4Se_4)[GaCl_4]_4$, and using antimony and tellurium gives $(Sb_3Te_4)[GaCl_4]$ (chapter 2.9) in an analogous reaction. Antimony is in octahedral coordination and connects two double ladder shaped SbTe chains. The same situation for antimony is present in the clusters $(Sb_7Te_8)^{5+}$ (chapter 2.1), $(Sb_7Se_8)^{5+}$, $(Sb_7Se_8Cl_2)^{3+}$ and $(Sb_7S_8Cl_2)^{5+}$ (chapter 2.2). The cube shaped clusters $(Pn_4Ch_4)^{4+}$ are existent for Bi/Te, Bi/Se, Bi/S [29,30] as well as for Sb/Te and Sb/Se (chapter 2.5). It had never been tried to synthesize a $(Sb_4S_4)^{4+}$ cluster. $(Sb_7Te_8)^{5+}$, $(Sb_7Se_8)^{5+}$, $(Sb_7S_8Cl_2)^{5+}$, $(Sb_4Te_4)^{4+}$, $(Sb_4Se_4)^{4+}$, $(Bi_4Se_4)^{4+}$ and $(Bi_4S_4)^{4+}$ can be obtained with copper(I) chloride as an additive to the gallium trichloride melt. Furthermore, the chlorido gallate salts of $(Bi_4Te_4)^{4+}$ and $(Bi_4Se_4)^{4+}$ are accessible in sodium gallate melts (compare Tab. A 5.8.5.1).

Although bismuth did not seem to be able to be coordinated octahedrally by tellurium, an experiment was performed to synthesize a hypothetical $(Bi_7Te_8)^{5+}$ cluster from a $Cu[GaCl_4]$ melt. As a result, $(Bi_4Te_4)[GaCl_4]_2[Ga_2Cl_7]$ crystallized.
In chapter 2.1 it was reported, that InCl and $InCl_2$ led to $(Sb_7Te_8)[GaCl_4]_3[Ga_2Cl_7]_2$. An analogous synthesis with bismuth and selenium was performed and PPh_4Cl was added to synthesize an hypothetical $(Bi_7Se_8)^{5+}$ cluster. The synthesis led to various compounds with incorporated $(Bi_4Se_4)^{4+}$, $(Bi_4Se_4)^{3+}$ and Bi_5^{3+} clusters.

2.16.1 Syntheses and EDX Analyses

$(Bi_4Te_4)[GaCl_4]_2[Ga_2Cl_7]$

Starting from elemental bismuth and tellurium did not succeed in the formation of crystalline products. Thus, 288.3 mg (0.36 mmol) bismuth telluride, 50.5 mg (0.16 mmol) bismuth trichloride, 174.3 mg gallium trichloride and 17.8 mg (0.18 mmol) copper(I) chloride were annealed in a vacuum ampoule to 100 °C. After 10 days black crystals were obtained in a sticky black melt. Smaller crystals showed the actual orange color of the compound in transmitted light.

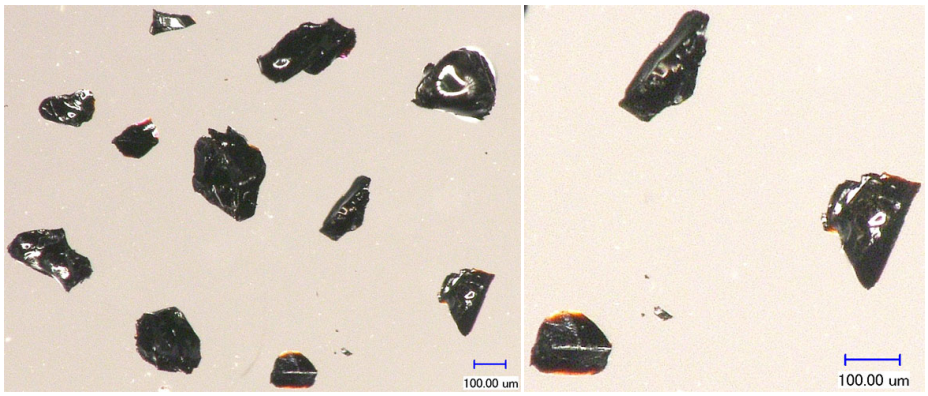

Fig. 2.16.1.1 Crystals of $(Bi_4Te_4)[GaCl_4]_2[Ga_2Cl_7]$ immersed in perfluorinated polyether.

The crystals, which were examined in the EDX analysis (Tab. 2.16.1.1), were collected from the edges of the reaction melt. They had clean and smooth surfaces. The analysis revealed a too high content of Ga, which can not be explained. In general, a too high Ga content was found rather often in measurements performed in this work and seems to be a systematic problem. The results for Bi, Te and Cl are close to the calculated contents. The analysis is in acceptable agreement with the sum formula.

A tentative reaction equation is:

$$4\ Bi_2Te_3 + 4\ BiCl_3 + 12\ GaCl_3 + 3\ CuCl \rightarrow 3\ (Bi_4Te_4)[GaCl_4]_2[Ga_2Cl_7] + 3\ CuCl_2$$

The EDX analysis reveals an accurate agreement with the sum formula besides a result for Ga, which is slightly above the expectation.

Tab. 2.16.1.1 Elemental composition of $(Bi_4Te_4)[GaCl_4]_2[Ga_2Cl_7]$ in atom-% and the Bi : Te ratio. Standard deviations given in brackets refer to the last significant digit.

$(Bi_4Te_4)[GaCl_4]_2[Ga_2Cl_7]$	Bi	Te	Ga	Cl	Bi : Te
Found	13.8(3)	14.0(3)	17.9(4)	54.1(3)	1 : 1.01
Calculated	14.8	14.8	14.8	55.6	1 : 1.00

$(Bi_4Se_4)[GaCl_4][SeGa_3Cl_9]$

28.4 mg (0.36 mmol) selenium, 50.5 mg (0.24 mmol) bismuth, 37.8 mg (0.12 mmol) bismuth trichloride, 174.0 mg (0.99 mmol) gallium trichloride, 60.0 mg tetraphenylphosphonium chloride and 33.4 (0.22 mmol) indium(I) chloride were filled in a glass ampoule under argon atmosphere. The ampoule was evacuated and flame sealed. After annealing at 100 °C for two to three weeks, several crystalline products could be obtained. $(Bi_4Se_4)[GaCl_4][SeGa_3Cl_9]$ crystallized as very small black needles. They were found mainly at the inner wall of the ampoule outside the reaction melt in a colourless solution, which was presumed to be $PPh_4[GaCl_4]$. The specific way of formation of the crystals indicates a formation from the gas phase or a diffusion within the reaction melt in $PPh_4[GaCl_4]$ along the wall of the ampoule and final crystallization. As further products, $Bi_5[GaCl_4]_3$[73] as red, square, plate-like crystals and $(Bi_4Se_4)[GaCl_4]_4$[30] as yellow, trigonal pyramidal crystals were found in several experiments and identified by unt cell determinations (Fig. 2.16.1.2).

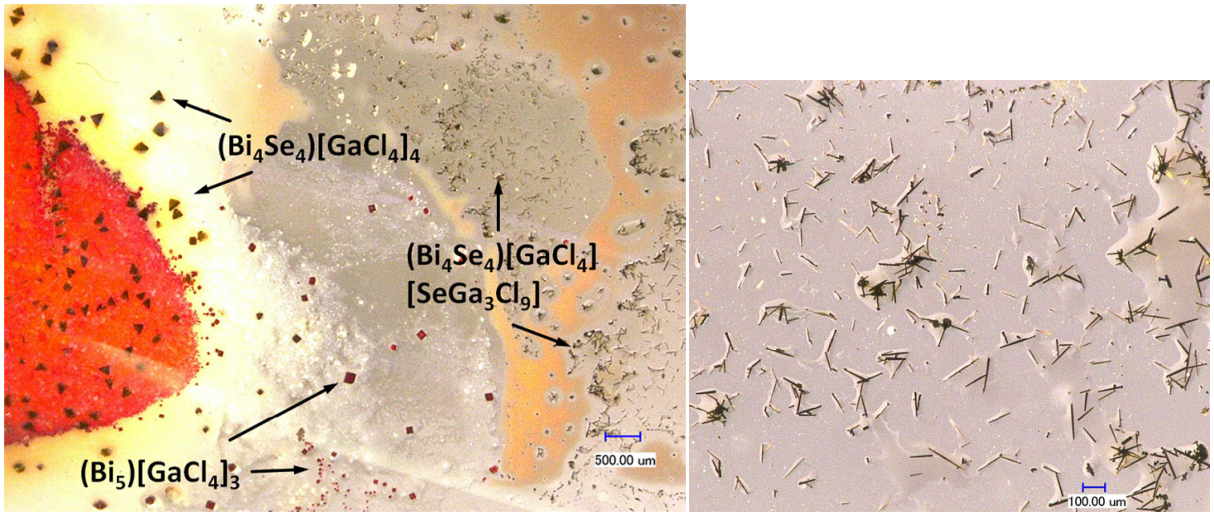

Fig. 2.16.1.2 Crystals of $(Bi_4Se_4)[GaCl_4][SeGa_3Cl_9]$ and the byproducts $(Bi_5)[GaCl_4]_3$ and $(Bi_4Se_4)[GaCl_4]_4$ in the reaction ampoule (left). On the right, crystals of $(Bi_4Se_4)[GaCl_4][SeGa_3Cl_9]$ are shown, exclusively.

The EDX analysis is in very good agreement with the calculated composition. Only the result for selenium comes out slightly too high, presumably due to an excess of this element on the crystal surface as found for tellurium in the case of $Ag(Sb_7Te_8)[GaCl_4]_6$ (chapter 2.1).

A tentative reaction equation is:

$$4\ Bi + 5\ Se + BiCl_3 + 4\ GaCl_3 + InCl \rightarrow (Bi_4Se_4)[GaCl_4][SeGa_3Cl_9] + InCl_3$$

Tab. 2.16.1.2 Elemental composition of $(Bi_4Se_4)[GaCl_4][SeGa_3Cl_9]$ in atom-% and the Bi : Te ratio. Standard deviations given in brackets refer to the last significant digit.

$(Bi_4Se_4)[GaCl_4][SeGa_3Cl_9]$	Bi	Se	Ga	Cl	Bi : Se
Found	14.6(3)	22.0(4)	15.1(4)	48.2(4)	1 : 1.51
Calculated	15.4	19.2	15.4	50	1 : 1.25

2.16.2 Crystal Structures of $(Bi_4Te_4)[GaCl_4]_2[Ga_2Cl_7]$ and $(Bi_4Se_4)[GaCl_4][SeGa_3Cl_9]$

$(Bi_4Te_4)[GaCl_4]_2[Ga_2Cl_7]$ crystallizes in space group *Pbca* and consists of $(Bi_4Te_4)^{3+}$ polycationic clusters and both $[GaCl_4]^-$ and $[Ga_2Cl_7]^-$ anions (Fig. 2.16.2.1). The crystallographic data are shown in table A 5.2.24.

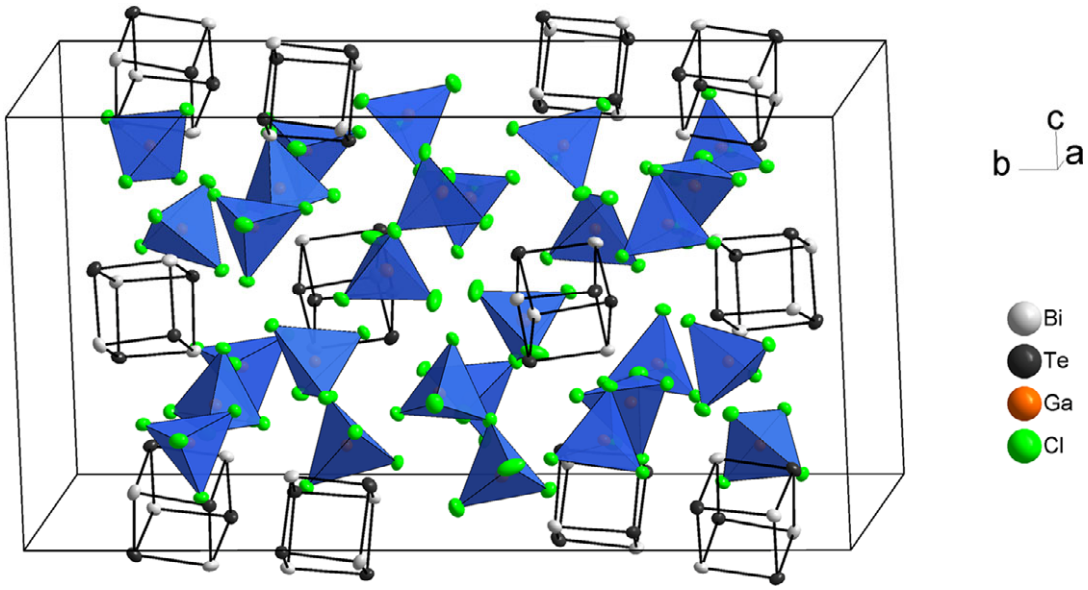

Fig. 2.16.2.1 The unit cell of the structure of $(Bi_4Te_4)[GaCl_4]_2[Ga_2Cl_7]$. The chlorido gallate anions are represented by discrete tetrahedra and double tetrahedra. The atoms are represented by thermal ellipsoids scaled to include a probability of 70 %.

The bond and angle parameters of the anions are in line with those found in $K[GaCl_4]$[50] and $K[Ga_2Cl_7]$.[51] Ga–Cl bond lenghts range between 2.122(4) and 2.317(4) Å, bond angles between 98.5(2) and 115.9(2)°.

The cube shaped cluster $(Bi_4Te_4)^{3+}$ has a lower positive charge compared to $(Bi_4Te_4)^{4+}$ [29] . Bi–Te bond lenghts of 2.945(1) to 3.001(1) in $(Bi_4Te_4)^{3+}$ correspond to the bond lenghts of 2.949(1) to 3.017(1) in $(Bi_4Te_4)^{4+}$. The angles within the cluster range from 85.13(3) to 94.39(3)° and show a slight stronger distortion compared to $(Bi_4Te_4)^{4+}$ (87.70(2) - 92.25(1)), which was confirmed by DFT calculations.[139]

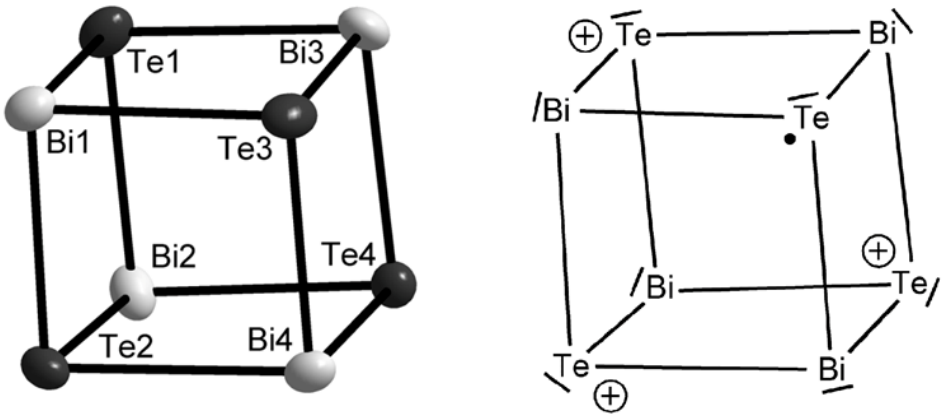

Fig. 2.16.2.2 The $(Bi_4Te_4)^{3+}$ cluster radical (left) and a possible Lewis valence formula (right). The Lewis formula of the $(Bi_4Se_4)^{3+}$ is analogous.

The coordination of the Bi and Te atoms by surrounding Cl atoms (A 5.6.14) is slightly weaker compared to $(Bi_4Te_4)^{4+}$, which is expected due to the lower positive charge of $(Bi_4Te_4)^{3+}$. Bi···Cl interactions start at 3.183(3) Å (3.05 Å in $(Bi_4Te_4)^{4+}$) and show an average length of 3.465 Å. Analysis of the Te···Cl interactions show one remarkable short contact of 3.543(4) Å (Te2···Cl11), but generally start at 3.702(3) Å (3.67 Å in $(Bi_4Te_4)^{4+}$) with an average of 3.829 Å (Tab. A 5.5.15). The positive charge is mainly localized on the Bi atoms.

$(Bi_4Se_4)[GaCl_4][SeGa_3Cl_9]$ crystallizes in the azentric space group *Cc* with a monoclinic angle of 89.961(1)°, which makes the crystal susceptible for twinning. No orthorhombic unit cell was found. Generally, crystals of this compound are weakly diffracting due to their small size. To obtain a reliable diffraction data set, a bigger crystal was chosen for measurement, which was twinned in a non-merohedral way by a 180° rotation along the direct *a* axis.

The obtained unit cell is in line with the unit cells, which had been found in former unit cell determinations of this compound. The unit cell relationship of the two twin components in direct space is $a_{TWIN} = a$, $b_{TWIN} = -b$ and $c_{TWIN} = -c$, in reciprocal space $a^*_{TWIN} = a^*$, $b^*_{TWIN} = -b^*$ and $c^*_{TWIN} = -c^*$ (Fig. 2.2.3.6) with the superposition matrix hkl_{TWIN} = (1 0 0, 0 -1 0, 0 0 -1). The structure refinement was carried out using the complete dataset and applying the twin matrix, which led to acceptable results (compare Tab. A 5.2.24). The non-centrosymmetry was ensured by a Flack *x* parameter of 0.132(9). Fig. 2.16.2.3 shows a pseudo hexagonality along the *c** axis.

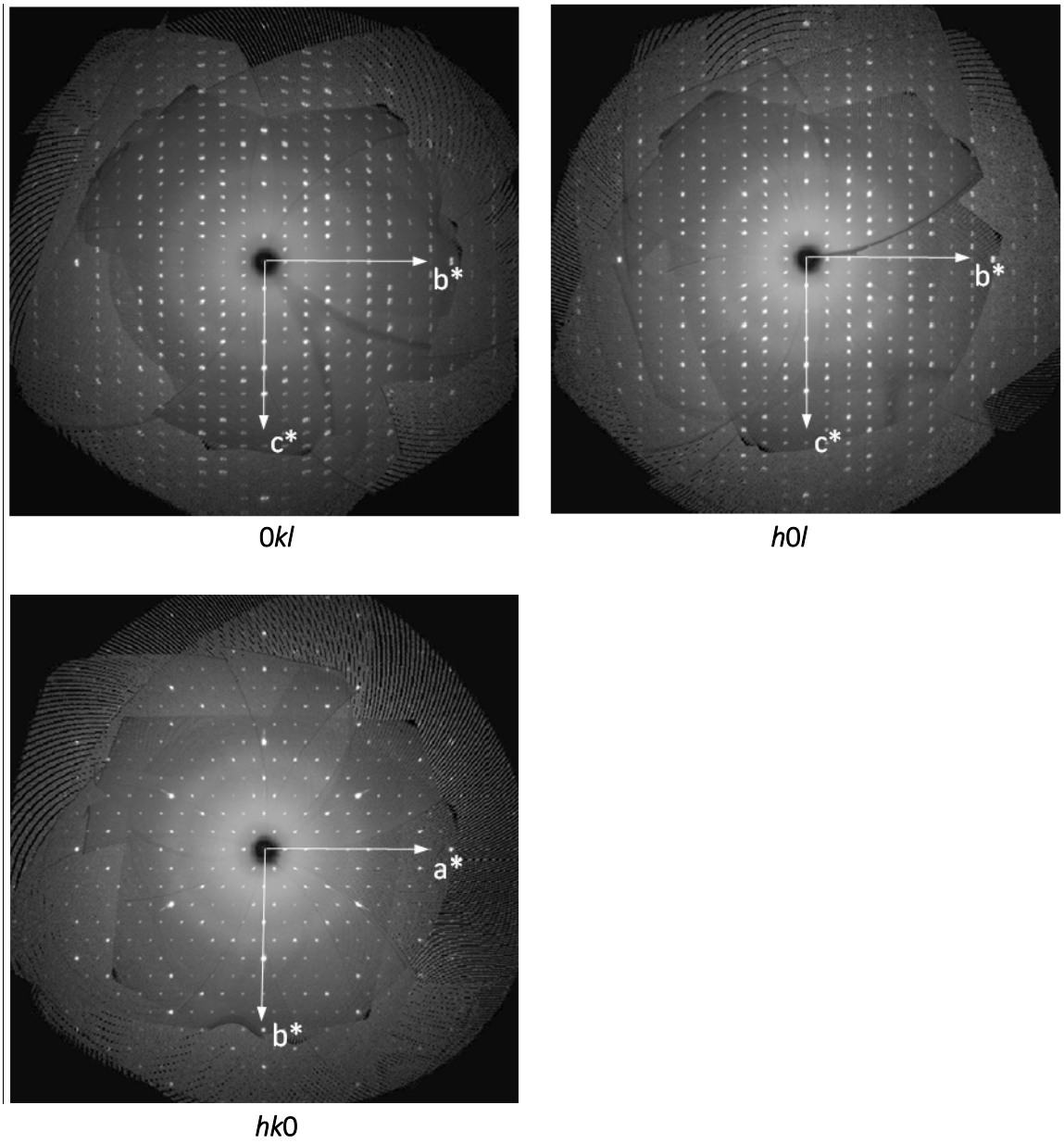

Fig. 2.16.2.3 Simulated precession images, derived from the area detector data, of three layers of $(Bi_4Se_4)[GaCl_4][SeGa_3Cl_9]$ at 123 K.

$(Bi_4Se_4)[GaCl_4][SeGa_3Cl_9]$ consists of $(Bi_4Se_4)^{3+}$ clusters analogous to $(Bi_4Te_4)^{3+}$ and both $[GaCl_4]^-$ and novel $[SeGa_3Cl_9]^{2-}$ anions. In contrast to the slightly higher distortion of the $(Bi_4Te_4)^{3+}$ cluster compared to its four-fold positively charged congener, the $(Bi_4Se_4)^{3+}$ cluster is more regular compared to $(Bi_4Se_4)^{4+}$. In the latter one, Bi–Se bonds range between 2.759(1) and 2.821(1) Å. In the three-fold positively charged congener the corresponding bond lengths are uniform between 2.772(4) and 2.790(5) Å. Bi–Se–Bi angles between 89.29(1) and 93.65(1)° and Se–Bi–Se angles between 86.15(1) and 90.60(1)° are found in $(Bi_4Se_4)^{4+}$. Bi–Se–Bi angles in $(Bi_4Se_4)^{3+}$ range between 90.7(2)° and 91.6(1)°. The Se–Bi–Se angles are found in the range of 88.5 - 89.2(2)°. The reduction of the charge seems to symmetrize the cluster in reverse way to its tellurium congener. The distances to Cl atoms of the coordinating anions (Fig. A 5.6.16) are short for Bi–Cl with 3.18(1) - 4.10(2) Å and long for Se–Cl with 3.57(2) - 3.80(1) Å. Additionally, a remakable short Bi–Cl contact of 3.07(1) Å is found for Bi3–Cl11. The associated $[GaCl_4]^-$ anion bridges between the clusters comparable to the Cl^- anions in the

structure of $(Bi_2Se_2)Cl[GaCl_4]$ with a Bi–Cl distance of 3.0875(5) (chapter 2.9). The crystal structure of $(Bi_4Se_4)[GaCl_4][SeGa_3Cl_9]$ exhibits a pseudo-hexagonal symmetry (Fig. 2.16.2.4).

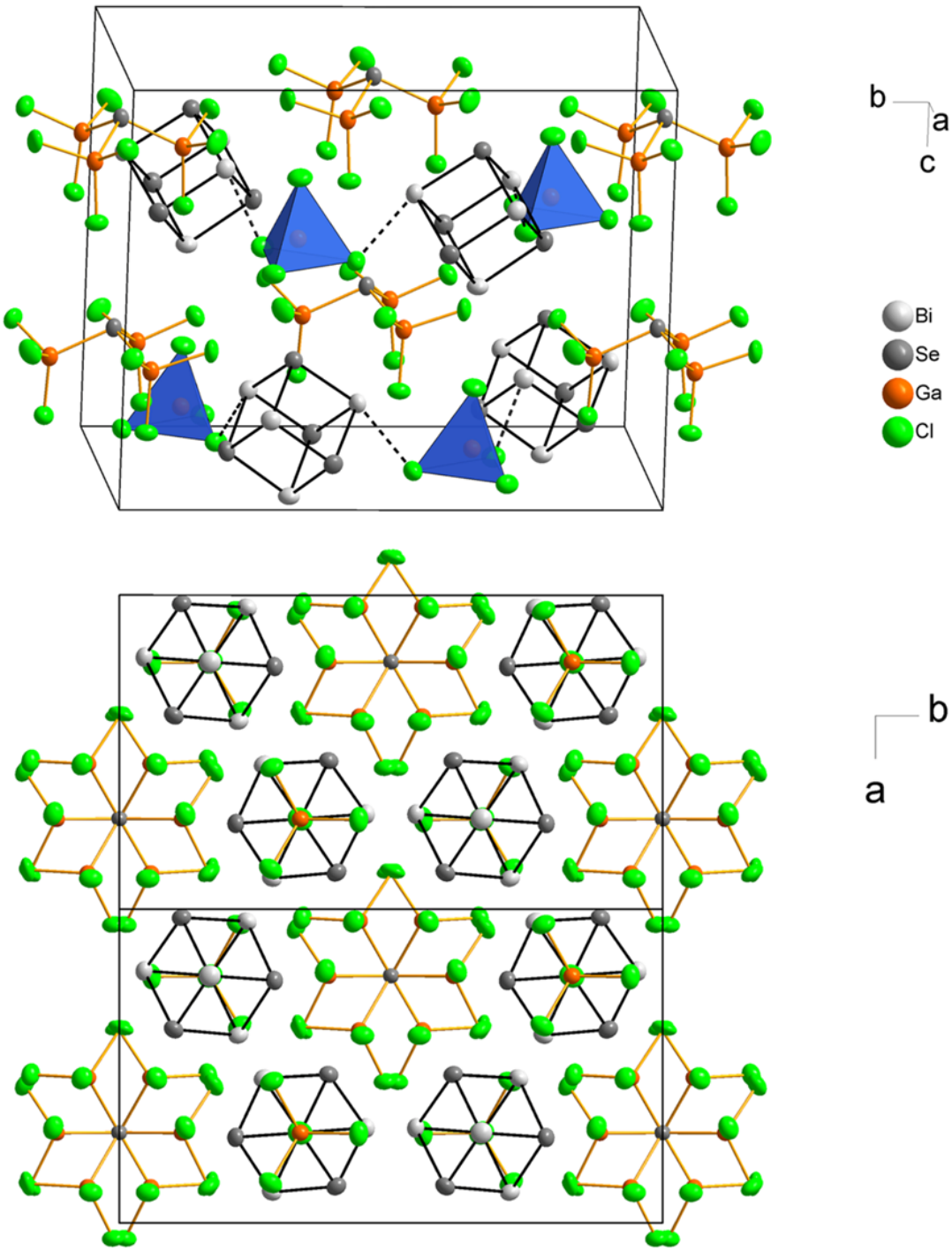

Fig. 2.16.2.4 The unit cell of the structure of $(Bi_4Se_4)[GaCl_4][SeGa_3Cl_9]$ in two different viewing directions. The chlorido gallate anions are represented by discrete tetrahedra (top). The short Bi3-Cl11 contact is marked with dashed lines. The view along the *c*-axis shows the pseudo-hexagonal symmetry of the structure. The atoms are represented by thermal ellipsoids scaled to include a probability of 70 %.

The structural parameters of the $[GaCl_4]^-$ anion reveal Ga–Cl bond lengths between 2.16(1) and 2.17(2) Å and Cl–Ga–Cl angles close to the ideal tetrahedral angle of 109.5° (107.7(5) - 111.3(4)°).

The complex anion $[SeGa_3Cl_9]^{2-}$ represents a novel tris-{trichlorido gallium}-selenide anion. A selenium atom is coordinated in trigonal pyramidal way be three $GaCl_3$ units.

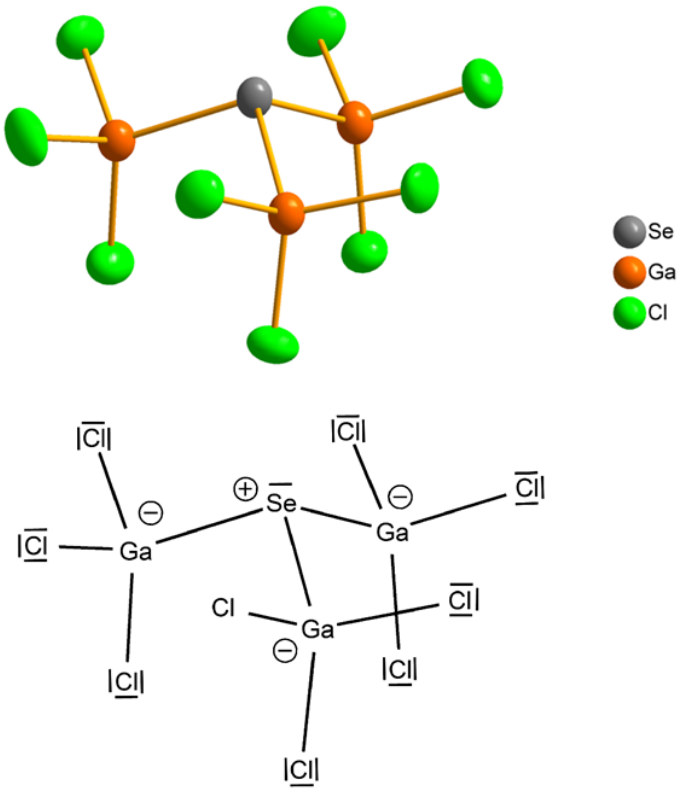

Fig. 2.16.2.5 The $[SeGa_3Cl_9]^{2-}$ anion in the structure of $(Bi_4Se_4)[GaCl_4][SeGa_3Cl_9]$ (top). The atoms are represented by thermal ellipsoids scaled to include a probability of 70 %. On bottom the corresponding Lewis formula is shown.

Ga–Se bond lengths range between 2.412(5) and 4.417(6) Å and are slightly shorter than those found in the different modifications of GaSe[140, 141, 142] and are in agreement with the average Ga–Se bond lengths in Ga_2Se_3[143]. Ga–Cl bond lengths are in expected ranges between 2.13(1) and 2.19(2) compared to $[GaCl_4]^-$.[50] The trigonal pyramidal coordination of Se by GaR_3 units (R = Me, Et) is already known from Se/Ga cubane shaped molecules like present in $[(Me_2EtC)Ga(\mu_3\text{-}Se)]_4$[144] with relatively small Ga–Se–Ga angles of 80.4(1)° - 80.9(1)° due to the cuboidal structure. In $[SeGa_3Cl_9]^{2-}$ these angles are larger with 103.0(2)° - 103.2(2)°.

2.16.3 Analysis of the Electronic Structure of the $(Bi_4Te_4)^{3+}$ Cluster

$(Bi_4Te_4)^{3+}$ and $(Bi_4Se_4)^{3+}$ are radicals. One additional electron is delocalized in the clusters consisting of 2e-2c bonds (Fig. 2.16.2.2). However, a diamagnetic susceptibility was found in a magnetic measurement of crystals of $(Bi_4Te_4)[GaCl_4]_2[Ga_2Cl_7]$ (Fig. 2.16.1.1) and an EPR analysis did not reveal any signal. Only noise was detected (Fig. 2.16.3.1).

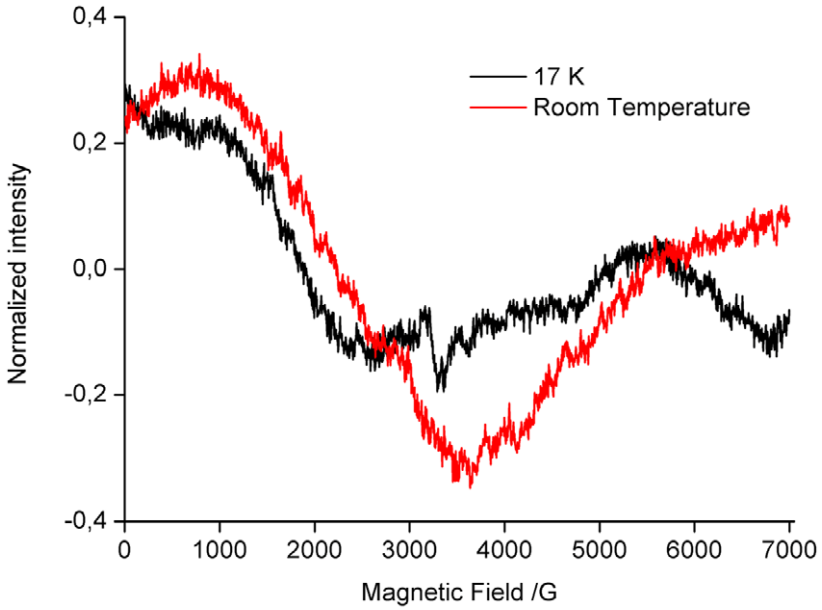

Fig. 2.16.3.1 Continuous wave X-band EPR spectra of crystals of $(Bi_4Te_4)[GaCl_4]_2[Ga_2Cl_7]$ (black) at 17 K and room temperature (red). Both spectra were recorded with 20 mM microwave power and 2 G modulation amplitude.

One possible reason could be a not sufficient microwave energy to stimulate the sample.
Another more probable reason for the EPR silence is a fast spin-lattice relaxation as a result of large spin-orbit coupling, [145] which increases from As^+ ($4p^2$) to Bi^+ ($6p^2$).[146] EPR examinination of bismuthinyl radicals in solution did not reveal any EPR signal between 298 and 114 K. In contrast, Sb^+ shows a very broad and weak signal.[145]

To get insight in the electronical structure of the $(Bi_4Te_4)^{3+}$ cluster, a molecular orbital scheme was calculated.

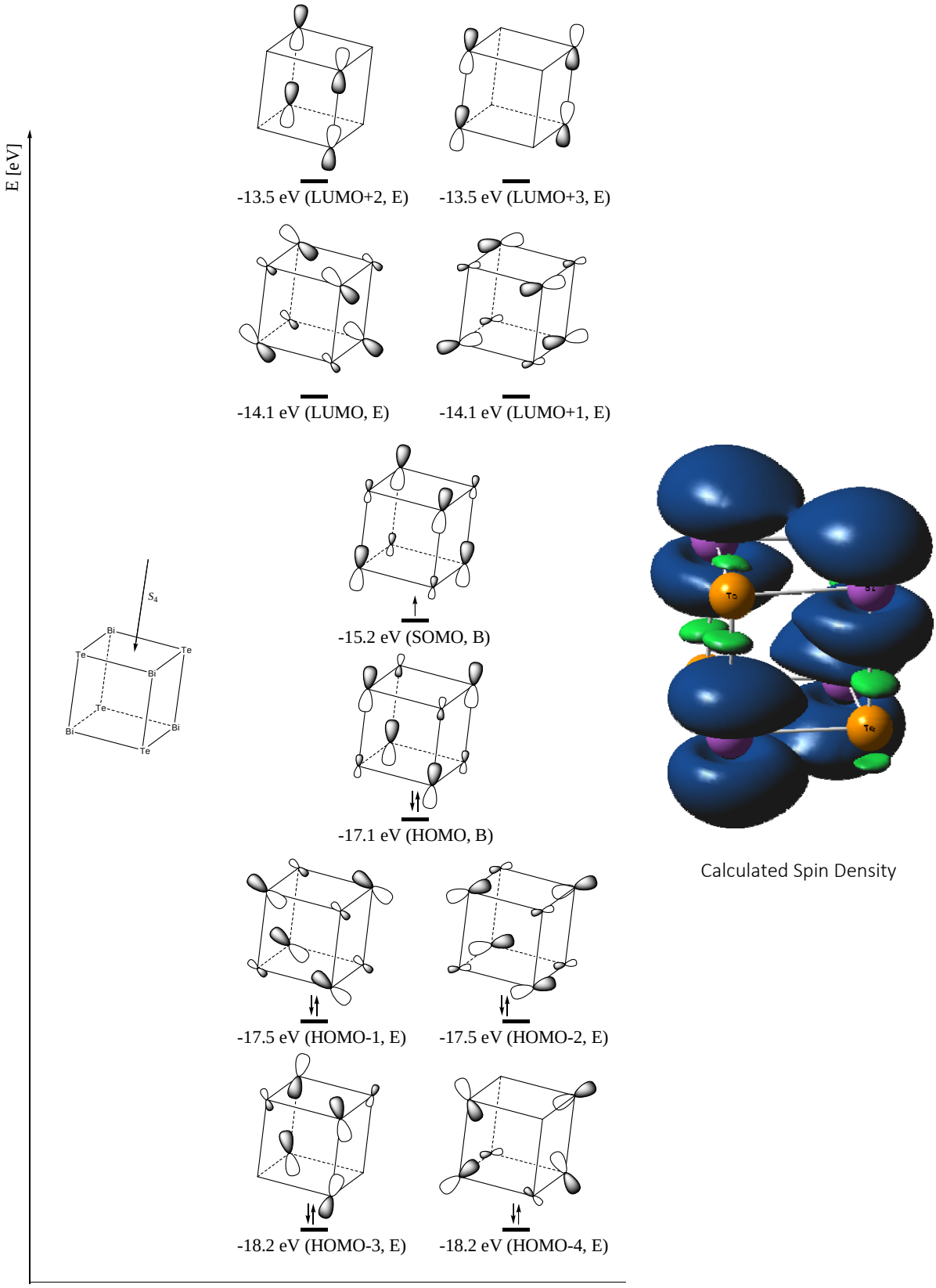

Fig. 2.16.3.2 MO scheme of the $(Bi_4Te_4)^{3+}$ cluster in the HOMO-LUMO region. Energies are given in electron volt. The symmetry races given in parentheses correspond to the S4 point group of the cluster. On the right the calculated spin density is illustrated, scaled at an isosurface value of 0.0008e·bohr^{-3}.*

* The theoretical treatment of the $(Bi_4Te_4)^{3+}$ cluster was performed by Dr. Gregor Schnakenburg.

Density functional calculations of the $(Bi_4Te_4)^{3+}$ polycationic cluster at the B3LYP/DEF2-TZVPPD level of theory corroborate the picture stated above. According to NBO calculations, the symmetry equivalent Bi atoms carry a positive charge of +0.9e, whereas the Te atoms carry a slightly negative partial charge of -0.15e. All Bi–Te bonds are strongly polarized towards the tellurium atoms (ca. 68 vs 32 %) and are build up from almost pure *p* atomic orbitals. The high occupancy of all Natural Bond Orbitals (>0.995 e per spin and orbital) and the low amount of non-Lewis electron density show the electron precise set-up of $(Bi_4Te_4)^{3+}$, where each atom carries a lone pair of electrons in a *s* atomic orbital and participates in three 2c-2e bonds to the adjacent atoms. The remaining electron resides in the singly occupied molecular orbital (SOMO). This orbital comprises the *pz*-orbitals of Bi in a constructive overlap within each of the planes orthogonal to the *S*4 symmetry axis, but destructive overlap between these two planes. This explains: a) the slight elongation of the Bi–Te bonds along the symmetry axis compared to the respective other Bi–Te bonds, and b) the strong delocalization of the unpaired electron over all Bi atoms giving a rational reason for the EPR silence of $(Bi_4Te_4)[GaCl_4]_2[Ga_2Cl_7]$.

3.0 Synopsis and Perspective

Synthetic work in chloridogallate melts yielded various novel compounds comprising novel mixed polycationic clusters and molecules build of pentele and chalcogen elements. This synthetic approach generally demonstrates a very promising way to obtain such clusters. It was found empirically, that several single positively charged metal ions are incoorporated in the compounds and/or have a crucial influence on the product formation. Generally, the cations Na^+, K^+, Rb^+, Cs^+, NH_4^+, In^+, Tl^+, Cu^+ and Ag^+ could be incorporated. The cations Li^+ and Au^+ led to specific products, but they were not incorporated. The Sb/Te system shows the highest variety of polycationic clusters and related compounds in the $GaCl_3$ melt approach.

$AsCl_3$, $SbCl_3$ and $BiCl_3$ turned out as suitable oxidants. It was found by various experiments that the use of $TeCl_4$ as oxidant led to $Te_4[Ga_2Cl_7]_2$ [116], solely. Consequently, only pentele trihalides were used.

The double cube shaped clusters $(Sb_7Ch_8)^{5+}$ (Ch = Te, Se) and $(Sb_7Ch_8Cl_2)^{3+}$ (Ch = Se, S) are the most complex ones found during this work. DFT calculations show that the two individual cubes are connected by multiple-centre bonds. As the only cluster of these double cube shaped cations $(Sb_7Te_8)^{5+}$ was obtained in a variety of compounds. One the one hand it crystallizes as ordinary chloridogallate salts, on the other hand it was isolated in the compounds $M(Sb_7Te_8)[GaCl_4]_6$ (M = Na, Cu, Ag), which show interesting dynamical phase transitions and the presence of a $Cu[GaCl_4]^-$ anion. These phenomena could be clarified by temperature dependend X-ray investigations.

The cube shaped clusters $(Sb_4Ch_4)^{4+}$ (Ch = Te, Se) form a series of compounds which are isotypic to those of $(Bi_4Ch_4)^{4+}$ (Ch = Te, Se, S). No experimental hints are obtained so far for the existence of the hypothetical $(Sb_4S_4)^{4+}$ cluster.

Prismatic $(Pn_2Te_4)^{2+}$ (Pn = As, Sb) clusters were found in individual compounds as well as in a series of 11 isotypic structures, which show a remarkable statistical disorder. The presence of specific isomers could be determined by the comparison of experimental and theoretical Raman spectra. $(As_2Te_4)^{2+}$ is the first discovered As-Te cluster. Further experiments, containing both As and Sb, yielded orange crystals as well but the crystal structure determinations were not performed yet. Maybe both pentele elements are incorporated together in the $(Pn_2Te_4)^{2+}$ clusters and give more insight in the inherent disorder of this cluster type.

The missing link between cube and prism shaped clusters, namely the heptatomic $(Sb_3Te_4)^{3+}$, was discovered and confirmed by DFT calculations. Unfortunately, all attempts to obtain this cluster in higher yield were not successful.

Besides discrete polycationic clusters, a large number of cationic chains were obtained and analyzed. $(Sb_2Te_2^{+})_n$, $(Sb_2Te_2^{2+})_n$, $(Sb_3Te_4^{+})_n$, $(SbTe_4^{+})_n$, and $(Bi_2Ch_2^{2+})_n$ (Ch = Te, Se) form ladder and double ladder chains as well as chains consisting of four- and five-membered rings. The preferred formation of heteronuclear bonds locates the Sb atom in the highest coordinated position in the $(SbTe_4^{+})_n$ chain.

A novel class of compounds was accessed with the syntheses of $CuCh_4[GaCl_4]$ (Ch = Se, Te) and $Cu_2Se_7[GaCl_4]_2$. Structural motives are chains of formal neutral chalcogen atoms, which are isolated from each other or bridged by $CuGaCl_4$ units. The presence of Cu(I) was confirmed by EPR analyses.

By using different oxidic adjuvants, the oxygen bridged hexachlorido oxo digallate anion, namely $[Ga_2Cl_6O]^{2-}$, was generated and crystallized with the homonuclear Te_4^{2+} and mixed $(Pn_2Te_4)^{2+/4+}$ clusters (Pn = As, Sb). The final question about the charge of the prismatic clusters, however, could not be answered.

Ga_2SbCl_7O was found coincidentally. It is a neutral molecule and structurally related to the $[Ga_2Cl_6O]^{2-}$ anion.

Finally, two further congeners of cube shaped clusters, the $(Bi_4Te_4)^{3+}$ and $(Bi_4Te_4)^{3+}$, were isolated. They exhibit very similar structural parameters as the higher charged $(Bi_4Ch_4)^{4+}$ (Ch = Te, Se). The silent EPR spectrum of $(Bi_4Te_4)[GaCl_4]_2[Ga_2Cl_7]$ is currently not fully understood. Further experiments should target at the yet hypothetical $(Bi_4S_4)^{3+}$ cation.

During the presented work, more than 1200 experiments in ampoules were performed. All characterized compounds besides $(Sb_2Te_4)_2[Ga_2Cl_6O]_4$ (chapter 2.15) are reproducible. Some general trends regarding the adjuvants and hypothetical clusters could be discovered. Cu(I) leads to three of four double cube shaped and cube shaped clusters. Four of six cationic chains are accessible with Na^+ and melts containing Cu(II) form chalcogen chains with formal neutral atoms. Experiments containing the oxidic adjuvants Pn_2O_3, Pn_2O_5 (Pn = As, Sb) and TeO_3 lead to prismatic polycationic clusters and the $[Ga_2Cl_6O]^{2-}$ anion.

PPh_4Cl turned out as an essential adjuvant for several syntheses. Besides that, the syntheses of known products were possible at lower temperatures and in less viscous melts, which facilitated the mechanical cleaning and separation of crystals significantly.

Arsenic was never found in chains and Bi does not seem be able to be coordinated octahedrally. In all obtained clusters, the chalcogen content is higher or equal compared to the pentele content. Even no examples in the literature can be found for clusters with higher pentele contents. Attempts should be done to synthesize such clusters. A possible start could be $Sb_8[GaCl_4]_2$[69] and its' reactions with chalcogens. The dissolution of $(Sb_7Te_8)[GaCl_4]_2[Ga_2Cl_7]_3$ in $PPh_4[GaCl_4]$ and reaction with AgCl at 100 °C yields $Ag(Sb_7Te_8)[GaCl_4]_6$. The preferred formation of heteronuclear over homonuclear clusters may be a driving force for the incorporation of chalcogen atoms to the homonuclear Sb cluster.

A comparison of all compounds obtained during this work exhibits a general fact of the charges. Neutral chalcogen chains were found. Cationic chains carry a charge of +1 or maximally +2. Higher charges up to +5 can only be realized in the case of discrete clusters. The bigger the cluster, the higher the charge which can be stabilized. A conceivable reason is the saturation with negative charges around the clusters, which is realized by the weakly coordinating chloridogallate anions. For example, the relatively big clusters $(Sb_7Ch_8)^{5+}$ (Ch = Te, Se) feature 16 anions in their vicinity (Figs. 2.1.3.3 and A 5.6.6). Polymeric cations can only be stabilized in two dimensions by negative charges, which explains the maximum charge of +2.

Due to a shortage of single crystal structure determinations in the majority of cases equal stoichiometric amounts of starting materials were used. For a more detailed investigation of the reaction media, these ratios should be varied to obtain more effective reaction conditions and increase the yields of the respective syntheses (,,fine tuning"). Sparsely attempts of reprodution led to the desired products, but still result in the same quantity and species of byproducts referred to the original syntheses. It may indicate, that the pentele/chalcogen ratio is no parameter, which has an influence on the product.

In contrast, the temperature plays an important role in all performed synthesis. In general, 100 °C turned out as the most advantageous temperature. Lower and higher temperatures lowered the yields in most cases. In some synthesis, the product formation can be controlled solely by the temperature, e. g. $(Sb_4Te_4)[GaCl_4]_4$ (88 °C) and $(Sb_7Te_8)[GaCl_4]_2[Ga_2Cl_7]_3$ (100 °C).

In general, crystals formed in the melts are systematically prone to problematic growth, which results in complex twinning. Several compounds were crystallized during the work, but the structure determinations did not lead to unambigous results. Attempts of reproduction should be done in suitable solvents and the gas phase.

The attempts to synthesize the following clusters in the chloridogallate system did not succeed: $(As_2Se_2^{+})_n$, $(As_2Te_2^{+})_n$, $(As_2Se_2^{2+})_n$, $(As_2Te_2^{2+})_n$, $(As_3Se_4^{+})_n$, $(As_3Te_4^{+})_n$, $(As_3Te_4)^{3+}$, $(As_7Te_8)^{5+}$, $(Sb_2Se_2^{+})_n$, $(Sb_2Se_2^{2+})_n$, $(Bi_2Se_2^{+})_n$, $(Bi_2Te_2^{+})_n$, $(Bi_2Te_4)^{2+}$, $(Bi_3Se_4^{+})_n$, $(Bi_3Te_4^{+})_n$, $(Bi_3Se_4)^{3+}$, $(Bi_3Te_4)^{3+}$, $(Bi_7Se_8)^{5+}$, $(Bi_7Te_8)^{5+}$. The $(Sb_2Te_2^{2+})_n$ could be obtained as a iodido aluminate salt, exclusively. Experiments with the pentele - chalcogen combinations Bi/Se and Bi/Te were only carried out initially. The pentele - chalcogen combination Sb/S was tried only once and the experiment led to $(Sb_7S_8Cl_2)[GaCl_4]_3$. These three combinations and additionally As/S, Bi/S and As/Se should be investigated more detailed for the formation of polycationic clusters.

Furthermore, syntheses corresponding to the syntheses in this work should be perfomed in chlorido aluminate, bromido aluminate/gallate and iodido aluminate/gallate melts to check for the hypothetical as well as for new clusters. The different products in comparable syntheses in chlorido aluminate [31] and gallate melts as well as the first impression of iodido aluminate melts indicate for a diverse product formation depending on the melts properties. In any case, the temperature has to be considered as an important parameter since $GaCl_3$ based melts exhibit the lowest melting point of all MX_3 melts (M = Al, Ga; X = Cl, Br, I).

Other projects could be the syntheses of mixed pentele and chalcogene clusters, respectively, in the melt approach. So far, only the mixed chalcogen clusters $(Te_3Se)^{2+}$, $(Te_2Se_2)^{2+}$, $(Te_2Se_8)^{2+}$, $(Te_{4.5}Se_{5.5})^{2+}$ and $(Te_2Se_6)^{2+}$, $(Te_xSe_{6-x})^{2+}$ and $(Te_xS_{6-x})^{2+}$ are known,[118,147,148] which exhibit related structures as homonuclear chalcogen clusters and heteronuclear pentele - chalcogen clusters.

Additionally the variety of adjuvants should be expanded to higher positively charged adjuvants (alkaline earth metal halides, transition metal halides and oxides). Synthetic attempts with $CuCl_2$ and $InCl_2$ directly led to a new class of compounds and a new individual compound.

The search for polycationic clusters in the melt approach is still sparsely explored. Plenty novel compounds and clusters are waiting to be discovered and analyzed.

4.0 Literature

[1] M. H. Klaproth, P. Klinzing*, Phil. Mag.* 1798, *1*, 78.
[2] C. F. Buchholz, *Gehlen's New J. Chem.* 1804, *3*, 7.
[3] G. Magnus, *Ann. Phys.* 1827, *10*, 491.
[4] G. Magnus, *Ann. Phys.* 1827, *14*, 328.
[5] N. Bartlett, D. H. Lohmann, *Proc. Chem. Soc.* 1960, *14*.
[6] N. Bartlett, D. H. Lohmann, *Proc. Chem. Soc.* 1962, *115*.
[7] A. R. Young, T. Hirata, S. I. Morrow, *J. Am. Chem. Soc.* 1964, *86*, 20.
[8] I. Solomon, R. I. Brabets, R. K. Uenishi, J. N. Keith, J. M. McDonough, *Inorg. Chem.* 1964, *3*, 457.
[9] J. Shamir, J. Binenboym, *Inorg. Chim. Acta* 1968, *2*, 37.
[10] J. N. Keith, I. J. Solomon, I. Sheft, H. H. Hyman, *Inorg. Chem.* 1968, *7*, 230.
[11] J. B. Beal, C. Pupp, W. E. White, *Inorg. Chem.* 1969, *8*, 828.
[12] J. Barr, R. J. Gillespie, R. Kapoor, K. C. Malhotra, *Can. J. Chem.* 1968, *46*, 149.
[13] I. D. Brown, D. B. Crump, R. J. Gillespie, D. P. Santry, *Chem. Commun.* 1968, 853.
[14] I. D. Brown, D. B. Crump, R. J. Gillespie, *Inorg. Chem.* 1971, *10*, 2319.
[15] N. J. Bjerrum, G. P. Smith, *J. Am. Chem. Soc.* 1968, *90*, 4472.
[16] N. J. Bjerrum, *Inorg. Chem.* 1970, *9*, 1965.
[17] T. W. Couch, D. A. Lokken, J. D. Corbett, *Inorg. Chem.* 1972, *11*, 357.
[18] J. Banister, P. J. Dainty, *Chem. Com.* 1969, 1187.
[19] A. C. Hazell, R. Gronbaek Hazell, *Acta Chem. Scand.* 1972, *26*, 1987-1995.
[20] P. Klinzing, W. Willing, U. Müller, K. Dehnicke, *Z. Anorg. Allg. Chem.* 1985, 529, 35-45.
[21] R. J. Gillespie, D. R. Slim, J. D. Tyrer, *J. Chem. Soc. Chem. Comm.* 1977, 253-255.
[22] T. Chivers, L. Fielding, W. G. Laidlaw, M. Trsic, *Inorg. Chem.* 1979, *18*, 3379-3388.
[23] H. W. Roesky, A. Hamza, *Angew. Chem.* 1976, *7*, 226-227.
[24] B. Krebs, G. Henkel, S. Pohl, H. W. Roesky, *Chem. Ber.* 1980, *113*, 226-232.
[25] R. J. Gillespie, J. P. Kent, J. F. Sawyer, *Inorg. Chem.* 1981, *20*, 3784-3799.
[26] S. Herler, P. Mayer, H. Nöth, A. Schulz, M. Suter, M. Vogt, *Angew. Chem.* 2001, *113*, 3270-3273.
[27] B. H. Christian, R.J. Gillespie, J. F. Sawyer, *Inorg. Chem.* 1981, *20*, 3410-3420.
[28] J. Beck, S. Schlüter, N. Zotov, *Z. Anorg. Allg. Chem.* 2005, *631*, 2450-2456.
[29] J. Beck, M. Dolg, S. Schlüter, *Angew. Chem*. 2001, *113*, 2347-2350.
[30] J. Beck, S. Schlüter, N. Zotov, *Z. Anorg. Allg. Chem.* 2004, *630*, 2512-2519.
[31] S. Schlüter, PhD thesis 2004, University of Bonn(http://hss.ulb.uni-bonn.de/2004/0333/0333.pdf).
[32] K. Biswas, Q. Zhang, I. Chung, J.-H. Song, J. Androulakis, A. J. Freeman, M. G. Kanatzidis, *J. Am. Chem. Soc.* 2010, *132*, 14760-14762.
[33] K. Biswas, I. Chung, J.-H. Song, C. D. Malliakas, A. J. Freeman, M. G. Kanatzidis, *Inorg. Chem.* 2013, *52*, 5657-5659.
[34] J. Beck, S. Schlüter, *Z. Anorg. Allg. Chem.* 2005, *631*, 569-574.
[35] F. Steden, PhD thesis 2002, University of Bonn.
[36] E. Ahmed, A. Isaeva, A. Fiedler, M. Haft, M. Ruck, *Chem. Eur. J.* 2011, *17*, 6847-6852.
[37] Q. Zhang, I. Chung, J. I. Jang, John B. Ketterson, M. G. Kanatzidis, *J. Am. Chem. Soc.* 2009, *131*, 9896-9897.
[38] E. Ahmed, J. Breternitz, M. F. Groh, A. Isaeva, M. Ruck, *Eur. J. Inorg. Chem.* 2014, *19*, 3037-3042.
[39] J. Beck, T. Marschall, *Z. Kristall.* 1995, *210*, 265-268; J. Beck, M. A. Pell, J. Richter, J. A. Ibers, *Z. Anorg. Allg. Chem.* 1996, *622*, 473-478.
[40] J. Beck, *Inorganic Chemistry in Focus II*, 2005, 35-52.

[41] J. Beck, G. Bock, *Z. Anorg. Allg. Chem.* 1996, *622*, 823-828.
[42] J. Beck, *Chem. Ber.* 1995, *128*, 23-27.
[43] J. Beck, G. Bock, *Angew. Chem.* 1995, *107*, 2739-2741.
[44] A. Baumann, J. Beck, T. Hilbert, *Z. Naturforsch.* 1999, *54b*, 1253-1259.
[45] J. Beck, *Angew. Chem.* 1990, *102*, 301-302.
[46] J. Beck, A. Fischer, A. Stankowski, *Z. Anorg. Allg. Chem.* 2002, *628*, 2542-2548.
[47] S. Brownridge, I. Krossing, J. Passmore, H. D. B. Jenkins, H. K. Roobottom, *Coord. Chem. Rev.* 2000, *197*, 397-481.
[48] A. Baumann, J. Beck, *Z. Anorg. Allg. Chem.* 2004, *630*, 2078-2082.
[49] G. W. Drake, G. L. Schimek, J. W. Kolis, *Inorg. Chem.* *1996*, *35*, 1740-1742.
[50] M. Gorlov, A. Fischer, L. Kloo, *Acta Cryst.* 2003, *E59*, 70-71.
[51] P. D. Mascherpa-Corral, P. Vitse, A. Potier, *Acta Cryst.* 1976, *B32*, 247-250.
[52] S. A. Semiletov, *Kristallografiya* 1956, *1*, 403-406.
[53] KPLOT, Rudolf Hundt, 1979, University of Bonn, Germany.
[54] W. Gebhardt, U. Krey, *Phasenübergänge und kritische Phänomene - Eine Einführung*, Vieweg-Verlag, Braunschweig, Germany, 1980.
[55] W. Hönle, *Z. Krist.* 1990, *191*, 141-142.
[56] R. W. G. Wyckoff, E. Posnjak, *J. Am. Chem. Soc.* 1922, *44*, 30-36.
[57] P. C. Burns, F. C. Hawthorne, *Am. Mineralog*. 1993, *78*, 187-189.
[58] M. H. Habibi, M. Montazerozohori, K. Barati, R. W. Harrington, W. Clegg, *Acta Crystallogr*. 2007, *C63*, m592-m594; P. J. Healy, J. C. McMurtrie, J. Bouzaid, *Acta Crystallogr*. 2010, *E66*, m493-m494; Q. Meng, Y. Chen, B. Li, S. Chen, S. Gao, *Acta Crystallogr*. 2011, *E67*, m226.
[59] W. Hoenle, B. Hettich, A. Simon, *Z. Naturforsch*. 1987, *42B*, 248-250.
[60] M. Jinxiao, H. Zhang, J-F. Deng, S.-Y. Mao, J.-T. Zhao, *Z. Kristallogr. New Cryst. Struct*. 2002, *217*, 479-480.
[61] R. C. Gearhart, J. D. Beck, R. H. Wood, *Inorg. Chem*. 1975, *14*, 2413-2416; R. Buscher, G. Lehmann, G. Henkel, B. Krebs, *Z. Naturforsch*. 1984, *39A*, 1204-1207.
[62] A. Lipka, *Acta Cryst. B* 1979, 35, 3020-3022.
[63] G. J. Schrobilgen, R. C. Burns, P. Granger, *J. Chem. Soc. Chem. Comm*. 1978, 957-960.
[64] M. J. Collins, R. J. Gillespie, J. F. Sawyer, G. J. Schrobilgen, *Inorg. Chem*. 1986, *25*, 2053-2057.
[65] R. C. Burns, M. J. Gillespie, G. J. Schrobilgen, *Inorg. Chem*. 1986, *25*, 4456-4469.
[66] S. Brownridge, L. Calhoun, H. D. B. Jenkins, R. S. Laitinen, M. P. Murchie, J. Passmore, J. Pietikäinen, J. M. Rautiainen, J. C. P. Sanders, G. J. Schrobilgen, R. J. Suontamo, H. M. Tuonen, J. U. Valkonen, C.-M. Wong, *Inorg. Chem*. 2009, *48*, 1938-1959.
[67] T. F. Kemp, A. Wong, M. E. Smith, P.T. Bishop, N. Carthey, *Solid State Nucl. Mag. Reson.* 2008, *34*, 224-227.
[68] L. A. Woodward, A. A. Nord, *J. Chem. Soc.* 1956, 3721-3722.
[69] M. Lindsjö, A. Fischer, L. Kloo, *Angew. Chem. Int. Ed.* 2004, *43*, 2540-2543.
[70] M. J. Taylor, *J. Chem. Soc. A* 1970, *623*, 2812-2814.
[71] S. I. Troyanov, T. Krahl, E. Kemnitz, *Z. Krist.* 2004, *219*, 88-92; W. Hoenle, *Z. Krist.* 1990, *191*, 141-142.
[72] J. Beck, K. Müller-Buschbaum, *Z. Anorg. Allg. Chem.* 1997, 409-413.
[73] M. Lindsjö, A. Fischer, L. Kloo, *Eur. J. Inorg. Chem.* 2005, *4*, 670-675.
[74] K.Wade, Adv. Inorg. *Chem. Radiochem.*, 1976, *18*, 1–66.
[75] P. Pyykkö, M. Atsumi, *Chem. Eur. J.* 2009, *15*, 186-197; A. G. Volkov, S. Paula, D. W. Deamer, *Bioelectrochem. Bioenergetics* 1997, *42*, 153-160.

[76] J. Beck, *Angew. Chem. 1991*, *103*, 1149-1151; J. Beck, *Z. Anorg. Allg. Chem.* 1993, *619*, 237-242; J. Beck, A. Fischer, A. Stankowski, *Z. Anorg. Allg. Chem.* 2002, *628*, 2542-2548.
[77] Drake, G. W.; Schimek, G. L.; Kolis, J. W. *Inorg. Chem.* 1996, *35*, 1740–1742.
[78] J. Beck, A. Stankowski, *Z. Naturforsch.* 2001, *56 b*, 453-457; J. Beck, A. Fischer, *Z. Anorg. Allg. Chem.* 2002, *628*, 369-372; C. Feldmann, D. Freudenmann, *Acta Cryst. C* 2012, *68*, i68-i70.
[79] A. Baumann, J. Beck, *Z. Anorg. Allg. Chem.* 2004, *630*, 2078–2080.
[80] J. Beck, T. Schlörb, *Phosphorus Sulfur Silicon Relat. Elem.* 1997, *124, 125*, 305-313.
[81] R. Kniep, D. Mootz, A. Rabenau, *Z. Anorg. Allg. Chem.* 1976, *422*, 17-38; J. Beck, M. A. Pell, J. Richter, J. A. Ibers, *Z. Anorg. Allg. Chem.* 1996, *622*, 473-478.
[82] G. P. Voutsas, P. J. Rentzeperis,D. Siapkas, *Z. Kristallogr.* 1983, *165*, 159-167; A. Ibanez, J. C. Jumas, J. Olivier-Fourcade, E. Philippot, M. J. Maurin, *Solid State Chem.* 1983, *48*, 272-283.
[83] A. V. Shevel'kov, E. V. Dikarev, R. V. Shpanchenko, B. A. Popovkin, *J. Solid State Chem.* 1995, 114, 379-384.
[84] G. P. Voutsas, P. J. Rentzeperis, D. Siapkas, *Z. Kristallogr.* 1986, 177, 117-124.
[85] J. Beck, *Coord. Chem. Rev*. 1997, *163*, 55-70; E. Ahmed, M. Ruck, *Coord. Chem. Rev*. 2011, *255*, 2892-2903.
[86] C. Peylhard, P. Teulon, A. Potier, *Z. Anorg. Allg. Chem.* 1981, *483*, 236-240.
[87] S. Pohl, *Z. Naturforsch.* 1983, *38b*, 1539-1542.
[88] S. Pohl, *Z. Anorg. Allg. Chem.* 1983, *498*, 15-19; S. Pohl, *Z. Anorg. Allg. Chem.* 1983, *498*, 20-24.
[89] C. Aubauer, T. M. Klapötke, P. Mayer, *Acta Cryst.* 2001, *E57*, i1-i2.
[90] M. Baudler, G. Wetter, *Z. Anorg. Allg. Chem.* 1964, *329*, 3-11.
[91] J. Trotter, T. Zobel, *Z. Krist.* 1966, 123, 67-72; S. Pohl, W. Saak, *Z. Krist.* 1984, 169, 177-184.
[92] H. Schäfer, M. Nimmewies, R. Laumanns, H. Wächter, *Z. Anorg. Allg. Chem.* 1980, *461*, 31-34.
[93] K. Hildebrandt, P. G. Jones, E. Schwarzmann, G. M. Sheldrick, *Z. Naturforsch.* 1982, *37b*, 1129-1131.
[94] J. D. Martin, B. R. Leafblad, R. M. Sullivan, P. D. Boyle, *Inorg. Chem.* 1998, *37*, 1341-1346.
[95] K. Yamada, Y. Tomita, T. Okuda, *J. Mol. Struct.* 1995, *345*, 219-227.
[96] C. Verries-Peyhard, *Compt. Rend.* 1982, *Serie C*, *295*, 171-174.
[97] W. Hönle, *Z. Kristall.* 1990, *191*, 141-142.
[98] R. Burnus, A. Zajonc, G. Meyer, *Z. Kristall.* 1994, 210, 61.
[99] C. Aubauer, G. Engelhardt, T. M. Klapötke, A. Schulze, *J. Chem. Soc., Dalton Trans.* 1999, 1729-1733.
[100] G. M. Begun, C. R. Boston, G. Torsi, G. Mamantov, *Inorg. Chem.* 1979, *10*, 886.889.
[101] G. Burns, F. H. Dacol, M. W. Shafer, *Solid State Com.* 1977, *24*, 753-757.
[102] A. J. Bradley, *Phil. Mag. Ser. 6* 1924, *48*, 477-497.
[103] R. Kniep, D. Mootz, A. Rabenau, *Angew. Chem.* 1973, *11*, 504-505.
[104] R. Kniep, D. Mootz, . Rabenau, *Z. Anorg. Allg. Chem.* 1976, *422*, 17-38.
[105] R. Kniep, H.-J. Beister, *Angew. Chem.* 1985, *97*, 399-400.
[106] R. Kniep, L. Korte, D. Mootz, *Z. Naturforsch.* 1982, *38b*, 1-6.
[107] W. Milius, *Z. Anorg. Allg. Chem.* 1990, *586*, 175-184; P. M. Carkner, H. M. Haendler, *J. Solid. State Chem.* 1976, *18*, 183-189; J. Fenner, A. Rabenau, *Z. Anorg. Allg. Chem.* 1976, *426*, 7-14.
[108] J. Fenner, *Acta Cryst. B* 1976, *32*, 3084-3086; W. Milius, *Z. Naturforsch.* 1989, *44b*, 990-992.
[109] A. Pfitzner, S. Zimmerer, *Z. Anorg. Allg. Chem.* 1995, *621*, 969-974.
[110] A. Pfitzner, S. Zimmerer, *Z. Anorg. Allg. Chem.* 1996, *622*, 853-857; T. Nilges, S. Zimmerer, D. Kurowski, A. Pfitzner, *Z. Anorg. Allg. Chem.* 2002, *628*, 2809-2814.

[111] W. Milius, A. Rabenau, *Z. Naturforsch.* 1988, *43b*, 243-244; A. Pfitzner, T. Nilges, H.-J. Deiserot, *Z. Anorg. Allg. Chem.* 1999, *625*, 201-206.
[112] H. M. Haendler, P. M. Carkner, *J. Solid State Chem.* 1979, *29*, 35-39; W. Milius, A. Rabenau, *Materials Research Bulletin* 1987, *22*, 1493-1497.
[113] A. Pfitzner, S. Zimmerer, *Z. Krist.* 1997, *212*, 203-207.
[114] T. W. Couch, D. A. Lokken, J. D. Corbett, *Inorg. Chem.* 1972, *11*, 357.
[115] J. Beck, M. Kasper, A. Stankowski, *Chem. Ber.* 1997, *130*, 1189-1192.
[116] M. Lindsjö, L. Kloo, *Acta Cryst.* 2005, *E61*, i18-i19.
[117] A. N. Kuznetsov, B. A. Popovkin, K. Stahl, M. Lindsjö, L. Kloo, *Eur. J. Inorg. Chem.* 2005, 4907-4913.
[118] P. Boldrini, I. D. Brown, M. J. Collins, R. J. Gillespie, E. Maharajh, D. R. Slim, J. F. Sawyer, *Inorg. Chem.* 1985, *24*, 4302-4307.
[119] J. Hartig, J. Steiner, A. Stößer, H. Schnöckel, *Chem. Eur. J.* 2007, *13*, 4475-4482.
[120] S. Geller, *J. Chem. Phys.* 1960, *33*, 676-684.
[121] R. C. Burns, R. J. Gillespie, W.-C. Luk, D. R. Slim, *Inorg. Chem.* 1979, *18*, 3986-3094.
[122] M. J. Buerger, S. B. Hendricks, *Zeitschr. f. Kristallogr.* 1938, 98, 1-30.
[123] SpringerMaterials - The Landolt-Börnstein Database, *II.2.3.1,* W. Pies, A. Weiss, 1980; M. Edstrand, *Arkiv Kemi* 1953, *6*, 89-112.
[124] C. Peylhard, P. Teulon, A. Potier, *Z. Anorg. Allg. Chem.* 1981, *483*, 236-240.
[125] M. Lindsjoe, A. Fischer, L. Kloo, *Angew. Chem. Int. Ed.* 2004, *116*, 2594-2597.
[126] J. D. Donaldson, A. Kjekshus, D. G. Nicholson, T. Rakke, *Acta Chem. Scand.* 1975, *29*, 803-809.
[127] The *Cambridge Structural Database CSD* contains 160 entries with the structure fragment Sb···Cl···Sb. An inspection of the respective Sb–Cl bond lengths in these bridging bonds revealed a broad range between 2.5 and 3.3 Å.
[128] M. Binnewies, *Z. Anorg. Allg. Chem*. 1983, *505*, 32-38.
[129] M. Binnewies, H. Schnöckel, *Chem. Rev.* 1990, *90*, 321-330.
[130] H. J. Breunig, M. Stanciu, R. Rösler, E. Lork, *Z. Anorg. Allg. Chem.* 1998, *624*, 1965-1968.
[131] H. J. Breuning, M. A. Mohammed, K. H. Ebert, *Polyhedron* 1994, *13*, 2471-2471.
[132] B. Räke, P. Müller, H. W. Roesky, I. Uson, *Angew. Chem. Int. Ed.* 1999, *38*, 2050-2051.
[133] U. Thewalt, F. Stollmaier, *Angew. Chem. Int. Ed.* 1982, *21*, 133-134; D. Jentsch, P. G. Jones, E. Schwarzmann, G. M. Sheldrick, *Acta Crystallogr*. *C* 1983, *39*, 1173-1174.
[134] J. Catterick, P. Thornton, *Adv. Inorg. Chem. Radiochem*. 1977, *20*, 291-362.
[135] M. Pazicky, F. Rominger, M. Limbach, *Acta Crystallogr*. *E* 2010, *66*, m724-m725.
[136] H. Schmidbaur, A. Kolb, E. Zeller, A. Schier, H. Bermuda, *Z. Anorg. Allg. Chem.* 1993, *619*, 1575-1579.
[137] A. Weiss, G. Nagorsen, A. Weiss, *Z. Anorg. Allg. Chem.* 1953, *274*, 151-168.
[138] B. Kamenar, B. Kaitner, S. Pocev, *J. Chem. Soc. Dalton Trans*. 1985, 2457-2458.
[139] Oral Communication, M. Ruck, July 2nd, Dresden.
[140] F. Jellinek, H. Hahn, *Z. Naturforsch.* 1961, *16*, 713-715.
[141] W. Schubert, E. Dörre, M. Kluge, *Z. Metallk.* 1955, *46*, 216.
[142] A. Kuhn, R. Chevalier, A. Rimsky, *Acta Cryst.* 1975, *B31*, 2841-2842.
[143] P. G. Ghemard, S. Jaulmes, J. Etienne, J. Flahhaut, *Acta Cryst.* 1983, *C38*, 968-971.
[144] C. J. Harlan, E. G. Gillan, S. G. Bott, A. R. Barron, *Organometallics* 1996, *15*, 5479-5488.
[145] S. Ishida, F. Hirakawa, K. Furuhawa, K. Yoza, T. Iwamoto, *Angew. Chem. Int. Ed.* 2014, *53*, 11172-11176.
[146] K. Wittel, R. Manne, *Theoret. Chim. Acta* 1974, *33*, 347-349.

[147] M. J. Collins, R. J. Gillespie, J. F. Sawyer, *Inorg. Chem.* 1987, *26*, 1476-1481.
[148] R. C. Burns, M. J. Collins, S. M. Eicher, R. J. Gillespie, J. F. Sawyer, *Inorg. Chem.* 1988, *27*, 1807–1813.
[149] G. M. Sheldrick, *Acta Cryst.* 2008, *A64*, 112-122.
[150] Z. Otwinowski, W. Minor, Program SCALEPACK, *Macromol. Crystallogr. A* 1997, *276*, 307-326.
[151] G. M. Sheldrick, Program SADABS, University of Göttingen, Germany, 2009.
[152] Diamond, *Program for Crystal Structure Visualisation*, Crystal Impact Comp., Bonn, Germany, 2005.
[153] NMR and Periodic Table, R. K. Harris, B. E. Mann, *Academic Press* 1978, 413.
[154] J. M. van den Berg, Acta Cryst. 1966, *20*, 905-910.
[155] G. Brinkmann, *Recl. Trav. Chim. Pays-Bas.* 1969, *88*, 275-285.

5.0 Appendix

A 5.1 Instruments, Analytics and Preparation

A 5.1.1 The Vacuum System and Tube Furnaces

The vacuum system consists of two main parts: the vacuum line and the argon line.
The vacuum line is connected to a rotary vane pump (Labovac PK 4 D), which generates low pressure down to $9.7 \cdot 10^{-3}$ mbar. In the case of volatile substances, a cooling trap can be used as a condenser before the pump (Fig. A 5.1.1.1).

Fig. A 5.1.1.1 The vacuum system.

The argon protecting gas is first led through a cascade of glass tubes filled with phosphorous pentoxide, molecular sieve, potassium hydroxide and silica gel to remove traces of water and organic gases. Afterwards it passes a silica tube with titanium lumps, heated to 600 °C, to remove oxygen, nitrogen and hydrogen before it finally reaches the argon line. The common argon excess pressure was 0.15 bar.
There are three connections for ampoules, for evacuating and filling them with argon.
Sublimations and dryings were done in horizontallly mounted glass tubes inserted into tube furnaces in dynamic vacuum. Additionally the vacuum system is elongated to a fume hood for performing syntheses in low pressure and argon atmosphere.
Tube furnaces used for syntheses were aligned in an angle of about 30° to the horizontal (Fig. A 5.1.1.2). All temperatures were adjusted by external thermometers at the exact position of the reaction melts within the furnaces.

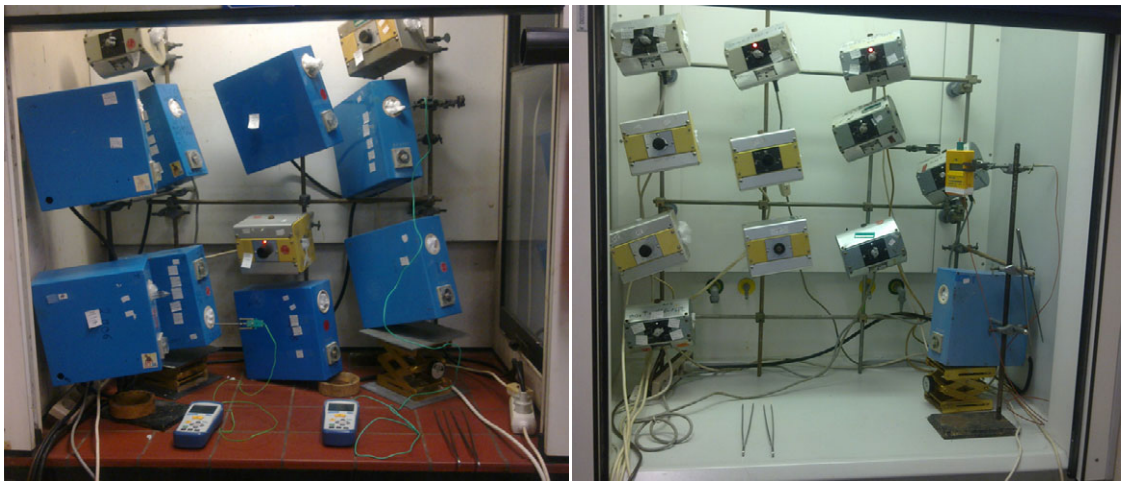

Fig. A 5.1.1.2 Fume hoods with tube furnaces and external thermometers.

A 5.1.2 The Glove Box

Preparative work was done in the glovebox exclusively (LabMaster 130, MBRAUN) because of the air sensitivity of all compounds (Fig. A 5.1.2.1).

Fig. A 5.1.2.1 The glove box LabMaster 130.

The glove box is equipped with one large and one small vacuum chamber to channel various materials in by evacuating and flooding with argon. The vacuum is generated by an Edwards RV12 rotary pump. The argon inside the glove box is circulating through a BTS catalyst and molecular sieve. The catalyst consists of finely dispersed copper and absorbs oxygen at its surface. Regularely the catalyst has to be regenerated at higher temperatures in a hydrogen stream to remove oxygen in form of water. The

molecular sieve (400 pm) absorbs water from the box atmosphere. By oxygen and water analyzers the box atmosphere is checked permanently. Optimal contents are less than 1 ppm, respectively.
In the front window a microscope (Leica MZ6) offering a 40x magnification lens is mounted, which can be used with both reflected and transmitted light.
For weighing substances the glove box is equipped with a balance (Sartorius BP615) and for sealing glass capillaries with a heatable tantal wire. Additionally, the glove box is equipped with a home-made apparature to measure electrical conductivities of crystals (Fig. A 5.1.2.2).

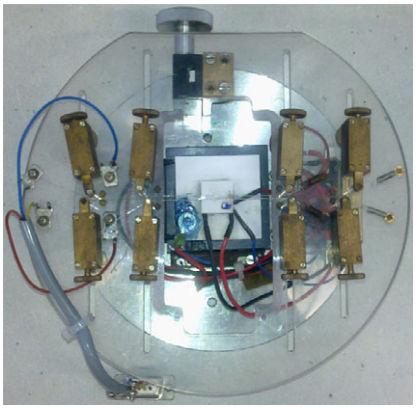

Fig. A 5.1.2.2 Cell for electrical conductivity measurements. Crystals are clamped by four platinum wires and pressed on the surface (white square) of a Peltier element.

Measurements of electrical conductivities of crystals can be performed inside the glove box between - 20 and 50 °C. The temperatures are contollable by a Peltier element (Fig. A 5.1.2.2). The crystals have to big enough to be contacted by two (> 0.2 mm) or four (> 0.6 mm) platinum wires.

A 5.1.3 Crystal Structure Determinations

Crystals were transferred immersed in perfluorinated polyether into the cold N_2 stream of the crystal cooling device of a diffractometer. In the present work a Bruker-Nonius Kappa-CCD and a Bruker Kappa ApexII CCD diffractometer, both equipped with graphite monochromatized Mo-K_α radiation, were used. In general, data collections were performed at –150 °C (123 K) or –173 °C (100 K). At these temperatures the crystals' covering polyether solidifies to glass and acts as a protection against hydrolysis. The deep temperatures are ensured by an external Oxford Cryosystems 600 Series cooling at the Kappa CCD and a Bruker cooling system at the ApexII.
All crystal structures were solved by direct methods and refined based on F^2 with anisotropic displacement parameters for all atoms.[149] Semi-empirical absorption corrections were applied to all data sets [150,151]. Crystallographic representations were performed with the Program Diamond.[152] The crystallographic data of all examined compounds are given in chapter A 5.2 in the apendix.

Fig. A 5.1.3.1 Nonius Kappa-CCD (left) and Bruker Kappa ApexII CCD (right).

A 5.1.4 Energy Dispersive Electron-Beam X-ray Fluorescence Analysis (EDX)

All compounds were examined for the composition via energy dispersive electron-beam X-ray fluorescence. Selected crystals were fixed on a carbon coated sample holder and broken to obtain fresh surfaces to examine the bulk material. The samples were transferred under exclusion of air into the chamber of a SPI Module Sputter Coater, where the crystals were sputtered with gold under low pressure (approx. 10^{-1} mbar, Edwards E2M5) using an argon plasma (Fig. A 5.1.4.1)

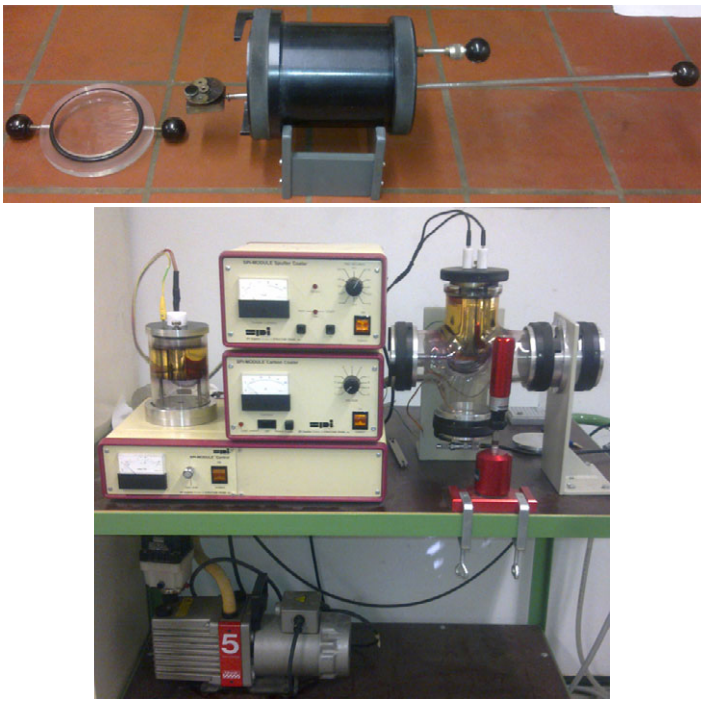

Fig. A 5.1.4.1 Transfer chamber with sample holder (top) and SPI Sputter Coater (bottom).

After this treatment they were transferred into the vacuum chamber to the digital scanning electron microscope ZEISS DSM 940 and examined under high vacuum with 20 kV accelerated electrons (detector PV9800, EDAX). The radiation source is a tungsten thermionic cathode. The vacuum is

generated first by a rotary pump (Edwards P2M8) and second by a turbomolecular pump (Fig. A 5.1.4.2).

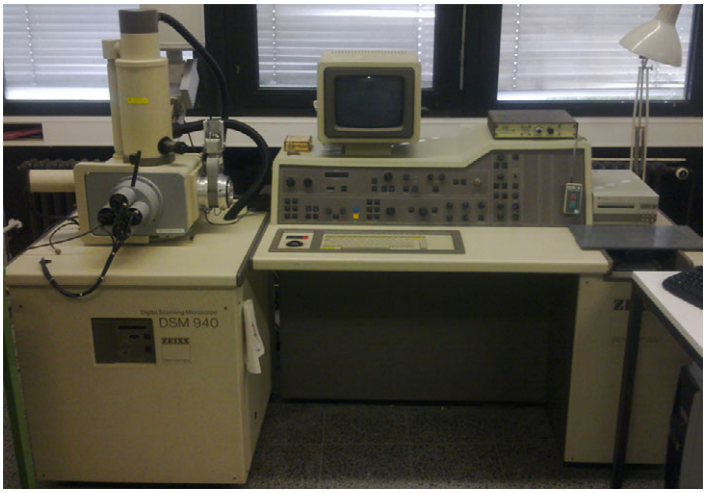

Fig. A 5.1.4.2 Scanning Electron Microscope ZEISS DSM 940. The control unit can be seen on the right side. The left modular unit consists of the turbomolecular pump (bottom) and the examination chamber with electron source and nitrogen dewar (top).

In all cases, around five crystals of the respective compound were examined with 5 - 10 point or area measurements each. In general, the examined crystals showed the problem to have gallium trichloride, tetraphenylphosphonium tetrachlorido gallate or metal gallate adherences on their surfaces. Consequently, the obtained values for gallium and chlorine came out too high for several substances. Depending on the actual position of the electron beam on the crystal surfaces, the amount of adherences varied, which led to high standard deviations on averaging the obtained values in some cases. However, in all reported tables certain element ratios are given, which are in fair agreement with the expected ratios.
An approved methode in cases of adherences of $PPh_4[GaCl_4]$ and $AsCl_3$ is the exposure to vacuum in the glovebox chamber before sputtering to remove the liquids at least partly.
In all EDX analyses performed in this work besides those of $(Sb_7S_8Cl_2)[GaCl_4]_3$ (Tab. 2.2.1.3) and $(Bi_4Se_4)[GaCl_4][SeGa_3Cl_9]$ (Tab. 2.16.1.2), the results for Ga are too high compared to the expected content based on the crystal structure. Crystals of $Cu[GaCl_4]$ were examined as a reference substance (Tab. A 5.1.4.1).

Tab. A 5.1.4.1 Elemental composition of $Cu[GaCl_4]$ in atom-% and the Cu : Ga ratio. Standard deviations given in brackets refer to the last significant digit.

$Cu[GaCl_4]$	Cu	Ga	Cl	Cu : Ga
Found	17.2(7)	18.9(6)	63(1)	1 : 1.10
Calculated	16.7	16.7	66.7	1 : 1.00

The results show a Cu : Ga ratio of 1 : 1.1, expected is 1 : 1.0. Since the obtained value for Cl is somewhat lower than expected, the higher result for Ga can not be explained by $GaCl_3$ adherences on the crystals surface. The reason for the too high Ga result is not clear since this effect did not occur in all analyses performed throughout this work.

A 5.1.5 Characterization by Raman Spectroscopy

Raman spectra were recorded with a Bruker Multiram spectrometer equipped with a Nd:YAG-Laser (λ = 1064 nm) and a germanium detector at resolutions of 1 cm^{-1} (Fig. A 5.1.5.1). The special feature of this detector is the prevention of fluorescence, which is a common problem of analyzing polycationic clusters with Raman spectroscopy.
50 - 300 crystals - depending on their size - were selected under argon atmosphere, cleaned in perfluorinated polyether (Fomblin Y, Sigma Aldrich) and fixed on the inner side of a glass tube. The glass tubes were annealed prior to use at 150 - 200 °C in dynamic vacuum (approx. $2 \cdot 10^{-2}$ mbar) for one day before to remove adsorbed moisture. The crystals were crushed to smaller pieces, accumulated in an area of 1 - 3 mm^2 and measured in the closed glass tube. The laser energies varied between 50 and 80 mW and 32 scans at a resolution of 1 cm^{-1} were chosen commonly.

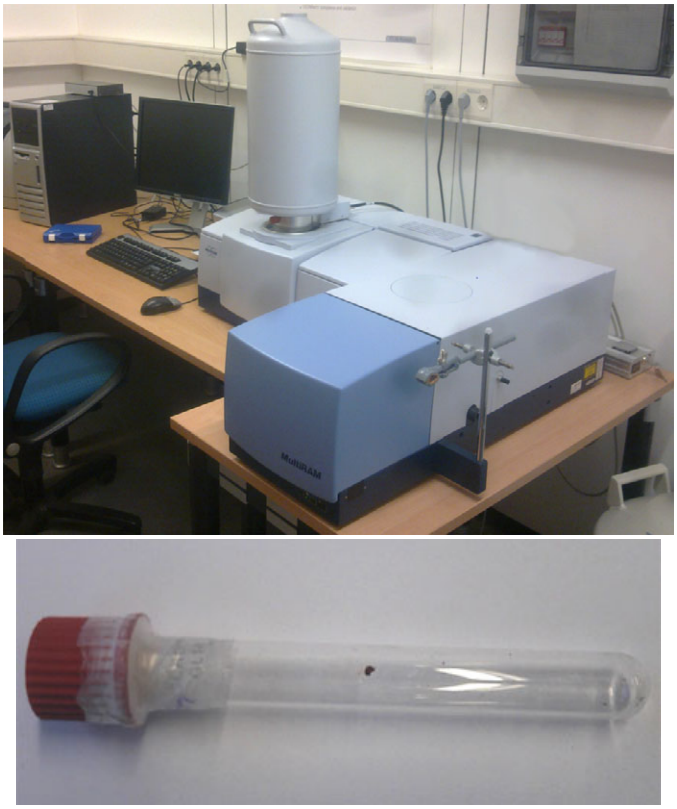

Fig. A 5.1.5.1 Bruker Multiram Raman spectrometer (top) and glass tube with cummulated crystals (bottom).

In general, it occured that crystalline gallium trichloride adopted the melts' colour and seemed to be the compound of interest. Gallium trichloride has a rather complex spectrum (Fig. A 5.1.5.2) and would falsify the spectrum of a compound containing a polycationic cluster or even make the measured spectrum useless. For comparison, Raman spectra of crystalline gallium trichloride and the empty sample holder were recorded, respectively. Reliable statements of the vibration frequencies of the examined substances can be made for wavenumbers above 100 cm^{-1}. The exciting laser causes signals at 74 and 78 cm^{-1} (Fig. A 5.1.5.2).

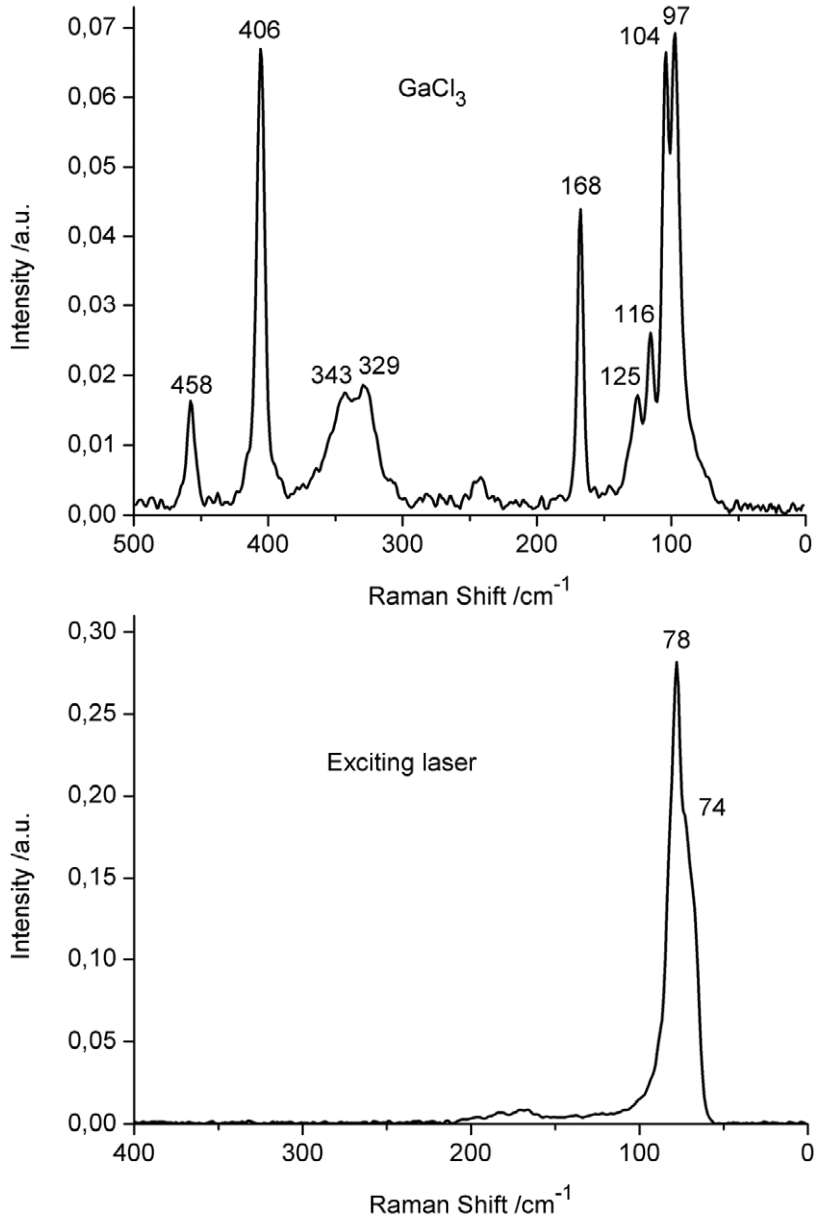

Fig. A 5.1.5.2 Raman spectra of crystalline gallium trichloride (top) and the exciting Raman laser (bottom).

A 5.1.6 ^{77}Se and ^{125}Te Solid State NMR Spectroscopy

All solid state NMR experiments were carried out using a Varian Infinity+ NMR spectrometer operating at 9.4 T (Fig. A 5.1.6.1).

Fig. A 5.1.6.1 NMR spectrometer Varian Infinity+ with open sample holder on the bottom. The rotation control unit is shown on the left.

The used samples were selected crystals of the respective compounds, which had been cleaned from adherences under immersion in perfluorinated polyether. Samples were filled into zirconia rotors by manual compressing. All crystalline materials turned out to be stable for about 3 weeks during all measurements under these conditions. Spectrometer frequencies were 76.54 MHz and 126.48 MHz for ^{77}Se and ^{125}Te, respectively. The magic angle spinning (MAS) technique was performed using a 4 mm Chemagnetics probe with zirconia rotors at several different rotation frequencies ranging from 12 to 17 kHz. The ^{77}Se spectra were acquired by using a 90˚ - τ - 90˚ echo sequence with a 90˚ pulse length of 3.8 µs, 1000 kHz spectral width, 8 ms acquisition time, recycle delay up to 5 s, and up to 80000 transients. 500 Hz line broadening was applied during data processing. Chemical shifts were referenced to Me_2Se and to Ph_2Te_2. Ph_2Te_2 is shifted by +422 ppm relative to Me_2Se[153].

A 5.1.7 Electron Paramagnetic Resonance Spectroscopy (EPR)

Crystals were cleaned from adherences in perfluorinated polyether and filled in EPR capillaries (ER221TUB-Q10 , inner diameter 1 mm) in the glovebox. The capillaries were fixed in a standard glass taper NS14, which was approximately tapered to the diameter of the capillary. The junction between the taper and the capillary was closed with Araldite 2-component-epoxy-glue. The glass construction was connected to the vacuum system and the capillary was sealed under low pressure (Fig. A 5.1.7.1).

Fig. A 5.1.7.1 The glass construction for EPR sample preparation.

The EPR data were acquired on a Bruker Elexsys E580 spectrometer (Fig. A 5.1.7.2). For the continuous wave (cw) X-band (9.7 GHz) EPR, a cylindrical TE011 cavity (Bruker, ER 4119HS) was utilized which was additionally equipped with an Oxford ESR900 helium cryostat for reaching lower temperatures. 2 or 20 mW microwave power with 2 or 5 G modulation amplitude and modulation frequency of 100 KHz were used.

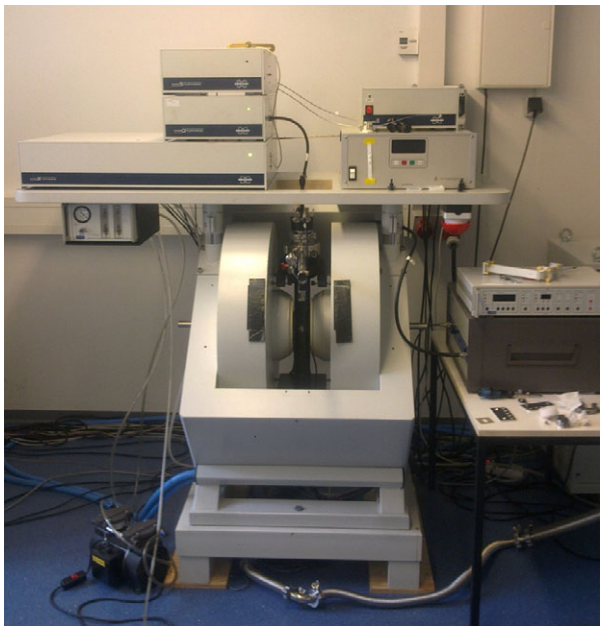

Fig. A 5.1.7.2 The Bruker Elexsys E580 EPR spectrometer.

A 5.1.8 X-ray Powder Diffraction

Powder diffractograms were recorded on Bruker D8 and STOE StadiP powder diffractometers, both equipped with germanium monochromatized Cu-K_α radiation.
Powders were prepared in the glovebox by grinding in a mortar, which was heated to 120 °C before and cooled down under reduced pressure to remove moisture. Samples were filled in capillaries of 0.5 mm outer diameter and sealed with an electrically heated tantal wire. Manually separated crystals were cleaned from adherences in perfluorinated polyether and filled in with a glass wire. Capillaries were preheated at 300 °C under low pressure to remove adsorbed moisture.
Data collections were performed in Debye-Scherrer mode and permanent sample rotation.

Fig. A 5.1.8.1 Bruker D8 (left) and STOE StadiP (right) powder diffractometers.

A 5.1.9 Differential Scanning Calorimetry (DSC)

For differential scanning calorimetric analyses manually selected crystals were filled in Al crucibles and examined in specified temperature ranges applying heating rates of 10 °C/min with a Netzsch DSC thermal analyzer. Due to the presence of the perfluorinated polyether Fomblin Y, which was used for crystal separation from the reaction melts, an individual scanning calorimetric analysis of the polyether was performed for comparison (Fig. A 5.1.9.1).

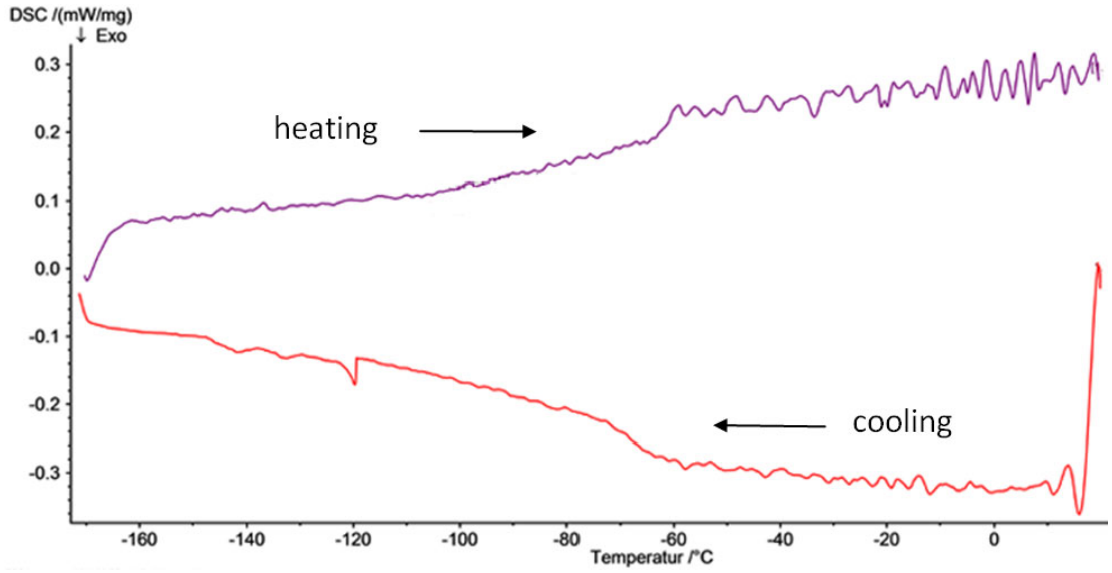

Fig. A 5.1.9.1 Differential scanning calorimetric plot of Fomblin Y between 113 and 210 K. Curve 1 (top) referres to the heating process, curve 2 (bottom) to the cooling process.

A 5.1.10 Mass Spectrometry (MS)

Chosen samples were analyzed by the Matrix-Assisted Laser Desorption/Ionization (MALDI) technique. Crystals were separated in perfluorinated polyether in the glove box, placed on a steel plate and covered with the matrix DCTB (*trans*-2-[3-(4-*tert*-Butylphenyl)-2-methyl-2-propenylidene] malononitrile). They were loaded to a Bruker Daltonik Autoflex II TOF/TOF spectrometer (Fig. A 5.1.10.1) and examined in positive mode under low pressure.

Fig. A 5.1.10.1 Bruker Daltonik Autoflex II TOF/TOF mass spectrometer.

A 5.1.11 Magnetic Measurements

Magnetic measurements were performed with a QD PPMS-VSM (Quantum Design Physical Property Measurement System - Vibrating Sample Magnetometer) with a nine Tesla magnet (Fig. A 5.1.11.1).

Fig. A 5.1.11.1 Quantum Design Physical Property Measurement System.

Crystals were separated and cleaned from adherences in perfluorinated polyether in the glove box. The were clamped between two plastic sample holders, tranferred to the magnetometer and examined in an external magnetic field of 1 T.

A 5.1.12 Crystal Photos

Crystal photos were taken with a KEYENCE Digital Microscope VHX-500F (Fig. A 5.1.12.1).

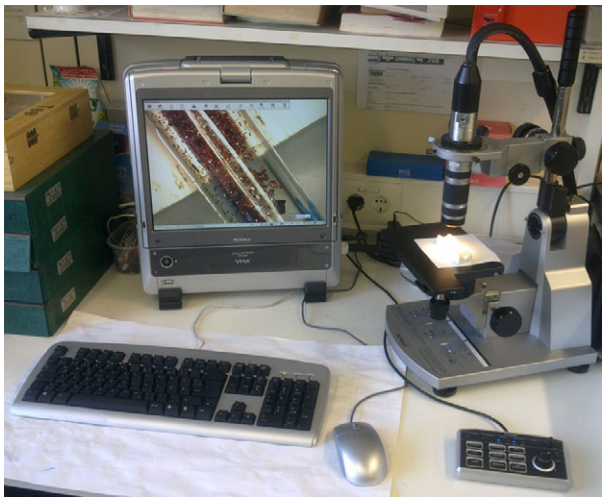

Fig. A 5.1.12.1 Video microscope KEYENCE VHX-500F.

Photos with up to 200x magnification can be taken. Several computional optimizations like depth of focus and different light modes are possible. Additionally a polarisation filter can be used to remove disturbing reflections e. g. of bend ampoule glass.

A 5.2 Crystallographic Data

Tab. A 5.2.1 Crystallographic data and details of the structure refinement for $(Sb_7Te_8)[GaCl_4]_3[Ga_2Cl_7]_2$ and $(Sb_7Te_8)[GaCl_4]_2[Ga_2Cl_7]_3$. Standard deviations given in brackets refer to the last significant digit.

Formula	$(Sb_7Te_8)[GaCl_4]_3[Ga_2Cl_7]_2$	$(Sb_7Te_8)[GaCl_4]_2[Ga_2Cl_7]_3$
Crystal system	triclinic, $P\bar{1}$	monoclinic, $P2_1/c$
Lattice constants / Å / °	a = 10.7593(1)	a = 18.1357(2)
	b = 15.6011(2)	b = 10.584(1)
	c = 18.8612(2)	c = 36.8524(4)
	α = 68.071(1)	
	β = 83.777(1)	β = 115.41(7)
	γ = 88.556(1)	
Unit cell volume / Å^3	2919.21(6)	6389.0(6)
Measurement temperature / K	123 (2)	123 (2)
Number of formula units Z	2	4
Calculated density / g·cm^{-3}	3.74	3.60
Absorption coefficient / mm^{-1}	11.472	11.024
Crystal size / mm^3	0.04 × 0.04 × 0.05	0.03 × 0.03 × 0.10
Absorption correction	multiscan [150]	multiscan [150]
Range of data collection	2.96° < θ < 30.11°	2.94° < θ< 30.0°
Number of measured reflections	17080	18474
Number of independent reflections	14035	13671
R_{int} on averaging reflections	0.0689	0.0519
Number of refined parameters	434	470
Ratio reflections / parameters	32.3	29.1
$R(\|F\|)$ for $F_o > 4\sigma(F_o)$	0.0298	0.0542
$R(\|F\|)$ for all reflections	0.0423	0.0312
$wR_w(F^2)$	0.0631	0.0621
GooF	1.035	1.023
max. and min. electron density / e·Å^{-3}	1.29 / –1.06	1.40 / –1.44

Tab. A 5.2.2 Crystallographic data and details of the structure refinement for $Na(Sb_7Te_8)[GaCl_4]_6$ and $Cu(Sb_7Te_8)[GaCl_4]_6$. Standard deviations given in brackets refer to the last significant digit.

Chemical Formula	$Na(Sb_7Te_8)[GaCl_4]_6$	$Cu(Sb_7Te_8)[GaCl_4]_6$
Crystal system, space group	triclinic, $P\bar{1}$	triclinic, $P\bar{1}$
Lattice constants / Å / °	a = 12.182(1)	a = 11.6397(5)
	b = 12.767(2)	b = 11.9955(6)
	c = 18.307(14)	c = 12.3109(9)
	α = 92.021(4)	α = 112.082(3)
	β = 90.129(3)	β = 111.468(3)
	γ = 105.793(4)	γ = 100.359(2)
Unit cell volume / Å^3	2737.9(5)	1378.2(1)
Measurement temperature / K	100(2)	100 (2)
Number of formula units Z	2	1
Calculated density / g·cm^{-3}	3.839	3.862
Absorption coefficient / mm^{-1}	11.659	11.948
Range of data collection	1.66° < θ < 30.03°	2.07° < θ < 29.94°
Number of independent reflections	15841	7220
Number of refined parameters	416	211
Ratio reflections / parameters	38.08	34.2
R_{int} on averaging reflections	0.0884	0.0277
Crystal size / mm^3	0.01 × 0.03 × 0.05	0.02 × 0.04 × 0.06
Absorption correction	multiscan [151]	multiscan [151]
$R(\|F\|)$ for $F_o > 4\sigma(F_o)$	0.0613	0.0185
$R(\|F\|)$ for all reflections	0.1539	0.0214
$wR_w(F^2)$	0.1384	0.303
GOOF	0.923	1.101
max. and min. electron density / e·Å^{-3}	2.10 / –2.02	2.55 / -0.94

Tab. A 5.2.3 Crystallographic data and details of the structure refinement for $Ag(Sb_7Te_8)[GaCl_4]_6$ at 123 and 163 K. Standard deviations given in brackets refer to the last significant digit.

Chemical Formula	$Ag(Sb_7Te_8)[GaCl_4]_6$	
Crystal system, space group	triclinic, $P\bar{1}$	triclinic, $P\bar{1}$
Lattice constants / Å / °	a = 18.2976(3)	a = 18.3421(7)
	b = 12.7806(2)	b = 12.7815(4)
	c = 26.9053(4)	c = 13.5212(5)
	α = 125.37(1)	α = 125.38(1)
	β = 132.37(1)	β = 132.23(1)
	γ = 91.75(1)	γ = 91.58(1)
Unit cell volume / Å^3	2753.0(2)	1383.71(9)
Measurement temperature / K	123(2)	163(2)
Number of formula units Z	2	1
Calculated density / g·cm^{-3}	3.92	3.90
Absorption coefficient / mm^{-1}	11.935	11.870
Range of data collection	2.91° < θ < 27.46°	3.00° < θ < 27.49°
Number of independent reflections	12568	5460
Number of refined parameters	426	215
Ratio reflections / parameters	29.50	25.40
R_{int} on averaging reflections	0.0630	0.056
Crystal size / mm^3	0.09 × 0.12 × 0.13	
Absorption correction	multiscan [150]	
$R(\|F\|)$ for $F_o > 4\sigma(F_o)$	0.038	0.046
$R(\|F\|)$ for all reflections	0.064	0.059
$wR_w(F^2)$	0.075	0.111
GOOF	1.076	1.061
max. and min. electron density / e·Å^{-3}	1.18 / –1.96	1.77 / -2.61

Tab. A 5.2.4 Crystallographic data and details of the structure refinement for $(Sb_7Se_8)[GaCl_4]_2[Ga_2Cl_7]_3$. Standard deviations given in brackets refer to the last significant digit.

Formula	$(Sb_7Se_8)[GaCl_4]_2[Ga_2Cl_7]_3$
Crystal system	triclinic, $P\bar{1}$
Lattice constants / Å / °	a = 10.8508(5)
	b = 15.5027(8)
	c = 18.932(1)
	α = 79.852(3)
	β = 84.040(3)
	γ = 70.709(3)
Unit cell volume / Å^3	2955.3(3)
Measurement temperature / K	100 (2)
Number of formula units Z	2
Calculated density / g·cm^{-3}	3.60
Absorption coefficient / mm^{-1}	12.972
Crystal size / mm^3	0.02 × 0.07 × 0.08
Absorption correction	multiscan [151]
Range of data collection	2.78° < θ < 26.37°
Number of measured reflections	11888
Number of independent reflections	6779
R_{int} on averaging reflections	0.1057
Number of refined parameters	469
Ratio reflections / parameters	14.45
$R(\|F\|)$ for $F_o > 4\sigma(F_o)$	0.0463
$R(\|F\|)$ for all reflections	0.102
$wR_w(F^2)$	0.086
GooF	0.837
max. and min. electron density / e·Å^{-3}	1.93 / –1.91

Tab. A 5.2.5 Crystallographic data and details of the structure refinement for $(Sb_7Se_8Cl_2)[GaCl_4]_3$ and $(Sb_7S_8Cl_2)[GaCl_4]_3$. Standard deviations given in brackets refer to the last significant digit.

Chemical Formula	$(Sb_7Se_8Cl_2)[GaCl_4]_3$	$(Sb_7S_8Cl_2)[GaCl_4]_3$
Crystal system, space group	monoclinic, $P2_12_12_1$	monoclinic, $P2_1$
Lattice constants / Å / °	a = 12.2027(7)	a = 17.002(1)
	b = 17.0089(9)	b = 11.991(1)
	c = 17.735(1)	c = 8.610(1)
		β = 93.199(8)
Unit cell volume / Å^3	3.681.0(4)	1752.9(3)
Measurement temperature / K	100(2)	123(2)
Number of formula units Z	4	2
Calculated density / g·cm^{-3}	3.951	3.437
Absorption coefficient / mm^{-1}	16.138	9.115
Range of data collection	2.35° < θ < 30.01°	1.20° < θ < 27.50°
Number of measured reflections	10726	5824
Number of independent reflections	1007	5426
Number of refined parameters	289	289
Ratio reflections / parameters	18.78	18.78
R_{int} on averaging reflections	0.0620	0.1050
Crystal size / mm^3	0.05 × 0.12 × 0.25	0.05 × 0.05 × 0.24
Absorption correction	multiscan [151]	multiscan [150]
$R(\|F\|)$ for $F_o > 4\sigma(F_o)$	0.0271	0.0494
$R(\|F\|)$ for all reflections	0.0310	0.0554
$wR_w(F^2)$	0.0612	0.1294
GOOF	1.035	1.069
max. and min. electron density / e·Å^{-3}	1.59 / –1.31	2.35 / –3.47
Flack x parameter	0.025(6)	0.03(3)

Tab. A 5.2.6 Crystallographic data and details of the structure refinement for $(Sb_4Te_4)[GaCl_4]_4$ and $(Sb_4Se_4)[GaCl_4]_4$. Standard deviations given in brackets refer to the last significant digit.

Chemical Formula	$(Sb_4Te_4)[GaCl_4]_4$	$(Sb_4Se_4)[GaCl_4]_4$
Crystal system, space group	tetragonal, $I\bar{4}$	tetragonal, $I\bar{4}$
Lattice constants / Å / °	a = 12.1392(6)	a = 11.868(1)
	b = 11.2384(6)	b = 10.904(1)
Unit cell volume / Å^3	1656.0(2)	1535.8(2)
Measurement temperature / K	100(2)	100(2)
Number of formula units Z	2	2
Calculated density / g·cm^{-3}	3.697	3.566
Absorption coefficient / mm^{-1}	11.155	13.044
Range of data collection	4.34° < θ < 29.99°	4.42° < θ < 28.27°
Number of measured reflections	2378	1900
Number of independent reflections	2248	1722
Number of refined parameters	64	64
Ratio reflections / parameters	35.1	26.9
R_{int} on averaging reflections	0.0215	0.041
Crystal size / mm^3	0.03 × 0.04 × 0.04	0.08 × 0.12 × 0.14
Absorption correction	multiscan [150]	multiscan [150]
$R(\|F\|)$ for $F_o > 4\sigma(F_o)$	0.014	0.020
$R(\|F\|)$ for all reflections	0.017	0.025
$wR_w(F^2)$	0.024	0.026
GOOF	0.872	0.949
max. and min. electron density / e·Å^{-3}	0.82 / -0.45	0.51 / -0.45
Flack x parameter	0.023(8)	0.038(7)

Tab. A 5.2.7 Crystallographic data and details of the structure refinement for $(Sb_3Te_4)[Ga_2Cl_7]_3$. Standard deviations given in brackets refer to the last significant digit.

Chemical Formula	$(Sb_3Te_4)[Ga_2Cl_7]_3$
Crystal system, space group	triklinic, $P\bar{1}$
Lattice constants / Å / °	a = 10.949(1)
	b = 12.411(1)
	c = 15.538(1)
	α = 72.428(1)
	β = 87.111(1)
	γ = 85.329(1)
Unit cell volume / Å^3	2005.77(6)
Measurement temperature / K	123(2)
Number of formula units Z	2
Calculated density / g·cm^{-3}	3.375
Absorption coefficient / mm^{-1}	10.204
Range of data collection	3.08° < θ < 27.54°
Number of measured reflections	9221
Number of independent reflections	8003
Number of refined parameters	307
Ratio reflections / parameters	26.1
R_{int} on averaging reflections	0.055
Crystal size / mm^3	0.034 × 0.140 × 0.236
Absorption correction	multiscan [150]
$R(\|F\|)$ for $F_o > 4\sigma(F_o)$	0.028
$R(\|F\|)$ for all reflections	0.036
$wR_w(F^2)$	0.066
GOOF	1.062
max. and min. electron density / e·Å^{-3}	3.13 / -1.58

Tab. A 5.2.8 Crystallographic data and details of the structure refinement for $(As_2Te_4)[Ga_2Cl_7]_2$ and $(Sb_2Te_4)[Ga_2Cl_7]_2$. Standard deviations given in brackets refer to the last significant digit.

Formula	$(As_2Te_4)[Ga_2Cl_7]_2$	$(Sb_2Te_4)[Ga_2Cl_7]_2$
Crystal system	monoclinic, *C*2/*c*	orthorhombic, $P2_12_12_1$
Lattice constants / Å / °	*a* = 22.2355(7)	*a* = 11.4957(2)
	b = 10.8036(3)	*b* = 12.0467(2)
	c = 14.0870(5)	*c* = 21.0554(4)
	β = 121.871(2)	
Unit cell volume / Å^3	2873.8(2)	2915.86(9)
Measurement temperature / K	123 (2)	123 (2)
Number of formula units *Z*	2	4
Calculated density / g·cm^{-3}	3.318	3.483
Absorption coefficient / mm^{-1}	11.27	10.669
Crystal size / mm^3	0.028 × 0.100 × 0.140	0.020 × 0.082 × 0.158
Absorption correction	multiscan [150]	multiscan [150]
Range of data collection	3.09° < θ < 27.50°	3.12° < θ < 27.47°
Number of measured reflections	3293	6683
Number of independent reflections	2398	5935
R_{int} on averaging reflections	0.0823	0.0750
Number of refined parameters	136	218
Ratio reflections / parameters	24.21	30.66
$R(\|F\|)$ for $F_o > 4\sigma(F_o)$	0.0477	0.0382
$R(\|F\|)$ for all reflections	0.0774	0.0469
$wR_w(F^2)$	0.1153	0.0849
GooF	1.089	1.079
max. and min. electron density / e·Å^{-3}	2.29 / –1.69	2.64 / –3.0
Flack *x* parameter	-	–0.011(8)

Tab. A 5.2.9 Crystallographic data and details of the structure refinement for $(Sb_2Te_4)[GaCl_4]_2$. Standard deviations given in brackets refer to the last significant digit.

Chemical Formula	$(Sb_2Te_4)[GaCl_4]_2$
Crystal system, space group	orthorhombic, $Pca2_1$
Lattice constants / Å / °	a = 16.092(2)
	b = 9.8024(9)
	c = 12.531(1)
Unit cell volume / Å^3	1976.7(3)
Measurement temperature / K	123(2)
Number of formula units Z	4
Calculated density / g·cm^{-3}	3.955
Absorption coefficient / mm^{-1}	12.243
Range of data collection	2.93° < θ < 29.71°
Number of measured reflections	5479
Number of independent reflections	3812
Number of refined parameters	146
Ratio reflections / parameters	37.53
R_{int} on averaging reflections	0.0963
Crystal size / mm^3	0.04 × 0.06 × 0.10
Absorption correction	multiscan [150]
$R(\|F\|)$ for $F_o > 4\sigma(F_o)$	0.0444
$R(\|F\|)$ for all reflections	0.0966
$wR_w(F^2)$	0.0625
GOOF	1.010
max. and min. electron density / e·Å^{-3}	3.36 / -2.49
Flack x parameter	–0.012(16)

Tab. A 5.2.10 Crystallographic data and details of the structure refinement for $M(As_2Te_4)[GaCl_4]_2$. Standard deviations given in brackets refer to the last significant digit.

Chemical Formula	M = K	M = Rb	M = Cs	M = NH_4	M = In	M = Tl
Crystal system, Space group	trigonal, $R\bar{3}c$	trigonal, $R\bar{3}c$	trigonal, $R\bar{3}c$	trigonal, $R\bar{3}c$	trigonal, $R\bar{3}c$	trigonal, $R\bar{3}c$
Lattice constants / Å	a = 11.7130(3)	a = 11.7781(2)	a = 11.8688(2)	a = 11.7641(1)	a = 11.7580(5)	a = 11.7367(2)
	c = 32.2627(8)	c = 32.1817(5)	c = 32.2903(8)	c = 32.1712(1)	c = 32.167(2)	c = 32.103(2)
Unit cell volume / $Å^3$	3833.3(2)	3866.25(14)	3939.27(16)	3855.81(7)	3851.3(4)	3829.8(2)
Mesurement temperature / K	123	123(2)	123(2)	123(2)	100(2)	123(2)
Calculated density / $g \cdot cm^{-3}$	3.467	3.557	3.611	3.392	3.647	3.900
Absorption coefficient / mm^{-1}	11.593	13.209	12.489	11.365	12.252	17.722
Crystal size / mm^3	0.040 × 0.053 × 0.160	0.078 × 0.108 × 0.176	0.065 × 0.071 × 0.530	0.070 × 0.095 × 0.151	0.020 × 0.050 × 0.120	0.042 × 0.171 × 0.195
Absorption correction	multi-scan[150]	multi-scan[150]	multi-scan[150]	multi-scan[150]	multi-scan[151]	multi-scan[151]
Range of data collection	2.91° < θ < 27.48°	3.23° < θ < 27.53°	3.21° < θ < 27.48°	3.23° < θ < 27.46°	3.29° < θ < 30.05°	3.23° < θ < 29.57°
Number of measured reflections	976	1001	1017	988	1259	1198
Number of independent reflections	870	979	842	862	1119	1057
R_{int} on averaging reflections	0.1996	0.0514	0.0862	0.0658	0.0964	0.0472
Number of refined parameters	44	44	44	45	44	44
Ratio reflections / parameters	22.18	22.75	23.11	22.45	28.61	27.23
$R(\|F\|)$ for $F_o > 4\sigma(F_o)$	0.0427	0.0309	0.0300	0.0270	0.0521	0.0309
$R(\|F\|)$ for all reflections	0.0481	0.0315	0.0433	0.0343	0.0564	0.0392
$wR_w(F^2)$	0.0958	0.0652	0.0619	0.0568	0.1002	0.0546
GOOF	1.163	1.222	1.123	1.207	1.172	1.104
max. and min. electron density / $e \cdot Å^{-3}$	0.70 / -0.82	0.15 / -0.71	0.18 / -1.00	0.13 / -0.79	0.27 / -1.37	0.27 / -1.06

Tab. A 5.2.11 Crystallographic data and details of the structure refinement for $M(Sb_2Te_4)[GaCl_4]_2$. Standard deviations given in brackets refer to the last significant digit.

Chemical Formula	M = K	M = Rb	M = Cs	M = NH_4	M = Tl
Crystal system, Space group	trigonal, $R\bar{3}c$	trigonal, $R\bar{3}c$	trigonal, $R\bar{3}c$	trigonal, $R\bar{3}c$	trigonal, $R\bar{3}c$
Lattice constants / Å	a = 11.8357(4)	a = 11.8860(2)	a = 11.9653(8)	a = 11.8748(2)	a = 11. 863(3)
	b = 32.879(1)	c = 32.8080(8)	c = 32.930(3)	c = 32.8882(9)	c = 32.756(8)
Unit cell volume / $Å^3$	3988.8(3)	4014.0(2)	4082.9(6)	4016.27(17)	3994(2)
Mesurement temperature / K	123(2)	123(2)	123(2)	123(2)	123(2)
Calculated density / $g·cm^{-3}$	3.566	3.658	3.712	3.489	3.973
Absorption coefficient / mm^{-1}	10.66	12.344	11.579	10.433	16.496
Crystal size / mm^3	0.034 × 0.040 × 0.081	0.080 × 0.012 × 0.165	0.040 × 0.040 × 0.005	0.035 × 0.052 × 0.69	0.030 × 0.040 × 0.060
Absorption correction	multi-scan[150]	multi-scan[150]	multi-scan[150]	multi-scan[150]	multi-scan[150]
Range of data collection	3.18° < θ < 27.45°	3.18° < θ < 29.95°	3.16° < θ < 29.20°	3.17° < θ < 27.48°	3.18° < θ < 29.13°
Number of measured reflections	981	1297	1237	1030	1124
Number of independent reflections	822	1081	839	902	854
R_{int} on averaging reflections	0.0531	0.0746	0.1179	0.0581	0.1075
Number of refined parameters	44	44	44	44	44
Ratio reflections / parameters	15.33	29.48	28.11	23.41	25.55
$R(\|F\|)$ for $F_o > 4\sigma(F_o)$	0.0415	0.0317	0.0454	0.0344	0.0570
$R(\|F\|)$ for all reflections	0.0518	0.0422	0.0857	0.0421	0.0651
$wR_w(F^2)$	0.1027	0.0661	0.0772	0.0740	0.0570
GOOF	0.1046	1.083	0.944	1.127	1.129
max. and min. electron density / $e·Å^{-3}$	0.18 / -1.32	0.15 / -1.23	3.46 / -0.24	0.14 / -1.08	1.25 / -1.51

Tab. A 5.2.12 Crystallographic data and details of the structure refinement for $(Sb_2Te_2)[GaCl_4]$. Standard deviations given in brackets refer to the last significant digit.

Formula	$(Sb_2Te_2)[GaCl_4]$
Crystal system	triclinic, $P\bar{1}$
Lattice constants / Å / °	a = 9.444(1)
	b = 13.418(1)
	c = 17.917(1)
	α = 75.372(1)
	β = 87.831(1)
	γ = 88.556(1)
Unit cell volume / Å^3	2195.28(7)
Measurement temperature / K	123(2)
Number of formula units Z	2
Calculated density / g·cm^{-3}	4.30
Absorption coefficient / mm^{-1}	13.437
Crystal size / mm^3	0.01 × 0.012 × 0.09
Absorption correction	multiscan [150]
Range of data collection	3.06° < θ < 27.54°
Number of measured reflections	10105
Number of independent reflections	7648
R_{int} on averaging reflections	0.0825
Number of refined parameters	325
Ratio reflections / parameters	23.53
$R(\|F\|)$ for $F_o > 4\sigma(F_o)$	0.0362
$R(\|F\|)$ for all reflections	0.0609
$wR_w(F^2)$	0.0663
GooF	1.065
max. and min. electron density / e·Å^{-3}	2.44 / –2.03

Tab. A 5.2.13 Crystallographic data and details of the structure refinement for $(Sb_2Te_2)I[AlI_4]$. Standard deviations given in brackets refer to the last significant digit.

Formula	$(Sb_2Te_2)I[AlI_4]$
Crystal system	monoclinic, *C*2/*m*
Lattice constants / Å / °	*a* = 10.2435(6)
	b = 8.5420(5)
	c = 17.4681(10)
	β = 97.905(2)
Unit cell volume / Å^3	1513.9(2)
Measurement temperature / K	123
Number of formula units *Z*	4
Calculated density / g·cm^{-3}	5.09
Absorption coefficient / mm^{-1}	17.554
Crystal size / mm^3	0.06 × 0.07 × 0.12
Absorption correction	multiscan [151]
Range of data collection	2.35° < θ < 29.57°
Number of measured reflections	4288
Number of independent reflections	2452
R_{int} on averaging reflections	0.0357
Number of refined parameters	101
Ratio reflections / parameters	42.46
$R(\|F\|)$ for $F_o > 4\sigma(F_o)$	0.0425
$R(\|F\|)$ for all reflections	0.0831
$wR_w(F^2)$	0.0874
GooF	1.046
max. and min. electron density / e·Å^{-3}	3.22 / –2.97

Tab. A 5.2.14 Crystallographic data and details of the structure refinement for $(Bi_2Te_2)Cl[GaCl_4]$ and $(Bi_2Te_2)Cl[GaCl_4]$. Standard deviations given in brackets refer to the last significant digit.

Chemical Formula	$(Bi_2Te_2)Cl[GaCl_4]$	$(Bi_2Se_2)Cl[GaCl_4]$
Crystal system, space group	monoclinic, *C*2/*m*	monoclinic, *C*2/*m*
Lattice constants / Å / °	*a* = 12.879(1)	*a* = 12.624(1)
	b = 4.224(1)	*b* = 4.049(1)
	c = 10.575(1)	*c* = 10.492(1)
	β = 98.535(2)	β = 99.945(4)
Unit cell volume / Å^3	569.07(2)	528.34(6)
Measurement temperature / K	123 (2)	123(2)
Number of formula units *Z*	2	2
Calculated density / g·cm^{-3}	5.37	5.17
Absorption coefficient / mm^{-1}	39.331	43.839
Range of data collection	3.20° < θ < 27.48°	3.28° < θ < 27.41°
Number of measured reflections	739	686
Number of independent reflections	713	569
Number of refined parameters	39	39
Ratio reflections / parameters	18.28	14.59
R_{int} on averaging reflections	0.0446	0.1029
Crystal size / mm^3	0.010 × 0.010 × 0.094	0.002 × 0.020 × 0.070
Absorption correction	multiscan [150]	multiscan [150]
$R(\|F\|)$ for $F_o > 4\sigma(F_o)$	0.0171	0.0382
$R(\|F\|)$ for all reflections	0.0184	0.0582
$wR_w(F^2)$	0.0389	0.0679
GOOF	1.064	1.057
max. and min. electron density / e·Å^{-3}	1.56 / –1.31	2.00 / –2.00

Tab. A 5.2.15 Crystallographic data and details of the structure refinement for $(Sb_3Te_4)[GaCl_4]$. Standard deviations given in brackets refer to the last significant digit.

Formula	$(Sb_3Te_4)[GaCl_4]$
Crystal system	monoclinic, *C*2/*m*
Lattice constants / Å / °	*a* = 14.453(1)
	b = 4.195(1)
	c = 12.899(1)
	β = 111.797(4)
Unit cell volume / Å^3	726.3(1)
Measurement temperature / K	123 (2)
Number of formula units *Z*	2
Calculated density / g·cm^{-3}	4.971
Absorption coefficient / mm^{-1}	15.919
Crystal size / mm^3	0.004 × 0.008 × 0.088
Absorption correction	multiscan [150]
Range of data collection	3.09° < θ < 27.50°
Number of measured reflections	899
Number of independent reflections	703
R_{int} on averaging reflections	0.0566
Number of refined parameters	44
Ratio reflections / parameters	15.98
$R(\|F\|)$ for $F_o > 4\sigma(F_o)$	0.0290
$R(\|F\|)$ for all reflections	0.0471
$wR_w(F^2)$	0.0488
GooF	1.089
max. and min. electron density / e·Å^{-3}	0.94 / –0.95

Tab. A 5.2.16 Crystallographic data and details of the structure refinement for $(SbTe_4)[Ga_2Cl_7]$. Standard deviations given in brackets refer to the last significant digit.

Formula	$(SbTe_4)[Ga_2Cl_7]$
Crystal system	monoclinic, $P2_1/n$
Lattice constants / Å / °	a = 7.1476(5)
	b = 18.854(2)
	c = 12.8699(8)
	β = 94.240(4)
Unit cell volume / Å^3	1729.7(2)
Measurement temperature / K	123 (2)
Number of formula units Z	4
Calculated density / g·cm^{-3}	3.916
Absorption coefficient / mm^{-1}	12.304
Crystal size / mm^3	0.008 × 0.010 × 0.17
Absorption correction	multiscan [150]
Range of data collection	3.06° < θ < 27.56°
Number of measured reflections	3848
Number of independent reflections	2486
R_{int} on averaging reflections	0.1223
Number of refined parameters	127
Ratio reflections / parameters	30.30
$R(\|F\|)$ for $F_o > 4\sigma(F_o)$	0.0507
$R(\|F\|)$ for all reflections	0.1027
$wR_w(F^2)$	0.0944
GooF	1.077
max. and min. electron density / e·Å^{-3}	1.71 / –1.25

Tab. A 5.2.17 Crystallographic data and details of the structure refinement for $(SbI_2)[AlI_4]$ and $Cu[AlI_4]$. Standard deviations given in brackets refer to the last significant digit.

Chemical Formula	$(SbI_2)[AlI_4]$	$Cu[AlI_4]$
Crystal system, space group	monoclinic, $P2_1/n$	monoclinic, $P\bar{4}2c$
Lattice constants / Å / °	a = 10.8457(8)	a = 11.8732(2)
	b = 11.3104(9)	
	c = 10.8493(8)	c = 12.1086(4)
	β = 93.971(2)	
Unit cell volume / Å^3	1327.6(2)	1706.98(8)
Measurement temperature / K	100 (2)	123 (2)
Number of formula units Z	4	8
Calculated density / g·cm^{-3}	4.553	4.655
Absorption coefficient / mm^{-1}	16.037	17.026
Range of data collection	2.61° < θ < 30.02°	3.37° < θ < 27.47°
Number of measured reflections	3822	1958
Number of independent reflections	3623	1566
Number of refined parameters	73	58
Ratio reflections / parameters	52.36	33.76
R_{int} on averaging reflections	0.0279	0.0714
Crystal size / mm^3	0.039 × 0.076 × 0.153	0.044 × 0.063 × 0.115
Absorption correction	multiscan [151]	multiscan [150]
$R(\|F\|)$ for $F_o > 4\sigma(F_o)$	0.0168	0.0238
$R(\|F\|)$ for all reflections	0.0188	0.0350
$wR_w(F^2)$	0.0361	0.0585
GOOF	1.272	1.061
max. and min. electron density / e·Å^{-3}	0.67 / –0.92	1.32 / –1.05

Tab. A 5.2.18 Crystallographic data and details of the structure refinement for $CuSe_4[GaCl_4]$ and $CuTe_4[GaCl_4]$. Standard deviations given in brackets refer to the last significant digit.

Chemical Formula	$CuSe_4[GaCl_4]$	$CuTe_4[GaCl_4]$
Crystal system, space group	monoclinic, $P2_1/c$	monoclinic, $P2_1/c$
Lattice constants / Å / °	a = 10.5187(8)	a = 11.024(1)
	b = 6.3759(5)	b = 6.867(1)
	c = 15.845(1)	c = 16.639(1)
	β = 111.663(5)	β = 112.53(1)
Unit cell volume / Å^3	987.6(2)	1163.58(7)
Measurement temperature / K	123 (2)	123 (2)
Number of formula units Z	4	4
Calculated density / g·cm^{-3}	3.974	4.484
Absorption coefficient / mm^{-1}	20.627	14.827
Range of data collection	2.08° < θ < 29.26°	3.25° < θ < 27.47°
Number of measured reflections	2680	2655
Number of independent reflections	2487	2121
Number of refined parameters	91	91
Ratio reflections / parameters	29.45	29.18
R_{int} on averaging reflections	0.0289	0.0961
Crystal size / mm^3	0.096 × 0.100 × 0.122	0.012 × 0.020 × 0.120
Absorption correction	multiscan [151]	multiscan [150]
$R(\|F\|)$ for $F_o > 4\sigma(F_o)$	0.0158	0.0305
$R(\|F\|)$ for all reflections	0.0185	0.0505
$wR_w(F^2)$	0.0331	0.0508
GOOF	1.122	1.074
max. and min. electron density / e·Å^{-3}	0.57 / –0.72	1.32 / –1.21

Tab. A 5.2.19 Crystallographic data and details of the structure refinement for $Cu_2Se_7[GaCl_4]_2$. Standard deviations given in brackets refer to the last significant digit.

Formula	$Cu_2Se_7[GaCl_4]_2$
Crystal system	monoclinic, *C*2/*c*
Lattice constants / Å / °	*a* = 9.0770(2)
	b = 16.1907(6)
	c = 14.3991(4)
	β = 101.54(1)
Unit cell volume / Å^3	2073.35(1)
Measurement temperature / K	123 (2)
Number of formula units *Z*	4
Calculated density / g·cm^{-3}	3.533
Absorption coefficient / mm^{-1}	17.895
Crystal size / mm^3	0.016 × 0.026 × 0.060
Absorption correction	multiscan [150]
Range of data collection	3.20° < θ < 27.46°
Number of measured reflections	2359
Number of independent reflections	1740
R_{int} on averaging reflections	0.0757
Number of refined parameters	87
Ratio reflections / parameters	27.11
$R(\|F\|)$ for $F_o > 4\sigma(F_o)$	0.0359
$R(\|F\|)$ for all reflections	0.0659
$wR_w(F^2)$	0.0651
GooF	1.067
max. and min. electron density / e·Å^{-3}	0.95 / –1.08

Tab. A 5.2.20 Crystallographic data and details of the structure refinement for $Te_4[Ga_2Cl_6O]$. Standard deviations given in brackets refer to the last significant digit.

Formula	$Te_4[Ga_2Cl_6O]$
Crystal system	monoclinic, $P2_1/c$
Lattice constants / Å / °	a = 8.5923(3)
	b = 12.5174(5)
	c = 11.8016(3)
	β = 95.235(2)
Unit cell volume / Å^3	1264.01(7)
Measurement temperature / K	123 (2)
Number of formula units Z	4
Calculated density / g·cm^{-3}	3.276
Absorption coefficient / mm^{-1}	10.006
Crystal size / mm^3	0.02 × 0.04 × 0.08
Absorption correction	multiscan [150]
Range of data collection	2.88° < θ < 29.12°
Number of measured reflections	3381
Number of independent reflections	2056
R_{int} on averaging reflections	0.1190
Number of refined parameters	100
Ratio reflections / parameters	33.81
$R(\|F\|)$ for $F_o > 4\sigma(F_o)$	0.0346
$R(\|F\|)$ for all reflections	0.0851
$wR_w(F^2)$	0.0540
GooF	0.890
max. and min. electron density / e·Å^{-3}	1.22 / –2.10

Tab. A 5.2.21 Crystallographic data and details of the structure refinement for $(As_2Te_4)[Ga_2Cl_6O]_2$ and $(Sb_2Te_4)[Ga_2Cl_6O]_2$. Standard deviations given in brackets refer to the last significant digit.

Chemical Formula	$(As_2Te_4)[Ga_2Cl_6O]_2$	$(Sb_2Te_4)[Ga_2Cl_6O]_2$
Crystal system, space group	monoclinic, *C*2	monoclinic, *C*2
Lattice constants / Å / °	*a* = 15.4664(3)	*a* = 15.7837(7)
	b = 10.0394(2)	*b* = 10.0742(5)
	c = 9.0336(2)	*c* = 9.0718(5)
	β = 95.257(2)	β = 94.456(3)
Unit cell volume / Å^3	1396.78(5)	1438.4(1)
Measurement temperature / K	123 (2)	123 (2)
Number of formula units *Z*	4	4
Calculated density / g·cm^{-3}	3.320	3.441
Absorption coefficient / mm^{-1}	11.494	10.634
Range of data collection	3.23° < θ < 27.46°	3.22° < θ < 29.13°
Number of measured reflections	3188	3738
Number of independent reflections	3067	2809
Number of refined parameters	137	139
Ratio reflections / parameters	23.27	26.89
R_{int} on averaging reflections	0.0612	0.0927
Crystal size / mm^3	0.075 × 0.154 × 0.174	0.047 × 0.100 × 0.120
Absorption correction	multiscan [150]	multiscan [150]
$R(\|F\|)$ for $F_o > 4\sigma(F_o)$	0.0229	0.0398
$R(\|F\|)$ for all reflections	0.0247	0.0613
$wR_w(F^2)$	0.0527	0.0836
GOOF	1.087	0.947
max. and min. electron density / e·Å^{-3}	0.68 / –0.73	0.70 / –1.38
Flack *x* parameter	0.58(2)	0.07(2)

Tab. A 5.2.22 Crystallographic data and details of the structure refinements for $(Sb_2Te_4)[Ga_2Cl_6O]_2$ and $(Sb_2Te_4)_2[Ga_2Cl_6O]_4$. Standard deviations given in brackets refer to the last significant digit.

Formula	$(Sb_2Te_4)[Ga_2Cl_6O]_2$	$(Sb_2Te_4)_2[Ga_2Cl_6O]_4$
Crystal system	monoclinic, $P2_1/n$	monoclinic, $C2$
Lattice constants / Å / °	a = 12.5006(1)	a = 23.1154(6)
	b = 18.3026(2)	b = 10.0372(3)
	c = 12.5193(1)	c = 18.6628(4)
	β = 92.471(1)	β = 97.632(2)
Unit cell volume / Å^3	2861.67(5)	4291.6(2)
Measurement temperature / K	123 (2)	123 (2)
Number of formula units Z	4	6
Calculated density / g·cm^{-3}	3.469	3.459
Absorption coefficient / mm^{-1}	10.747	10.692
Crystal size / mm^3	0.070 × 0.086 × 0.110	0.054 × 0.065 × 0.168
Absorption correction	multiscan [150]	multiscan [150]
Range of data collection	3.17° < θ < 30.06°	3.01° < θ < 27.52°
Number of measured reflections	8381	9552
Number of independent reflections	7257	8258
R_{int} on averaging reflections	0.0519	0.0705
Number of refined parameters	263	327
Ratio reflections / parameters	31.87	29.21
$R(\|F\|)$ for $F_o > 4\sigma(F_o)$	0.0276	0.0464
$R(\|F\|)$ for all reflections	0.0358	0.0586
$wR_w(F^2)$	0.0601	0.1057
GooF	1.085	1.045
max. and min. electron density / e·Å^{-3}	1.56 / –1.12	3.16 / –3.02
Flack x parameter	-	0.42(3)

Tab. A 5.2.23 Crystallographic data and details of the structure refinement for Ga_2SbCl_7O. Standard deviations given in brackets refer to the last significant digit.

Formula	Ga_2SbCl_7O
Crystal system	monoclinic, $P2_1/m$
Lattice constants / Å / °	a = 6.6666(3)
	b = 14.4635(7)
	c = 6.8768(3)
	β = 116.890(2)
Unit cell volume / Å^3	591.38(5)
Measurement temperature / K	123(2)
Number of formula units Z	2
Calculated density / g·cm^{-3}	2.950
Absorption coefficient / mm^{-1}	8.319
Crystal size / mm^3	0.118 × 0.085 × 0.037
Absorption correction	multiscan [150]
Range of data collection	3.32° < θ < 27.41
Number of measured reflections	1399
Number of independent reflections	1285
R_{int} on averaging reflections	0.0608
Number of refined parameters	55
Ratio reflections / parameters	25.43
$R(\|F\|)$ for $F_o > 4\sigma(F_o)$	0.0396
$R(\|F\|)$ for all reflections	0.0434
$wR_w(F^2)$	0.0998
GooF	1.246
max. and min. electron density / e·Å^{-3}	1.64 / –0.72

Tab. A 5.2.24 Crystallographic data and details of the structure refinements for $(Bi_4Te_4)[GaCl_4]_2[Ga_2Cl_7]$ and $(Bi_4Se_4)[GaCl_4][SeGa_3Cl_9]$. Standard deviations given in brackets refer to the last significant digit.

Chemical Formula	$(Bi_4Te_4)[GaCl_4]_2[Ga_2Cl_7]$	$(Bi_4Se_4)[GaCl_4][SeGa_3Cl_9]$
Crystal system, space group	orthorhombic, *Pbca*	monoclinic, *Cc*
Lattice constants / Å / °	a = 12.2519(3)	a = 10.8767(3)
	b = 31.7263(9)	b = 18.8217(6)
	c = 16.8949(5)	c = 14.9405(5)
		β = 98.961(1)
Unit cell volume / Å^3	6567.2(3)	3058.5(2)
Measurement temperature / K	123 (2)	123 (2)
Number of formula units Z	8	4
Calculated density / g·cm^{-3}	4.363	4.279
Absorption coefficient / mm^{-1}	29.286	33.475
Range of data collection	2.93° < θ < 27.46	3.48° < θ < 27.48
Number of measured reflections	7473	6974
Number of independent reflections	5746	6093
Number of refined parameters	244	236
Ratio reflections / parameters	30.62	29.55
R_{int} on averaging reflections	0.0944	0.01232
Crystal size / mm^3	0.030 × 0.076 × 0.080	0.036 × 0.037 × 0.102
Absorption correction	multiscan [150]	multiscan [150]
$R(\|F\|)$ for $F_o > 4\sigma(F_o)$	0.0520	0.0502
$R(\|F\|)$ for all reflections	0.0750	0.0613
$wR_w(F^2)$	0.1214	0.1168
GOOF	1.110	1.049
max. and min. electron density / e·Å^{-3}	4.33 / –4.00	2.47 / –2.09
Flack *x* parameter	-	0.132(9)

A 5.3 Occupation Factors of Heavy Atom Positions in Sb-Te Polycationic Clusters

Since the atomic scattering factors of Sb and Te are very similar, special care had to be taken for the correct assignment of the respective atomic positions, which was possible on the basis of the diffraction data in most cases. The atom positions of the polycationic clusters were initially treated as occupied solely by Te and refined with free occupation parameters. Because of the slightly higher scattering factor of Te the atomic positions occupied by Sb are thus falsely assigned and are expected to obtain an occupation factor of less than 1. In most structure determinations, this method allowed for a reliable assignment of the atomic positions.

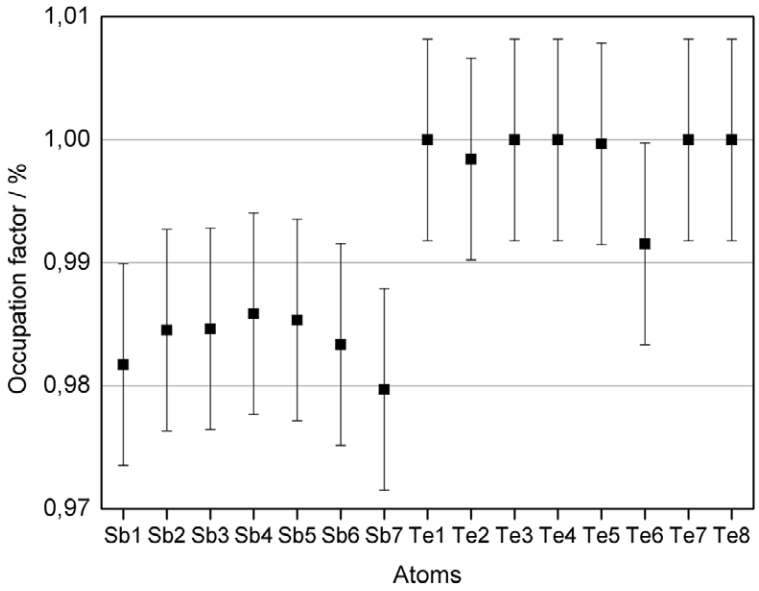

Fig. A 5.3.1 Graphical representation of the Sb/Te atom assignments in the structure of $(Sb_7Te_8)[GaCl_4]_3[Ga_2Cl_7]_2$. Depicted are the obtained occupation factors of the atomic sites of the $(Sb_7Te_8)^{5+}$ cluster when the structure is refined with all atom positions assumed to be occupied by Te exclusively. The standard deviations are indicated by vertical bars.

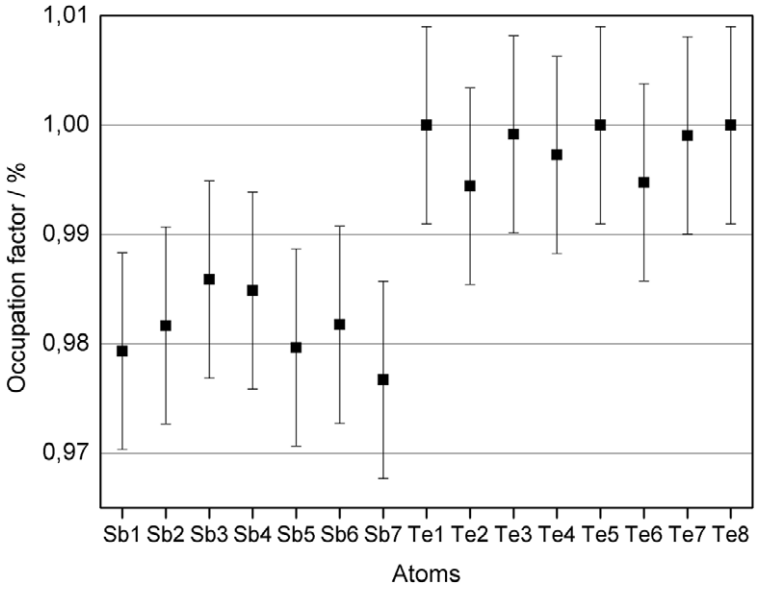

Fig. A 5.3.2 Graphical representation of the Sb/Te atom assignments in the structure of $Na(Sb_7Te_8)[GaCl_4]_6$. Depicted are the obtained occupation factors of the atomic sites of the $(Sb_7Te_8)^{5+}$ cluster when the structure is refined with all atom positions assumed to be occupied by Te exclusively. The standard deviations are indicated by vertical bars.

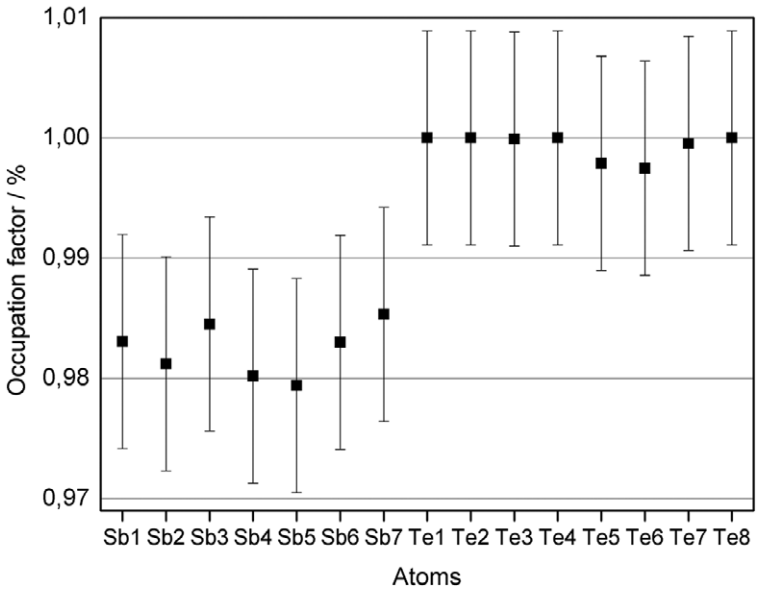

Fig. A 5.3.3 Graphical representation of the Sb/Te atom assignments in the structure of $Ag(Sb_7Te_8)[GaCl_4]_6$ at 123 K. Depicted are the obtained occupation factors of the atomic sites of the $(Sb_7Te_8)^{5+}$ cluster when the structure is refined with all atom positions assumed to be occupied by Te exclusively. The standard deviations are indicated by vertical bars.

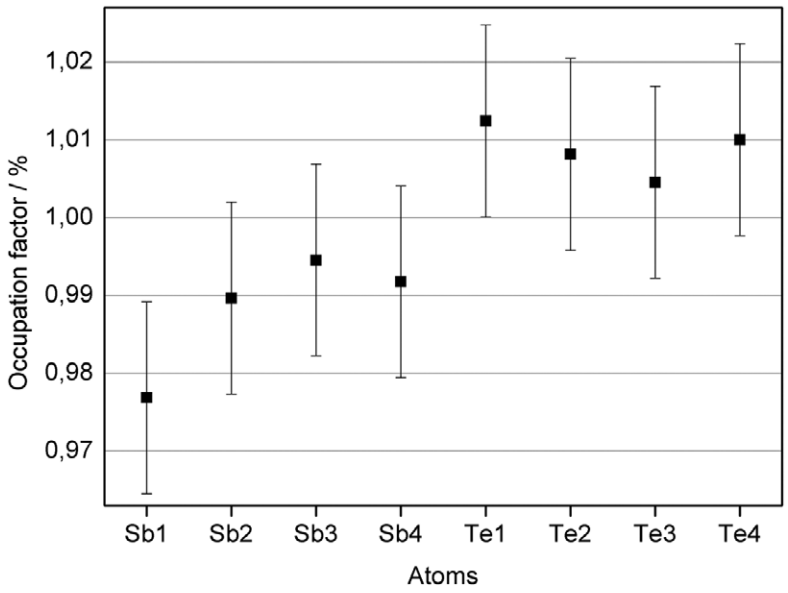

Fig. A 5.3.4 Graphical representation of the Sb/Te atom assignments in the structure of $Cu(Sb_7Te_8)[GaCl_4]_6$. Depicted are the obtained occupation factors of the atomic sites of the $(Sb_7Te_8)^{5+}$ cluster when the structure is refined with all atom positions assumed to be occupied by Te exclusively. The standard deviations are indicated by vertical bars.

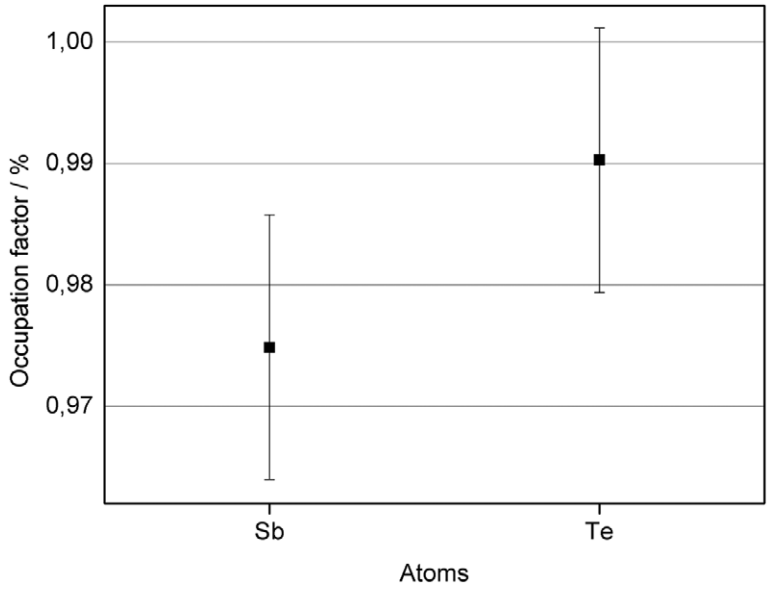

Fig. A 5.3.5 Graphical representation of the Sb/Te atom assignments in the structure of $(Sb_4Te_4)[GaCl_4]_4$. Depicted are the obtained occupation factors of the atomic sites of the $(Sb_4Te_4)^{4+}$ cluster when the structure is refined with all atom positions assumed to be occupied by Te exclusively. The standard deviations are indicated by vertical bars.

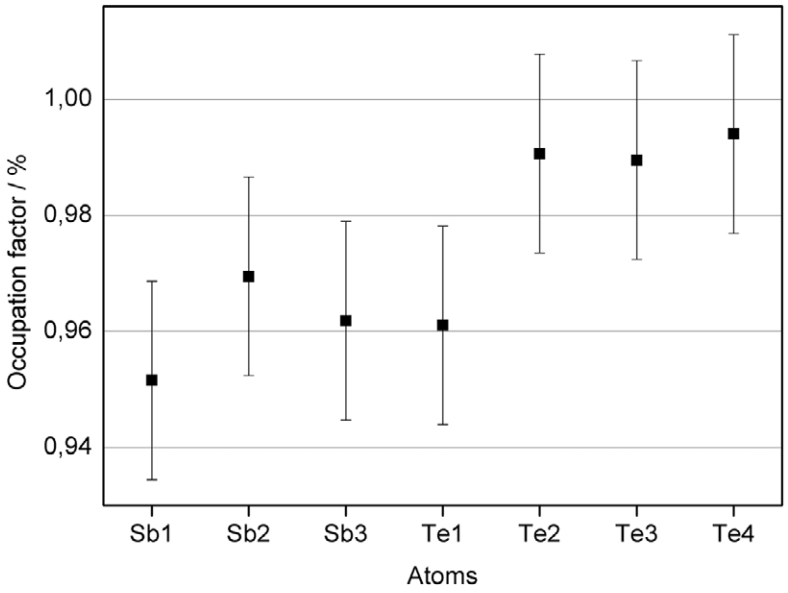

Fig. A 5.3.6 Graphical representation of the Sb/Te atom assignments in the structure of $(Sb_3Te_4)[Ga_2Cl_7]_3$. Depicted are the obtained occupation factors of the atomic sites of the $(Sb_3Te_4)^{3+}$ cluster when the structure is refined with all atom positions assumed to be occupied by Te exclusively. The standard deviations are indicated by vertical bars.

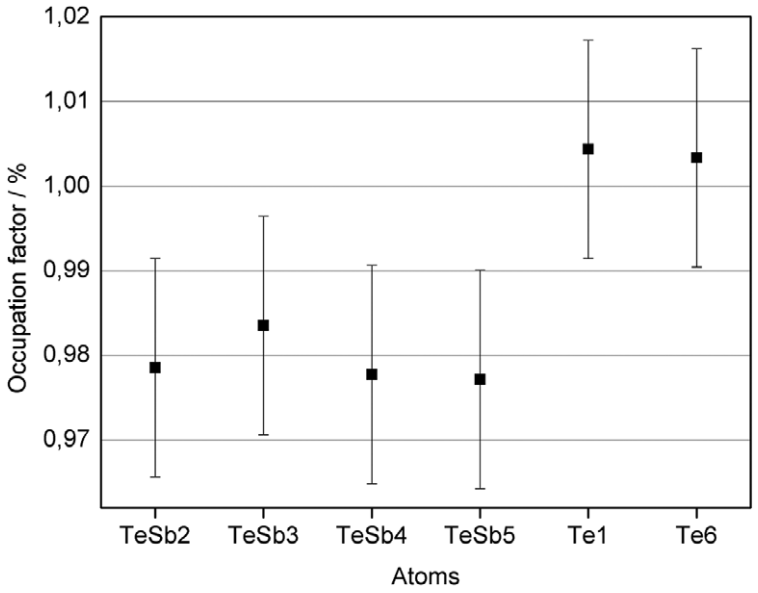

Fig. A 5.3.7 Graphical representation of the Sb/Te atom assignments in the structure of $(Sb_2Te_4)[Ga_2Cl_7]_2$. Depicted are the obtained occupation factors of the atomic sites of the $(Sb_2Te_4)^{2+}$ cluster when the structure is refined with all atom positions assumed to be occupied by Te exclusively. The standard deviations are indicated by vertical bars.

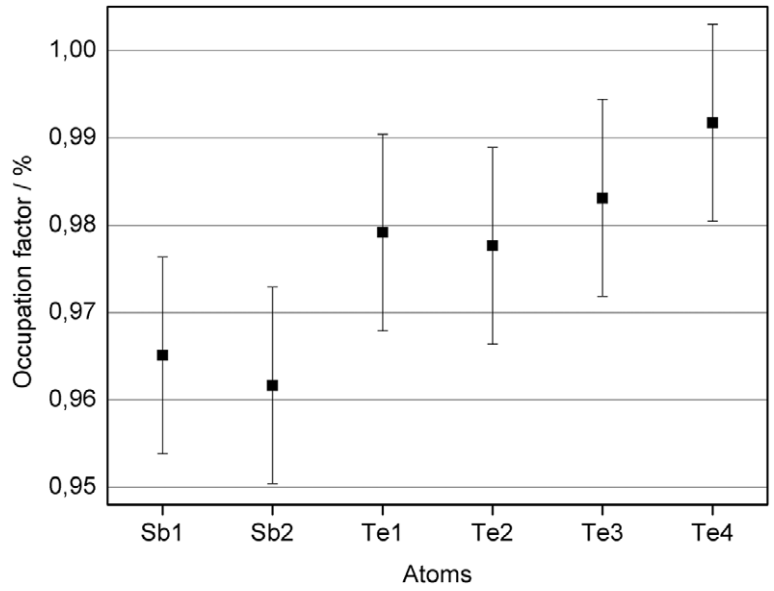

Fig. A 5.3.8 Graphical representation of the Sb/Te atom assignments in the structure of $(Sb_2Te_4)[GaCl_4]_2$. Depicted are the obtained occupation factors of the atomic sites of the $(Sb_2Te_4)^{2+}$ cluster when the structure is refined with all atom positions assumed to be occupied by Te exclusively. The standard deviations are indicated by vertical bars.

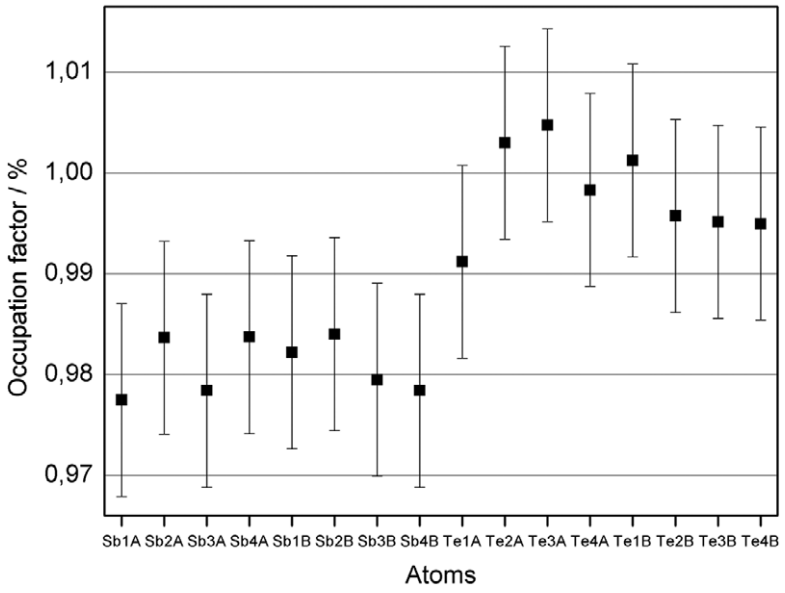

Fig. A 5.3.9 Graphical representation of the Sb/Te atom assignments in the structure of $(Sb_2Te_2)[GaCl_4]$. Depicted are the obtained occupation factors of the atomic sites of the $(Sb_2Te_2^{+})_n$ cluster when the structure is refined with all atom positions assumed to be occupied by Te exclusively. The standard deviations are indicated by vertical bars.

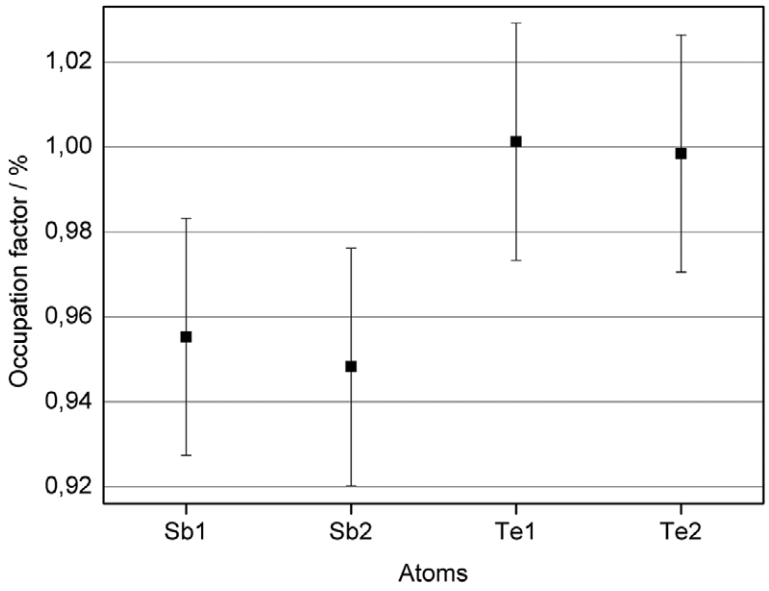

Fig. A 5.3.10 Graphical representation of the Sb/Te atom assignments in the structure of $(Sb_2Te_2)I[AlI_4]$. Depicted are the obtained occupation factors of the atomic sites of the $(Sb_2Te_2^{2+})_n$ cluster when the structure is refined with all atom positions assumed to be occupied by Te exclusively. The standard deviations are indicated by vertical bars.

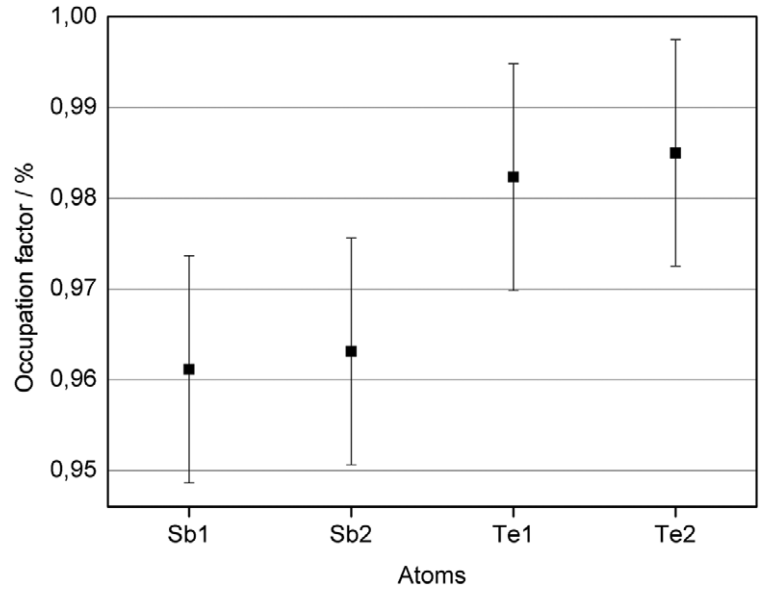

Fig. A 5.3.11 Graphical representation of the Sb/Te atom assignments in the structure of $(Sb_3Te_4)[GaCl_4]$. Depicted are the obtained occupation factors of the atomic sites of the $(Sb_3Te_4^{+})_n$ cluster when the structure is refined with all atom positions assumed to be occupied by Te exclusively. The standard deviations are indicated by vertical bars.

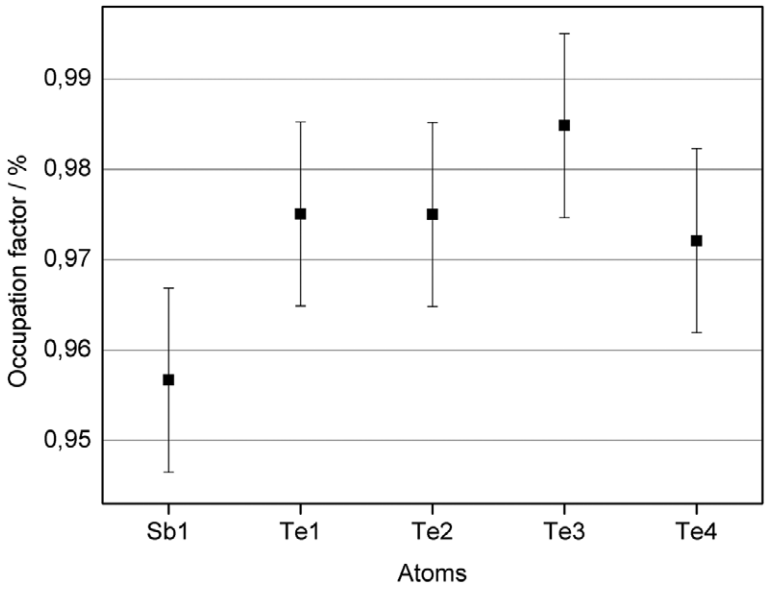

Fig. A 5.3.12 Graphical representation of the Sb/Te atom assignments in the structure of $(SbTe_4)[Ga_2Cl_7]$. Depicted are the obtained occupation factors of the atomic sites of the $(SbTe_4^+)_n$ cluster when the structure is refined with all atom positions assumed to be occupied by Te exclusively. The standard deviations are indicated by vertical bars.

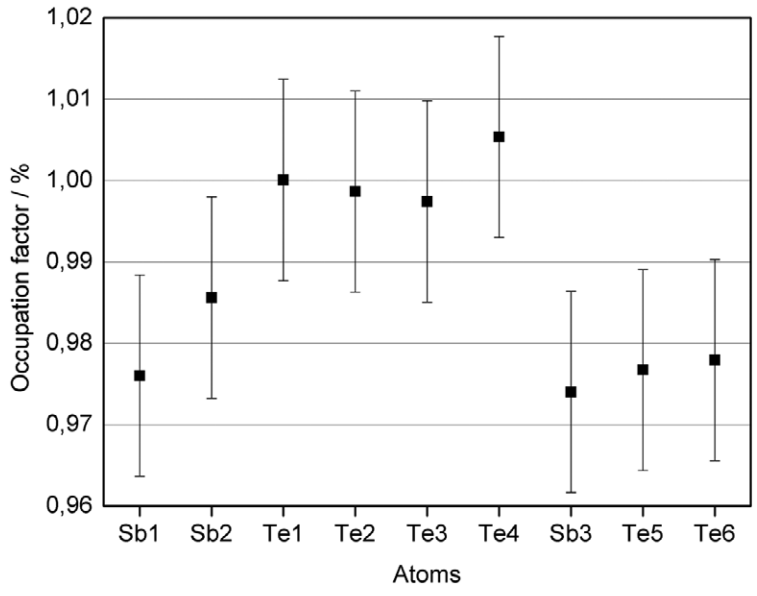

Fig. A 5.3.13 Graphical representation of the Sb/Te atom assignments in the structure of $(Sb_2Te_4)_2[Ga_2Cl_6O]_2$. Depicted are the obtained occupation factors of the atomic sites of the $(Sb_2Te_4)^{4+}$ clusters when the structure is refined with all atom positions assumed to be occupied by Te exclusively. The standard deviations are indicated by vertical bars.

A 5.4 Intramolecular Bond Lengths in Polycationic Clusters

Tab. A 5.4.1 Intramolecular bond lengths of the $(Sb_7Te_8)^{5+}$ cluster in the crystal structure of $(Sb_7Te_8)[GaCl_4]_3[Ga_2Cl_7]_2$ / Å. Standard deviations given in brackets refer to the last significant digit.

Bond	Length	Bond	Length
Sb1–Te1	2.9205(4)	Sb2–Te1	2.9056(4)
Sb1–Te3	3.1860(4)	Sb2–Te2	2.8830(4)
Sb1–Te4	2.9892(4)	Sb2–Te3	2.8009(4)
Sb1–Te5	2.9318(4)	Sb3–Te2	2.8803(4)
Sb1–Te7	3.2264(4)	Sb3–Te3	2.8340(4)
Sb1–Te8	3.0957(4)	Sb3–Te4	2.8853(4)
		Sb4–Te1	2.8682(4)
		Sb4–Te2	2.8867(4)
		Sb4–Te4	2.8486(4)
		Sb5–Te5	2.8838(4)
		Sb5–Te6	2.8844(5)
		Sb5–Te7	2.7886(4)
		Sb6–Te5	2.8768(4)
		Sb6–Te6	2.8569(4)
		Sb6–Te8	2.8258(4)
		Sb7–Te6	2.9072(4)
		Sb7–Te7	2.8163(4)
		Sb7–Te8	2.8696(4)

Tab. A 5.4.2 Intramolecular bond lengths of the $(Sb_7Te_8)^{5+}$ cluster in the crystal structure of $(Sb_7Te_8)[GaCl_4]_2[Ga_2Cl_7]_3$ / Å. Standard deviations given in brackets refer to the last significant digit.

Bond	Length	Bond	Length
Sb1–Te1	2.9025(5)	Sb2–Te1	2.9042(5)
Sb1–Te3	3.1356(5)	Sb2–Te2	2.8579(5)
Sb1–Te4	3.1556(5)	Sb2–Te3	2.8005(5)
Sb1–Te5	2.9605(5)	Sb3–Te2	2.9058(5)
Sb1–Te7	3.2334(5)	Sb3–Te3	2.8612(5)
Sb1–Te8	2.9514(5)	Sb3–Te4	2.8672(4)
		Sb4–Te1	2.9060(5)
		Sb4–Te2	2.8554(5)
		Sb4–Te4	2.7903(5)
		Sb5–Te5	2.8883(5)
		Sb5–Te6	2.8934(5)
		Sb5–Te7	2.8026(5)
		Sb6–Te5	2.8619(5)
		Sb6–Te6	2.8874(5)

		Sb6–Te8	2.8562(5)
		Sb7–Te6	2.8867(5)
		Sb7–Te7	2.7956(5)
		Sb7–Te8	2.9032(5)

Tab. A 5.4.3 Intramolecular bond lengths of the $(Sb_7Te_8)^{5+}$ cluster in the crystal structure of $Na(Sb_7Te_8)[GaCl_4]_6$ / Å. Standard deviations given in brackets refer to the last significant digit.

Bond	Length	Bond	Length
Sb1–Te1	2.991(2)	Sb2–Te1	2.879(2)
Sb1–Te3	2.999(1)	Sb2–Te2	2.915(1)
Sb1–Te4	3.010(2)	Sb2–Te3	2.848(2)
Sb1–Te5	3.012(2)	Sb3–Te2	2.869(1)
Sb1–Te7	3.044(2)	Sb3–Te3	2.850(2)
Sb1–Te8	3.014(1)	Sb3–Te4	2.860(2)
		Sb4–Te1	2.863(2)
		Sb4–Te2	2.851(1)
		Sb4–Te4	2.861(2)
		Sb5–Te5	2.843(2)
		Sb5–Te6	2.886(2)
		Sb5–Te7	2.863(2)
		Sb6–Te5	2.866(2)
		Sb6–Te6	2.859(2)
		Sb6–Te8	2.845(2)
		Sb7–Te6	2.874(2)
		Sb7–Te7	2.850(1)
		Sb7–Te8	2.855(2)

Tab. A 5.4.4 Intramolecular bond lengths of the $(Sb_7Te_8)^{5+}$ cluster in the crystal structure of $Ag(Sb_7Te_8)[GaCl_4]_6$ / Å at 123 K. Standard deviations given in brackets refer to the last significant digit.

Bond	Length	Bond	Length
Sb1–Te1	3.003(2)	Sb2–Te1	2.860(1)
Sb1–Te3	3.016(1)	Sb2–Te2	2.857(1)
Sb1–Te4	3.007(2)	Sb2–Te3	2.864(2)
Sb1–Te5	3.014(2)	Sb3–Te2	2.871(2)
Sb1–Te7	3.034(2)	Sb3–Te3	2.859(1)
Sb1–Te8	3.007(2)	Sb3–Te4	2.857(1)
		Sb4–Te1	2.873(2)
		Sb4–Te2	2.909(1)
		Sb4–Te4	2.850(2)
		Sb5–Te5	2.862(1)
		Sb5–Te6	2.870(2)
		Sb5–Te7	2.849(1)
		Sb6–Te5	2.847(1)

		Sb6–Te6	2.866(2)
		Sb6–Te8	2.864(1)
		Sb7–Te6	2.896(1)
		Sb7–Te7	2.871(2)
		Sb7–Te8	2.846(2)

Tab. A 5.4.5 Intramolecular bond lengths of the $(Sb_7Te_8)^{5+}$ cluster in the crystal structure of $Cu(Sb_7Te_8)[GaCl_4]_6$ / Å at 100 K. Standard deviations given in brackets refer to the last significant digit.

Bond	Length	Bond	Length
Sb1–Te1	3.0057(3)	Sb2–Te2	2.8575(4)
Sb1–Te2	3.0171(3)	Sb2–Te3	2.8670(4)
Sb1–Te3	3.0138(3)	Sb2–Te4	2.8659(4)
		Sb3–Te1	2.8449(4)
		Sb3–Te3	2.8580(4)
		Sb3–Te4	2.8775(4)
		Sb4–Te1	2.8525(4)
		Sb4–Te2	2.8750(4)
		Sb4–Te4	2.8946(4)

Tab. A 5.4.6 Intramolecular bond lengths of the $(Sb_7Se_8)^{5+}$ cluster in the crystal structure of $(Sb_7Se_8)[GaCl_4]_2[Ga_2Cl_7]_3$ / Å at 100 K. Standard deviations given in brackets refer to the last significant digit.

Bond	Length	Bond	Length
Sb1–Se1	2.719(2)	Sb2–Se1	2.690(2)
Sb1–Se3	3.013(2)	Sb2–Se2	2.672(2)
Sb1–Se4	2.977(2)	Sb2–Se3	2.579(2)
Sb1–Se5	2.730(2)	Sb3–Se2	2.691(2)
Sb1–Se7	3.111(2)	Sb3–Se3	2.649(2)
Sb1–Se8	2.7512)	Sb3–Se4	2.655(2)
		Sb4–Se1	2.696(2)
		Sb4–Se2	2.674(2)
		Sb4–Se4	2.589(2)
		Sb5–Se5	2.689(2)
		Sb5–Se6	2.714(2)
		Sb5–Se7	2.581(2)
		Sb6–Se5	2.663(2)
		Sb6–Se6	2.683(2)
		Sb6–Se8	2.681(2)
		Sb7–Se6	2.709(2)
		Sb7–Te7	2.604(2)
		Sb7–Te8	2.679(1)

Tab. A 5.4.7 Intramolecular bond lengths of the $(Sb_7Se_8Cl_2)^{3+}$ cluster in the crystal structure of $(Sb_7Se_8Cl_2)[GaCl_4]_3$ / Å at 100 K. Standard deviations given in brackets refer to the last significant digit.

Bond	Length	Bond	Length
Sb1–Se1	2.7316(7)	Sb2–Se1	2.6955(7)
Sb1–Se3	3.0306(7)	Sb2–Se3	2.5847(7)
Sb1–Se4	2.8397(7)	Sb3–Se2	2.5919(6)
Sb1–Se5	2.7652(7)	Sb3–Se3	2.6349(6)
Sb1–Se7	3.0542(7)	Sb3–Se4	2.6533(7)
Sb1–Se8	2.844(8)	Sb4–Se1	2.6925(6)
		Sb4–Se2	2.5752(6)
		Sb4–Se4	2.6239(7)
		Sb5–Se5	2.6875(7)
		Sb5–Se7	2.5798(7)
		Sb6–Se5	2.7020(6)
		Sb6–Se6	2.5750(6)
		Sb6–Se8	2.6077(7)
		Sb7–Se6	2.5915(6)
		Sb7–Se7	2.6230(6)
		Sb7–Se8	2.666(8)
		Sb2–Cl1	2.377(2)
		Sb5–Cl2	2.401(2)

Tab. A 5.4.8 Intramolecular bond lengths of the $(Sb_7S_8Cl_2)^{3+}$ cluster in the crystal structure of $(Sb_7S_8Cl_2)[GaCl_4]_3$ / Å at 123 K. Standard deviations given in brackets refer to the last significant digit.

Bond	Length	Bond	Length
Sb1–S1	2.580(4)	Sb2–S1	2.564(4)
Sb1–S3	2.707(4)	Sb2–S2	2.439(4)
Sb1–S4	2.968(4)	Sb2–S3	2.477(4)
Sb1–S5	2.744(4)	Sb3–S2	2.439(4)
Sb1–S7	2.983(4)	Sb3–S3	2.536(4)
Sb1–S8	2.607(4)	Sb3–S4	2.490(4)
		Sb4–S1	2.582(4)
		Sb4–S4	2.427(4)
		Sb5–S5	2.527(4)
		Sb5–S6	2.444(4)
		Sb5–S7	2.501(5)
		Sb6–S5	2.460(4)
		Sb6–S6	2.434(4)
		Sb6–S8	2.571(4)
		Sb7–S7	2.438(4)
		Sb7–S8	2.562(4)
		Sb4–Cl2	2.367(5)
		Sb7–Cl1	2.389(4)

Tab. A 5.4.9 Intramolecular bond lengths of the $(Sb_4Te_4)^{4+}$ and $(Sb_4Se_4)^{4+}$ clusters in the crystal structures of $(Sb_4Ch_4)[GaCl_4]_4$ / Å at 100 K. Standard deviations given in brackets refer to the last significant digit.

$(Sb_4Te_4)^{4+}$		$(Sb_4Se_4)^{4+}$	
Bond	Length	Bond	Length
Sb–Te	2.8635(4)	Sb–Se	2.7631(7)
Sb–Te	2.8658(4)	Sb–Se	2.6670(6)
Sb–Te	2.9377(4)	Sb–Se	2.6627(6)

Tab. A 5.4.10 Intramolecular bond lengths of the $(Sb_3Te_4)^{3+}$ cluster in the crystal structure of $(Sb_3Te_4)[Ga_2Cl_7]_3$ / Å at 123 K. Standard deviations given in brackets refer to the last significant digit.

Bond	Length
Sb1–Te1	2.7390(5)
Sb1–Te2	2.8382(5)
Sb1–Te3	2.9752(5)
Sb2–Te1	2.7367(5)
Sb2–Te2	2.8508(5)
Sb2–Te4	2.9464(5)
Sb3–Te2	2.8680(5)
Sb3–Te3	2.8450(5)
Sb3–Te4	2.8433(5)
Te3–Te4	2.7471(5)

Tab. A 5.4.11 Intramolecular bond lengths of the $(Sb_2Te_4)^{2+}$ clusters in the crystal structures of $(Sb_2Te_4)[Ga_2Cl_7]_2$ (left) and $(Sb_2Te_4)[GaCl_4]_2$ (right) / Å at 123 K. Standard deviations given in brackets refer to the last significant digit.

$(Sb_2Te_4)^{2+}$		$(Sb_2Te_4)^{2+}$	
Bond	Length	Bond	Length
SbTe2–Te1	2.698(2)	Sb1–Sb2	2.678(2)
SbTe2–bTe3	2.752(2)	Sb1–Te1	2.690(2)
SbTe2–SbTe5	3.116(2)	Sb1–Te4	3.596(2)
SbTe3–Te1	2.725(1)	Sb2–Te1	2.795(2)
Sb Te3–SbTe4	3.069(2)	Sb2–Te3	2.974(2)
SbTe4–Te6	2.719(2)	Te1–Te2	2.974(2)
SbTe4–SbTe5	2.754(2)	Te2–Te3	2.788(2)
SbTe5–Te6	2.706(1)	Te2–Te4	2.703(2)
Te1–Te6	3.305(2)	Te3–Te4	2.703(2)

Tab. A 5.4.11 Intramolecular bond lengths of the $(Sb_2Te_2^+)_n$ chains in the crystal structure of $(Sb_2Te_2)[GaCl_4]$ / Å at 123 K. Standard deviations given in brackets refer to the last significant digit.

$(Sb_2Te_2)^+$ (chain a)		$(Sb_2Te_2)^+$ (chain b)	
Bond	Length	Bond	Length
Sb1–Te1a	2.8335(7)	Sb1b–Te1b	2.8455(7)
Sb1a–Te1a	2.8407(8)	Sb1b–Te1b	2.8415(7)
Sb2a–Te2a	2.8203(7)	Sb2b–Te1b	3.0028(8)
Sb2a–Te3a	2.8368(7)	Sb2b–Te2b	2.8049(7)
Sb3a–Te1a	2.9749(8)	Sb2b–Te3b	2.8149(7)
Sb3a–Te2a	2.8040(7)	Sb3b–Te2b	2.8222(7)
Sb3a–Te3a	2.8288(7)	Sb3b–Te3b	2.8320(7)
Sb4a–Te3a	3.0460(8)	Sb4b–Te3b	3.0126(8)
Sb4a–Te4a	2.8133(7)	Sb4b–Te4b	2.8267(7)
Sb4a–Te4a	2.7982(7)	Sb4b–Te4b	2.8048(7)

Tab. A 5.4.12 Intramolecular bond lengths of the $(Bi_2Te_2^{2+})_n$ and $(Bi_2Te_2^{2+})_n$ chains in the crystal structures of $(Bi_2Ch_2)Cl[GaCl_4]$ / Å at 123 K. Standard deviations given in brackets refer to the last significant digit.

$(Bi_2Te_2)^{2+}$		$(Bi_2Se_2)^{2+}$	
Bond	Length	Bond	Length
Bi–Te	2.9631(5)	Bi–Se	2.781(1)
Bi–Te	2.9673(3)	Bi–Se	2.782(2)

Tab. A 5.4.13 Intramolecular bond lengths of the $(Sb_2Te_2^{2+})_n$ chain in the crystal structure of $(Sb_2Te_2)I[AlI_4]$ / Å at 123 K. Standard deviations given in brackets refer to the last significant digit.

Bond	Length
Sb1–Te1	2.8059(9)
Sb1–Te1	2.962(1)
Sb1–Te2	2.918(1)
Sb2–Te1	3.095(1)
Sb2–Te2	2.8238(9)
Sb2–Te2	2.947(1)

Tab. A 5.4.14 Intramolecular bond lengths of the $(Sb_3Te_4)^+$ chain in the crystal structure of $(Sb_3Te_4)[GaCl_4]$ / Å at 123 K. Standard deviations given in brackets refer to the last significant digit.

Bond	Length
Sb1–Te1	3.0257(5)
Sb1–Te2	3.0280(7)
Sb2–Te1	2.8686(9)
Sb2–Te1	3.5375(8)
Sb2–Te2	2.8876(7)

Tab. A 5.4.15 Intramolecular bond lengths of the $(SbTe_4)^+$ chain in the crystal structure of $(SbTe_4)[Ga_2Cl_7]$ / Å at 123 K. Standard deviations given in brackets refer to the last significant digit.

Bond	Length
Sb–Te1	3.0597(14)
Sb–Te1	2.8328(14)
Sb–Te4	3.1400(14)
Sb–Te4	2.8170(14)
Te1–Te2	2.7501(14)
Te2–Te3	2.6960(15)
Te3–Te4	2.7442(14)

Tab. A 5.4.16 Chosen intramolecular bond lengths in the crystal structures of $Ch_4Cu[GaCl_4]$ / Å at 123 K. Standard deviations given in brackets refer to the last significant digit.

$CuSe_4[GaCl_4]$		$CuTe_4[GaCl_4]$	
Bond	Length	Bond	Length
Se1–Se2	2.3225(4)	Te1–Te2	2.7471(7)
Se1–Se4	2.4321(4)	Te1–Te4	2.8444(6)
Se2–Se3	2.3724(4)	Te2–Te3	2.7710(7)
Se3–Se4	2.3576(4)	Te3–Te4	2.7070(6)
Se1–Cu	2.4158(5)	Te1–Cu	2.582(1)
Se3–Cu	2.4557(4)	Te3–Cu	2.5853(9)
Se4–Cu	2.4478(5)	Te4–Cu	2.558(1)
Cu–Cl1	2.3354(7)	Cu–Cl1	2.432(2)

Tab. A 5.4.17 Chosen intramolecular bond lengths in the crystal structure of $Cu_2Se_7[GaCl_4]_2$ / Å at 123 K. Standard deviations given in brackets refer to the last significant digit.

Bond	Length
Se1–Se1’	2.3210(8)
Se1–Se2	2.3313(9)
Se2–Se3	2.3983(8)
Se3–Se4	2.3390(8)
Se2–Cu	2.4091(9)
Se3–Cu	2.399(1)
Cu–Cl1	2.331(2)
Cu–Cl4	2.395(2)

Tab. A 5.4.18 Intramolecular bond lengths of the $(Bi_4Te_4)^{3+}$ cluster in the crystal structure of $(Bi_4Te_4)[GaCl_4]_2[Ga_2Cl_7]$ / Å at 123 K. Standard deviations given in brackets refer to the last significant digit.

Bond	Length
Bi1–Te1	2.9721(9)
Bi1–Te2	2.945(1)
Bi1–Te3	2.988(1)
Bi2–Te1	2.964(1)
Bi2–Te2	2.9864(9)
Bi2–Te4	2.972(1)
Bi3–Te1	2.980(1)
Bi3–Te3	2.988(1)
Bi3–Te4	2.959(1)
Bi4–Te2	3.001(1)
Bi4–Te3	2.962(1)
Bi4–Te4	2.9654(9)

Tab. A 5.4.19 Intramolecular bond lengths of the $(Bi_4Se_4)^{3+}$ cluster in the crystal structure of $(Bi_4Se_4)[GaCl_4][SeGa_3Cl_9]$ / Å at 123 K. Standard deviations given in brackets refer to the last significant digit.

Bond	Length
Bi1–Se1	2.778(5)
Bi1–Se3	2.787(4)
Bi1–Se4	2.788(5)
Bi2–Se2	2.772(4)
Bi2–Se3	2.774(5)
Bi2–Se4	2.786(4)
Bi3–Se1	2.790(5)
Bi3–Se2	2.775(4)
Bi3–Se4	2.772(4)
Bi4–Se1	2.774(4)
Bi4–Se2	2.777(4)
Bi4–Se3	2.785(5)

A 5.5 Sb···Cl and Te···Cl Distances Around Polycationic Clusters

The interactions between the pentele and chalcogen atoms of the polycationic clusters and the chlorine atoms of the coordinating anions were analyzed up to 4 or 4.1 Å. Generally, the Pn···Cl distances are shorter than the Ch···Cl distances due to a higher positive charge on the pentele atoms. Consequently, this analysis is a useful tool to confirm the Sb and Te positions in Sb-Te clusters since these elements are difficult to distinguish on basis of X-ray diffraction data.

Tab. A 5.5.1 Intermolecular distance ranges of the Sb and Te atoms within the $(Sb_7Te_8)^{5+}$ cluster to the surrounding Cl atoms up to 4 Å in the crystal structure of $(Sb_7Te_8)[GaCl_4]_3[Ga_2Cl_7]_2$. Standard deviations given in brackets refer to the last significant digit.

Contact	Range	Contact	Range
Sb1 ··· Cl	-	Te1 ··· Cl	3.590(1) - 3.721(2)
Sb2 ··· Cl	3.129(1) - 3.992(2)	Te2 ··· Cl	3.593(1) - 3.826(2)
Sb3 ··· Cl	3.127(2) - 3.900(2)	Te3 ··· Cl	3.525(1) - 3.933(1)
Sb4 ··· Cl	3.102(2) - 3.371(1)	Te4 ··· Cl	3.534(2) - 3.748(2)
Sb5 ··· Cl	3.239(2) - 3.923(1)	Te5 ··· Cl	3.488(1) - 3.876(2)
Sb6 ··· Cl	3.233(2) - 3.845(1)	Te6 ··· Cl	3.614(1) - 3.853(1)
Sb7 ··· Cl	3.096(2) - 3.488(1)	Te7 ··· Cl	3.539(1) - 3.760(2)
		Te8 ··· Cl	3.584(1) - 3.918(2)

Tab. A 5.5.2 Intermolecular distance ranges of the Sb and Te atoms within the $(Sb_7Te_8)^{5+}$ cluster to the surrounding Cl atoms up to 4 Å in the crystal structure of $(Sb_7Te_8)[GaCl_4]_2[Ga_2Cl_7]_3$. Standard deviations given in brackets refer to the last significant digit.

Contact	Range	Contact	Range
Sb1 ··· Cl	-	Te1 ··· Cl	3.465(1) - 3.914(1)
Sb2 ··· Cl	3.154(2) - 3.495(1)	Te2 ··· Cl	3.460(2) - 3.957(2)
Sb3 ··· Cl	3.153(2) - 3.794(1)	Te3 ··· Cl	3.546(2) - 3.795(2)
Sb4 ··· Cl	3.194(2) - 3.970(1)	Te4 ··· Cl	3.525(1) - 3.904(2)
Sb5 ··· Cl	3.164(2) - 4.008(1)	Te5 ··· Cl	3.718(1) - 3.987(2)
Sb6 ··· Cl	3.071(1) - 3.872(2)	Te6 ··· Cl	3.504(2) - 3.943(1)
Sb7 ··· Cl	3.155(2) - 4.005(1)	Te7 ··· Cl	3.484(2) - 3.769(1)
		Te8 ··· Cl	3.637(1) - 3.946(1)

Tab. A 5.5.3 Intermolecular distance ranges of the Sb and Te atoms within the $(Sb_7Te_8)^{5+}$ cluster to the surrounding Cl atoms up to 4 Å in the crystal structure of $Na(Sb_7Te_8)[GaCl_4]_6$. Standard deviations given in brackets refer to the last significant digit.

Contact	Range	Contact	Range
Sb1 ··· Cl	-	Te1 ··· Cl	3.636(4) - 3.900(4)
Sb2 ··· Cl	3.074(4) - 3.670(4)	Te2 ··· Cl	3.433(4) - 3.755(4)
Sb3 ··· Cl	3.185(4) - 3.835(4)	Te3 ··· Cl	3.666(4) - 3.976(4)
Sb4 ··· Cl	3.202(4) - 3.931(4)	Te4 ··· Cl	3.623(4) - 3.958(4)
Sb5 ··· Cl	3.199(4) - 3.776(4)	Te5 ··· Cl	3.673(4) - 3.976(4)
Sb6 ··· Cl	3.201(4) - 3.841(4)	Te6 ··· Cl	3.576(4) - 3.862(4)
Sb7 ··· Cl	3.183(4) - 3.912(4)	Te7 ··· Cl	3.635(4) - 3.832(4)
		Te8 ··· Cl	3.396(4) - 3.778(4)

Tab. A 5.5.4 Intermolecular distance ranges of the Sb and Te atoms within the $(Sb_7Te_8)^{5+}$ cluster to the surrounding Cl atoms up to 4 Å in the crystal structure of $Ag(Sb_7Te_8)[GaCl_4]_6$. Standard deviations given in brackets refer to the last significant digit.

Contact	Range	Contact	Range
Sb1 ··· Cl	-	Te1 ··· Cl	3.653(3) - 3.919(3)
Sb2 ··· Cl	3.190(5) - 3.942(3)	Te2 ··· Cl	3.474(4) - 3.993(4)
Sb3 ··· Cl	3.191(5) - 3.944(5)	Te3 ··· Cl	3.626(3) - 3.796(4)
Sb4 ··· Cl	3.117(3) - 3.791(3)	Te4 ··· Cl	3.671(5) - 3.883(3)
Sb5 ··· Cl	3.162(4) - 3.904(3)	Te5 ··· Cl	3.459(4) - 3.828(4)
Sb6 ··· Cl	3.202(4) - 3.874(4)	Te6 ··· Cl	3.549(4) - 3.907(4)
Sb7 ··· Cl	3.184(4) - 3.737(4)	Te7 ··· Cl	3.670(5) - 3.878(3)
		Te8 ··· Cl	3.656(5) - 3.962(3)

Tab. A 5.5.5 Intermolecular distance ranges of the Sb and Te atoms within the $(Sb_7Te_8)^{5+}$ cluster to the surrounding Cl atoms up to 4 Å in the crystal structure of $Cu(Sb_7Te_8)[GaCl_4]_6$. Standard deviations given in brackets refer to the last significant digit.

Contact	Range	Contact	Range
Sb1 ··· Cl	-	Te1 ··· Cl	3.8018(9) - 3.881(1)
Sb2 ··· Cl	3.1587(9) - 4.0087(9)	Te2 ··· Cl	3.6804(9) - 3.917(1)
Sb3 ··· Cl	3.193(1) - 3.0049(9)	Te3 ··· Cl	3.565(1) - 3.8074(9)
Sb4 ··· Cl	3.1764(9) - 3.643(1)	Te4 ··· Cl	3.529(1) - 3.965(1)

Tab. A 5.5.6 Intermolecular distances and distance ranges of the Sb and Te atoms within the $(Sb_4Te_4)^{4+}$ cluster to the surrounding Cl atoms up to 4 Å in the crystal structure of $(Sb_4Te_4)[GaCl_4]_4$. Standard deviations given in brackets refer to the last significant digit.

Contact	Distance / Range	Contact	Distance / Range
Sb ··· Cl1	2.9753(9)	Te ··· Cl1	3.8537(9)
Sb ··· Cl2	3.6482(9)	Te ··· Cl2	3.842(1)
Sb ··· Cl3	3.144(1) - 3.702(1)	Te ··· Cl3	3.6478(9)
Sb ··· Cl4	3.1556(9)	Te ··· Cl4	3.691(1) - 3.692(1)

Tab. A 5.5.7 Intermolecular distance ranges of the Sb and Te atoms within the $(Sb_3Te_4)^{3+}$ cluster to the surrounding Cl atoms up to 4 Å in the crystal structure of $(Sb_3Te_4)[Ga_2Cl_7]_3$. Standard deviations given in brackets refer to the last significant digit.

Contact	Range	Contact	Range
Sb1 ··· Cl	3.242(2) - 3.951(2)	Te1 ··· Cl	3.674(2) - 3.986(2)
Sb2 ··· Cl	3.201(2) - 3.685(2)	Te2 ··· Cl	3.472(1) - 3.754(1)
Sb3 ··· Cl	3.220(2) - 3.738(2)	Te3 ··· Cl	3.231(2) - 3.844(1)
		Te4 ··· Cl	3.499(2) - 4.007(1)

Tab. A 5.5.8 Intermolecular distance ranges of the Sb and Te atoms within the $(Sb_2Te_4)^{2+}$ cluster to the surrounding Cl atoms up to 4 Å in the crystal structure of $(Sb_2Te_4)[Ga_2Cl_7]_2$. Standard deviations given in brackets refer to the last significant digit.

Contact	Distance / Range	Contact	Distance / Range
TeSb2 ··· Cl	3.509(5) - 3.876(5)	Te1 ··· Cl	3.576(4) - 3.821(3)
TeSb3 ··· Cl	3.285(4) - 3.903(3)	Te6 ··· Cl	3.499(4) - 3.908(4)
TeSb4 ··· Cl	3.467(3) - 3.940(3)		
TeSb5 ··· Cl	3.652(4) - 3.988(4)		

Tab. A 5.5.9 Intermolecular distance ranges of the Sb and Te atoms within the $(Sb_2Te_4)^{2+}$ cluster to the surrounding Cl atoms up to 4 Å in the crystal structure of $(Sb_2Te_4)[GaCl_4]_2$. Standard deviations given in brackets refer to the last significant digit.

Contact	Distance / Range	Contact	Distance / Range
Sb1 ··· Cl	3.452(5) - 3.996(5)	Te1 ··· Cl	3.506(4) - 3.960(5)
Sb2 ··· Cl	3.449(4) - 3.959(5)	Te2 ··· Cl	3.445(5) - 3.726(4)
		Te3 ··· Cl	3.481(5) - 3.982(5)
		Te4 ··· Cl	3.595(4) - 3.846(5)

Tab. A 5.5.10 Intermolecular distance ranges of the Sb and Te atoms within the $(Sb_2Te_2^+)_n$ cluster to the surrounding Cl atoms up to 4 Å in the crystal structure of $(Sb_2Te_2)[GaCl_4]$. Standard deviations given in brackets refer to the last significant digit.

Contact	Range	Contact	Range
Sb1A ··· Cl	3.440(2) - 3.897(2)	Te1A ··· Cl	3.742(2) - 3.896(2)
Sb2A ··· Cl	3.389(2) - 3.739(2)	Te2A ··· Cl	3.807(2) - 3.907(2)
Sb3A ··· Cl	3.328(2) - 3.961(2)	Te3A ··· Cl	3.724(2) - 3.927(2)
Sb4A ··· Cl	3.385(2) - 3.731(2)	Te4A ··· Cl	3.513(2) - 4.001(2)
Sb1B ··· Cl	3.409(2) - 3.790(2)	Te1B ··· Cl	3.617(2) - 3.877(2)
Sb2B ··· Cl	3.245(2) - 3.902(2)	Te2B ··· Cl	3.456(2) - 3.851(2)
Sb3B ··· Cl	3.459(2) - 3.614(2)	Te3B ··· Cl	3.381 (2) - 3.971(2)
Sb4B ··· Cl	3.224(2) - 3.788(2)	Te4B ··· Cl	3.656(2) - 3.969(2)

Tab. A 5.5.11 Intermolecular distance ranges of the Sb and Te atoms within the $(Sb_2Te_2^{2+})_n$ cluster to the surrounding I atoms up to 4 Å in the crystal structure of $(Sb_2Te_2)I[AlI_4]$. Standard deviations given in brackets refer to the last significant digit.

Contact	Range	Contact	Range
Sb1 ··· I	3.199(2) - 3.797(1)	Te1 ··· I	3.8640(9) - 3.9864(9)
Sb2 ··· I	3.051(1) - 3.800(1)	Te2 ··· I	3.8248(9) - 3.9731(9)

Tab. A 5.5.12 Intermolecular distance ranges of the Sb and Te atoms within the $(Sb_3Te_4^+)_n$ cluster to the surrounding Cl atoms up to 4 Å in the crystal structure of $(Sb_3Te_4)[GaCl_4]$. Standard deviations given in brackets refer to the last significant digit.

Contact	Range	Contact	Range
Sb1 ··· Cl	-	Te1 ··· Cl	3.546(2)
Sb2 ··· Cl	3.291(4) - 3.830(2)	Te2 ··· Cl	3.590(4) - 3.926(4)

Tab. A 5.5.13 Intermolecular distance ranges of the Sb and Te atoms within the $(SbTe_4^+)_n$ cluster to the surrounding Cl atoms up to 4 Å in the crystal structure of $(SbTe_4)[Ga_2Cl_7]$. Standard deviations given in brackets refer to the last significant digit.

Contact	Range	Contact	Range
Sb1 ··· Cl	3.536(5) - 3.760(6)	Te1 ··· Cl	3.573(4) - 3.806(4)
		Te2 ··· Cl	3.500(4) - 3.763(4)
		Te3 ··· Cl	3.577(4) - 3.882(4)
		Te4 ··· Cl	3.566(4) - 3.973(4)

Tab. A 5.5.14 Intermolecular distance ranges of the Sb and Te atoms within the $(Sb_2Te_4)^{4+}$ clusters to the surrounding Cl atoms up to 4 Å in the crystal structure of $(Sb_2Te_4)_2[Ga_2Cl_6O]_4$. Standard deviations given in brackets refer to the last significant digit.

Contact	Range	Contact	Range
Sb1 ··· Cl	3.553(4) - 4.060(4)	Te1 ··· Cl	3.573(6) - 3.911(4)
Sb2 ··· Cl	3.463(4) - 3.936(4)	Te2 ··· Cl	3.531(5) - 3.787(4)
Sb3 ··· Cl	3.440(5) - 4.032(6)	Te3 ··· Cl	3.353(4) - 3.986(4)
		Te4 ··· Cl	3.453(5) - 3.742(4)
		Te5 ··· Cl	3.586(5) - 3.949(6)
		Te6 ··· Cl	3.595(5) - 3.968(6)

Tab. A 5.5.15 Intermolecular distance ranges of the Bi and Te atoms within the $(Bi_4Te_4)^{3+}$ cluster to the surrounding Cl atoms up to 4 Å in the crystal structure of $(Bi_4Te_4)[GaCl_4]_2[Ga_2Cl_7]$. Standard deviations given in brackets refer to the last significant digit.

Contact	Range	Contact	Range
Bi1 ··· Cl	3.307(4) - 3.566(3)	Te1 ··· Cl	3.733(4) - 3.860(3)
Bi2 ··· Cl	3.183(3) - 4.015(4)	Te2 ··· Cl	3.543(4) - 3.946(4)
Bi3 ··· Cl	3.507(4) - 3.754(4)	Te3 ··· Cl	3.702(3) - 3.945(4)
Bi4 ··· Cl	3.218(4) - 3.635(4)	Te4 ··· Cl	3.706(4) - 3.933(3)

Tab. A 5.5.16 Intermolecular distance ranges of the Bi and Se atoms within the $(Bi_4Se_4)^{3+}$ cluster to the surrounding Cl atoms up to 4.1 Å in the crystal structure of $(Bi_4Se_4)[GaCl_4][SeGa_3Cl_9]$. Standard deviations given in brackets refer to the last significant digit.

Contact	Range	Contact	Range
Bi1 ··· Cl	3.603(9) - 4.10(2)	Se1 ··· Cl	3.59(2) - 3.80(1)
Bi2 ··· Cl	3.20(2) - 4.04(1)	Se2 ··· Cl	3.64(1) - 3.65(2)
Bi3 ··· Cl	3.18(1) - 4.05(1)	Se3 ··· Cl	3.57(2) - 3.80(1)
Bi4 ··· Cl	3.18(2) - 4.04(2)	Se4 ··· Cl	3.59(2) - 3.79(2)

A 5.6 Coordination Spheres of Discrete Polycationic Clusters

The coordination spheres of all discrete polycationic clusters were analyzed. Generally, the number of coordinating anions corresponds to the cluster's charge. Higher charged clusters need a higher number of weakly coordinating anions to be stabilized.

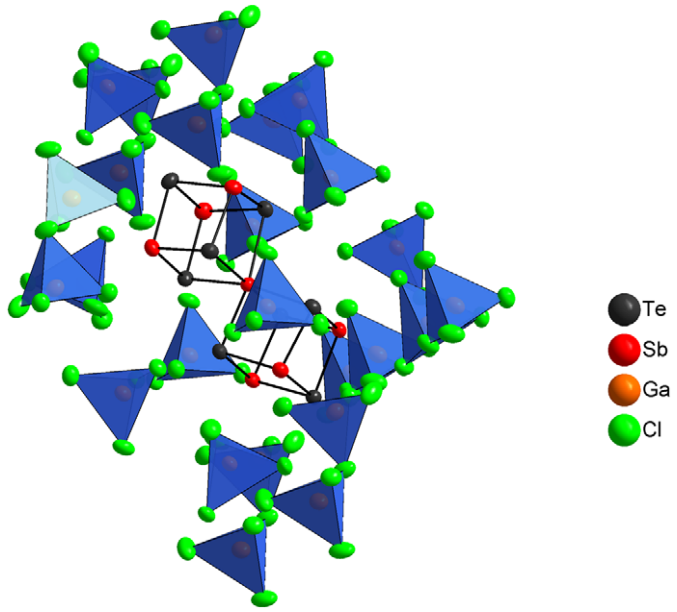

Fig. A 5.6.1 The coordination sphere of the $(Sb_7Te_8)^{5+}$ cluster by surrounding $[GaCl_4]^-$ and $[Ga_2Cl_7]^-$ ions in the structure of $(Sb_7Te_8)[GaCl_4]_3[Ga_2Cl_7]_2$. The atoms are represented by thermal ellipsoids scaled to include a probability of 80 %. The $[GaCl_4]^-$ and $[Ga_2Cl_7]^-$ ions are shown as discrete tetrahedra and double tetrahedra.

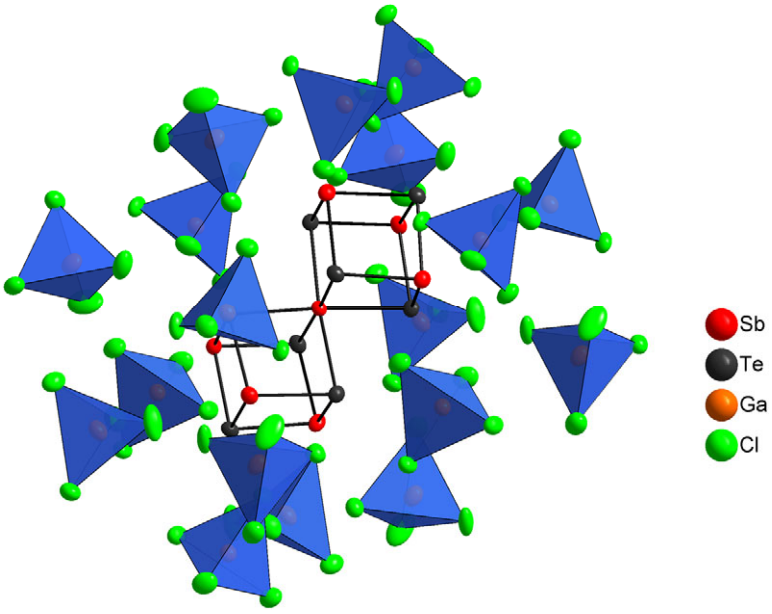

Fig. A 5.6.2 The coordination sphere of the $(Sb_7Te_8)^{5+}$ cluster by surrounding $[GaCl_4]^-$ ions in the structure of $Na(Sb_7Te_8)[GaCl_4]_6$. The atoms are represented by thermal ellipsoids scaled to include a probability of 80 %. The $[GaCl_4]^-$ ions are shown as discrete tetrahedra. Na^+ ions are omitted for clarity.

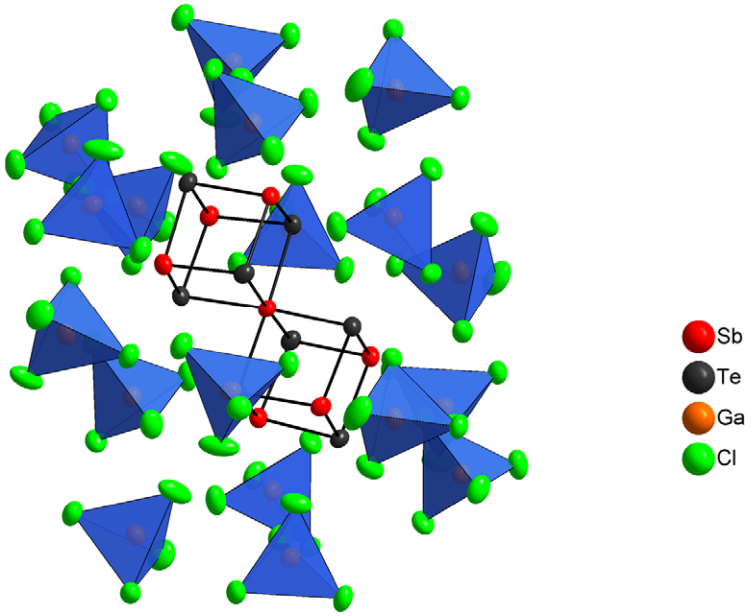

Fig. A 5.6.3 The coordination sphere of the $(Sb_7Te_8)^{5+}$ cluster by surrounding $[GaCl_4]^-$ ions in the structure of $Ag(Sb_7Te_8)[GaCl_4]_6$. The atoms are represented by thermal ellipsoids scaled to include a probability of 80 %. The $[GaCl_4]^-$ ions are shown as discrete tetrahedra. Ag^+ ions are omitted for clarity.

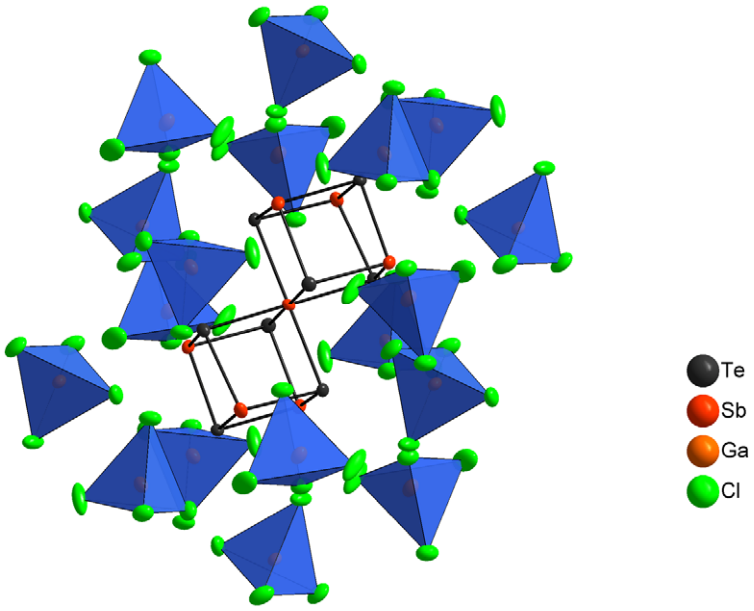

Fig. A 5.6.4 The coordination sphere of the $(Sb_7Te_8)^{5+}$ cluster by surrounding $[GaCl_4]^-$ ions in the structure of $Cu(Sb_7Te_8)[GaCl_4]_6$. The atoms are represented by thermal ellipsoids scaled to include a probability of 80 %. The $[GaCl_4]^-$ ions are shown as discrete tetrahedra. Cu^+ ions are omitted for clarity.

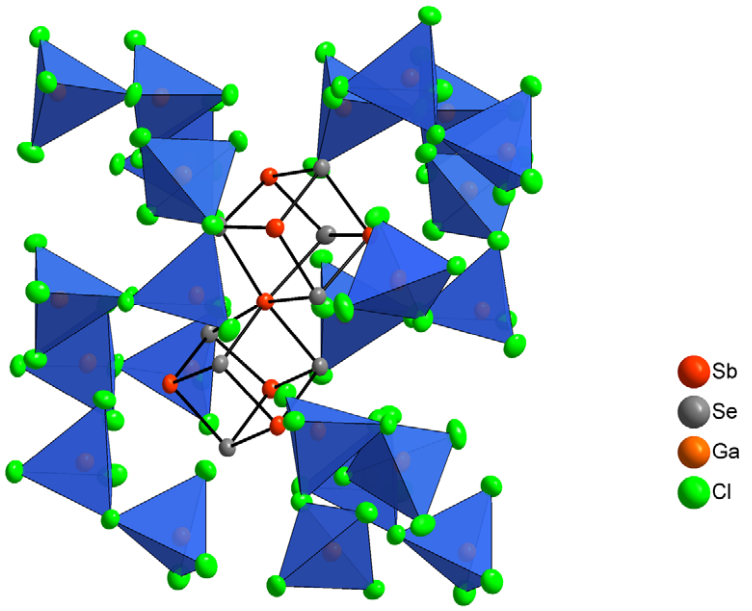

Fig. A 5.6.6 The coordination sphere of the $(Sb_7Se_8)^{5+}$ cluster by surrounding $[GaCl_4]^-$ and $[Ga_2Cl_7]^-$ ions in the structure of $(Sb_7Se_8)[GaCl_4]_2[Ga_2Cl_7]_3$. The atoms are represented by thermal ellipsoids scaled to include a probability of 80 %. The $[GaCl_4]^-$ and $[Ga_2Cl_7]^-$ ions are shown as discrete tetrahedra and double tetrahedra.

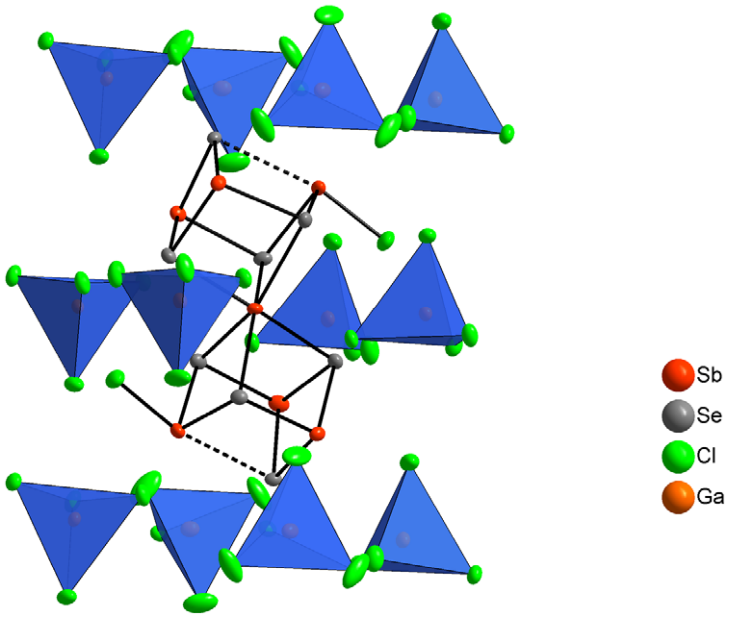

Fig. A 5.6.7 The coordination sphere of the $(Sb_7Se_8Cl_2)^{3+}$ cluster by surrounding $[GaCl_4]^-$ ions in the structure of $(Sb_7Se_8Cl_2)[GaCl_4]_3$. The atoms are represented by thermal ellipsoids scaled to include a probability of 80 %. The $[GaCl_4]^-$ ions are shown as discrete tetrahedra.

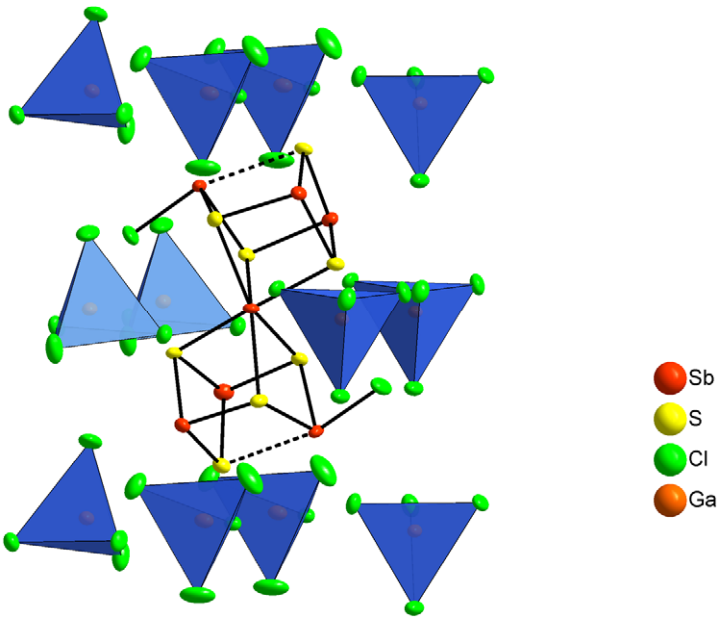

Fig. A 5.6.8 The coordination sphere of the $(Sb_7S_8Cl_2)^{3+}$ cluster by surrounding $[GaCl_4]^-$ ions in the structure of $(Sb_7S_8Cl_2)[GaCl_4]_3$. The atoms are represented by thermal ellipsoids scaled to include a probability of 80 %. The $[GaCl_4]^-$ ions are shown as discrete tetrahedra.

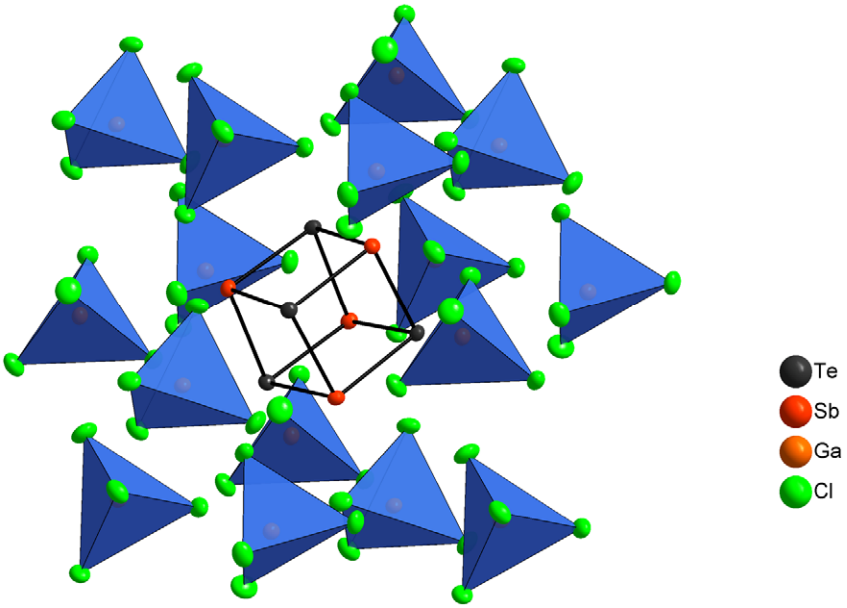

Fig. A 5.6.9 The coordination sphere of the $(Sb_4Te_4)^{4+}$ cluster by surrounding $[GaCl_4]^-$ ions in the structure of $(Sb_4Te_4)[GaCl_4]_4$. The atoms are represented by thermal ellipsoids scaled to include a probability of 80 %. The $[GaCl_4]^-$ ions are shown as discrete tetrahedra.

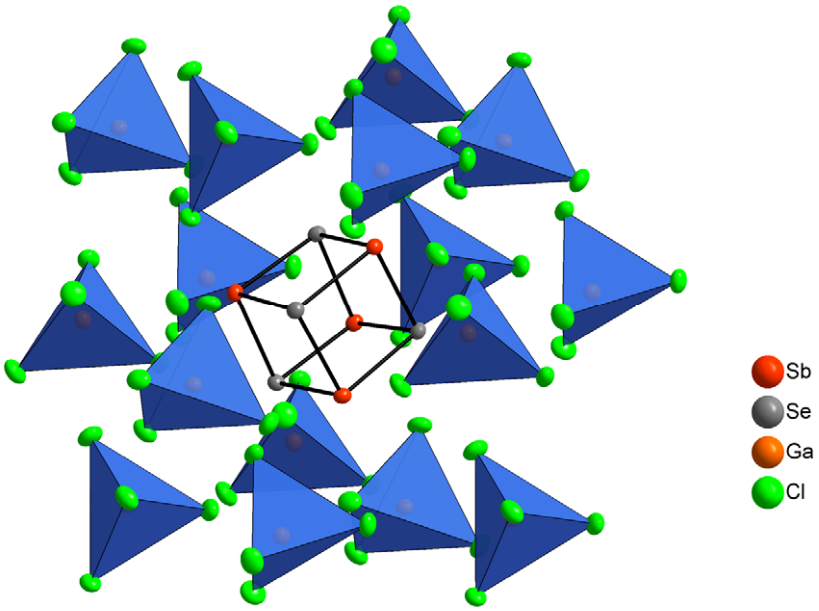

Fig. A 5.6.10 The coordination sphere of the $(Sb_4Se_4)^{4+}$ cluster by surrounding $[GaCl_4]^-$ ions in the structure of $(Sb_4Se_4)[GaCl_4]_4$. The atoms are represented by thermal ellipsoids scaled to include a probability of 80 %. The $[GaCl_4]^-$ ions are shown as discrete tetrahedra.

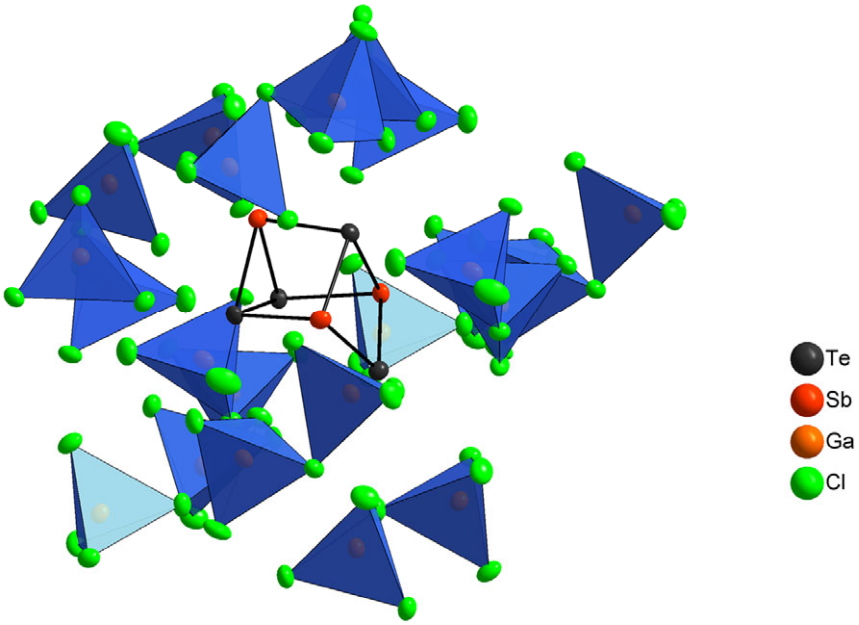

Fig. A 5.6.11 The coordination sphere of the $(Sb_3Te_4)^{3+}$ cluster by surrounding $[Ga_2Cl_7]^-$ ions in the structure of $(Sb_3Te_4)[Ga_2Cl_7]_3$. The atoms are represented by thermal ellipsoids scaled to include a probability of 80 %. The $[Ga_2Cl_7]^-$ ions are shown as discrete double tetrahedra.

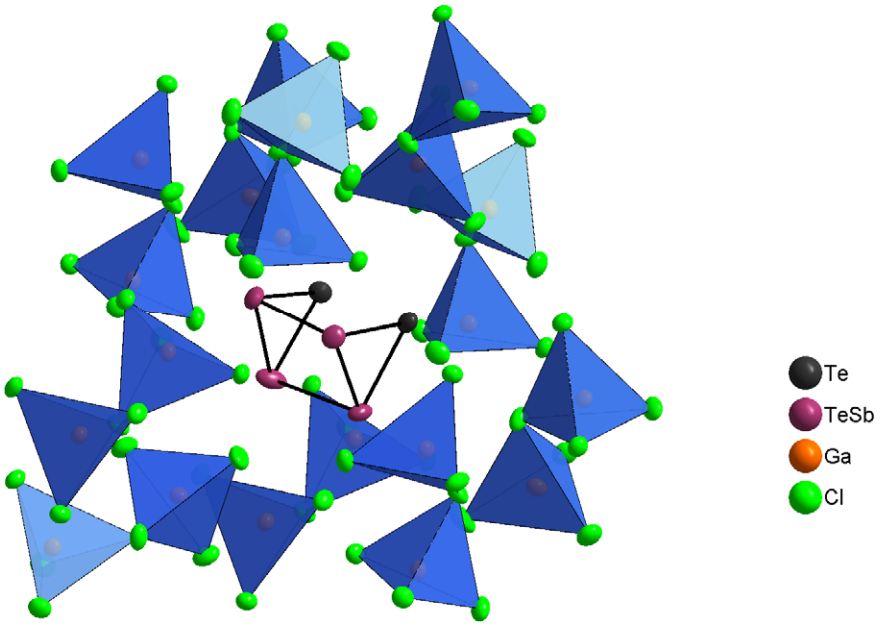

Fig. A 5.6.12 The coordination sphere of the $(Sb_2Te_4)^{2+}$ cluster by surrounding $[Ga_2Cl_7]^-$ ions in the structure of $(Sb_2Te_4)[Ga_2Cl_7]_2$. The atoms are represented by thermal ellipsoids scaled to include a probability of 50 %. The $[Ga_2Cl_7]^-$ ions are shown as discrete double tetrahedra.

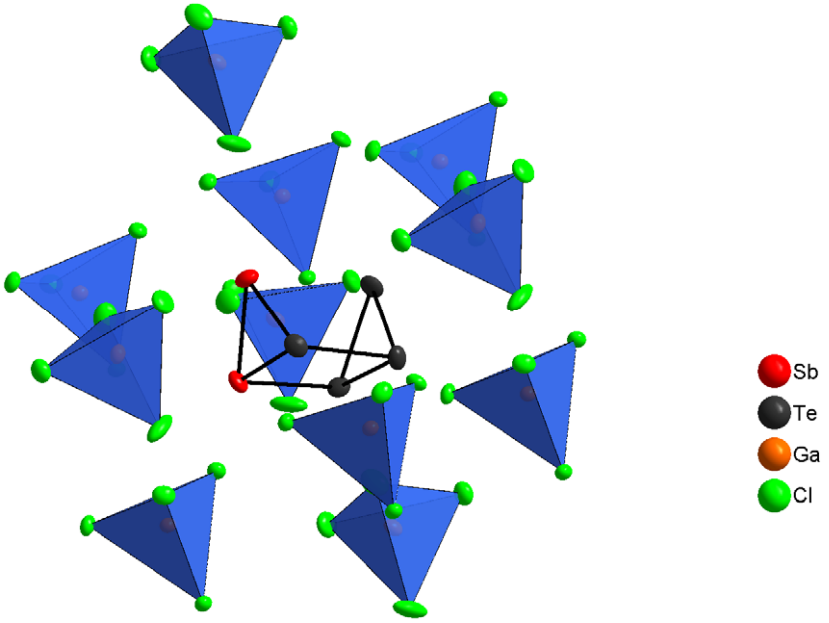

Fig. A 5.6.13 The coordination sphere of the $(Sb_2Te_4)^{2+}$ cluster by surrounding $[GaCl_4]^-$ ions in the structure of $(Sb_2Te_4)[GaCl_4]_2$. The atoms are represented by thermal ellipsoids scaled to include a probability of 50 %. The $[GaCl_4]^-$ ions are shown as discrete double tetrahedra.

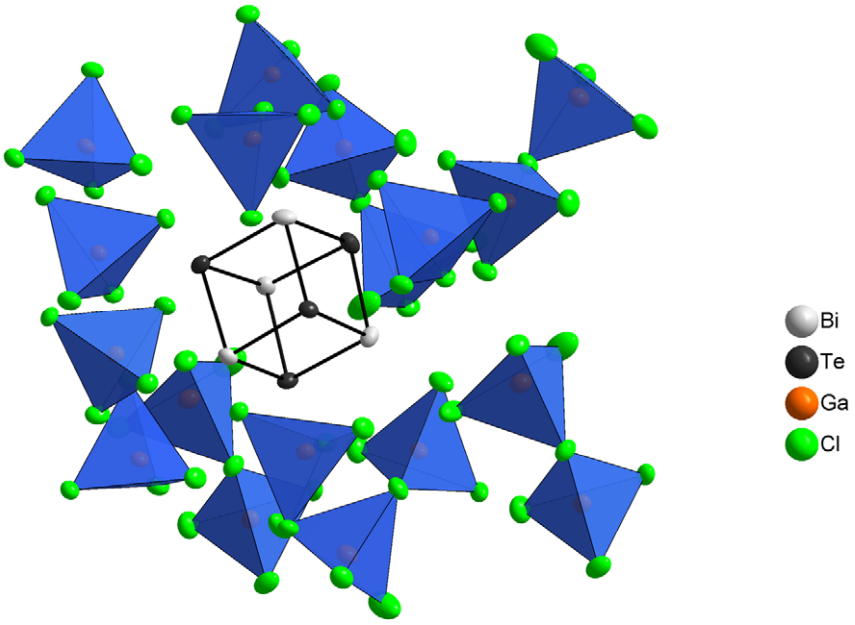

Fig. A 5.6.14 The coordination sphere of the $(Bi_4Te_4)^{3+}$ cluster by surrounding $[GaCl_4]^-$ and $[Ga_2Cl_7]^-$ ions in the structure of $(Bi_4Te_4)[GaCl_4]_2[Ga_2Cl_7]$. The atoms are represented by thermal ellipsoids scaled to include a probability of 70 %. The $[GaCl_4]^-$ and $[Ga_2Cl_7]^-$ ions are shown as discrete tetrahedra and double tetrahedra.

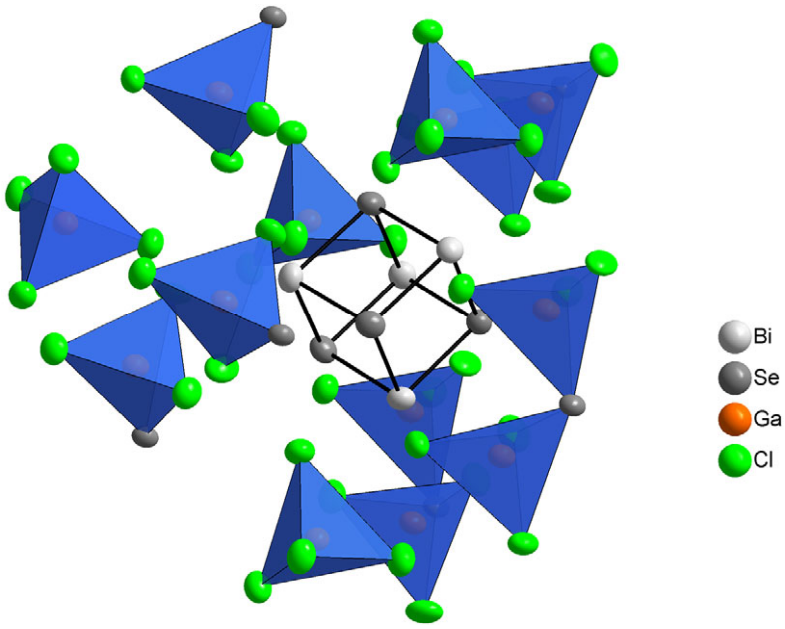

nn

Fig. A 5.6.15 The coordination sphere of the $(Bi_4Se_4)^{3+}$ cluster by surrounding $[GaCl_4]^-$ and $[SeGa_3Cl_9]^{2-}$ ions in the structure of $(Bi_4Se_4)[GaCl_4][SeGa_3Cl_9]$. The atoms are represented by thermal ellipsoids scaled to include a probability of 70 %. The $[GaCl_4]^-$ ions are shown as discrete tetrahedra. For clarity, the $[SeGa_3Cl_9]^{2-}$ anions are shown only partly as $SeGaCl_3$ and $SeGa_2Cl_6$ tetrahedra and double tetrahedra.

A 5.7 Calculated Raman Vibrational Modes of Polycationic Clusters and Anions

For orientation in the Raman spectra of novel compounds, calculations of the clusters and anions vibration modes were performed with DFT methods.

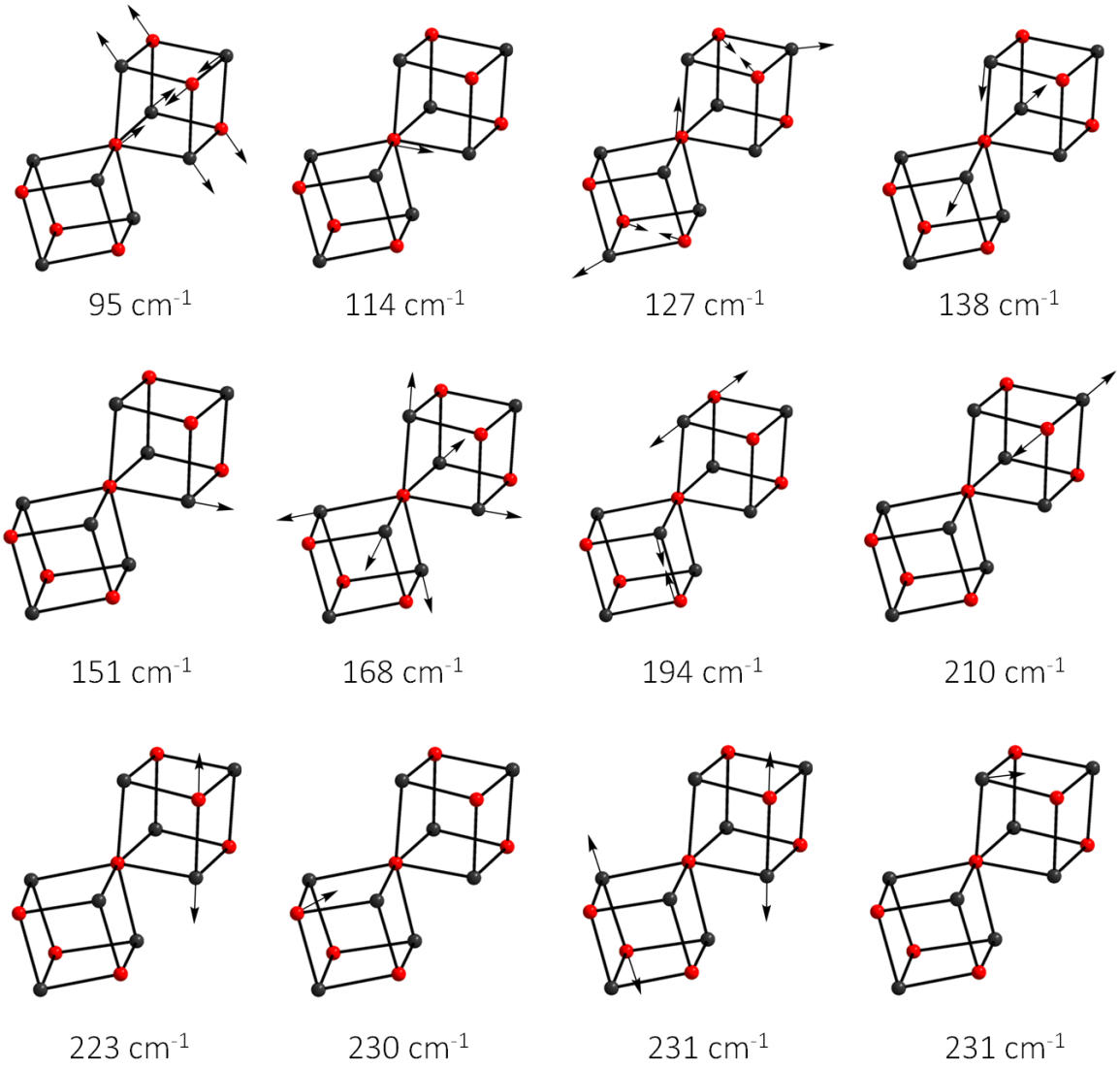

Fig. A 5.7.1 Calculated vibration modes of the $(Sb_7Te_8)^{5+}$ cluster (B3LYP/TZV(2d/sp)). Directions of strongest vibrational displacements are indicated by black arrows. Only the strongest displacements are indicated.

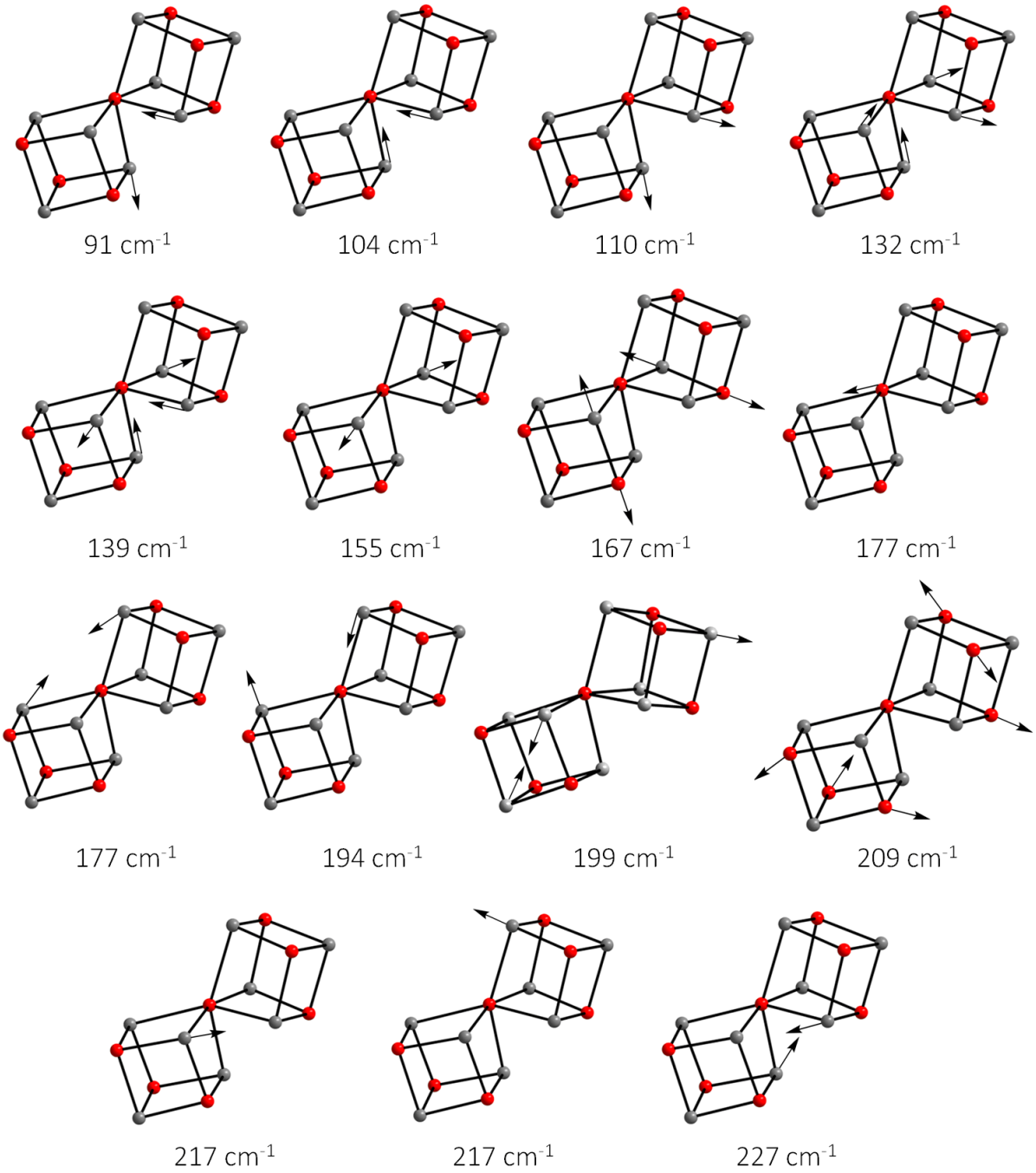

Fig. A 5.7.2 Calculated vibration modes of the $(Sb_7Se_8)^{5+}$ cluster (B3LYP/TZV(2d/sp)). Directions of strongest vibrational displacements are indicated by black arrows. Only the strongest displacements are indicated.

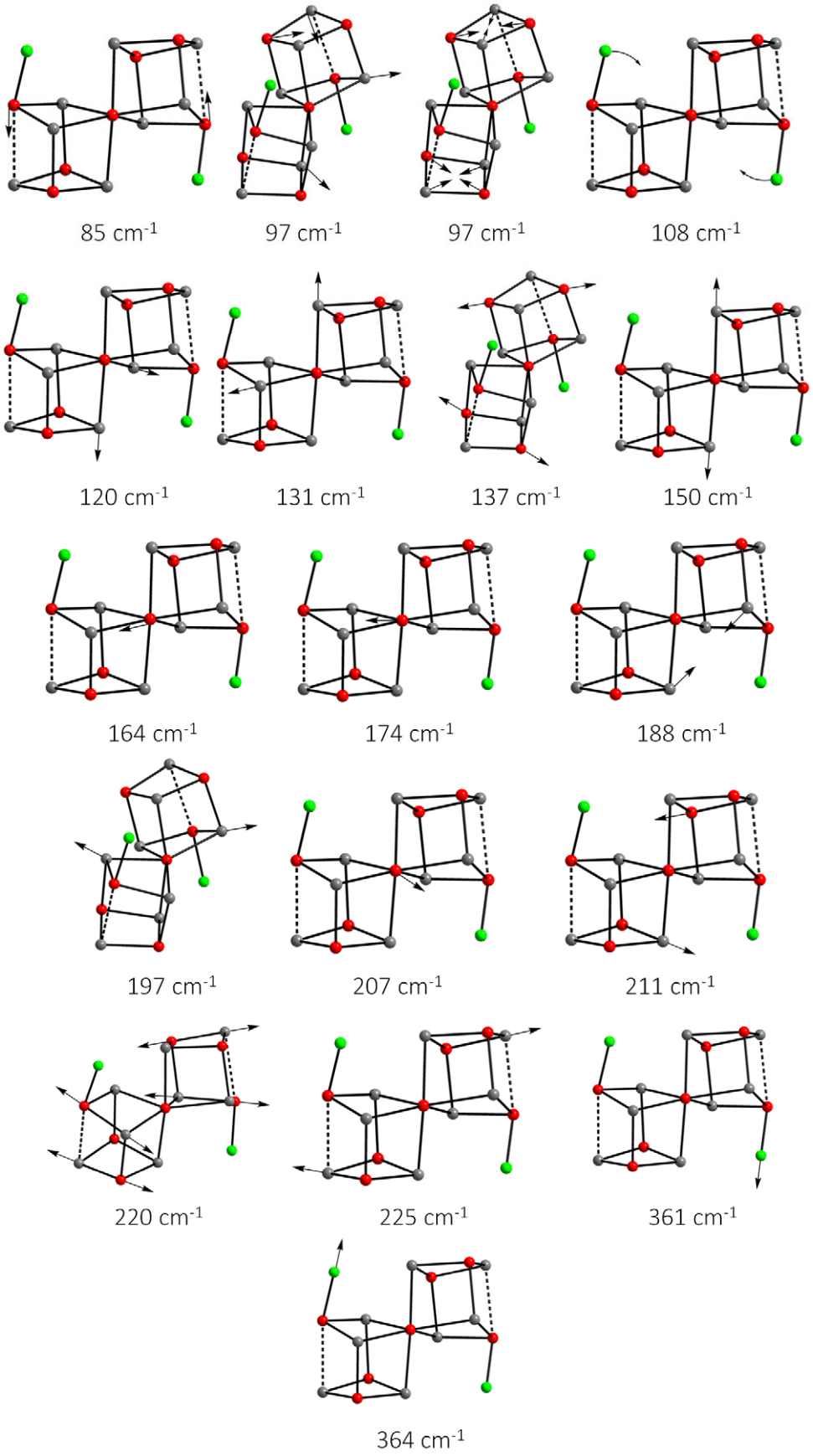

Fig. A 5.7.3 Calculated vibration modes of the $(Sb_7Se_8Cl_2)^{3+}$ cluster (B3LYP/TZV(2d/sp)). Directions of strongest vibrational displacements are indicated by black arrows. Only the strongest displacements are indicated.

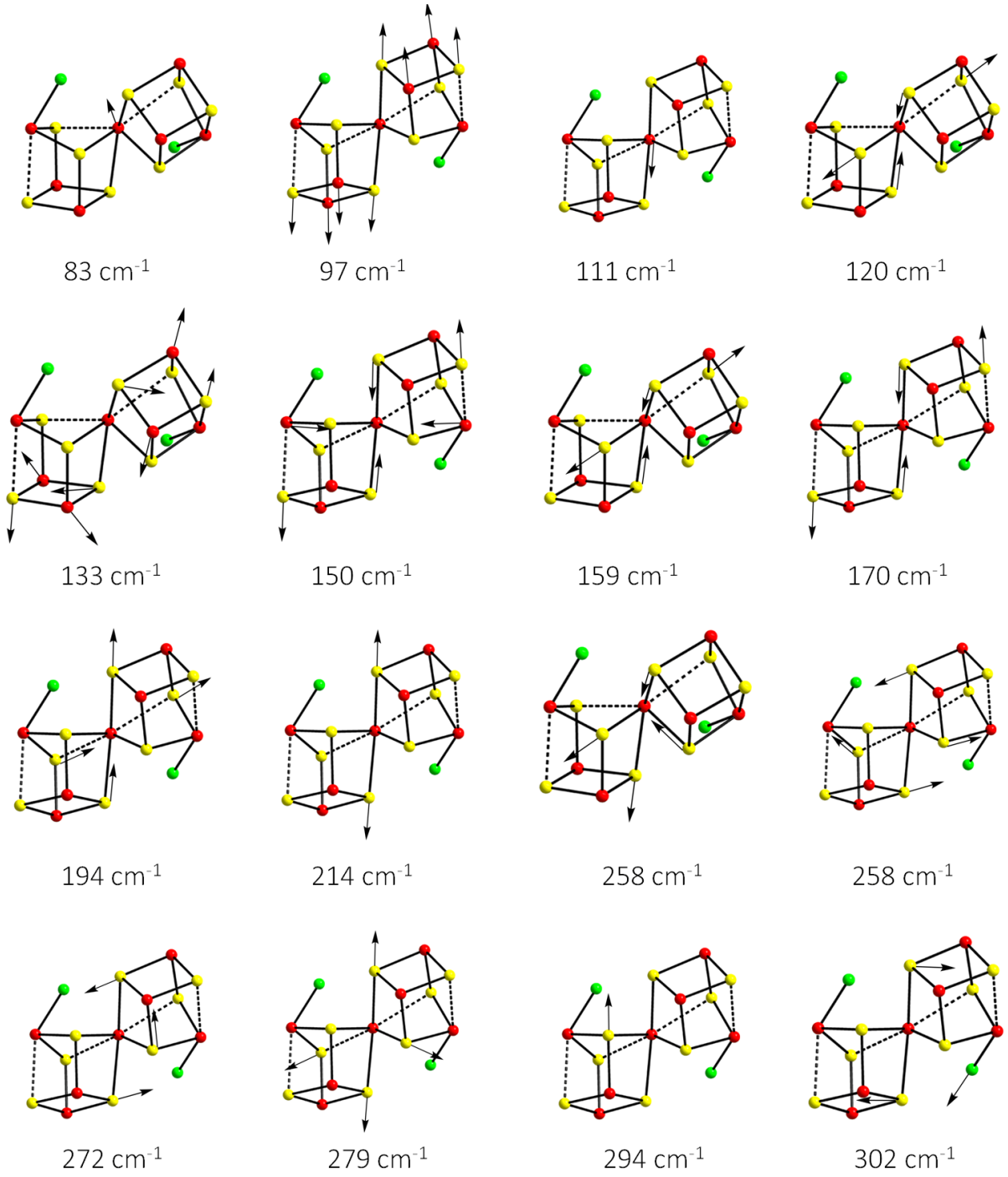

Fig. A 5.7.4 Calculated vibration modes of the $(Sb_7S_8Cl_2)^{3+}$ cluster (B3LYP/TZV(2d/sp)). Directions of strongest vibrational displacements are indicated by black arrows. Only the strongest displacements are indicated.

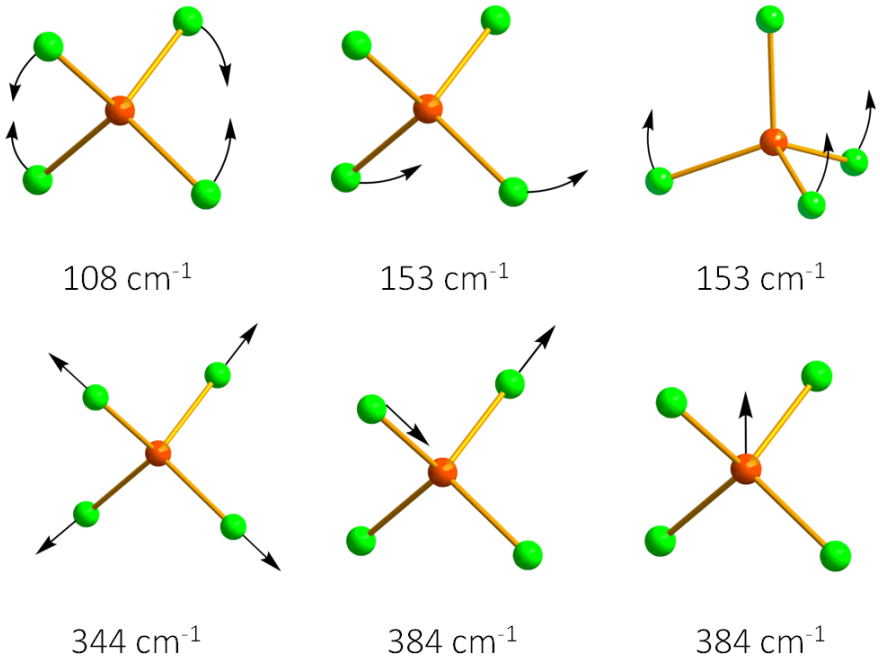

Fig. A 5.7.5 Calculated vibration modes of the $[GaCl_4]^-$ anion (B3LYP/TZV(2d/sp)). Directions of vibrational displacements are indicated by black arrows. Only the strongest displacements are indicated.

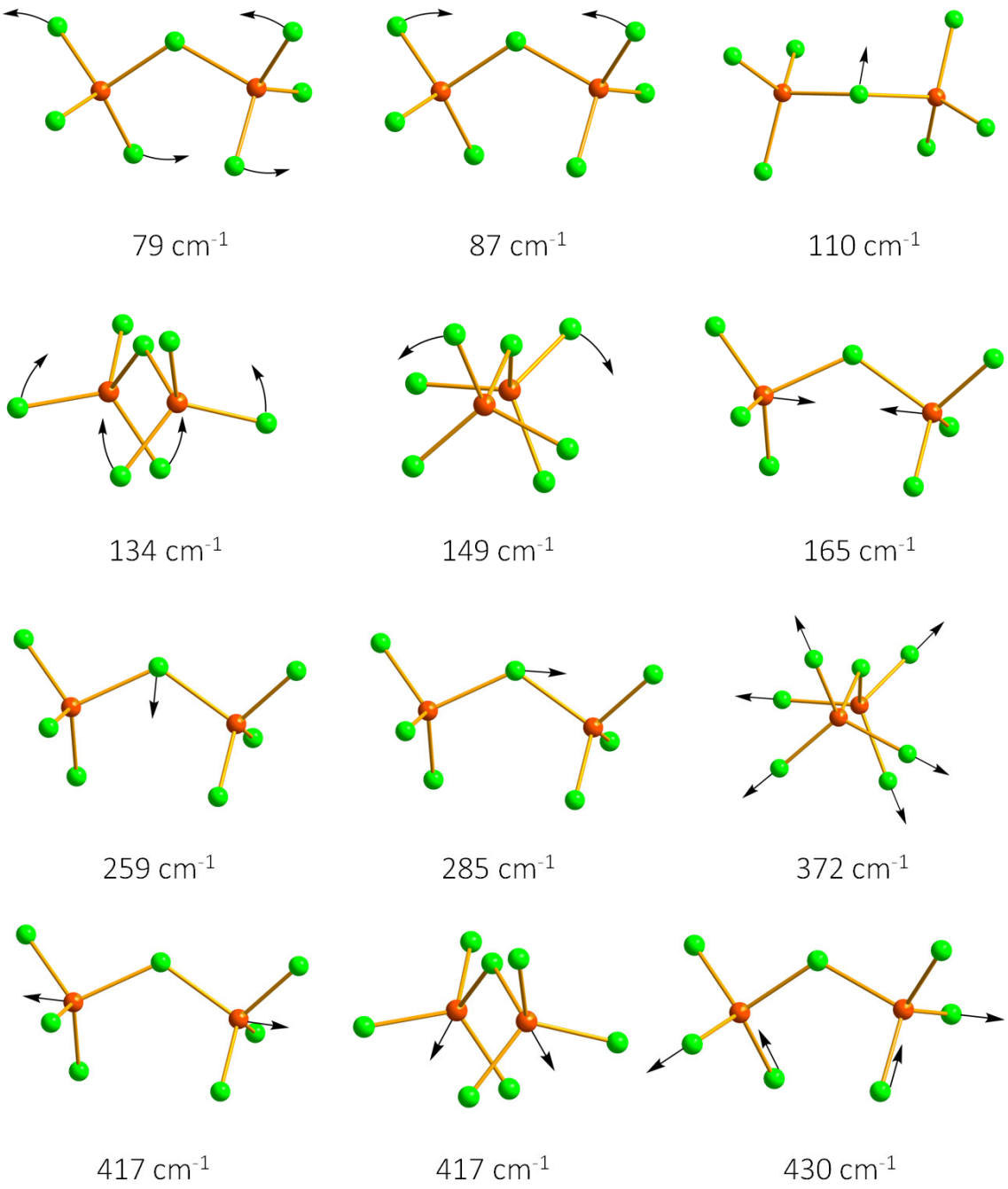

Fig. A 5.7.6 Calculated vibration modes of the $[Ga_2Cl_7]^-$ anion (B3LYP/TZV(2d/sp)). Directions of vibrational displacements are indicated by black arrows. Only the strongest displacements are indicated.

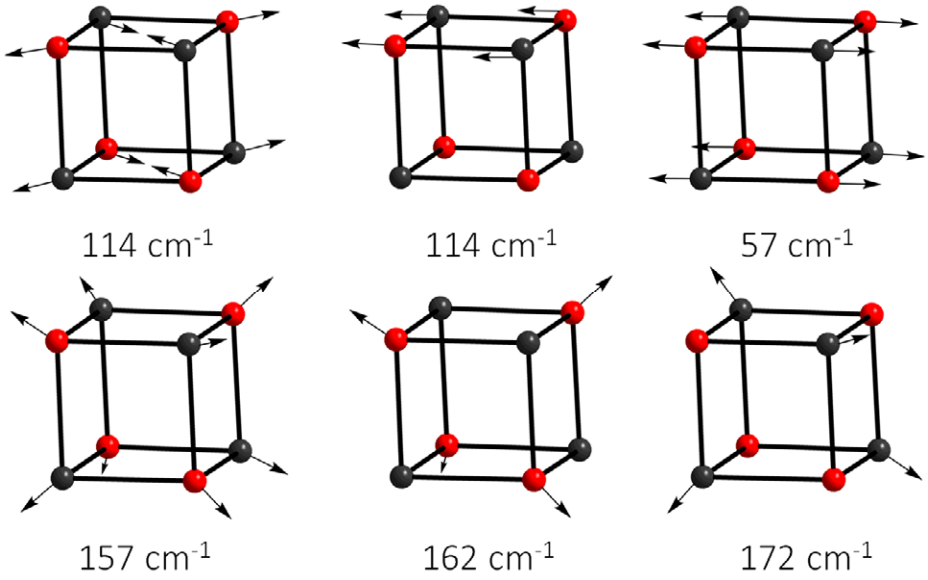

Fig. A 5.7.7 Calculated vibration modes of the $(Sb_4Te_4)^{4+}$ cluster (B3LYP/TZV(2d/sp)). Directions of strongest vibrational displacements are indicated by black arrows. Only the strongest displacements are indicated.

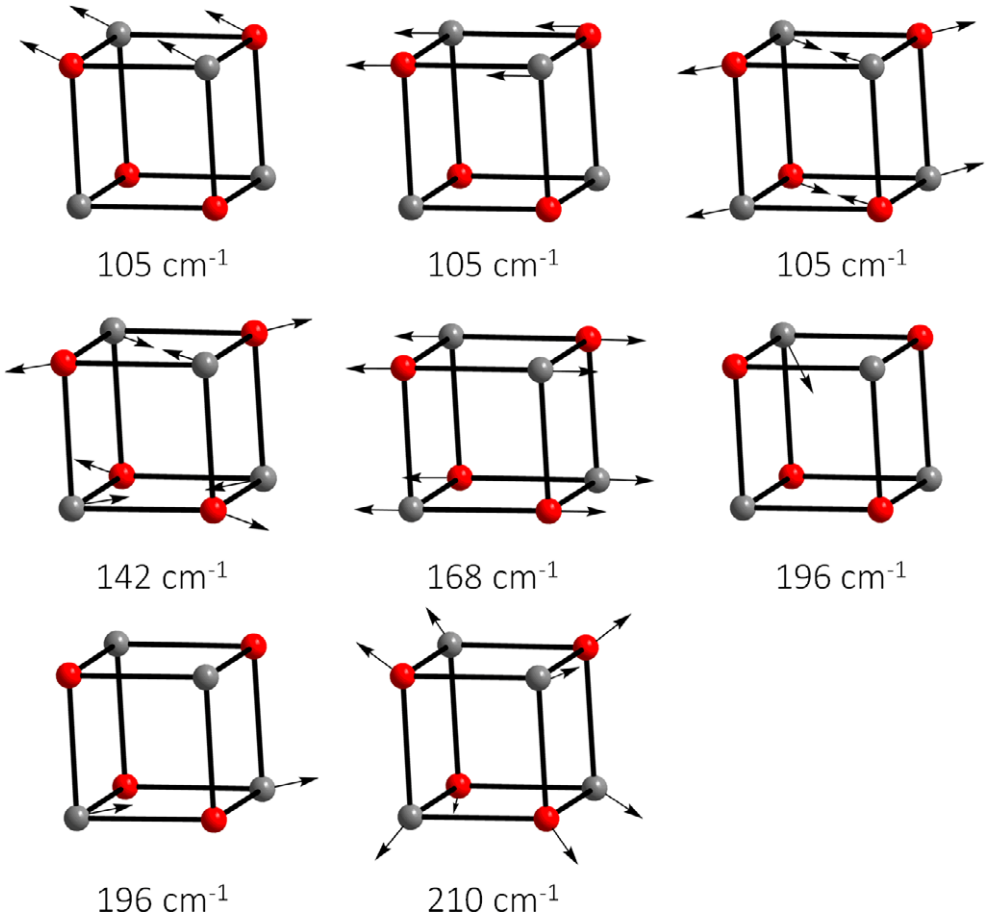

Fig. A 5.7.8 Calculated vibration modes of the $(Sb_4Se_4)^{4+}$ cluster (B3LYP/TZV(2d/sp)). Directions of strongest vibrational displacements are indicated by black arrows. Only the strongest displacements are indicated.

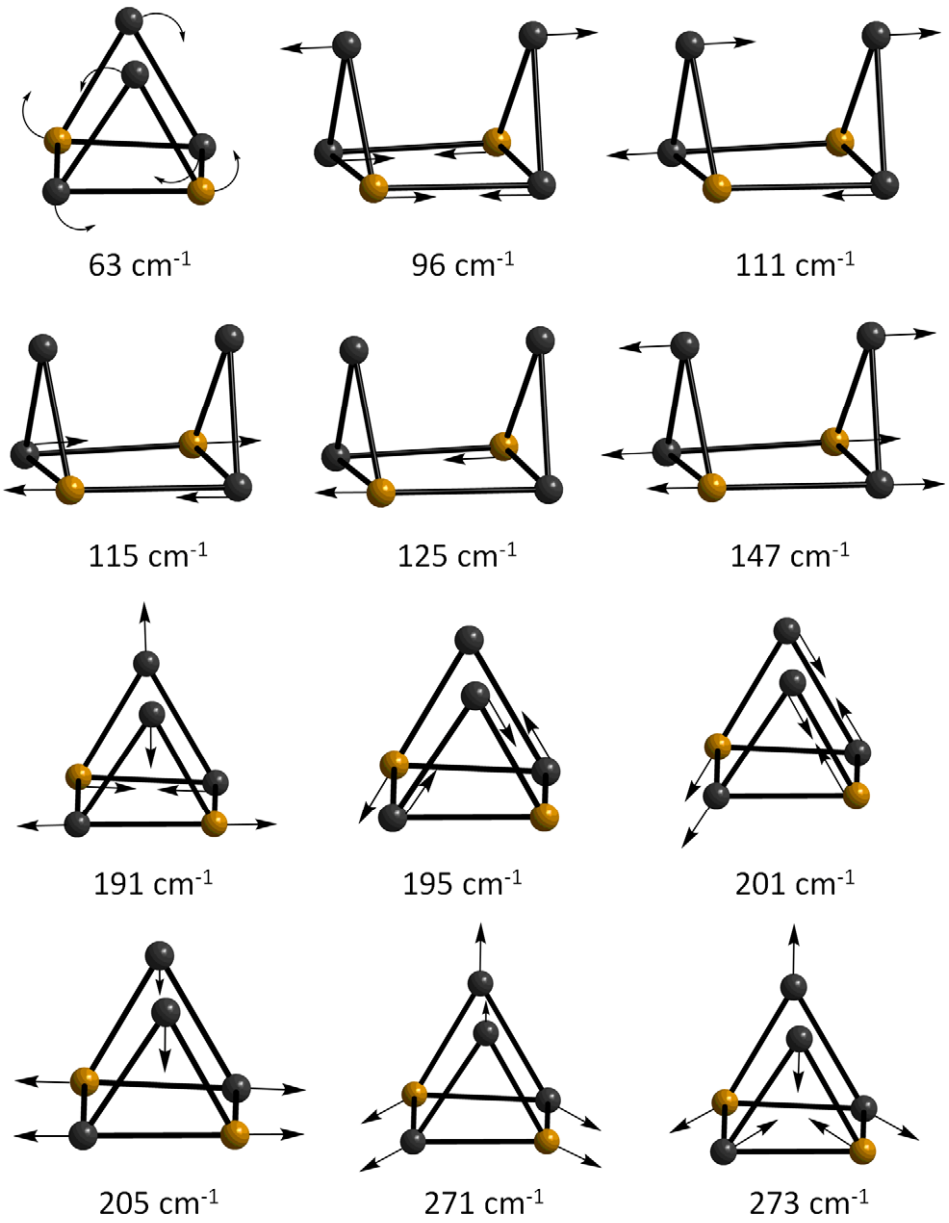

Fig. A 5.7.9 Calculated vibration modes of isomer 1 of $(As_2Te_4)^{2+}$ (B3LYP/TZV(2d/sp)). Directions of vibrational displacements are indicated by black arrows. Only the strongest displacements are indicated.

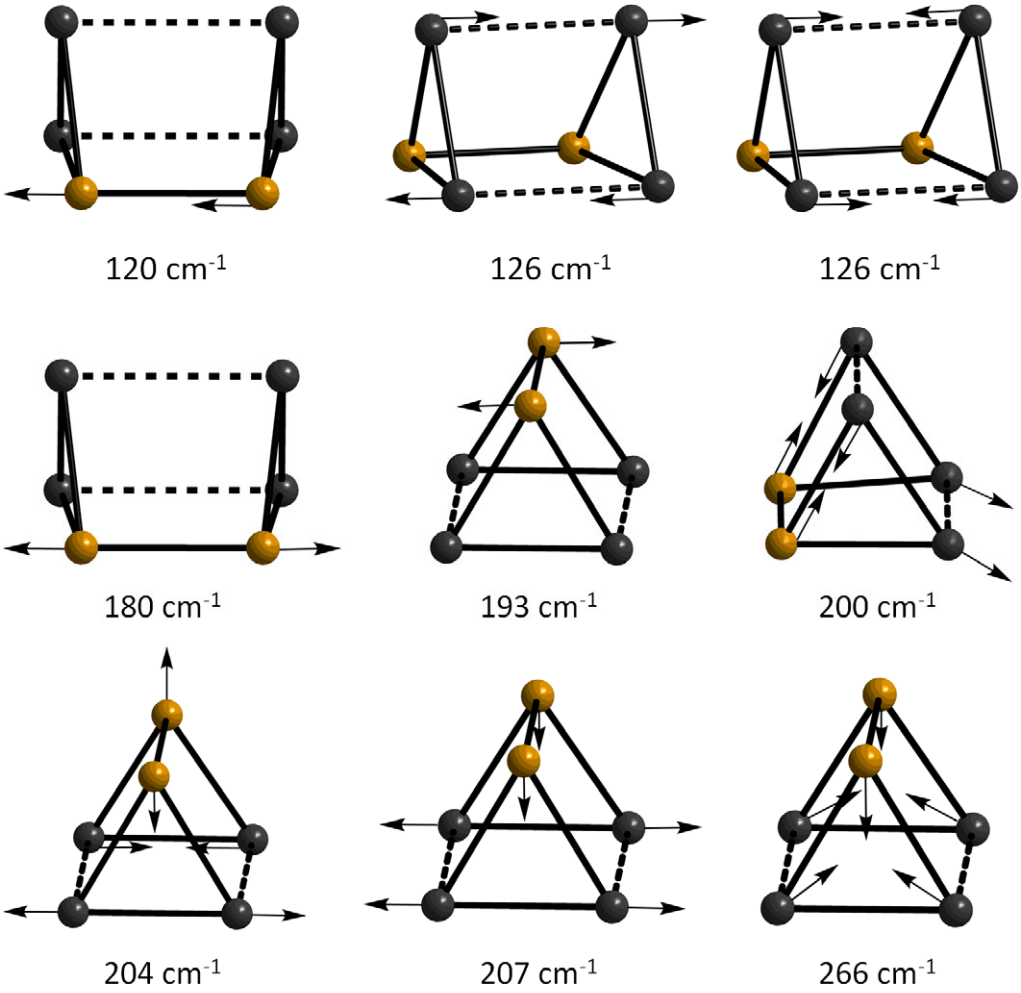

Fig. A 5.7.10 Calculated vibration modes of isomer 2 of $(As_2Te_4)^{2+}$ (B3LYP/TZV(2d/sp)). Directions of vibrational displacements are indicated by black arrows. Only the strongest displacements are indicated.

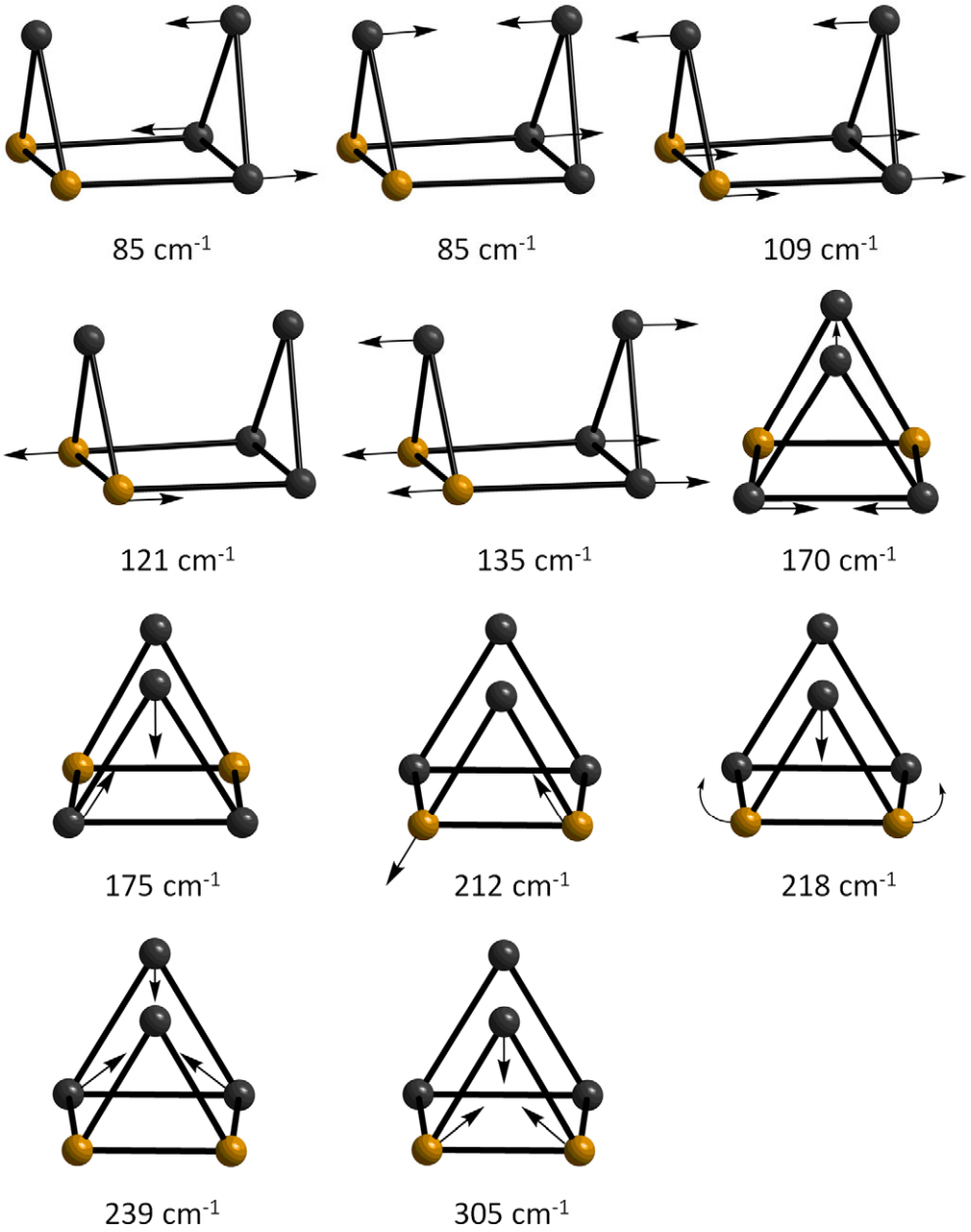

Fig. A 5.7.11 Calculated vibration modes of isomer 3 of $(As_2Te_4)^{2+}$ (B3LYP/TZV(2d/sp)). Directions of vibrational displacements are indicated by black arrows. Only the strongest displacements are indicated.

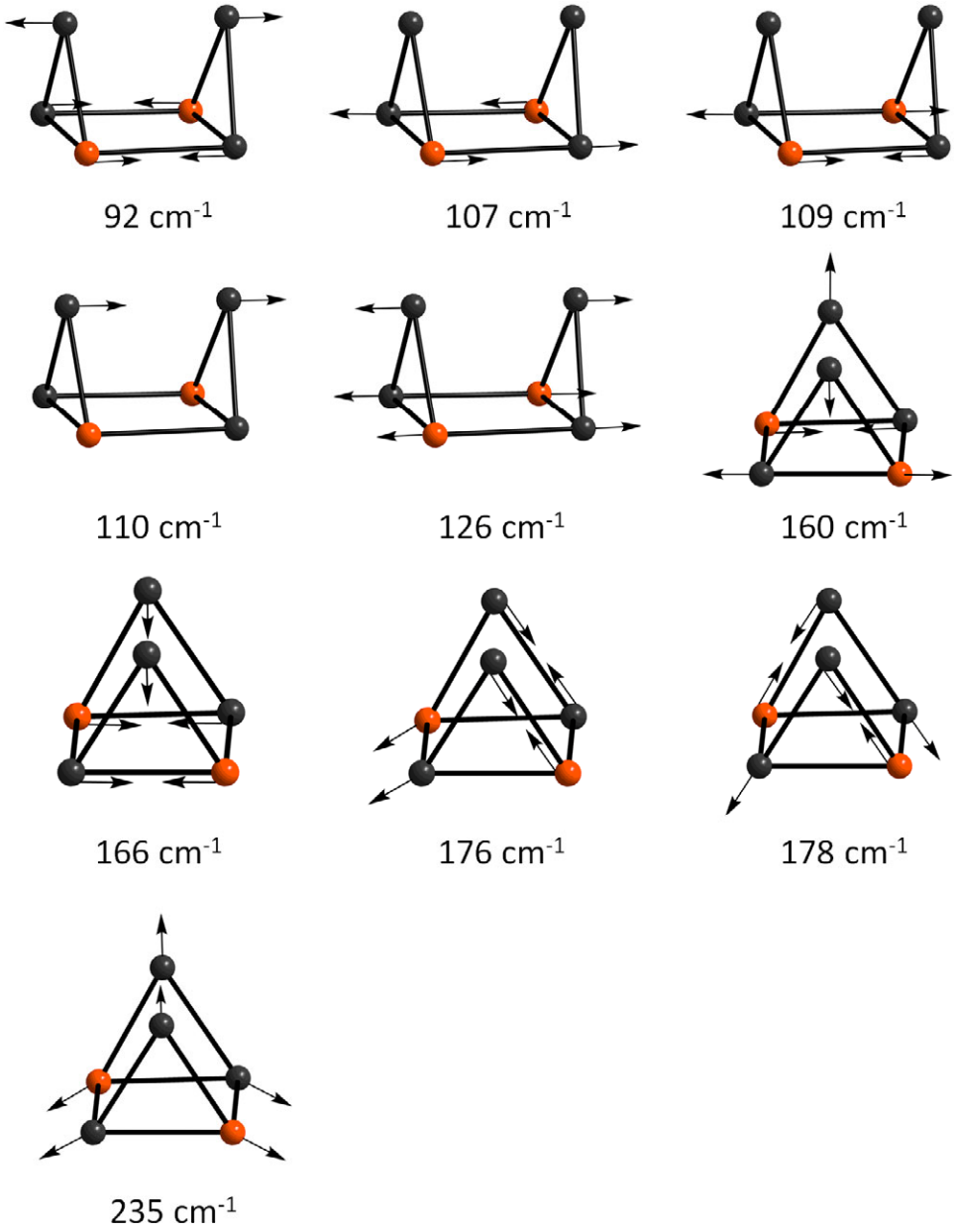

Fig. A 5.7.12 Calculated vibration modes of isomer 1 of $(Sb_2Te_4)^{2+}$ (B3LYP/TZV(2d/sp)). Directions of vibrational displacements are indicated by black arrows. Only the strongest displacements are indicated.

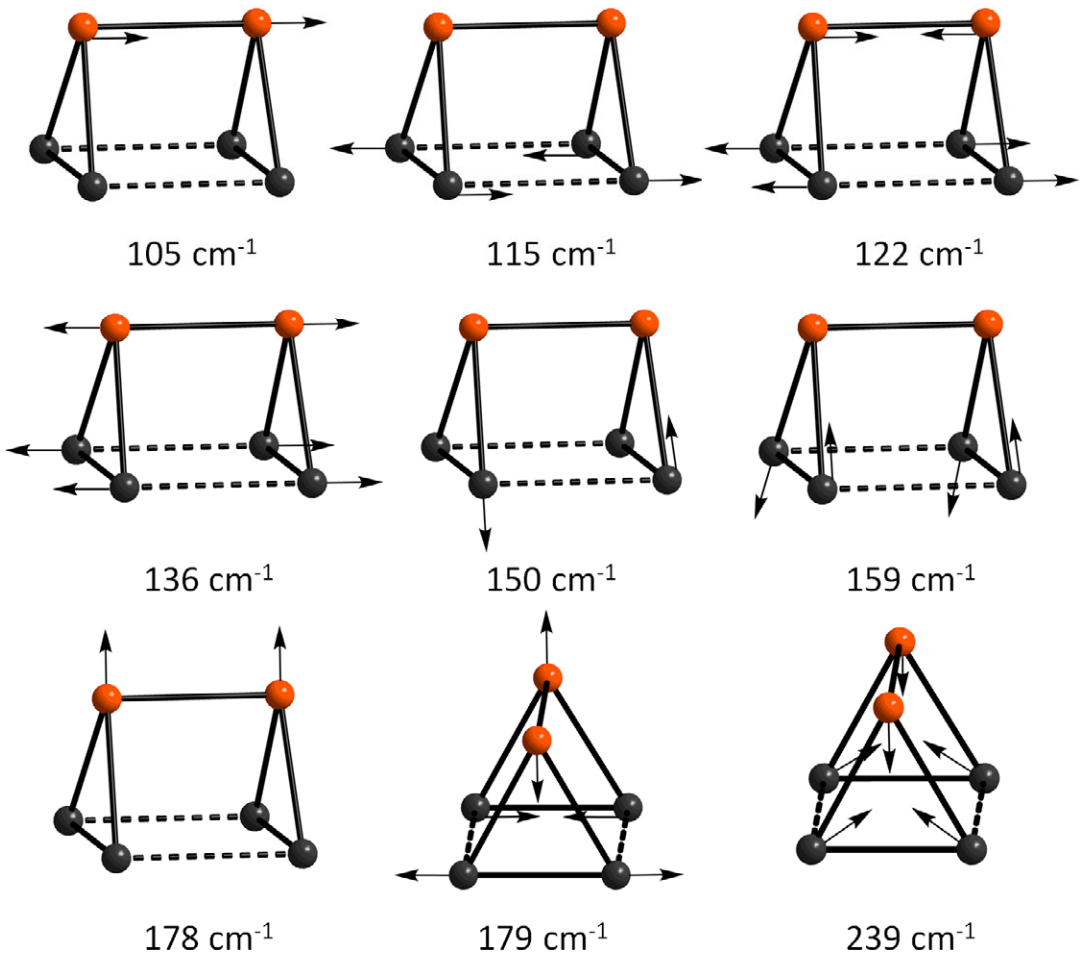

Fig. A 5.7.13 Calculated vibration modes of isomer 2 of $(Sb_2Te_4)^{2+}$ (B3LYP/TZV(2d/sp)). Directions of vibrational displacements are indicated by black arrows. Only the strongest displacements are indicated.

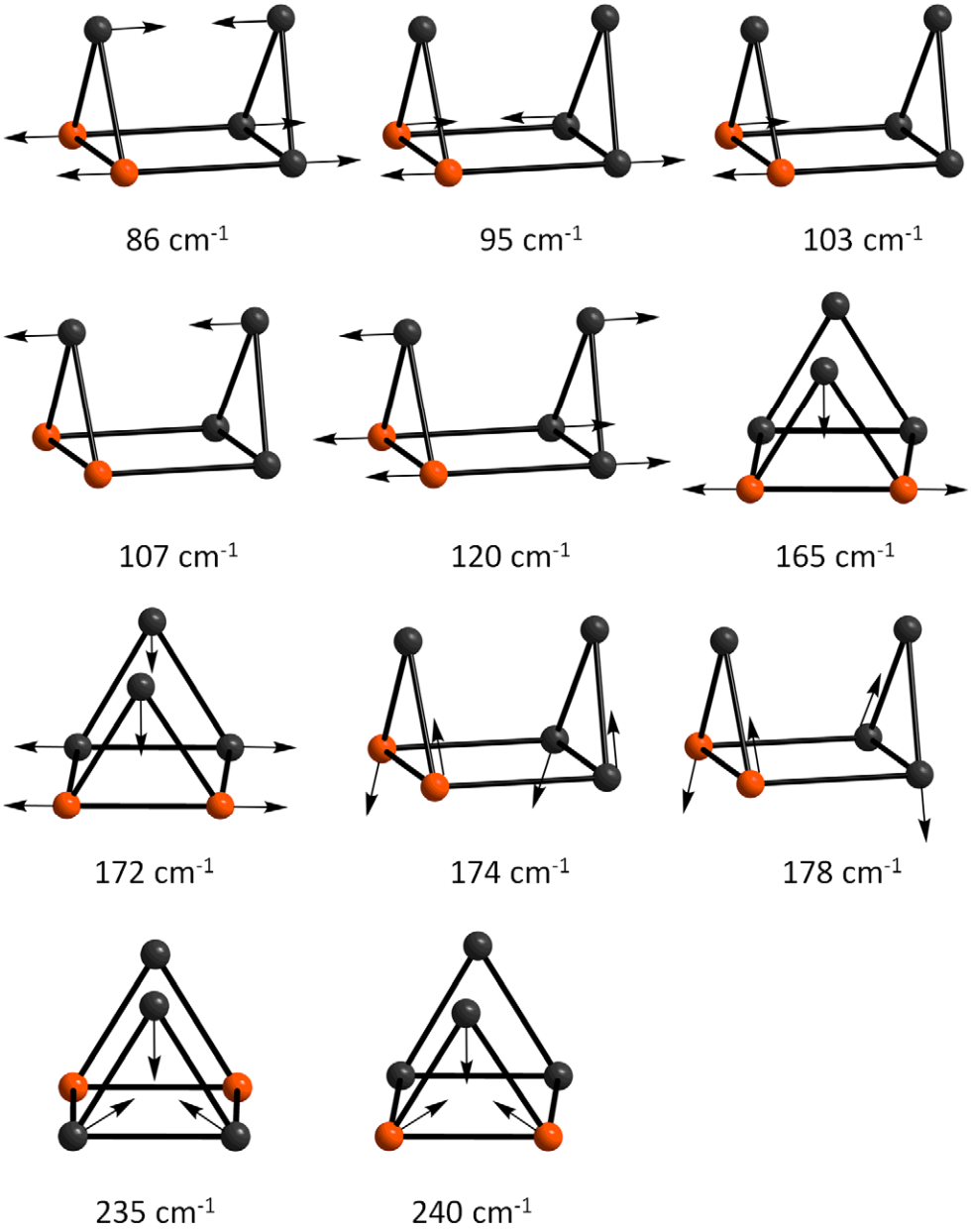

Fig. A 5.7.14 Calculated vibration modes of isomer 3 of $(Sb_2Te_4)^{2+}$ (B3LYP/TZV(2d/sp)). Directions of vibrational displacements are indicated by black arrows. Only the strongest displacements are indicated.

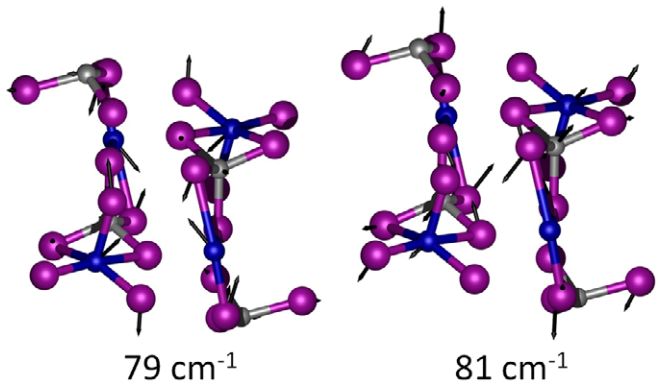

79 cm^{-1} 81 cm^{-1}

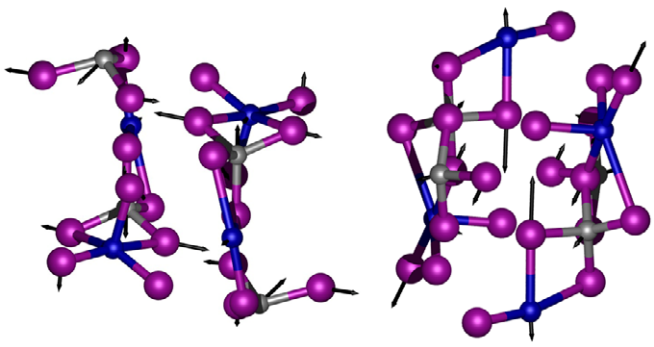

94 cm^{-1} 99 cm^{-1}

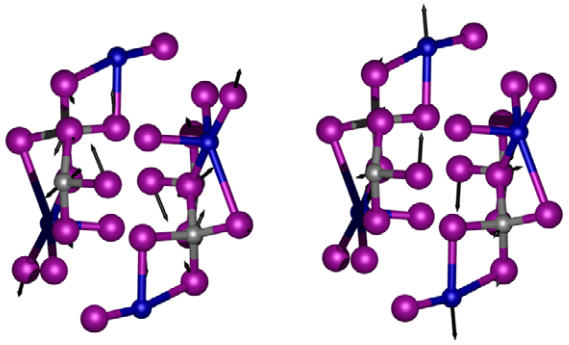

108 cm^{-1} 109 cm^{-1}

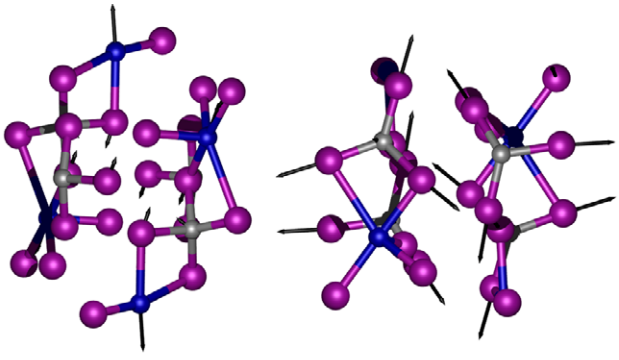

126 cm^{-1} 149 cm^{-1}

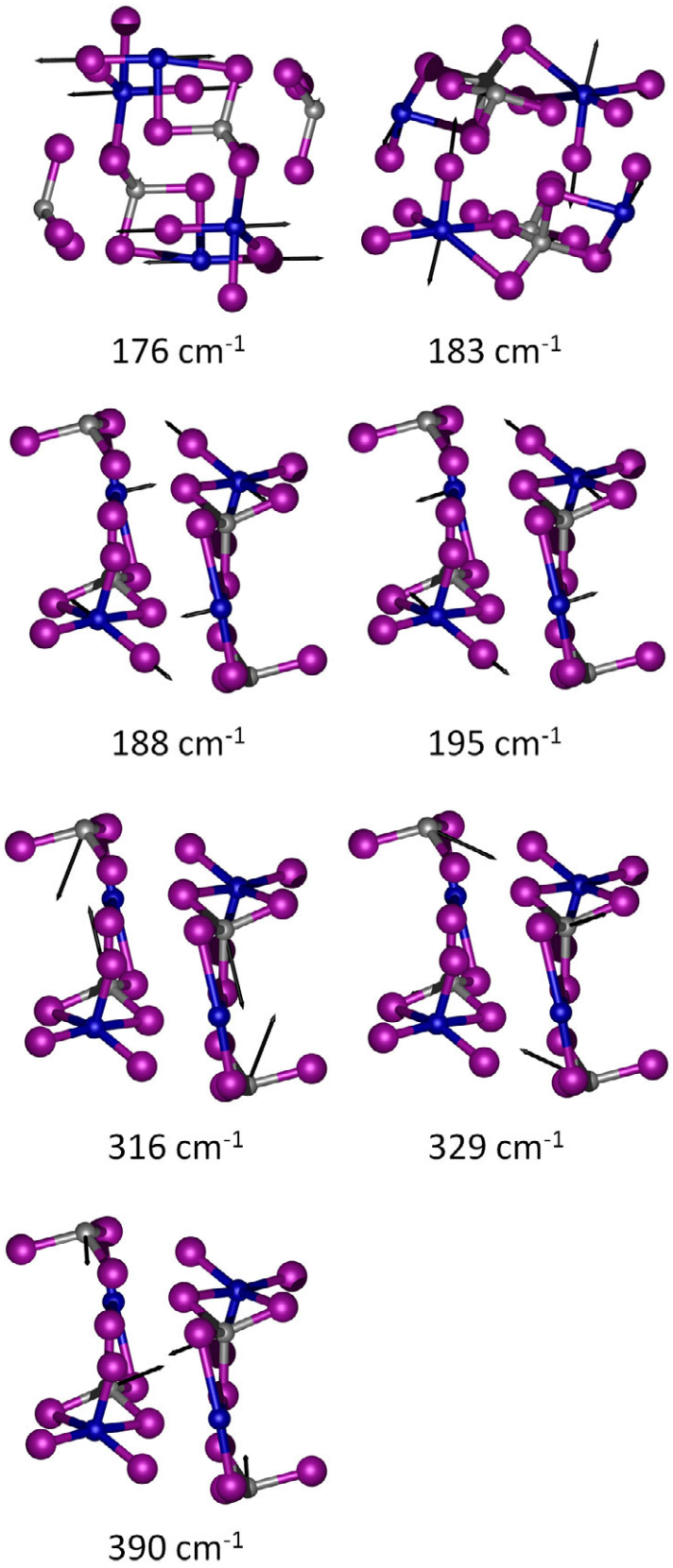

Fig. A 5.7.15 Calculated vibration modes of $(SbI_2)[AlI_4]$ (PW1PW). Directions of vibrational displacements are indicated by black arrows.

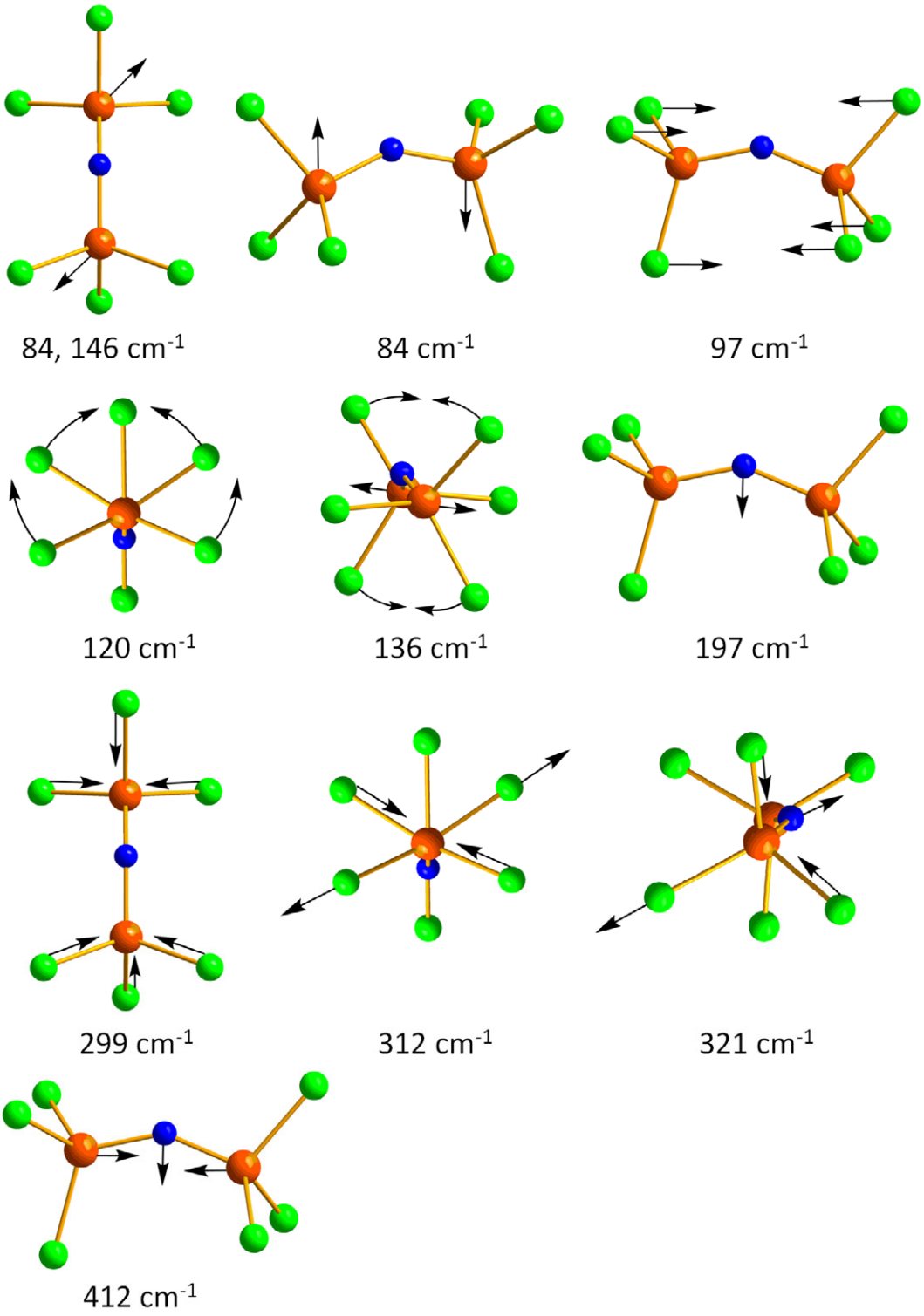

Fig. A 5.7.16 Calculated vibration modes of the $[Ga_2Cl_6O]^{2-}$ anion (B3LYP/TZV(2d/sp)). Directions of vibrational displacements are indicated by black arrows. Only the strongest displacements are indicated.

A 5.8 Programs and Chemicals

A 5.8.1 Synthesis of Gallium(III) Chloride

Gallium trichloride was synthesized from gallium metal at 60 °C in a chlorine gas stream.
Figure A 5.8.1.1 shows the glass construction for synthesis. After evacuating and heating to remove adsorbed moisture gallium was placed in the bent glass tube and molten in an oil bath. Hereinafter a chlorine gas stream was led through the liquid gallium. Gallium trichloride crystallized behind the melt in form of white crystals.
After two hours the glass apparature was closed with a stop cock and transferred into the glove box. The upper end was cut and gallium trichloride was taken out with a glass rod.

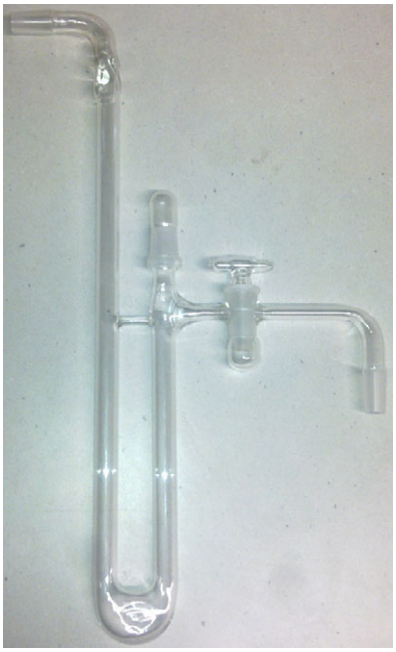

Fig. A 5.8.1.1 Glass apparature for the synthesis of gallium trichloride. Chlorine gas is led through from the right.

The disadvantages of this synthesis were the low yield of gallium trichloride and the residues of unreacted gallium which had to be discarded to keep the glass apparature undestroyed.

A 5.8.2 Synthesis of Indium(I) Chloride

The syntheses of InCl proceeds according to the equation:

$$2\ In + InCl_3 \xrightarrow[7d]{300\ °C} 3\ InCl$$

0,459 g (4 mmol) In and 0.442g (2 mmol) $InCl_3$ were closed in an ampoule (lengths 13 mm, wall thickness 2.5 mm, outer diameter 20 mm) in the glovebox and flame sealed under low pressure (approx. $2 \cdot 10^{-2}$ mbar). The ampoule was heated to 300 °C for 7 days in a horizontal tube furnace with

a slight temperature gradient. InCl deposited as dark red drops at the colder end of the ampoule. During cooling down to room temperature the drops solidified and changed their colour to orange and gold (Fig. A 5.8.2.1).

Fig. A 5.8.2.1 InCl in two different colours in the reaction ampoule.

Both phases were ground in mortars to a yellow powder, respectively, and powder diffractograms were recorded, one is shown in Fig. A 5.8.2.2.

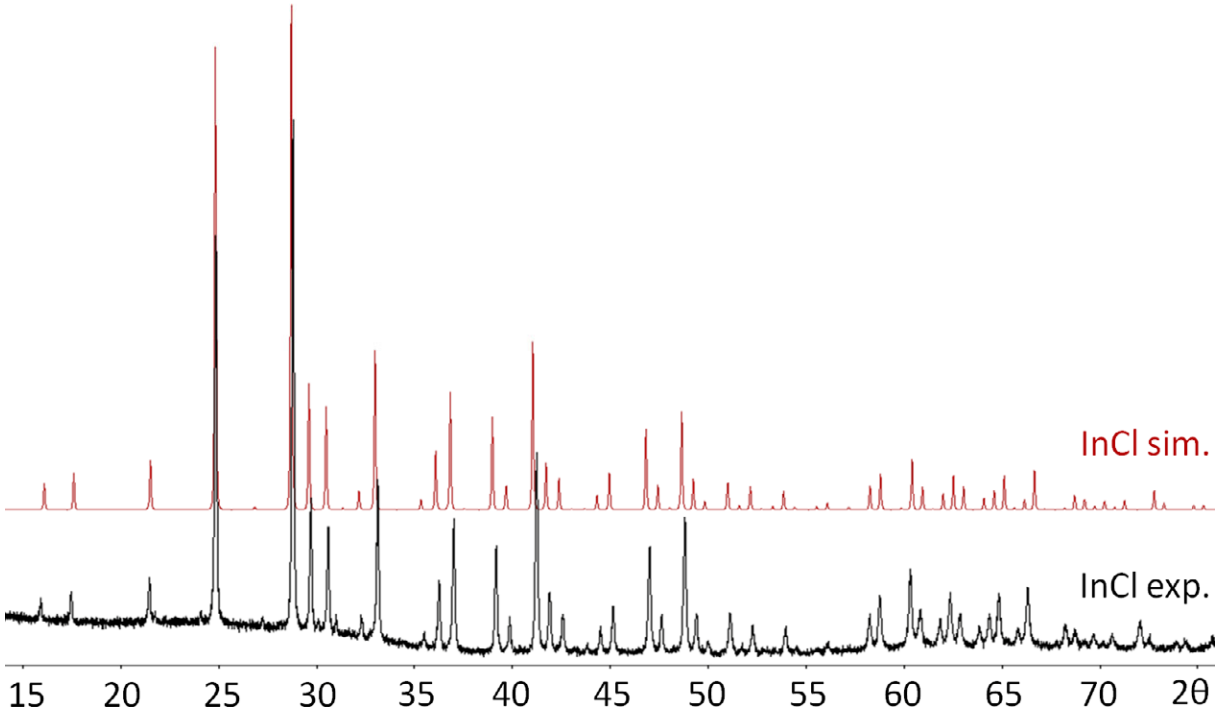

Fig. A 5.8.2.2 Powder diffractogram of the yellow InCl phase (black) and calculated diffractogram of yellow InCl[154] from the database (red).

Both recorded diffractograms show the same pattern and go along with this of yellow InCl[154], which is the room temperature modification of this compound.
Thus orange and golden solidified drops were ground together and used for further syntheses. In general, InCl was prepared shortly before it was needed. After some weeks it slowly became grey in the glovbox presumable due to the disproportionation to the educts In and $InCl_3$.

One synthetic run for InCl did not succeed. Instead of InCl, colourless crystalline $InCl_2$[155] was obtained (Fig. A 5.8.2.3). Another phase, giving an intensive reflection at 47.66° and less intensive reflexions at 6.18°, 30.28°, 33.07°, 35.75°, 40.37°, 71.98° and 74.17° could not be identified with the database.

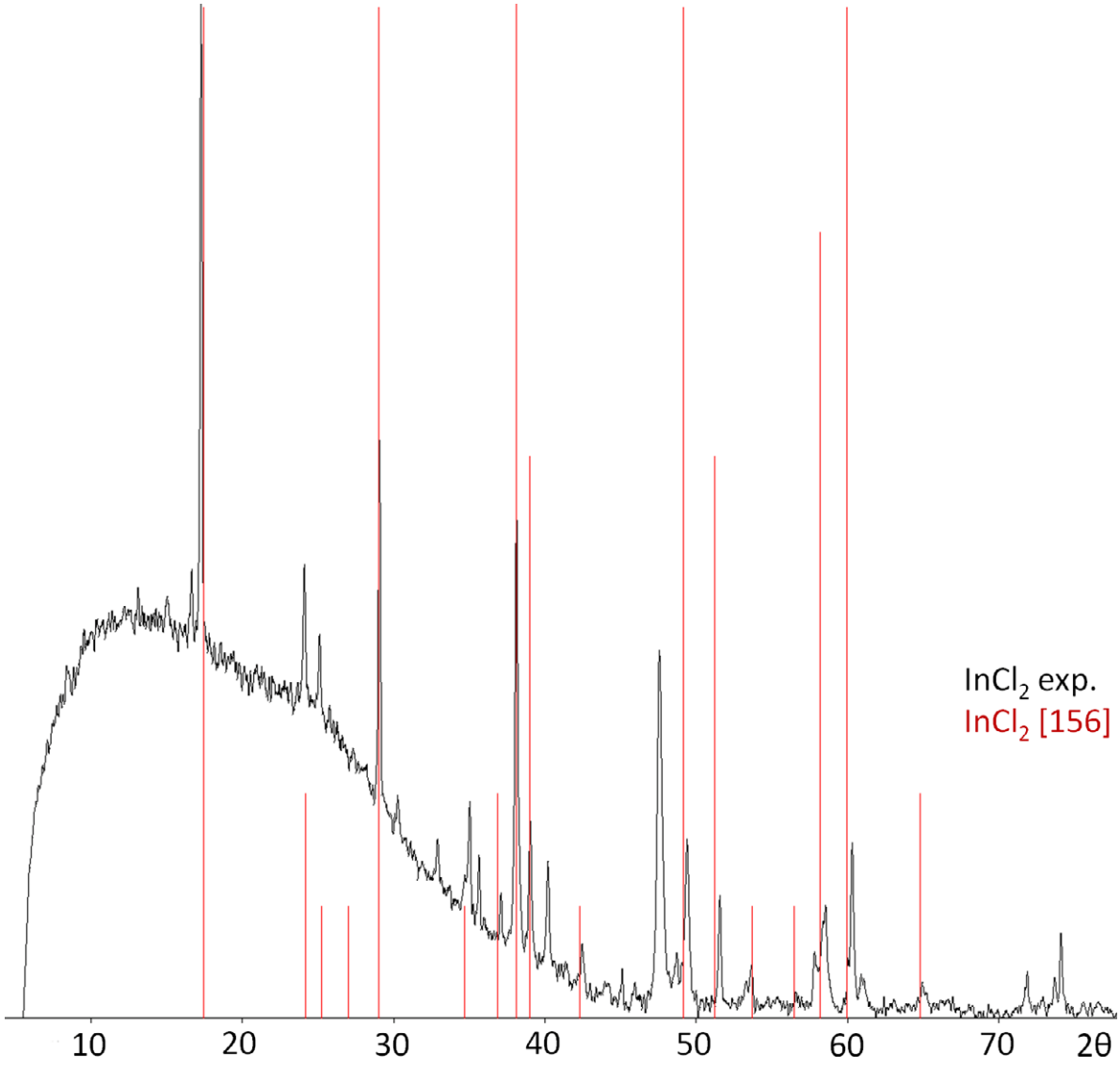

Fig. A 5.8.2.3 Experimental powder diffractogram of $InCl_2$ (black) and diffractogram of $InCl_2$[155] from the database (red).

A 5.8.3 Programs

For operating instruments, analyzing and evaluating data as well as data representation, various programs were used, which are collocated in Tab. A 5.8.3.1.

Tab. A 5.8.3.1 Used programs during the work.

Program	Function	Developer
WinGX	Interface for crystal structure refinement programs	L. J. Farrugia
ShelXL	Crystal structure refinement	George M. Sheldrick
Diamond 3	Visualisation of crystal structures	Crystal Impact
FindIt	ICSD Database	Fachinformationszentrum Karlsruhe
Match 2	Analysis of powder diffractograms	Crystal Impact
Collect	X-Ray data collection	Nonius B. V.
Data Collection APEXII	X-Ray data collection	Bruker AXS
HKL2000	Processing of X-Ray diffraction data	Z. Otwinowski, W. Minor
SAINT	Processing of X-Ray diffraction data	Bruker AXS
TWINABS	Absorption correction for datasets of twinned crystals	Bruker AXS
EvalCCD	X-Ray reflection intensity evaluation	A. J. M. Duisenberg L. M. J. Kroon-Batenburg A. M. M. Schreurs A. J. M. Duisenberg
Phi/Chi-Scans	Compiling accurate Cells from area-detector images	R. W. W. Hooft A. M. M. Schreurs, J. Kroon
Cell Now	Unit cell determination	George M. Sheldrick
Opus	Recording Raman spectra	Opus Software
Genesis Spectrum	Recording and evaluating EDX spectra	EDAX Inc.
WinXPOW	Recording powder diffraction data	Fa. Stoe & Cie
DIFFRAC Plus XRD Commander	Recording powder diffraction data	Bruker AXS Inc.
Origin 8G	Statistic calculations, data plotting	OriginLab Corporation
Microsoft Word 2003	Text processing	Microsoft Corporation
Microsoft Excel 2003	Spreadsheet	Microsoft Corporation
Microsoft Powerpoint 2003	Preparation of figures for representation	Microsoft Corporation
Adobe Photoshop CS4	Preparation of figures for representation	Adobe Systems Incorporated
ChemBioDraw Ultra 11	Constructing chemical formulae	CambridgeSoft

A 5.8.4 Chemicals and Purifications

Tab. A 5.8.4.1 show the educts, which were used in the presented work and their purifications before syntheses.

Tab. A 5.8.4.1 Educts and their melting points, treatments before synthesis and suppliers.

Educt	Mp*/°C	Supplier	Treatment
Ga	29	Alfa Aesar (99,9999 %)	/
S	113	No Information	dried at 100 °C under low pressure
As	817	Avacado (> 99.9999 %)	subl. at 380 °C under low pressure
Se	217	Merck (> 99.5 %)	subl. at 180 °C under low pressure
Sb	630	Diedel-De Haen (> 99.995 %)	subl. at 630 °C under low pressure
Te	450	Riedel-De Haen (> 99.5 %)	subl. at 430 °C under low pressure
Bi	271	Merck, (> 99 %)	subl. at 730 °C under low pressure
In	156.6	Sigma Aldrich (99.99 %)	/
Sb_2Te_3	629	Alfa Aesar (99 %)	/
Sb_2S_3	75	Alfa Aesar (99.999 %)	/
Ga_2O_3	1795	Alfa Aesar (> 99.999 %)	dried at 100 °C under low pressure
As_2O_3	312	Sigma Aldrich (99.995 %)	dried at 100 °C under low pressure
As_2O_5	730	Alfa Aesar (99.9 %)	dried at 65 °C under low pressure
Sb_2O_3	654	Merck (> 99 %)	dried at 100 °C under low pressure
Sb_2O_5	2000	Sigma Aldrich (99.999 %)	dried at 65 °C under low pressure
TeO_2	733	No information	dried at 150 °C under low pressure
PbO_2	290	No information	dried at 70 °C under low pressure
LiCl	614	No information	dried at 100 °C under low pressure
NaCl	801	KMF (> 99.82 %)	dried at 100 °C under low pressure
KCl	773	Merck (> 99.5 %)	dried at 100 °C under low pressure
RbCl	715	Sigma Aldrich (> 99 %)	dried at 100 °C under low pressure
CsCl	646	Merck (extra pure)	dried at 100 °C under low pressure
NH_4Cl	335	Merck (> 99 %)	dried at 100 °C under low pressure
InCl	225	/	/
TlCl	430	No information	dried at 100 °C under low pressure
CuCl	170	Sigma Aldrich (> 99 %)	dried at 100 °C under low pressure
AgCl	455	Riedel-De Haen (no inform.)	dried at 100 °C under low pressure
AuCl	430	Alfa Aesar (> 99.99 %)	/
Hg_2Cl_2	383	No information	dried at 60 °C under low pressure
NaI	662	No Information	/
CuI	602	No Information	/
AgI	557	Alfa Aesar (99.999 %)	/
$GaCl_3$	77.9	Alfa Aesar (> 99.999 %)	/
$AsCl_3$	Bp. 130.2	Acros Organics (> 99.5 %)	/
$SbCl_3$	73	ABCR (> 99.5 %)	/
$SbCl_5$	Bp. 140	Merck (no information)	/
$BiCl_3$	232	No information	/

$TeCl_4$	224	No Information	dried at 120 °C under low pressure
AlI_3	191	Alfa Aesar (99.999 %)	/
SbI_3	168	Alfa Aesar (99.998 %)	/
PPh_4Cl	276	Alfa Aesar (98 %)	dried at 100 °C under low pressure
$InCl_2$	262	/	/
$InCl_3$	586	No information	/
$Se(CH_3)_2$	Bp. 52.8	Alfa Aesar (99.1 %)	/
Te_2Ph_2	65 - 67	Alfa Aesar (98 %)	/

* taken from the respective MSDS data sheet or entry in the GESTIS database

A 5.8.5 Summary of Successful Syntheses

The following table gives an overview about the successful syntheses during the presented work.

Tab. A 5.8.5.1 Successful syntheses during the present work.

Educt basis	Adjuvants	Conditions	Product
Sb, Te, $SbCl_3$, $GaCl_3$	NaCl	130 - 160 °C	
	KCl	140 °C	
	PPh_4Cl	50 - 140 °C	$(Sb_3Te_4)[GaCl_4]$
Sb, Te, $SbCl_3$, $GaCl_3$	NaCl	125 -> 105 °C	
Sb_2Te_3, $SbCl_3$, $GaCl_3$	NaCl, Sb_2O_3	100 °C	$(Sb_2Te_2)[GaCl_4]$
Sb, Te, $SbCl_3$, $GaCl_3$	KCl	100 - 160 °C	
	KCl, PPh_4Cl	100 °C	
Sb_2Te_3, $SbCl_3$, $GaCl_3$	KCl, PPh_4Cl	100 °C	$K(Sb_2Te_4)[GaCl_4]_3$
Sb, Te, $SbCl_3$, $GaCl_3$	RbCl	100 - 140 °C	
	RbCl, PPh_4Cl	100 °C	$Rb(Sb_2Te_4)[GaCl_4]_3$
Sb, Te, $SbCl_3$, $GaCl_3$	CsCl	88 °C,	
	CsCl, PPh_4Cl	100 °C	$Cs(Sb_2Te_4)[GaCl_4]_3$
Sb, Te, $SbCl_3$, $GaCl_3$	NH_4Cl	100 - 120 °C	
	NH_4Cl, PPh_4Cl	100 °C	
Sb_2Te_3, $SbCl_3$, $GaCl_3$	NH_4Cl, PPh_4Cl	100 °C	$NH_4(Sb_2Te_4)[GaCl_4]_3$
Sb, Te, $SbCl_3$, $GaCl_3$	TlCl	100 - 120 °C	
	TlCl, PPh_4Cl	120 °C	
Sb_2Te_3, $SbCl_3$, $GaCl_3$	TlCl, PPh_4Cl	120 °C	$Tl(Sb_2Te_4)[GaCl_4]_3$
Sb, Te, $SbCl_3$, $GaCl_3$	LiCl, Sb_2O_3	100 °C	
	Sb_2O_3, PPh_4Cl	50 °C	
	TeO_3, PPh_4Cl	50 °C	$(Sb_2Te_4)[Ga_2Cl_6O]_2$
Sb, Te, $SbCl_3$, $GaCl_3$	NaCl, Sb_2O_3	100 °C	
	NaCl, PPh_4Cl	100 °C	$Na(Sb_2Te_4)[GaCl_4]_3$
Sb, Te, $SbCl_3$, $GaCl_3$	Ga_2O_3	100 °C	
	AgCl	120 °C	

	NaCl	200 °C	$(Sb_3Te_4)[Ga_2Cl_7]_3$
Sb, Te, $SbCl_3$, $GaCl_3$	CuCl	88 °C	$(Sb_4Te_4)[GaCl_4]_4$
Sb, Te, $SbCl_3$, $GaCl_3$	LiCl, NaCl	100 °C	
	NaCl, Sb_2O_3	100 °C	
	NaCl, PPh_4Cl	100 °C	$Na(Sb_7Te_8)[GaCl_4]_6$
Sb, Te, $SbCl_3$, $GaCl_3$	LiCl, NaCl	100 °C	$(Sb_7Te_8)[GaCl_4]_5$*
Sb, Te, $SbCl_3$, $GaCl_3$	AgCl, PPh_4Cl	100 °C	
$(Sb_7Te_8)[GaCl_4]_2[Ga_2Cl_7]_3$, $SbCl_3$, $GaCl_3$	AgCl, PPh_4Cl	100 °C	$Ag(Sb_7Te_8)[GaCl_4]_6$
Sb, Te, $SbCl_3$, $GaCl_3$	NaCl	100 °C	
	InCl	100 °C	
	$InCl_2$, PPh_4Cl	100 °C	
	$InCl_2$	100 °C	
	Hg_2Cl_2, PPh_4Cl	100 °C	$(Sb_7Te_8)[GaCl_4]_3[Ga_2Cl_7]_2$
Sb, Te, $SbCl_3$, $GaCl_3$	CuCl	100 °C	
	Hg_2Cl_2	100 °C	
Sb_2Te_3, $SbCl_3$, $GaCl_3$	CuCl	100 °C	
	NaCl	100 °C	$(Sb_7Te_8)[GaCl_4]_2[Ga_2Cl_7]_3$
Sb, Te, $SbCl_3$, $GaCl_3$	PPh_4Cl	100 °C	
	Sb_2O_5, PPh_4Cl	100 °C	$Te_4[Ga_2Cl_6O]$
Bi, Te, $SbCl_3$, $GaCl_3$	$CuCl_2$, PPh_4Cl	100 °C	
Sb, Te, $SbCl_3$, $GaCl_3$	$CuCl_2$, PPh_4Cl	100 °C	
	LiCl, CuCl	88 °C	$CuTe_4[GaCl_4]$
Sb, Te, $SbCl_3$, $GaCl_3$	Sb_2O_3	50 °C	Ga_2SbCl_7O
Sb, Te, $SbCl_3$, $GaCl_3$	Sb_2O_3, PPh_4Cl	50 - 100 °C	
	Sb_2O_5, PPh_4Cl	50 - 100 °C	
	TeO_3, PPh_4Cl	50 - 100 °C	
	Sb_2O_5	100 °C	$(Sb_2Te_4)[Ga_2Cl_6O]_2$
Sb, Te, $SbCl_3$, $GaCl_3$	Sb_2O_5	100 °C	
	NaCl, Sb_2O_3	100 °C	$Te_6(SbCl_3)[Ga_2Cl_6O]_2$*
Sb, Te, $SbCl_3$, $GaCl_3$	TeO_2	50 °C	$(SbTe_4)[Ga_2Cl_7]$
Sb, Te, $SbCl_5$, $GaCl_3$		50 - 120 °C	
	NaCl	100 °C	
	AuCl	50 °C	
Sb, $TeCl_4$, $GaCl_3$	NaCl	88 - 100 °C	
Bi, Te, $BiCl_3$, $GaCl_3$	$CuCl_2$, PPh_4Cl	100 °C	$Te_4[Ga_2Cl_7]_2$**[116]
Sb, Te, $SbCl_3$, $GaCl_3$	Sb_2S_3, PPh_4Cl	50 - 100 °C	$(Sb_2Te_4)[Ga_2Cl_7]_2$*
Sb, Te, $SbCl_3$, $GaCl_3$	$InCl_2$, PPh_4Cl	100 °C	$(Sb_2Te_4)[Ga_2Cl_7]_2$
Sb, Te, $SbCl_3$, $GaCl_3$	PPh_4Cl	88 °C	
	LiCl, PPh_4Cl	100 °C	
	$CuCl_2$, PPh_4Cl	100 °C	$(Sb_2Te_4)[GaCl_4]_2$

As, Te, $AsCl_3$, $GaCl_3$	KCl	100 - 140 °C	$K(As_2Te_4)[GaCl_4]_3$
As, Te, $AsCl_3$, $GaCl_3$	RbCl	100 - 140 °C	$Rb(As_2Te_4)[GaCl_4]_3$
As, Te, $AsCl_3$, $GaCl_3$	CsCl	100 - 140 °C	
	CsCl, PPh_4Cl	50 °C	$Cs(As_2Te_4)[GaCl_4]_3$
As, Te, $AsCl_3$, $GaCl_3$	NH_4Cl	100 - 120 °C	$NH_4(As_2Te_4)[GaCl_4]_3$
As, Te, $AsCl_3$, $GaCl_3$	InCl	100 - 120 °C	$In(As_2Te_4)[GaCl_4]_3$
As, Te, $AsCl_3$, $GaCl_3$	TlCl	120 °C	$Tl(As_2Te_4)[GaCl_4]_3$
As, Te, $AsCl_3$, $GaCl_3$	PPh_4Cl	50 - 140 °C	
	NaCl, Sb_2O_3	100 - 120 °C	
	AuCl	50 °C	
	KCl	88 °C	$(As_2Te_4)[Ga_2Cl_7]_2$
As, Te, $AsCl_3$, $GaCl_3$	AgCl, PPh_4Cl	100 °C	$Ag(As_2Te_4)[GaCl_4]_3$
As, Te, $AsCl_3$, $GaCl_3$	As_2O_3, PPh_4Cl	50 - 100 °C	
	As_2O_5, PPh_4Cl	50 - 100 °C	$(As_2Te_4)[Ga_2Cl_6O]_2$
Sb, Se, $SbCl_3$, $GaCl_3$		100 °C	
	PPh_4Cl	50 - 120 °C	
	LiCl	100 °C	
	NaCl	100 °C	
	KCl	100 °C	
	RbCl	100 °C	
	AgCl, PPh_4Cl	100 °C	
	LiCl, PPh_4Cl	100 °C	
	NH_4Cl, PPh_4Cl	100 °C	
	CsCl, PPh_4Cl	100 °C	$(Sb_7Se_8Cl_2)[GaCl_4]_3$
Sb, Se, $SbCl_3$, $GaCl_3$	CuCl	88 - 100 °C	
	AgCl	100 °C	
	Au(tht)Cl/PPh_4Cl	100 °C	
	CuCl/PPh_4Cl	100 °C	
	Sb_2O_3/PPh_4Cl	100 °C	$(Sb_7Se_8)[GaCl_4]_2[Ga_2Cl_7]_3$
Sb, Se, $SbCl_3$, $GaCl_3$	CuCl	100 → 20 °C	$(Sb_4Se_4)[GaCl_4]_4$
Bi, Se, $BiCl_3$, $GaCl_3$	$CuCl_2$, PPh_4Cl	100 °C	$CuSe_4[GaCl_4]$
Sb, Se, $SbCl_3$, $GaCl_3$	$CuCl_2$, PPh_4Cl	100 °C	$Cu_2Se_7[GaCl_4]_2$
Sb_2S_3, $SbCl_3$, $GaCl_3$	CuCl	100 °C	$(Sb_7S_8Cl_2)[GaCl_4]_3$
Bi, Te, $BiCl_3$, $GaCl_3$		120 °C	
	NaCl	100°C	
	PPh_4Cl	100 - 140 °C	$(Bi_2Te_2)Cl[GaCl_4]$
Bi_2Te_3, $BiCl_3$, $GaCl_3$	CuCl	100 °C	$(Bi_4Te_4)[GaCl_4]_2[Ga_2Cl_7]$
Bi, Te, $BiCl_3$, $GaCl_3$	NaCl	100 - 170 °C	$(Bi_4Te_4)[GaCl_4]_4$**
Bi, Te, $BiCl_3$, $GaCl_3$	Hg_2Cl_2, PPh_4Cl	100 °C	
Bi, Se, $BiCl_3$, $GaCl_3$	InCl	88 - 100 °C	
Bi, $BiCl_3$, $GaCl_3$	PPh_4Cl	100 °C	$Bi_5[GaCl_4]_3$**[72]

Bi, Se, $BiCl_3$, $GaCl_3$		100°C	$(Bi_2Se_2)Cl[GaCl_4]$
Bi, Se, $BiCl_3$, $GaCl_3$	NaCl	80 - 140 °C	
	CuCl, PPh_4Cl	100 °C	
	InCl, PPh_4Cl	100 °C	$(Bi_4Se_4)[GaCl_4]_4$**
Bi, S, $BiCl_3$, $GaCl_3$	CuCl	88 - 100 °C	
Bi, S, $BiCl_3$, $GaCl_3$	CuCl, PPh_4Cl	100 °C	
Bi_2S_3, $BiCl_3$, $GaCl_3$	CuCl	100 °C	$(Bi_4S_4)[GaCl_4]_4$**
Sb_2Te_3, SbI_3, AlI_3	NaI	170 °C	$(Sb_2Te_4)I[AlI_4]$
CuI, AlI_3		100 - 190 °C	$Cu[AlI_4]$
SbI_3, AlI_3		190 °C	$(SbI_2)[AlI_4]$

* crystal structure clearly evident, but data sets not sufficient for presentation

** compound or isotypic compound already known

Declaration of Originality

I hereby declare that this thesis, entiteld “Heteronuclear Polycationic Clusters from Group 15 and 16 Elements Synthesized in Chloridogalllate Melts” represents my original work and that I have used no other sources except those indicated by footnotes and citations.
All data, tables, figures and text citations, which have been reproduced from any other source, including the internet, have been explicitly acknowledged as such.